HEAT TRANSFER UNDER AN IMPINGING SLOT JET

by

© Adriaan R.P. van Heiningen

A Thesis Submitted to the Faculty of Graduate Studies and Research in Partial Fulfillment of the Requirements for the Degree of Doctor of Philosophy

Department of Chemical Engineering
McGill University
Montreal

April 1982

To

Magriet

and

Willem, Jan and Hanna

ABSTRACT

The flow field and heat transfer characteristics for both a laminar and a turbulent confined impinging slot jet were calculated numerically, with the turbulence properties for the latter case being incorporated via the turbulent viscosity concept and the two equation $k-\varepsilon$ model of turbulence. These computer simulations gave good predictions except for the stagnation region for the turbulent jet.

An experimental facility was developed for measurement of local heat transfer under a single confined turbulent jet impinging on a rotating cylinder with or without throughflow at the surface. With a high sensitivity, fast response thin film heat flux sensor it was possible to obtain accurate heat transfer profiles of high resolution for a wide range of jet Reynolds numbers and impingement surface velocities at impingement surface spacings of 2.6 and 6 nozzle widths. An analysis is given of measurement of heat transfer with an impermeable sensor for the case of throughflow at the impingement surface.

RESUME

Les caractéristiques de l'écoulement et du transfert de chaleur d'un jet rectangulaire confiné ont été prédits numériquement en résolvant simultanément les équations de Navier Stokes et celles de conservation de l'énergie pour le cas de jets laminaires et turbulents. Dans le dernier cas les propriétés turbulentes ont été incorporées par le concept d'une viscosité turbulente et le modèle de turbulence "k-ε" à deux équations.

Une installation expérimentale a été conçue pour mesurer le transfert local de chaleur sous un jet turbulent confiné frappant un cylindre rotatif avec ou sans aspiration à la surface. Avec une jauge pour flux de chaleur du type à couche mince conçue pour une grande sensibilité on a pu obtenir des profils du nombre de Nusselt avec une haute résolution. Ces caractéristiques ont été mesurées à deux espacements entre la sortie de la buse et la surface d'impact pour un plage étendue de nombre de Reynolds et de vitesse de la surface d'impact. Une analyse est aussi présentée dans le cas d'aspiration à la surface d'impact.

ACKNOWLEDGEMENTS

I would like to express my gratitude to Dr. W.J.M. Douglas for his encouragement, financial support and help during the long period it took to complete this thesis. Especially his stay for a few weeks at my residence in Holland gave me the momentum to complete this work.

I also would like to thank Dr. A.S. Mujumdar for his constructive advice and stimulating discussions on many aspects of this work as well as for the friendship which developed between our families.

Also a special word of thanks to Ir. Th.H. van der Meer at the Department of "Technische Natuurkunde", Technical University of Delft, The Netherlands for assisting with the complete rerun of the numerical calculations on turbulent impinging slot jet at the computer center in Delft.

The contributions of my successors on this subject, Mr. Bing Huang and Mrs. Suna Polat in replotting the heat transfer profiles on a digital plotter are gratefully acknowledged. Help of summer students Messrs. P. Lee and H. Bernstein was appreciated.

The actual manufacturing of the experimental equipment, as well as other services given by the many persons at the machine shops of the Chemical Engineering Department and of the Pulp and Paper Research Institute of Canada, under the guidance of respectively Mr. A. Krish and Mr. D.P.W. Pounds, was of course

most important.

For help in manufacturing the heat flux sensor, the heart of the experimental equipment, and assistance with the data acquisition programming and very valuable comments on instrumentation I would like to thank, respectively, Dr. M. Jain and Mr. L.J. Vroomen.

I also wish to express my appreciation to the Directors of NORIT for allowing leaves of absence to complete the writing of this thesis.

I am also thankful to the National Research Council of Canada and the Pulp and Paper Research Institute of Canada for their scholarship support, and to my father and mother for their financial help and moral support to complete this work.

For the typing of the manuscript and the preparation of the figures I would like to thank Miss P. Fong and Mr. B. Gavin.

Last, but not least, I would like to thank my wife Magriet and my mother-in-law for their moral support and endurance especially during the completion of the writing of this manuscript.

TABLE OF CONTENTS

ABSTRACT

RESUME

ACKNOWLEDGEMENTS i

TABLE OF CONTENTS iii

LIST OF FIGURES x

LIST OF TABLES xx

NOMENCLATURE xxii

CHAPTER 1. INTRODUCTION 1

1.1 Introduction 1

1.2 Background Information and Industrial Motivation 2

1.3 Objective and Strategy 10

1.4 Previous Work on Single Impinging Slot Jets 14

1.4.1 The Flowfield of an Impinging Slot Jet 15

1.4.2 Heat and Mass Transfer under an Impinging Slot Jet 26

1.5 Outline of the Thesis 41

CHAPTER 2. NUMERICAL PREDICTIONS 47

2.1 Introduction 47

2.2 Laminar Impinging Slot Jet 49

2.2.1 Mathematical Description of the Problem 51

2.2.2 Numerical Procedure 62

2.2.2.1 Factors Influencing the Convergence of the Procedure 65

		2.2.2.2 Factors Influencing the Accuracy of the Procedure	80
	2.2.3 Results and Discussion		109
		2.2.3.1 Effect of Reynolds Number and Jet Velocity Profile	110
		2.2.3.2 Effect of Nozzle to Impingement Surface Spacing	134
		2.2.3.3 Effect of Throughflow at the Impingement Surface	144
		2.2.3.4 Effect of Temperature Dependent Physical Properties	169
		2.2.3.5 Effect of Prandtl Number	173
2.3	Turbulent Impinging Slot Jet		179
	2.3.1 Mathematical Formulation		183
		2.3.1.1 Turbulence Model and Final Set of Equations	184
		2.3.1.2 Derivation of Transport Equations for k and ε	187
		2.3.1.3 Boundary Conditions	191
		2.3.1.4 Capabilities and Limitations of the k - ε Model	193
	2.3.2 Numerical Procedure		197
		2.3.2.1 Finite Difference Grid	199
		2.3.2.2 Finite Difference Equation for Scalar Variables	199
		2.3.2.3 Finite Difference Equation for Velocities	203
		2.3.2.4 Finite Difference Equation for Pressure	204

2.3.2.5 Insertion of Boundary Conditions 206

2.3.2.6 Computational Procedures 209

2.3.3 Results and Discussion 210

2.3.3.1 Effect of Wall-flux Laws and Treatment of Diffusion and Source Terms in the k and ε Equations 212

2.3.3.2 Analysis of Turbulence Modelling in the Stagnation Region 226

2.3.3.3 Effect of Re_j and H/w on the Heat Transfer Distribution 230

2.4 Summary and Conclusions 241

CHAPTER 3. EXPERIMENTAL EQUIPMENT AND PROCEDURES 264

3.1 Overall Design Conception 264

3.2 The Experimental Facility 270

3.3 The Heat Flux Sensor 278

3.3.1 Description of the Sensor 278

3.3.1.1 Selection of Type of Heat Flux Sensor 278

3.3.1.2 Manufacture of the Heat Flux Sensor 282

3.3.1.3 Calibration of the Heat Flux Sensor 288

3.3.1.4 Instrumentation for the Heat Flux Measurement 293

3.3.2 Computation of Instantaneous Local Heat Flux 295

3.3.3 Display of Nusselt Number Profiles 300

3.4	Instrumentation		301
	3.4.1	Circumferential Position Marker	301
	3.4.2	Instrumentation for Pressure Measurement	303
	3.4.3	Auxiliary Instrumentation	303
	3.4.4	Electrical Noise Reduction	305
3.5	Testing and Calibration of the Equipment		306
	3.5.1	Nozzle Flowrate Calibration	306
	3.5.2	Temperature Distribution in the Nozzles	314
	3.5.3	Temperature Effect at an Adiabatic Impingement Surface	320
	3.5.4	Temperature Measurement at the Back of the Heat Flux Sensor	325
	3.5.5	Elimination of Axial Heat Conduction along the Impingement Cylinder	326
	3.5.6	Symmetry of the Flow and Two Dimensionality in the Wall Jet Region	334
	3.5.7	Characterization of the Porous Stainless Steel	343
3.6	Effect of Operating Procedures on Nusselt Number Profiles		345
	3.6.1	Number of Rotations Averaged for a Profile	345
	3.6.2	Filtering of Noise from the Heat Flux Sensor Signal	351
	3.6.3	Number of Measurements to Define a Profile	354
CHAPTER 4.	EXPERIMENTAL RESULTS AND DISCUSSION		358
4.1	Introduction		358

4.2	Temperature Independent Correlation of Impingement Heat Transfer with Temperature Dependent Physical Properties		359
4.3	Impingement Heat Transfer without Surface Motion or Throughflow		376
	4.3.1	Lateral Profiles of Local Heat Transfer	378
	4.3.2	Stagnation Point Heat Transfer	393
	4.3.3	Heat Transfer Distribution in the Stagnation Region	401
	4.3.4	The Secondary Heat Transfer Maximum	405
	4.3.5	Heat Transfer Distribution in the Wall Jet Region	408
	4.3.6	Average Heat Transfer	420
4.4	Influence of Impingement Surface Motion		428
	4.4.1	Lateral Profiles of Local Heat Transfer	429
	4.4.2	Stagnation Point Heat Transfer	449
	4.4.3	Heat Transfer Distribution in the Stagnation Region	453
	4.4.4	The Secondary Heat Transfer Maximum	455
	4.4.5	Heat Transfer Distribution in the Wall Jet Region	460
	4.4.6	Average Heat Transfer	463
4.5	Influence of Throughflow at the Impingement Surface		473
	4.5.1	Lateral Profiles of Local Heat Transfer	478
	4.5.2	Significance of the Impermeable Sensor Results	494
4.6	Summary and Conclusions		500

CHAPTER 5.	CONCLUSIONS	519
5.1	Contribution to Knowledge	519
5.2	Recommendations and Suggestions for Future Work	524
REFERENCES		528
APPENDIX 1.	Derivation of the Boundary Condition of the Vorticity at the Wall	541
APPENDIX 2.	Convection and Diffusion Terms in Equation (2.28)	545
APPENDIX 3.	Derivation of Coefficients in Recursive Solutions of Finite Difference Equations (2.43) and (2.44)	549
APPENDIX 4.	A Study of Two Finite Difference Schemes and Matrix Inversion Techniques to Solve the Vorticity Stream Function Equations	551
APPENDIX 5.	Derivation of Equations (2.45) and (2.46) for Artificial Viscosity and Velocity	572
APPENDIX 6.	Influence of Throughflow on the "Papridryer" Drying Rates	576
APPENDIX 7.	Impingement Surface Temperature Fluctuation	579
APPENDIX 8.	Resolution of Surface Temperature of the Sensor	582
APPENDIX 9.	On the Use of Hot and Cold-Film Sensors for Skin Friction and Heat Transfer Measurements in Impingement Flows	584
APPENDIX 10.	Response Time of the Heat Flux Sensor	590
APPENDIX 11.	Test Assembly to Measure Thermal Conductivity	592

APPENDIX 12.	Thermal Conductivity of Sintered Metal Powders at Room Temperature	598
APPENDIX 13.	Sensitivity of Thin Film Resistance Thermometers	607
APPENDIX 14.	Self Heating of the Heat Flux Sensor	609
APPENDIX 15.	Derivation of Equations (3.8) and (3.9)	611
APPENDIX 16.	Derivation of Equation (3.19)	615
APPENDIX 17.	Numerical Prediction of the Flow Field and Impingement Heat Transfer Caused by a Laminar Slow Jet	616
APPENDIX 18.	Flow and Heat Transfer Characteristics of a Turbulent Slot Jet Impinging on a Moving Wall	621

LIST OF FIGURES

Figure	Caption	Page
1.1	Schematic view of cylindrical confined impingement apparatus	13
1.2	Two-dimensional impinging jet	16
1.3	Conceptual model of vortex-pair generation	21
1.4	Local heat transfer distribution at H/w = 2 and $Re_j \approx 11000$	31
1.5	Local heat transfer distribution at H/w = 8 and $Re_j \approx 11000$	32
1.6	Local heat transfer distribution at H/w = 16 and $Re_j \approx 11000$	33
1.7	Local heat transfer distribution at H/w = 8 and $Re_j \approx 50000$	34
1.8	Correlation of stagnation point heat transfer	37
2.1	Impinging jet system for numerical prediction	52
2.2	Computational grid for H/w = 4	68
2.3	Effect of the grid on stability of the numerical procedure	70
2.4	Convergence characteristics of finite difference schemes	72
2.5a	Effect of difference scheme on stream function contours for $Re_j = 100$	85
2.5b	Effect of difference scheme on transfer properties of the impingement surface for $Re_j = 100$	86
2.6a	Effect of difference scheme on stream function contours for $Re_j = 950$	87
2.6b	Effect of difference scheme on transfer properties of the impingement surface for $Re_j = 950$	88
2.7a	Effect of difference scheme on axial temperature distribution in stagnation region	90

Figure	Caption	Page
2.7b	Effect of difference scheme on velocity distribution in stagnation region	90
2.8	Effect of treatment of corner vorticity on free streamline contours ($\psi = -0.125$)	95
2.9a	Effect of corner vorticity treatment on development of jet velocity profile	97
2.9b	Effect of corner vorticity treatment on centerline axial velocity decay	98
2.10a	Effect of corner vorticity treatment on skin friction distribution	99
2.10b	Effect of corner vorticity treatment on heat transfer distribution	100
2.11	Effect of boundary condition at boundary III on flow development	104
2.12	Effect of boundary condition at boundary III on heat transfer distribution	106
2.13a	Effect of length of impingement surface on flow characteristics	107
2.13b	Effect of length of impingement surface on heat transfer distribution	108
2.14	Free streamline contours	111
2.15	Vorticity contours for a flat jet velocity profile	112
2.16	Vorticity contours for a parabolic jet velocity profile	113
2.17	Isotherms $T^* = 0.90$ for a flat jet velocity profile	114
2.18	Location and development of the maximum velocity parallel to the impingement surface for a parabolic jet velocity profile	116
2.19	Location and development of the maximum velocity parallel to the impingement surface for a flat jet velocity profile	117

Figure	Caption	Page
2.20	Development of U_1^* velocity distribution for a flat jet velocity profile	119
2.21	Development of U_2^* velocity distribution for a flat jet velocity profile	120
2.22	Heat transfer and skin friction distribution for a flat jet velocity profile	122
2.23	Heat transfer and skin friction distribution for a parabolic jet velocity profile	123
2.24	Effect of Reynolds number on stagnation point heat transfer	127
2.25	Comparison with experimental heat transfer distribution of Gardon and Akfirat	131
2.26	Comparison with experimental heat transfer distribution of Sparrow and Wong	132
2.27	Centerline axial velocity decay	133
2.28	Stability of numerical procedure at H/w = 12	136
2.29	Effect of impingement surface spacing on free streamline contours	138
2.30	Effect of impingement surface spacing on jet velocity profile development	139
2.31	Effect of impingement surface spacing on heat transfer distribution at the impingement surface	142
2.32	Effect of impingement surface spacing on skin friction distribution at the impingement surface	143
2.33	Effect of throughflow on location of the free streamline	145
2.34	Effect of throughflow on centerline axial velocity decay	147
2.35	Effect of throughflow on U_2^* velocity profile	148
2.36	Effect of throughflow on wall jet development	149

Figure	Caption	Page
2.37	Effect of throughflow on location of maximum wall jet velocity	150
2.38	Effect of throughflow on skin friction distribution	153
2.39	Effect of throughflow on heat transfer distribution	154
2.40	Effect of difference scheme and length of permeable plate	155
2.41	Effect of throughflow on change in skin friction	158
2.42	Effect of throughflow on change in heat transfer	159
2.43	Effect of throughflow on change in transport rates at the impingement surface	163
2.44	Effect of throughflow on drying rate of mill Papridryer	166
2.45	Effect of variable properties on skin friction distribution	171
2.46	Effect of variable properties on heat transfer distribution	172
2.47	Effect of variable properties and throughflow on heat transfer distribution	174
2.48	Effect of Prandtl number on heat transfer distribution for a flat jet velocity profile	177
2.49	Effect of Prandtl number on heat transfer distribution for a parabolic jet velocity profile	178
2.50	Scalar and vector grid	200
2.51	Pressure distribution along impingement surface	216
2.52	Development of the maximum wall jet velocity	218
2.53	Velocity distribution in the wall jet region	219

Figure	Caption	Page
2.54	Turbulent kinetic energy development near the axis of symmetry	221
2.55	Turbulent kinetic energy distribution in the wall jet region	223
2.56	Heat transfer distribution along the impingement surface for H/w = 2.6 and Re_j = 10400	224
2.57	Development of the maximum wall jet velocity for H/w = 6	231
2.58	Spreading of the wall jet half-width	233
2.59	Velocity distribution in the wall jet region	234
2.60	Heat transfer distribution along the impingement surface for H/w = 2.6 and Re_j = 20200	235
2.61	Heat transfer distribution along the impingement surface for H/w = 6 and Re_j = 5200	237
2.62	Heat transfer distribution along the impingement surface for H/w = 6 and Re_j = 8100	239
2.63	Heat transfer distribution along the impingement surface for H/w = 8 and Re_j = 20750	240
3.1a	General view of experimental facility before installation in laboratory	266
3.1b	General view of experimental facility after installation in laboratory	267
3.2	Schematic diagram of experimental facility	271
3.3	Close-up photograph of SIMTEST apparatus	272
3.4	The heat flux sensor	283
3.5	Calibration curve of heat flux sensor	289
3.6	Thermal conductivity of Pyroceram® 9606	290
3.7	Thermal diffusivity of Pyroceram 9606	291
3.8	Specific heat of Pyroceram 9606	292
3.9	Electrical circuit of the pressure transducer	304

Figure	Caption	Page
3.10	Design of nozzle blocks	307
3.11	Static pressure along nozzle midplane	308
3.12	Relation between static pressure at the nozzle exit and plenum chamber pressure for H/w = 6	310
3.13	Relation between static pressure at the nozzle exit and plenum chamber pressure for H/w = 2.6	311
3.14	Discharge coefficient for 14.1 mm nozzle as a function of plenum chamber pressure	315
3.15	Discharge coefficient for 6.2 mm nozzle as a function of plenum chamber pressure	316
3.16	Temperature decrease across the nozzles caused by expansion	318
3.17	Temperature distribution in the nozzle of the heating jet	319
3.18	Temperature distribution in the nozzle of the cooling jet	321
3.19	Adiabatic wall temperature effect for the heating jet	323
3.20	Adiabatic wall temperature effect for the cooling jet	324
3.21	Electrical circuit for temperature measurement at back of sensor	327
3.22	Effect of power input of heating lamps on heat transfer distribution for the heating jet	330
3.23	Effect of power input of heating lamps on heat transfer distribution for the cooling jet	331
3.24	Velocity distribution in heating jet exit ducts	336
3.25	Velocity distribution in cooling jet exit ducts	337

Figure	Caption	Page
3.26	Velocity distribution in annular confinement section for heating jet	338
3.27	Uniformity in permeability of porous cylinder	344
3.28	Effect of number of rotations for averaging the heat transfer distribution	347
3.29	Effect of frequency of low-pass filter on the heat transfer distribution	352
3.30a	Heat transfer distribution for the cooling jet at 239 measurements per rotation	355
3.30b	Heat transfer distribution for the cooling jet at 412 measurements per rotation	356
3.30c	Heat transfer distribution for the cooling jet at 718 measurements per rotation	357
4.1	Test of physical property evaluation basis with stagnation point heat transfer for $H/w = 6$	364
4.2	Test of physical property evaluation basis with stagnation point heat transfer for $H/w = 2.6$	365
4.3a	Test of physical property evaluation basis with average heat transfer for $H/w = 6$	366
4.3b	Test of physical property evaluation basis with secondary heat transfer maximum for $H/w = 6$	366
4.4a	Test of physical property evaluation basis with average heat transfer for $H/w = 2.6$	371
4.4b	Test of physical property evaluation basis with secondary heat transfer maximum for $H/w = 2.6$	372
4.5	Lateral profiles of Nu_j at $H/w = 6$: Effect of Re_j	382

Figure	Caption	Page
4.6	Lateral profiles of Nu_j at H/w = 6: Comparison of results	385
4.7	Lateral profiles of Nu_j at H/w = 2.6: Effect of Re_j	388
4.8	Lateral profiles of Nu_j at H/w = 2.6: Comparisons of results for Re_j 9400 to 12000	392
4.9	Lateral profiles of Nu_j at H/w = 2.6: Comparisons of results for Re_j = 52200	394
4.10	Stagnation point heat transfer at H/w = 2.6: Effect of Re_j	396
4.11	Stagnation point heat transfer at H/w = 6.0: Effect of Re_j	397
4.12	Heat transfer distribution in the stagnation region at H/w = 2.6: Effect of Re_j	402
4.13	Heat transfer distribution in the stagnation region at H/w = 6.0: Effect of Re_j	403
4.14	Secondary heat transfer maximum at H/w = 2.6: Effect of Re_j	406
4.15	Secondary heat transfer maximum at H/w = 6: Effect of Re_j	407
4.16	Heat transfer in the wall jet region at H/w = 6: Effect of Re_j and M_{V_s}	410
4.17	Heat transfer in the wall jet region at H/w = 6: Comparison of results	412
4.18	Heat transfer in the wall jet region at H/w = 2.6: Effect of Re_j and M_{V_s}	417
4.19	Correlation of average heat transfer for H/w = 6	422
4.20	Average heat transfer at H/w = 6: Comparison of correlations	423
4.21a	Correlations of average heat transfer at H/w = 2.6	426
4.21b	Comparison of present correlation for average heat transfer for experimental H/w spacings	427

Figure	Caption	Page
4.22	Effect of M_{V_s} on lateral profile of heat transfer at Re_j = 8200 and H/w = 6	434
4.23	Effect of M_{V_s} on lateral profile of heat transfer at Re_j = 11000 and H/w = 6	435
4.24	Effect of M_{V_s} on lateral profile of heat transfer at Re_j = 13900 and H/w = 6	436
4.25	Effect of M_{V_s} on lateral profile of heat transfer at Re_j = 11000 and H/w = 2.6	437
4.26	Effect of M_{V_s} on lateral profile of heat transfer at Re_j = 23000 and H/w = 2.6	438
4.27	Effect of M_{V_s} on lateral profile of heat transfer at Re_j = 51000 and H/w = 2.6	439
4.28	Effect of M_{V_s} on lateral profile of heat transfer at H/w = 2.6	451
4.29	Effect of M_{V_s} on stagnation point heat transfer at H/w = 6	452
4.30	Effect of M_{V_s} on heat transfer distribution in stagnation region for H/w = 2.6	454
4.31	Effect of M_{V_s} on location of secondary heat transfer maxima at H/w = 2.6	457
4.32	Effect of M_{V_s} on location of secondary heat transfer maxima for impingement surface leaving stagnation, H/w = 6	458
4.33	Effect of M_{V_s} on secondary heat transfer maxima at H/w = 2.6	459
4.34a	Effect of M_{V_s} and upper integration limit on average heat transfer for H/w = 2.6	464
4.34b	Effect of M_{V_s} and upper integration limit on average heat transfer for H/w = 2.6	465
4.35	Effect of M_{V_s} and upper integration limit on average heat transfer for H/w = 6	466
4.36	Average heat transfer between four symmetrically placed jets and a rotating cylinder, as measured by Fechner	469

Figure	Caption	Page
4.37	Average heat transfer between symmetrically placed jets and a rotating cylinder, as measured by Fechner	470
4.38	Effect of impermeable sensor on impingement heat transfer with throughflow	475
4.39	Effect of M_{U_s} on lateral profiles of heat transfer at Re_j = 5200 and H/w = 6	479
4.40	Effect of M_{U_s} on lateral profiles of heat transfer at Re_j = 11100 and H/w = 6	483
4.41	Effect of M_{U_s} on lateral profiles of heat transfer at Re_j = 13800 and H/w = 6	484
4.42	Effect of M_{U_s} on lateral profiles of heat transfer at Re_j = 16300 and H/w = 2.6	490
4.43	Effect of M_{U_s} on lateral profiles of heat transfer at Re_j = 24600 and H/w = 2.6	491
4.44	Effect of M_{U_s} on lateral profiles of heat transfer at Re_j = 55000 and H/w = 2.6	492
4.45	Effect of M_{U_s} on lateral profiles of heat transfer at Re_j = 88000 and H/w = 2.6	493
4.46	Effect of impingement surface motion on heat transfer distribution at H/w = 6 and the highest throughflow	495
4.47	Effect of impingement surface motion on heat transfer distribution at H/w = 2.6 and the highest throughflow	496
4.48	Effect of M_{U_s} on lateral profiles of heat transfer at H/w = 6 and high impingement surface speed	497
4.49	Effect of M_{U_s} on lateral profiles of heat transfer at H/w = 2.6 and high impingement surface speed	498
All.1	Test assembly for thermal conductivity measurements	593
All.2	Typical output of thermal conductivity experiment	595

LIST OF TABLES

Table	Title	Page
1.1	Operating conditions and geometry of pilot-and mill "Papridryer"	11
1.2	Experimental conditions and heat/mass transfer correlations for a single slot jet impinging on a flat stationary and impermeable surface	27
2.1	Coefficients in Equation (2.11)	56
2.2	Non-dimensional coefficients in Equation (2.11)	57
2.3	Relative size of artificial viscosity and velocity	92
2.4	Range of parameters for laminar jet calculations	109
2.5	Comparison of alternate bases for St_o for a flat nozzle exit velocity profile	125
2.6	Comparison of alternate bases for St_o for a parabolic nozzle exit velocity profile	126
2.7	Effective exchange coefficients and source terms in Equation (2.103)	198
2.8	Range of parameters for turbulent jet calculations	211
2.9	Location of near-wall grid line	213
3.1	Comparison between numerical and experimental maximum recovery pressure	313
3.2	Effect of power input of heating lamps on local and average heat transfer	333
3.3	Properties of porous stainless steel	343
3.4	Effect on average Nusselt number for cooling jet of number of rotations averaged	351
3.5	Effect of frequency of filtering of heat flux sensor signal on stagnation point measurement	353

Table	Title	Page
4.1	Range of parameters for experiments with SIMTEST apparatus	360
4.2a,b	Effect of (T_j-T_s) on heat transfer for the heating jet	367
4.3a,b	Effect of (T_s-T_j) on heat transfer for the cooling jet	369
4.4	Operating conditions and results for influence of Re_j at $H/w = 6$	379
4.5	Operating conditions and results for influence of Re_j at $H/w = 2.6$	380
4.6	Coefficients in Equation (4.9) for the average heat transfer at $H/w = 2.6$	424
4.7	Operating conditions and results for influence of M_{V_s} at $H/w = 6$	430
4.8	Operating conditions and results for influence of M_{V_s} at $H/w = 2.6$	431
4.9	Operating conditions and results for influence of M_{V_s} at $H/w = 6$	485
4.10	Operating conditions and results for influence of M_{V_s} at $H/w = 2.6$	487

NOMENCLATURE

$\bar{a}$	potential flow constant in equation (1.1)
$\bar{a}_{eff}$	average effective thermal diffusivity of the turbulent boundary layer, m^2/s
a_g	thermal diffusivity of gold film of sensor, m^2/s
a_j	coefficient in equation (2.42)
a_s	thermal diffusivity of pyroceram sensor, m^2/s
a_{UR}	underrelaxation factor in equation (2.36)
a_ϕ	coefficient in equation (2.11)
A	sensitivity of sensor in equation (1) of Appendix 13, $V/^oC$
AE,AW,AN,AS	coefficients in the convection terms of equation (2.28); see also equation (2.32) and Appendix 2
A_j	coefficient in equation (2.41)
$A_{\phi j}$	coefficient in equation (2.37)
b	negative part of source term in equation (2.105)
b_j	coefficient in equation (2.42)
b_ϕ	coefficient in equation (2.11)
BE,BW,BN,BS	coefficients in the diffusion terms of equation (2.28); see also equation (2.31) and Appendix 2
B_j	coefficient in equation (2.41)
$B_{\phi j}$	coefficient in equation (2.37)
c	positive part of source term in equation (2.105)
c_ϕ	coefficient in equation (2.11)
C	constant in equation (2.75)
C_D	discharge coefficient
CE,CW,CN,CS	coefficients in equation (2.28); see also equations (2.29) and (2.30) for the laminar jet. Also

	coefficients in equations (2.104), (2.110) and (2.111) for respectively the scalar variables, the velocities and the pressure in the turbulent jet case.
C_f	skin friction coefficient in equation (2.56)
C_j	coefficient in equation (2.42)
C_p	specific heat, J/kg-K
$C_{\varepsilon_1}, C_{\varepsilon_2}$	constants in equation (2.88), equal to respectively 1.44 and 1.92
C_μ	constant in equation (2.69), equal to 0.09
C'_μ	constant in equation (2.70)
$C_{\phi j}$	coefficient in equation (2.37)
C_1	constant in equation (2.100), equal to 1.5
d	thickness of gold film, μm
d_j	coefficient in equation (2.42)
d_ϕ	coefficient in equation (2.11)
D	diffusion coefficient, m^2/s
D_C	diameter of impingement cylinder, m
D_H	hydraulic diameter of slot nozzle, m
D_x	area on which pressure acts in equation (2.110), m^2
E	constant in equation (2.91), equal to 9.793
$E_{\Delta T}$	EMF of thermocouple, V
f	fraction of jet flow being removed through the porous surface
F_ϕ	half of mass flux, momentum flux and energy flux entering through the nozzle with ϕ respectively P', U and T; see equation (2.121)
Fo	Fourier number, $a_g t/d^2$ in equation (1) of Appendix 10
Fo_t	turbulent Fourier number, $\bar{a}_{eff} t/\delta^2$

G	generation term in equation (2.83), $(\frac{\partial u_i}{\partial x_j} + \frac{\partial u_j}{\partial x_i})(\frac{\partial u_i}{\partial x_j})$, s^{-2}
h	layer thickness in calculation procedure of heat flux in equation (3.8), μm
H	spacing, nozzle-to-impingement surface, mm
H_v	heat of evaporation in equation (2.66), kJ/kg
I	gridline number in x_1-direction
$\bar{I}$	electrical current in equation (1) in Appendix 13, A
IN	last gridline number in x_1-direction
J	gridline number in x_2-direction
JN	last gridline number in x_2-direction
k	turbulence kinetic energy, m^2/s^2
K	permeability, $\mu U_s/(\Delta P)$ in equation (3.22), m
K_1	constant, $(T_j-T_s)\rho_j U_j C_p/H_v$ in equation (1) of Appendix 6, $^{J}kg/m^2-s$
K_2	constant in equation (2.67)
K_d	amplification (gain) of DATAC amplifier
ℓ'	turbulence length scale in equation (2.70), m
L	length of gold film in equation (2) in Appendix 13, mm
L_p	length of impingement surface from stagnation point, m
L_s	thickness of sample for thermal conductivity measurement in Appendix 11, mm
M_f	expression in equation (2.120a), kg/m^2-s
M_{U_s}	impingement surface throughflow velocity mass ratio, $\rho_s U_s/(\rho_j U_j)$
M_{V_s}	impingement surface velocity mass ratio, $\rho_s V_s/(\rho_j U_j)$
N_R	number of rotations

Nu	Nusselt number, $\frac{\alpha w}{\lambda}$
Nu_{jis}	Nusselt number obtained with the impermeable sensor in equation (4.13)
Nu_{jm}	Nusselt number at the secondary heat transfer peak, $\alpha w/\lambda_j$
p'	fluctuating pressure component, N/m^2(Pa)
p_j	coefficient in equation (2.44)
P	mean pressure component, N/m^2(Pa)
P'	correction on mean pressure component in equation (2.112), N/m^2(Pa)
P^*	estimate of mean pressure component in equation (2.112), N/m^2(Pa)
$\tilde{P}$	production of turbulence kinetic energy, $-\overline{u_i u_j}\frac{\partial u_i}{\partial x_j}$ in equation (2.124), m^2/s^3
$\tilde{P}_{ij}$	production of turbulent stress, $-\{\overline{u_j u_k}\frac{\partial u_i}{\partial x_k} + \overline{u_i u_k}\frac{\partial u_j}{\partial x_k}\}$ in equation (2.81), m^2/s^3
P_j	coefficient in equation (2.43)
ΔP_n	pressure difference over jet nozzle, $P_p - P_{sj} = \frac{1}{2}\rho_j U_j^2$, N/m^2(Pa)
P_{sj}	static pressure at nozzle exit, N/m^2(Pa)
P_p	plenum chamber pressure, N/m^2(Pa)
P_{sm}	maximum static pressure at the impingement surface, N/m^2(Pa)
Pe	Peclet number, $U(\Delta X)/a$
Pr	Prandtl number, $\mu C_p/\lambda$
q	heat flux, W
q_j	coefficient in equation (2.44)
q_{sm}	maximum self-heating power of sensor in equation (2) of Appendix 13, W
Q_j	coefficient in equation (2.43)

r	radial distance, m
r_j	coefficient in equation (2.44)
R	resistance, Ω
R_d	drying rate in equation (2.66), $kg/m^2/s$
R_j	coefficient in equation (2.43)
R_s	resistance of sensor
R_v	variable resistance in wheatstone bridge of sensor circuit, Ω
R_ϕ	summation of relative residuals at all grid points in equation (2.121)
Re	Reynolds number, $\rho Uw/\mu$
Ri	turbulent Richardson number, $\frac{k^2}{\varepsilon^2}\frac{U_\theta}{r^2}\left(\frac{\partial(rU_\theta)}{\partial r}\right)$ in equation (2.102)
RP	underrelaxation factor
s	surface area of sample for thermal conductivity measurement in Appendix II, m^2
S	length of impingement surface from nozzle centerline, mm
S_f	false source term in equation (2.109)
S_i	source term in equation (2.71), $kg/m^2\text{-}s^2$
S_ρ	source term due to variable density in equation (2.8), $kg/m^3\text{-}s^2$
S_μ	source term due to variable viscosity in equation (2.8), $kg/m^3\text{-}s^2$
S_ϕ	source term in equation (2.103)
Sc	Schmidt number, ν/D
Sh	Sherwood number, $\beta w/D$
St	Stanton number, $\alpha/(\rho UC_p)$
SUMNW	sum of the nondimensional vorticity at all inner grid points
t	time, s

T	mean component of temperature, ^{o}C
T_f	film temperature, $(T_j + T_s)/2$, ^{o}C
T_j	temperature at jet nozzle, ^{o}C
T_p	plenum chamber temperature, ^{o}C
T_S	sensor temperature, ^{o}C
T_s	impingement surface temperature
ΔT_S	average temperature difference between central and other two thermocouples at the back of the sensor, ^{o}C
Tu_a	turbulence intensity at the location of the impingement surface, when the impingement surface is not present (arrival turbulence intensity)
u'	fluctuating component of velocity, m/s
u^+	skin friction velocity in equation (2.91)
u	mean component of velocity, m/s
U_a	artificial velocity in equation (2.46), m/s
U_m	maximum wall jet velocity, m/s
U_s	throughflow velocity, m/s
U_θ	angular velocity, m/s
$U_{\phi j}$	coefficient in equation (2.38)
V	volume of integration, m^3
V_s	impingement surface velocity, m/s
V_t	turbulent velocity in equation (2.75), m/s
w	nozzle width, mm
W	width of gold film in equation (2) in Appendix 13, m
X	coordinate, m
X_{psm}	location where static pressure at the impingement surface is maximal, m
y	distance from the wall, m

y^+	nondimensional distance from the wall in equation (2.92)
z	penetration depth of heat wave in equation (3.13), mm

Greek Letters

α	heat transfer coefficient in equation (2.57), W/m^2-^oC
α_t	thermal coefficient of resistance in equation (1) of Appendix 13, $^oC^{-1}$
β	mass transfer coefficient, m/s
γ	fluctuating component of temperature, ^oC
γ_t	constant in equation (2.100), equal to 0.6
δ	boundary layer thickness, mm
δ_f	film resistivity in equation (5) of Appendix 13, Ωm
δ_m	distance of maximum wall jet velocity location from the wall, m
δ_s	sublayer thickness in equation (3.23), μm
ε	dissipation rate of turbulence kinetic energy, m^2/s^3
μ	dynamic viscosity, kg/m-s
μ_{eff}	effective viscosity, $\mu + \mu_t$, kg/m-s
μ_t	turbulent viscosity in equation (2.69), kg/m-s
ν	kinematic viscosity, m^2/s
ν_a	artificial viscosity in equation (2.45), m^2/s
ρ	density, kg/m^3
ω	vorticity in equation (2.7), s^{-1}
ω_m	circular frequency in equation (1) of Appendix 7, s^{-1}
ψ	stream function in equations (2.5) and (2.6), kg/m-s

λ	thermal conductivity, W/m/^{o}C
ϕ	general variable
Γ	general exchange coefficient in equation (2.103)
Γ_a^*	nondimensional artificial diffusion in equation (2.50)
Γ_{eff}	effective thermal exchange coefficient in equation (2.80), kg/m-s
τ_m	cycle time of fastest heat flux, s
τ_0	cycle time for one rotation of the drum in equation (3.13), s
τ_s	shear stress at the wall in equation (2.56), kg/m-s^2
σ_k	turbulent Prandtl number for the turbulence kinetic energy in equation (2.85), equal to 1.0
σ_ε	constant in equation (2.88), equal to 1.217
κ	constant in equation (2.91), equal to 0.4187

Subscripts

cp	constant properties
eff	effective, summation of laminar and "turbulent" contribution
f	physical properties determined at T_f
j	physical properties determined at T_j, or at location of the nozzle exit
ℓ	lower
nw	near-wall
o	at stagnation point
t	turbulent
s	physical properties determined at T_s, or location at impingement surface
N,E,S,W,P	at location of grid nodes N, E, S, W and P; see Figure 2.1

ϕ	general variable

Superscripts

o	estimated
*	nondimensionalized, i.e. divided by length scale w, H, velocity U_j and/or physical properties at the nozzle exit. For temperature, see equation (2.12).
$\overline{}$	averaged

CHAPTER 1

INTRODUCTION

1.1 Introduction

This thesis is concerned with measurement and prediction of heat transfer distribution under a confined impinging slot jet, at the surface of a rotating porous cylinder, with the possibility of throughflow at the impingement surface. The prime motivation comes from the large increase in drying rate that results from combining impingement and throughflow drying in the drying of paper. This potential was demonstrated a decade ago in a pilot plant (Burgess et al. (23)) and full size mill experiment (Burgess et al. (24)) in Québec. Newsprint drying rates obtained with this "Papridryer" process were one order of magnitude larger than with the conventional steam-heated cylinder drying process. The new process has the additional potential of enabling rapid corrections to the cross-machine direction moisture profile of the paper and eliminating "sheet flutter" at high newsprint machine speeds.

Because of lack of data for such a complicated system at the time the pilot and mill Papridryer were conceived, the design can in no way be considered optimal. It is the objective of the present work to make a contribution to the basic knowledge necessary for improved designs of the Papridryer and of similar impingement systems. Thus an experimental program was conceived to provide heat transfer data on a simulated Papri-

dryer system, including establishing the influence of important variables such as impingement cylinder surface velocity, throughflow rate, temperature difference between jet and impingement surface and separation distance between jet nozzle and impingement surface. In parallel with the experimental program noted, the objective of this thesis was furthered through development of a computer simulation model of the flow and heat transfer for this complex system, the results of the experimental program providing a test of this computer simulation.

1.2 Background Information and Industrial Motivation

Impinging jets are used industrially because of high transport rates which can be obtained at the impingement surface. Moreover, impinging jets provide the potential of fine and fast control of local transfer rates by varying the jet velocity, size of the nozzle opening, etc. Depending upon the application, either round or slot jets can be selected, used individually, in a row or in a multiple array. Likewise, alternate designs for the flow of the spent fluid from the system after impingement provide a further design parameter. Applications include processes such as tempering of glass, annealing of non-ferrous metals, drying of paper, textiles and photographic film, and cooling of turbine blades, electronic components and paper mill calender rolls.

High transfer rates may be further enhanced by the use of throughflow at the impingement surface, which may involve the application of suction beneath this surface. The combination

of both impinging jets and throughflow was demonstrated for the drying of newsprint in a pilot plant (Burgess et al. (23)) and a full size mill in Canada (Burgess et al. (24)). In this "Papridryer" process the wet paper passes over about 300 degrees of the circumference of a rotating cylinder, which is pattern drilled, wire mesh covered and subjected to moderate vacuum. The cylinder is surrounded by a high-velocity hood in which a row of holes for the spent air exhaust is located between each slot nozzle. Some of the hot air from the impinging jets is drawn through the wet newsprint and, in so doing, evaporates water in the sheet. The larger fraction of the impingement air serves to evaporate water from the surface of the sheet before exhausting into the air return system. Part of this exhaust air passes to an air heater for reuse as impingement air, while part of the stream is vented. The basic advantages of the Papridryer are high drying rates and the very rapid cross-machine direction moisture profile corrections, made possible by control of jet velocity independently in different sections of the high-velocity hood. Moreover, as the paper is firmly pressed against the cylinder due to the pressure drop across the sheet, there is the additional advantage of elimination of "sheet flutter" which, especially when the moisture content of the paper is still high, can lead to sheet breakage and loss of paper machine operating time. The high heat transfer rates and sheet stabilization over regions of critical moisture content on a single Papridryer cylinder allow high newsprint machine speeds not attainable with conventional dryers involving many

steam-heated cylinders.

Fundamental studies of the flow and heat transfer characteristics of a confined jet impinging on a fast moving surface, with or without throughflow, had never been undertaken prior to the present study. Recently Crotogino and Allenger (35) simulated the drying rates in the Papridryer process by a linear combination of the transfer rates due to throughflow and jet impingement, neglecting the influence of impingement surface velocity, confinement and jet interaction. Some experimental data for a single unconfined slot jet impinging on a porous rotating cylinder have been published by Baines and Keffer (8, 9) since the original Papridryer publication of Burgess et al. However, the techniques used by Baines and Keffer are either not applicable or are inaccurate for impinging jet flows, as has been pointed out by van Heiningen et al. (147) of the McGill group. Considering the lack of basic data for such a complicated system at the time the pilot plant and mill-trial Papridryer were conceived, it is clear that these designs represent only a first, important step. Certainly the influence that parameters such as impingement surface velocity, throughflow rate, confinement, nozzle to impingement surface spacing, jet flow rate, temperature difference between jet and impingement surface, exert on the flow, heat and mass transfer characteristics must be known in order to develop optimum designs for specific industrial applications.

There are only a few studies reported concerning the influence of impingement surface motion on heat transfer. Average

heat transfer between a heated rotating cylinder and an unconfined cooling impinging slot jet has been investigated by Kays and Bjorklund (75), Yildiz (155) and Fechner (40), while recently Subba Raju and Schlünder (142) studied average heat transfer between a cooling impinging slot jet and a heated, continuous moving flat surface. The latter study reported an increase in heat transfer by a factor two for relatively low surface velocities. All these studies report only average heat transfer rates because of the obvious experimental problems to measure local heat transfer rates at a moving surface under an impinging jet. Thus there were no prior reports of local heat transfer rates for a moving impingement surface. Finally, Hardisty (57) reports that the effect of a moving surface on the flow field in the impingement region was negligible for the ink drying process. As the relative velocities in the ink drying process are comparable to the relative velocities in the experimental work of Subba Raju and Schlünder (142) mentioned earlier, there is a clear conflict between these claims.

The influence of throughflow on impingement heat transfer has received even less attention than surface motion. Most of the reported work has been done by the Impinging Jet Group of the Department of Chemical Engineering at McGill University. A preliminary investigation of the effect of suction on the flow characteristics in the free jet region of a two-dimensional jet was done by Abdul-Wahab et al. (1). Baines and Keffer (9) showed the influence of suction on boundary layer development for an confined impinging two-dimensional jet at a fixed

throughflow velocity and a fixed jet velocity. More detailed information on the effect of suction on the mean flow and turbulence intensity are given by Obot (105) for turbulent impinging round jet. Preliminary experimental heat transfer measurements under a turbulent impinging round jet by Obot (103) showed that the effect of applying small, uniform suction at the impingement surface is to increase the heat transfer along the test plate. Most recently a Ph.D. thesis completed by Saad (125) focussed on multiple impinging slot jets, including the influence of throughflow on heat transfer at the stationary impingement surface. Finally, numerical simulations by van Heiningen et al. (148) and Saad et al. (126) of respectively the laminar confined slot and round jet showed a constant increase in heat transfer along the impingement surface as a result of uniform throughflow. There remains a lack of reliable experimental data on the effect of suction on heat transfer under an impinging slot jet.

The effect on heat transfer of impingement surface spacing from the nozzle exit is one of the most investigated parameters. It has been well-established for an unconfined slot jet with a low turbulence intensity at the nozzle exit that the highest average heat and mass transfer is obtained at an impingement surface spacing of about 8 nozzle widths (Korger and Krizek (78), Schlünder et al. (133) and Cadek (26)). The generally accepted explanation for this behaviour, given by Gardon and Akfirat (44), is that at small separation distances the potential core mean velocity is constant while the turbulence level increases rapidly

with separation distance, leading to heat transfer coefficients increasing with separation distance. With further increases in separation distance, axial mean velocity of the jet decreases and even though the turbulence continues to increase, but more slowly now, the net effect is a decrease in impingement heat transfer coefficient. The maximum heat transfer occurs at a separation of about 8 nozzle widths and 6 nozzle diameters for respectively slot and round jets. For a fully developed turbulent slot jet at the nozzle exit, Folayan (41) also finds that the maximum heat transfer is obtained at a separation of 8 nozzle widths, independent of the impingement angle, except at an impingement angle of 60° where he reports the maximum to be at a separation of 6w. However, it is probable that interaction between the impingement flow and the flow induced by rotation of the impingement cylinder affects the impingement surface spacing for maximum heat transfer. This expectation is confirmed by the study of Sparrow et al. (137) on effect of crossflow on impingement heat transfer. Here the optimum separation distance for a round impinging slot jet is substantially reduced for a ratio of jet to crossflow mass velocity of 4. Throughflow at the surface further complicates the flow field. Therefore for the industrially important application of drying paper by a Papridryer process, the separation distance for maximum heat transfer may be quite different from the value for impingement on a stationary surface without throughflow. Thus the combination of throughflow at a moving impingement surface clearly should be investigated further.

Despite the extensive amount of literature on impinging jets it is indeed surprising and unfortunate that the effect of confinement has received practically no attention. Essentially all studies have been carried out with unconfined jets, i.e. with the impingement surface fully exposed to the surroundings. As unconfined impinging jets entrain large amounts of fluid from the surroundings, the flow and heat transfer characteristics of confined and unconfined impingement systems could be expected to differ significantly. However, most important process applications of impinging jets require confinement of the impingement system in order to recover the spent fluid without entrainment from the surroundings. Although the McGill University group has focussed on confined impingement systems, the only other investigation of confined jets is that of Folayan (41) for a single slot jet impinging on a flat, stationary surface. For the one value of jet Reynolds number investigated he found that the heat transfer under a jet with a fully developed exit mean velocity profile was reduced by confinement of the impingement flow with a plate parallel to the impingement surface. The jet velocity profile at the exit of the nozzle described for the Papridryer system would however be flat. Because of the limited extent of the Folayan study it is apparent that the industrially important variable, confinement, warrants detailed investigation.

Another variable which has received little or no attention is the influence of temperature difference between jet and impingement surface. The temperature difference in experimental studies has generally been kept constant and at a level of only

20^{o}-70^{o}C. Alternately, heat transfer has been obtained indirectly with such techniques as water evaporation or naphthalene sublimation which are the mass transfer equivalents of heat transfer data at low ΔT. This lack of both high ΔT and variable ΔT experimental data is again both surprising and unfortunate considering the large thermal driving force in important industrial applications, as for example turbine blade cooling and paper drying with temperature differences respectively up to 500^{o}C (Livingood et al. (85)) and 350^{o}C (Burgess et al. (23)). Other parameters which, though important, will not be discussed here are impingement angle, multiple jet interaction and geometry of the exhaust ports in a confined system, as these effects are beyond the scope of the present study.

From the foregoing discussion it is clear that a complete understanding of the influence of all parameters in the complex flow and temperature field of a slot jet impinging on a moving porous surface would require an enormous amount of difficult experimental work. Experimental work cannot be eliminated but may be reduced through following the alternate path of obtaining quantitative information via a theoretical calculation, provided that the theoretical calculation is sufficiently general to incorporate the important parameters affecting the flow and temperature field. The only theoretical approach with the potential of fulfilling this requirement is numerical solution of the complete partial differential equations which describe the various physical processes.

The first attempt to predict the flow and temperature field

of a turbulent impinging slot jet with such a general numerical procedure was by Wolfshtein (153). He solved the equations of motion and energy for two-dimensional flow together with a modelled form of the turbulent kinetic energy equation. The effect of turbulence on the mean flow was incorporated via the turbulent viscosity concept. Turbulent viscosity was calculated algebraically from turbulent kinetic energy and an assumed length scale. Reasonable agreement is obtained with experimental heat transfer data of Gardon and Akfirat (44). However, for large Reynolds numbers the deviations become excessive. Later, Russell and Hatton (123) obtained a slightly better agreement with a measured length scale distribution as input. The problem of prescribing the length scale was eliminated by Folayan (41) by calculating the length scale from a modelled form of the differential equation of the dissipation rate of turbulent kinetic energy. The comparison of local experimental and numerical heat transfer coefficients show discrepancies less than 30% at any position. Considering the complexity of the flow, the agreement is encouraging for further development of such a general numerical simulation model for the much more complex Papridryer configuration. Due to the still early stage of application of numerical fluid mechanics to such complex flows, experimental testing of such computer simulation models is essential.

1.3 Objective and Strategy

The objective of the present work is to obtain experimental data for heat transfer between a confined impinging slot jet and

a moving porous surface with throughflow at the surface and to develop a general prediction method for a confined impingement system. More specifically, for the experimental part of the study, the objective was to measure the local heat transfer distributions as a function of:

(1) separation distance between the jet nozzle and the impingement surface

(2) jet Reynolds number

(3) temperature difference between the jet and the impingement surface

(4) impingement surface velocity

(5) throughflow rate

The operating conditions and geometry of the pilot plant and mill-trial Papridryer (Burgess et al. (23, 24)) shown in Table 1.1 served as a guide in selection of the range of these parameters.

TABLE 1.1. Operating Conditions and Geometry of Pilot and Mill Papridryer

	Pilot Papridryer	Mill Papridryer
Drum diameter (mm)	381	1524
Nozzle width (mm)	0.51	1.27
Nozzle-surface separation (mm)	8.4	12.7-19.1
Internozzle spacing (mm)	38.1	76.2
Jet temperature (^{o}C)	177-427	173-344
Jet velocity (m/s)	12.2-96.5	41.1-85.3
Paper speed (m/s)	2.0-3.6	9.6-9.9
Throughflow velocity (m/s)	0.046-0.269	0.051-0.203

As in the Papridryer system, the central component of the present experimental facility is a rotating cylindrical impingement surface. Overall steady-state operation is achieved through use of two slot jets, one hot and one cold, impinging on the rotating cylinder from 180° opposed positions. The flow field of the heating jet and cooling jet is separated by two skimmer plates midway between the nozzles very close to the surface of the impingement cylinder. Throughflow was achieved by forming the impingement cylinder from porous metal and providing for suction within the cylinder. The impingement system was closed with a confinement surface concentric with the impingement surface. The spent air after impingement exhausts through exit ports located at the confinement surface at positions 90° on either side of the respective inlet nozzle. Care was taken to minimize variations in flow and temperature in the axial direction along the impingement cylinder so as to minimize experimental equipment end effects. Thus the flow and temperature fields were a close approximation to two-dimensional. A heat flux sensor of unique design, small in size and with exceptionally fast response time, was located in the impingement cylinder surface so as to provide the local heat transfer distribution. A schematic representation of this conception for an experimental facility is shown as Figure 1.1.

With respect to the computer simulation aspect of the study, a key factor determining the approach taken is the fact that the flow under consideration is recirculating, turbulent and extremely complex due to such additional parameters as

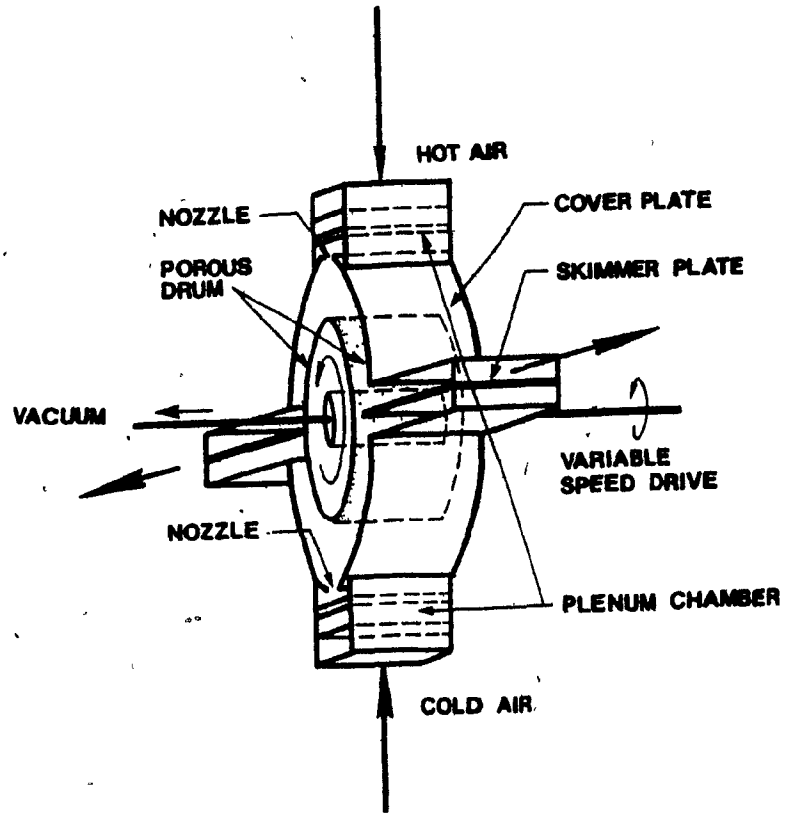


FIGURE 1.1. Schematic view of cylindrical confined impingement apparatus

throughflow at the impingement surface. The computational programs developed by D.B. Spalding and co-workers at Imperial College, London, for recirculating flows are sufficiently general that they were chosen for development to incorporate as many features as possible of the complex, Papridryer type flow. It is judged more productive to attempt to expand the capability of those programs to more complex flows rather than to expend effort in developing new programs. This then was the strategy adopted for the objective of predicting the flow and heat transfer of laminar and turbulent confined impinging slot jets, these predictions to be tested with results from the experimental aspect of the investigation.

1.4 Previous Work on Single Impinging Slot Jets

In describing previous work, attention will be restricted to single impinging slot jets as work with round jets and multiple jets is not directly relevant. Moreover, several reviews on impinging jets have been published during the last decade. The flow characteristics of impinging jets were reviewed by J.W. Gauntner et al. (46) and Hardisty (56), while the reviews by Arganbright and Resch (5), Mujumdar and Douglas (100), Hardisty (57), Martin (88) and Obot et al. (104) concentrated on the heat and mass transfer at the impingement surface. Furthermore, of two recent Ph.D. theses, that of Obot (105) on the flow characteristics and heat transfer for a single turbulent impinging round jet provides also a very extensive review on flow, heat and mass transfer of impinging jets in general, while

the thesis of Saad (125) on flow and heat transfer under multiple inpinging slot jets, provides a literature review mainly focussed on transport processes under multiple impinging slot jets.

1.4.1 The Flow Field of an Impinging Slot Jet

Poreh and Cermak (110) were the first to identify the four characteristic flow regions of a turbulent impinging slot jet. The regions are (see Figure 1.2): zone of flow establishment (I), free jet region (II), impingement region (III) and wall jet region (IV).

The zone of flow establishment (I) extends to the tip of the potential core of the jet. The length of the potential core is defined as the axial distance from the nozzle exit over which the mean velocity remains equal to the jet velocity at the nozzle exit. The point of ending of the potential core is determined by the rate of growth of the two mixing layers originating at the edges of the nozzle. Nozzle design has a major influence on the flow field in region I, because it determines the jet profile, turbulence level at the nozzle exit, and hence the rate of penetration of the mixing layers into the potential core. Special attention to slot nozzle design in impinging jet studies has been paid by Cadek (26) and Dosdogru (37), and for round nozzles by Obot (105). Depending on the shape of the slot nozzle, Dosdogru (37) found the length of the potential core to increase from about 2 nozzle widths for a sharp edged slot, to about 4-1/2 nozzle widths for a slot formed by two plates at a small included angle, and finally to about 8 nozzle widths for a slot nozzle

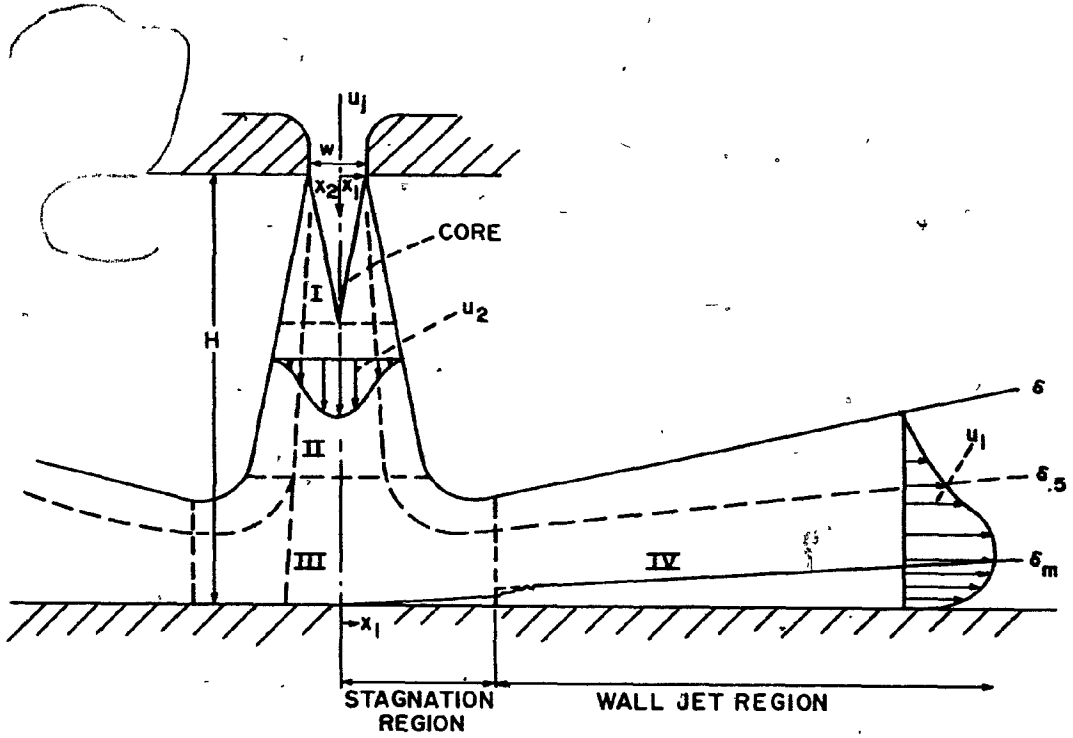


FIGURE 1.2. Two-dimensional impinging jet

shaped as the ASME long-radius nozzle, i.e. a nozzle with a short elliptical entrance, and a discharge coefficient close to 1.0.

Provided that the impingement surface spacing from the nozzle is sufficiently large, there is a region of established flow (II), which has the same characteristics as the corresponding established flow region of a free slot jet. The flow field is characterized by the associated processes of decrease of centerline velocity and spreading of the jet in the transverse direction. Further details concerning free jets are available in texts such as Hinze (60), Abramovitch (2) and Schlichting (131). Measurements of the turbulence properties in a free slot jet are reported by Gutmark and Wygnanski (52). Recently, the axial mean velocity and axial turbulence intensity of a confined impinging slot jet have been measured by Saad (125) from the nozzle exit almost to the impingement surface. These measurements of turbulence again point out that although the potential core is by definition the region in which mean velocity remains unchanged from that at the nozzle exit, the turbulence level in the potential core region changes greatly long before the main velocity changes.

The impingement region (III) is characterized by an increased static pressure as a result of the sharp decrease in axial mean velocity close to impingement. Velocity and turbulence measurements in this region have been relatively scarce, especially at impingement surface spacings of about 8 nozzle widths which give rise to the highest heat transfer. The distribution of axial and transverse mean velocity in the impingement

region of a two-dimensional jet was measured by Beltaos and Rajaratnam (13) at the exceptionally large spacing of H/w = 67.5. Dosdogru (37) measured axial velocity decay in the impingement region for the important spacing range of $2 \leq H/w \leq 10$, and correlated his data within 10% by a potential flow constant $\bar{a}$, similar to plane stagnation flow (Schlichting (131)) as

$$\bar{a} = \frac{\partial U_2}{\partial X_2} = |1.022 - 0.0236\ H/w|\ U_j/w \qquad (1.1)$$

Having taken account of the accumulated data on axial velocity decay Gutmark et al. (54) concluded that the impinging slot jet is not affected by the impingement surface until a distance from impingement of about 0.25H, which may be taken as axial extent of the impingement region. Some measurements of axial velocity and turbulence in the impingement region of a confined slot jet are documented by Saad (125) at H/w = 19. Saad found that, for H/w = 19, the sharp drop in axial mean velocity at the approach to the impingement surface occurred at 0.21H from impingement. Thus Saad's estimate of the axial extent of the impingement region, 0.21H, and that of Gutmark, 0.25H, are in reasonable agreement. The extent of the region within which axial mean velocity is affected by the presence of the impingement surface is conventionally used as the criterion for defining the boundaries of the impingement region. However, it should be noted that the boundaries of the region within which turbulence is affected is significantly different. Thus Saad (125) found that, for H/w = 19, axial turbulence velocity is not affected by the presence of the

impingement surface even as close as 1w from impingement. According to his measurements, axial turbulence intensity is of course affected at the same distance, 0.21H, from impingement, but only through the drop in axial mean velocity which begins at that location. For a round jet Obot (105) found the same difference between the distance from the impingement surface that its presence affected axial mean velocity and axial turbulence velocity. It is interesting to note that the large difference in variation of axial mean velocity and axial turbulence velocity in the region extending from the nozzle exit was pointed out in the discussion of the flow establishment region (I). In that case the axial turbulence velocity increases sharply immediately downstream of the nozzle exit while axial mean velocity remains constant throughout the considerable length of the potential core. Approaching impingement, this difference is in effect reversed, as axial mean velocity is affected 0.21H away from impingement while the measurements of Saad (which are consistent with those of Obot for a normal jet) indicate that axial turbulence velocity is unaffected as little as 0.05H from impingement, the closest measured by Saad.

Development of the maximum velocity parallel to the impingement surface has been established for an unconfined slot jet by Schauer and Eustis (128) and Kumada and Mabuchi (79) for respectively $H/w = 40$ and $2 \leq H/w \leq 40$. A definition of the lateral extent of the impingement region is the position where the pressure gradient at the impingement surface becomes zero again. For relatively large values of H/w the data of Beltaos and

Rajaratnam (13) and Schauer and Eustis (128) indicate that for an unconfined slot jet this position is located at $x_1/H = 0.35$. The value of $x_1/H = 0.35$ can also be obtained from the pressure distributions obtained by Cadek at $8 \leq H/w \leq 32$. For spacings, H/w, of 2 and 4 the axial extent is respectively about 1.6w and 1.9w. Saad (125) has taken an extensive set of profiles of impingement surface pressure. For two values of nozzle slot width, w, and for dimensionless spacings, H/w, of 4.8 and 16 for both nozzles, Saad (125) found that profiles of normalized impingement surface pressure superimpose to a single profile when x/H is used as the lateral dimension. He finds that the half-pressure width is 0.15H, while the profiles drop to 5% of the stagnation pressure at a lateral position of about 0.5H. Thus Saad's results indicate that the lateral extent of the impingement region for a confined slot jet is somewhat greater than 0.5H but less than 1H.

A very informative study is the flow visualization of transformation of the shear vortex sheets in the zone of flow establishment (II) into well-ordered vortex-pair structures in the impingement region by Yokobori et al. (156). The conceptual model for the vortex-pair generation is shown in Figure 1.3. These well ordered structures are only discernible in the stagnation region for $4 \leq H/w \leq 12$, i.e. at spacings giving rise to the highest heat transfer in the impingement region. The high transport rates at these spacings are attributed by Yokobori et al. (156) to the renewal of the boundary layer by the vortex-pairs and to the high turbulence intensity accompanying these

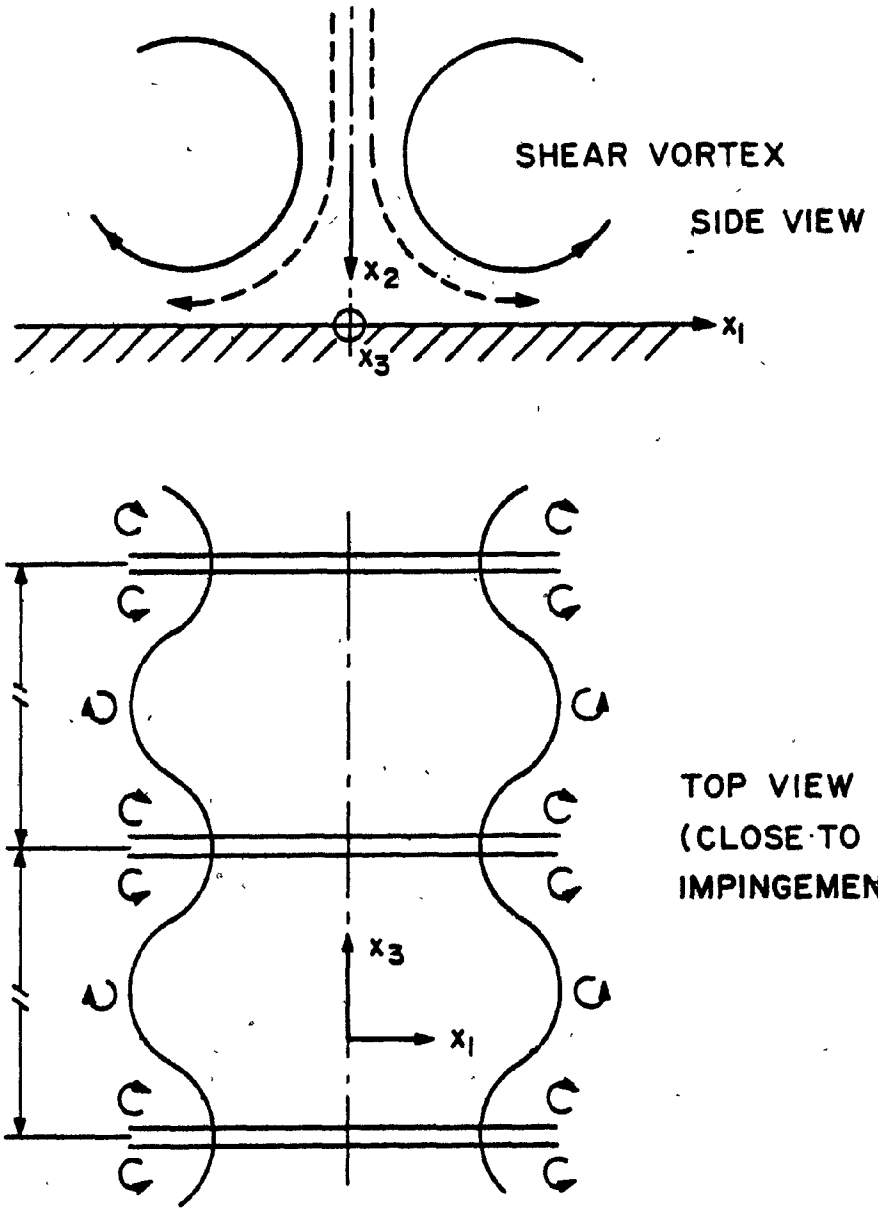


FIGURE 1.3. Conceptual model of vortex-pair generation

vortex pairs. The large scale structures are not found by Gutmark et al. (54) for H/w = 100. Gutmark et al. (54) are the first investigators who measured on the centerline of an impinging slot jet all the terms, except for the pressure-velocity correlation, in the three components of the turbulence kinetic energy equation. The influence of the impingement surface is to increase the anisotropy of the three components of normal stress. This behaviour is attributed to the deformation of vortex lines, i.e. stretching in the x_1-direction and compression in the x_2-direction (see Figure 1.3). The turbulence kinetic energy and the shear stress contours were measured by Russell and Hatton (123) for H/w = 31.5. There is, however, some doubt whether their data can be used quantitatively, because of the three-dimensional effects resulting from the unrealistically small aspect ratio , 6, of their nozzle and the presence of side-plates to prevent lateral spreading of the jet. The measurements show a gradual decrease of the turbulence kinetic energy along the midplane in the impingement region, in agreement with Gutmark et al. (54) at H/w = 100 and Saad (125) at H/w = 19. Other interesting findings by Gutmark et al. (54) are, that the turbulence properties of the jet are changed from their equilibrium level at only $\leq 0.15H$ from the plate, and that there is a general trend of energy transfer towards the large scale eddies as the impingement plate is approached. This last effect is studied in more detail by Gutmark et al. (53) for a round jet at an impingement surface spacing of 10 nozzle diameters.

Finally the measurements made by Scheuter and Dosdogru

(129, 130) and Baines and Keffer (8) with a surface hot-film probe mounted flush with impingement surface should be mentioned. As explained by van Heiningen et al. (147) and Black and Hardisty (16), these measurements cannot be used to obtain heat transfer in the impingement region as is done by Scheuter and Dosdogru (129) because Reynolds analogy is invalid in this region. Moreover, the hot film technique is not applicable for accurate measurement of skin friction in the stagnation region. This limitation explains the discrepancies between results obtained with this technique by Baines and Keffer (8) and velocity measurements in the boundary layer obtained with a hot wire probe. The inaccuracy of the hot film technique for measurement of skin friction in the stagnation region is related to the effect of a pressure gradient on the velocity profile in the boundary layer, noted long ago by Brown (20). It is interesting to note however that the hot film measurements of skin friction of Baines and Keffer (8) and Scheuter and Dosdogru (129) at H/w = 4 display two maxima in skin friction. The first maximum, located at $X_1/w \simeq 1$, is attributed to transition of the accelerating lateral flow into the decelerating wall jet. The second maximum, at 5w to 7w from stagnation, has been attributed to the gradual transition of the initial laminar stagnation flow to a turbulent wall jet. A different explanation for the origin of the second peak is given by Popiel and Trass (109). They conclude from detailed flow visualization measurements of an impinging round jet that the maximum is caused by coherent wall eddies. In this respect it should also be noted that Scheuter

and Dosdogru (129) found that the second skin friction peaks disappear at H/w ≈ 12. This observation may be related to that of Yokobori et al. (156) finding that for a slot jet vortex-pairs are no longer discernible after this same spacing, H/w ≈ 12.

The wall jet region (IV) has the same characteristics as the flow issuing from a plane slit parallel to a surface. Such a flow can be treated in two parts; an inner layer where the effect of the surface is present and an outer layer which is characterized by the features of a free turbulent jet. Wall jet velocity profiles for an unconfined impinging slot jet with a low turbulence level at the nozzle exit have been measured by Schauer and Eustis (128) and Beltaos and Rajaratnam (13) for spacing, H/w, of respectively 20 and 40, and 66.15 and 43.6. Wall jet velocity profiles for an impinging slot jet fully turbulent at the nozzle exit have been documented by Folayan (41) for spacings, H/w, of 6 and 12. Kumada and Mabuchi (79) measured the maximum velocity decay in the wall jet region of an unconfined impinging slot jet at $2 \leq H/w \leq 40$. Velocity measurements in the wall jet region for a confined impinging slot jet have however not been reported yet.

Two aspects of the impingement surface are important for industrial applications, i.e. surface motion and surface curvature. No publications exist concerning the influence of impingement surface motion on the flow pattern of an impinging slot jet. The influence of cylindrical curvature of the impingement surface has been studied by Kumada et al. (80) and Kumada et al. (81) for spacings, H/w, of respectively 2, 8 and 40. The ratio

of impingement cylinder diameter, D_c to nozzle width, w, was varied between 3.75 and 25. The potential flow solution of a slot jet impinging on a circular cylinder is given by Miyazaki and Sparrow (98). Measurements of mean and turbulent velocities for a 2-dimensional turbulent wall jet over a cylinder are reported by Wilson and Goldstein (152).

The effect of throughflow on the impingement flow field of a 2-dimensional jet was the subject of an exploratory study by Abdul-Wahab et al. (1). At Re_j = 5680 the throughflow velocity was varied between 0.21 and 0.43 m/s for a jet velocity of 13.5 m/s, i.e. equivalent to ratios of throughflow velocity to jet velocity, U_s/U_j, of 1.5% and 3.2%, which is larger than the values reported by Burgess et al. (23, 24) for the Papridryer process. The results of Abdul-Wahab et al. show a slightly faster decay of the jet centerline mean velocity with throughflow than without and a reduction across the jet of the axial fluctuating velocity component. On the contrary, for $11400 \leq Re_j \leq 30200$, Saad (125) found that a throughflow velocity, U_s, in the range 0.1 - 0.3 m/s, caused an increase in the axial mean velocity at 0.25H from the impingement surface of about 4-6 times the throughflow velocity, independent of both Re_j and x/w, and no consistent effect on the fluctuating velocity. The reported effect of throughflow on axial mean velocity at this distance from the impingement surface is quite surprising since the results of Saad and of Gutmark et al. (54) indicate that presence of an impermeable surface is not felt by an impinging jet that far from impingement.

In the wall jet region of an impinging round jet, for throughflow rates in the range $0.2 < U_s/U_j < 0.8\%$, Obot (105) reports an increase in lateral velocity, no change in turbulence velocity, and hence a slight decrease in streamwise turbulence intensity adjacent to the impingement surface. With throughflow at a level of $U_s/U_j = 0.29\%$ for $U_j = 52.7$ m/s for a rotating surface, Baines and Keffer (9) report a slight increase in the maximum wall jet velocity with throughflow. With conflicting results from the limited studies yet available, it is clear that further work is required to establish the effects that throughflow at the impingement surface has on the flow field.

Finally, for a detailed literature review of the dependence of the transition of a laminar impinging jet to a turbulent jet one is referred to Section 2.2.

1.4.2 Heat and Mass Transfer Under an Impinging Slot Jet

The range of experimental conditions and the principal correlations obtained by investigators of heat or mass transfer under a single impinging slot jet are given in Table 1.2. Although the study by Saad (125) is primarily of multiple slot jets, the cases for which there is negligible jet interaction have been included in Table 1.2. Descriptions of experimental techniques may be obtained from the original references. The Reynolds number Re_j range covered is from 10^2 to 10^5, the nozzle width w from 0.25 to 40 mm and impingement surface spacing, H/w, from 0.25 to 40. The mass transfer studies were done with water evaporation or naphthalene and ethylsalicylate evaporation,

TABLE 1.2. Experimental Conditions and Heat/Mass Transfer Correlations for a Single Slot Jet Impinging on a Flat Stationary and Impermeable Surface

Author(s)	Range of Parameters of Reported Experiments							Confined Jet	Correlations and Range of Validity Comments
	Re_j	w, mm	H/w	x/w	T_j (°C)	ΔT (°C)	Pr (or Sc)		
Metzger (93), 1962	1500 to 5000	0.25 to 2.03	2 to 20	6.25 to 100	20	≤ 50 air cooling	0.71	No	$\overline{St}_x = 0.547\ Re_x^{-0.434} Pr^{-0.63}$ for $7 < H/w < 10$ and $3 < x/w < 50$
Schauer and Eustis (128), 1963	20300 to 53000	12.7	40	≤ 76	20	10 air cooling	0.71	No	very complex correlations
Gardon and Akfirat (44, 45), 1965, 1966	450 to 50000	1.59 3.18 6.35	0.5 to 40	≤ 40	20	air cooling	0.71	No	$Nu_{oj} = 1.2\ Re_j^{0.58} (H/w)^{-0.62}$ for $H/w > 14$, $Re_j > 2000$ $\overline{Nu}_j = 0.506\ Re_j^{0.62} (\frac{x}{H})^{-0.38} (\frac{H}{w})^{-0.69}$ for $H/w > 8$, $Re_j > 2000$
Korger and Krizek (78), 1966	6000 to 38000	5.0, 10.0 20.0 40.0	0.25 to 40	≤ 20	20	20 naphthalene sublimation	2.5	No	$Nu_{oj} = Re^{0.66} (H/w)^{-0.66}$

TABLE 1.2. (continued)

Author(s)	Range of Parameters of Reported Experiments							Confined Jet	Correlations and Range of Validity Comments
	Re_j	w, mm	H/w	x/w	T_j (°C)	ΔT (°C)	Pr (or Sc)		
Cadek (26), 1968	4600 to 102000	6.35 12.7 25.4	2 to 32	≤ 36	24.4	70 air cooling	0.71	No	$\overline{Nu}_j = 0.506\ Re_j^{0.62} (\frac{x}{H})^{-0.38} (\frac{H}{w})^{-0.69}$ for H/w > 8, Re_j > 2000
Schlünder et al. (133), 1970	1500 to 45000	2, 5 10 20	1 to 40	≤ 50	~ 20	water evaporation	0.59	No	$\overline{Nu}_j/Pr^{0.42} = 1.53(2\ Re_j)^m/(x/w + H/w + 2.78)$ with $m = 0.695 - 2/(x/w + 6.12 + 0.8(H/w)^{1.33})$ for $4 \leq H/w \leq 20$ and $4 \leq x/w \leq 50$
Kumada and Mabuchi (79), 1970	10000 to 15000	5 and 10	2 to 40	< 30	~ 30	naphthalene sublimation	2.5	No	$Nu_{jo}/Pr^{0.43} = 1.42\ Re_j^{0.58}(H/w)^{-0.62}$ for $10 \leq H/w \leq 40$
Cartwright and Russell (30), 1972	25000 to 110000	6.35	8 to 47	≤ 150	20	air cooling	0.71	No	$Nu_{oj} = 0.489\ Re^{0.672}(H/w)^{-0.604}$ for 16 < H/w < 47
Sparrow and Wong (139), 1975	150 to 950	6.35	2 to 20	≤ 5½	~ 20	naphthalene sublimation	2.5	No	$Nu_o \propto Re_j^{0.6}$

TABLE 1.2. (continued)

Author(s)	Range of Parameters of Reported Experiments							Confined Jet	Correlations and Range of Validity Comments
	Re_j	w, mm	H/w	x/w	T_j (^oC)	ΔT (^oC)	Pr (or Sc)		
Folayan (42), 1977	3500 7100	5	2, 6, 8, 12	$\leq$ 40	45	20 air heating	0.71	Yes	fully turbulent jet at nozzle exit
Masliyah and Nguyen (89), 1978	90 to 300	0.75 1.0 1.5	4 and 8	$\leq$ 30	~ 20	ethylsalicylate evaporation	2.85	No	$Sh = 0.512(x/B)^{-0.73}(Re_j)^{0.55}$ for $1 \leq x/w \leq 30$ local mass transfer
Saad (125), 1981	3330 to 20740	2.5	8 to 24	$\leq$ 32	~ 30	~ 30 air cooling	0.71	Yes	$\overline{Nu}_j = 0.63\ Re_j^{0.63}(\frac{x}{H})^{-0.55}(\frac{H}{w})^{-0.80}$ for $1.5 \leq x/H \leq 4$, $8 \leq H/w \leq 24$ and $3330 \leq Re_j \leq 20740$

Study of Metzger (93) was of average heat transfer. All other studies obtained local transfer rates.

leading to Schmidt numbers (Sc) of respectively 0.58, 2.5 and 2.85. The heat transfer studies were generally performed with a constant temperature difference between the jet at the nozzle exit and the impingement surface. The level of the temperature difference, 10^{o}-70^{o}C, is much smaller than that in such important industrial applications as turbine blade cooling and paper drying.

The most detailed local heat/mass transfer profiles obtained in the studies reported in Table 1.2 are compared in Figures 1.4 to 1.7. The mass transfer data of Korger and Krizek (78) and of Schlünder et al. (133) are converted to heat transfer under air jets by expressing the local transfer rates as $Nu_j \left(\frac{Sc}{0.71}\right)^{0.42}$. For heat transfer, Sc is taken as 0.71. The exponent 0.42 is taken in accordance with the recommendations of Hansen (55) for effect of Prandtl or Schmidt number on turbulent heat and mass transfer rates. This exponent was first used by Schlunder and Gnielinski (132) when comparing heat and mass transfer studies of turbulent impinging round jets. In the English literature an exponent of 0.40 is generally used (Sparrow and Wong (139), Kumada and Mabuchi (79) and Masliyah and Nguyen (89)).

The agreement between the sets of data in Figures 1.4 to 1.7 is quite good, considering differences in measurement techniques, nozzle sizes and design, velocity profile and turbulence level at the nozzle exit and the variable of jet confinement. The very close agreement for H/w = 16 in Figure 1.6 compared with the spread of data at H/w = 2 in Figure 1.4 indicates that

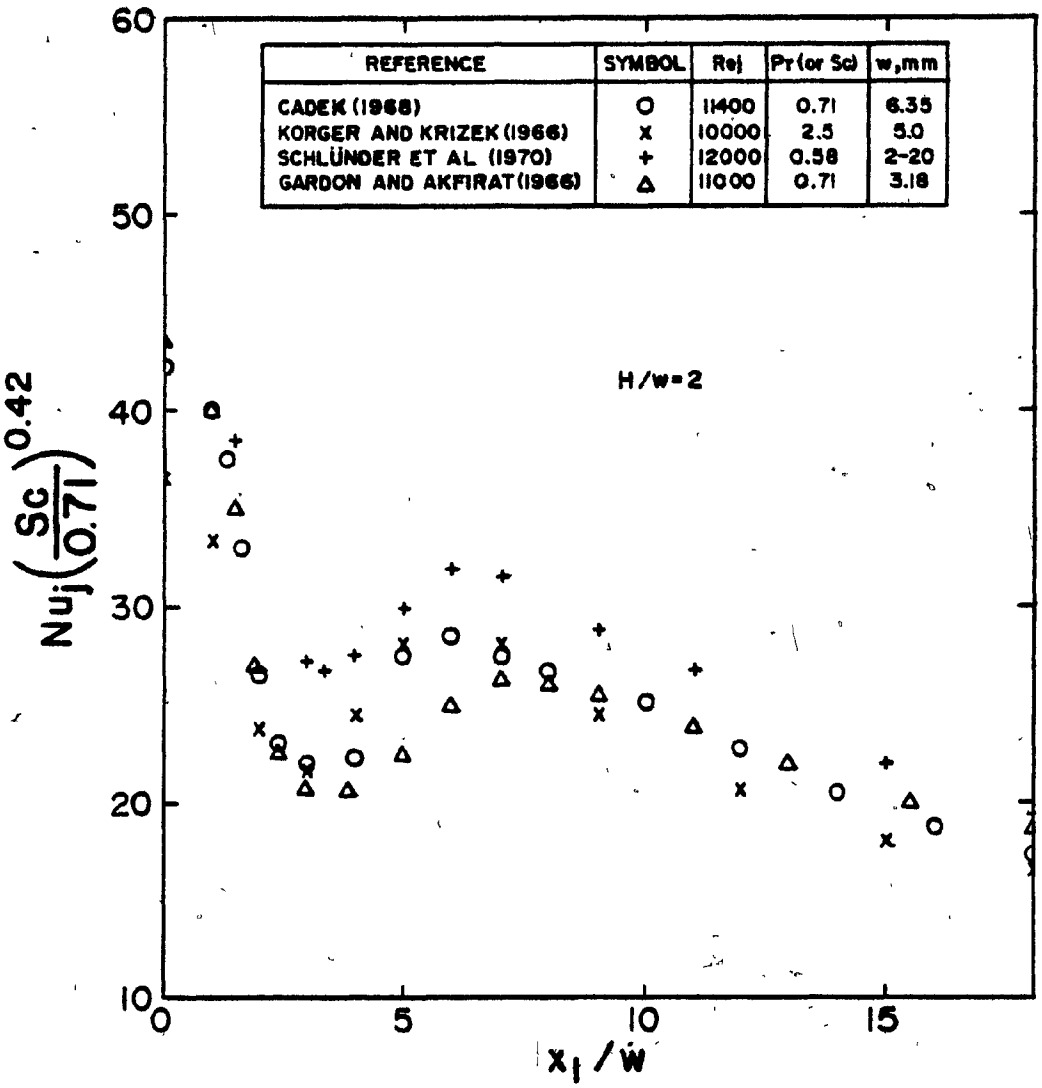


FIGURE 1.4. Local heat transfer distribution at H/w = 2 and $Re_j \simeq 11000$

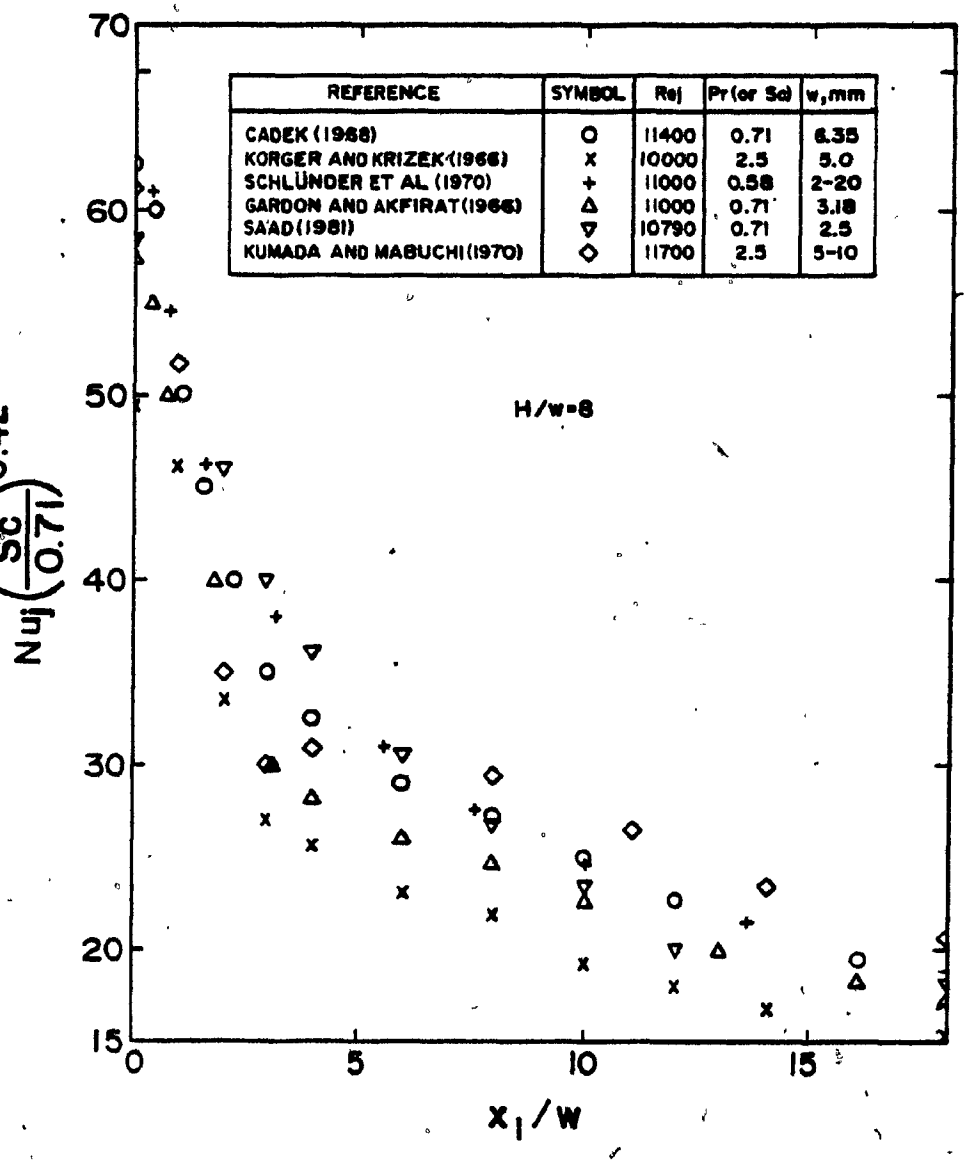


FIGURE 1.5. Local heat transfer distribution at H/w = 8 and $Re_j \simeq 11000$

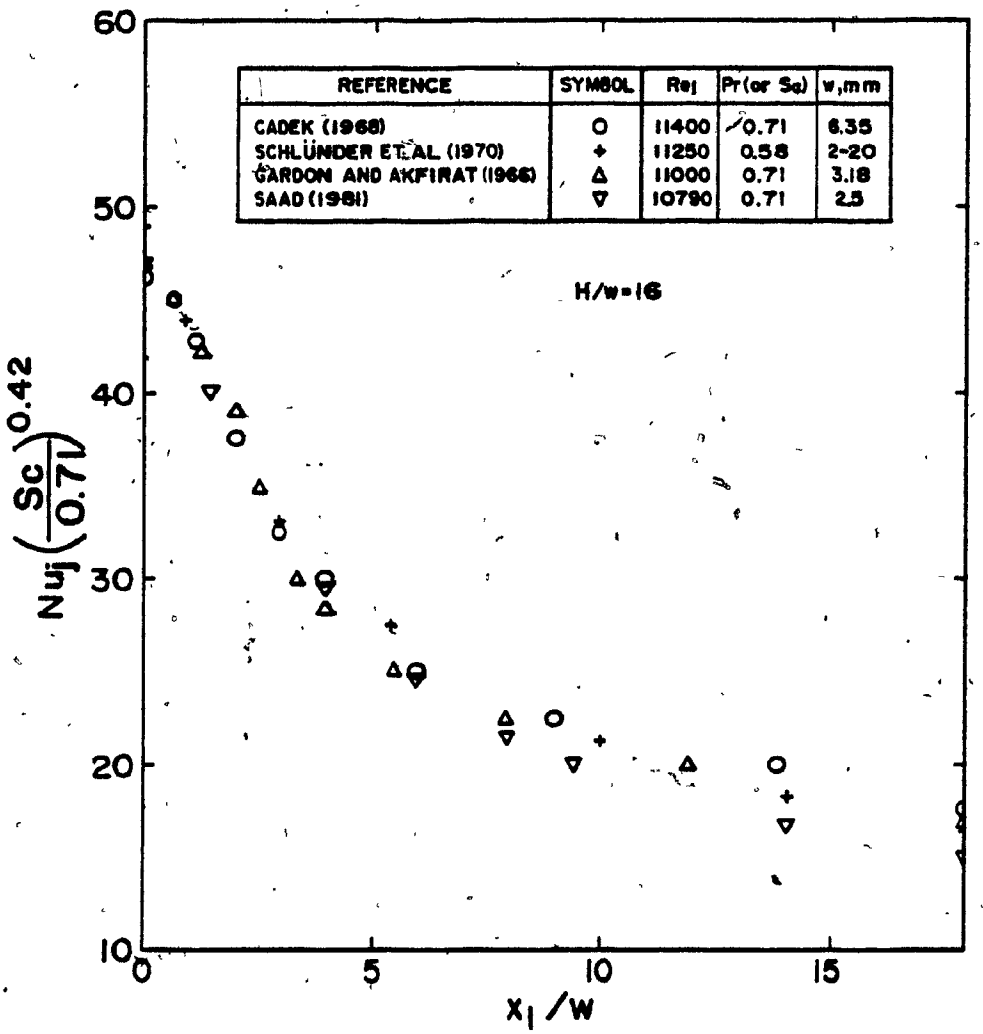


FIGURE 1.6. Local heat transfer distribution at H/w = 16 and $Re_j \simeq 11000$

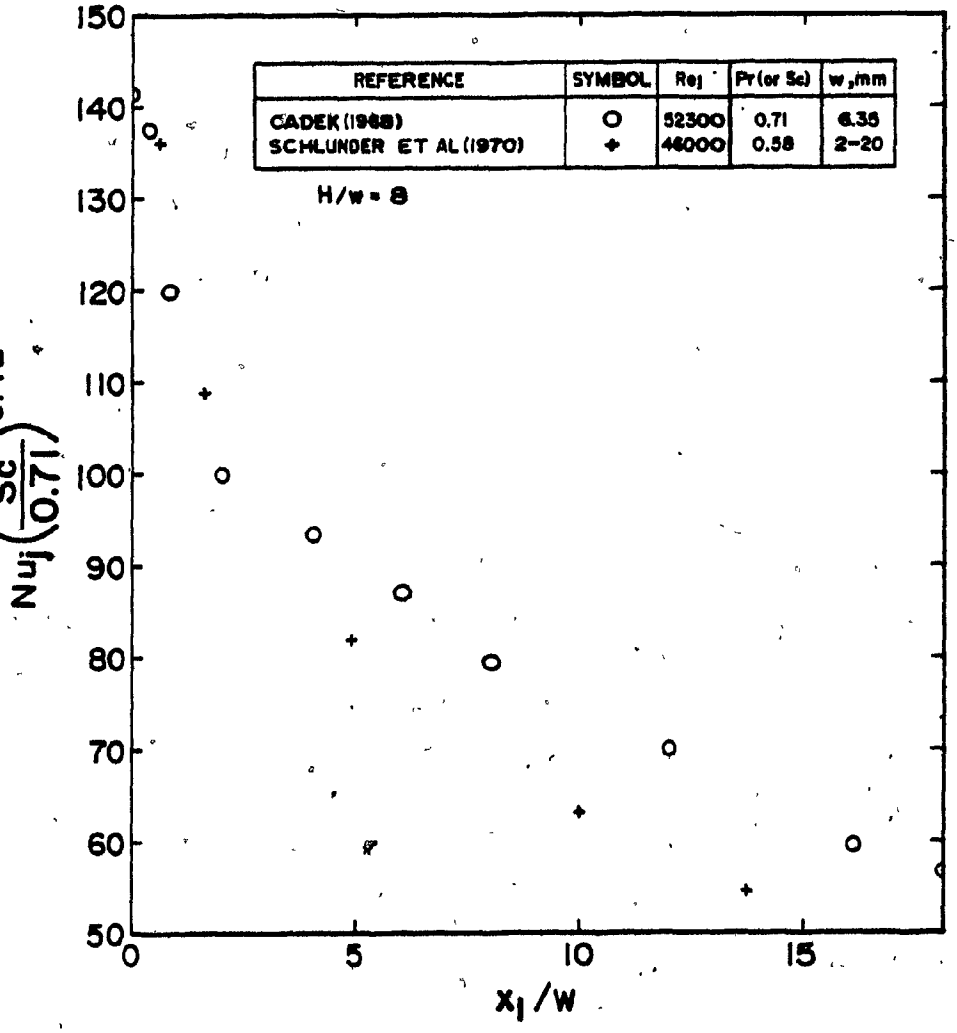


FIGURE 1.7. Local heat transfer distribution at $H/w = 8$ and $Re_j \simeq 50000$

nozzle geometry and other upstream boundary conditions are only important at relatively small impingement surface spacings.

The shape of the transfer profiles over spacings, H/w, of 2, 8 and 16 vary considerably as can be seen from Figures 1.4, 1.5 and 1.6, with the secondary maxima for spacings as close as H/w = 2 disappearing at a high spacing. The explanation for this behaviour, first given by Gardon and Akfirat (44), is that the minimum marks the onset of boundary layer transition from laminar to turbulent, while the maximum marks completion of this transition. The onset of transition can be related to the end of the region of steep pressure gradients at the impingement surface, such gradients providing the mechanism for maintaining a laminar-like boundary layer under fully turbulent jets. Transfer rates in the stagnation region increase for H/w > 2 due to the enhancing effect of mixing-induced turbulence on heat transfer in a laminar-like boundary layer subjected to a favourable pressure gradient. Outside the potential core region the axial jet velocity starts to decrease, while the absolute turbulence level continues to rise, reaching a maximum a spacing, H/w, of about 8-10 (Saad (125), leading to maximum stagnation point transfer rates at about H/w ≈ 8. The location of the minima and maxima in transfer rates for H/w < 8 are reported by Cadek (26) as well as by Saad (125)) to shift towards the stagnation point with increasing Re_j. Although by H/w = 8, Figure 1.5, the off-stagnation peaks no longer occur, there remains some indication of change in the character of the flow because an abrupt change in slope of the profiles occurs in the region 2w to 4w

from stagnation. The change again becomes more significant with increasing Re_j, as can be seen in Figure 1.7. At $H/w = 8$ Cadek (26) obtains a small secondary maximum at $x_1/w = 3.5$ again when Re_j is increased to 102700. At $H/w = 16$ the change of slope in the profiles has disappeared and a perfectly bell-shaped distribution, Figure 1.6, is obtained. The absence of evidence of boundary layer transition from the heat transfer profiles at large H/w spacings could be taken as indicating that the boundary layer is turbulent from the outset. On the other hand, examination of stagnation point transfer rates at $H/w = 16$ and 40 measured by Cadek (26), Schlünder et al. (133), Gardon and Akfirat (45) and Saad (125) for $Re_j \geq 2000$ in Figure 1.8 shows that Nu_{oj} is well represented by the correlation of Gardon and Akfirat (45)

$$Nu_{oj}\left(\frac{Sc}{0.71}\right)^{0.42} = 1.2\ Re_j^{0.58}(H/w)^{-0.62} \qquad (1.2)$$

It is notable that the Re_j exponent in this correlation, 0.58, is still much closer to 0.5, the value corresponding to a laminar boundary layer, than to the 0.8 exponent typical of turbulent boundary layers.

With respect to flow phenomena in the impingement region the view of Yokobori et al. (156) is pertinent, namely, that the well ordered structures in the stagnation region for $4 < H/w < 12$ play an important role in enhancement of stagnation heat and mass transfer rates. The mechanism is thought to be a periodic surface boundary layer renewal caused by the vortex-

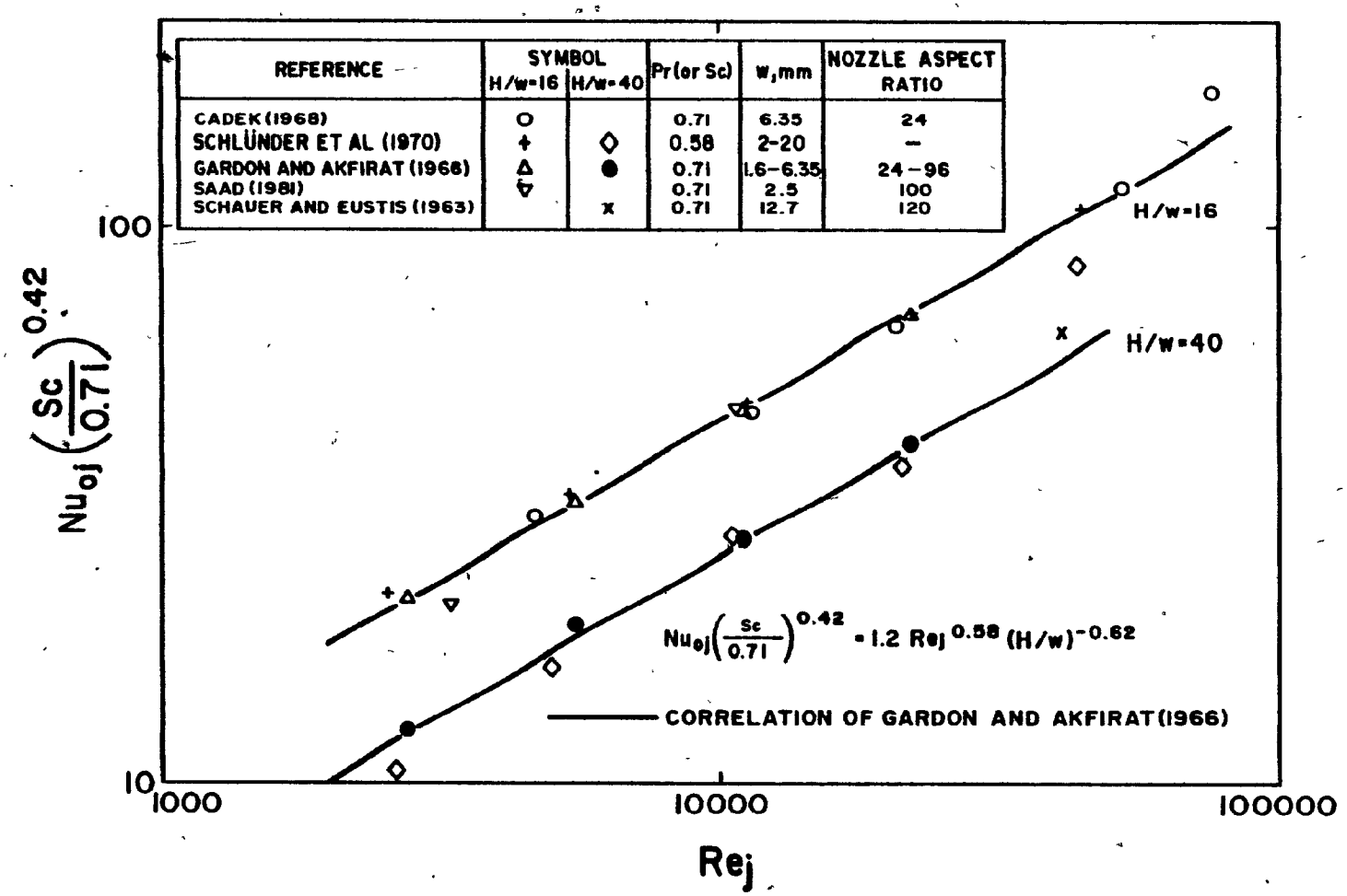


FIGURE 1.8. Correlation of stagnation point heat transfer

pairs in the stagnation region.

In the wall jet region the Re_j exponent is very close to the turbulent boundary layer value of 0.8, as is shown by Cadek and Zerkle (25). Thus even at large values of impingement surface spacing such as H/w = 16, transfer rates in the stagnation and wall jet region still show a clear distinction between behaviour characteristic of respectively laminar and turbulent boundary layer flow. The evidence available is consistent with the hypothesis that, when the transfer rates in the stagnation region are enhanced strongly by the action of a highly turbulent jet, the stagnation region boundary layer remains laminar-like but with transfer rates across it strongly enhanced by turbulent effects. Consequently the transition from this modified laminar boundary layer to a fully turbulent one takes place without the production of the off-stagnation peaks which occur at close impingement surface spacings. Another possible explanation for the bell-shaped curve, given by Gardon and Akfirat (44), is that the transition becomes gradual because of the more gradual diminution of pressure gradients at increasing H/w. However, it has already been noted that Saad (125) demonstrated that normalized impingement surface pressure profiles in the impingement region collapse to a single profile when lateral distance is expressed as X_1/H, this single general profile applying for the wide range of impingement surface spacings, H/w, from 4 to 16.

The effect of turbulence intensity in increasing stagnation

point heat transfer has been quantified by Cadek (26), by comparing his experimental heat transfer results with a theoretical solution based on the experimental pressure distribution in the stagnation region and laminar boundary layer theory. It appeared that for each H/w the turbulence augmentation effect was about constant over the entire stagnation region. Cadek (26) did not correlate the increase in heat transfer with axial turbulence intensity because this parameter was not measured. Later Andreyev et al. (4) applied essentially the same procedure to the measurements of Gardon and Akfirat (44) to correlate the effect of axial turbulence intensity with enhancement of stagnation heat transfer. Now Saad (125) has correlated enhancement of stagnation heat transfer with arrival turbulence intensity $(Tu_a)^n$, the turbulence intensity in a free jet at the same distance from the nozzle exit as the actual impingement surface spacing from the nozzle. On this basis he obtained values for the exponent n of 0.41 for $4 < H/w < 8$ but only 0.10 for $8 < H/w < 16$. The larger value of the exponent n for spacings of 4 to 8 could be related to the presence of a large fraction of low frequency turbulence at this range of spacings, caused by the ordered structures in the stagnation region. This explanation is consistent with Mujumdar (99) having shown that low frequency turbulence energy is more effective in increasing transfer rates at the forward stagnation point of a cylinder. The decrease in exponent, n, with increasing levels of turbulence may also reflect the decreasing potential for increase of heat transfer as the transfer rate is enhanced. At values of

Re_j of 2000 and 80000 the actual rates of heat transfer according to equation (1.2) of Gardon and Akfirat (45), shown in Figure 1.8, correspond at H/w = 16 to increases of 82% and 145% above the values given by the theoretical analysis of Cadek (26) based on laminar boundary layer theory. For H/w < 14 the best practice would be to consult those references of Figure 1.8 having nozzle design and upstream boundary conditions most similar to the case of interest.

Transfer rates in the wall jet region are proportional to Re_j^n with values of n variously reported as 0.8 (Kumada and Mabuchi (80) and many others) and 0.8571 (Cadek (26)). Consequently the relative contribution of wall jet transfer to the total transfer increases with increasing Re_j. One reflection of this difference is that the off-stagnation maxima are lower than the stagnation peak at low Re_j but become larger than the stagnation peak at high Re_j. For conditions which do not give rise to off-stagnation peaks, this difference changes the shape of the heat transfer profiles. This effect makes it impossible to obtain a generalized profile for heat transfer distribution, as has been established by Saad (125).

The three important correlations reported for average heat and mass-transfer rates under a single impinging slot jet, those of Gardon and Akfirat (45), Schlünder et al. (133) and Saad (125), are given in Table 1.2. The correlation of Schlünder et al. (133) has the widest range of applicability and gives almost the same results as the correlation of Gardon and Akfirat (45), as was shown by Obot et al. (104).

With respect to laminar slot jets, experimental heat and mass transfer studies have been reported by Gardon and Akfirat (45), Sparrow and Wong (139) and Masliyah and Nguyen (89). The latter two studies relate to jets with a fully developed velocity profile at the nozzle exit, while the first study was done with a velocity profile intermediate between fully developed and flat. A large influence of velocity profile at the nozzle exit has also been shown in the numerical work of van Heiningen et al. (147). The range of validity of laminar flow for an impinging slot jet is discussed in detail subsequently in Section 2.2.

The influence of throughflow and impingement surface motion, a prime motivation of this work, has already been reviewed in Section 1.2.

All analytical solutions for heat and mass transfer under an impinging slot jet are based on matching at their connecting boundaries the analytical or semi-analytical solutions of the flow in the four characteristic regions (Figure 1.2). Subsequently the thermal boundary layer equation is solved to obtain the transfer rate at the wall. This procedure has been applied by Miyazaki and Silberman (97) and Sparrow and Lee (138) to the impingement region of a laminar slot jet at small H/w spacing for respectively a flat and a parabolic velocity profile at the nozzle exit. The flow and thermal boundary layer equations were solved numerically, while the velocity along the surface, obtained from the inviscid flow analysis, was used as the "free stream" boundary condition. For a flat exit profile and H/w $\geq$ 1.5 Miyazaki and Silberman (97) derive for stagnation heat

transfer

$$Nu_{oj} = 0.51\ Re_j^{0.5} Pr^{0.373} \tag{1.3}$$

For a parabolic velocity profile and $H/w > 0.5$ the stagnation results of Sparrow and Lee (138) can be written as

$$Nu_{oj} = 1.00\ Re_j^{0.5} Pr^{0.373} \tag{1.4}$$

Comparison of equations (1.3) and (1.4) shows that at the same Re_j the stagnation heat or mass transfer is effectively doubled by changing the velocity profile from flat to parabolic. It should be remembered that these solutions are valid only as long as jet entrainment effects are negligible. The solution has been extended to a uniform slot jet impinging on a circular cylinder by Miyazaki and Sparrow (98).

A similar approach was used by Schauer and Eustis (128), Cadek (26) and Kumada and Mabuchi (79) for the stagnation region of turbulent slot jets, but in this case the "free stream" boundary condition was obtained from experiments or from the wall pressure distribution. Good agreement between theory and experiments was found by Cadek (26) for $H/w \leq 4$. For $H/w \geq 5$ the experimental results are progressively higher than the theory because of the effect of turbulence discussed earlier. In the turbulent wall jet region the three references mentioned above follow essentially the same path as Myers *et al.* (101, 102) for a plane turbulent wall jet, by dividing the flow into two regions. The so-called "inner" layer of the wall jet is

solved using integral techniques and is patched to the "outer" layer at the point of maximum velocity. The "outer" layer is assumed to behave as a free jet at a distance $X_1 + H$ from the jet exit plane. The thermal boundary is also handled by the integral method. Finally, the heat transfer is calculated using a modified Reynolds analogy. Good agreement with experimental data are reported.

The more general iterative finite difference techniques for solution of the full governing equations describing the flow and heat transfer of an impinging slot jet have been reported by Wolfshtein (153), Russell and Hatton (123) and Folayan (41). This numerical work was discussed in Section 1.2 and will be analyzed in detail in Section 2.3.

1.5 Outline of the Thesis

Chapter 2 is devoted to the numerical prediction of a confined impinging slot jet by solving the full equations of motion and thermal energy with finite difference techniques. In the first part of Chapter 2, concerned with the laminar jet, the approach of Gosman *et al.* (49) is applied to solve the equations of motion in their vorticity-stream function form. After investigation of the accuracy and convergence properties of the program when applied to the confined laminar impinging jet flow configuration, the influence of Reynolds number, impingement surface spacing, temperature variable properties and through-flow rate on the flow and heat transfer characteristics are discussed. The so-called "TEACH-T" program of the Imperial

College Group, London is then applied to solve the velocity-pressure form of the equations of motion for the case of a confined turbulent impinging jet. The effect of turbulence on the mean flow was incorporated via the turbulent viscosity concept, while the turbulent viscosity itself was calculated algebraically from the turbulent kinetic energy and the dissipation rate of the turbulent kinetic energy, both described by a partial differential transport equation. The impingement heat transfer results obtained with this so-called two-equation turbulence model are strongly influenced by the use of laminar or turbulent wall-flux laws and on the treatment of diffusion and source terms in the k and ε equations. Five numerical predictions of impingement heat transfer are compared with experimental heat transfer distributions obtained in Chapter 4 for spacings, H/w, of 2.6 and 6.0, each at two Reynolds numbers, as well as with one experiment of Cadek (26) for H/w = 8.0. Recommendations are given for development of an improved method of numerical prediction.

In Chapter 3 the experimental equipment and procedures are described. The experimental facility was built for study of local heat transfer under a single confined turbulent jet of air impinging on a moving surface with or without throughflow at the surface. The moving surface was obtained by forming the impingement surface as the cylindrical porous wall of a rotating drum, 0.482 m in diameter. Two slot jets, one hot and one cold, impinging on this surface from 180° opposed positions provided overall steady-state operation. The length of each

slot, 203 mm, equalled the length of the cylindrical impingement surface. The experimental facility was closed with circular plates at the ends of the rotating cylinder and with a cylindrical confinement hood concentric with and at a spacing H = 37 mm from the 0.482 m diameter impingement surface. The experimental equipment, called the SIMTEST apparatus, was designed for future use with a wide range of spacings H. In the present work, however, the spacing was fixed at H = 37 mm which, with selection of fixed nozzle widths, w, of 6.2 and 14.1 mm for the hot and cold jets respectively, corresponded to dimensionless spacings, H/w, of 6.0 and 2.6. The design with nozzles of different widths for the heating and cooling jets on the opposite sides of the impingement cylinder had the advantage that for each experimental run, results for the two spacings, H/w, were provided simultaneously.

Local heat transfer was measured with a high sensitivity, fast response, thin film heat flux sensor. With this sensor it is possible to achieve essentially instantaneous monitoring of the surface temperature of the sensor with a resolution of about $0.001^{\circ}C$ at a sampling speed of 5000 measurements per second. Local Nusselt number could be determined from this measurement of surface temperature through solution of the unsteady-state heat conduction equation. Use of a computer for on-line data acquisition permits determination of about 500 values of local Nusselt number per rotation. Profiles of local Nusselt number are produced by a plotter directly as computer output from the data processing. After testing and calibration of the equipment

and investigation of the influence of a number of operating procedures on the results, the SIMTEST apparatus was used to generate Nusselt number profiles.

The experimental results are discussed in Chapter 4. The influence of size of the temperature driving force is studied first. For the moderate temperature range of this study (ΔT to $50^{o}C$) it is found possible to eliminate the influence of the temperature dependency of physical properties on the heat transfer profiles, irrespective of whether it is a heating or a cooling jet. The influence of Reynolds number on local and average heat transfer results, obtained without throughflow and at low speeds of rotation, is presented next. The analysis of effect of Reynolds number considers the overall heat transfer profiles as well as heat transfer at the stagnation point, in the stagnation region, at the off-stagnation maximum, in the wall jet region and finally the integrated mean heat transfer. Analysis of the influence of impingement surface motion on heat transfer includes consideration of implications of this variable for the "Papridryer" design. Finally, the extent to which influence on heat transfer of throughflow at the impingement surface can be studied with an impermeable sensor is discussed.

In the final chapter, 5, the important contributions of this study and suggestions for further work are presented.

CHAPTER 2

NUMERICAL PREDICTIONS

2.1 Introduction

The numerical predictions of the flow and temperature field of a confined impinging slot jet presented in this chapter are obtained by solving the full equations of motion and thermal energy with finite difference techniques. Two quite different numerical schemes are used, one for the laminar case, the other for the turbulent jet. The flow and geometrical conditions for validity of the laminar flow assumption are discussed. For the laminar jet case the equations of motion and thermal energy are transformed into the equivalent vorticity-stream function form. Following Gosman et al. (49), the transformed equations of motion and thermal energy are represented by a general differential equation and subsequently approximated by a general finite difference equation. Application of the finite difference equation for all variables at each grid point, together with the boundary conditions, leads in an iterative procedure to a converged solution of the variables at all the grid points. After investigation of the accuracy and convergence properties of the vorticity-stream function program when applied to the laminar impinging jet configuration, the influence of flow, geometric and physical property variables on the flow and heat transfer characteristics are predicted.

For the turbulent jet the velocity-pressure form of the equations of motion and the thermal energy equation are solved with the so-called "TEACH-T" program of the Imperial College

group (Gosman, Patankar, Spalding and others). The effect of turbulence on the mean flow is incorporated via the turbulent viscosity concept, while the turbulent viscosity itself is calculated algebraically from the turbulent kinetic energy, k, and the dissipation rate of turbulent kinetic energy, ε; both described by a partial differential transport equation. A turbulence model of this kind is called a two-equation turbulence model. As with the laminar jet calculations, the equations for turbulent flow and thermal energy are cast into a general partial differential equation, although in contrast to the vorticity-stream function program, a staggered grid is used in TEACH-T for respectively the velocities and all scalar quantities (k, ε, temperature T and pressure P) in the finite difference approximation. The finite difference equations relating the velocities and scalar quantities at the grid nodes are solved together with the boundary condition in an iterative procedure until convergence is reached. Numerical predictions of heat transfer at the impingement surface for the five computer simulations made are compared with experimental heat transfer distributions obtained in Chapter 4 as well as with one experiment of Cadek (26). The differences between predicted and experimental heat transfer distributions in the stagnation and early wall jet region are attributed to the turbulent viscosity concept of the two-equation turbulence model as well as to the boundary conditions describing the transport of momentum and temperature to the impingement surface. Based on this investigation several recommendations are given to improve the prediction of heat transfer in the stagnation region.

2.2 Laminar Impinging Slot Jet

The two-dimensional impinging jet system is shown in Figure 2.1. The symmetry of the system implies a stationary impingement surface. At some considerable distance from the stagnation point the impingement surface is made impermeable for reasons of the numerical computational procedures, as will be discussed subsequently. The flow field is closed by a confinement surface parallel to the impingement surface. The laminar flow condition requires that the jet Reynolds number Re_j and geometric parameters, dimensionless spacing of the impingement surface from the nozzle exit, H/w, and dimensionless distance from the stagnation point X_1/w, remain within certain limits. Before stating the regions of validity for laminar flow, a qualitative description of the impinging jet flow will be given.

Upon emergence from the nozzle exit the outer layers of the jet stream entrain fluid from the environment, thereby setting up a mixing zone. The inner layers of the jet stream, the so-called potential core, are not involved in the mixing process. The mixing zone progressively reduces the size of this core, which eventually disappears (Sparrow and Wong (139)). Turbulence is generated by the mixing process in the region of high lateral gradients in mean velocity. The gradients and thus the mixing will decrease when the jet velocity profile at the nozzle exit is changed from flat to parabolic. The gradients also decrease when the flow field is closed by a confinement surface, as will be shown subsequently. Consequently the regions of validity for the laminar flow assumption for the present impinging jet system

are conservative when they are derived from experiments without a confinement surface. The lower the value of Re_j, the larger the distance from the nozzle exit for which the jet retains its laminar character. When the jet is still laminar on impact, the flow remains laminar in the impingement region due to favorable pressure gradients in this region. Beyond the impingement region the wall jet eventually becomes turbulent under the influence of free stream turbulence generated at the outer layers of the jet and in the absence of the strongly favorable pressure gradient that exists only in the impingement region (Gardon and Akfirat (44)). This transition occurs at larger values of X_1/w when Re_j and H/w are decreased.

There is considerable experimental evidence available for the general nature of flow of laminar impinging jets. Schuh and Pettersson (134) conclude from their average heat transfer results for an unconfined impinging slot jet with an almost flat velocity profile at the nozzle exit that the jet is laminar at $H/w = 4$ for $Re_j \leq 1300$ and X_1/w up to 50. On closer examination of the data, the transition to turbulent flow must have taken place somewhere between $Re_j = 630$ and 1260.

Gardon and Akfirat (45) measured local heat transfer under an unconfined impinging slot jet with a fast response heat flux sensor. The slower turbulent heat transfer fluctuations could be measured with the sensor. The velocity profile at the nozzle exit was intermediate between flat and parabolic. From the data it can be concluded that the jet was still laminar on impact for $Re_j = 450$ when $H/w < 45$, or for $Re_j = 650$ when $H/w < 11$, or for

Re_j = 950 when H/w < 8. At H/w = 4 and Re_j = 950 the wall jet remains laminar up to X_1/w = 5. For Re_j = 450 and H/w = 4 transition does not occur up to the maximum distance from the stagnation point in this experiment, X_1/w = 50.

Sparrow and Wong (139) measured local heat transfer under an unconfined, initially laminar impinging slot jet with the naphthalene sublimation technique. The velocity profile at the nozzle exit was parabolic. Their results roughly confirm the conditions derived from the data of Gardon and Akfirat for the jet to be laminar on impact. The small humps in the heat transfer distribution for $Re_j \geq 650$ and $2 \leq H/w \leq 10$ in the region of $1 \leq X_1/w \leq 3$ are attributed to free stream turbulence.

Finally, the flow visualization techniques of Marple et al. (87) showed that an impinging jet system, as shown in Figure 2.1, with a flat velocity profile at the nozzle exit, is still laminar at X_1/w = 5 for Re_j = 1150 and H/w = 1.

At the three values of Re_j investigated in the present study, 100, 450 and 950, it can therefore be concluded from previous studies that the laminar flow assumption used in the present numerical calculation is valid for all cases studied, except for $X_1/w > 5$ for the case of Re_j = 950 and H/w = 4.

2.2.1 Mathematical Description of the Problem

The flow field and temperature distribution of the impinging jet system are described by the continuity equation, the Navier-Stokes equations and the energy equation , which are based on the conservation laws of respectively mass, momentum

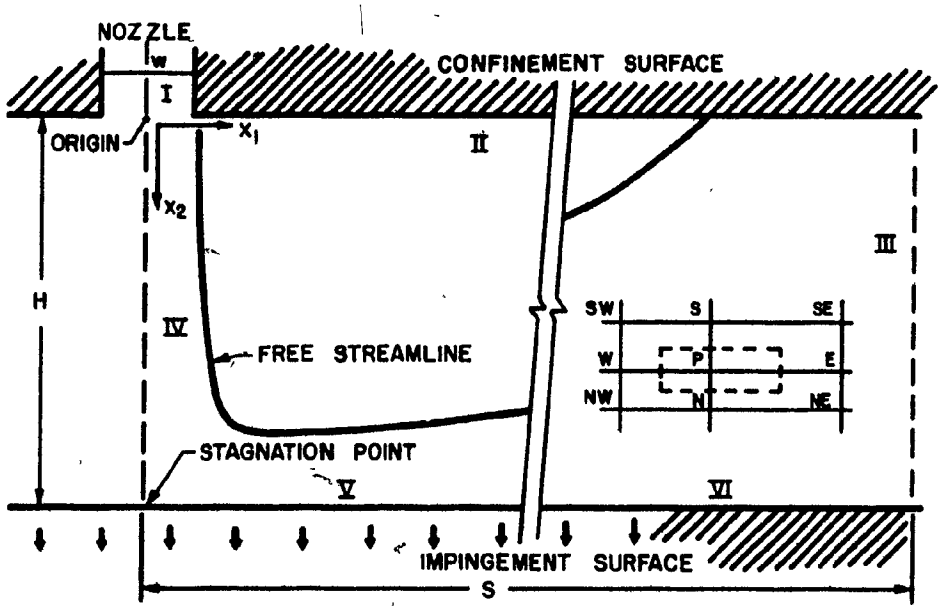


FIGURE 2.1. Impinging jet system for numerical prediction

and energy. When the flow is laminar and steady, the equations take the following form in two-dimensional Cartesian coordinates

(a) Continuity equation

$$\frac{\partial \rho U_1}{\partial X_1} + \frac{\partial \rho U_2}{\partial X_2} = 0 \tag{2.1}$$

(b) Navier-Stokes equation

X_1 component

$$\rho U_1 \frac{\partial U_1}{\partial X_1} + \rho u_2 \frac{\partial U_1}{\partial X_2} = - \frac{\partial P}{\partial X_1} + \frac{\partial}{\partial X_1}\left[\mu\left(2 \frac{\partial U_1}{\partial X_1} - \frac{2}{3} \nabla \cdot \underline{U}\right)\right]$$

$$+ \frac{\partial}{\partial X_2}\left[\mu\left(\frac{\partial U_1}{\partial X_2} + \frac{\partial U_2}{\partial X_1}\right)\right] \tag{2.2}$$

X_2 component

$$\rho U_1 \frac{\partial U_2}{\partial X_1} + \rho U_2 \frac{\partial U_2}{\partial X_2} = - \frac{\partial P}{\partial X_2} + \frac{\partial}{\partial X_2}\left[\mu\left(2 \frac{\partial U_2}{\partial X_2} - \frac{2}{3} \nabla \cdot \underline{U}\right)\right]$$

$$+ \frac{\partial}{\partial X_1}\left[\mu\left(\frac{\partial U_1}{\partial X_2} + \frac{\partial U_2}{\partial X_1}\right)\right] \tag{2.3}$$

when buoyancy effects are neglected.

(c) Energy equation

$$\frac{\partial (\rho U_1 T)}{\partial X_1} + \frac{\partial (\rho U_2 T)}{\partial X_2} = \frac{\partial}{\partial X_1}\left(\frac{\lambda}{C_p} \frac{\partial T}{\partial X_1}\right) + \frac{\partial}{\partial X_2}\left(\frac{\lambda}{C_p} \frac{\partial T}{\partial X_2}\right) \tag{2.4}$$

In this formulation of the energy equation, viscous dissipation and temperature change due to compression are neglected. This assumption as well as neglect of buoyancy effects are checked in the discussion of results. Other restrictions to the energy equation in this form are that specific heat is temperature independent and the fluid is an ideal gas.

With the introduction of the stream function ψ, the continuity equation is automatically satisfied. The stream function is a scalar quantity defined by

$$\rho U_1 = \frac{\partial \psi}{\partial X_2} \tag{2.5}$$

and

$$\rho U_2 = - \frac{\partial \psi}{\partial X_1} \tag{2.6}$$

By cross differentiation of the two components of the Navier-Stokes equation, subtraction and introduction of the vorticity defined as

$$\omega = \frac{\partial U_2}{\partial X_1} - \frac{\partial U_1}{\partial X_2} \tag{2.7}$$

The vorticity equation is obtained

$$\frac{\partial (\rho U_1 \omega)}{\partial X_1} + \frac{\partial (\rho U_2 \omega)}{\partial X_2} = \frac{\partial^2}{\partial X_1^2}(\mu\omega) + \frac{\partial^2}{\partial X_2^2}(\mu\omega) + S_\rho + S_\mu \tag{2.8}$$

with S_ρ, the term due to variable density defined as

$$S_\rho = \frac{\partial}{\partial X_1}\left(\frac{U_1^2 + U_2^2}{2}\right)\frac{\partial \rho}{\partial X_2} - \frac{\partial}{\partial X_2}\left(\frac{U_1^2 + U_2^2}{2}\right)\frac{\partial \rho}{\partial X_1} \qquad (2.9)$$

The term S_μ, due to variable viscosity, is defined as

$$S_\mu = 2\,\frac{\partial^2}{\partial X_1^2}\left(\mu\,\frac{\partial U_1}{\partial X_2}\right) - 2\,\frac{\partial^2}{\partial X_2^2}\left(\mu\,\frac{\partial U_2}{\partial X_1}\right) + 2\,\frac{\partial^2}{\partial X_1 \partial X_2}\left(\mu\left[\frac{\partial U_2}{\partial X_2} - \frac{\partial U_1}{\partial X_1}\right]\right) \qquad (2.10)$$

The advantage of the introduction of vorticity is elimination of pressure from the Navier-Stokes equations, while the 2 components of the Navier-Stokes equations are reduced to one equation.

The primitive variables U_1 and U_2 in equations (2.4), (2.7) and (2.8) are replaced by the stream function ψ by using equations (2.5) and (2.6). Following Gosman *et al.* (49), the three resulting equations which describe the flow and temperature field of the laminar jet system can be represented by the general differential equation

$$a_\phi\left[\frac{\partial}{\partial X_1}\left(\phi\,\frac{\partial \psi}{\partial X_2}\right) - \frac{\partial}{\partial X_2}\left(\phi\,\frac{\partial \psi}{\partial X_1}\right)\right] - \frac{\partial}{\partial X_1}\left[b_\phi\,\frac{\partial}{\partial X_1}(c_\phi \phi)\right]$$

$$- \frac{\partial}{\partial X_2}\left[b_\phi\,\frac{\partial}{\partial X_1}(c_\phi \phi)\right] + d_\phi = 0 \qquad (2.11)$$

where ϕ is the general dependent variable. The coefficients a_ϕ, b_ϕ, c_ϕ and d_ϕ for the three alternate variables are listed in Table 2.1.

---

* van Heiningen *et al.* (149) found the so-called "vorticity-velocity" scheme of Chien and Schetz (31) to be invalid in that mass is not conserved because, in differentiation of the continuity equation, $(\partial/\partial x)[(\partial u/\partial x) + (\partial v/\partial y) + (\partial w/\partial z)] = 0$ is also satisfied by $(\partial u/\partial x) + (\partial v/\partial y) + (\partial w/\partial z) =$ constant.

TABLE 2.1. Coefficients in Equation (2.11)

ϕ	a_ϕ	b_ϕ	c_ϕ	d_ϕ
ω	1	1	μ	$- S_\rho - S_\mu$
ψ	0	$1/\rho$	1	$- \omega$
T	1	λ/C_p	1	0

With introduction of dimensionless variables, the mathematical formulation of the problem is freed from arbitrarily selected units. The impingement surface spacing, H, and the average jet velocity U_j are the characteristic length and velocity used for nondimensionalization. For nondimensionalization of the physical properties, conditions at the nozzle exit are used. The nondimensional variables are:

$$\left.\begin{aligned} \omega^* &= \frac{\partial U_2^*}{\partial X_1^*} - \frac{\partial U_1^*}{\partial X_2^*} \\ \rho^* U_1^* &= \frac{\partial \psi^*}{\partial X_2^*} \quad \text{and} \quad \rho^* U_2^* = - \frac{\partial \psi^*}{\partial X_1^*} \\ T^* &= (T - T_w)/(T_j - T_w) \end{aligned}\right\} \qquad (2.12)$$

with $U_1^* = U_1/U_j$, $U_2^* = U_2/U_j$, $X_1^* = X_1/H$ and $X_2^* = X_2/H$ and $\rho^* =$

ρ/ρ_j and $\mu^* = \mu/\mu_j$. As equation (2.11) is completely general it remains unchanged, while the variables and coefficients are now nondimensional. The nondimensional coefficients are listed in Table 2.2.

TABLE 2.2. Nondimensional Coefficients for Equation (2.11)

ϕ^*	a_ϕ^*	b_ϕ^*	c_ϕ^*	d_ϕ^*
ω^*	1	$\frac{w}{H}\frac{1}{Re_j}$	μ^*	$-S_\rho^* - \frac{w}{H}\frac{1}{Re_j}S_\mu^*$
ψ^*	0	$1/\rho^*$	1	$-\omega^*$
T^*	1	$\frac{w}{H}\frac{\mu^*}{Re_j Pr}$	1	0

S_ρ^* and S_μ^* are the same as S_ρ and S_μ in respectively equations (2.9) and (2.10), but an * as superscript as on all the variables. The three nondimensional differential equations describe any laminar, steady two-dimensional flow (with the minor restrictions noted during derivation of the equations). The characteristics of a specific impinging jet system are introduced by the boundary conditions. Since the equations are elliptic in nature, Roache (117), boundary conditions must be specified at all boundaries in Figure 2.1.

Boundary I: The Nozzle Exit

From the fully developed velocity profile between two infinite parallel plates given by Schlichting (131)

$$U_2^* = 3/2\{1 - 4(H/w)^2 X_1^{*2}\} \tag{2.13}$$

one can derive

$$\psi^* = -3/2\ X_1^*\{1 - 4/3(H/w)^2 X_1^{*2}\} \tag{2.14}$$

$$\omega^* = -12(H/w)^2 X_1^* \tag{2.15}$$

and $$T^* = 1 \tag{2.16}$$

For a flat velocity profile the conditions are

$$\psi^* = -X_1^* \tag{2.17}$$

$$\omega^* = 0 \tag{2.18}$$

and $$T^* = 1 \tag{2.19}$$

Boundary II: Confinement Surface

Since the confinement surface is impermeable, the value of the stream function along it is equal to the stream function value at the corner of the nozzle exit, i.e.

$$\psi^* = -\frac{1}{2}\ w/H \tag{2.20}$$

$$T^* = 1 \tag{2.21}$$

The no-slip boundary condition is used to generate the boundary condition for the vorticity (see Appendix 1).

$$\omega_W^* = - \frac{3(\psi_{NW}^* - \psi_W^*)}{(\frac{3}{8}\rho_W^* + \frac{5}{8}\rho_{NW}^*)(\Delta X_2^*)^2} - \frac{1}{2}\frac{(\frac{1}{4}\rho_W^* + \frac{3}{4}\rho_{NW}^*)}{(\frac{3}{8}\rho_W^* + \frac{5}{8}\rho_{NW}^*)}\omega_{NW}^* \tag{2.22}$$

with ψ_{NW}^*, ω_{NW}^* and ρ_{NW}^* the values of the variables ΔX_2^* from the confinement surface.

Equation (2.22) is derived using an integral approach and the assumption that vorticity varies linearly with distance from the wall. Another boundary condition for the vorticity is obtained from the assumption that vorticity near the wall is constant. This boundary condition is not preferred, however, since Gosman et al. (49) have shown that the uniform vorticity near the wall assumption does not agree with the numerically obtained vorticity profile near the wall. Moreover van Heiningen et al. (148) have shown that more accurate predictions are obtained for wall-deflected flows when employing the incompressible equivalent of equation (2.22). Which assumption should be used for vorticity variation near the wall from the point of view of numerical stability will be discussed subsequently.

A derivation from Taylor series expansion of an equation slightly different than (2.22) is given in Appendix 1 .

Boundary III: Outflow Region

Several boundary conditions for the outflow boundary are discussed by Roache (117). From the point of view of numerical stability it is advantageous to specify completely the variables at the outflow boundary. In fact, the conditions are now known at the exit. The boundary conditions recommended by Gosman et al. (49) in such a case are

$$\frac{\partial \psi^*}{\partial X_1^*} = \frac{\partial \omega^*}{\partial X_1^*} = \frac{\partial T^*}{\partial X_1^*} = 0 \qquad (2.23)$$

These conditions correspond to taking the streamlines parallel to the duct walls and ω^* and T uniform along the streamlines. With only outflow at Boundary III the choice of boundary conditions (2.23) has not much influence on the velocity and temperature distribution in the remainder of the computational area, Gosman (49). Under certain conditions inflow occurs over part of Boundary III. For such cases, several boundary conditions other than equation (2.23) were tested to establish the sensitivity of the flow and temperature field in the impingement region to the outflow boundary conditions. This aspect is discussed further subsequently.

Boundary IV: Axis of Symmetry

From the symmetry conditions one can derive

$$\psi^* = \omega^* = \frac{\partial T^*}{\partial X_1^*} = 0 \qquad (2.24)$$

Boundary V: Permeable Impingement Surface

With uniform throughflow the stream function becomes

$$\psi^* = - \frac{U_s}{U_j} X_1^* \tag{2.25}$$

Further

$$T^* = 0 \tag{2.26}$$

and for the vorticity, equation (2.22) is used.

Boundary VI: Impermeable Impingement Surface

At some distance from the stagnation point the surface is made impermeable in order to be able to specify parallel outflow at Boundary III. Also, for an impingement surface permeable to the outflow Boundary IV, there would be inflow near the surface at the outflow boundary, which is undesirable from a computational viewpoint. The boundary conditions for ω^* and T^* are the same as at Boundary V. The stream function is constant and equal to

$$\psi^* = - \frac{U_s}{U_j} X_{1T}^* \tag{2.27}$$

where X_{1T}^* is the nondimensional length of the permeable surface from the stagnation point.

The impinging jet problem is now completely described by the three differential equations for ω^*, ψ^* and T^* and the

appropriate boundary conditions. In the next section the numerical procedure for solution of the set of equations is presented.

2.2.2 Numerical Procedure

The equations described in the previous section can be solved by the method of finite differences. The finite difference scheme of Gosman et al. (49) was adopted for solution of the equations. As details of the scheme are comprehensively described in the book by Gosman et al. only the results of their analysis and changes made will be noted.

The general partial differential equation (2.11) in non-dimensional form is integrated over the control volume indicated by dashed lines, inset on Figure 2.1. The resulting general finite difference equation (F.D.E.), after making assumptions concerning the behaviour of ω^* and ψ^* within the control volume and along its boundaries, is

$$\phi_P^* = (CE_\phi \phi_E^* + CW_\phi \phi_W^* + CN_\phi \phi_N^* + CS_\phi \phi_S^* - d_{\phi P}^*)/ \\ (CE_{\phi,P} + CW_{\phi,P} + CS_{\phi,P} + CN_{\phi,P}) \qquad (2.28)$$

where

$$CE_\phi = |AE_\phi| + AE_\phi + c_{\phi E}^* BE_\phi \quad \text{in the "upwind" scheme} \qquad (2.29)$$

or

$$CE_\phi = \frac{1}{2}(c^*_{\phi E}\cdot BE_\phi + |AE_\phi| + |c^*_{\phi E}\cdot BE_\phi - |AE_\phi||) + AE_\phi \qquad (2.30)$$

in the "hybrid" scheme

with $CE_{\phi,P}$ equal to CE_ϕ with $c^*_{\phi E}$ replaced by $c^*_{\phi,P}$

and $$BE_\phi = (b^*_{\phi E} + b^*_{\phi P})/((X^*_{1E} - X^*_{1P})(X^*_{1E} - X^*_{1W})) \qquad (2.31)$$

$$AE_\phi = \frac{1}{2}\, a^*_\phi(\psi^*_S + \psi^*_{SE} - \psi^*_N - \psi^*_{NE})/((X^*_{2N} - X^*_{2S})(X^*_{1E} - X^*_{1W})) \qquad (2.32)$$

with similar expressions for CW_ϕ, CN_ϕ and CS_ϕ (see Appendix 2 for the other A's and B's).

Gosman et al. derive equation (2.28) with a flow-oriented (upwind) difference formulation for the non-linear convective terms. This leads to the "upwind" scheme of equation (2.29). A combination of central and upwind differences is used for the convective terms in the "hybrid" scheme (2.30) following Runchal (122) and Spalding (136). Because of their greater accuracy (Roache), central differences are used whenever instability is not produced. Central differences are used when the convection contribution $|AE_\phi|$ is smaller than the diffusion contribution $c^*_{\phi E}\cdot BE_\phi$. Upwind differences are used when the diffusion contribution is smaller than term $|AE_\phi|$. The general F.D.E. is applicable for each of the three variables ω^*, ψ^* and T^* at each grid point (except for the boundaries) of a grid covering the complete flow field.

After initializing the variables at all grid points, variables are successively updated at all inner grid points with the use of equation (2.28). The gradient-type boundary conditions are used to update variables at boundaries. This iterative process is repeated until the relative change of variables at all grid nodes is smaller than a specified value. The solution is then said to have converged. In order to limit computing time, initialization of the program was done by reading in the vorticity, stream function and temperature field of a previous converged solution which was as close as possible to the case to be calculated.

The convergence condition is that the residual

$$|(\phi_P^{*m} - \phi_P^{*m-1})/\phi_r^*| < 10^{-3} \tag{2.33}$$

must be satisfied at all grid points for all the dependent variables. ϕ_r represents the reference value for the different dependent variables, i.e. $\omega_r^* = 1$, $\psi_r^* = \psi^*_{\text{nozzle corner}}$ and $T_r^* = T^*_{\text{nozzle corner}}$. ϕ_r^* is not taken to be ϕ_P^{*m} as is done by Gosman et al. (49) because ω_P^{*m} can be very close to zero somewhere in the flow field. Because the location in the flow field of the maximum residual varies during the iterative process (the location of the maximum residual was printed), a plot of the maximum residual for each dependent variable against the iteration number does not give a smooth curve. A smooth curve is however obtained by plotting as a function of iteration number the sum of each dependent variable SUMNW (vorticity), SUMNF (stream

function) and SUMNT (temperature) at the inner grid points. The SUMNW will be used for graphical presentation of convergence of the solution because the vorticity is the last variable to stabilize.

2.2.2.1 Factors Influencing the Convergence of the Procedure

In order to obtain a converged solution the iterative procedure must be stable. The conditions for stability of the iterative procedure are given by Gosman et al. (49) as

(i) $$\left|(CE_\phi + CW_\phi + CN_\phi + CS_\phi)/(CE_{\phi,P} + CW_{\phi,P} + CN_{\phi,P} + CS_{\phi,P})\right| \leq 1 \qquad (2.34)$$

should be satisfied by all variables at each grid point inside the calculation domain. Since the C's are always positive with the "upwind" and "hybrid" scheme, this condition will be satisfied for all variables, except when the flow is compressible, because then the coefficients a_ϕ^*, b_ϕ^* and c_ϕ^* are not constant as is required in the derivation of (2.34).

(ii) $$\left|(CE_\phi + CW_\phi + CN_\phi + CS_\phi)/(CE_{\phi,P} + CW_{\phi,P} + CN_{\phi,P} + CS_{\phi,P})\right| < 1 \qquad (2.35)$$

should be satisfied by at least one grid point in the calculation domain. This condition is satisfied by boundary conditions of the Dirichet type (fixed boundary

condition) because the ratio can be considered as being zero.

(iii) The C's and $d^*_{\phi,P}$ must not vary too greatly from one cycle of iteration to another.

One way of limiting the variations of the C's and $d^*_{\phi,P}$ is under-relaxation

$$\phi_P^{*m} = \phi_P^{*m-1} + a_{UR}(\phi_P^{*m} - \phi_P^{*m-1}) \qquad (2.36)$$

where the superscript m denotes the iteration number. ϕ_P^{*m-1} is the value of ϕ^* at grid point P calculated with equation (2.28) during the m^{th} iteration. The under-relaxation parameter a_{UR} is a number between 0 and 1.

With this perspective on the solution procedure, six factors influencing convergence may now be reviewed.

(a) Grid Choice

In almost all the computer calculations a 29 x 23 gridline mesh in respectively the X_1^* and X_2^* direction was used. A non-uniform grid was chosen because a fine mesh was required in regions where large gradients in the dependent variables could be expected, such as near the impingement and confinement surfaces and near the axis of symmetry under the nozzle exit. A coarser grid could be used in the middle of the flow field and in the region far from the axis of symmetry where gradients are expected to be much smaller.

A grid which was used in many computations for H/w = 4 is

shown in Figure 2.2. The location of the gridline adjacent to the impingement plate is determined by the requirement that it lie within the linear gradient region of the variables ω^* and T^*, as for calculation of skin friction and heat transfer at the surface the assumptions of respectively $\frac{\partial \omega^*}{\partial X_2^*}$ = constant and $\frac{\partial T^*}{\partial X_2^*}$ = constant are made (see Section 2.2.2.2). The spacing ΔX_2^* between the impingement surface and the adjacent gridline varied from 0.01 to 0.0025 for all computational runs. The increase in spacing between gridlines parallel to the wall varied from 30 to 40%, i.e. always smaller than the maximum value of 50% recommended by Gosman et al. (49) for stability reasons. The spacing ΔX_2^* between the confinement surface and the adjacent gridline was kept at 0.01. In the X_1^* direction, the corner of the jet always coincided with the sixth gridline parallel to the axis of symmetry. After the tenth gridline, the spacing was monotonically increased by a constant factor varying from 1.15 to 1.3 in different computational runs. It is clear from Figure 2.2 that grid cells with a very large aspect ratio are formed in the lower right-hand corner of the flow field.

For $Re_j \geq 450$ and $H/w \geq 4$ the free streamline shown in Figure 2.1 was not expected to reattach to the confining surface until $X_1^* \geq 15$. Since inclusion of the complete recirculating area required such a large grid, it was decided to allow inflow at the top of Boundary III and investigate whether this inflow had any influence on the solution (see Section 2.2.2.2(d)).

Another factor was that it appeared very difficult to get a converged solution with very elongated grid cells, which would

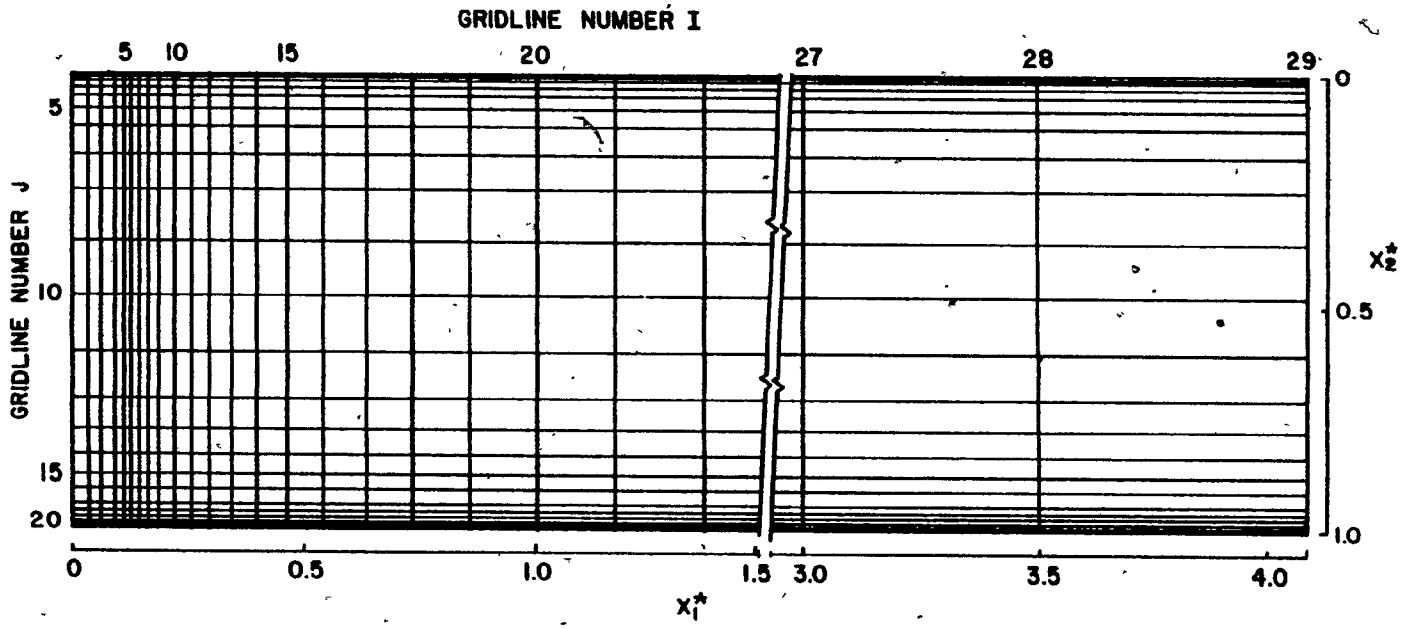


FIGURE 2.2. Computational grid for H/w = 4

be formed when the recirculating area was completely covered by the more elongated grid. With an elongated grid, the extent and magnitude of the recirculating flow continued to oscillate. The influence on stability of the aspect ratio of grid cells near Boundary III will be shown by comparing computations for Re_j = 450 and H/w = 8 obtained with three different grids. The only difference between the three grids (29 x 23 gridlines) is the increase in the spacing ΔX_1^* between gridlines, starting from the tenth gridline. The separation between successive gridlines is increased by respectively a factor of 1.15, 1.20 and 1.25, leading to a total length of the computational area of X_1^* = S/H = 1.63, 2.90 and 5.24. The aspect ratio of the grid cell in the lower right-hand corner of the grid are respectively 43, 96 and 208. The smallest aspect ratios at Boundary III are respectively 1.5, 4 and 8. The number of iterations required for convergence are respectively 104, 121 and 310. The normal convergence criteria were used. The same flow and temperature field were used for initialization of the computations.

Shown in Figure 2.3 is the development of the sum of vorticity at all inner grid points (SUMNW) during the computation. The first 200 iterations for S/H = 5.24 have been deleted. The small oscillations in SUMNW are almost absent for S/H = 1.63, showing the greater stability of the finer grid. The solutions obtained in the region $X_1^* \leq 1.0$ are almost exactly the same for the three runs (see Section 2.2.2.2).

The destabilizing effect of an elongated grid has also been found by Saad (124) for a laminar impinging round jet. He en-

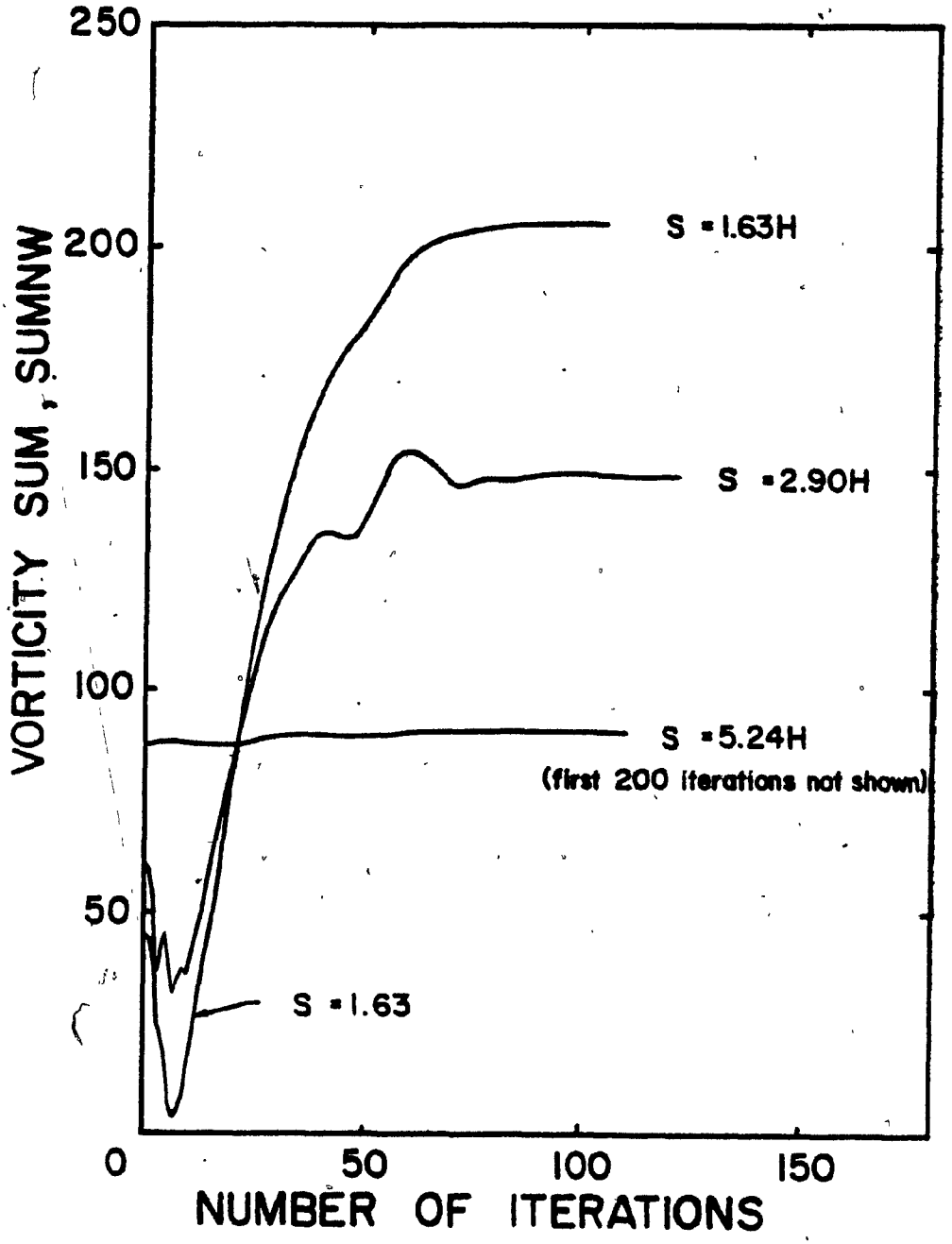


FIGURE 2.3. Effect of the grid on stability of the numerical procedure

countered convergence problems when the radius of the confining surface was larger than about 15 times the nozzle diameter, when using a 21 x 24 grid. The qualitative explanation for the instability is as follows. The result of the high aspect ratio of grid cells near the walls is that the vorticity and stream function at P (see Figure 2.1) are almost solely dependent on the vorticity and stream function at N, S and P. Thus an error in the center of the flow field propagates and possibly amplifies in the direction of the wall because the stabilizing effect of convection from neighbouring grid points W and E is not felt numerically, and the error in vorticity is not corrected at the boundary due to the gradient-type of boundary condition for vorticity at the wall.

(b) Difference Scheme

The upwind scheme was more stable than the hybrid scheme as can be seen in Figure 2.4, where the sum of vorticity at the inner grid nodes is given as a function of number of iterations. In both cases the grid shown in Figure 2.2 is used. The first hundred iterations with the upwind scheme are shown in the upper right-hand corner of Figure 2.4. In the next 198 iterations a converged solution is obtained with the upwind scheme. The converged solution is used as input for the computer program with the hybrid scheme. The solution does not converge in 200 iterations, and it is doubtful whether a converged solution can be obtained at all. It should be mentioned that for the case considered here, the recirculation area is completely covered by

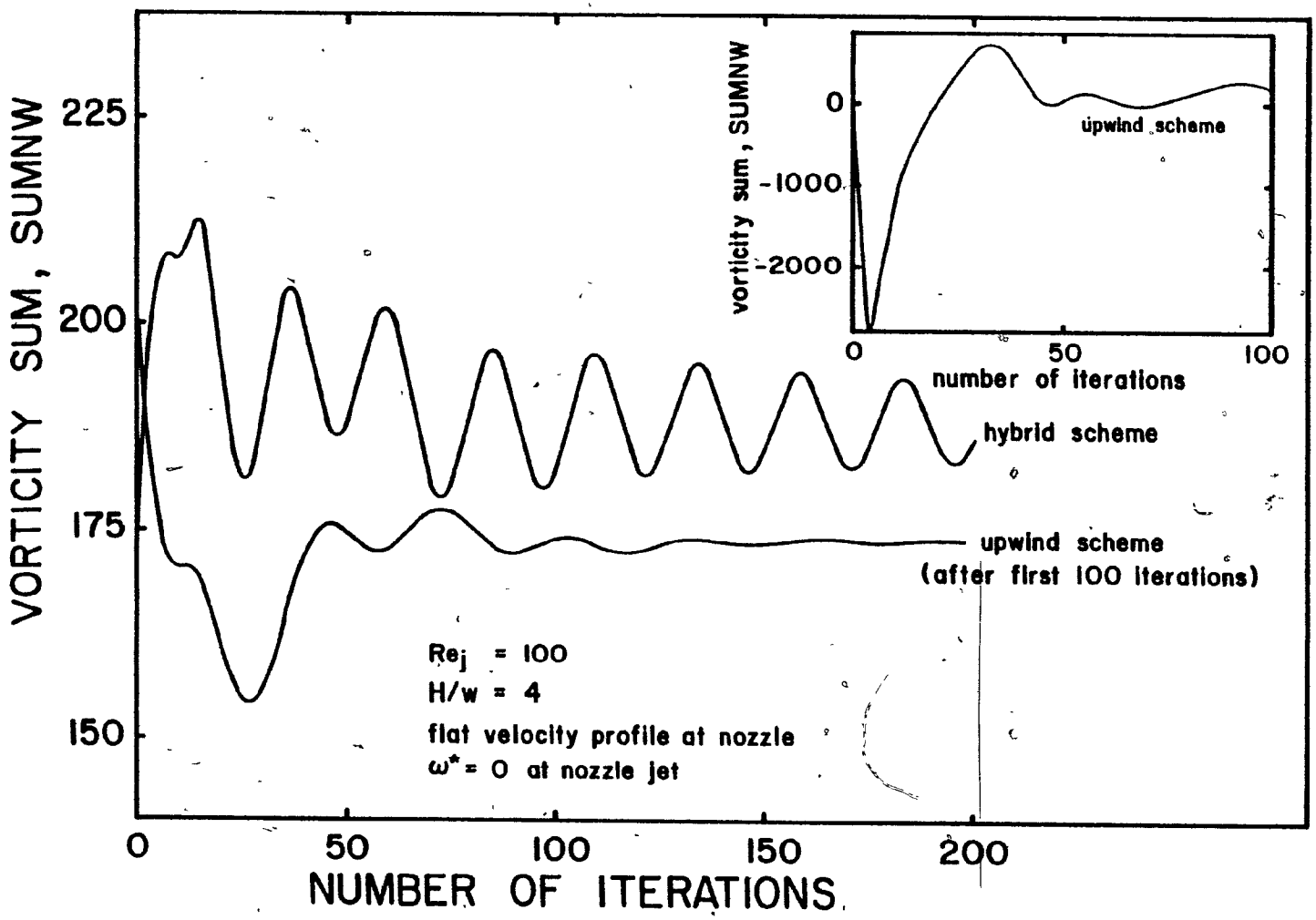


FIGURE 2.4. Convergence characteristics of finite difference schemes

the computational grid, and only outflow occurs at Boundary III When stream function contours are plotted during the iterative process it is seen that the recirculation area keeps oscillating. It is interesting to note that a converged solution was obtained in 300 iterations with the hybrid scheme by shortening the length of the 29 x 23 grid to S/H = 3.26 and using an under-relaxation factor of 0.7 for the vorticity. The converged solution with the upwind scheme was used as the starting flow and temperature field for the latter case.

(c) Scanning Procedure

Two methods of updating the variables were tested. In the first method, vorticity was updated at all grid points before recalculating the stream function for the whole flow field. In the second method, all variables were updated at one grid point before moving to the next grid point. In the last method, the vorticity and stream function develop almost simultaneously, while in the first method the stream function field is calculated for a frozen vorticity field, and vice versa. The variations in vorticity were found to be substantially smaller in the first few iterations when using the second method. Because the total number of iterations were nearly equal, the first scanning method was used in all further work.

Stability was also improved when the grid was scanned along lines perpendicular to rather than parallel to the impingement surface. A further improvement was obtained when the grid lines perpendicular to the surface under the nozzle were scanned in

the direction of the impingement surface while for the remaining gridlines the scanning direction was reversed (i.e. following the flow). For example, for $Re_j = 450$, $H/w = 8$ and a flat velocity profile at the nozzle, a converged solution was obtained in 310 iterations. Without reversing the scanning direction the solution was still far from converged after 400 iterations.

(d) Under-relaxation

When the computational procedure would not converge for the reason described under (a), under-relaxation of vorticity and sometimes of the stream function were tried (see equation (2.36)). It was found that the residuals of vorticity and stream function were reduced but the stability of solution was hardly influenced. The smallest under-relaxation factor tried was 0.3 for both vorticity and stream function.

(e) Boundary Conditions

It is well-known that boundary conditions affect the stability and rate of convergence of a numerical procedure (Roache, Gosman). Convergence is slower when the boundary condition is in the form of a prescribed gradient because errors in the flow field, which propagate to the boundary, will not be eliminated by the gradient-type boundary condition. The fact that the vorticity residuals were generally the last to satisfy the convergence criteria is consistent with the presence of gradient-type of boundary conditions for vorticity along most boundaries. Three different sets of boundary conditions were tried at Boundary III:

(1) $\frac{\partial \omega^*}{\partial X_1^*} = \frac{\partial \psi^*}{\partial X_1^*} = 0$ (or $U_1^* =$ constant and $U_2^* = 0$)

(2) $\frac{\partial \omega^*}{\partial X_1^*} = \frac{\partial^2 \psi^*}{\partial X_1^{2*}} = 0$ when outflow occurs,

or $\frac{\partial^2 \psi^*}{\partial X_1^{2*}} = \omega^* = 0$ when inflow occurs, i.e. entrainment of irrotational flow along streamlines of constant curvature.

(3) $\frac{\partial \omega^*}{\partial X_1^*} = \frac{\partial \psi^*}{\partial X_1^*} = 0$ when outflow occurs,

or $\omega^* = 0$ and $\psi^* = \psi^*_{\text{nozzle corner}}$ when inflow occurs.

For $Re_j = 450$, $H/w = 8$ and a flat velocity profile at the nozzle it was found that the highest rate of convergence occurred with set (3), closely followed by set (1), while set (2) led to significantly slower convergence. This finding is in agreement with the remark of Roache (117) that stability of the procedure is improved when variables at boundaries are as closely defined as possible. The most realistic boundary condition is boundary condition set (2). However boundary condition set (1) was subsequently used throughout the study because of stability reasons and the fact that conditions at Boundary III will subsequently be shown to scarcely influence flow and heat transfer characteristics in the regions of prime interest, the impingement and

wall jet regions.

Following Gosman et al. (49) the wall vorticities in the general substitution formula (2.11) have been eliminated by use of equation (2.22). The resulting "implicit formulation" for vorticity at the gridline adjacent to the walls has been used throughout this work because of the better stability properties.

(f) Matrix Inversion Technique

Solution of the set of non-linear equations represented by (2.28) and the finite difference approximations of the boundary conditions is obtained by the point iteration method called the Gauss-Seidel method (i.e. values of dependent variable are used as soon as they come available). Block iteration methods were also tried in the hope of increasing the rate of convergence. In block methods, vorticity and stream function values are updated successively or simultaneously along gridlines using respectively the tridiagonal matrix algorithm (T.M.A.) or bi-tridiagonal matrix algorithm (B.T.M.A.).

In the T.M.A. given by Carnahan et al. (28) and Roache (117) the F.D.E. (2.28), rewritten as

$$\phi_j^* = A_{\phi j}\phi_{j+1}^* + B_{\phi j}\phi_{j-1}^* + C_{\phi j} \qquad (2.37)$$

can be solved by the recursive solution

$$\phi_j^* = U_{\phi j} + V_{\phi j}\phi_{j+1}^* \qquad (2.38)$$

with $$U_{\phi j} = \frac{B_{\phi j} U_{\phi j-1} + C_{\phi j}}{1 - B_{\phi j} V_{\phi j-1}} \tag{2.39}$$

and $$V_{\phi j} = \frac{A_{\phi j}}{1 - B_{\phi j} V_{\phi j-1}} \tag{2.40}$$

$U_{\phi 1}$ and $V_{\phi 1}$ are determined with equation (2.38) and the boundary conditions for the dependent variable ϕ^* (i.e. for a fixed boundary condition $V_{\phi 1} = 0$ and $U_{\phi 1} = \phi_1^*$). Then the coefficients $U_{\phi j}$ and $V_{\phi j}$ are determined with equations (2.39) and (2.40) for $j = 2$ to JN-1, where JN is the total number of grid points along a gridline parallel to the axis of symmetry. For a gradient-type boundary condition at the other end of the gridline ϕ_{JN}^* is obtained by solving equation (2.38) for $j = JN-1$ together with the F.D. formulation of the boundary condition. Finally ϕ_j^* is calculated for $j = JN-1$ to 1 with equation (2.38).

The B.T.M.A. is given by Von Rosenberg (151), and its application to the vorticity and stream function equation is as follows. The F.D.E. (2.28) for vorticity and stream function is rewritten as:

$$\omega_j^* = A_j \omega_{j+1}^* + B_j \omega_{j-1}^* + C_j \tag{2.41}$$

and $$\psi_j^* = a_j \psi_{j+1}^* + b_j \psi_{j-1}^* + c_j + d_j \omega_j^* \tag{2.42}$$

The two recursive solutions of (2.41) and (2.42) are

$$\omega_j^* = P_j \omega_{j+1}^* + Q_j + R_j \psi_{j+1}^* \tag{2.43}$$

and $$\psi_j^* = p_j\psi_{j+1}^* + q_j + r_j\omega_{j+1}^* \qquad (2.44)$$

The coefficients of equations (2.43) and (2.44) are listed in Appendix 3. As with the T.M.A., the coefficients are first calculated using the BC's for ω^* and ψ^* starting at one end of the gridline. After reaching the other end of the gridline the ω^*'s and ψ^*'s are back calculated using the BC's for ω^* and ψ^* at this end of the gridline. The finite difference equation for the temperature is again solved with the T.M.A.

The two algorithms were first tried for a simpler but similar flow, viz. plane stagnation flow (see Appendix 4). From these numerical experiments it was found that application of the T.M.A. along gridlines perpendicular to the impingement wall led to an unstable procedure. Reasons for this behaviour are because of the lag between vorticity and stream function when the T.M.A. is applied first to vorticity and then the stream function, and because of the strong linkage between ω^* and ψ^*, especially at the wall via the no-slip condition. The procedure became stable when the lag between vorticity and stream function was removed by application of the B.T.M.A. (the lag between ω^* and ψ^* due to the nonlinear terms is of course not removed by the B.T.M.A.). The number of iterations required to get a converged solution for plane stagnation flow is an order of magnitude lower for the block method with the B.T.M.A. than for the Gauss-Seidel point iteration technique. Alternating the procedure along gridlines perpendicular to the wall and then parallel to the wall led to longer computing times. When the

block method with the B.T.M.A. along lines perpendicular to the walls was applied to the impinging jet case for $Re_j = 450$, $H/w = 8$ and a flat velocity profile, the solution was converging for the first 20-25 iterations, but then the residuals continued to oscillate without further convergence. The oscillations are due to the movement of several recirculating regions adhering to the confinement surface. The flow field in the impingement and wall jet region however was not too far from the converged solution obtained by the Gauss-Seidel point iteration technique. Alternating the B.T.M.A. procedure along gridlines perpendicular to the wall and then parallel to the wall made the procedure more unstable. No cure has been found for the instability when using the B.T.M.A. for the impinging jet case. Therefore the block method of matrix inversion was abandoned in favor of the Gauss-Seidel point iteration technique in all further work.

2.2.2.2 Factors Influencing the Accuracy of the Procedure

(a) Difference Scheme

Use of upwind differences leads to an error called "artificial diffusion" (Roache) or "false diffusion" (Wolfshtein). Roache (119) derived an expression for artificial viscosity for the "first" upwind scheme by the method of Taylor series expansion. In the "first" upwind scheme, velocity is assumed constant over the entire control volume. The present numerical procedure is the integral version of the so-called "second" upwind difference (Roache) where the effect of variation in velocity is taken into account. The expression for relative artificial viscosity resulting from the present numerical scheme is derived in Appendix 5 for a uniform grid as

$$\nu_a/\nu_j = \frac{1}{2} U^* \Delta X^* Re_j \frac{H}{w} \tag{2.45}$$

Another numerical error inherent to the second upwind difference is

$$U_a/U_j = -\frac{1}{2} \Delta X^* \frac{\partial U^*}{\partial X^*} \tag{2.46}$$

which will be called artificial velocity (U and ΔX^* are in the same direction).

These two errors are absent in the central difference form of the hybrid scheme (see Appendix 4). The central difference form is used when, for example $|AW_\phi| < C^*_{\phi W} BW_\phi$, or for $\phi = \omega^*$ when

$$\frac{\frac{1}{2}(U^*_{1P} + U^*_{1W})(X^*_{1P} - X^*_{1W})}{\mu^*_w} < 2\,\frac{w}{H}\,\frac{1}{Re_j} \tag{2.47}$$

When U^*_{1W}, approximated by a Taylor series expansion

$$U^*_{1W} = U^*_{1P} - (X^*_{1P} - X^*_{1W})\left.\frac{\partial U^*_1}{\partial X^*_1}\right|_P + O\left[(X^*_{1P} - X^*_{1W})^2\right] \tag{2.48}$$

is inserted in equation (2.47) second and higher order terms are neglected, one obtains

$$\frac{1}{2}\left[2\,U^*_{1P} - (X^*_{1P} - X^*_{1W})\left.\frac{\partial U^*}{\partial X^*_1}\right|_P\right](X^*_{1P} - X^*_{1W})/\mu^*_w < 2\,\frac{w}{H}\,\frac{1}{Re_j}$$

or generally for incompressible flow

$$\frac{1}{2}\,U^*\Delta X^*\left[1 - \frac{1}{2}(\Delta X^*/U^*)\,\frac{\partial U^*}{\partial X^*}\right]/\mu^*_w < \frac{1}{Re_j\,(H/w)} \tag{2.49}$$

When the higher order term $\frac{1}{2}(\Delta X^*/U^*)\,\frac{\partial U^*}{\partial X^*}$ is neglected in (2.49), it follows from comparison of equation (2.49) with (2.45) that $\nu_a/\nu_j < 1$ in the upwind scheme when the diffusive contribution is larger than the convective contribution in the same direction. When $\nu_a/\nu_j > 1$ the diffusive contribution is smaller than the convective contribution. This explains why the conductive contribution is eliminated in the hybrid scheme when the convective contribution is larger, i.e. because the conductive contribution is already accounted for via the artificial diffusion introduced by the upwind difference.

From the above analysis it is clear that the hybrid scheme is more accurate than the upwind scheme at all ratios of convective to diffusive contribution because the hybrid scheme selects central differences when the diffusive contribution is larger than the convective contribution but selects upwind differences with omission of the diffusion terms when the convective contribution is larger than the diffusive contribution. The hybrid scheme is also stable because central differences are used only when the local cell Reynolds number or local cell Peclet number ≤ 2 (Runchal).

However, the upwind form of the hybrid scheme can lead to large errors when the flow cuts across the grid at an angle and there are strong crossflow gradients. The magnitude of these errors are discussed by Wolfshtein (154), de Vahl Davis and Mallinson (36) and by Raithby (113). The expression for the artificial diffusion given by de Vahl Davis and Mallinson (36) is

$$\Gamma_a^* = \frac{\sqrt{U_1^{*2} + U_2^{*2}}\,(\Delta X_1^*)(\Delta X_2^*)\sin(2\theta)}{4[\Delta X_2^*(\sin^3\theta) + \Delta X_1^*(\sin^3\theta)]}\,(Pe)\,\frac{H}{w} \qquad (2.50)$$

θ being the angle between the flow and the x_1-direction. The absolute numerical error as a result of the upwind differences will be very small in solution of the thermal energy equation because $\Gamma_a^* >> 1$ occurs outside the boundary layer where gradients in the temperature are essentially absent, i.e. where $T^* = 1.0$ everywhere. Inside the thermal boundary layer $\Gamma_a^* \leq 1$ (see

Fig. 2.7a) because of the closely spaced grid and because the angle between the flow and the gridlines parallel to the wall is very small. Significant numerical errors are possible when solving the vorticity equation because there are flow regions outside the boundary layer with $\Gamma_a^* >> 1$ and significantly large gradients in vorticity. The error in the jet mixing layer, which is one of these regions, is reduced by refining the grid. The error in the immediate neighbourhood of the jet corner is discussed subsequently. It should be remembered however that the vorticity gradients in all other regions of $\Gamma_a^* >> 1$ are about zero, i.e. 10^2 smaller than the gradients in the boundary layer.

In order to quantify the false diffusion effect in the boundary layer, the finite difference schemes were applied to a flow similar to the impinging jet but for which an exact solution is available, namely, plane stagnation flow. The non-uniform grid used for plane stagnation flow was similar to that chosen for the impinging jet. Except for the lowest Reynolds number ($Re_H = 10$), the hybrid scheme resulted in upwind differences in the x_1-direction and central differences in the x_2-direction inside the boundary layer of plane stagnation flow. Thus in this case the difference between the hybrid and upwind scheme occurs in the treatment of the x_2-direction convection term. From the results given in more detail in Appendix 4 it can be concluded that of the two procedures, the hybrid scheme is clearly the more accurate. Most important, the error in heat transfer at the wall is considerably lower with the hybrid

scheme. The maximum error in normalized vorticity at the wall with the hybrid scheme is about 10% for $Re_H = 1000$ immediately adjacent to the axis of symmetry. Generally along the wall the error in normalized vorticity is 2 to 8%. The error is completely eliminated when central differences are used in both the x_1 and x_2-direction, as is the case for $Re_H = 10$ and $X_1^* < 1.0$.

The influence of the difference scheme on the numerical solution of the impinging jet is shown in Figures 2.5 and 2.6. Figure 2.5(a) illustrates that for $Re_j = 100$, the upwind scheme predicts a slightly deeper penetration of the jet in the impingement region, followed by a faster spreading of the jet in the wall jet region, as compared to the hybrid scheme. Heat transfer in the stagnation region shown in Figure 2.5(b) is lower for the hybrid scheme, as was found also for the case of plane stagnation flow. Differences in skin friction results are significant only in the wall jet region, predicted values there being lower for the upwind scheme due to faster spreading of the wall jet. The crosshatched areas in Figure 2.5(a) indicate regions where the hybrid difference scheme selects upwind differences. In the area of positive slope crosshatching, convection in the x_2-direction is approximated by upwind differences while negative slope crosshatching denotes convection in the x_1-direction approximated by upwind differences. Thus central differences are used in regions where crossflow diffusion is important, i.e. the mixing region of the jet and the boundary layers on both walls. Consequently, the solution with the

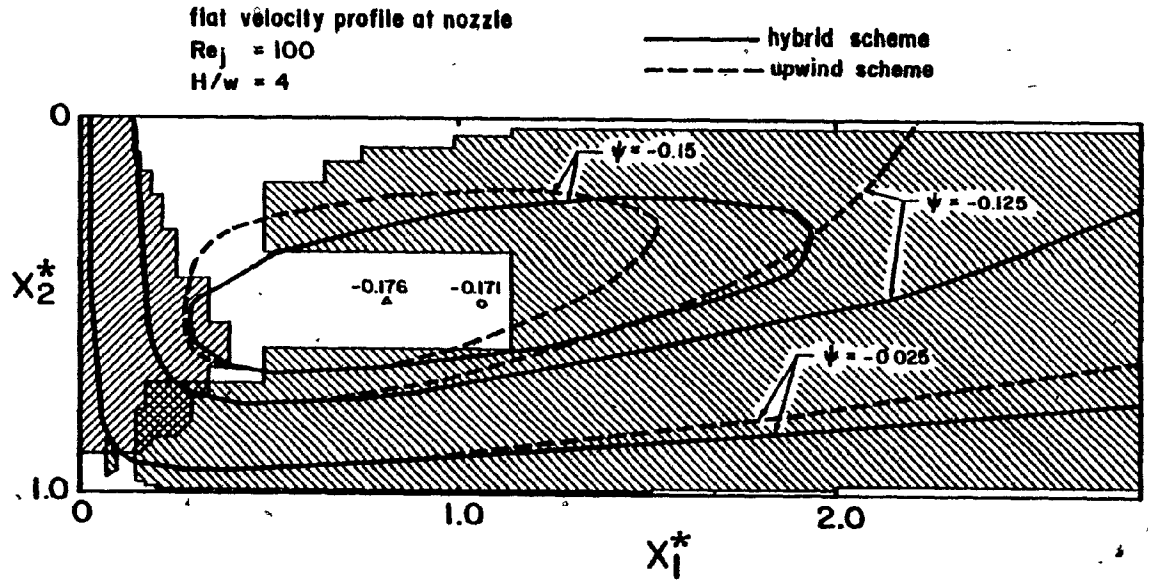


FIGURE 2.5a. Effect of difference scheme on stream function contours for $Re_j = 100$

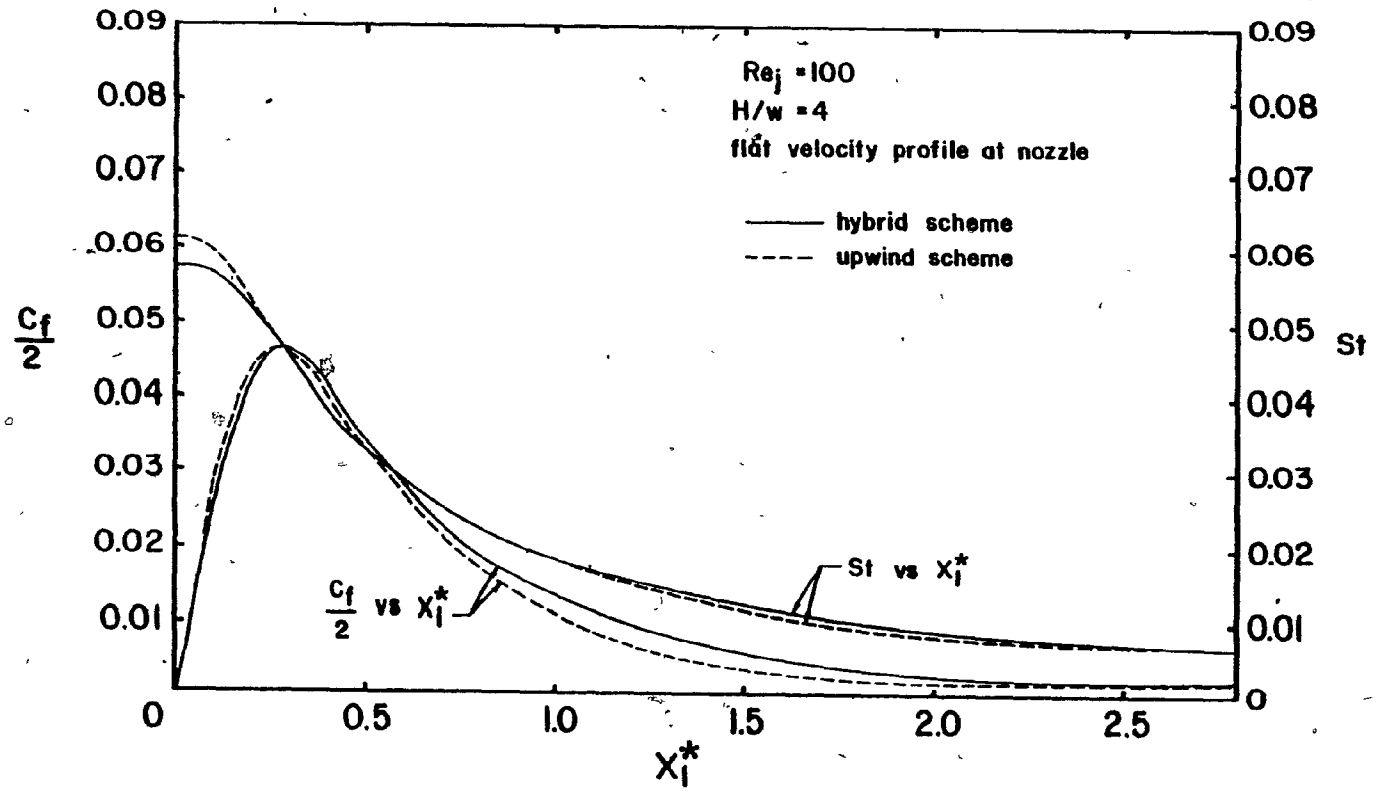


FIGURE 2.5b. Effect of difference scheme on transfer properties of the impingement surface for $Re_j = 100$

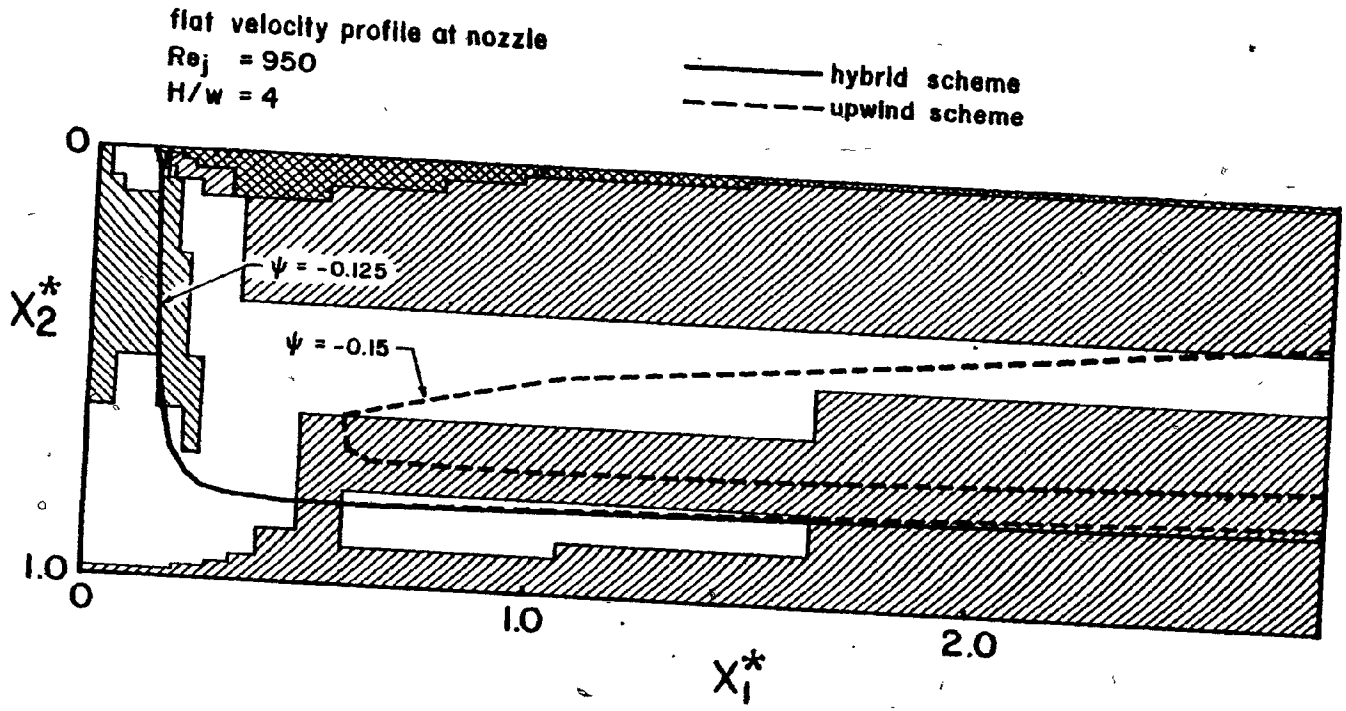


FIGURE 2.6a. Effect of difference scheme on stream function contours for $Re_j = 950$

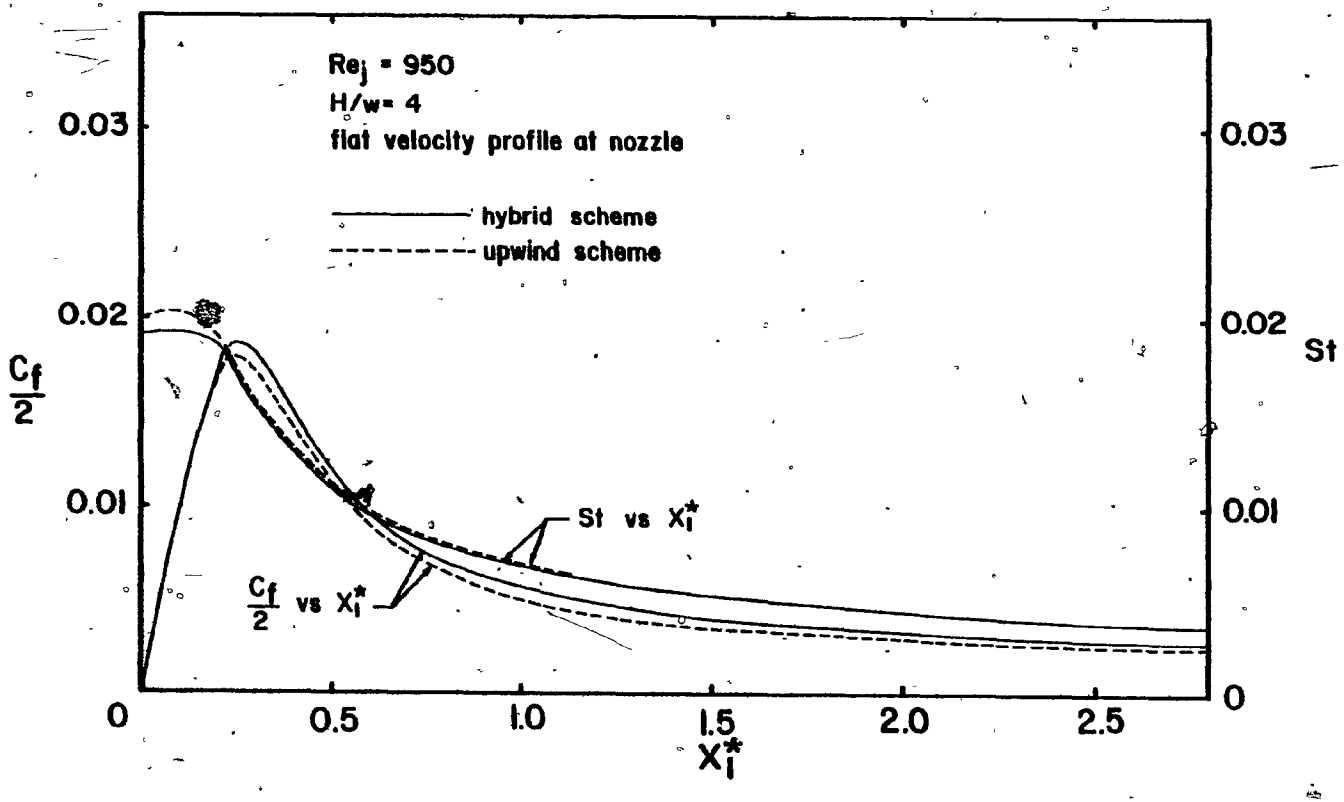


FIGURE 2.6b. Effect of difference scheme on transfer properties of the impingement surface for $Re_j = 950$

hybrid scheme can be considered more accurate than that from the upwind scheme. In the areas of Figure 2.6(a) identified by crosshatching of positive and negative slope, diffusion in respectively the x_2 and x_1-direction is approximated by central differences in the hybrid scheme. So the flow regions where central differences are used for the diffusion terms are smaller for $Re_j = 950$, but still cover most regions where crossflow diffusion is important.

The calculated velocity and temperature distributions in the stagnation region for $Re_j = 950$ shown in Figure 2.7 demonstrate that differences between the two schemes are very small. As with plane stagnation flow, the predicted thermal gradient at the plate is marginally steeper and the thermal boundary layer correspondingly thicker with the upwind difference scheme. This behaviour results from the fact that close to the wall artificial convection dominates over artificial diffusion, while the converse exists further from the wall. When artificial velocities and viscosities (Appendix 5) are included in calculation of local Reynolds number at the grid points, one obtains the relation (2.51) given on the following page. The results of application of this formula at the grid nodes on the axis of symmetry inside the thermal boundary layer are given in Table 2.3. From the table it follows that the increase in local Reynolds number due to artificial velocity dominates over the decreasing effect of artificial viscosity for grid nodes adjacent to the impingement surface. Further from the wall the situation is reversed. At the grid node J = 18, the local

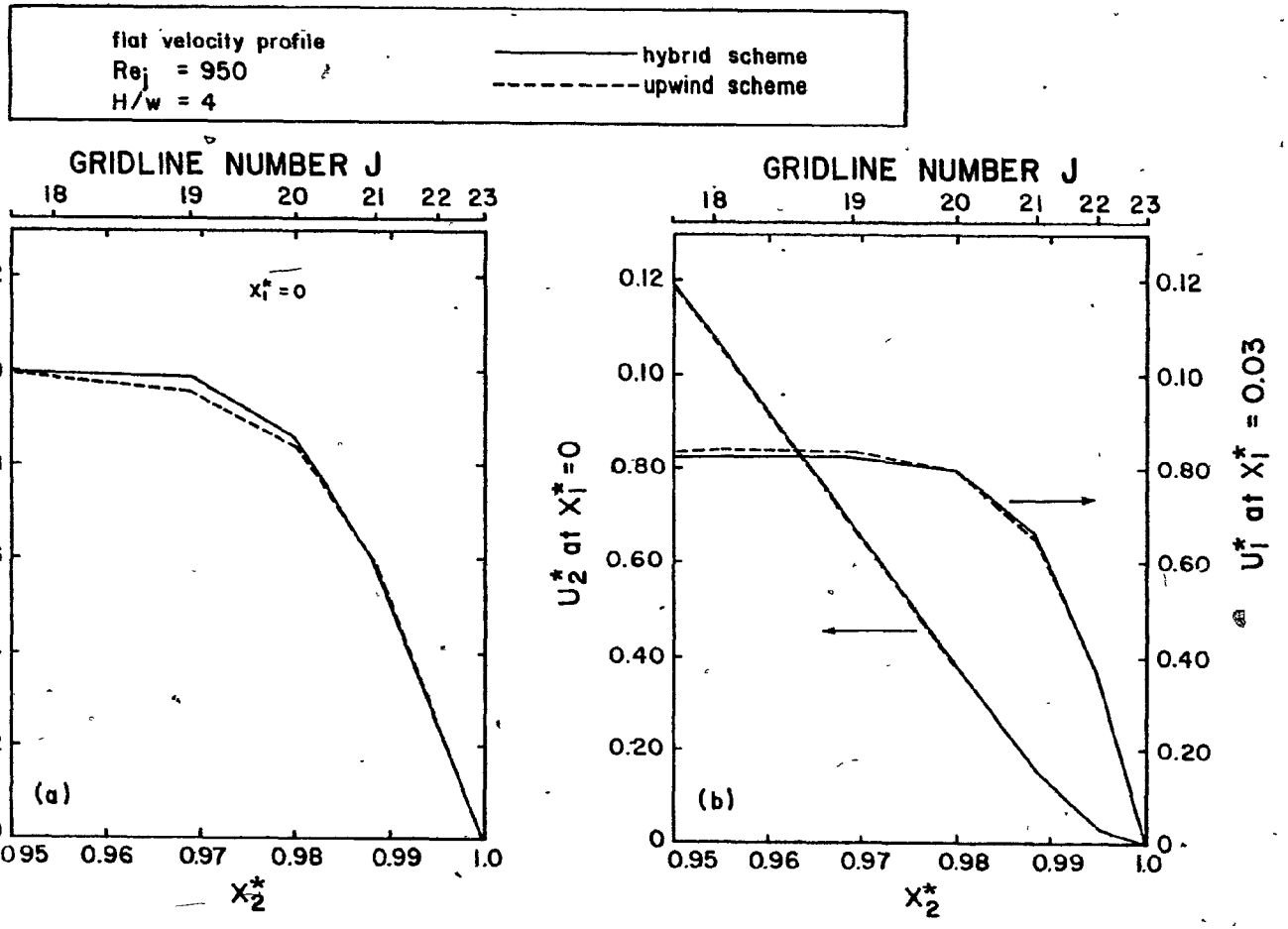


FIGURE 2.7a. Effect of difference scheme on axial temperature distribution in stagnation region

FIGURE 2.7b. Effect of difference scheme on velocity distribution in stagnation region

$$\frac{Re_{upwind}}{Re_{central}}$$

$$= \frac{\left[1 - \frac{(X_i^*-X_{i-1}^*)^2}{(X_{i+1}^*-X_{i-1}^*)} \frac{1}{U_i^*} \frac{\partial U^*}{\partial X^*}\bigg|_i - \frac{[(X_{i+1}^*-X_i^*)-(X_i^*-X_{i-1}^*)]}{(X_{i+1}^*-X_{i-1}^*)}\right]\left[1 - \frac{1}{2} U_i^*[(X_{i+1}^*-X_i^*)-(X_i^*-X_{i-1}^*)] \, Re \, \frac{H}{w}\right]}{\left[1 + U_i^* \frac{(X_i^*-X_{i-1}^*)^2}{(X_{i+1}^*-X_{i-1}^*)} \, Re \, \frac{H}{w}\right]\left[1 + \frac{1}{2} \frac{[(X_{i+1}^*-X_i^*)-(X_i^*-X_{i+1}^*)]}{U_i^*} \frac{\partial U^*}{\partial X^*}\bigg|_i\right]}$$

(2.51)

TABLE 2.3.

Relative size of artificial viscosity and velocity

Gridline Number, I	$\frac{Re_{upwind}}{Re_{central}}$	Pe_{local}
22	1.87	0.024
21	1.31	0.172
20	0.91	0.621
19	0.64	1.578
18	0.49	3.534

Peclet number is larger than 2, leading to upwind differencing for the hybrid scheme. Since the hybrid scheme is more accurate, all subsequent results are derived from use of this difference scheme.

(b) Selection of Grid

It is evident that the finer the grid, the more accurate the solution. However, economy requires that the number of grid nodes be kept to a minimum. It was found that use of a grid finer than that shown in Figure 2.2 hardly influenced the solution. A non-uniform, 29 x 23, grid was therefore used for almost all numerical predictions. The non-uniformity of the grid was such that closely spaced gridlines were present in regions with large gradients in ω^* and T^*. The influence of uniformity of the grid on accuracy for plane stagnation flow is reported in Appendix 4. The results show an improvement in accuracy with a uniform grid for the hybrid scheme. This finding is a consequence of introduction of artificial viscosity and

velocity terms when using a non-uniform grid (see equations (12) and (13) in Appendix 5). With the upwind scheme accuracy in vorticity at the wall can increase or decrease when changing from a uniform to non-uniform grid depending on the relative magnitude of the artificial viscosity and velocity introduced by the non-uniformity and upwind differences (see equations (14) and (15) in Appendix 5). Use of a uniform grid often results in an increase in the number of gridlines because the gridline adjacent to the impingement surface should be within the very thin, linear gradient region for ω^* and T^*. This requirement is necessary because heat transfer and skin friction at the impingement surface are calculated with equations (2.57) and (2.22) which are based on the assumptions of linear variation of T^* and ω^* with distance. For plane stagnation flow it can be shown that equations (3.9) and (2.22) describe the exact solution within about 1% when $T^*_{ns} < 1/3$. As the stagnation region of an impinging jet resembles plane stagnation flow, the requirement of $T^*_{ns} < 1/3$ was also adhered to for all calculations of the impinging jet case.

(c) Treatment of Vorticity at the Corner of the Nozzle

It was found that alternate treatments of vorticity at the corner of the nozzle had a pronounced effect on predicted flow and heat transfer characteristics of the impinging jet. Roache and Mueller (118), who tested 7 methods, suggest use of discontinuous values of corner vorticity, which means that the vorticity in the F.D.E. at the two grid nodes adjacent to the cor-

ner is evaluated from the stream function difference between that grid node and the corner. Gosman and Samuelsen (50) recommend use of a single-valued corner vorticity, considering the corner as a part of the wall which is parallel to the dominant flow. They recommend discontinuous values when the flows along the two walls are of the same magnitude. In the present case, where the inlet flow conditions are specified directly at the nozzle exit, the two methods reduce to using either equation (2.22) (Roache and Mueller's recommendation), or a constant corner vorticity value (Gosman and Samuelsen's recommendation) in the F.D.E. for the vorticity at the inner grid node adjacent to the wall.

The two procedures were tested for both a uniform and a parabolic velocity profile at the nozzle exit. The resulting free stream function contours starting from the nozzle corner are shown in Figure 2.8. Location of the streamline $\psi^* = -0.125$ was determined by linear interpolation. The differences are small for the parabolic but pronounced for the flat velocity profile at the nozzle exit. For both velocity profiles, the iteration at the corner leads to a more realistic spreading of the jet, i.e. a streamline which diverges but not too sharply. It should be mentioned that the sudden increase in jet width of about 15% at the first gridline under the nozzle for the flat velocity profile, obtained with iteration of the corner vorticity, results from only 2% of the jet mass flow crossing the vertical gridline coincident with the nozzle wall.

Development of the lateral profile of axial velocity under

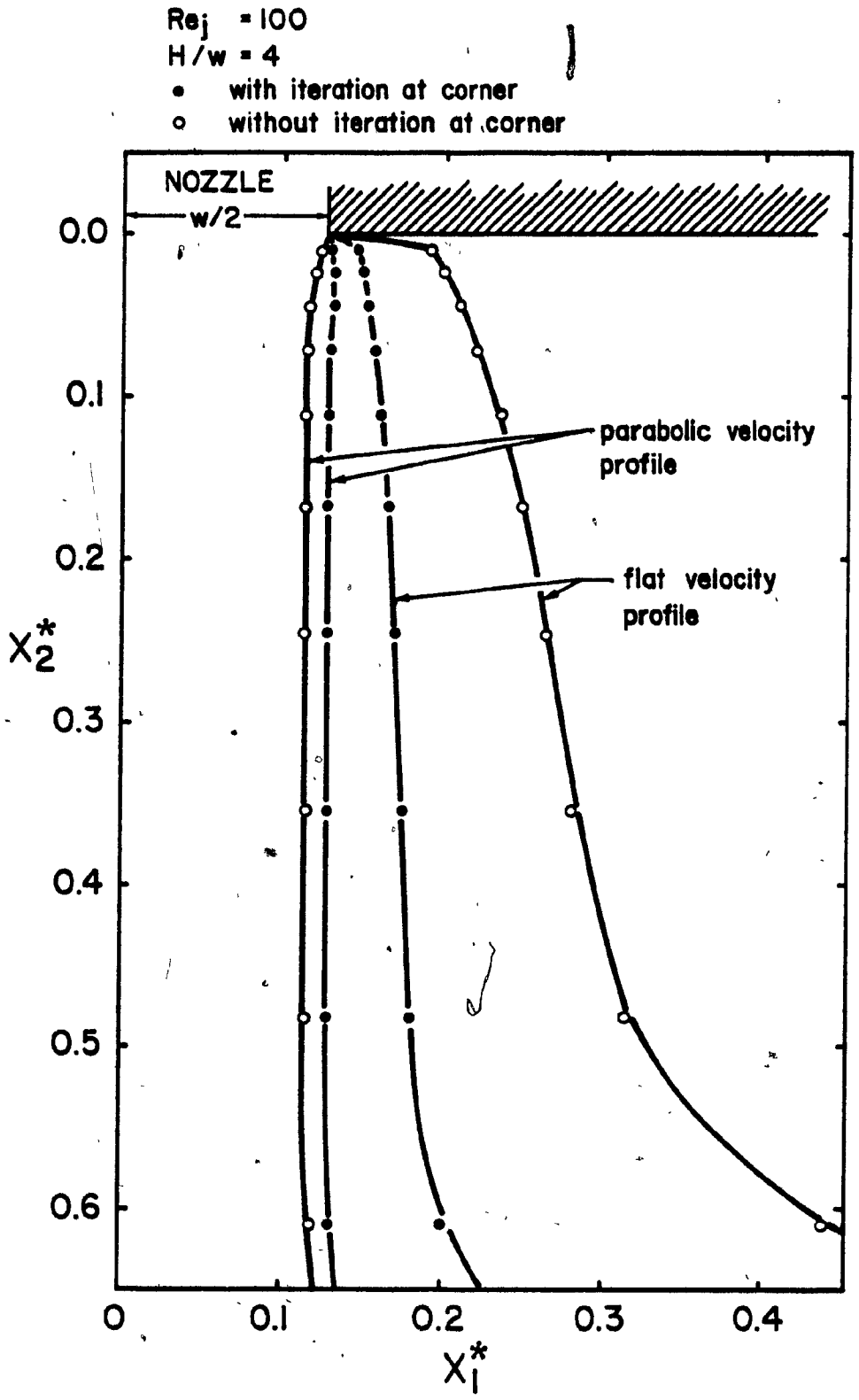


FIGURE 2.8. Effect of treatment of corner vorticity on free streamline contours ($\psi = -0.125$)

the nozzle for the two alternate treatments of vorticity at the corner is shown in Figure 2.9(a). Use of a constant vorticity, $\omega^* = 0$, at the corner is seen to predict a more rapid spreading of the jet and decay of centerline axial velocity. Also shown in Figure 2.9(a) are velocities on the gridlines at $X_2^* = 0.01$ and $X_2^* = 0.024$ calculated from the theoretical solution of the "plane half-jet" given by Schlichting (pg. 175). As the solution with iteration of vorticity at the corner agrees well with the theoretical solution while the other solution does not, iteration of corner vorticity is confirmed as leading to a more realistic development of jet velocity profile. For completeness, profiles of centerline axial velocity decay from nozzle exit to impingement are shown in Figure 2.9(b) for the four cases of corner vorticity treatment.

The influence of these two methods of treating corner vorticity on prediction of conditions at the impingement surface is shown by Figures 2.10(a) and (b). The results for both skin friction, Figure 2.10(a), and Stanton number, Figure 2.10(b), indicate that corner vorticity treatment is not particularly important for a parabolic velocity profile but has a large effect on predicted results with a flat velocity profile at the nozzle exit. The vorticity at the corner for case Ia and IIa (Figure 2.10) is respectively -6.825 and -65.88.

Another method of treating vorticity at the corner is given by Bui (22). Here the separation is forced at a right-angle from the corner by setting the stream function at the first downstream grid node equal to the stream function value at the

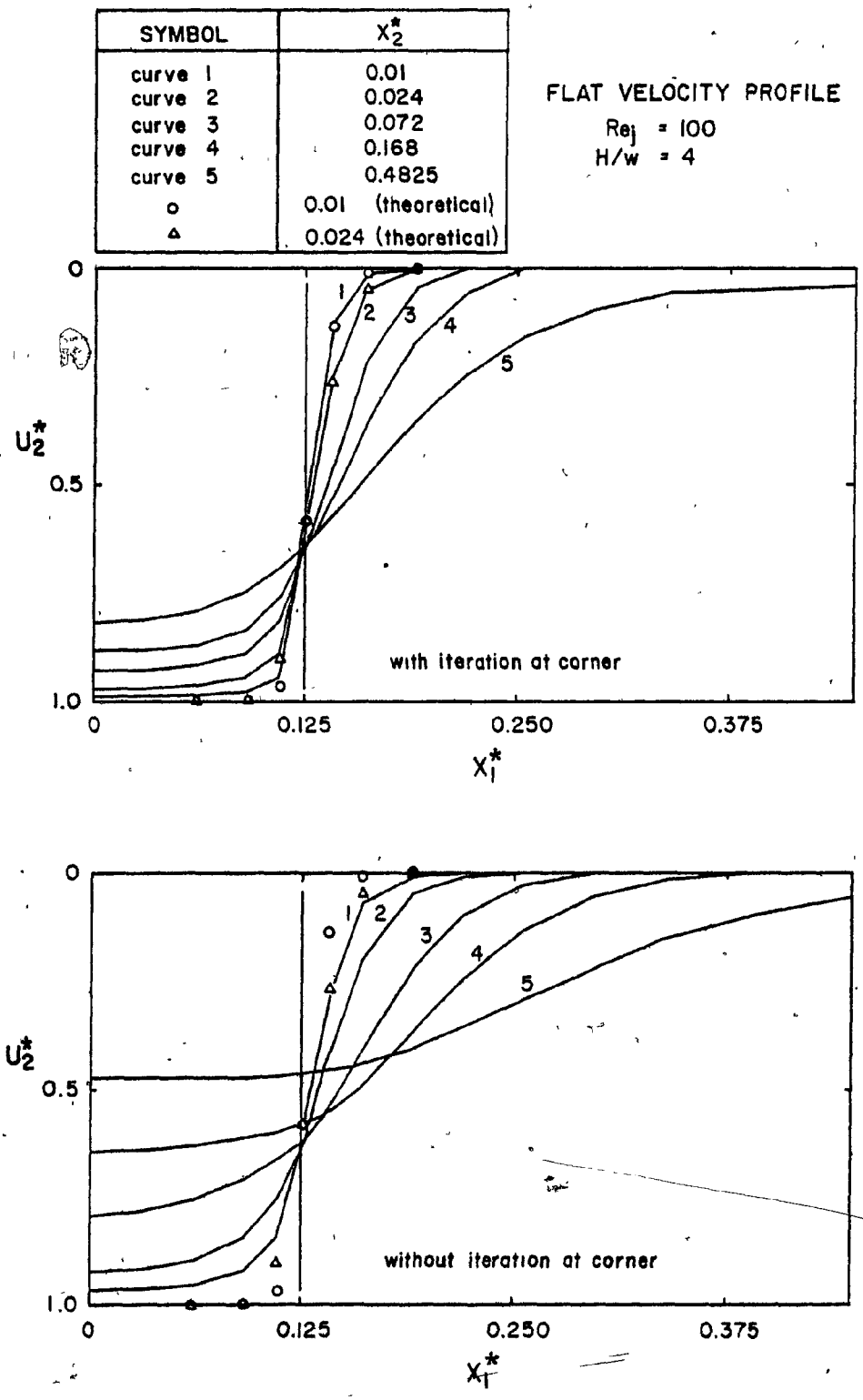


FIGURE 2.9a. Effect of corner vorticity treatment on development of jet velocity profile

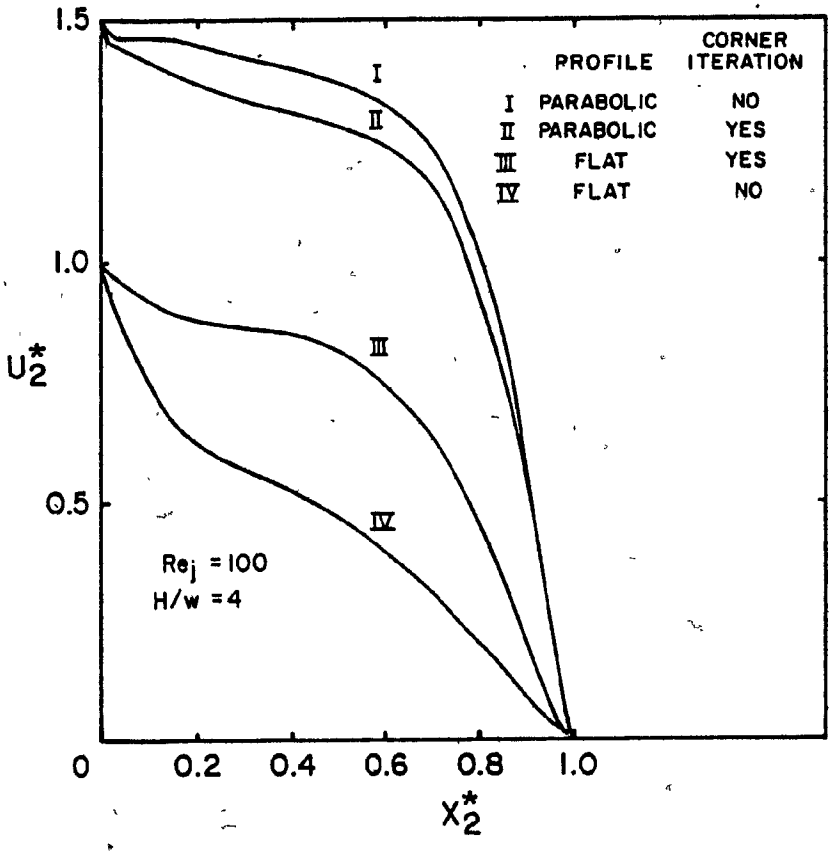


FIGURE 2.9b. Effect of corner vorticity treatment on centerline axial velocity decay

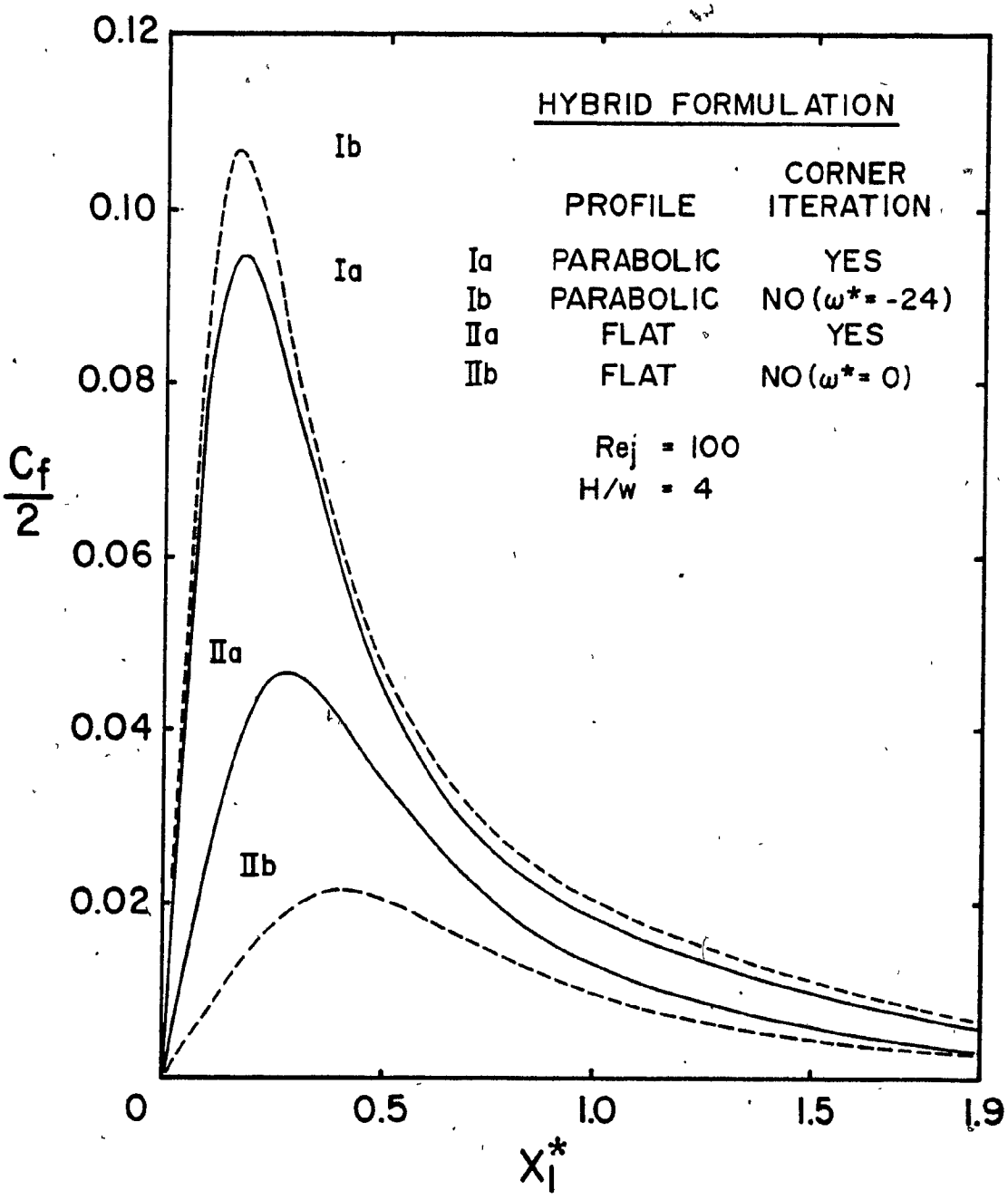


FIGURE 2.10a. Effect of corner vorticity treatment on skin friction distribution

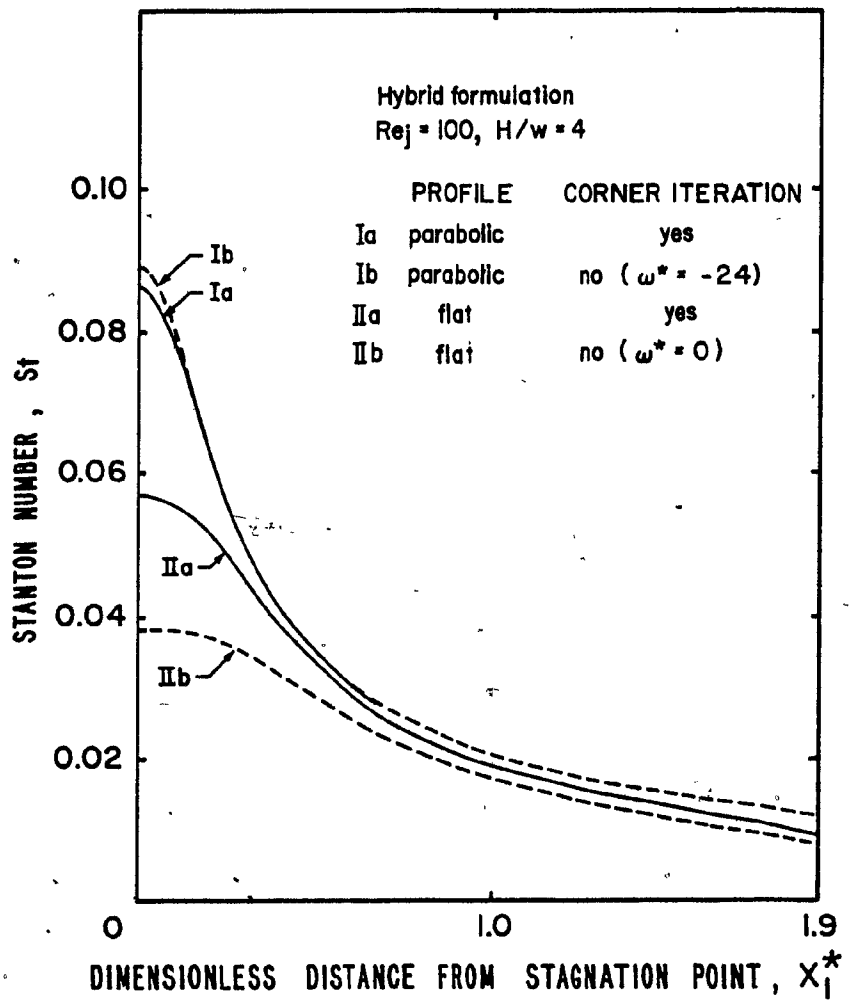


FIGURE 2.10b. Effect of corner vorticity treatment on heat transfer distribution

corner. Vorticity at the downstream grid node is calculated from equation (2.28) with stream function as the dependent variable. When Bui's method was tested for a round impinging jet (Saad) it was found that the sudden expansion of the jet occurred after the first gridline below the nozzle.

Only by using a staggered grid for ω^* and ψ^* can one circumvent the corner vorticity problem. However, Roache (117) recommended against such a grid because of deterioration of accuracy of the vorticity boundary condition at the wall.

After these tests and considerations the conclusion was to select for the numerical predictions of the present study the procedure suggested by Roache and Mueller, i.e. with iteration of vorticity at the corner. In a study undertaken subsequently by Huang (63) it was shown that by using the primitive variables (instead of vorticity and stream function) in the numerical solution a smooth decay was obtained for the axial velocity of a round jet impinging on a flat surface, i.e. the rather abrupt changes immediately downstream of the nozzle exit, apparent in Figure 2.9(a), were eliminated.

(d) Boundary Conditions

Inaccuracies may be introduced via boundary conditions. Specification of boundary conditions at the spent flow exit, Boundary III, (Figure 2.1) presents a problem because the entrainment of fluid by the jet may result in an inflow adjacent to the confinement surface at this boundary. In the beginning of this work it was felt that Boundary III should be located

sufficiently far from the axis of symmetry to ensure only outflow at this boundary. With only outflow at Boundary III, the solution would be insensitive to a "wrong" specification of the boundary condition since such information would be convected out of the control volume. However, use of this criterion either required too many gridlines or destabilized the numerical solution (see Section 2.2.2.1(a)). On the other hand, with an undefined inflow over part of Boundary III, errors due to a not completely correct boundary condition would be convected into the control volume. Fortunately it was established that, although alternate boundary conditions at Boundary III strongly affected the results in the recirculation area, their influence was scarcely felt in the impingement and early wall jet regions which are of major concern.

Boundary conditions at Boundary III tested were

a) Streamlines parallel to the impingement and confinement surfaces and no variation of vorticity in the x_1-direction, i.e.

$$\frac{\partial \psi^*}{\partial x_1^*} = \frac{\partial \omega^*}{\partial x_1^*} = 0 \qquad (2.52)$$

b) Slope of the streamlines at Boundary III equal to the slope of the streamlines immediately inside Boundary III. Vorticity is irrotational when inflow occurs, otherwise vorticity does not vary in the x_1-direction, i.e.

$$\frac{\partial^2 \psi}{\partial x_1^{*2}} = \frac{\partial \omega}{\partial x_1^*} = 0 \qquad (2.53)$$

or $$\omega^* = 0 \qquad (2.54)$$

when inflow occurs.

c) As in a), only when inflow would develop, the flow is blocked by an impermeable but frictionless wall, i.e. equation (2.52) or

$$\psi^* = -\frac{1}{2}\frac{w}{H} \qquad (2.55)$$

when inflow occurs.

The effect on calculated flow and heat transfer results caused by these alternate forms of specifying the boundary condition at the spentflow exit boundary is now reviewed. Development of the free streamline $\psi^* = 0.0625$ with boundary conditions a), b) and c) is shown in the lower part of Figure 2.11 for $Re_j = 450$ and $H/w = 8$. The effect of changing the outflow boundary condition propagates only about 2H from the outflow boundary back into the wall jet region, which in this case corresponds to about 2 gridlines back to I = 27 from the exit gridline, I = 29. The influence that alternate boundary conditions have in the recirculation area is shown in the upper part of Figure 2.11. It is clear that the quite significant differences in the predicted inflow and profile of lateral velocity, U_1^*, which exist at $X_1^* = 4.198$, I = 28, i.e. at about 1H back from the exit boundary effectively disappear by $X_1^* = 2.167$, I = 25, i.e. by about

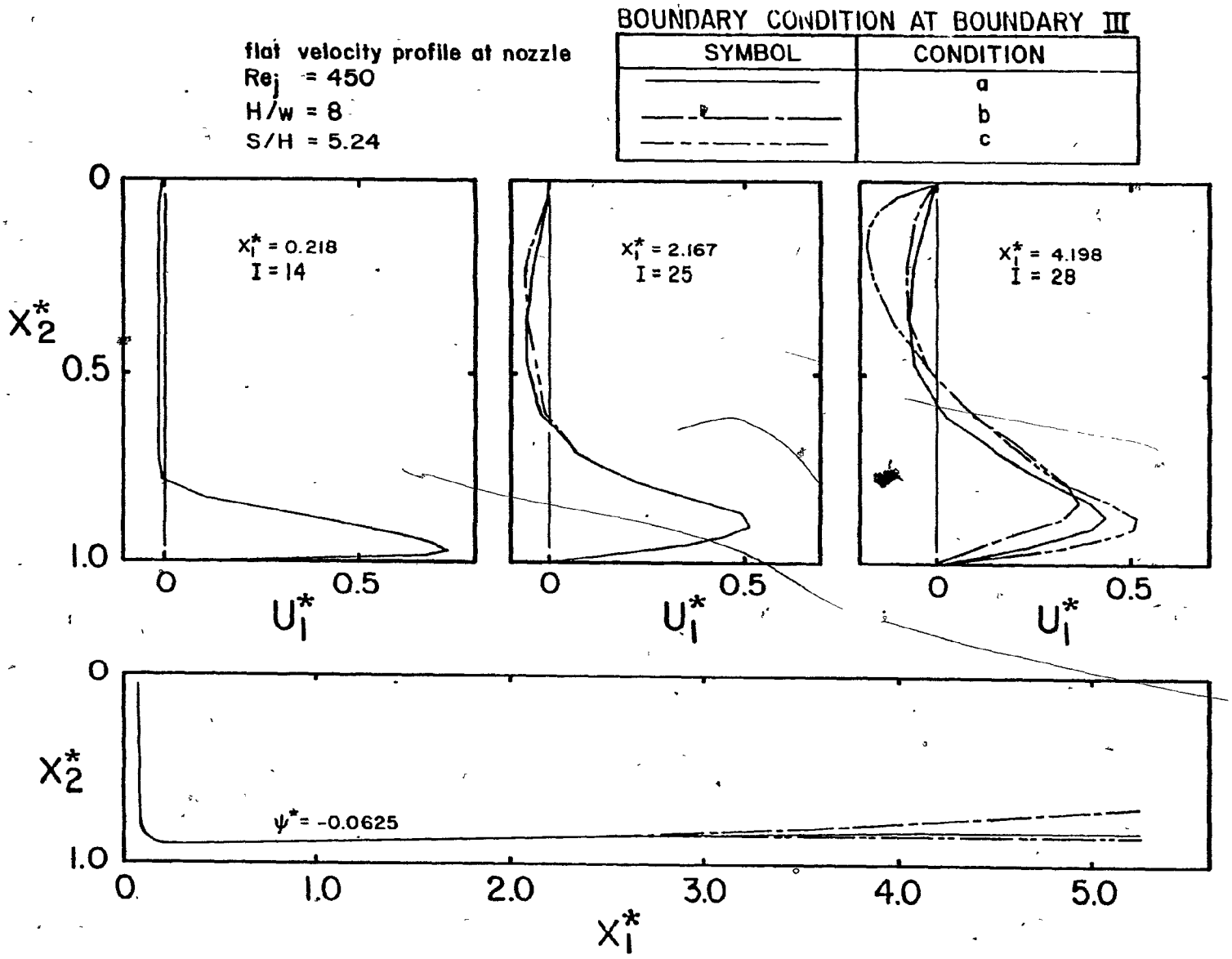


FIGURE 2.11. Effect of boundary condition at boundary III on flow development

3H from the outflow boundary. The effect on calculated heat transfer at the impingement surface related to choice between these three forms for the exit flow boundary condition is illustrated on Figure 2.12. Although significant effects propagate back for about 2H from the exit, by a distance 3H back from an exit boundary located at S = 5.24H from stagnation, the effects on heat transfer become negligible. As the prime interest is in heat transfer in the impingement and early wall jet region, the choice of alternate exit boundary (III) conditions is in general not important. Similar results were found for skin friction, the differences in $\frac{C_f}{2}$ being smaller than 0.0002 for $0 \leq X_1^* \leq 2.17$. Based on these findings, boundary conditions a) are used in all further calculations.

The influence of lateral extent of impingement surface, S, from nozzle centerline to the spentflow exit, i.e. between boundaries III and IV, is shown on Figures 2.13(a) and (b). As the effect of any change on conditions at the impingement surface is of prime interest, the predicted results for skin friction and Stanton number are most relevant. If one uses as a basis of comparison the case for the longest impingement surface, i.e. S/H = 5.24, the effect of using shorter impingement surfaces is seen to be an increase in C_f or St for a region beginning at the spentflow exhaust boundary (III) and extending back for a distance of about 2H from the outflow boundary. In other words, from the stagnation point out to about 1H from the stagnation point the values of C_f and St are independent of lateral extent of the confined slot jet system, after which C_f and

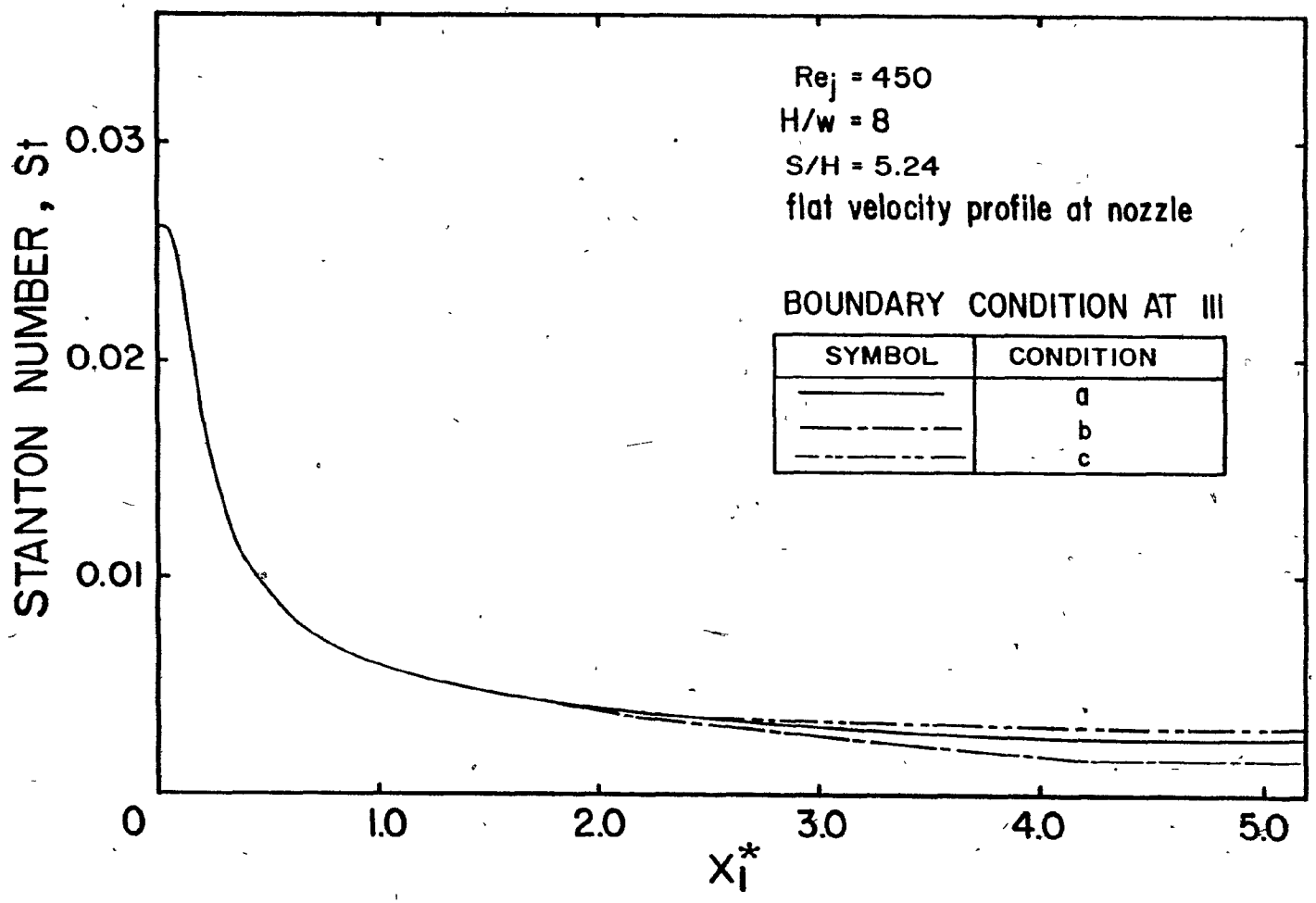


FIGURE 2.12. Effect of boundary condition at boundary III on heat transfer distribution

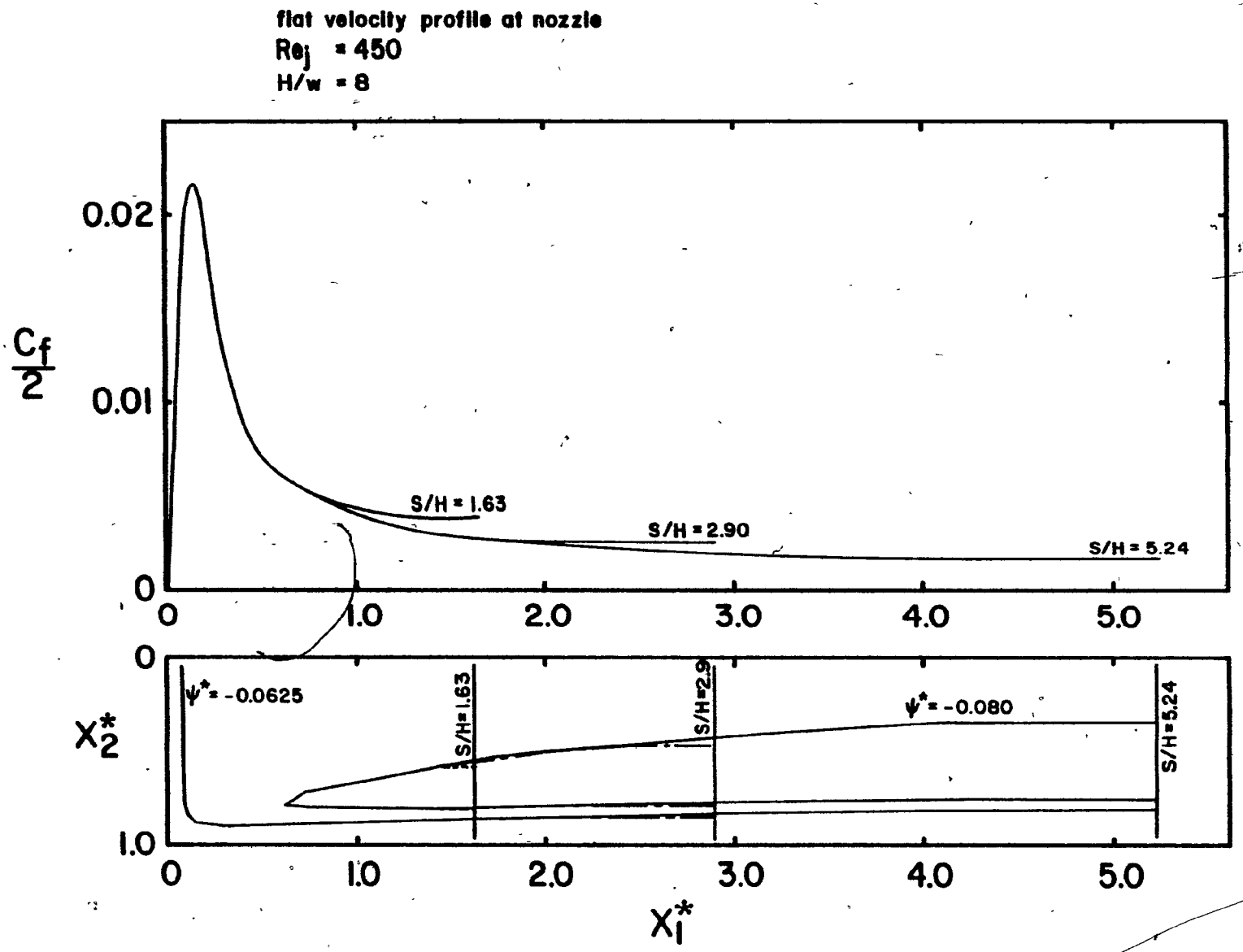


FIGURE 2.13a. Effect of length of impingement surface on flow characteristics

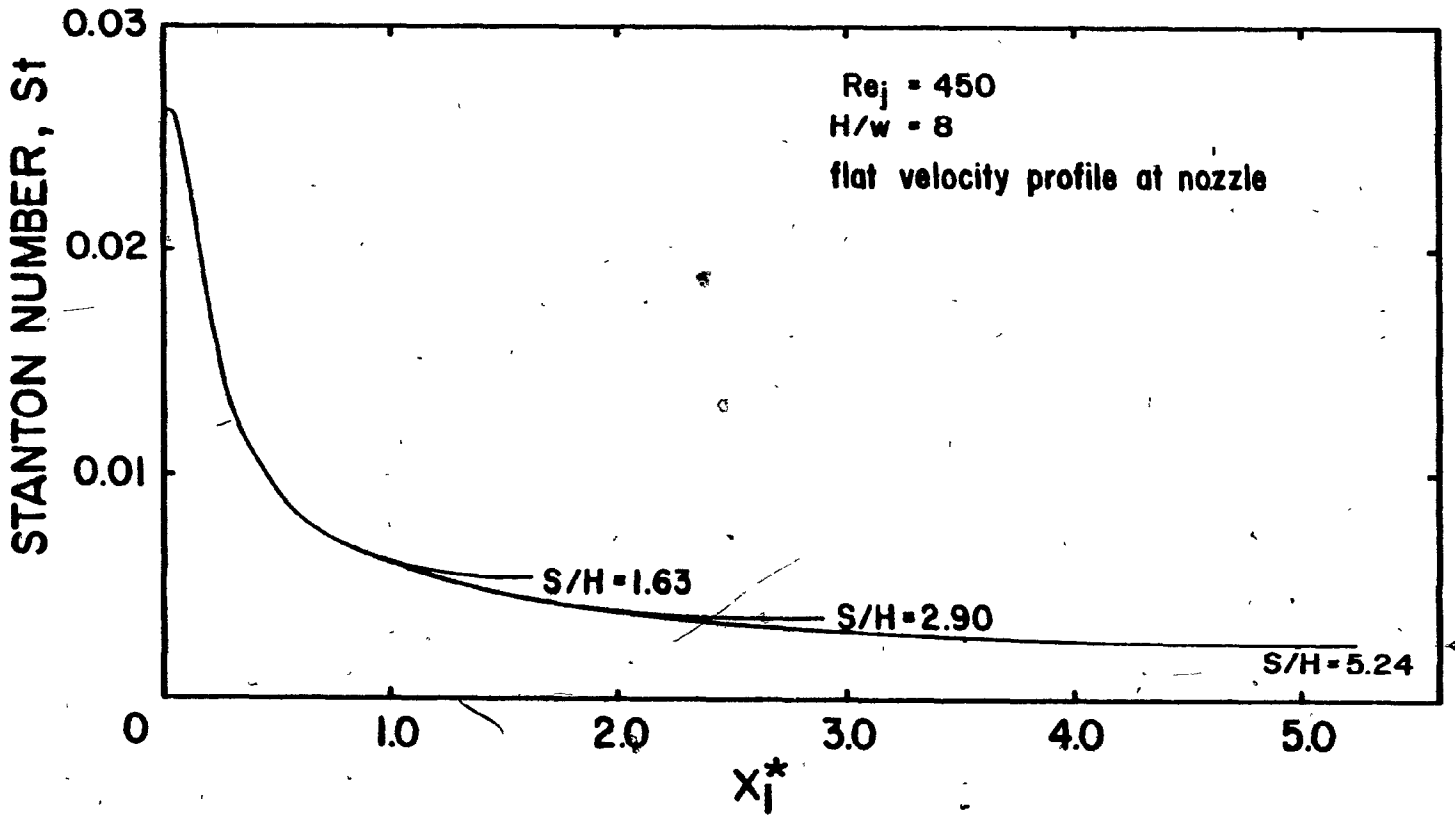


FIGURE 2.13b. Effect of length of impingement surface on heat transfer distribution

St for shorter impingement surfaces increase significantly relative to values for a long impingement surface.

2.2.3 Results and Discussion

The range of parameters used in this study is given in Table 2.4.

TABLE 2.4.

Range of parameters for laminar jet calculations

Re_j	100, 450, 950
H/w	4, 8, 12, 16
Velocity profile	Flat, Parabolic, Intermediate
U_s^*	-0.01, 0, 0.01, 0.025
Pr	0.73, 2.5, 7.0
T_s/T_j	1, 0.667, 0.5

A converged solution is obtained in the form of the stream function, vorticity, temperature and velocities at each grid node including the boundaries. The important transfer properties at the impingement surface, nondimensional skin friction, $C_f/2$, and nondimensional heat transfer, St, are derived respectively from the vorticity and temperature gradient at the impingement surface. Thus

$$\frac{C_f}{2} = \frac{\tau_s}{\rho_j U_j^2} = \frac{\mu_s^* \omega_s^*}{Re_j \; H/w} \qquad (2.56)$$

and

$$St = \frac{\alpha}{\rho_j U_j C_p} = \frac{(T_s^* - T_{ns}^*)k_s^*}{\Delta X_2^* \, Re_j Pr \, H/w} \qquad (2.57)$$

Preference is given to St over Nu for representation of heat transfer because, in contrast to Nusselt number, Stanton number is independent of any characteristic length, of which there are two for impinging jets, i.e. w or H.

2.2.3.1 Effect of Reynolds Number and Jet Velocity Profile

Results of the computations for three Reynolds numbers and two velocity profiles at the nozzle exit, parabolic and flat, are displayed in Figures 2.14(a) and (b) in the form of the free streamline, in Figures 2.15 and 2.16 in the form of the vorticity contours, and in Figure 2.17 in the form of the isotherm $T^* = 0.9$. Unless stated otherwise, the other parameters are: $U_s^* = 0$, $Pr = 0.73$, and $T_s/T_j = 1$. The free streamline results in Figure 2.14 show a closed recirculation region for $Re_j = 100$. For the higher Reynolds numbers, a solution was obtained with inflow at Boundary III (the influence of inflow at Boundary III is discussed in Section 2.2.2.2 (d)). The occurrence of a slight contraction of the jet below the nozzle for a parabolic profile attracts attention. By contrast, for a flat profile the jet expands continuously. The free streamline is found significantly closer to the impingement surface for the parabolic velocity profile owing to its higher momentum and spreading

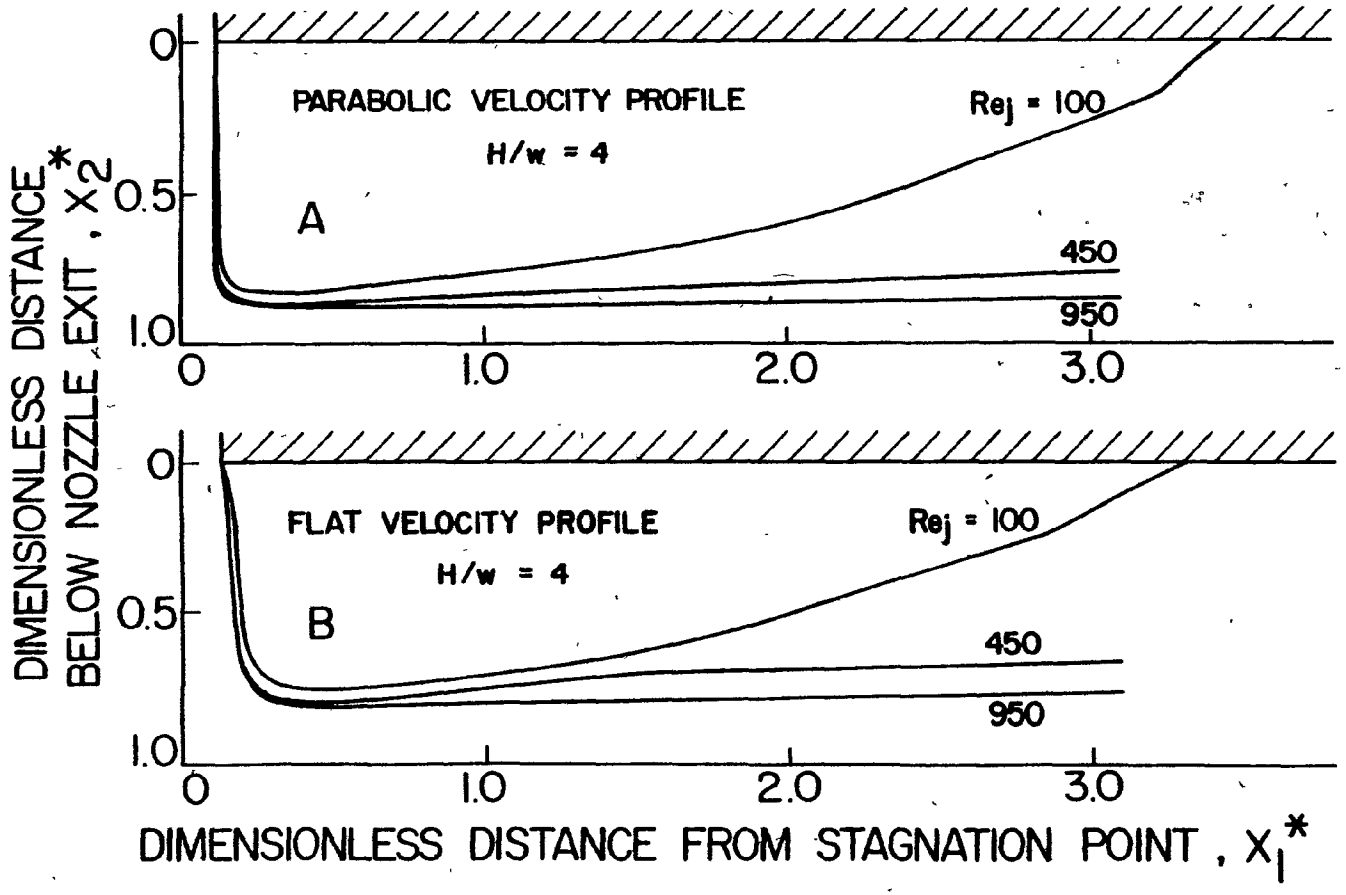


FIGURE 2.14. Free streamline contours

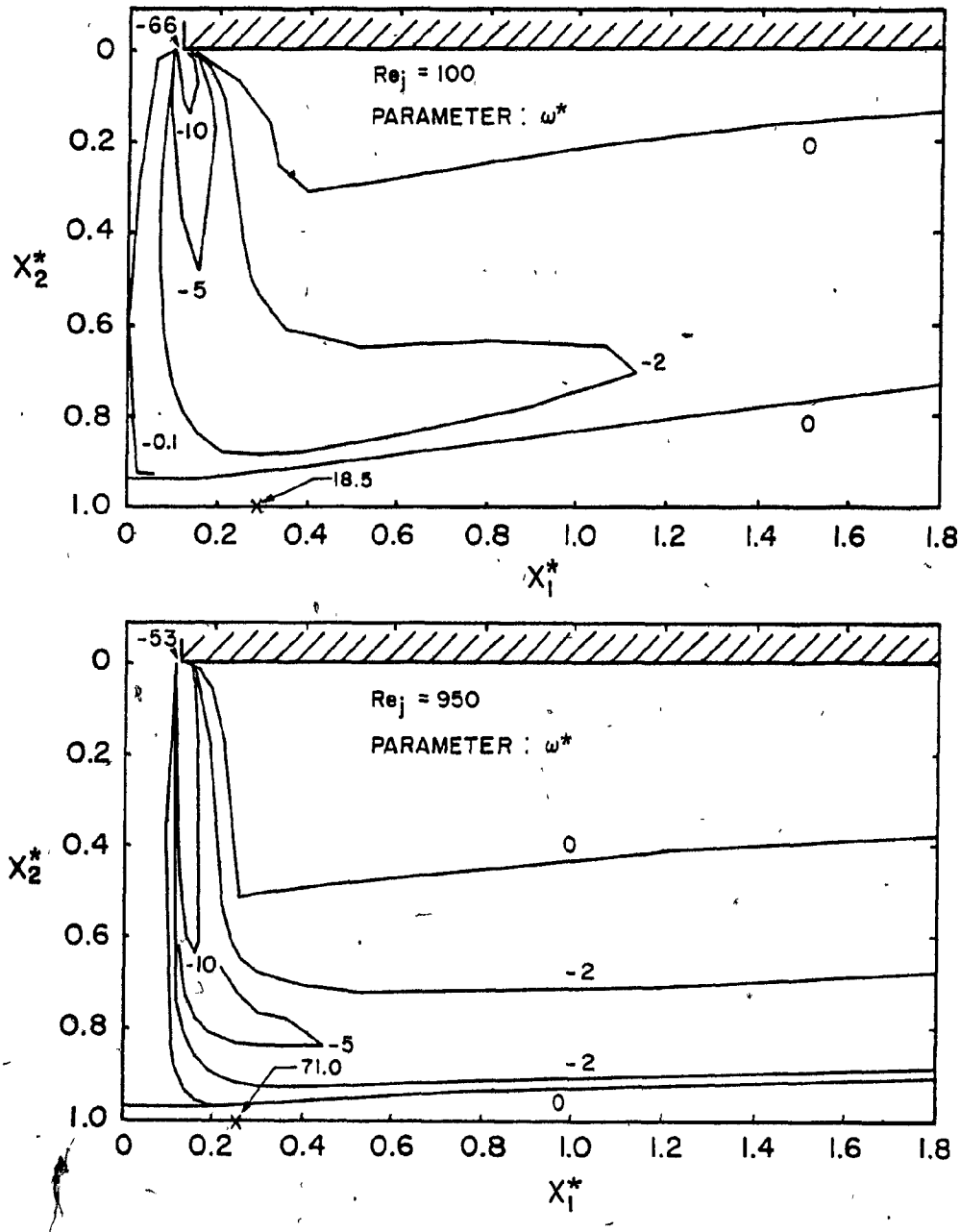


FIGURE 2.15. Vorticity contours for a flat jet velocity profile

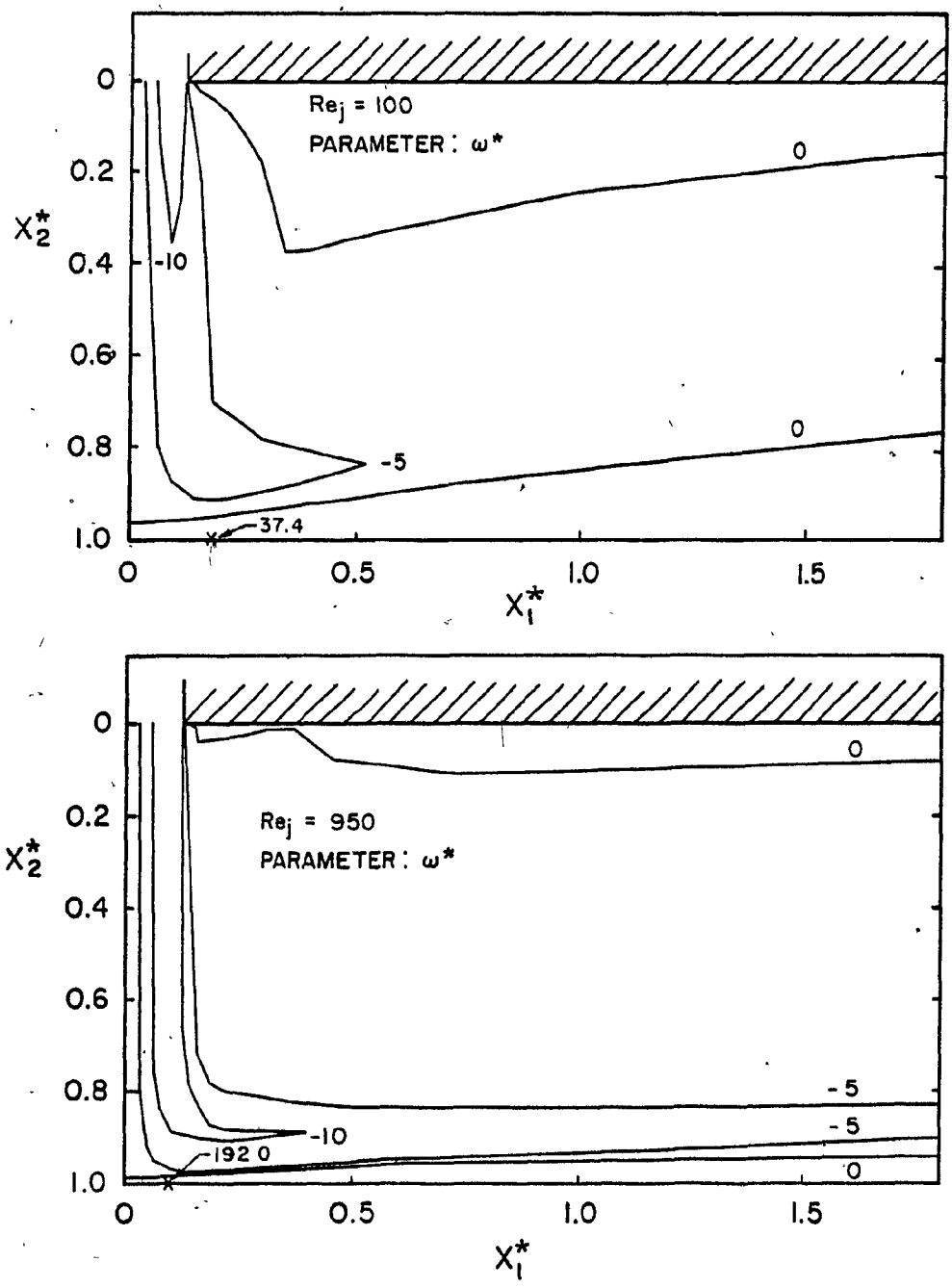


FIGURE 2.16. Vorticity contours for a parabolic jet velocity profile

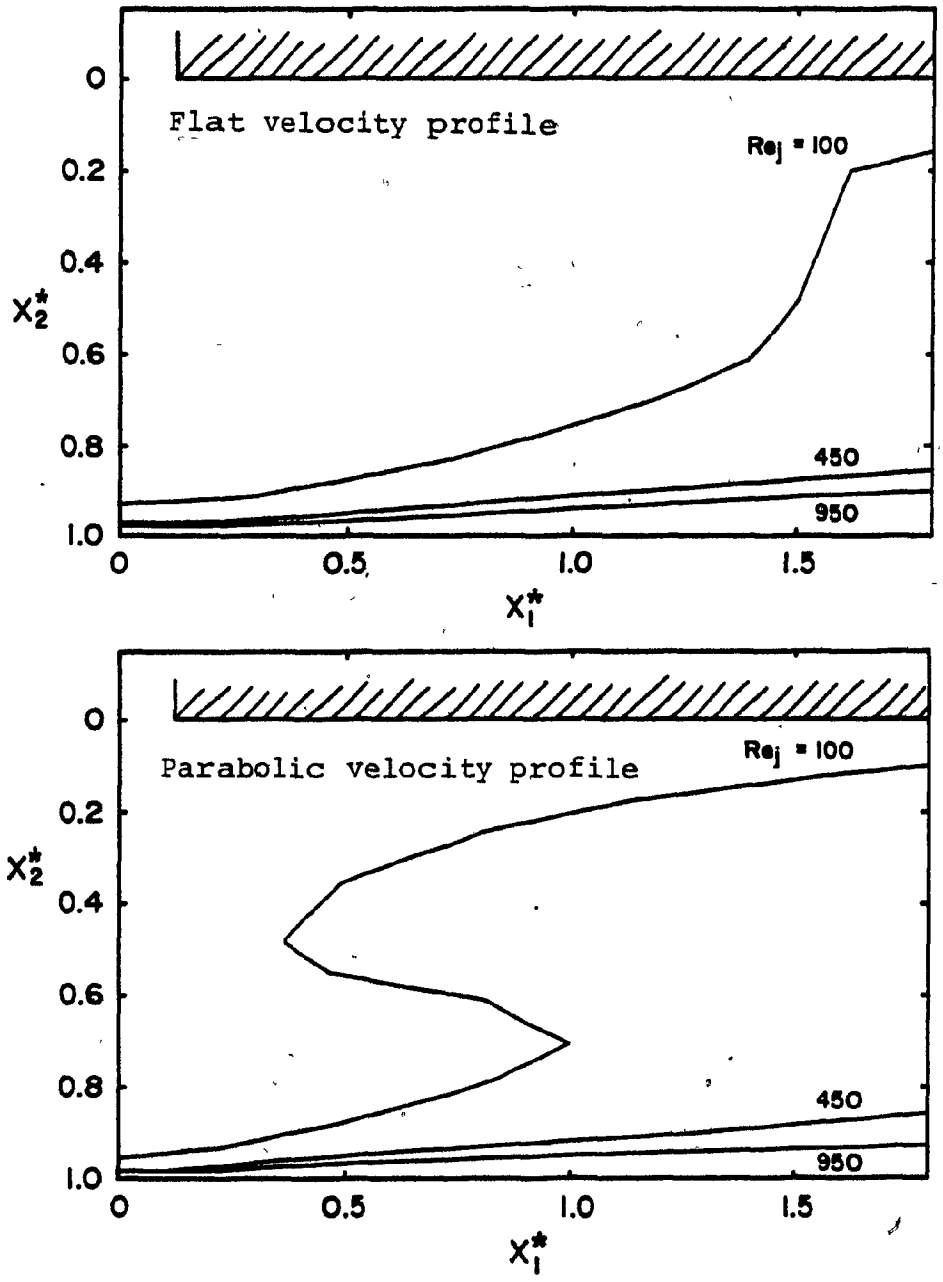


FIGURE 2.17. Isotherms T* = 0.90

characteristics. Consequently, the velocity and temperature gradients in the impingement region are steeper for a jet with a parabolic than a flat velocity profile at the nozzle exit. For example, in Figure 2.17 the isotherm $T^* = 0.9$ is closer to the plate in the impingement region for the parabolic profile. Also in Figures 2.15 and 2.16 the maximum vorticity at the impingement surface (location marked by an X) is much higher with the parabolic profile. Another feature from Figures 2.15 and 2.16 is the slower diffusion of the vorticity with increasing Reynolds number and parabolic velocity profile. The large amount of vorticity generated at the corner of the jet with a flat velocity profile spreads over the whole width of the jet before impingement for $Re_j = 100$, while for $Re_j = 950$ there is hardly any spreading.

As the numerical predictions of Chapter 2 are concerned mainly with skin friction and heat transfer in the impingement region, inspection of the velocity distributions in this region is of interest. The development and location of the maximum velocity parallel to the plate for the parabolic and flat velocity profile are shown, respectively, in Figures 2.18 and 2.19. For the parabolic inlet profile, development of the maximum velocity parallel to the impingement surface in Figure 2.18 is compared with the velocity distribution along the surface obtained by Sparrow and Lee (138) assuming inviscid flow. With increasing Reynolds number (or decreasing influence of viscosity), development of the velocity parallel to the impingement surface approaches the inviscid solution. Also note that the

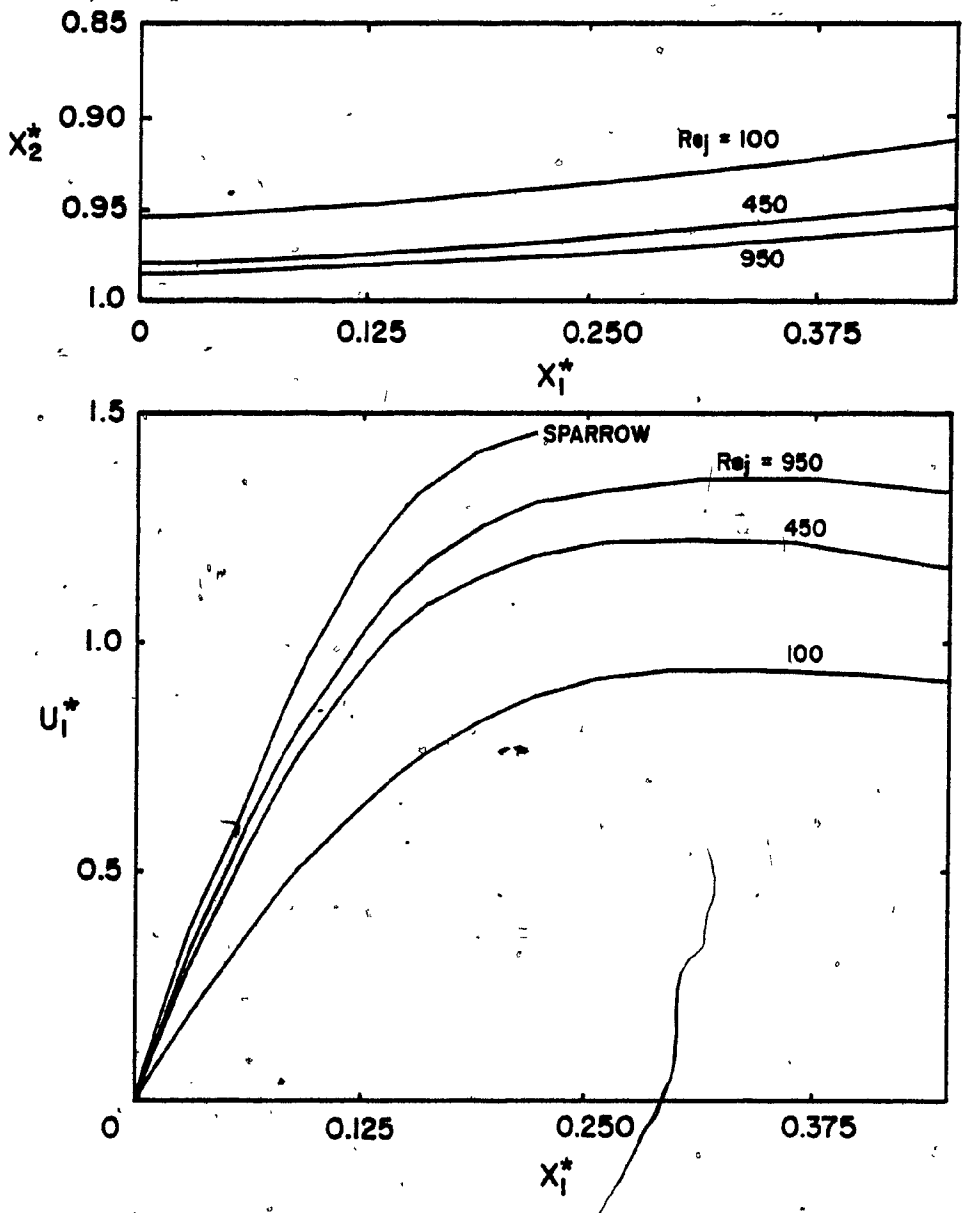


FIGURE 2.18. Location and development of the maximum velocity parallel to the impingement surface for a parabolic jet velocity profile

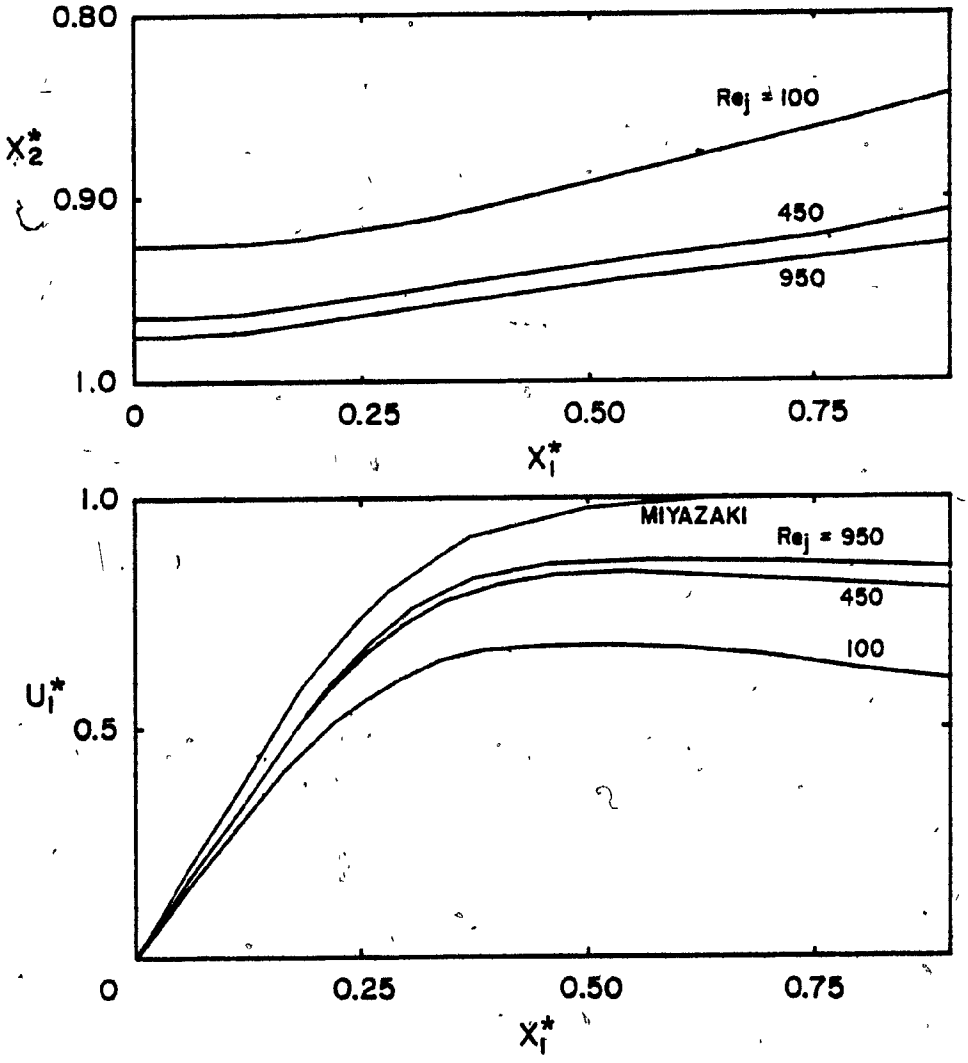


FIGURE 2.19. Location and development of the maximum velocity parallel to the impingement surface for a flat jet velocity profile

slope $\partial U_1^*/\partial X_1^*$ at $X_1^* = 0$, important when comparisons are made for heat transfer, is higher with the inviscid analysis. The location of the maximum velocity parallel to the wall, given in the upper part of Figure 2.18, quantifies the thickness of the boundary layer. Results for the flat inlet velocity profile jet are compared in Figure 2.19 with the inviscid flow results of Miyazaki and Silberman (97). The same trends as in Figure 2.18 are apparent (note the factor of 2 difference in the x-axis scales). The spreading of the boundary layer shown in the upper part of Figure 2.19 is shown more clearly in Figure 2.20 for Re_j of 100 and 950. The location of the maximum velocity for Re_j = 950 is difficult to determine because of the flatness of the profile in the stagnation region. This is not the case for Re_j = 100, because the U_2^* velocity profile in the impingement region, shown in Figure 2.21, is not flat, i.e. the mixing zone of the jet has already reached the axis of symmetry before entering the stagnation region (see also Figure 2.9). The different behaviour of the jets for Re_j = 100 and for Re_j = 450 and 950 is in agreement with the classification of jets by McNaughton and Sinclair (92) for a round jet, i.e. a "dissipated laminar jet" when the jet Reynolds number is smaller than 300 and a "fully laminar jet" when the jet Reynolds number is between 300 and 1000. Sparrow and Lee (138) in their theoretical analysis neglect the influence of viscous diffusion when $Re_j \geq 100$. The maximum in the U_2^* velocity profile evident in Figure 2.21 for Re_j = 950 is caused by the numerical error inherent to the upwind form of the hybrid differencing scheme (see Section

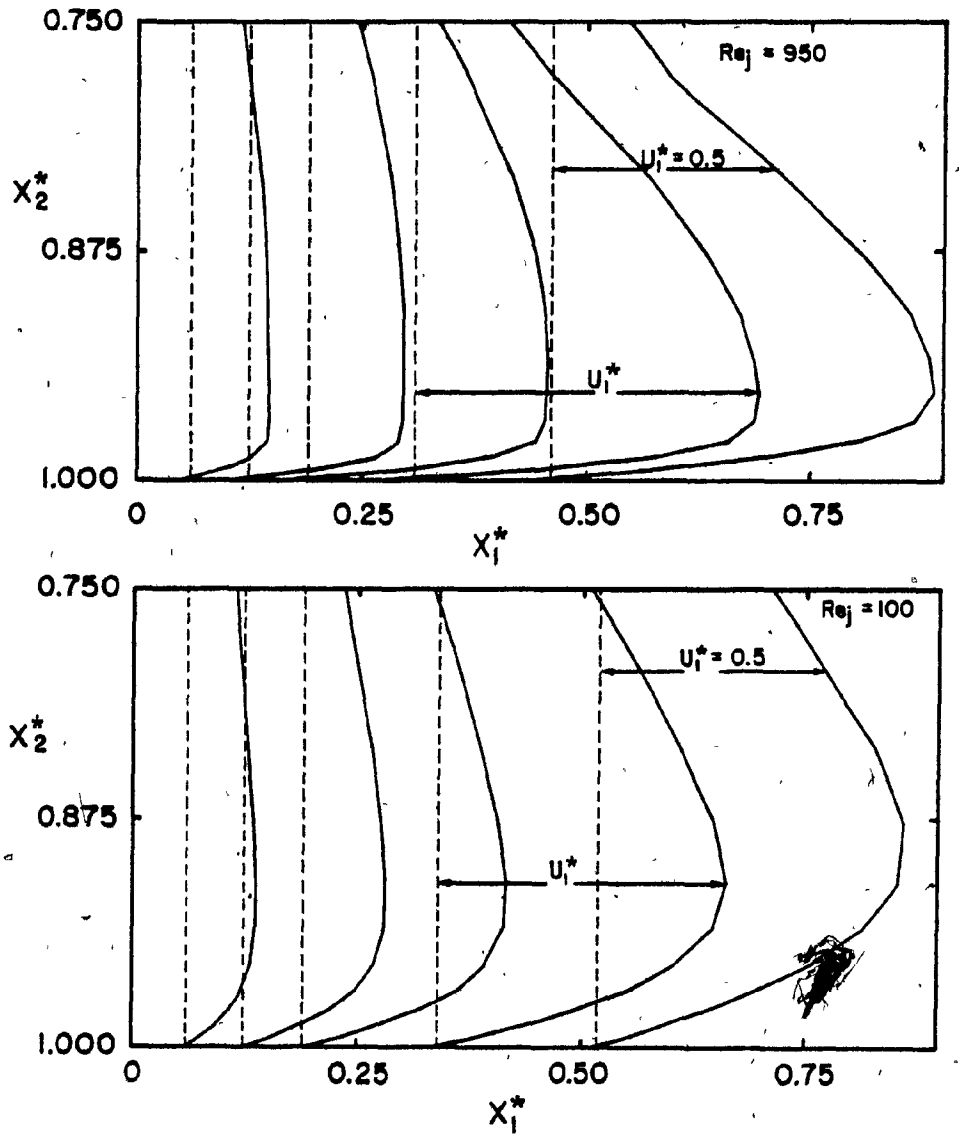


FIGURE 2.20. Development of U_1^* velocity distribution for a flat jet velocity profile

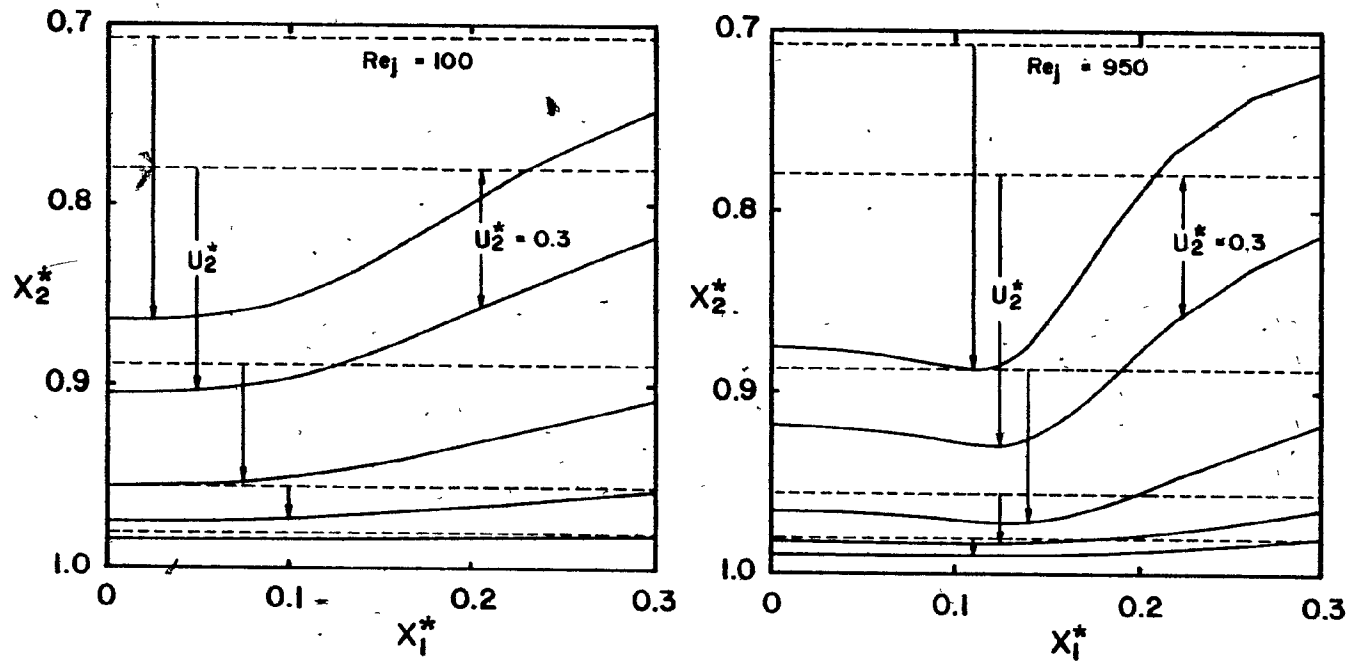


FIGURE 2.21. Development of U_2^* velocity distribution for a flat jet velocity profile

2.2.2.2 (a)). As with plane stagnation flow, the underprediction of the velocity in the X_2^*-direction decreases with increasing distance from the stagnation line. Because of the finite width of the jet, the U_2^* velocity eventually decreases with increasing X_1^*, leading to the maximum at $X_1^* \approx 0.125$ in Figure 2.21.

The lateral profiles of dimensionless heat transfer and skin friction at the impingement surface in the form of respectively $Nu_j/\sqrt{Re_j}$ and $\frac{1}{2} C_f\sqrt{Re_j}$ are given in Figures 2.22 and 2.23 for the two nozzle exit velocity profiles. The results clearly show that the simple Reynolds analogy, $St = \frac{1}{2} C_f$, is completely invalid in the stagnation region, a fact not always recognized by previous workers. The use of $\sqrt{Re_j}$ in representation of these profiles for laminar flow allows comparison of the present computations with the inviscid analysis of references (138) and (97).

Considering first the case of a flat velocity profile at the nozzle exit, the results of Miyazaki and Silberman (97) are represented in Figure 2.22 by two curves, independent of Re_j. The curves for $Re_j = 100$ from the present numerical study deviate the most from the inviscid flow analysis of Miyazaki and Silberman because of the significant spreading and retardation of the jet before impact at this low a Reynolds number. This effect is clearly shown in Figures 2.9 and 2.27.

The maximum heat transfer should be found at the stagnation point. For the case of a flat velocity profile the slight increase in heat transfer rate at about w/2 from the stagnation point for $Re_j = 450$ and 950 is again caused by the error in the

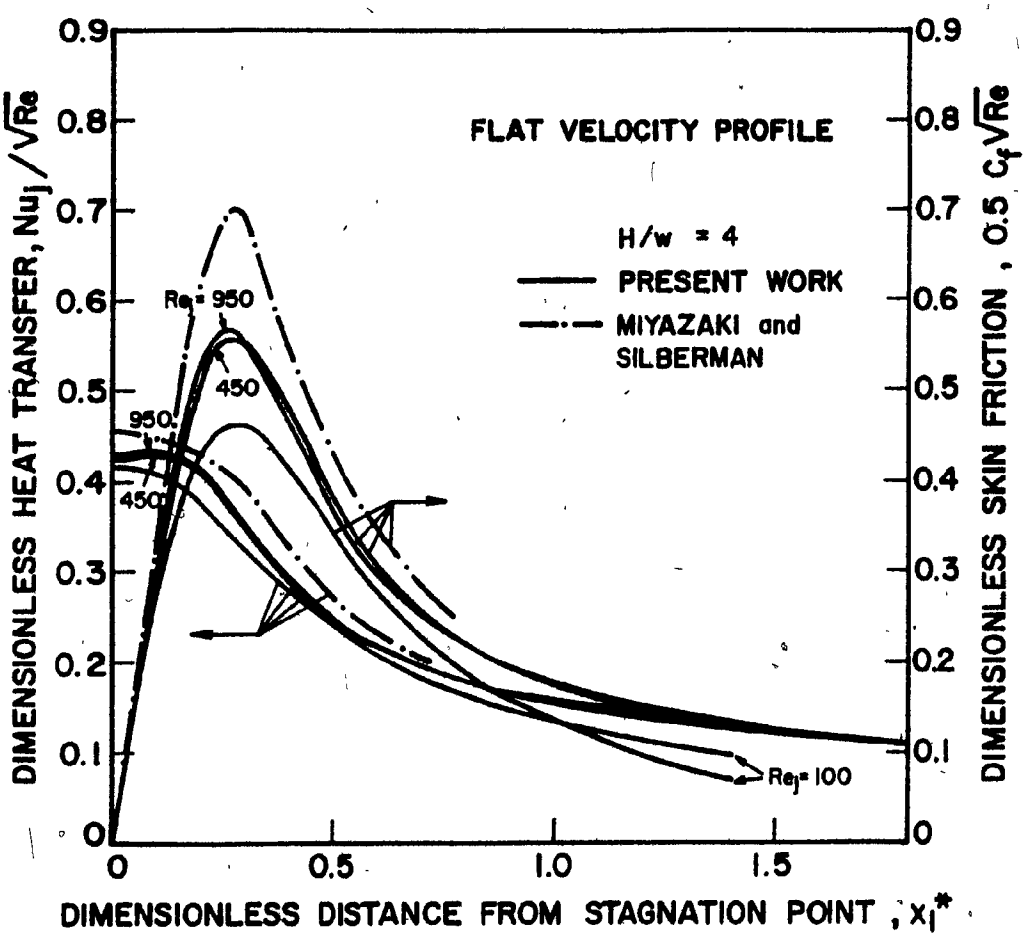


FIGURE 2.22. Heat transfer and skin friction distribution for a flat jet velocity profile

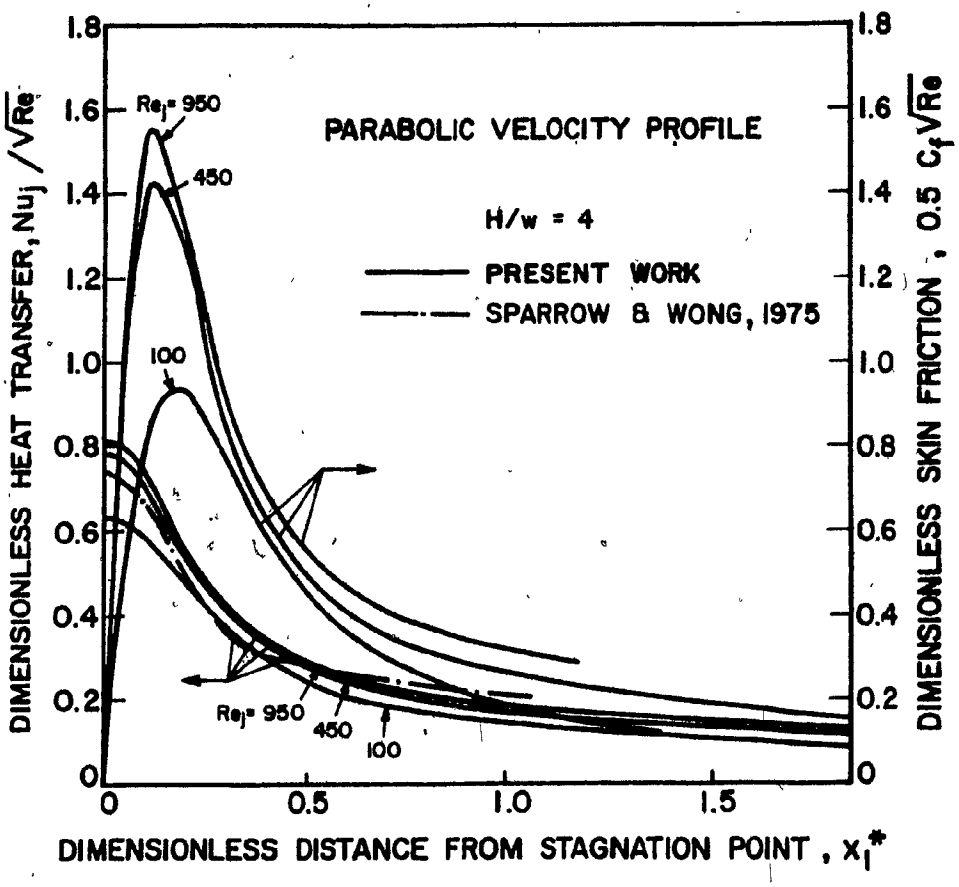


FIGURE 2.23. Heat transfer and skin friction distribution for a parabolic jet velocity profile

numerical differencing scheme. The location of this maximum coincides with the maximum of U_2^* in Figure 2.21. By analogy with the results for plane stagnation flow (see Appendix 4), stagnation point heat transfer will be slightly overpredicted with the hybrid differencing scheme. The maximum skin friction is located at slightly more than one nozzle width from the stagnation point.

The relation given by Sparrow and Lee (138) between stagnation heat transfer and the U_1^* velocity gradient at the stagnation point (obtained from their inviscid flow analysis) can be rewritten as

$$St_o = 0.690(dU_1^*/dX_1^*)^{\frac{1}{2}}/(Re_j \cdot H/w)^{\frac{1}{2}} \qquad (2.58)$$

for an impinging jet when Pr = 0.73. Equation (2.58) is obtained from the exact solution of the boundary layer equations. Insertion of the gradient of the maximum velocity parallel to the wall at the stagnation point (see Figure 2.19), for dU_1^*/dX_1^*, in equation (2.58), for the three values of Re_j gives for a flat velocity profile the values of St_o in the third column of Table 2.5. The good agreement of St_o in the third column with the numerically obtained St_o in the fourth column of Table 2.5 show that the numerical results are internally consistent. The last column in Table 2.5 is obtained when $dU_1^*/dX_1^* = 3.145$, calculated by Miyazaki and Silberman (97) from their potential flow analysis, is inserted in equation (2.58). The values in this column are consistently higher than the numerical predicted St_o because

TABLE 2.5. Comparison of Alternate Bases for St_o for a Flat Nozzle Exit Velocity Profile

Re_j	$(dU_1^*/dX_1^*)_{0,max}$	St_o (1)	St_o (2)	St_o (3)
100	2.60	.0557	.0570	.0612
450	2.73	.0269	.0274	.0288
950	2.75	.0186	.0191	.0198

(1) St_o calculated with equation (2.58) and $(dU_1^*/dX_1^*)_{0,max}$

(2) St_o numerical prediction from present work

(3) St_o calculated with equation (2.58) and $dU_1^*/dX_1^* = 3.145$

the value of $(dU_1^*/dX_1^*)_{0,max}$ from the present study is always smaller than 3.145 as a result of the decrease in the calculated axial jet velocity immediately after the nozzle exit (see Figure 2.27).

For the parabolic velocity profile jet the maximum skin friction at the wall is located approximately in line with the nozzle wall, i.e. at w/2 from the stagnation point. Thus for the case of H/w = 4 shown in Figure 2.23 this maximum occurs at about $X_1^* = H/8$. It is particular striking that the stagnation heat transfer for a parabolic velocity profile is 1.5 to 1.9 times that for a flat velocity profile. This is in agreement with the ratio of almost two, predicted by Sparrow and Lee (138). For the maximum skin friction at the wall, this ratio for the two inlet profiles is about 2.7 at $Re_j = 950$.

For a jet with a parabolic velocity profile at the nozzle exit, application of equation (2.58) leads to a set of results comparable to those of Table 2.5. Thus the last column in Table 2.6 is calculated with equation (2.58) and $dU_1^*/dX_1^* = 12.1$, obtained by Sparrow and Lee for the inviscid flow analysis. As for the flat inlet profile, the values for St_o are higher when based on the inviscid flow solution. The close agreement of the latter two columns again proves the internal consistency of the numerical results.

TABLE 2.6. Comparison of Alternate Bases for St_o for a Parabolic Nozzle Exit Velocity Profile

Re_j	$(dU_1^*/dX_1^*)_{0,max}$	$St_o^{(1)}$	$St_o^{(2)}$	$St_o^{(3)}$
100	6.10	.0852	.0862	.1200
450	9.63	.0505	.0505	.0566
950	10.58	.0364	.0358	.0389

Bases (1), (2) and (3) are as described with Table 2.5.

The last two columns of both Tables 2.5 and 2.6 are displayed as the two light lines in Figure 2.24, the two heavy lines being for the predicted results of the present study (basis (2) in Tables 2.5 and 2.6). The St_o values obtained in the present study are proportional to $Re_j^{-0.49}$ and $Re_j^{-0.4}$ for the flat and parabolic velocity profile, respectively, in agreement with the

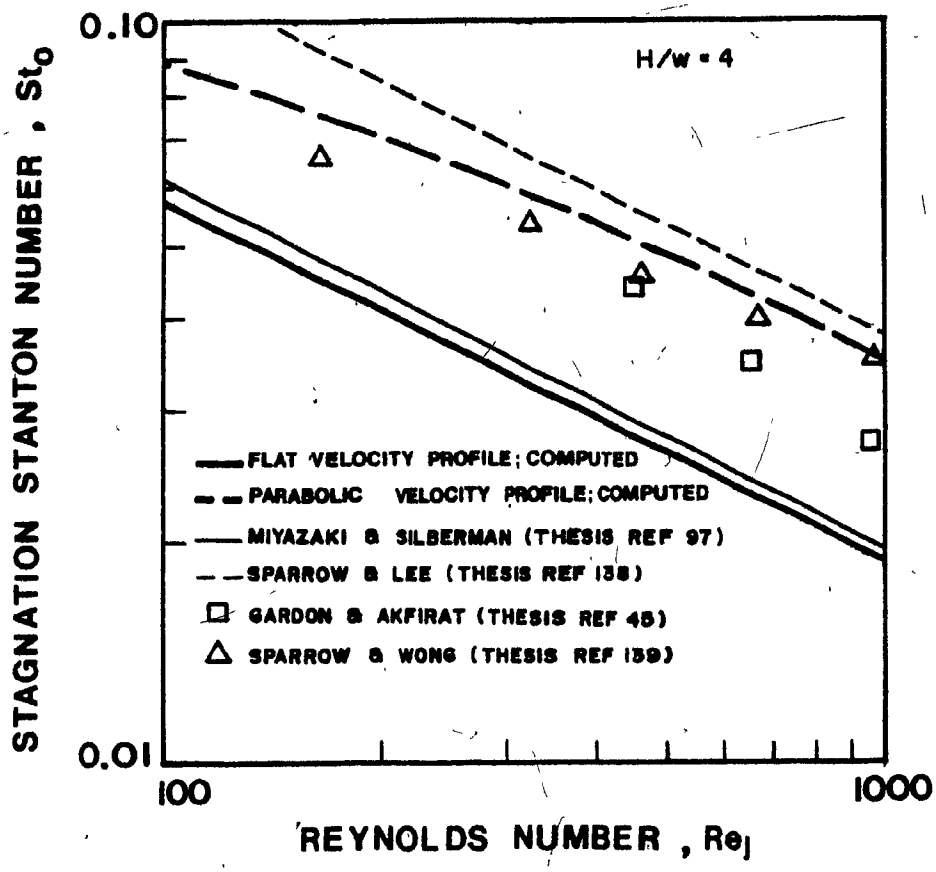


FIGURE 2.24. Effect of Reynolds number on stagnation point heat transfer

correlation of Sparrow and Wong (139). The finding by Saad (124) of St_o proportional to $Re^{-0.64}$ for a parabolic round jet seems unlikely, since for laminar flow a power slightly less negative than -0.5 is expected as a result of the decreasing influence of viscosity for increasing Re_j. The underprediction of heat transfer at higher Re found by Saad is probably due to too coarse a grid near the impingement surface. Saad reports having set the spacing of the gridline next to the impingement surface at 1/32 of the nozzle diameter. The linear temperature gradient assumption would be valid out to this grid spacing only for Nusselt numbers not larger than about 10. However, Nusselt numbers up to more than 50 are reported. The finding of St_o proportional to $Re^{-0.44}$ by Huang et al. (64) for a round jet with a parabolic jet profile and a small swirl (producing only a slight reduction in the heat transfer) is in reasonable agreement with the present findings.

Also included in Figure 2.24 are the heat transfer equivalents of the experimental mass transfer data of Sparrow and Wong (139) for impingement on a naphthalene plate of an unconfined slot jet with a parabolic velocity profile at the nozzle exit. For Sc = 2.5 and Pr = 0.73 the conversion was made on the basis of Nu = 0.6225 Sh, this relation being derived from the theoretical analysis of Sparrow and Lee (138). The mass transfer data at H/w = 4 are obtained by interpolation of their results at spacings of 2 and 5. The good agreement apparent between this derived data of Sparrow and Wong and the numerical results of the present study may be taken in part as indicating

that the absence of a confinement surface in their experimental set-up has only a minor effect on stagnation point conditions.

The experimental data of Gardon and Akfirat (45) are intermediate between the numerical results for flat and parabolic velocity profiles probably because the velocity profiles generated in their nozzle were intermediate between these two limiting cases. Therefore it may be inferred that Gardon and Akfirat's correlation for stagnation heat transfer, in which Nu_o is proportional to $Re^{0.32}$, includes an effect of velocity profile at the nozzle exit as an unspecified dependent variable, i.e. with increasing Re_j the velocity profile at the nozzle becomes flatter, thereby reducing the overall dependence of Nu_o on Re. This interpretation was tested by using as input to the numerical procedure the velocity profile that would have been generated in their nozzle for $Re_j = 450$. The velocity profile at the exit of a nozzle 8w in length was obtained from Schlichting (131). Agreement between the experimental data and the computer results is excellent except at the stagnation point, as can be seen in Figure 2.25. The difference between the computer and experimental results near the stagnation point are due in part to the averaging effect of the heat flux sensor used by Gardon and Akfirat, the size of which can be seen from Figure 2.25 to be sufficiently large to affect experimental Nu_o values significantly. It can be inferred from the large differences in St_o between the parabolic and flat velocity profile jet recorded on Figure 2.24 that a slightly higher jet velocity at the axis of symmetry leads to a considerable higher stagnation heat transfer.

It is also apparent from Figure 2.25 that the influence on heat transfer of a confining surface is small, with the higher heat transfer being obtained without a confinement surface. Thus for applications which require a confinement surface, use of predictions correct for an unconfined jet would lead to values higher than would actually be obtained.

A further check of results computed by methods of the present study with experimental results is shown in Figure 2.26. Here the mass transfer distributions obtained by Sparrow and Wong (139) for a fully developed laminar slot jet at spacings, H/w, of 2 and 5 are compared with the present computation at H/w = 4, all at Re_j = 450. As before, their mass transfer results for Sc = 2.5 are converted to heat transfer at Pr = 0.73 through the relation Nu = 0.6225 Sh. Their impingement surface extended only 5.5w from stagnation, i.e. to S/H of only 2.75 and 1.1 for their H/w spacings of 2 and 5, respectively. The increase of transfer rates near the edge of the impingement surface has been noted in connection with Figure 2.13(b). Although all comparisons were made at Re_j = 450, it should be noted that if a correction is made for the aspect ratio of the slot jet, as pointed out by Sparrow and Lee (138), the equivalent Reynolds number should be 475.

Discussion of the effects of Reynolds number and jet velocity profile is concluded with reference to the axial velocity decay of the jet, shown in Figure 2.27. The nondimensional axial velocity decay profiles tend to become independent of Reynolds number at the upper end of the Re_j range investigated.

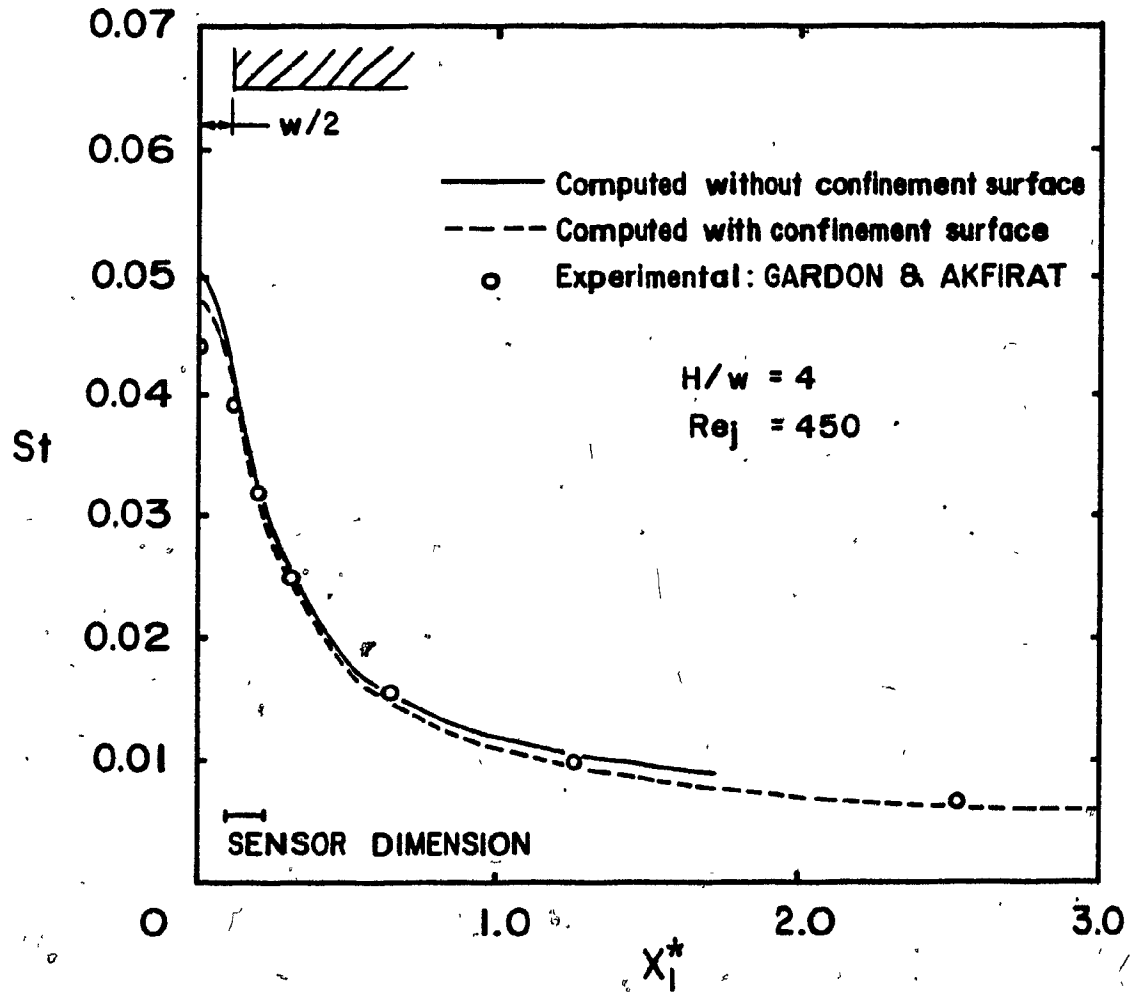


FIGURE 2.25. Comparison with experimental heat transfer distribution of Gardon and Akfirat

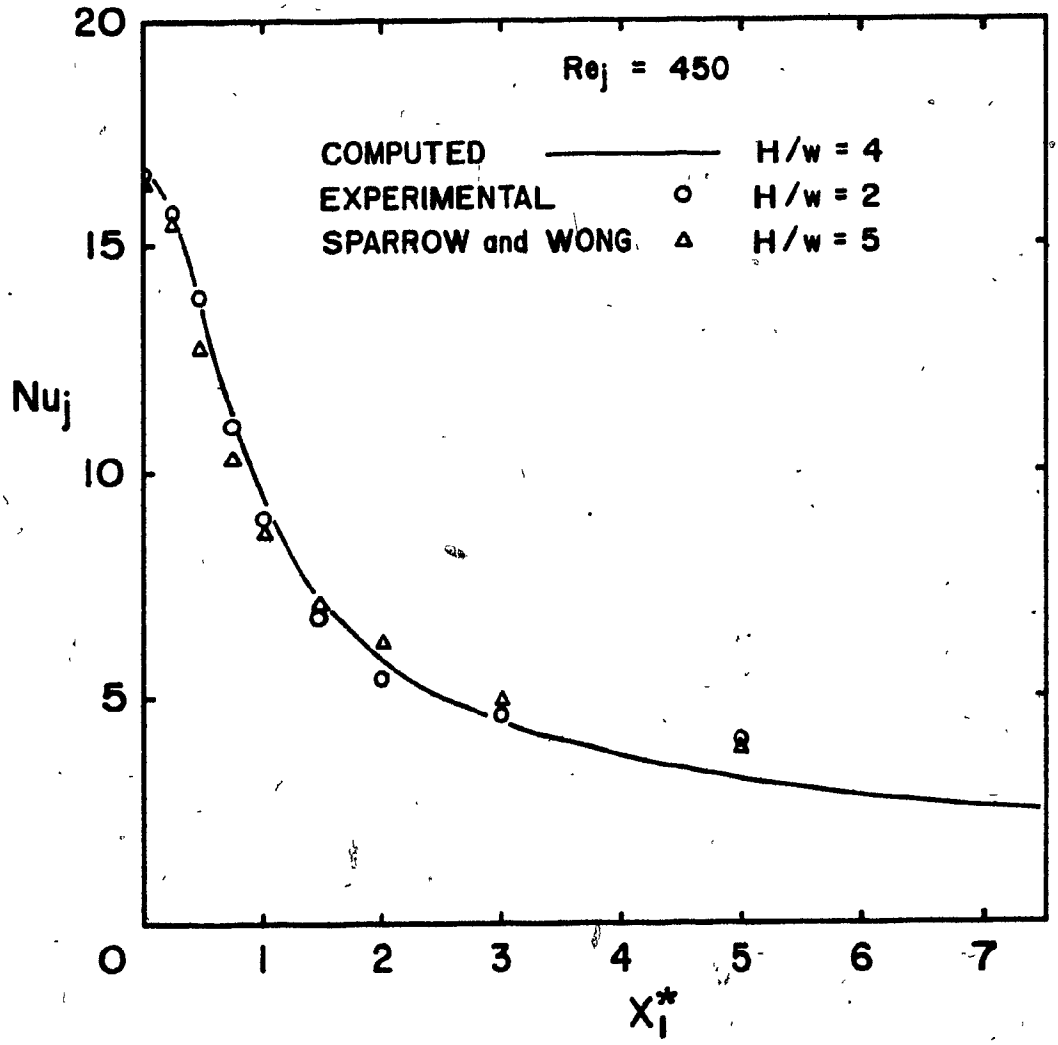


FIGURE 2.26. Comparison with experimental heat transfer distribution of Sparrow and Wong

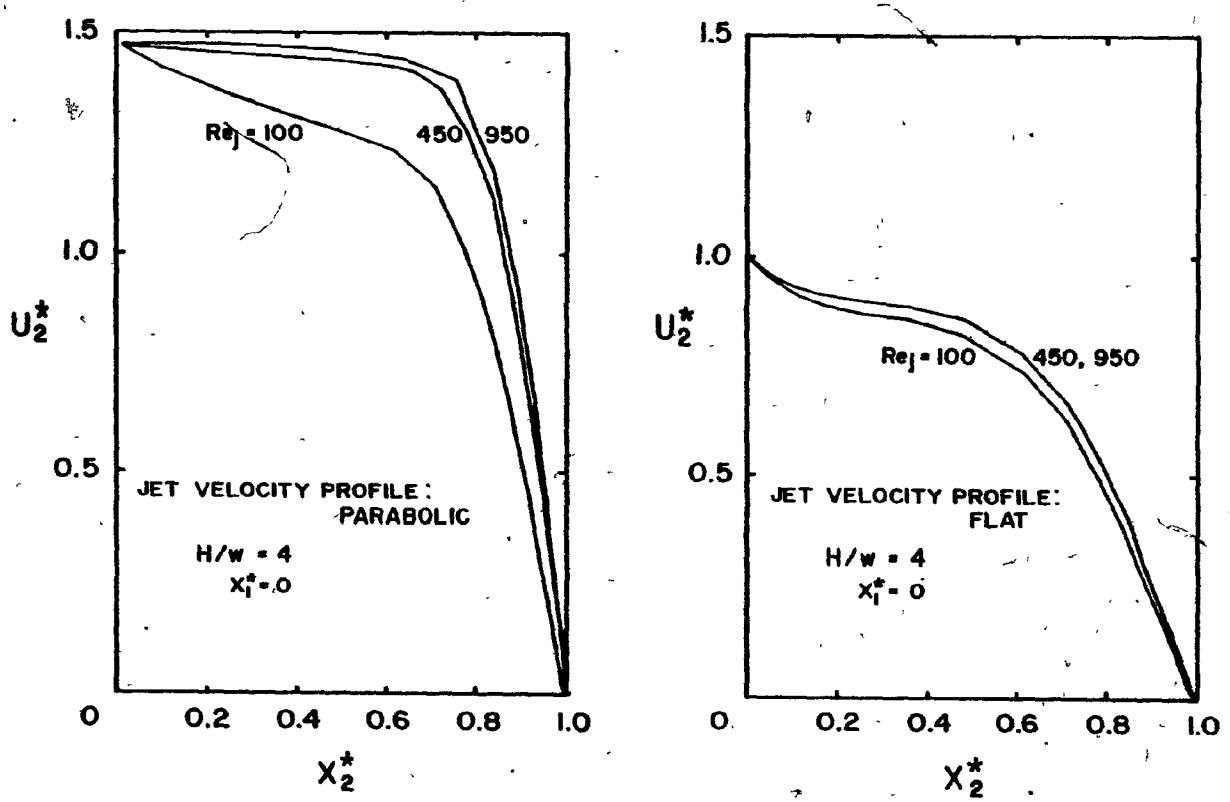


FIGURE 2.27. Centerline axial velocity decay

Viscous effects are responsible for the faster decay at Re_j = 100. The steep velocity decay immediately downstream of the nozzle exit for all Re must be due to the vorticity calculated at the edge of the nozzle because at these Reynolds numbers the axial velocity at the nozzle exit is not disturbed by downstream events. Support for this view is provided by Samuels and Wetzel (127) who found that at these Reynolds numbers the jet fluid is not "aware" of the exit until this position is actually reached. With the parabolic velocity profile the sudden velocity decay amounts for all three Reynolds numbers to less than 2% of the nozzle exit velocity. For the flat velocity profile the initial decrease in axial velocity persists over a considerably longer distance from the nozzle exit. Since this much decrease is physically unrealistic, the computed heat transfer results in the stagnation region for the flat velocity profile are thought to be underpredicted by 5 to 10%. For a square laminar jet Samuels and Wetzel (127) found experimentally that for Reynolds numbers larger than 160 the axial diffusion of momentum can be ignored, resulting in a collapse of the axial velocity decay to a single curve when axial distance is divided by Reynolds number. It is clear from Figure 2.27 that for the present results, division of X_2^* by Re_j would not lead to a single curve due to the sudden decrease in axial velocity at the nozzle exit for both jet velocity profiles.

2.2.3.2 Effect of Nozzle to Impingement Surface Spacing

The effect of impingement surface spacing, H/w, for values

of 4, 8 and 12 was investigated for $Re_j = 450$ and a flat velocity profile at the nozzle exit. It was difficult to obtain a converged solution at H/w = 12 and impossible at H/w = 16 even by underrelaxing the wall and field vorticities by a factor 0.5. This convergence problem, discussed qualitatively in Section 2.2.2.1 (a), will be considered first as it limited the range of data for impingement surface spacing.

Shown in Figure 2.28 is the development of the sum of the vorticity at all the inner field grid points (SUMNW) during the computation for the case of H/w = 12. Note that the scale of SUMNW is enlarged 500 times after 400 iterations. The underrelaxation factors were set equal to 1.0. During the first 360 iterations a smooth damped sinusoidal behaviour was obtained for SUMNW. Enlargement of the scale for SUMNW after 400 iterations reveals that the changes in SUMNW from iteration to iteration were larger than the average change in SUMNW over many iterations, leading to the noisy behaviour shown. After 500 iterations the largest variations in the vorticity occur at Boundary III at the separation between inflow and outflow. The absolute value of the vorticity variation is of the order O(1) which is equal in order of magnitude to the vorticity at this location. This means that after 500 iterations the convergence criterium has not been fulfilled. However when the skin friction and heat transfer distribution along the impingement surface after 400 iterations are compared with the same distributions after 500 iterations, then it is found that the maximum differences are respectively smaller than 2 and 1%. Therefore

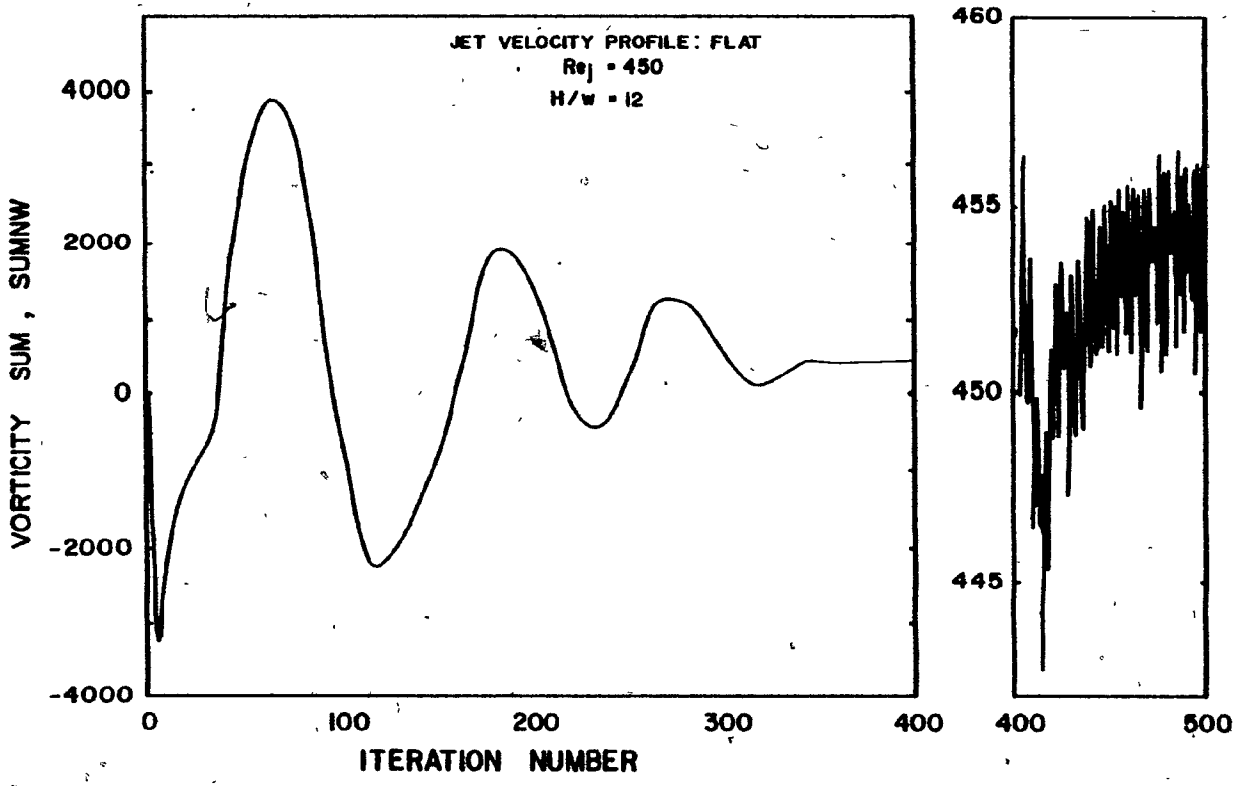


FIGURE 2.28. Stability of numerical procedure at H/w = 12

the solution obtained after 500 iterations can be considered converged when the recirculation area is not taken into consideration. For H/w = 16 the fluctuations in the recirculation area were so large that the whole flow field was affected.

The free streamline contours for H/w spacings of 4, 8 and 12 are shown in Figure 2.29. The length of the impingement surface, as S/w, was respectively 16.4, 13.1 and 13.1 or, as S/H, was 4.1, 1.64 and 1.09. It is clear that over this range of H/w, impingement surface spacing has little influence on the location of the free streamline with respect to the impingement surface. On detailed inspection it may be seen that the free streamline for H/w = 12 approaches the stagnation point somewhat closer than for H/w = 8, but not as close as for H/w = 4. Between impingement surface spacings of from 2 to 9 the spreading of the jet is only about 10%. This behaviour and the increase in jet width immediately downstream of the nozzle exit is reflected also in the centerline axial velocity decay profiles of Figure 2.30(a). Unrealistically strong reductions in centerline axial velocity during the first 1w after the nozzle exit is apparent for all three impingement surface spacings, 4w, 8w and 12w, although the effect is somewhat less pronounced for the spacing H/w = 4. Alternately, looking at the profiles from the perspective of the impingement surface it can be seen that its influence is felt by the centerline axial velocity starting at about 3w from impingement. This region of influence is about 1½ times that obtained by the theoretical analysis made by Miyazaki and Silberman (97). By contrast, Figure 2.27

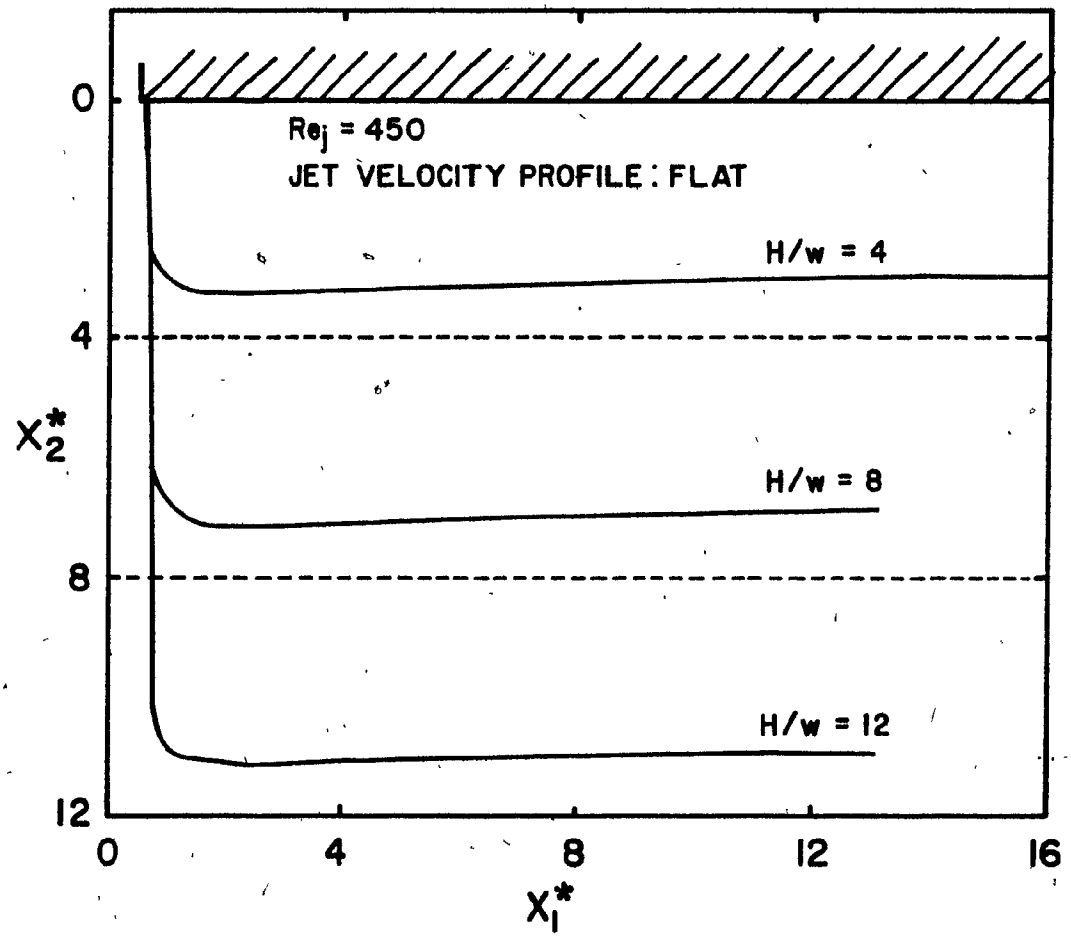


FIGURE 2.29. Effect of impingement surface spacing on free streamline contours

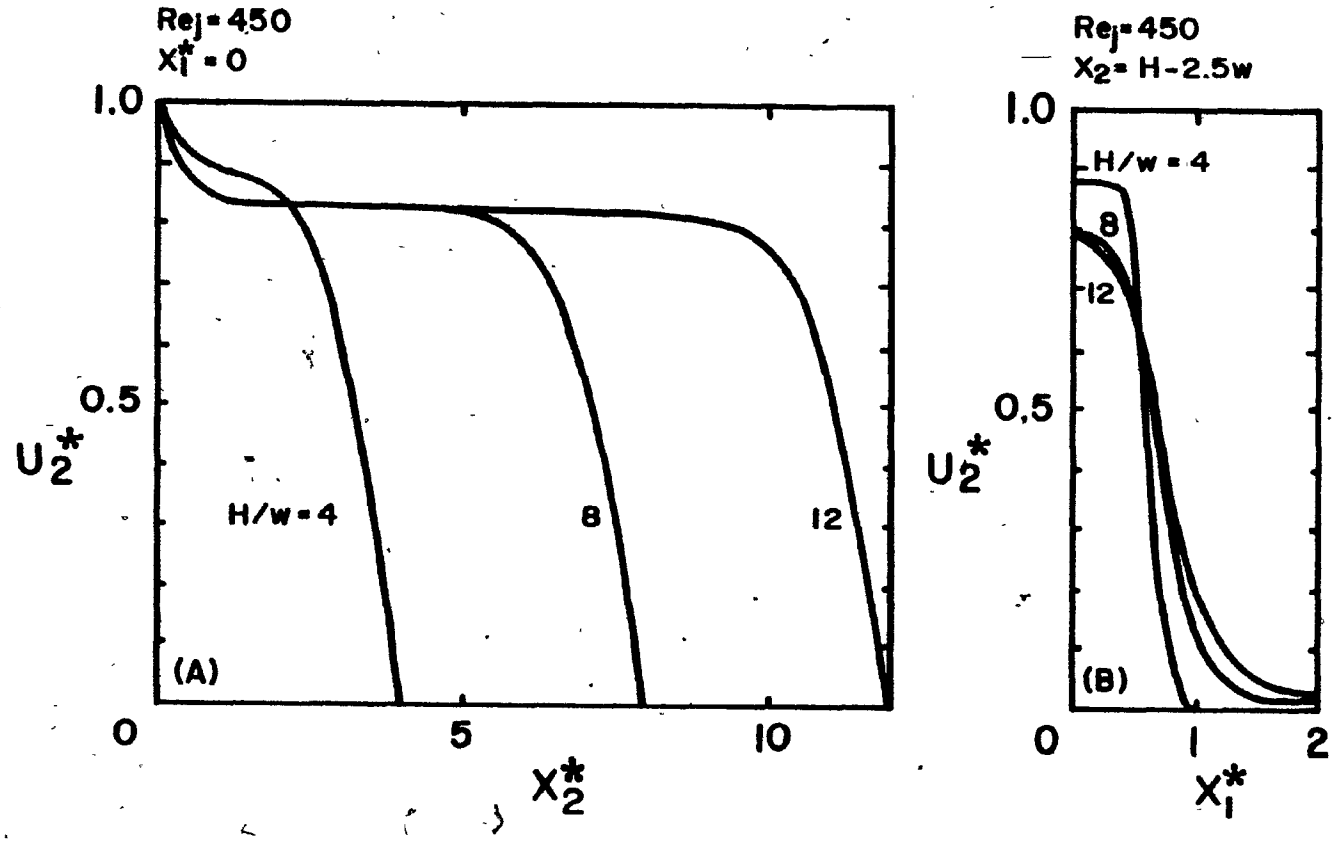


FIGURE 2.30. Effect of impingement surface spacing on jet velocity profile development

indicates that for a jet with a parabolic nozzle exit velocity profile, the influence of the impingement surface on centerline axial velocity is felt to only about 1.5w from the surface when H/w = 4, independent of Re_j. This extent of influence of the impingement surface is about 1.5 times the distance obtained theoretically by Sparrow and Lee (138). The somewhat larger extent of influence found in the present numerical study may be attributed to the effect of viscosity, not included in the Sparrow and Lee analysis.

Lateral profiles of axial velocity at a distance of 2.5w from the impingement surface are shown in Figure 2.30(b) for H/w spacings of 4, 8 and 12. At this separation the influence of the impingement surface is only beginning to be felt. The velocity profiles given by the solution for a two-dimensional laminar free jet of Schlichting (131) are of limited use and cannot be compared to those of the present study because Schlichting's solution is valid only for distances larger than $0(\frac{Re_j}{10})$ nozzle width downstream from the nozzle exit. By 10.5w from the nozzle exit, i.e. at 2.5w from impingement for H/w = 12 spacing, the influence of viscosity has just penetrated to the axis of symmetry, leading to a somewhat sharper lateral profile of axial mean velocity for H/w = 12 than for H/w = 8. From Schlichting's theoretical solution of the "plane half-jet" it can be derived that the influence of viscosity has penetrated to the axis of symmetry when $X_2/w \approx 0.02\ Re_j$, i.e. at $X_2/w = 9$ for $Re_j = 450$. This estimate based on Schlichting's theoretical solution is then seen to coincide with the findings of the

present study, as presented in the profiles of Figure 2.30(b).

Although a jet with a parabolic velocity profile at the nozzle exit assumes a steadily less peaked velocity profile with increasing distance from the nozzle, the velocity profile of a jet leaving the nozzle with a flat velocity profile first changes in the direction of becoming more peaked around the nozzle centerline before this trend eventually reverses with the profile finally becoming less peaked. Figure 2.30(b) shows that up to 10.5w from the nozzle exit the profile of an initially flat jet at $Re_j = 450$ is still becoming more peaked near the jet centerline. Thus for an initially flat jet, this effect of development of an increasingly peaked profile explains the otherwise curious effect of the slightly higher stagnation heat transfer for $H/w = 12$ than for $H/w = 8$, apparent in Figure 2.31. Except for small differences in the stagnation region, the heat transfer distributions out to $X_2/w = 12$ are all quite similar for impingement surface spacings from 4w to 12w. The corresponding skin friction distributions given in Figure 2.32 show the same trends, although indicating that heat transfer is slightly less sensitive to the H/w spacing than is skin friction. It should be kept in mind that the results noted in this section for effect of impingement surface spacing are for an inlet jet with an initially flat velocity profile at $Re_j = 450$. Thus although the trends for effect of H/w with jets of other nozzle exit velocity profiles and Re_j will be similar, the quantitative aspects depend on these two parameters as well.

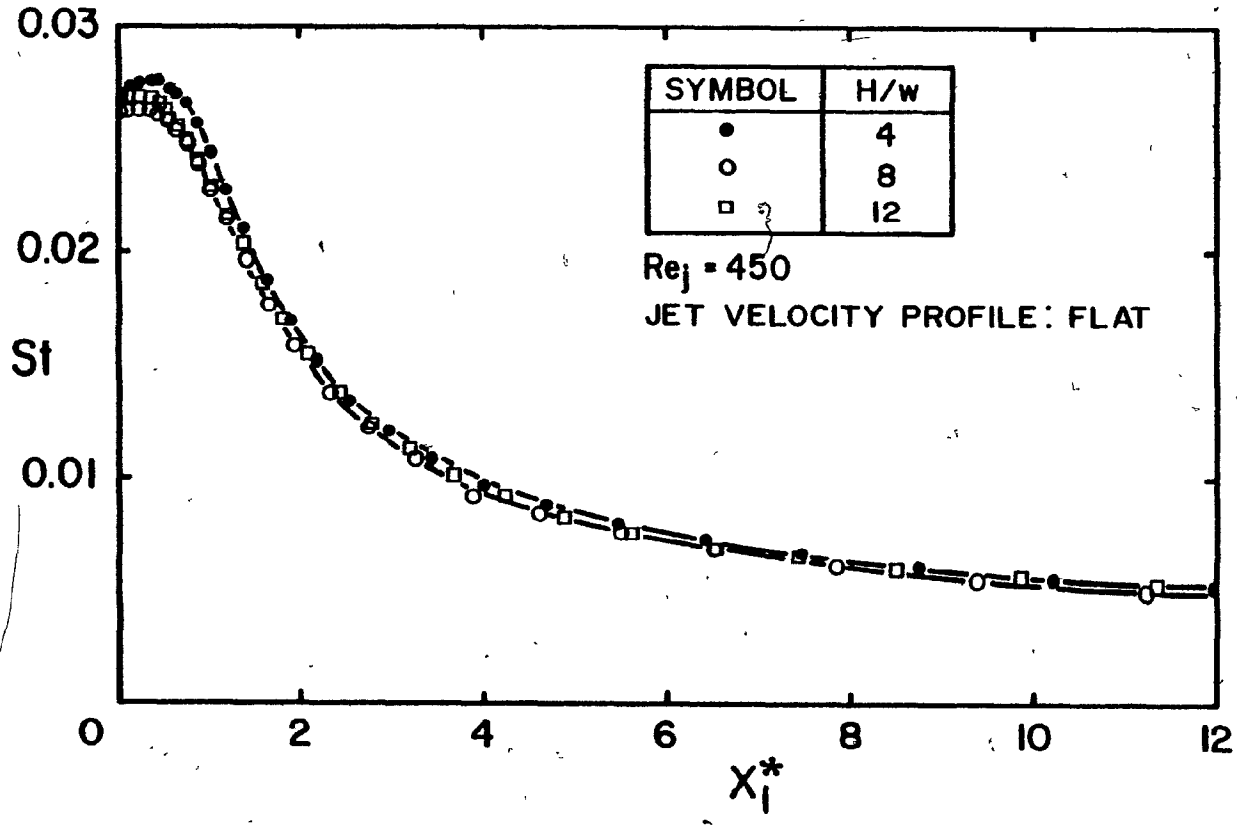


FIGURE 2.31. Effect of impingement surface spacing on heat transfer distribution at the impingement surface

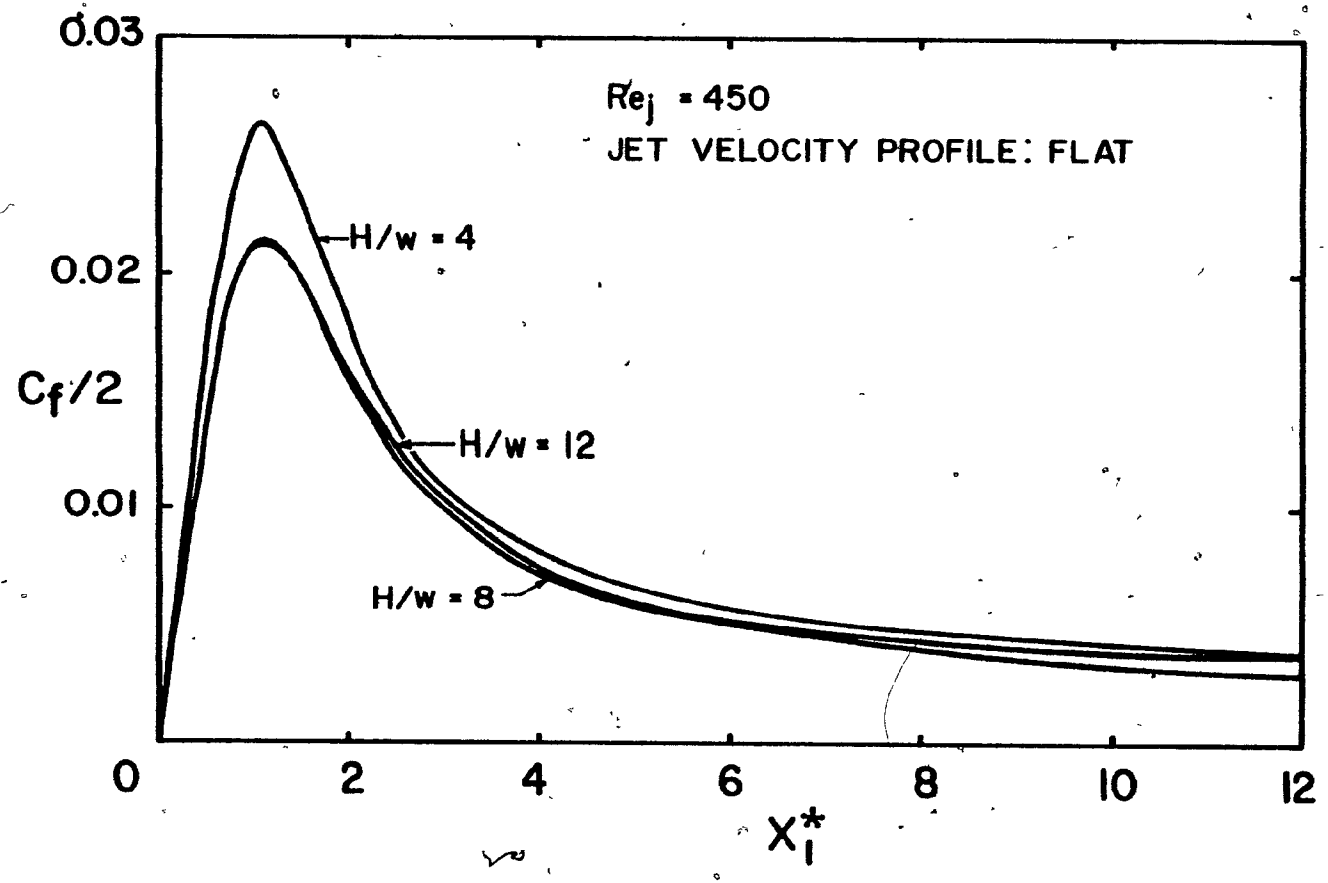


FIGURE 2.32. Effect of impingement surface spacing on skin friction distribution at the impingement surface

2.2.3.3 Effect of Throughflow at the Impingement Surface

The effect on flow and heat transfer of throughflow into the impingement surface was studied using the hybrid finite difference scheme for $Re_j = 100$, $H/w = 4$ and a parabolic velocity profile at the nozzle exit. The ratios between the mass velocity at the impingement surface and the nozzle, M_{U_S}, were -0.01, 0, 0.01 and 0.025. Consistent with the sign convention for U_2 velocity normal to the impingement surface, a positive value of M_{U_S} indicates throughflow into the surface while a negative value indicates a blowing or evaporative velocity from the surface into the jet flow. Shown in Figure 2.33 are the free streamlines for three flow rates at the impingement surface. Also shown are the locations of the recirculation eye. The value of the stream function at the center of recirculation is -0.190, independent of M_{U_S}, indicating that over the range of variables studied the maximum entrained flow is about 50% of the jet flow, independent of the direction and amount of surface throughflow. As expected, the size of the recirculation region increases and the free streamline moves closer to impingement surface with increasing M_{U_S}. For the computational reasons discussed in connection with equation (2.27) and in order to ensure a reasonable net outflow at Boundary III (Figure 2.1) for throughflow rates as high as $M_{U_S} = 0.025$, the impingement surface was made permeable from the stagnation point only up to $X_1^* = 3.0 = X_{1S}^*$. As will be shown later, a significant increase in X_{1S}^* for $M_{U_S} = 0.01$ did not appreciably change the results in the impingement and wall jet region up to one to two I-gridlines before the start of the im-

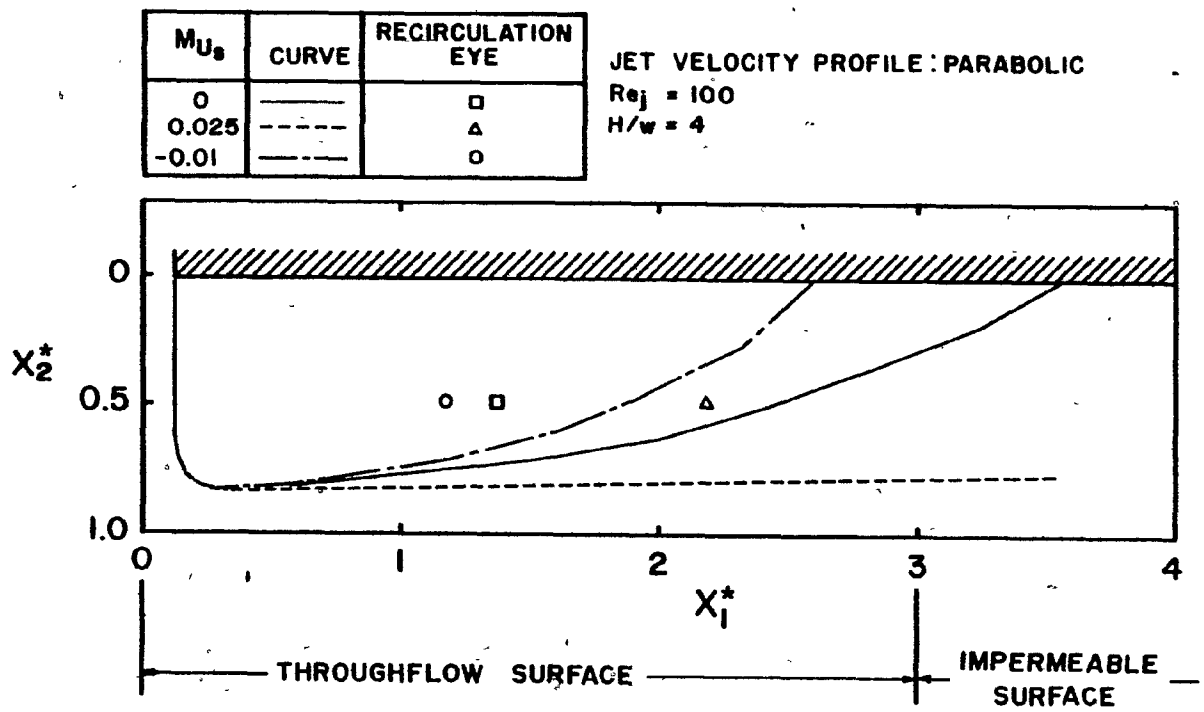


FIGURE 2.33. Effect of throughflow on location of the free streamline

permeable section. Thus results of the present study with a small impermeable section of impingement surface near the outflow are representative of systems in which throughflow occurs across the entire impingement surface.

Effects of throughflow on the velocity distributions are shown in Figures 2.34 to 2.37. The influence of the throughflow on centerline axial velocity decay begins at about 1.5w from the impingement surface, i.e. at $X_2^* = 0.625$ in Figure 2.34. It is significant that this is at the same location where the influence of an impermeable impingement surface is felt by a parabolic jet at H/w = 4 (see Section 2.2.3.2). The difference between the axial velocity U_2^* at the centerline with or without throughflow was always smaller than 1.5 M_{U_s}, a finding which may be seen more clearly in Figure 2.35. Here it may also be seen that the absolute value of the change in axial velocity because of throughflow is essentially the same over the full width of each profile. The experimental measurements of effect of throughflow made by Obot (105) and Abdul-Wahab et al. (1) are inconsistent with the present findings. In the region outside the impingement region these investigators obtained respectively an increase in the U_2 velocity for a turbulent impinging round jet and a decrease in the U_2 velocity for a turbulent impinging slot jet. In agreement with the present calculations are the numerical results of Saad (124) and Huang (63) for a laminar impinging round jet, both of which show that throughflow at the impingement surface does not affect the flow outside the impingement region.

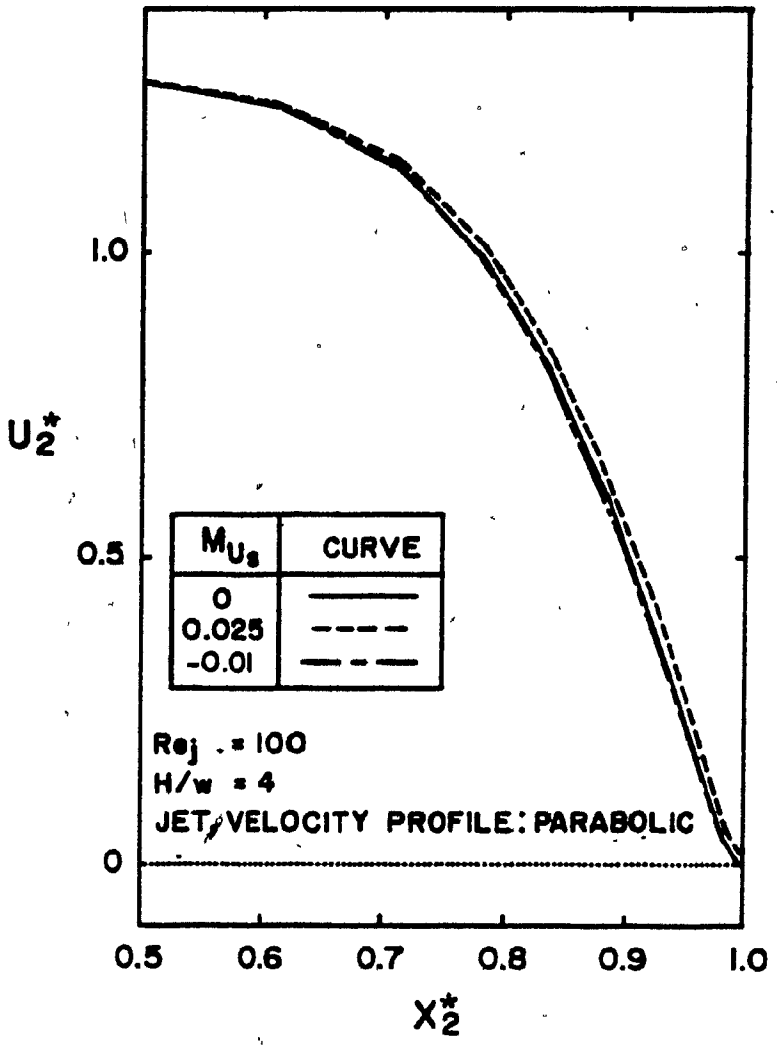


FIGURE 2.34. Effect of throughflow on centerline axial velocity decay

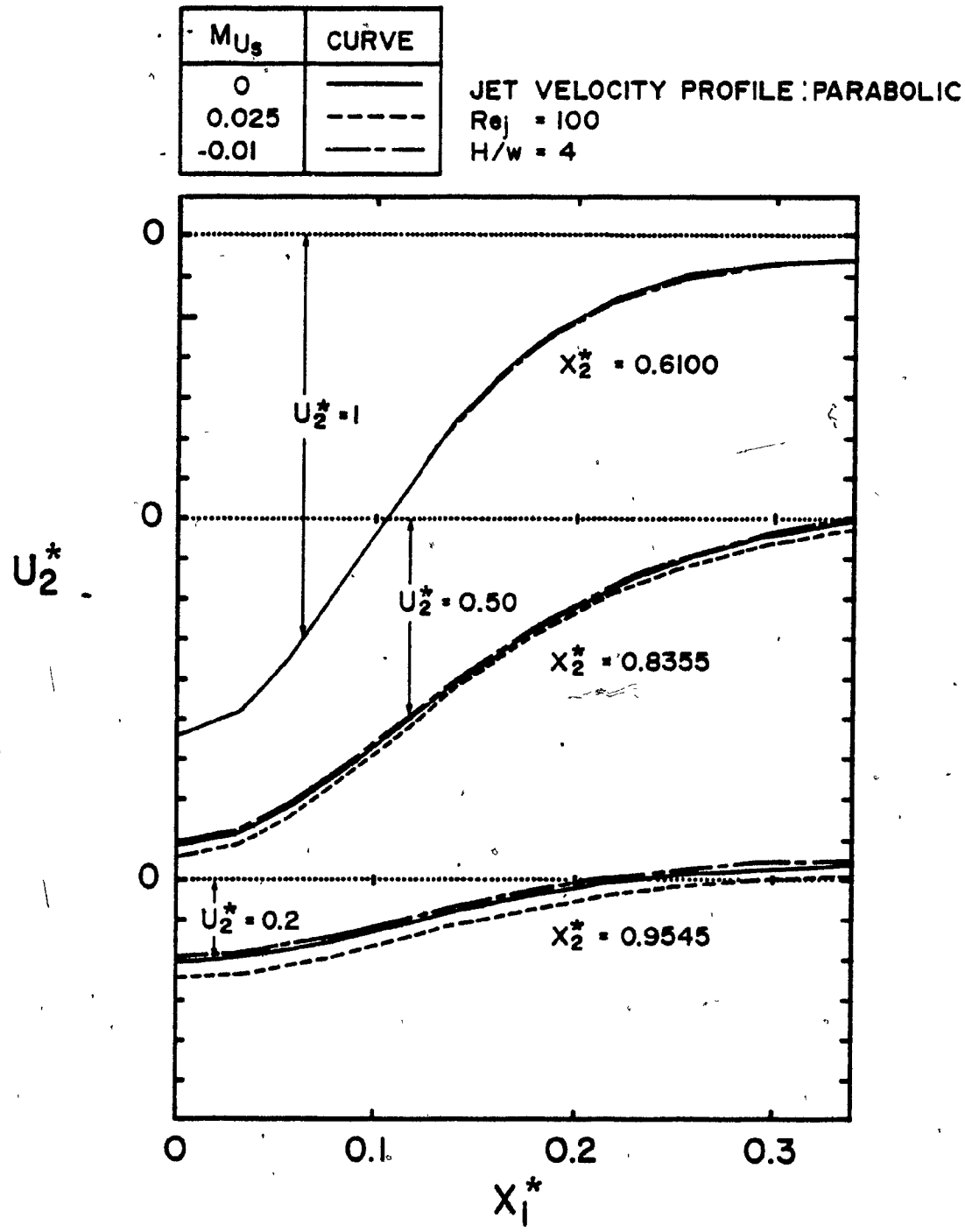


FIGURE 2.35. Effect of throughflow on U_2^* velocity profile

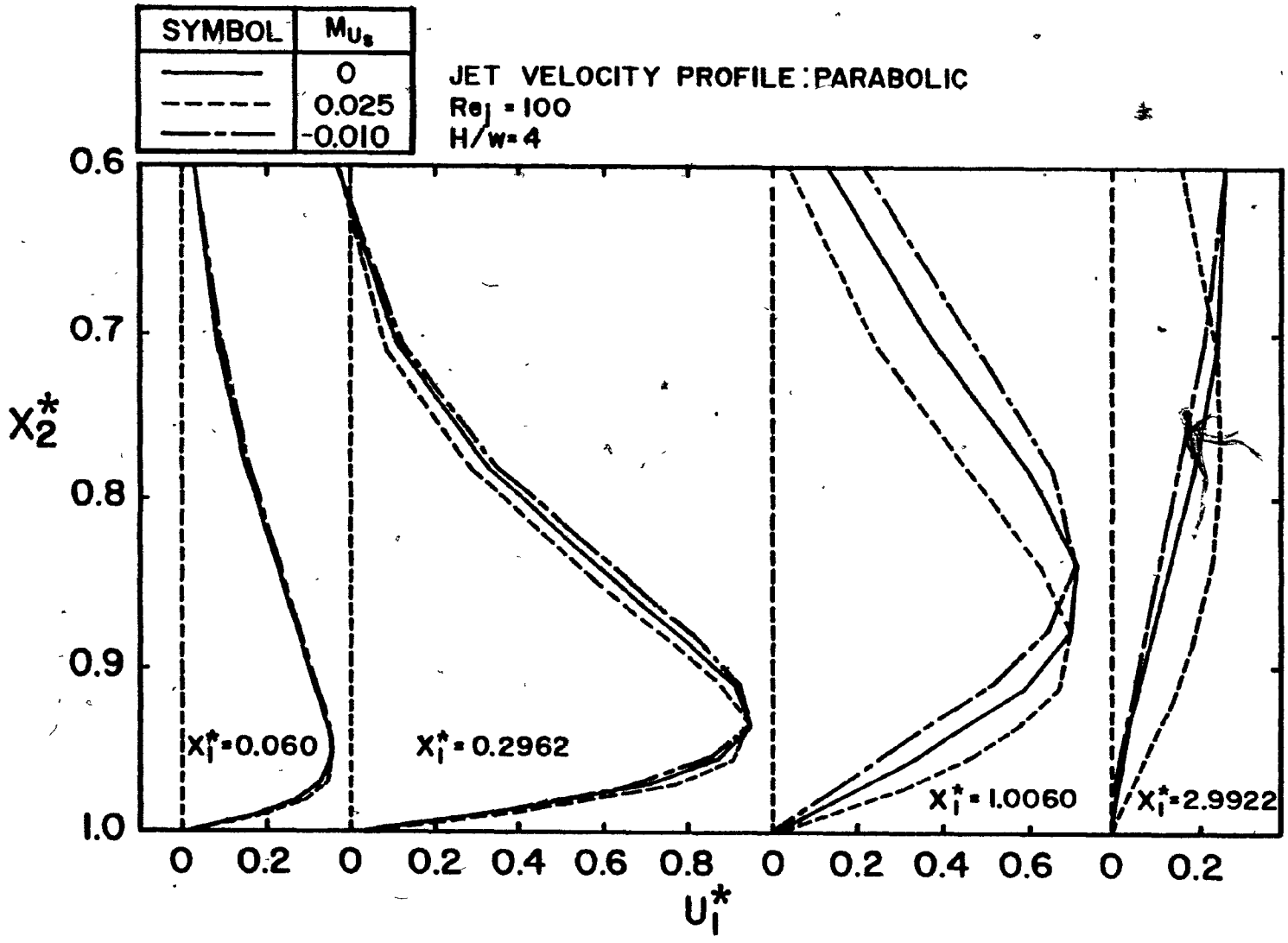


FIGURE 2.36. Effect of throughflow on wall jet development

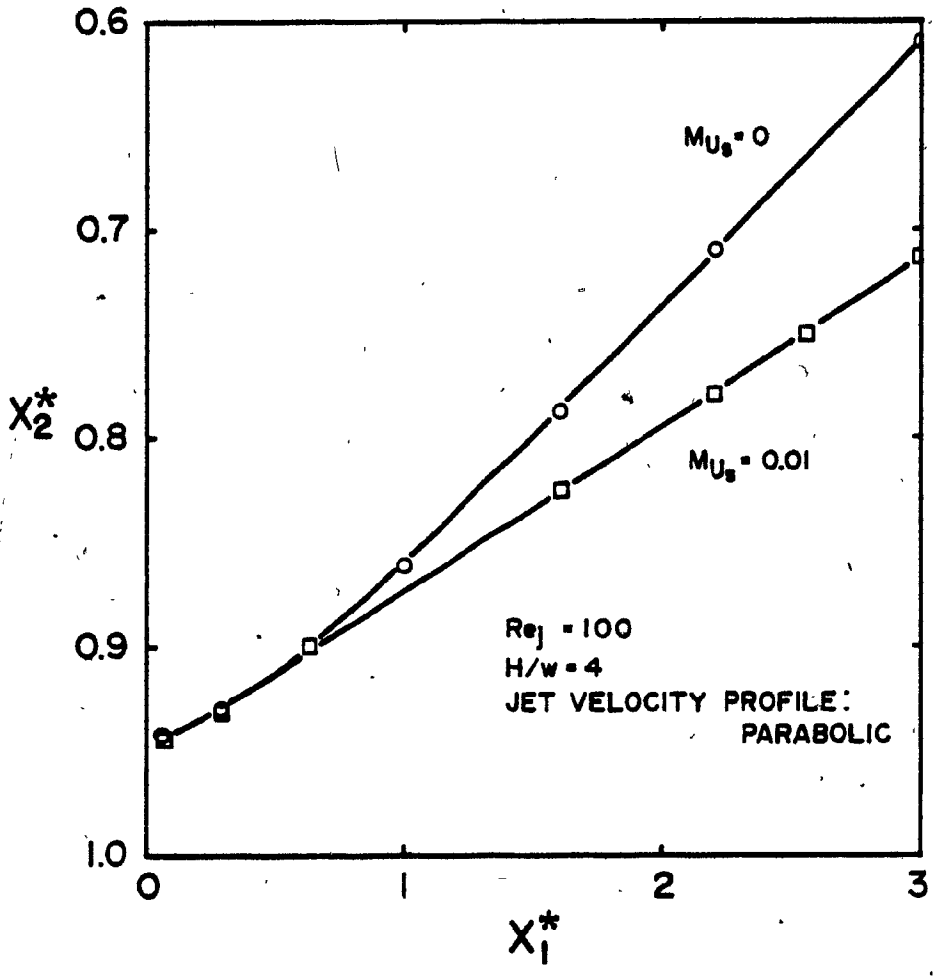


FIGURE 2.37. Effect of throughflow on location of maximum wall jet velocity

The influence of throughflow on development of the flow along the impingement surface is documented in Figures 2.36 and 2.37. As expected, the location of the maximum lateral velocity is shifted towards the impingement surface with throughflow and vice versa with blowing. With or without throughflow the distance of the maximum lateral velocity from the impingement surface increases linearly with distance from the stagnation point but Figure 2.37 indicates that even as small a throughflow as $M_{U_s} = 0.01$ has a strong effect on the location of this lateral velocity maximum. By contrast, any change in maximum lateral velocity caused by throughflow is at most a small effect whereas displacement of the position of the velocity maximum is quite sensitive to throughflow rate. Even for as high a throughflow rate as $M_{U_s} = 0.025$ and at a location as far from stagnation as $X_1^* = 3$, a combination which corresponds to 60% of the jet flow having been removed through the impingement surface, the magnitude of the maximum wall jet velocity is hardly affected. This finding is consistent with that of Baines and Keffer (9) for a turbulent slot jet impinging on a large porous cylinder. With throughflow at a rate of $M_{U_s} = 0.0029$ and spacing H/w = 2 they found an increase of a few percent in the maximum velocity at $X_1^* = 5.25$, i.e. at 10.5w from stagnation. Obot (105) on the other hand reported a significant increase of 11% in the maximum wall jet velocity for an impinging round jet with $M_{U_s} = 0.0029$ at 6 nozzle diameters from the stagnation point, a measurement which appears questionable in the light of the findings of Baines and Keffer and of the present investigation.

As can be seen in Figures 2.38 and 2.39, throughflow at the impingement surface does not change the general shape of the lateral profiles of transfer rates along the surfaces. The effect of a normal velocity at the impingement surface on skin friction, $C_f/2$, and heat transfer, St, parallels that on axial velocity, U_2^*, already noted, i.e. throughflow causes an increase in C_f and St while blowing (negative throughflow) causes an equivalent decrease, the absolute magnitude of these changes being essentially constant over the entire extent of the C_f and St profiles. Increases in heat transfer resulting from throughflow if expressed on a percentage basis therefore increase with distance from stagnation.

Before beginning quantitative analysis of the influence of throughflow on transfer rates, some evidence concerning the influence of two other factors in the presence of throughflow will be considered, i.e. the effect of extent of the impermeable section of the impingement surface and of the choice of finite difference scheme. Shown in Figure 2.40 are the increase in $C_f/2$ and in St due to throughflow for impingement surfaces in which the length of permeable section with throughflow is 12w ($X_{1S}^* = 3$, $H/w = 4$) and 30w ($X_{1S}^* = 6$, $H/w = 5$). Thus the results on Figure 2.40 reflect the influence of three variables, X_{1S}^*, H/w and the finite difference scheme used. When results are expressed as $(St - St_{M_{U_S}=0})$ and $(C_f - C_{f_{M_{U_S}=0}})/2$, the small difference in H/w is not significant, so all differences may be ascribed to the other two parameters. As the influence of the impermeable section beginning only at 12w or 30w from stagnation

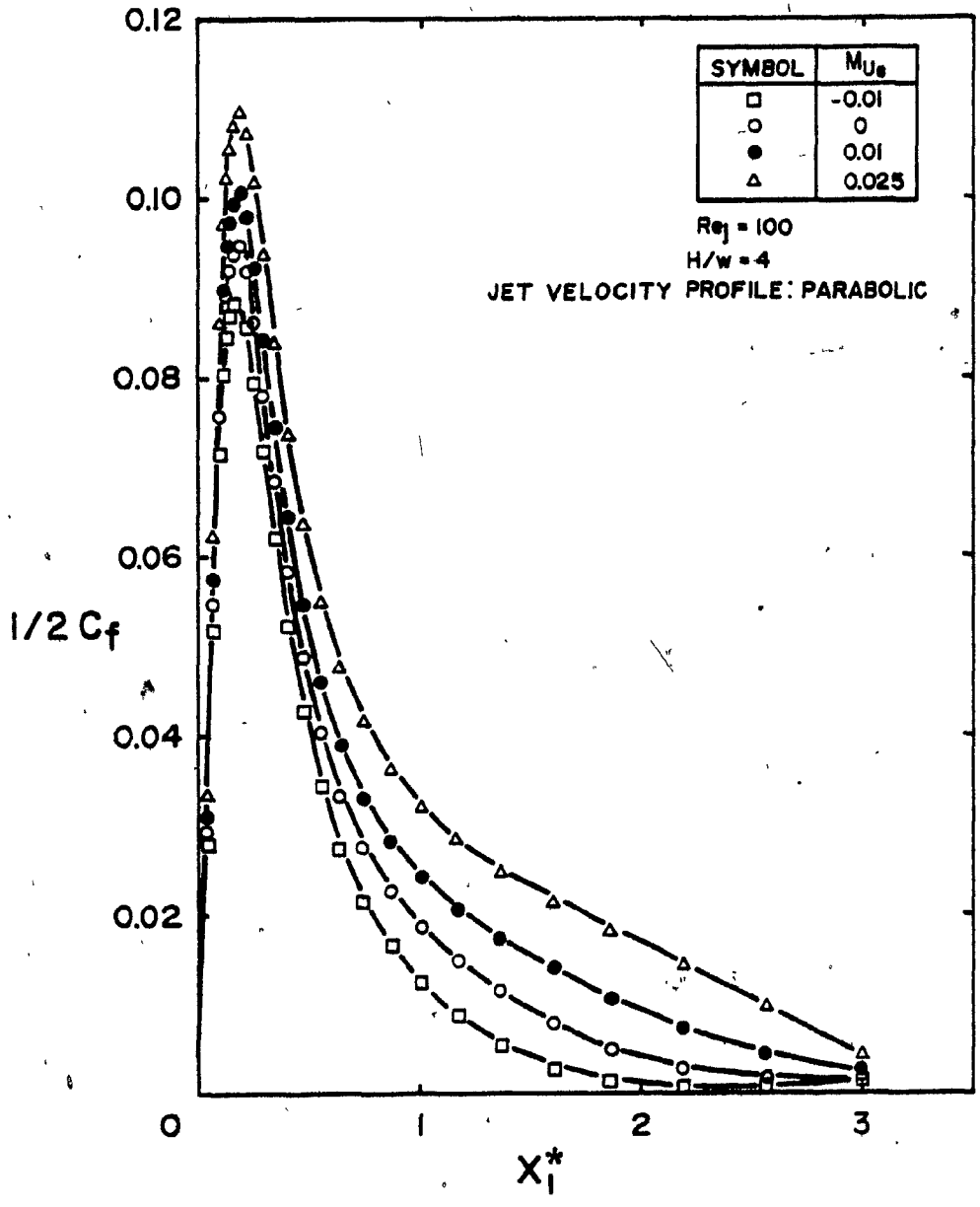


FIGURE 2.38. Effect of throughflow on skin friction distribution

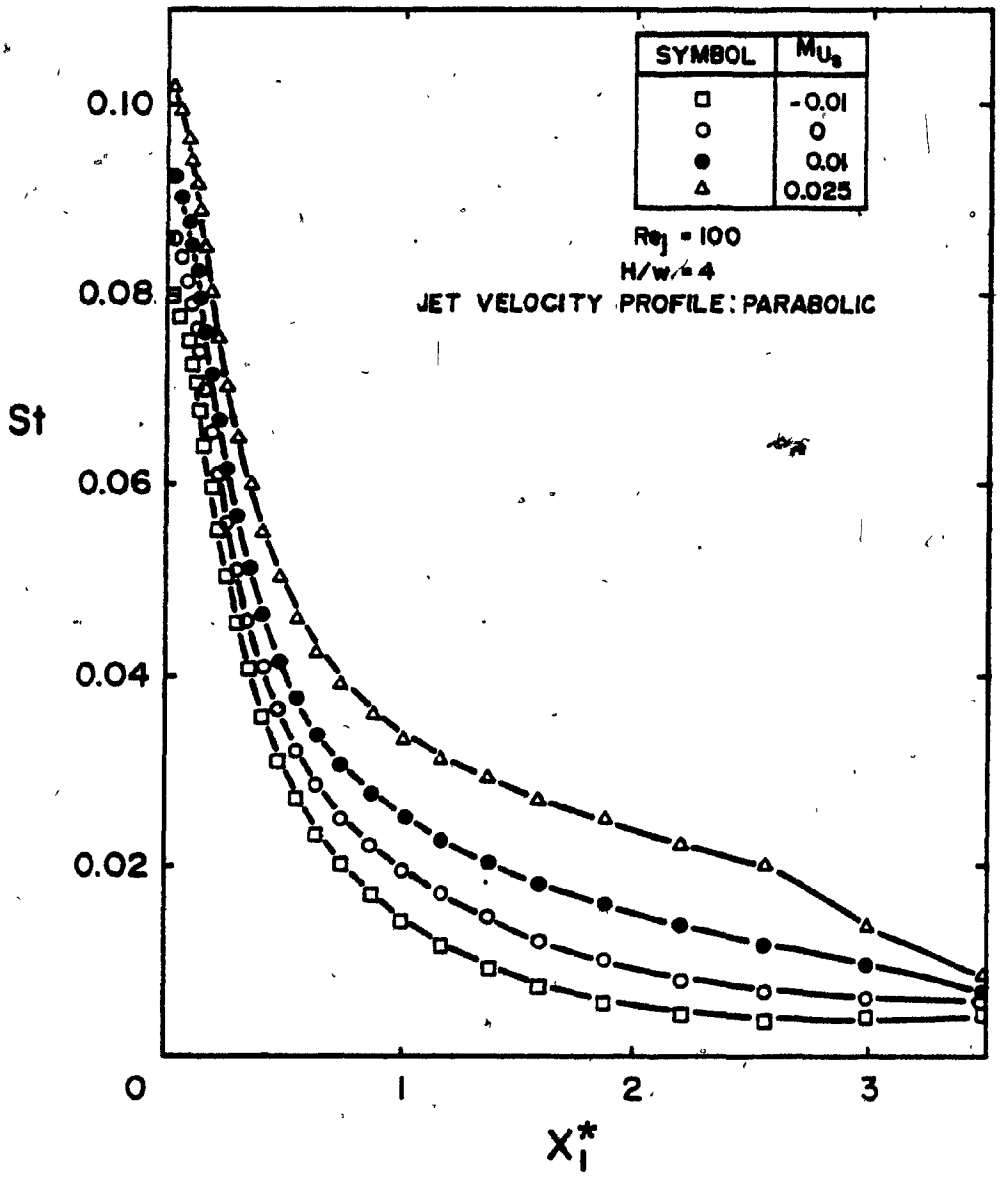


FIGURE 2.39. Effect of throughflow on heat transfer distribution

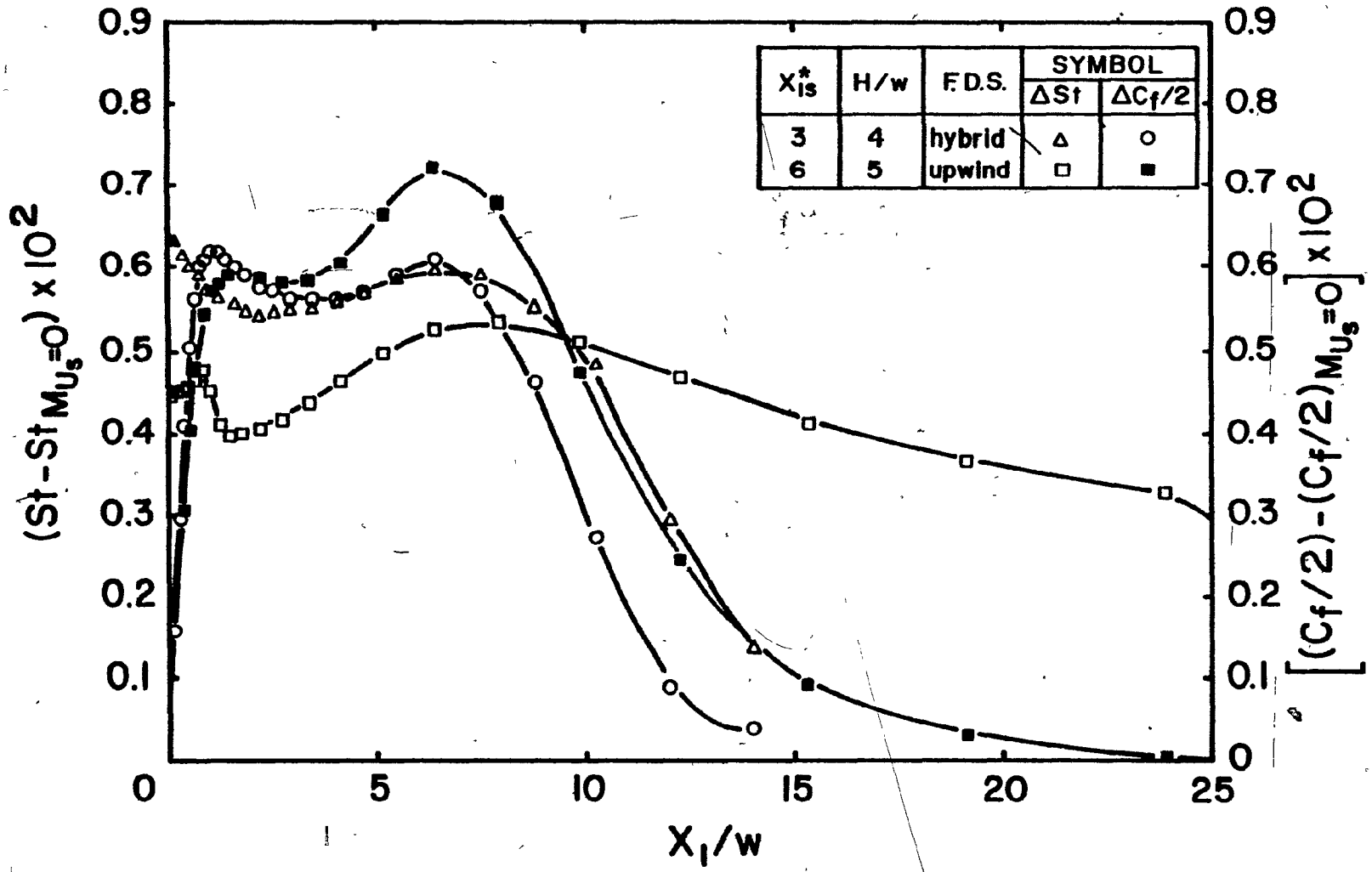


FIGURE 2.40. Effect of difference scheme and length of permeable plate

is not felt in the stagnation or early wall jet region, the differences in results here may then be attributed entirely to the difference scheme. Thus the lower increase in St out to about $X_1/w = 8$ when the upwind scheme is used is in agreement with the analysis of Gosman et al. (pg 141-147) for laminar Couette flow with mass injection through the walls as they likewise found that the upwind scheme leads to underprediction of transport rates at the impingement surface. They recommended the hybrid scheme (called "PD" by Gosman) as leading to a more accurate solution. Out to the same position, $X_1/w = 8$, the Figure 2.40 results indicate that the change in finite difference scheme has no consistent effect on computed skin friction. It is understandable that choice of finite difference scheme could produce significant changes for the case with throughflow since false diffusion thereby becomes larger in a region where diffusive transport of vorticity and temperature perpendicular to the impingement surface become dominant over convective transport. As to influence of extent of the impermeable outer section of the impingement surface, it appears that the presence of an impermeable section begins to be felt at about 5w upstream of the start of the impermeable section, although the profile for skin friction by the upwind scheme with a 30w wide permeable surface shows a drop after $X_1/w = 7$ for computational reasons not easily identifiable. More work is needed to clarify these effects.

The influence of throughflow on the change in skin friction $C_f/2$ and heat transfer as St are shown in Figures 2.41 and 2.42. The skin friction $C_f/2$ increases with throughflow and decreases

with blowing from the surface. The change goes from zero at the stagnation point to a maximum (or minimum for blowing) at the position where the stagnation flow changes into a wall jet, i.e. at the distance from stagnation where U_1^* reaches its maximum, as may be seen by reference to Figure 2.18. The absolute value of the change then stays approximately the same to about $X_1^* = 1.5$, regardless of the magnitude or direction of M_{U_s}. As the impingement surface becomes impermeable at $X_{1S}^* = 3$, the reduction in effect of throughflow over the region $1.5 < X_1^* < 3$ is presumed to reflect the extent of influence of the outer section without throughflow.

Similar general behaviour for effect of throughflow is obtained for the change in St, as displayed in Figure 2.42. The principal difference in effect on heat transfer from that on skin friction is that the maximum change in St is located at the stagnation point, where there is no effect on C_f. The broad region out to about 1.5H or 6w over which the effect of throughflow is approximately constant applies for both St and C_f.

Also shown in Figures 2.41 and 2.42 are the theoretical changes in $C_f/2$ and St when throughflow is applied, as calculated by the analytical approaches of Mickley et al. (96) and Spalding (136). In these methods the actual boundary layer is replaced by a Couette flow model under the assumption that variations in the flow direction parallel to the impingement surface are negligible compared to those perpendicular to it. It is further assumed that the boundary layer thickness is uninfluenced by the blowing process. The resulting equations are

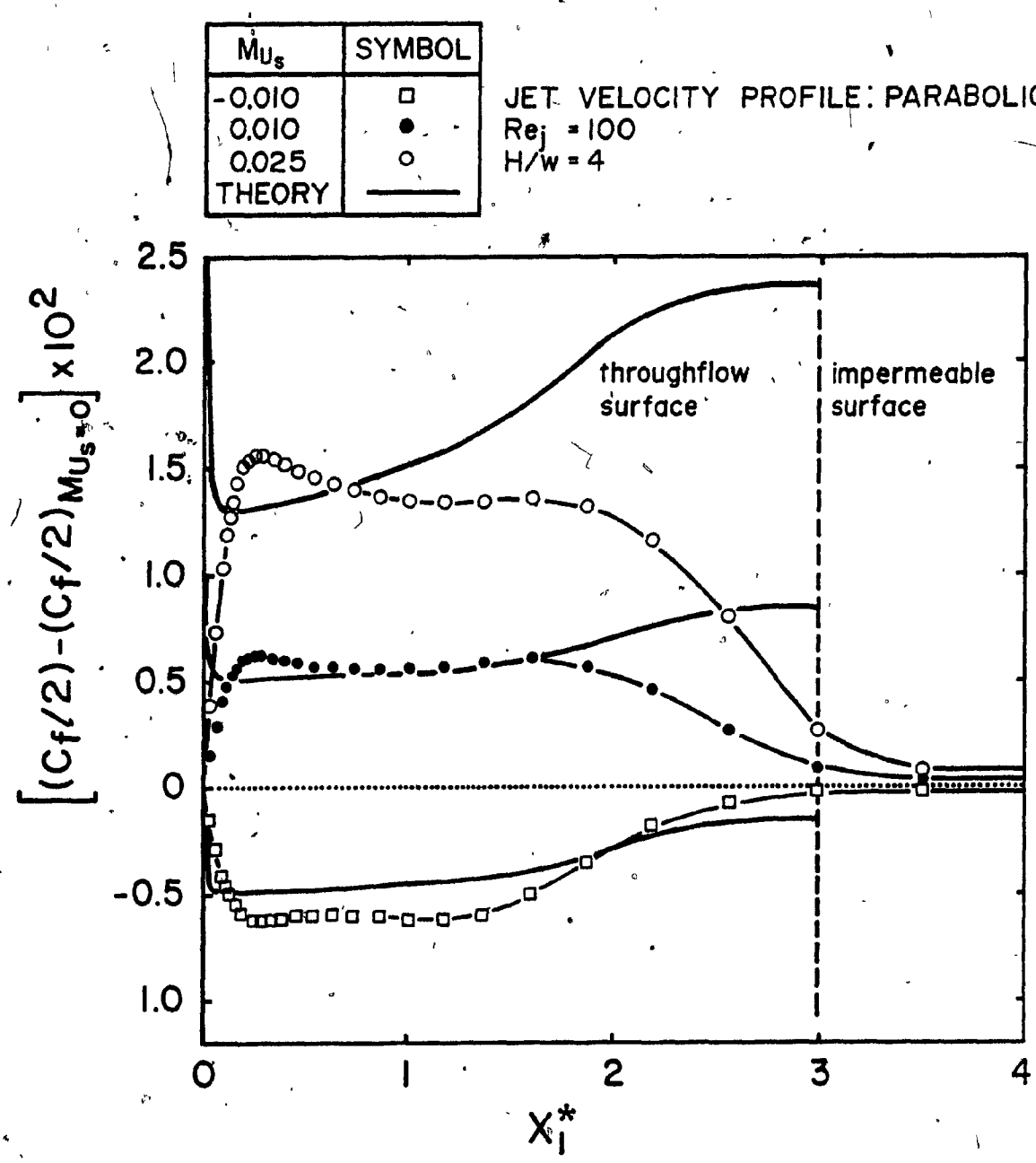


FIGURE 2.41. Effect of throughflow on change in skin friction

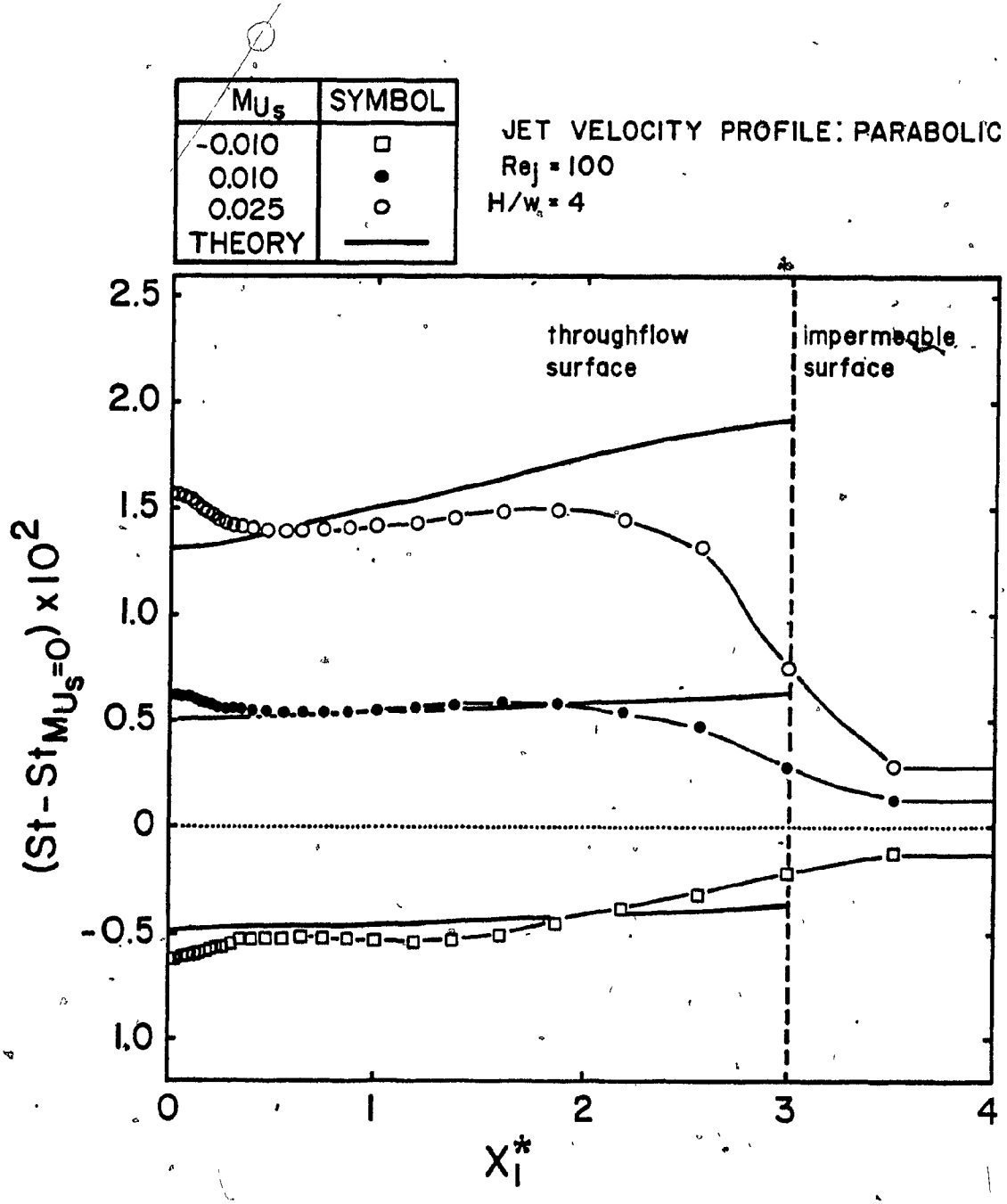


FIGURE 2.42. Effect of throughflow on change in heat transfer

$$\frac{C_f}{C_{f_{M_{U_s}=0}}} = \frac{\frac{-2M_{U_s}}{C_f}}{\exp\left(\frac{-2M_{U_s}}{C_{f_{M_{U_s}=0}}}\right) - 1} \qquad (2.59)$$

and

$$\frac{St}{St_{M_{U_s}=0}} = \frac{\frac{-M_{U_s}}{St}}{\exp\left(\frac{-M_{U_s}}{St_{M_{U_s}=0}}\right) - 1} \qquad (2.60)$$

The theoretical lines in Figures 2.41 and 2.42 are then calculated with equations (2.59) and (2.60) respectively. For throughflow this means that for $0 < M_{U_s}/St_{M_{U_s}=0} < 0.3$ the increase in Stanton number can be approximated with an accuracy better than 90% by

$$St - St_{M_{U_s}=0} = \frac{1}{2} M_{U_s} \qquad (2.61)$$

For $M_{U_s}/St_{M=0} > 2.3$ the increase in St can be approximated with an accuracy better than 90% by

$$St - St_{M_{U_s}=0} = M_{U_s} - St_{M_{U_s}=0} \qquad (2.62)$$

Relations similar to (2.61) and (2.62) can be derived for $(C_f - C_{f_{M_{U_s}=0}})/2$.

In view of the assumptions made in the theoretical analyses of Spalding (136) and Mickley et al. (96) the agreement between the numerical results and those determined using Couette flow theory is remarkably good, especially for the heat transfer. For example, in the stagnation region the variations in U_1 in the x_1-direction can definitely not be ignored, and the boundary layer thickness in the wall jet region is influenced appreciably by throughflow (as can be seen in Figure 2.37), contrary to the assumptions in the Couette flow analyses. It is therefore expected that for skin friction in the stagnation region, agreement between the numerical results and this analytic theory would be poor. This type of error in the theory with respect to skin friction is not present for heat transfer because the temperature variations in the x_1-direction in the stagnation region are quite small.

The linear relation between M_{U_s} and increase in St suggested by equation (2.61) is tested by presentation of the results in terms of $(St - St_{M_{U_s}=0})/M_{U_s}$ and $(C_f - C_{f_{M_{U_s}=0}})/2M_{U_s}$ in Figure 2.43. With $X^*_{1S} = 3$, only the region out to about 1.5H is relevant to this test because beyond that position the gradual transition begins from impingement with throughflow to impingement without throughflow. Thus out to about $X^*_1 = 1.5$ the lines for both skin friction and heat transfer effectively collapse for M_{U_s} of 0.01 and 0.025, and nearly so for $M_{U_s} = -0.01$ also. This behaviour proves the proportionality of the increase in $C_f/2$ and St with

M_{U_s}. The average increase in St in the impingement and early wall jet region as a result of throughflow can be seen from Figure 2.43 to be quite well correlated by

$$(St - St_{M_{U_s}=0}) = 0.58\ M_{U_s} \qquad (2.63)$$

It is of interest to analyze the results of other investigators of the effect of throughflow using the above model of the present study. Thus for a laminar round impinging jet with throughflow, the numerical results of Huang (63) and Saad (124), respectively with and without the presence of a swirl velocity at the nozzle, were reanalyzed on the basis of Figure 2.43. The increase in St obtained by Huang for an initially parabolic profile jet of Reynolds number 950 with an impingement surface spacing of 1.5 nozzle diameters was found to be well described by equation (2.63) up to about 7 nozzle diameters from the stagnation point (or up to about 50% of the jet flow being removed by throughflow). It is notable that this excellent agreement extends the applicability of the present model to an impingement system with the combined vortex which accompanies a swirling jet. The data of Saad, also for a jet Reynolds number of 950 but without swirl at the nozzle, and with impingement surface spacings of 8 and 12 nozzle diameters, are described by $(St - St_{M_{U_s}=0})/M_{U_s} = 0.6 \pm 0.1$ up to 2 nozzle diameters from the stagnation. Thus the model developed in the present study is seen to represent adequately the results of two other investigations at significantly different conditions.

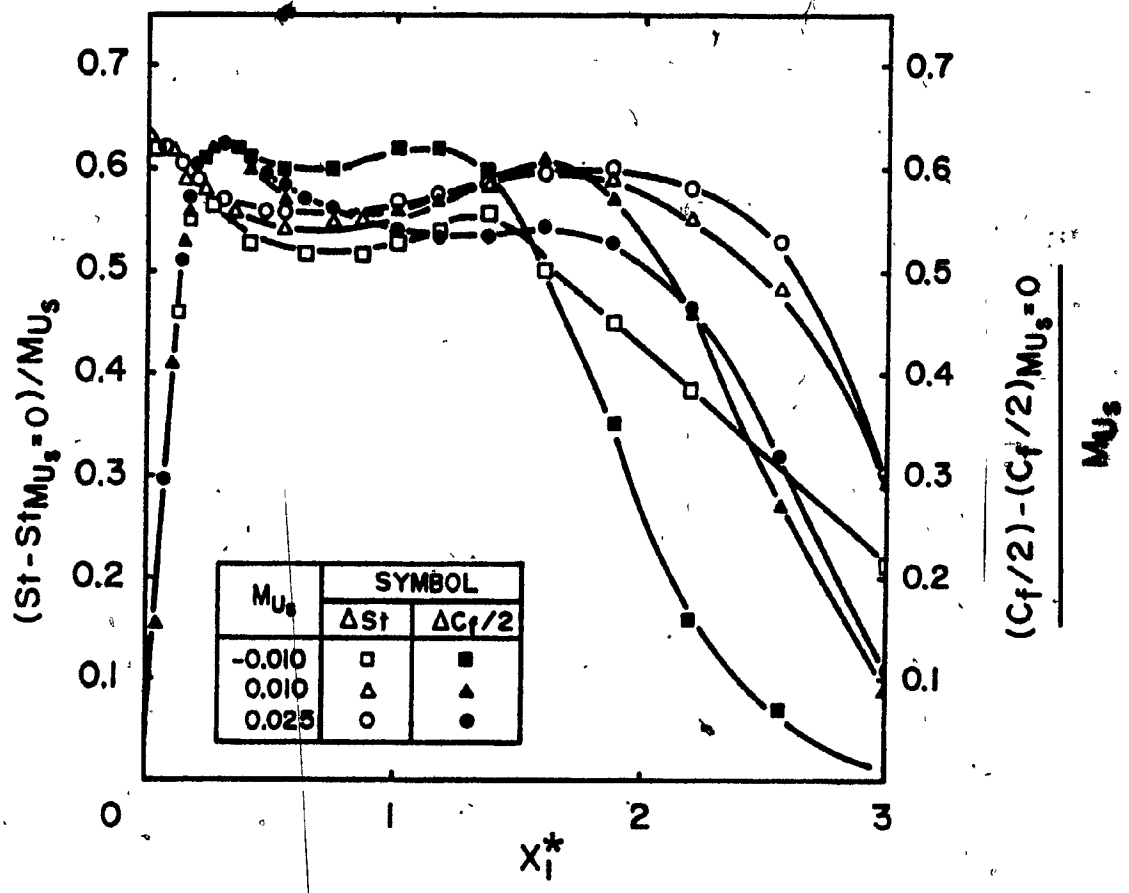


FIGURE 2.43. Effect of throughflow on change in transport rates at the impingement surface

As the increase in St due to throughflow is independent of the fraction of the jet flow withdrawn through the impingement surface, f, up to large values of f (i.e. f ≈ 0.5 for M_{U_s} = 0.025), the average increase in St can be reasonably estimated by

$$\overline{St} - \overline{St}_{M_{U_s}=0} = 0.58\, M_{U_s} \qquad (2.64)$$

However when f = 1, $\overline{St} = M_{U_s}$, so that equation (2.64) cannot hold up to f = 1.

The model developed here may be compared with the simple linear combination of the heat transfer contributions of throughflow and impingement as recently suggested by Crotogino and Allenger (35). Their linear combination can be rearranged into a form consistent with the present analysis, as follows

$$\overline{St} - \overline{St}_{M_{U_s}=0} = M_{U_s} - f\, \overline{St}_{M_{U_s}=0}$$

or

$$\overline{St} - \overline{St}_{M_{U_s}=0} = \left(1 - 2\,\frac{S}{H}\,\frac{H}{w}\,\overline{St}_{M_{U_s}=0}\right) M_{U_s} \qquad (2.65)$$

With equation (2.65) the increase in heat transfer with throughflow for the throughflow described in Figure 2.39 would be underestimated by 10%-20%. Although this chapter concerns only laminar flow, the present findings for the influence of throughflow

on heat transfer merit extrapolation to turbulent flow, because the Couette flow theory of Spalding (136) and Mickley et al. (96) can also be applied to turbulent flow, by conceptually replacing the laminar sublayer by Couette flow. Therefore the influence of throughflow on the experimental drying rates of the full scale "Papridryer" as reported by Burgess et al. (24) were reanalyzed using both equations (2.64) and (2.65) in order to provide a comparison between the Crotogino and Allenger approach (2.65) and that developed in the present study (2.64). This comparative analysis was carried out assuming heat transfer to be the rate determining step, so that

$$R = \frac{\overline{St}}{\Delta H_v} (T_j - T_s) \rho_j U_j C_{pj} = K_1 \overline{St} \qquad (2.66)$$

with R the drying rate in $kg/m^2/s$ and ΔH_v the heat of evaporation in J/kg.

The results of this analysis (described in detail in Appendix 6) are shown in Figure 2.44. The drying rate R in $kg/m^2/s$ increases linearly with M_{U_s} when using equation (2.64), which is based on the present numerical calculation (notation "present theory"), or equation (2.65), based on the linear combination of heat transfer contributions due to throughflow and impingement (notation "linear combination"). Both theoretical lines start at the drying rate without throughflow, obtained from the paper of Crotogino and Allenger. The magnitude of the slope of the experimental line is better predicted with the use of equation (2.64) based on the theory developed in the present

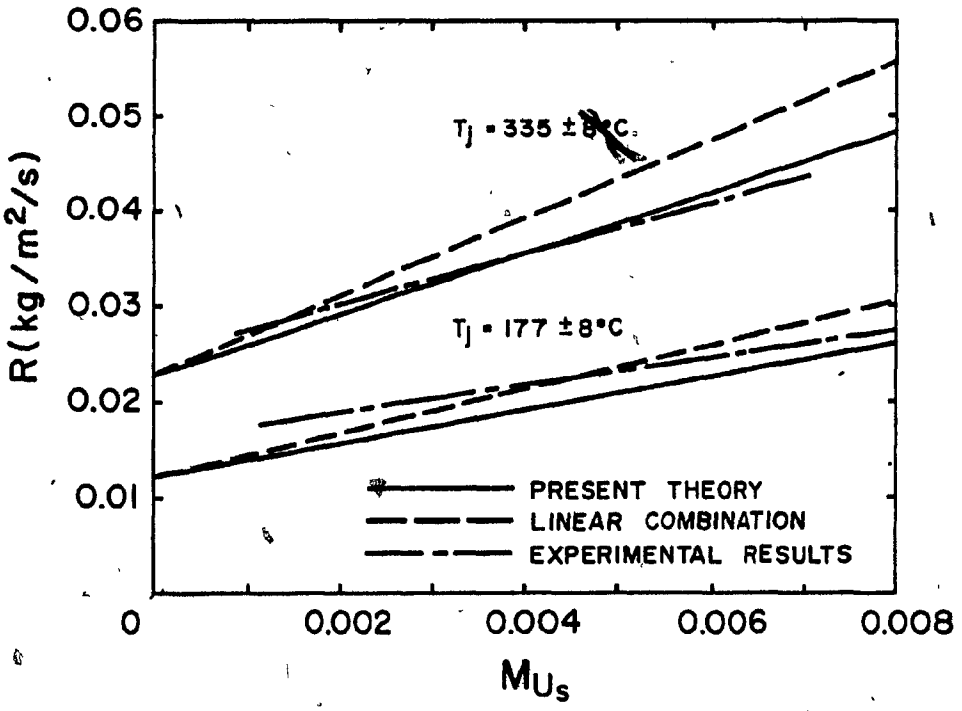


FIGURE 2.44. Effect of throughflow on drying rate of mill Papridryer

study. It should also be noted that the results obtained by Crotogino and Allenger coincide, as they should, with the straight line obtained with the use of equation (2.65).

Consideration of the effect of throughflow will be completed with a discussion of the turbulent impinging slot jet work of Baines and Keffer (7, 8 and 9). Using a hot-wire probe technique, they measured skin friction for normal and oblique impingement on a rotating drum, 0.61 m in diameter, with throughflow at the impingement surface. The drum surface was permeable over a circumferential distance of only 0.089 m. Air could be sucked through this small porous section, with or without drum rotation. They obtained skin friction from the velocity measured with a hot-wire probe mounted in the drum, in the center of the porous section. The hot wire, 5 μm in diameter, was kept at a constant distance of 25 μm from the surface. They report that, when applying throughflow at a rate of $M_{U_s} = 0.0029$ for $Re_j = 6600$, the local and average shear stress along the drum surface was increased by roughly a constant amount. To that extent their findings are similar to those of the present numerical work.

It is useful to examine the procedure by which Baines and Keffer correlated the increase in average skin friction. They used the equation, based on an overall momentum balance,

$$\left(\frac{\overline{C_f}}{2} - \frac{\overline{C_f}}{2}\bigg|_{M_{U_s}=0}\right)/M_{U_s} = K_2\,(\overline{U_m} + V_s)/V_s \qquad (2.67)$$

with V_s being the lateral velocity of the impingement surface, i.e. the circumferential speed of the drum surface, $\overline{U_m}$ the average value of the maximum fluid velocity parallel to the impingement surface over the region of interest, and K_2 a constant. The inclusion of circumferential speed V_s on the right side of equation (2.67) seems illogical because the effect of impingement surface motion is already included in $\frac{1}{2} C_{f_{M_{U_s}=0}}$. Their values of the constant K_2 vary between 0.1 and 0.3 with most of the values around 0.3, when skin friction is averaged from $0 \leq X_1/w \leq 16$. With $\overline{U_m} \approx \frac{1}{2} U_j$, the right side of equation (2.67) is only about 1/4 to 1/3 of the constant 0.58 obtained in the present work.

There is however a strong indication that their hot-wire technique cannot be used to measure the effect of suction on skin friction. In addition to the disagreement between their results and those of the present study as noted in the preceding paragraph, further evidence is provided by the effect of suction on the "windage" shear stress measurements made by Baines and Keffer. They obtained the "windage" shear stress with the jet assembly removed from the rotating drum. At a rotational speed of V_s = 10.2 m/s and without suction the skin friction $\frac{C_f}{2}$ was measured to be 0.00465. When applying suction at a velocity of 0.152 m/s, or M_{U_s} = 0.015, the skin friction $\frac{C_f}{2}$ was increased to 0.00865. For this type of boundary flow at such a strong suction rate (i.e. $M_{U_s} > 0.01$), the skin friction can theoretically be calculated quite accurately by setting $\frac{1}{2} C_f = M_{U_s}$ i.e. the viscous transport is completely inhibited and the total shear

stress is equal to the hydrodynamic sink drag. In this perspective their experimentally obtained increase in $\frac{C_f}{2}$ of only 0.27 M_{U_s} is totally unrealistic. Thus there is conclusive evidence that the hot-wire probe cannot measure the influence of suction on the skin friction, and that these results of Baines and Keffer are in error.

2.2.3.4 Effect of Temperature Dependent Physical Properties

The influence of the temperature difference between a heating jet and the impingement surface was studied for $Re_j = 100$, $H/w = 5$ and a parabolic velocity profile at the nozzle exit. The values used for nondimensional temperature at the impingement surface, T_s/T_j, were 1.0, 2/3 and 1/2. For a constant impingement surface temperature of 300 K, the corresponding jet temperatures were 300, 450 and 600 K. Viscosity of air was calculated using the Van Driest interpolation formula

$$\frac{\mu}{\mu_j} = \left(\frac{T}{T_j}\right)^{3/2} \left(\frac{T_j + 110}{T + 110}\right) \qquad (2.68)$$

where μ_j is the viscosity at the jet temperature in K. Thermal conductivity was calculated from the viscosity using the fact that the Prandtl number and the specific heat of air are almost independent of temperature over the range considered. The term S_μ^* (see equation (2.10) and Table 2.2) could be neglected.

The results indicated that the nondimensional vorticity and temperature gradient at the impingement surface were quite different between the cases of variable and constant physical prop-

erties. However, when the vorticity and temperature gradient at the impingement surface are expressed respectively in the form of the skin friction coefficient $C_f/2$ and the Stanton number St, with physical properties based at the jet nozzle temperature (see equations (2.56) and (2.57)) there is only a small influence for different T_s/T_j, as can be seen in Figures 2.45 and 2.46.

This numerical result is in agreement with the theoretical solutions for influence of temperature dependent fluid properties on two-dimensional stagnation flow and laminar boundary layer flow over a flat plate without a pressure gradient (Kays). The differences between predicted values for St and $C_f/2$ in the stagnation region are due not only to the fluid properties but to the use of slightly too large a spacing between the impingement surface and the adjacent gridline, i.e. the J = 22 gridline. As a consequence of a wider than ideal spacing to the near-wall gridline the assumption of a linear variation of T^* and ω^* with distance from the wall is not fully satisfied. For example, T^* at the stagnation line on the near-wall gridline increases from 0.3045 to 0.3858 to 0.4352 for the three values of T_s/T_j, 1.0, 2/3 and 1/2.

Another frequently used method of allowing for temperature dependent physical properties is the method whereby physical properties appearing in the nondimensional groups are evaluated at the film temperature, i.e. $(T_j + T_s)/2$. When this is done for the present results and the variation in Re at the nozzle, caused by the evaluation of ν at $(T_j + T_s)/2$, is eliminated by dividing Nu and the vorticity by $\sqrt{Re}$ (as is required for laminar

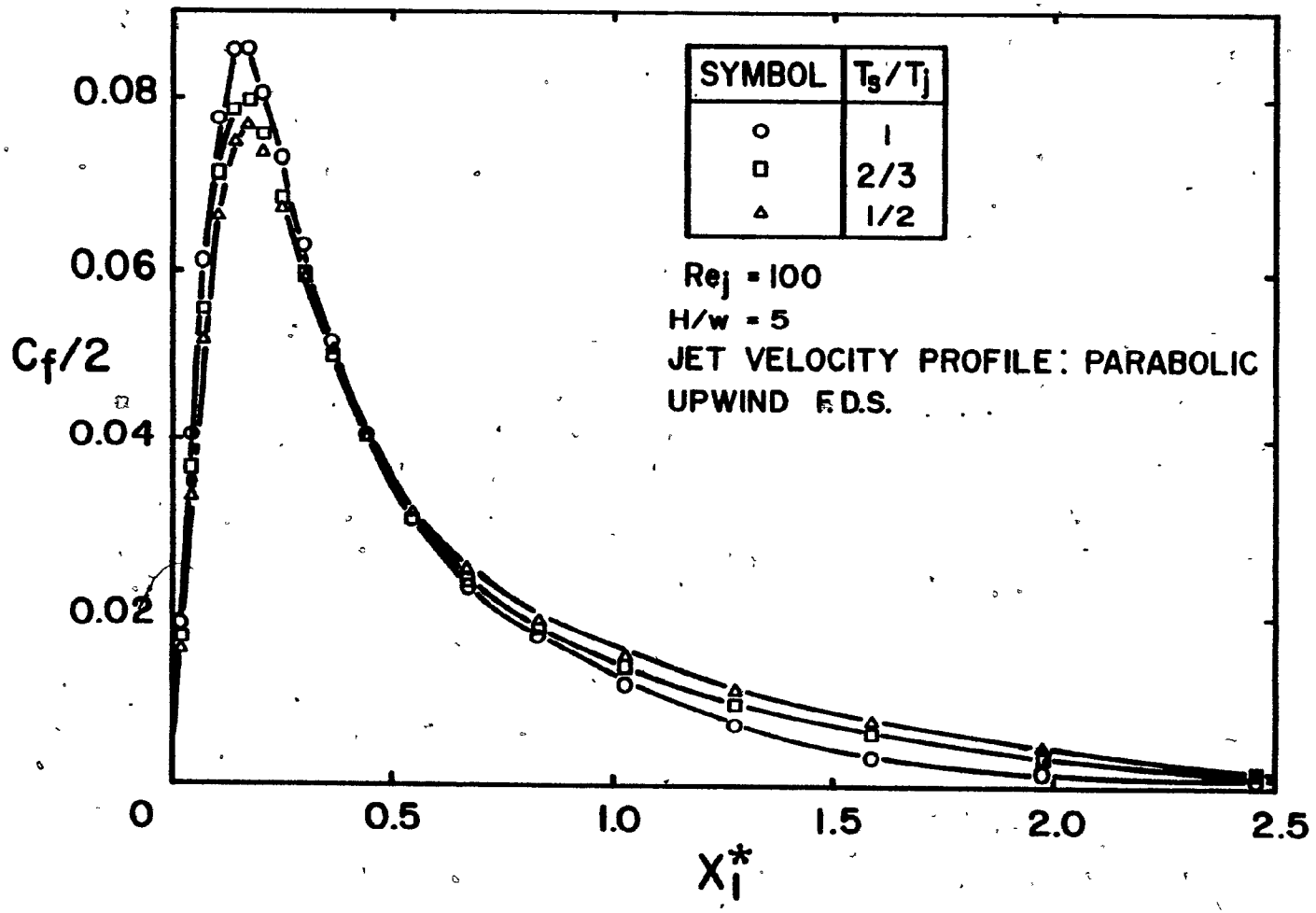


FIGURE 2.45. Effect of variable properties on skin friction distribution

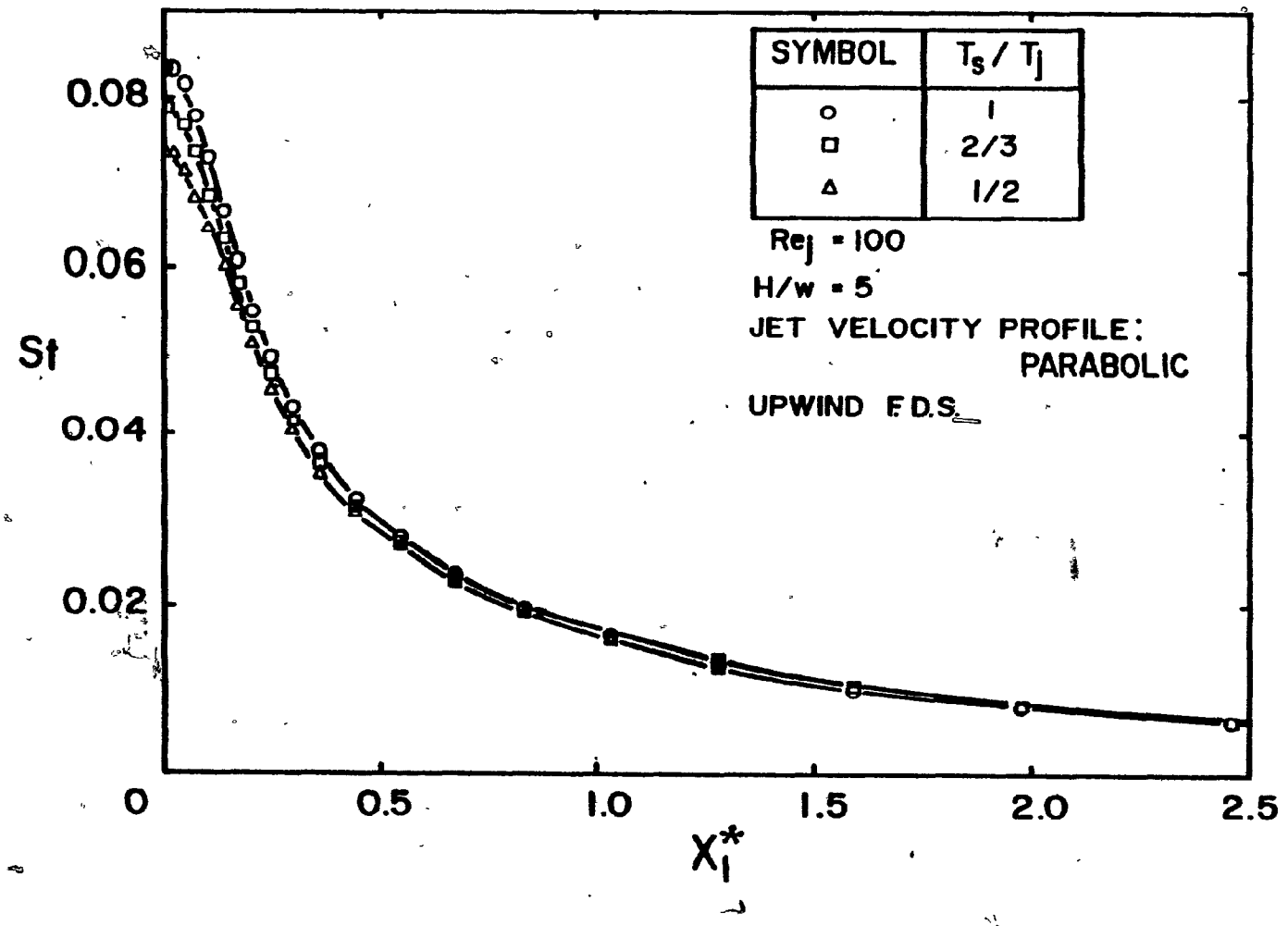


FIGURE 2.46. Effect of variable properties on heat transfer distribution

flow) a slightly larger difference is obtained between the results for the same three values of T^*, i.e. 1, 2/3 and 1/2.

The use of throughflow presents additional ways in which alternate methods of treating temperature dependent physical properties may affect the calculated performance of an impingement system. Similar findings are obtained in the experimental part of the present study and are presented in Section 4.2. For a throughflow rate of $U_s^* = 0.01$ for the variable property case, use of $T_s/T_j = 2/3$ leads to larger withdrawal of fluid through the impingement surface than for $T_s/T_j = 1$, i.e. the values of $M_{U_s} = \rho_s^* U_s^*$ are respectively 0.015 and 0.01.

As normalized throughflow rate expressed as M_{U_s} has been used in Figures 2.33-2.46 and throughout this section, it is of interest to examine the effectiveness of an alternate normalized variable, U_s^*. The failure of the data to collapse on a single curve in Figure 2.47 when U_s^* is used is a further indication that M_{U_s} is the preferred nondimensional variable for representation of throughflow. In a word, M_{U_s} not U_s^* determines the effect of throughflow on heat transfer.

2.2.3.5 Effect of Prandtl Number

Measurements of heat and mass transfer under impinging jets have been reported for experimental systems of Prandtl and Schmidt numbers over the range 0.71 to 3300. Thus heat transfer experiments have been made for values of Prandtl number of 0.71, 3.0-7.0 and 84.7-150.7 for respectively the air jet of Gardon and Akfirat (45), the water jets of McMurray *et al.*

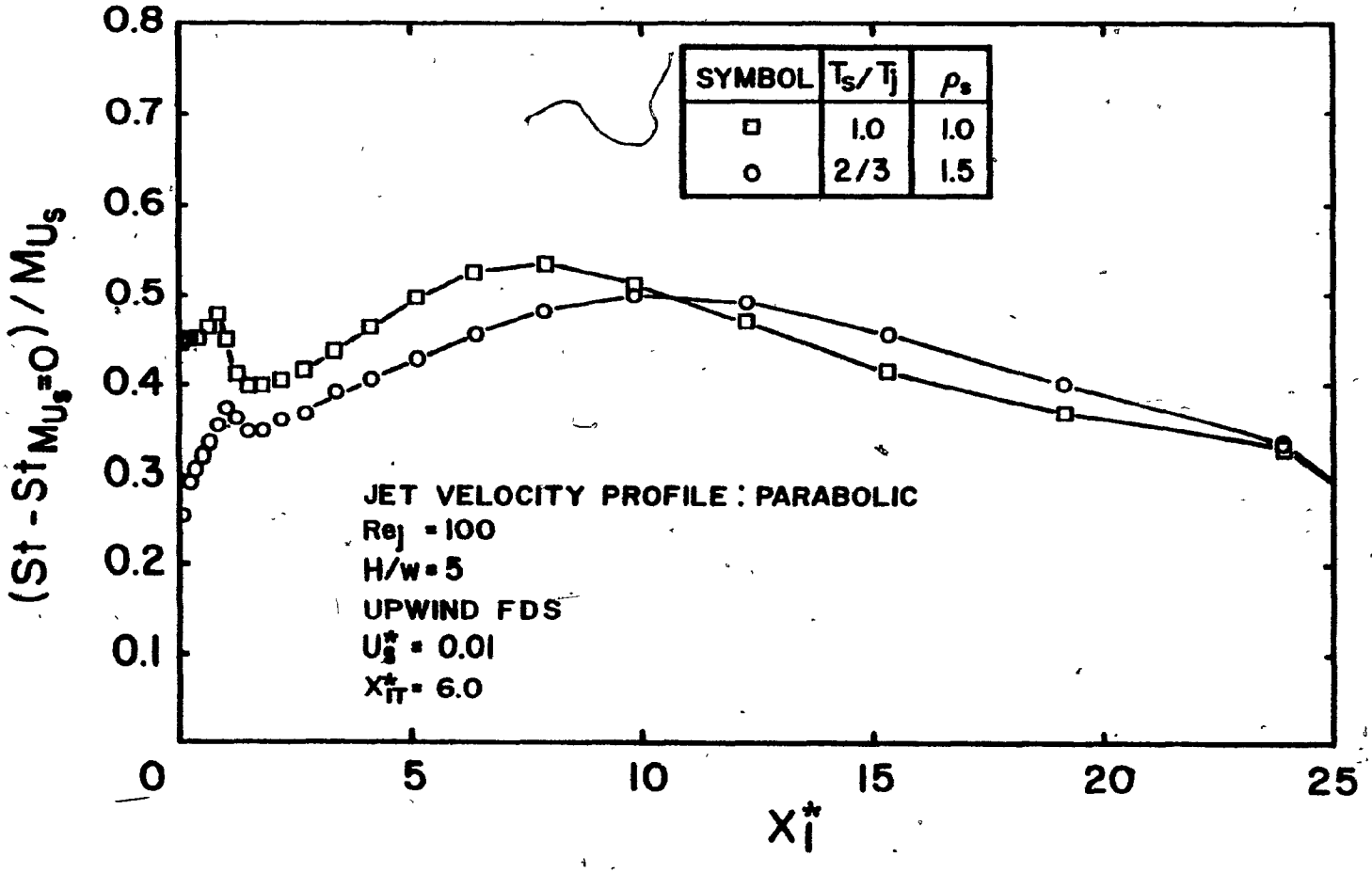


FIGURE 2.47. Effect of variable properties and throughflow on heat transfer distribution

(91) and D.E. Metzger et al. (95) and the lubricating oil jets of D.E. Metzger et al. (94). Mass transfer experiments have been reported for values of Schmidt number of 0.59, 2.5 and 2420-3300 for respectively an air jet on a water wet surface, Schlünder and Gnielinski (132), for an air jet on a naphthalene surface, Sparrow and Wong (139) and for potassium ferri- and ferro cyanide in a sodium hydroxide solution, Kataoka and Mizushina (72). Because of the wish to integrate data from such diverse experimental systems as well as to apply general correlations to diverse systems of practical interest there is a need to have a proven procedure for incorporation of Pr and Sc.

The influence of Prandtl (or Schmidt number) on heat (or mass) transfer can be eliminated by multiplying the Stanton number (or mass transfer equivalent of the Stanton number) by Pr^n (or Sc^n). As reported by Schlichting (131) it can be derived that n varies between the limits of 1/2 and 2/3 for Pr (or Sc) approaching 0 and ∞, respectively. The values of the exponent n used most frequently in impinging jet literature are 2/3, 0.60 and 0.58 for respectively Pr (or Sc) approaching ∞ for the analysis of Sibulkin (135) for heat transfer near the forward stagnation point of a body of revolution for $0.6 \leq Pr \leq 2.0$, and from the German literature, i.e. Martin (88). In 1972 Miyazaki and Silberman (97) correlated the influence of Pr on stagnation point heat transfer under an impinging slot jet with a flat velocity profile at the nozzle as $Pr^{0.627}$ for $0.7 \leq Pr \leq 10$. Correlation of the 1975 theoretical results of Sparrow and Lee (138)

for a parabolic velocity profile over the same range of Prandtl numbers also yields $Pr^{0.627}$. It is of interest to note that these 1975 results of Sparrow and Lee on the influence of Pr are exactly the same as the results obtained in 1938 by Squire (140) for the forward stagnation point heat transfer of a body of revolution.

In the present work, the effect of the Prandtl number was studied for $Re_j = 100$, $H/w = 4$ and a flat and parabolic velocity profile at the nozzle exit. Numerical solutions were obtained for Pr = 0.73, 2.5 and 7.0. In view of the above analysis the present heat transfer results are presented as $St(Pr)^{0.627}$ in Figures 2.48 and 2.49. The influence of Pr on the heat transfer distributions for Prandtl numbers of 0.73, 2.5 and 7.0 is thereby essentially eliminated. Also shown in Figures 2.48 and 2.49 is the power n in $St(Pr)^n$ as obtained by the method of the least squares. It can be seen that n varies from 0.613 at the stagnation point to 0.63 and 0.645 at $X_1^* = 2.0$ for respectively a flat and parabolic velocity profile. From these results and those from the literature one can conclude that the power n should be 0.627 When the impingement mass transfer data obtained with the naphthalene sublimation technique are compared with the heat transfer data obtained with an air or water jet. It appears that a power of 0.60 is more appropriate for mass transfer data obtained with the water evaporation technique.

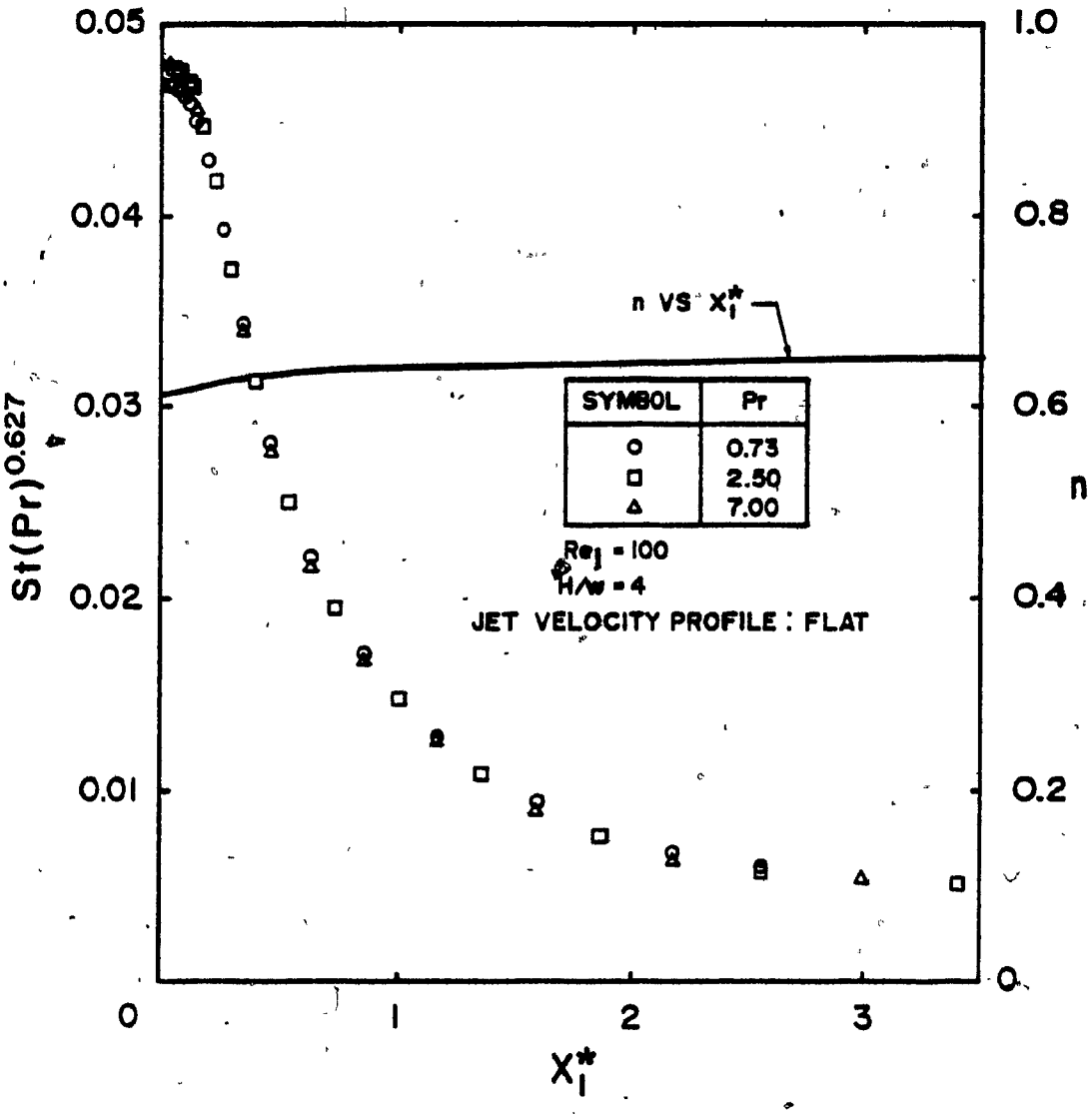


FIGURE 2.48. Effect of Prandtl number on heat transfer distribution for a flat jet velocity profile

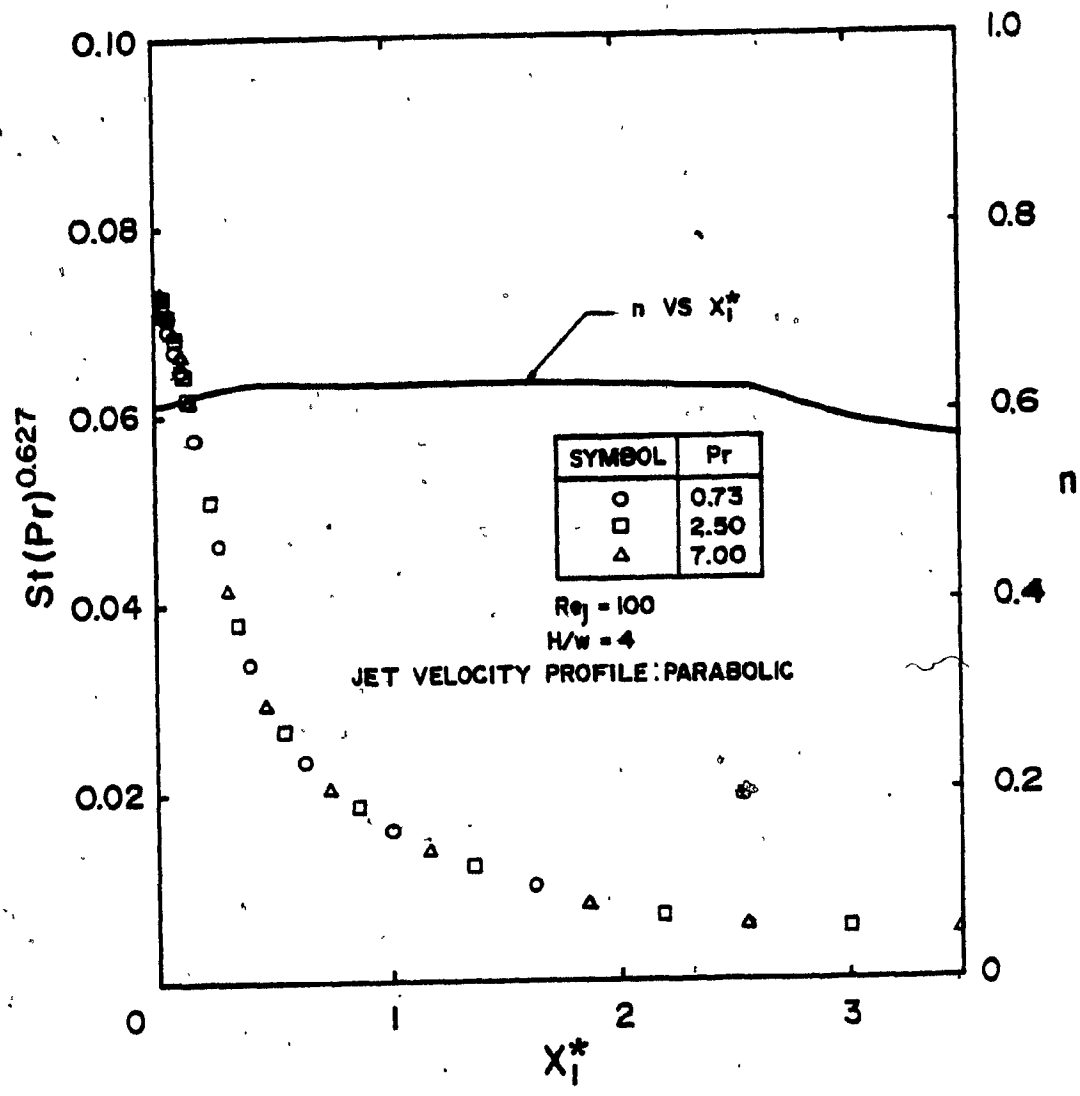


FIGURE 2.49. Effect of Prandtl number on heat transfer distribution for a parabolic jet velocity profile

2.3 Turbulent Impinging Slot Jet

In this section numerical solutions are obtained for a turbulent impinging slot jet of the same flow configuration as the laminar impinging jet shown in Figure 2.1. This configuration differs from that for the experimental study described subsequently in Chapters 3 and 4 in the use of a stationary, flat, impermeable impingement surface while the experimental investiation involved a moving, curved impingement surface and included modification of the flow field by throughflow at the surface. The effects of use of an impingement surface which is curved, moving and permeable were not included in the numerical simulation because it is necessary first to develop a numerical procedure capable of reliably predicting the flow and temperature fields for turbulent impinging slot jets without these additional complicating factors. Therefore the results obtained in this section are only a first step towards simulating the experimental results obtained with the Simtest apparatus described in Chapters 3 and 4.

Two alternate theoretical approaches have been followed for turbulent impinging jet calculations:

(a) the two-layer model, i.e. an inviscid flow-boundary layer for the impingement region and an "inner" and "outer" layer for the wall jet region

(b) iterative finite difference methods for numerical solution of the full governing equations

The first category was reviewed in Section 1.4 while the present section develops the comprehensive approach of solving the

full governing equations, as envisioned in the second of these theoretical approaches.

Numerical solution of the equations of motion and energy is obtained with the so-called "TEACH-T" program of the group of Gosman, Patankar, Spalding and many others at Imperial College, University of London. The version used was that provided at the course "Turbulent Recirculating Flows - Prediction and Measurement", given at Pennsylvania State University, July 28-August 1, 1975. As this program is well-suited for solving recirculating flows such as occur in the flow field of confined impinging jets, Figure 2.1, this program is adopted rather than developing yet another scheme. The time-averaged equations of motion are solved in their primitive form, i.e. with the velocity and pressure as dependent variables, as opposed to the vorticity-stream function approach. The turbulent fluxes in the Navier-Stokes equations and thermal energy equation are determined using the concept of a turbulent viscosity and a turbulent thermal conductivity via a constant turbulent Prandtl number. The turbulent viscosity μ_t is in turn evaluated with a so-called "two-equation" model, in this case from an algebraic relation with the turbulence kinetic energy k and the dissipation rate of turbulence kinetic energy ε,

$$\mu_t = C_\mu \rho k^2/\varepsilon \qquad (2.69)$$

with differential equations describing the transport of k and ε from the 1972 publication of Launder and Spalding on turbulent models (83).

The equations of motion in their vorticity-stream function form were solved numerically together with a "one-equation" turbulence model for turbulent viscosity by Wolfshtein in 1968 (154), Russell and Hatton in 1972 (123) and Bower et al. in 1977 (19). The turbulent viscosity was computed from

$$\mu_t = C'_\mu \rho k^{\frac{1}{2}} \ell \qquad (2.70)$$

with $C'_\mu = 0.227$ used by all three references

and $$\frac{\ell}{y} = 1 - e^{-0.016\ Re_k}$$

with $$Re_k = \frac{k^{\frac{1}{2}} y}{\nu} = 1.83\ y^+$$

At the edge of the wall region when $Re_k = 21.23$ (or $y^+ = 11.63$)

then $$\frac{\ell}{y} \approx 0.29$$

In a later (August 1969) report Wolfshtein used a two-equation model of turbulence to obtain turbulence viscosity, μ_t. In this model μ_t is again described by equation (2.70) but ℓ is replaced by $\ell = \sqrt{k/\Omega}$, Ω being turbulence vorticity squared. Then the differential equations describing the transport of k and Ω are solved. Wolfshtein and Bower et al. used an assumed length scale throughout the flow field, while Russell and Hatton made use of both the assumed length scale of Wolfshtein and their own measured length scale distribution. Reasonable agreement is obtained by Wolfshtein (154) between his computed impingement heat

transfer distribution and the experimental data of Gardon and Akfirat (45) at H/w = 8. However for $Re_j > 10^4$ the deviations become substantial - close to 40% at the stagnation point for $Re_j = 22000$. Comparisons of the theoretical and experimental contour plots of turbulence kinetic energy, shear stress and eddy diffusivity by Russell and Hatton indicate that the measured length scale distribution leads to better agreement with measured values. The thermal energy equation was not solved by Russell and Hatton. A complicating factor in their experimental study is a significant deviation from two-dimensional flow, as analyzed in Section 3.5.6. The centerline velocity and turbulence kinetic energy predicted by Bower et al. (19) do not agree with the measurements. The differences are attributed to inaccuracy of the required turbulence length scale.

The problem of prescribing the length scale which recurs through the three studies described above was eliminated in an approach published in 1976 by Folayan (41) who also used the present two-equation turbulence model based on k and ε. The differences between Folayan's case and the present study are

(1) A flat velocity profile with a low level of turbulence is used as the nozzle exit boundary condition in the present work while Folayan prescribes fully developed turbulent flow.

(2) In the present study the flow field is constrained by a confinement surface while Folayan prescribes inflow along this boundary.

It is interesting to note however that Folayan made heat trans-

fer measurements with and without a confining plate. He obtains reasonable agreement between measured and computed mean velocities parallel to the impingement surface up to $X_1/w = 20$ for spacings, H/w, of 6 and 12. Local heat transfer coefficients differ by less than 30% at any position. Although Folayan claimed an improvement over the 1968 numerical predictions of Wolfshtein it should be mentioned that, at $Re_j = 7100$, Folayan's predictions in the critical impingement region are not better than those of Wolfshtein. Finally it is noted by Folayan that isotropy of the turbulence properties, implied in the turbulent viscosity concept of the k-ε model, is not confirmed by the experimental measurements of Russell and Hatton. However he recommended that use of a Reynolds stress model is not justified until further work on eliminating the difficulties and developing the merits of the two-equation model is carried out. The present study represents a further contribution to the two-equation model approach.

2.3.1 Mathematical Formulation

The derivation of the transport equations of mean momentum for turbulent flow, unaffected by gravitational, hydrodynamic or other external force fields, and the corresponding thermal energy equation is conveniently provided by Bird et al. (15). In cartesian coordinates the transport equation of mean momentum is given by

$$\frac{D\rho u_i}{Dt} = \frac{\partial}{\partial x_j}\left(\mu \frac{\partial u_i}{\partial x_j} - \rho\overline{u_i' u_j'}\right) - \frac{\partial P}{\partial x_i} + S_i \qquad (2.71)$$

with

$$S_i = \frac{\partial}{\partial x_j}\left(\mu \frac{\partial u_j}{\partial x_i}\right) - \frac{2}{3}\frac{\partial}{\partial x_i}\left(\mu \frac{\partial u_j}{\partial x_j}\right) \qquad (2.72)$$

The last term of equation (2.72) is generally neglected because it is quite small, becoming zero for incompressible flow. The effect of turbulence on the mean flow is represented by the term, $\rho\overline{u_i'u_j'}$, called the Reynolds stress. Hinze (60) has shown that this term is really an additional momentum transfer term, usually of the opposite sign to $\frac{\partial u_i}{\partial x_j}$. A closed system of equations is formed by equation (2.71), together with a constitutive equation for $\rho\overline{u_i'u_j'}$ and the continuity equation

$$\frac{\partial \rho}{\partial t} + \frac{\partial}{\partial x_i}(\rho u_i) = 0 \qquad (2.73)$$

2.3.1.1 Turbulence Model and Final Set of Equations

For the derivation of a constitutive equation for $\rho\overline{u_i'u_j'}$ the approach of Launder and Spalding (83) is followed. In Prandtl's mixing-length theory the mixing length, ℓ, is defined as the average distance through which a turbulent blob of fluid moves before it merges with its surroundings, by analogy with the free mean path of molecules in the kinetic theory of gases (111). As a consequence of this analogy, the dominant turbulent stress component $-\rho\overline{u_1'u_2'}$ for thin shear flows takes the same form as the equivalent laminar shear stress component, i.e.

$$-\rho\overline{u_1'u_2'} = \mu_t \frac{\partial u_1}{\partial x_2} \qquad (2.74)$$

with the turbulent viscosity μ_t being defined as

$$\mu_t = C\rho|V_t|\ell \tag{2.75}$$

whereby $|V_t|$ is some representative, positive turbulent velocity. The turbulent viscosity concept can be generalized by analogy with the laminar shear stress for incompressible flow as

$$-\rho\overline{u_i'u_j'} = \mu_t\left(\frac{\partial u_i}{\partial x_j} + \frac{\partial u_j}{\partial x_i}\right) - \frac{2}{3}\,\delta_{ij}\rho k \tag{2.76}$$

In this form the Reynolds stress can be used in turbulent flows with more than one dominant flow direction, as in the case for the confined impinging jet. Kolmogorov in 1942 (77) and independently, Prandtl in 1945 (111), proposed that $|V_t|$ should be proportional to the square root of the turbulent kinetic energy, k. Jones and Launder (70) proposed in 1972 that the length scale, ℓ, characterizing the energy containing eddies (i.e. the turbulent blobs of fluid, as stated earlier) should be proportional to the dissipation length scale, $k^{3/2}/\varepsilon$, so that equation (2.75) becomes

$$\mu_t = C_\mu\rho k^2/\varepsilon \tag{2.69}$$

with ε the dissipation rate of turbulence kinetic energy. The The representation of $-\rho\overline{u_i'u_j'}$ by equations (2.76) and (2.69) together with transport equations for k and ε (to be derived subsequently) is called the Energy-Dissipation Turbulent Viscosity model, in short, the k-ε model of turbulence.

One of the advantages of this model over those based on Prandtl's mixing length hypothesis, where μ_t is determined from an algebraic formula containing for example the local velocity gradient and the distance from the wall, is that the k-ε model takes account of the transport of turbulence via the transport equations for k and ε. The advantage of the two-equation k-ε model over the one-equation model with μ_t represented by equation (2.70) is that the problem of specifying the length scale is eliminated.

With these assumptions the transport equation of mean momentum is obtained by insertion of equation (2.76) in (2.71) to give

$$\frac{D(\rho u_i)}{Dt} = \frac{\partial}{\partial x_j}\left(\mu_{eff}\frac{\partial u_i}{\partial x_j}\right) - \frac{\partial P}{\partial x_i} + \frac{\partial}{\partial x_j}\left(\mu_{eff}\frac{\partial u_j}{\partial x_i}\right) \tag{2.77}$$

with $$\mu_{eff} = \mu + \mu_t = \mu + C_\mu \rho \frac{k^2}{\varepsilon} \tag{2.78}$$

The constant in equation (2.78) is derived from near-wall turbulence data, where the local equilibrium situation is approached, as $C_\mu = 0.09$. Equations (2.77) and (2.78) together with the continuity equation and the modelled transport equations for k and ε, respectively equations (2.86) and (2.88), form the final closed set of equations describing the turbulent flow.

Temperature in the turbulent flow field is described by the thermal energy equation for compressible flow neglecting viscous dissipation, buoyancy effects and heating due to compression

(i.e. ideal gas) as

$$\frac{D(\rho T)}{Dt} = \frac{\partial}{\partial x_j}\left(\Gamma_{eff}\frac{\partial T}{\partial x_j}\right) \tag{2.79}$$

with $$\Gamma_{eff} = \frac{\mu}{Pr} + \frac{\mu_t}{Pr_t} \tag{2.80}$$

and Pr_t being the turbulent Prandtl number. Extensive numerical calculations of the Imperial College group give $Pr_t = 0.9$. In equation (2.80) the assumption is made that the turbulent heat flux, $-\rho C_p \overline{u_i'\gamma}$, can be approximated by $\lambda_t \frac{\partial T}{\partial x_i}$ in analogy with the Fourier's law, with γ being the fluctuating component of the temperature and λ_t the turbulent thermal conductivity.

2.3.1.2 Derivation of Transport Equations for k and ε

The differential equation for transport of turbulent kinetic energy is derived from the exact equation governing transport of kinematic Reynolds stress $-\overline{u_i'u_j'}$. The derivation of this equation,

$$\frac{D\overline{u_i'u_j'}}{Dt} = -\left[\overline{u_j'u_k'}\frac{\partial u_i}{\partial x_k} + \overline{u_i'u_k'}\frac{\partial u_j}{\partial x_k}\right] + \overline{\frac{p'}{\rho}\left(\frac{\partial u_i'}{\partial x_j} + \frac{\partial u_j'}{\partial x_i}\right)}$$

(i) (ii)

$$+ \frac{\partial}{\partial x_k}\left[\nu\frac{\partial \overline{u_i'u_j'}}{\partial x_k} - \overline{u_i'u_j'u_k'} - \overline{\frac{p'}{\rho}(\delta_{jk}u_i' + \delta_{ik}u_j')}\right] - 2\nu\,\overline{\frac{\partial u_i'}{\partial x_k}\frac{\partial u_j'}{\partial x_k}}$$

(iii) (iv)

(2.81)

is available from Hinze (60). The terms (i) to (iv) are respectively, the production $\tilde{P}_{ij}$ of turbulent stress, the pressure-strain correlation, the diffusive transport terms and the dissipation term. The kinematic Reynolds stress is contracted to the turbulence kinetic energy, k, by setting i = j or $\overline{u_i' u_j'} = 2k$. Application of this contraction to equation (2.81) together with the continuity equation gives rise to the exact transport equation of turbulence kinetic energy,

$$\frac{Dk}{Dt} = -\overline{u_i' u_k'} \frac{\partial u_i}{\partial x_k} + \frac{\partial}{\partial x_k} \left(\nu \frac{\partial k}{\partial x_k} - \overline{u_i' k} - \frac{\overline{p u_i'}}{\rho} \right) - \nu \overline{\left(\frac{\partial u_i'}{\partial x_k} \right)^2} \qquad (2.82)$$

In order to solve equation (2.82) the terms on the right side must be replaced by suitable approximations, which are now presented. Substitution of equation (2.76) in the first term gives, with substitution of j for k,

$$-\overline{u_i' u_j'} \frac{\partial u_i}{\partial x_j} = \nu_t \left(\frac{\partial u_i}{\partial x_j} + \frac{\partial u_j}{\partial x_i} \right) \left(\frac{\partial u_i}{\partial x_j} \right) = \nu_t G \qquad (2.83)$$

where $$G = \left(\frac{\partial u_1}{\partial x_2} + \frac{\partial u_2}{\partial x_1} \right)^2 + 2 \left(\frac{\partial u_1}{\partial x_1} \right)^2 + 2 \left(\frac{\partial u_2}{\partial x_2} \right)^2$$

in two-dimensional Cartesian coordinates. The last two correlations in the second term of (2.82) are modelled as for molecular thermal diffusion, i.e.

$$\left(\overline{u_i' k} + \overline{\frac{p}{\rho} u_i'} \right) = - \frac{\nu_t}{\sigma_k} \frac{\partial k}{\partial x_j} \qquad (2.84)$$

with σ_k being the turbulent Prandtl number for the kinetic energy. By definition, the last term on the right side of (2.82) is replaced by

$$\nu \overline{\left(\frac{\partial u_i'}{\partial x_j}\right)^2} = \varepsilon \tag{2.85}$$

Insertion of equations (2.83) to (2.85) in (2.82) gives the modelled form of the transport equation for k as

$$\frac{Dk}{Dt} = \frac{\partial}{\partial x_j}\left[\left(\frac{\nu_t}{\sigma_k} + \nu\right)\frac{\partial k}{\partial x_j}\right] + \nu_t G - \varepsilon \tag{2.86}$$

Computer optimizations by the Imperial College group indicate that $\sigma_k = 1.0$.

The exact transport equation of the dissipation rate of turbulent kinetic energy may be obtained as shown in 1968 by Harlow and Nakayama (58), by multiplying the x_ℓ derivative of the instantaneous velocity component of the Navier-Stokes equation by $2\nu \frac{\partial u_i'}{\partial x_\ell}$, and time averaging. Tennekes and Lumley (145) have shown that in flows of high turbulence Reynolds number, $R_T = k^2/\nu\varepsilon$, the exact transport equation for ε takes the form

$$\frac{D\varepsilon}{Dt} = -\frac{\partial}{\partial x_k}\left[\nu u_k' \overline{\left(\frac{\partial u_i'}{\partial x_\ell}\right)^2} + \frac{\nu}{\rho}\overline{\frac{\partial p'}{\partial x_\ell}\frac{\partial u_k'}{\partial x_\ell}}\right] - 2\nu \overline{\frac{\partial u_i'}{\partial x_k}\frac{\partial u_i'}{\partial x_\ell}\frac{\partial u_k'}{\partial x_\ell}} - 2\overline{\left[\nu \frac{\partial^2 u_i'}{\partial x_k^2}\right]^2}$$

(i) (ii) (iii)

(2.87)

The arguments presented in 1972 by Launder and Spalding (83) for modelling the terms in equation (2.87) are repeated here. Term (i) is responsible for the diffusive transport of ε and is represented by $\frac{\partial}{\partial x_k}\left(\frac{\nu_t}{\sigma_\varepsilon}\frac{\partial \varepsilon}{\partial x_k}\right)$. Terms (ii) and (iii) represent collectively the net effect of generation of ε due to vortex stretching of turbulent filaments and its destruction by viscous action. These two terms are large and of opposite sign so that they balance each other and therefore are treated together, being represented as

$$C_{\varepsilon_1}\nu_t\frac{\varepsilon}{k}\left(\frac{\partial u_i}{\partial x_k}+\frac{\partial u_k}{\partial x_i}\right)\frac{\partial u_i}{\partial x_k}-C_{\varepsilon_2}\frac{\varepsilon^2}{k}$$

Insertion of the modelled forms in (2.87) and taking $j = k$ gives the final form of the transport equation of ε as

$$\frac{D\varepsilon}{Dt}=\frac{\partial}{\partial x_j}\left(\frac{\nu_t}{\sigma_\varepsilon}\frac{\partial \varepsilon}{\partial x_j}\right)+C_{\varepsilon_1}\nu_t\frac{\varepsilon}{k}G-C_{\varepsilon_2}\frac{\varepsilon^2}{k} \qquad (2.88)$$

From the decay of turbulence behind a grid it is estimated that $C_{\varepsilon_2} = 1.92$, while from the properties of near-wall turbulence it is determined that $C_{\varepsilon_1} = 1.44$. Finally for near-wall turbulence, where the convective transport of ε is negligible and the production of turbulence energy is equal to ε, it can be shown that $\sigma_\varepsilon = \kappa^2/\left[(C_{\varepsilon_2} - C_{\varepsilon_1})\sqrt{C_\mu}\right]$. Then with $\kappa = 0.4187$ and $C_\mu = 0.09$ one obtains $\sigma_\varepsilon = 1.217$. These values are simply quoted without rounding off and in no way imply that these parameters are known to such accuracy.

2.3.1.3 Boundary Conditions

Conditions at the various boundaries shown in Figure 2.1, with dimensions expressed in the SI system, are given below.

Boundary I: The Nozzle Exit

For a flat velocity profile with a low level of turbulence the dimensional boundary conditions are

$$u_1 = 0 \quad , \quad u_2 = U_j \quad , \quad T = T_j \quad \text{and} \quad k = 3/2(0.005\ U_j)^2 \qquad (2.89)$$

The dissipation rate is set equal to

$$\varepsilon = 2k^{3/2}/w \qquad (2.90)$$

Boundary II: Confinement Surface

Because the transport equations derived in this chapter are only appropriate for flow regions where the Reynolds number of turbulence is high, the boundary conditions for T, u_1, k and ε are applied in the fully turbulent, near-wall region, not at the wall. So the velocity u_1 is matched to the following version of the law of the wall

$$u_1^+ = \frac{u_1}{\sqrt{\tau_s/\rho}} = \frac{1}{\kappa} \ln(Ey^+) \qquad (2.91)$$

with y^+ the nondimensional distance from the wall defined as

$$y^+ = \frac{\rho y \sqrt{\tau_s/\rho}}{\mu} \qquad (2.92)$$

and $\kappa = 0.4187$ and $E = 9.793$. When $y^+ \leq 11.63$ the laminar law $u_1^+ = y^+$ is used.

For the turbulence kinetic energy, k, the diffusive transport of k at the wall is set equal to zero. Furthermore, the relation from equilibrium turbulence near the wall

$$k = (\tau_s/\rho)/C_\mu^{\frac{1}{2}} \tag{2.93}$$

is used to evaluate the dissipation term in the transport equation of k.

The dissipation rate of turbulence kinetic energy, ε, near the wall is fixed by the requirement that the length scale varies linearly with distance from the wall, as can be inferred from equations (2.93), (2.91) and (2.69). From these equations it can be derived that

$$\varepsilon = C_\mu^{3/4} k^{3/2}/\kappa y \tag{2.94}$$

is valid in the near-wall region.

The temperature is matched to the law of the wall for the temperature given by Launder and Spalding as

$$\frac{(T - T_j)\sqrt{\tau_s \rho}}{q_s/C_p} = \frac{Pr_t}{\kappa}\left[\ln E y^+ + 9.24\left[\left(\frac{Pr}{Pr_t}\right)^{3/4} - 1\right]\kappa\right] \tag{2.95}$$

with $Pr = 0.71$, $Pr_t = 0.90$ and q_s the heat flux at the wall in kW/m^2. When $y^+ < 11.63$ the laminar law $q_s = k\dfrac{(T - T_s)}{y}$ is used.

For u_2 no special measures have to be taken for the near-wall grid node. The u_2 velocity at the wall is set to zero.

Boundary III: Outflow Region

The outflow region was set at 12.5H from the stagnation point, i.e. sufficiently far to ensure only outflow at this boundary. The boundary conditions are

$$\frac{\partial u_1}{\partial x_1} = \frac{\partial T}{\partial x_1} = \frac{\partial k}{\partial x_1} = \frac{\partial \varepsilon}{\partial x_1} = u_2 = 0 \qquad (2.96)$$

Boundary IV: Axis of Symmetry

$$\frac{\partial u_2}{\partial x_1} = \frac{\partial T}{\partial x_1} = \frac{\partial k}{\partial x_1} = \frac{\partial \varepsilon}{\partial x_1} = u_1 = 0 \qquad (2.97)$$

Boundary V: Impingement Surface

The same boundary conditions as for the confinement surface are used except for the temperature, where in equation (2.95) T_j is replaced by T_s.

2.3.1.4 Capabilities and Limitations of the k-ε Model

The value of the constant C_μ in equation (2.69) can be derived from the transport equation for k, equation (2.86), for near-wall turbulence. Together with the boundary layer assumptions and the "local-equilibrium" assumption, i.e. that turbulence can be presumed to be produced and dissipated at the same location, equation (2.86) reduces to

$$\nu_t \left(\frac{\partial u_1}{\partial x_2}\right)^2 = \varepsilon \qquad (2.98)$$

which is again the mathematical statement of "local-equilibrium" for thin shear flows

$$\text{or} \qquad C_\mu = \left(\frac{\tau_s/\rho}{k}\right)^2 \qquad (2.99)$$

From experiments it is known that in the near-wall region $\frac{\tau_s/\rho}{k} = 0.3$ so that $C_\mu = 0.09$. In the k-ε turbulent viscosity model, C_μ is consequently taken to be constant at 0.09 everywhere in the flow field.

Later, Launder (82) and Rodi (120) have shown for two-dimensional thin shear flows that the turbulent viscosity concept with μ_t given by equation (2.69) can be derived by a modest simplification of the modelled form of the exact transport equation of the Reynolds stress (equation (2.81)). The assumptions are:

(1) The rate of variation of $\overline{u_i u_j}/k$ along a streamline is much smaller than the variation of $\overline{u_i u_j}$.

(2) The pressure-strain correlation in the Reynolds stress equation (2.81) is modelled by

$$\overline{\frac{p'}{\rho}\left(\frac{\partial u_i'}{\partial x_j} + \frac{\partial u_j'}{\partial x_i}\right)} = -C_1 \frac{\varepsilon}{k}\left(\overline{u_i' u_j'} - \frac{2}{3}\delta_{ij}k\right) - \gamma_t\left(\tilde{P}_{ij} - \frac{2}{3}\delta_{ij}\tilde{P}\right) \qquad (2.100)$$

with $\tilde{P}_{ij}$ the production term in equation (2.81), $\tilde{P} = -\overline{u_i'u_j'}\frac{\partial u_i}{\partial x_j}$ the production of turbulent kinetic energy and the constants C_1 and γ_t respectively 1.5 and 0.6. The so-called "near-wall correction term" (Irwin (66)) is not included in this form of the pressure-strain correlation.

(3) The flow is a turbulence equilibrium flow, i.e. $\tilde{P} = \varepsilon$. If the last assumption is not made, it can be derived for two-dimensional thin shear flow that

$$-\rho\overline{u_1'u_2'} = \frac{2}{3}\frac{(1-\gamma_t)}{C_1}\frac{(C_1 - 1 + j\tilde{P}/\varepsilon)}{(C_1 - 1 + \tilde{P}/\varepsilon)^2}\rho\frac{k^2}{\varepsilon}\frac{\partial u_1}{\partial x_2} \qquad (2.101)$$

This is an effective viscosity relationship with C_μ being a function of $\tilde{P}/\varepsilon$. When $\tilde{P}/\varepsilon$ increases, C_μ decreases, and vice versa.

Launder in 1975 termed the modelling of the Reynolds stress as in (2.101) as "algebraic stress modelling" or ASM for short. Launder attributed the surprisingly good results of the k-ε model with a constant C_μ of 0.09, to the turbulent stresses being at least two orders of magnitude smaller than typical dynamic pressures, so that the turbulent shear stress gradients are only significant in the thin shear layers near the wall, a region where the ratio $\tilde{P}/\varepsilon$ is reasonably constant and of magnitude about unity. In the main flow where the stress gradients are not large, a variable C_μ scarcely affects the flow because gradients of static pressure provide the main forces on any fluid element.

Launder furthermore recommended the following modifications to the k-ε model in certain flow situations:

(1) For axisymmetric flows, different values of C_μ and C_{ε_2} should be used, as pointed out in 1973 by Launder et al. (84).

(2) For weak shear flows, as for jets, wakes and flow behind self-propelled bodies, the ASM version of the k-ε model (equation (2.101)) should be used, since $\tilde{P}/\varepsilon$ is significantly less than 1 in such flows of essentially zero pressure gradient.

(3) For thin shear flows over curved surfaces the coefficient C_{ε_2} in the ε equation (2.88) should be replaced by $C_{\varepsilon_2}(1 - 0.25\,Ri)$ with Ri, the Richardson number defined as

$$Ri = \frac{k^2}{\varepsilon^2}\frac{U_\theta}{r^2}\frac{\partial(rU_\theta)}{\partial r} \qquad (2.102)$$

For a positive Richardson number, i.e. for flows where the angular momentum increases with radius such as for a boundary layer developing over a convex surface, the sink term (containing C_{ε_2}) in the ε equation is reduced, thus leading to higher levels of ε and hence lower effective viscosities, as shown by Priddin (112).

(4) For flows where the near-wall region is not well described by the form of the law of the wall given in equation (2.91), such as for flows with

(a) throughflow at the wall

(b) steep streamwise pressure gradients

(c) steep temperature gradients at the wall

new wall laws must be developed which take account of these special conditions.

Yet another approach would be to extend the calculations directly to the wall. In this case the so-called low Reynolds number k-ε model of Jones and Launder (70) should be used which also models the viscous effects and which could be neglected for high turbulence Reynolds numbers. However Launder has noted that this route is not practicable for recirculating flows because the number of grid nodes necessary in the wall region to obtain a grid independent solution is prohibitively large.

2.3.2 Numerical Procedure

The steady state form of the equations described in Section 2.2, with the exception of the continuity equation, can be cast into a general partial differential equation with the aid of Cartesian tensor notation as

$$\frac{\partial(\rho u_i \phi)}{\partial x_i} - \frac{\partial(\Gamma_{\phi eff}(\partial\phi/\partial x_i))}{\partial x_i} - S_\phi = 0 \qquad (2.103)$$

with ϕ being u_1, u_2, k, ε and T, and $\Gamma_{\phi eff}$ respectively μ_{eff}, $\Gamma_{k,eff}$, $\Gamma_{\varepsilon,eff}$ and λ_{eff}/C_p. For uniform density, the effective exchange coefficients $\Gamma_{\phi eff}$ and the source term S_ϕ for the different dependent variables are listed in Table 2.7. It should be noted that in the original TEACH-T program, μ_t in S_k, S_ε and $\Gamma_{\varepsilon,eff}$ were replaced by $\mu_{eff} = \mu_t + \mu$, as will be discussed in Section 2.3.3.1.

TABLE 2.7.

Effective exchange coefficients and source terms in Equation (2.10.3)

ϕ	$\Gamma_{\phi eff}$	S_ϕ
u_1	$\mu_t + \mu$	$\frac{\partial}{\partial x_j}\left(\mu_{eff}\frac{\partial u_j}{\partial x_1}\right) - \frac{\partial P}{\partial x_1}$
u_2	$\mu_t + \mu$	$\frac{\partial}{\partial x_j}\left(\mu_{eff}\frac{\partial u_j}{\partial x_2}\right) - \frac{\partial P}{\partial x_2}$
k	$\mu_t/\sigma_k + \mu$	$\mu_t G - \rho\varepsilon$
ε	μ_t/σ_ε	$C_{\varepsilon_1}\frac{\varepsilon}{k}\mu_t G - C_{\varepsilon_2}\rho\frac{\varepsilon^2}{k}$
T	$\mu_t/Pr_t + \mu/Pr$	0

In order to solve the general partial differential equation (2.103) it must be transformed into a finite difference equation. The transformation is described first in the 1972 paper by Caretto et al. (27). The solution procedure of the TEACH-T program is exactly the same as the SIMPLE ("Semi-Implicit Method for Pressure-Linked Equations) procedure described by Caretto et al. More details about the solution procedure are given by Patankar (106) and Gosman et al. (48).

2.3.2.1 Finite Difference Grid

Transformation of the partial differential equation into a finite difference equation is based on the principle of control volume integration, just as in the vorticity-stream function (ω-ψ) procedure described in Section 2.2.2. However, in contrast to one aspect of the procedure for the ω-ψ program, a staggered grid is used in the TEACH-T program for respectively the velocities (u_i) and all the scalar quantities (k, ε, T, P, μ and ρ). The vector and scalar grid are represented by respectively the dashed and solid lines in Figure 2.50. The advantage of a staggered grid is two-fold. First, for the cross-hatched control volume in Figure 2.50, the velocity normal to a face is calculated for a point on that face, which makes it convenient to write the convective flux of a scalar at that face as well as to write the mass conservation for that control volume. Second, in the momentum equations the difference of pressure between two adjacent scalar nodes can be used to "drive" the velocity component for a vector node midway between the scalar nodes.

2.3.2.2 Finite Difference Equation for Scalar Variables

The convection and diffusion terms of the dependent scalar variables are integrated over the shaded control volume of Figure 2.50 using Gauss' theorem and the assumption of linear variation of density and effective exchange coefficient between grid nodes. Depending on the relative size of the diffusive and convective contributions to the surface integral (obtained after application of the Gauss theorem, central or upwind differences are used,

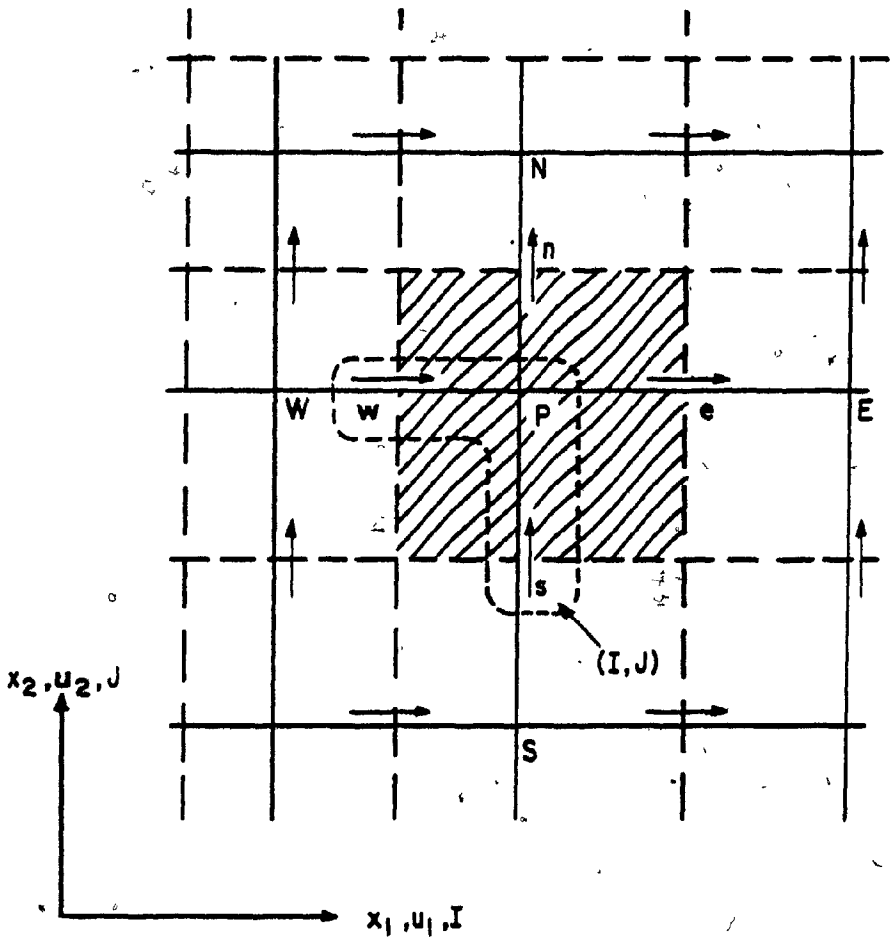


FIGURE 2.50. Scalar and vector grid

i.e. the hybrid scheme is used, just as in the ω-ψ program. Details of the hybrid scheme are as given in Section 2.2 concerning the laminar jet. Thus the finite difference equation becomes

$$\phi_P = (CE_\phi\phi_E + CW_\phi\phi_W + CN_\phi\phi_N + CS_\phi\phi_S + \int_V S_\phi dV)/$$

$$(CE_\phi + CW_\phi + CN_\phi + CS_\phi) \qquad (2.104)$$

with

$$CW_\phi = \begin{cases} \Gamma_{\phi w}(\delta x_{2ns})/(\delta x_{1PW}) + \rho_w u_{1w}(\delta x_{2ns})/2 & \text{when } -2 < Pe_w < 2 \\ + \rho_w u_{1w}(\delta x_{2ns}) & \text{for } Pe_w \geq 2 \\ 0 \quad \text{for } Pe_w \leq -2 \end{cases}$$

and $Pe_w = (\rho_w u_{1w})(\delta x_{1PW})/\Gamma_{\phi w}$

$\rho_w = (\rho_W + \rho_P)/2$

$\Gamma_{\phi w} = (\Gamma_{\phi W} + \Gamma_{\phi P})/2$

δx_{2ns} = distance between n and s

δx_{1PW} = distance between P and W

$\int_V S_\phi dV$ = volume integral of source term S_ϕ over shaded area

The source term $\int_V S_\phi dV$ requires special treatment in order to avoid stability problems. Although S_ϕ is non-linear the integral is linearized as

$$\int_V S_\phi dV = b\phi_P + c \qquad (2.105)$$

with b being negative and c positive. Insertion of (2.105) in (2.104) gives

$$\phi_P = (CE_\phi\phi_E + CW_\phi\phi_W + CN_\phi\phi_N + CS_\phi\phi_S + c)/$$

$$(CE_\phi + CW_\phi + CN_\phi + CS_\phi - b) \qquad (2.106)$$

It is clear that the formulation of $\int_V S_\phi dV$ as in (2.105) increases the stability of the iterative solution of equation (2.106), since the equations (2.34) and (2.35) are valid (cf Section 2.2.2.1). For the turbulent kinetic energy, $\int_V S_k dV$ is replaced by

$$(-\rho \frac{\varepsilon_P}{k_P} k_P + \mu_{t_P} G_P)\delta V$$

or

$$\int_V S_k dV = - \frac{C_\mu \rho_P^2 k_P (\delta V)}{\mu_{t_P}} k_P + \mu_{t_P} G_P (\delta V) \qquad (2.107)$$

with δV being the shaded cell control volume and G_P the product of velocity gradients defined in equation (2.83) and evaluated at node P. The energy-dissipation source is expressed as

$$\int_V S_\varepsilon dV = - \frac{C_{\varepsilon_2} \rho_P \varepsilon_P (\delta V)}{k_P} \varepsilon_P + C_{\varepsilon_1} C_\mu \rho_P k_P G_P (\delta V) \quad (2.108)$$

An extra term is added to the source term to avoid stability problems during the first iterations when a net outflow from the control volume can lead to all zero coefficients in the denominator of equation (2.106). The term is

$$S_{false} = (\max(0, \Sigma c))(\phi_P^* - \phi_P)$$

or

$$S_{false} = - (\max(0, \Sigma c))\phi_P + (\max(0, \Sigma c))\phi_P^* \quad (2.109)$$

with $\max(0, \Sigma c)$ being the net mass outflow or zero when there is a net mass inflow, and ϕ_P^* the value of ϕ_P at the previous iteration. This false source term is taken up in the finite difference equation in the same way as the regular source term. This procedure is followed for all the variables, i.e. also u_1, u_2 and the so-called pressure correction.

2.3.2.3 Finite Difference Equation for Velocities

The treatment of the momentum equation is essentially the same as for the scalar variables, except for the location of the control volumes which are now centered around the velocity locations, i.e. displaced halfway towards S and W for respectively u_1 and u_2 shown in Figure 2.50. The interpolation which is sometimes necessary for the velocities, densities and viscosities is done in such a way that the final difference equation is

conservative. Thus the difference equation for the velocity u_1 takes the form

$$u_{1P} = (CE_{u_1} u_{1E} + \ldots + CS_{u_1} u_{1S} + \int_V S'_{u_1} dV + D_x(P_W - P_P))/$$

$$(CE_{u_1} + \ldots + CS_{u_1}) \qquad (2.110)$$

with D_x the area on which the pressure acts and S'_{u_1} the source term, $(P_W - P_P)$ the pressure gradient term. (Note that the nodes P and W are at a different location for the pressure and the velocity.)

2.3.2.4 Finite Difference Equation for Pressure

Since the values of the pressure P are not known in advance, the best estimate of the pressure field, denoted by P^*, is substituted in (2.110) to obtain a preliminary velocity field u_1^* and u_2^*. Consequently equation (2.110) becomes

$$u^*_{1P} = (CE_{u_1} u^*_{1E} + \ldots + CS_{u_1} u^*_{1S} + \int_V S'_{u_1} dV + D_x(P^*_W - P^*_P))/$$

$$(CE_{u_1} + \ldots + CS_{u_1}) \qquad (2.111)$$

The true pressure P is related to the estimated pressure by

$$P = P^* + P' \qquad (2.112)$$

where P' is the so-called pressure correction. The true velocity u_1 is related to u_1^* via

$$u_{1W} = u^*_{1W} + \left.\frac{\partial u_1}{\partial P}\right|_W (P'_W - P'_P) \tag{2.113}$$

with $\left.\frac{\partial u_1}{\partial P}\right|_W$ estimated from equation (2.110) as

$$\left.\frac{\partial u_1}{\partial P}\right|_W \approx D_x/(CE_{u_1} + CW_{u_1} + CN_{u_1} + CS_{u_1})$$

one obtains

$$u_{1W} = u^*_{1W} + \frac{D_x(P'_W - P'_P)}{(CE_{u_1} + CW_{u_1} + CN_{u_1} + CS_{u_1})} \tag{2.114}$$

Substitution of equations of the type of (2.114) in the continuity equation which is integrated over the shaded control volume of Figure 2.50 gives a finite difference equation for the pressure correction P'

$$P'_P = (CE_P P'_E + CW_P P'_W + CN_P P'_N + CS_P P'_S + SP)/$$

$$(CE_P + CW_P + CN_P + CS_P) \tag{2.115}$$

with $CW_P = \rho_w (D_x)^2/(CE_{u_1} + CW_{u_1} + CN_{u_1} + CS_{u_1})$

and $SP = (\rho_w u^*_{1w} - \rho_e u^*_{1e})D_x + (\rho_s u^*_{2s} - \rho_n u^*_{2n})D_y$

2.3.2.5 Insertion of Boundary Conditions

It is convenient to let the physical boundaries of the flow problem coincide with the vector grid, i.e. with the dashed lines in Figure 2.50. Consequently only the grid nodes of velocities perpendicular to a physical boundary are located on a physical boundary.

Except for solid boundaries and for the pressure correction P', insertion of the boundary conditions given in Section 2.3.1.3 is straightforward. If values of the dependent variable are known for the boundary nodes, these values are simply used where they appear as the neighbours of the internal nodes near the boundary. When the boundary condition is in the form of a specified flux, then the difference equations for the near-boundary nodes are modified by use of the boundary condition information, thus eliminating the unknown values. For example, at the axis of symmetry the flux of u_2 momentum across this boundary is set to zero, by setting CW_{u_2} to zero.

Boundary conditions for the pressure correction are very simple. Usually either velocity or pressure is specified at a boundary. When velocity normal to the boundary is specified, there would be no correction to this velocity, and thus a boundary condition of zero normal gradient is appropriate for the P' equation. When pressure at the boundary is specified, the estimated pressure P^* at the boundary is equated to the given pressure P, so that P' at the boundary must be zero.

The wall boundary condition for the tangential velocity is incorporated in the finite difference procedure with the use of

the law of the wall given by equation (2.91). Equation (2.91) can be rewritten with the use of equation (2.93) as

$$\tau_s = - \rho C_\mu^{\frac{1}{4}} k^{\frac{1}{2}} u_1 \kappa/(\ln E y^+) \tag{2.116}$$

the negative sign indicating that the wall exerts a force on the control volume in the direction opposite to the flow. This expression is incorporated into the finite difference scheme by setting the shear force expression at the wall in the finite difference equation (2.111) for the grid node P near the wall equal to zero and adding

$$- (\rho_P C_\mu^{\frac{1}{4}} k_P K(\delta x_1)/(\ln E y_P^+)) u_{1P}$$

to the source term expressed as equation (2.105), with δx_1 being $\frac{1}{2}\ \delta x_{2EW}$ of the vector grid.

A similar procedure is followed for kinetic energy, when the flux of kinetic energy across the solid boundary for grid node P is set to zero and the source term given by equation (2.111) is changed by noting that, by making the boundary layer approximation, a fraction of $\int_V \mu_t G dV$ can be replaced as,

$$\int_V \mu_t \left(\frac{\partial u_1}{\partial x_2} + \frac{\partial u_2}{\partial x_1}\right)^2 dV \approx \tau_s u_P \delta V / y_P \tag{2.117}$$

while the normal expression for $\int_V \rho \varepsilon dV$ is replaced by

$$\int \rho \varepsilon dV = \left[\frac{\rho_P C_\mu^{\frac{3}{4}} k_P^{\frac{1}{2}}}{\kappa y_P} \ln(Ey^+) \right] (\delta V) k_P \qquad (2.118)$$

The dissipation rate at the near-wall grid point P is calculated by replacing the finite difference equation at the near-wall grid node by relation (2.94), i.e.

$$\varepsilon_P = C_\mu^{3/4} k_P^{3/2} / (\kappa y_P) \qquad (2.119)$$

The wall boundary condition for temperature given by equation (2.95) is incorporated in the finite difference procedure in the same way as for tangential velocity. So equation (2.95) is rewritten as

$$q_S/C_P = \frac{- \rho C_\mu^{\frac{1}{4}} k_P^{\frac{1}{2}} (T_P - T_S)}{Pr_t \left[\frac{1}{\kappa} \ln(Ey^+) + 9.24 \left[\left(\frac{Pr}{Pr_t} \right)^{\frac{3}{4}} - 1 \right] \right]} \qquad (2.120)$$

the negative sign indicating the heat flux direction of the wall, relative to the control volume, opposite to that of the temperature gradient at the wall. This expression is incorporated in the finite difference scheme by setting the expression for heat flux at the wall in finite difference equation (2.106) for the grid node P to zero and adding $- M_f(\delta x_1) + M_f(\delta x_1)$ to respectively b and c of equation (2.106) with M_f defined as

$$M_f = \frac{\rho_P C_\mu^{\frac{1}{4}} k_P^{\frac{1}{2}}}{Pr_t \left[\frac{1}{\kappa} \ln(Ey^+) + 9.24 \left[\left(\frac{Pr}{Pr_t} \right)^{\frac{3}{4}} - 1 \right] \right]}$$

and δx_1 being $\frac{1}{2}\ \delta x_{2EW}$ of the scalar grid.

A closed set of finite difference equations has now been obtained. Their solution is obtained by solving equations (2.111), (2.115), (2.112), (2.114) and (2.106) for respectively u^*, P', P, u and the remaining scalar variables, together with the boundary conditions, over and over again in this order, until convergence.

2.3.2.6 Computation Procedures

The finite difference equations for the dependent variables u_1, u_2, P', k, ε and T are solved along the N-S line, using the tridiagonal matrix algorithm described in Section 2.2.2.1 (f). The grid is swept three times for each dependent variable (except for P' which is swept five times) before proceeding to the next variable. The underrelaxation factors for u_1, u_2, P', k, ε, T and μ_t are respectively 0.5, 0.5, 1.0, 0.7, 0.7, 0.7 and 0.7.

The solution is considered converged when the summation of the absolute relative residual R_ϕ over all the grid points is smaller than 0.015 for each of the variables u_1, u_2, P' and T. R_ϕ is defined as

$$\sum_{\text{all grid nodes}} \left| CE_\phi \phi_E + \ldots CS_\phi \phi_S + c - (CE_\phi + \ldots CS_\phi - b)\phi_P \right| / F_\phi \qquad (2.121)$$

with F_ϕ being respectively half of the mass flux, momentum flux

and energy flux entering through the nozzle for ϕ as P', u and T, respectively. The computing time for a converged solution was of the order of 4 minutes cpu time on an IBM 360.

2.3.3 Results and Discussion

As stated at the outset of Section 2.3, results obtained here by numerical prediction are but the first step towards simulation of results obtainable experimentally with the Simtest apparatus which comprise Chapters 3 and 4 of the present study. As numerical simulation of turbulent impinging jets has not yet been achieved fully satisfactorily for the basic case of a flat, stationary, impermeable impingement surface due to the many difficulties already apparent, no attempt was made to incorporate the yet more difficult conditions of impingement surface motion, curvature and throughflow. Thus the present section treats some of the problems encountered in computer simulation for the case of a flat, stationary, impermeable impingement surface. The six combinations of jet Reynolds number, Re_j, and nozzle to impingement surface spacing, H/w, which were investigated for the confined impingement system shown in Figure 2.1 are listed in Table 2.8. The cases for H/w = 2.6 and 6 correspond to experimental runs with the Simtest apparatus in the present study, while the case for H/w = 8 corresponds to an experimental run of Cadek (26). Several grid distributions and boundary condition treatments were used for the cases listed in Table 2.8, as discussed subsequently in Section 2.3.3.1.

TABLE 2.8.

Range of parameters for turbulent jet calculations

H/w	Re_j
2.6	10400 and 20200
6	5200 and 8100
8	20750

After obtaining a converged solution in the form of velocities, static pressure, k, ε, T and μ_{eff} at all the grid points, the skin friction and heat transfer at the impingement surface are calculated as $C_f/2$ and St, as follows:

$$C_f/2 = \tau_s/(\rho_j U_j^2) \tag{2.122}$$

and

$$St = \frac{C_\mu^{\frac{1}{4}} k^{\frac{1}{2}} (T_p - T_s)}{Pr_t U_j (T_j - T_s) \left[\frac{1}{K_p} \ln(Ey_p^+) + 9.24\left[\left(\frac{Pr}{Pr_t}\right)^{\frac{3}{4}} - 1\right]\right]} \tag{2.123}$$

It should be noted that the solutions are obtained with constant physical properties, i.e. the influence of temperature on viscosity and density is not included, the differential equations given in Table 2.7 of Section 2.3.2 being for constant density flows. This is not a severe restriction for the present moderate temperature differences between the jet and impingement surface, especially noting that except for the near impingement

surface grid line, the temperature in the impingement region and a large part of the wall jet region differs little from the nozzle exit. However for simulation of performance with large temperature differences at least the wall boundary conditions should be adjusted to allow for variations in the variable properties (cf. recommendation (4), Section 2.3.1.4). Finally, for moderate temperature differences the influence of variable properties on heat transfer can be allowed for through a nondimensional treatment validated in Section 4.2.

2.3.3.1 Effect of Wall-Flux Laws and Treatment of Diffusion and Source Terms in the k and ε Equations

A non-uniform grid is used, analogous to that shown in Figure 2.2 for the vorticity-stream function program. For the reasons given in Section 2.2.2.1 (a), a closely spaced grid is used under the jet, near the confinement surface and especially near the impingement surface. The length of the confinement surface is set at 12.5H, leading to only outflow at Boundary III for turbulent flow. A 22 x 16 gridline mesh in respectively the x_1 and x_2-direction is used for most runs. The distribution of the 22 gridlines in the x_1-direction is the same in all cases. The number of gridlines in the x_2-direction is 15 or 16, the distribution of these gridlines being varied considerably.

Location of the gridlines parallel to the impingement surface, found to be a key parameter, is now documented. The separation between the impingment surface and the adjacent gridline was varied in five steps between 1.64×10^{-3}H and 19.64×10^{-3}H for Re_j = 10400 and H/w = 2.6, as listed in Table 2.9.

TABLE 2.9.

Location of near-wall grid line

Case	Number of Gridlines in x_2-direction	ΔX^*_{2Pn}	μ_t in $\Gamma_{\epsilon\,eff}$ and S_ϕ for $\phi = k$ and $\phi = \epsilon$
1	16	1.64×10^{-3}	$\mu_t + \mu_{laminar}$
2	16	3.00×10^{-3}	$\mu_t + \mu_{laminar}$
3	16	6.00×10^{-3}	μ_t
4	16	9.82×10^{-3}	μ_t
5	15	19.64×10^{-3}	μ_t

Cases 1 and 2 have the same grid distribution except for the 5 gridlines adjacent to the impingement surface. The grid distribution of cases 3, 4 and 5 differs significantly from cases 1 and 2, the only difference with cases 3, 4 and 5 being the location of the last 3 or 4 gridlines before impingement.

The differences in results between these five test spacings derive not simply from the size of the cells adjacent to the impingement surface because, in addition to that effect, the program was written so that a choice is made between the use of laminar or turbulent wall flux laws depending on the location, expressed as y^+, of the near-wall gridline. Specifically, if a near-wall grid point is located such that

$$y^+ = \rho k^{\frac{1}{2}} C_\mu^{\frac{1}{4}} y/\mu \leq 11.63$$

then laminar wall flux walls for temperature and velocity parallel to the wall are used, and as well the dissipation term of the kinetic energy equation is treated correspondingly differently than when $y^+ > 11.63$. If a near-wall grid point is located at $y^+ > 11.63$, the turbulent wall flux boundary conditions given in Section 2.3.1.3 are used.

Yet another important distinction between the first two and the last three cases is the treatment of the source and diffusion terms in the turbulence kinetic energy equation and the equation for the dissipation of turbulence kinetic energy (see Table 2.7). In the last three cases the viscosity in the above-mentioned terms is correctly represented by μ_t. However, in the first two cases the viscosity was taken to be $\mu_{eff} = \mu_t + \mu_{laminar}$ because the TEACH-T program provided was in the form with μ_{eff} in all terms of the differential equation of k and ε. This treatment is inconsistent with the modelling of the equations in the form of (2.86) and (2.88) respectively. As μ_t is generally many orders of magnitude larger than the laminar viscosity, the difference between μ_{eff} and μ_t can normally be ignored. However, in the potential core region of an impinging jet, μ_t is unfortunately of the same order of magnitude as μ, leading to significantly different results depending on whether the program uses μ_t, as is correct, or uses the μ_{eff} for μ_t as occurred for the reason cited when cases 1 and 2 were run.

The influence of the two forms of the diffusion and source terms in the equations of k and ε and of the effect of use of laminar or turbulent wall fluxes is examined by reference to

the computed distributions of pressure, velocity, turbulence kinetic energy and heat transfer along the impingement surface, beginning with consideration of the pressure profiles. Shown in Figure 2.51 is the normalized static pressure along the impingement surface relative to the pressure at the center of the nozzle exit (which was set at zero). Even between the two extremes of the five cases listed in Table 2.9 the difference is small and, moreover, agreement with the inviscid solution of Strand (141) in the impingement region is good at this close spacing. The close agreement between the cases at the two extremes and the theoretical solution does not prove that the computer program correctly simulates the confined impinging jet, but rather that the overall features of the present internal flow is pressure dominated and therefore relatively insensitive to the effect of wall-flux laws and use of μ_{eff} or μ_t in the diffusion and source terms of the k and ε equation, or even generally to the treatment of the turbulent stresses. This interpretation is reinforced by the characteristic static pressure recovery in the wall jet region of the confined impinging jet because the magnitude of the maximum pressure recovery is in close agreement with the experimental results obtained with the curved flow in the Simtest apparatus and the results obtained by application of overall equations of conservation of mass, momentum and energy, discussed subsequently in Section 3.5.1. The small negative relative static pressure in the beginning of the wall jet region was also found experimentally by Saad (125).

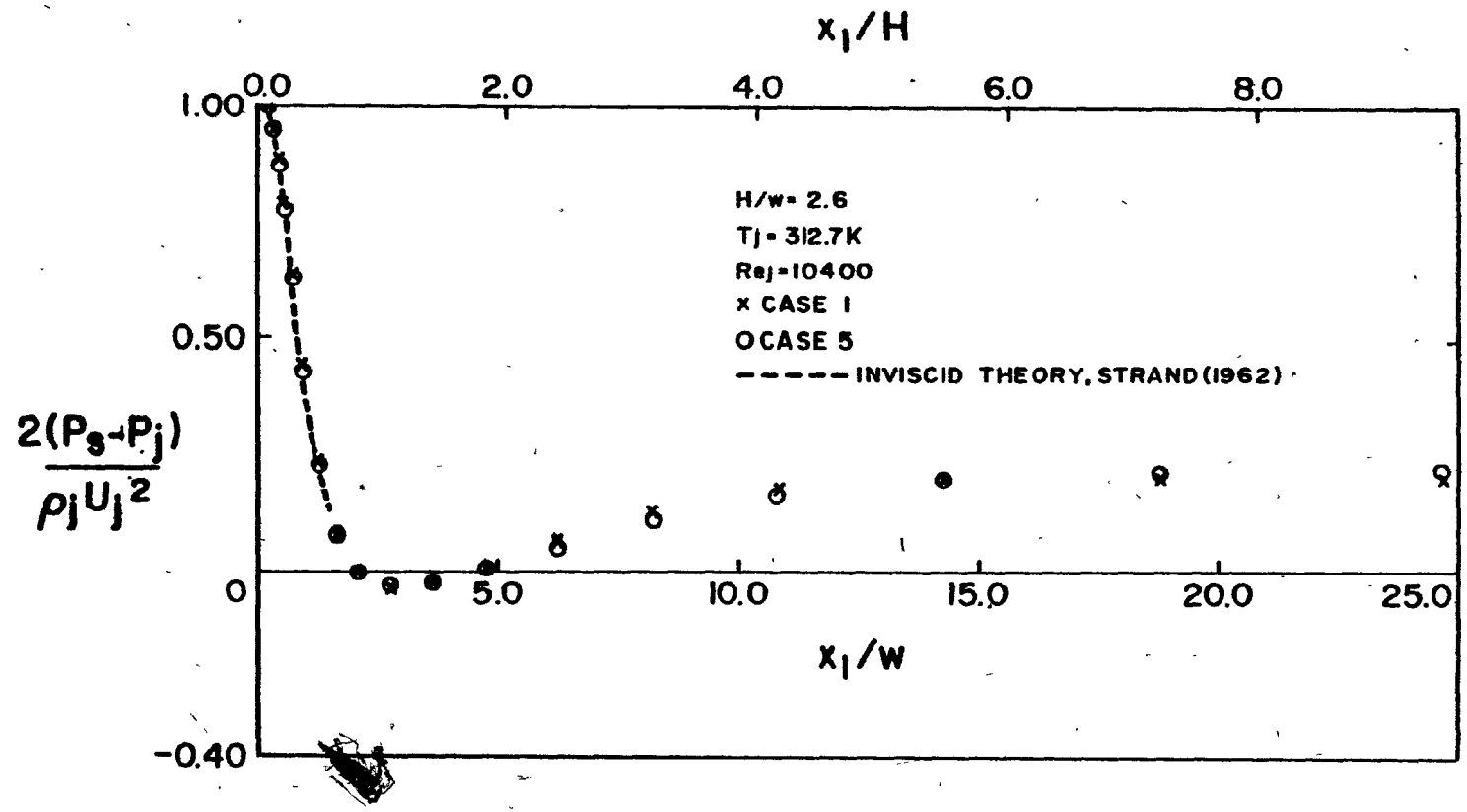


FIGURE 2.51. Pressure distribution along impingement surface

By contrast, differences between the maximum lateral velocities along the impingement surface for the five cases of Table 2.9 are significant in the wall jet region, as can be seen in Figure 2.52. There is little difference in the maximum velocities computed for cases 1 and 2, indicating that near-wall gridline spacing in the range of those cases is unimportant. However, it appears that the computed maximum wall jet velocities are erroneously low for cases 1 and 2 because of the incorrect use of μ_{eff} in place of μ_t in the source and diffusion terms of the k and ε equations. Even for cases 3, 4 and 5 where the problem concerning μ_t is not present, the computed maximum wall jet velocities decay faster than found experimentally by Kumada and Mabuchi (79) for an unconfined slot jet impinging on a flat plate and by Baines and Keffer (7,8) for an unconfined slot jet impinging on a cylinder of diameter 320.5w. Definitive conclusions cannot be made because maximum wall jet velocity would be expected to decay more quickly in the confined impingement system for which the computations were made than for the unconfined jets of the two experimental studies cited.

The profile of lateral (u_1) velocity between the impingement and confinement surfaces is shown at two lateral positions in Figures 2.53(a) and (b). By reference to Figure 2.52 it can be seen that the first position, $x_1 = 3.19w = 1.23H$, is at the beginning of the wall jet region, just past the position where u_m passes through its maximum, while the location of the Figure 2.53(b) profile, $x_1 = 16.5w = 6.35H$, is quite far out in the wall jet region. Results of the two extreme cases in Figure

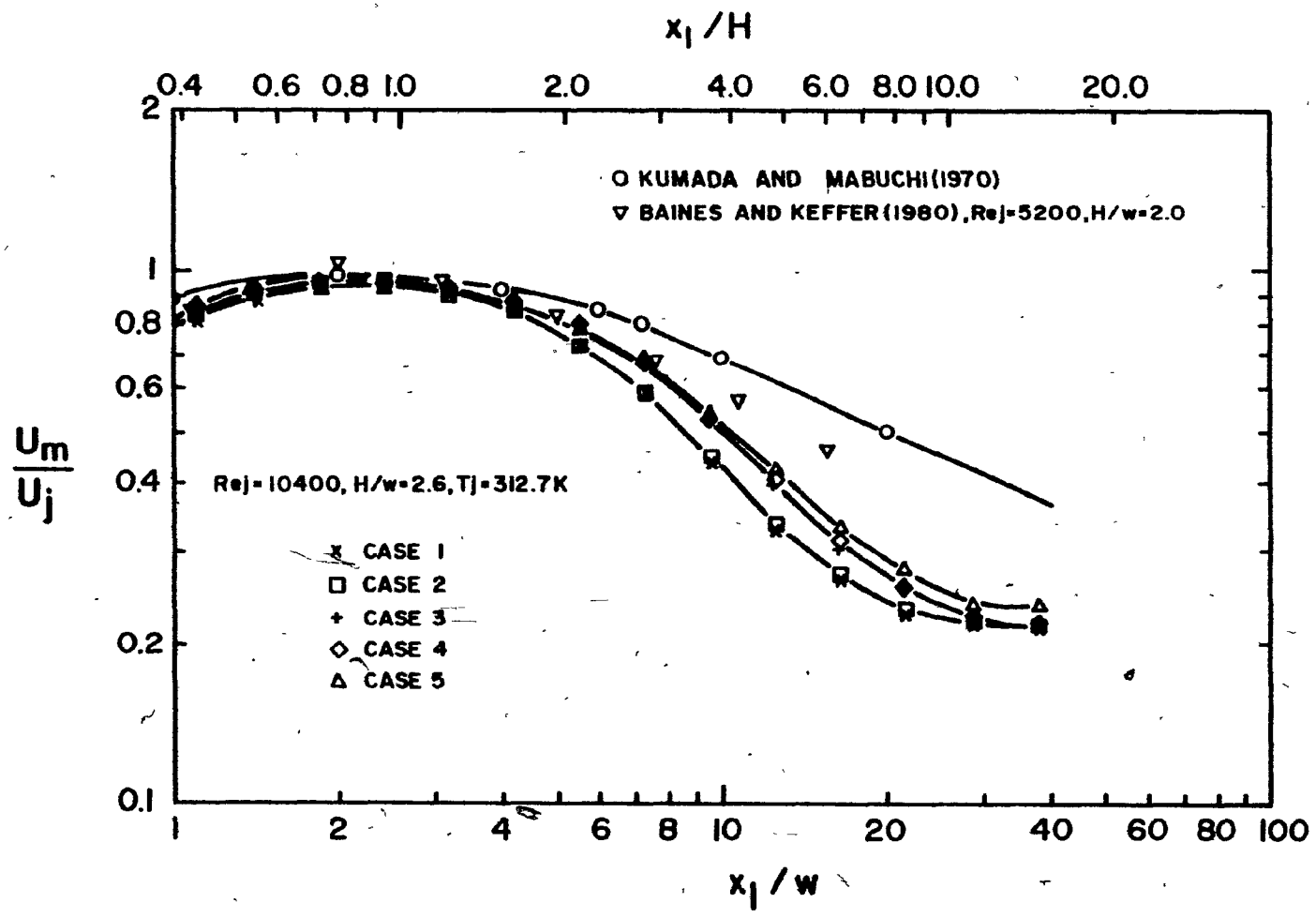


FIGURE 2.52. Development of the maximum wall jet velocity

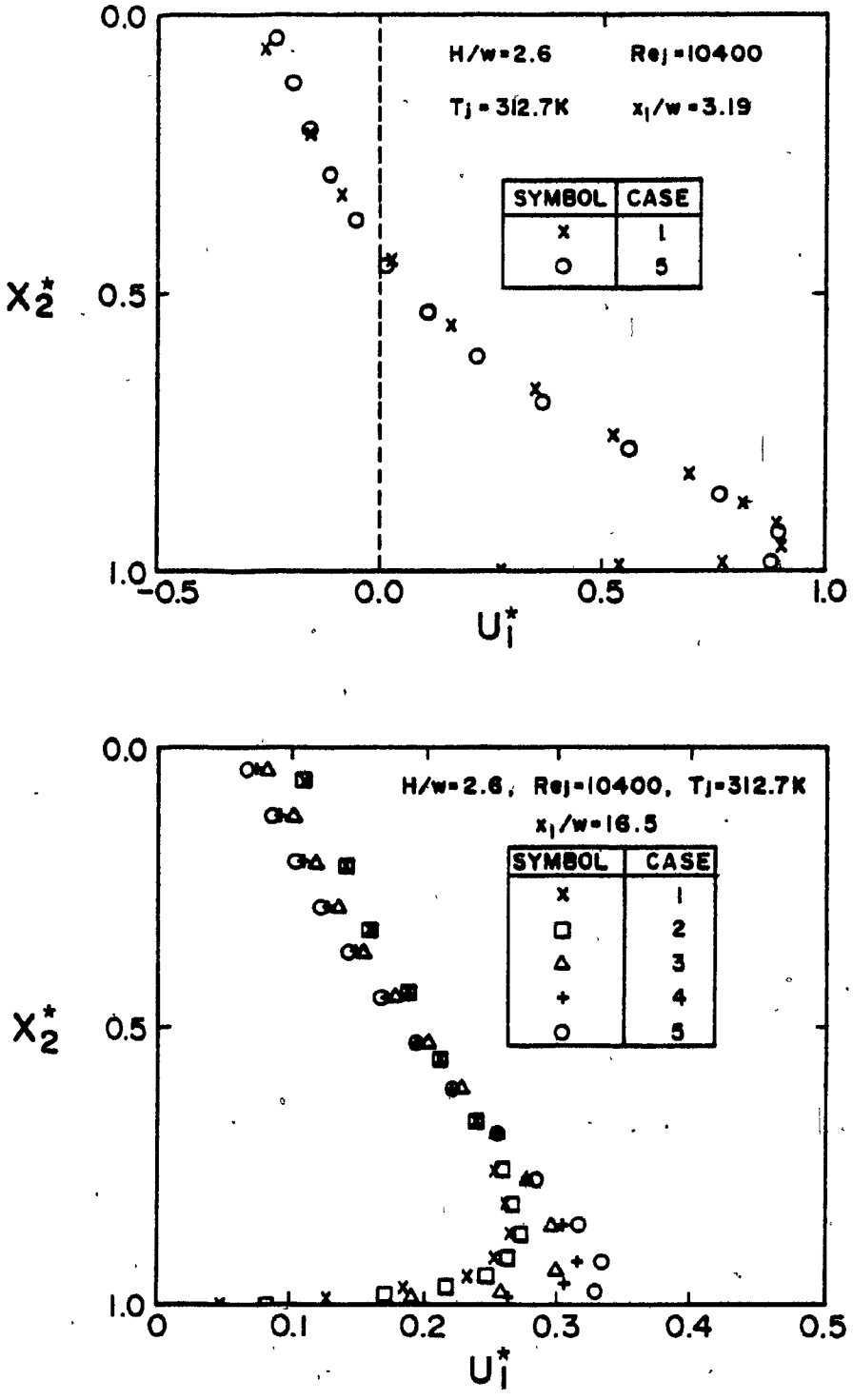


FIGURE 2.53. Velocity distribution in the wall jet region

2.53(a) again show that at the beginning of the wall jet region, the major part of the flow is still dominated by the dynamic pressures and is insensitive to the computational variables being examined.

A different situation exists in Figure 2.53(b). Here cases 1 and 2 are again distinctly different from cases 3, 4 and 5, indicating the importance of treating μ_t correctly. For cases 1, 2 and 3, the near-wall gridline is at $y^+ < 11.63$ over the entire impingement surface, hence the laminar flux laws are used throughout whereas for case 5, this gridline is always at $y^+ > 11.63$, leading to consistent selection of "turbulent" boundary conditions. Case 4 is intermediate, i.e. for $0.5 \leq x_1/w \leq 9.52$, turbulent laws are selected while in the stagnation and far wall jet regions the near-wall gridline is at $y^+ < 11.63$. Thus Figure 2.53(b) confirms that the different treatment of viscosity (turbulent or effective) and the choice between laminar or turbulent wall flux boundary conditions can produce significant variations in computed wall jet velocities close to the impingement surface.

The differences in results computed for the five cases are very pronounced when the turbulent kinetic energy distribution along the gridline at $x_1/w = 0.06$ (i.e. just off the axis of symmetry) is considered in Figure 2.54. The biggest differences are again due to the treatment of the viscosity. With the use of μ_{eff} in the source and diffusion terms of the k and ε equation it appears that especially the diffusion of turbulence kinetic energy from the mixing layer to the axis of symmetry be-

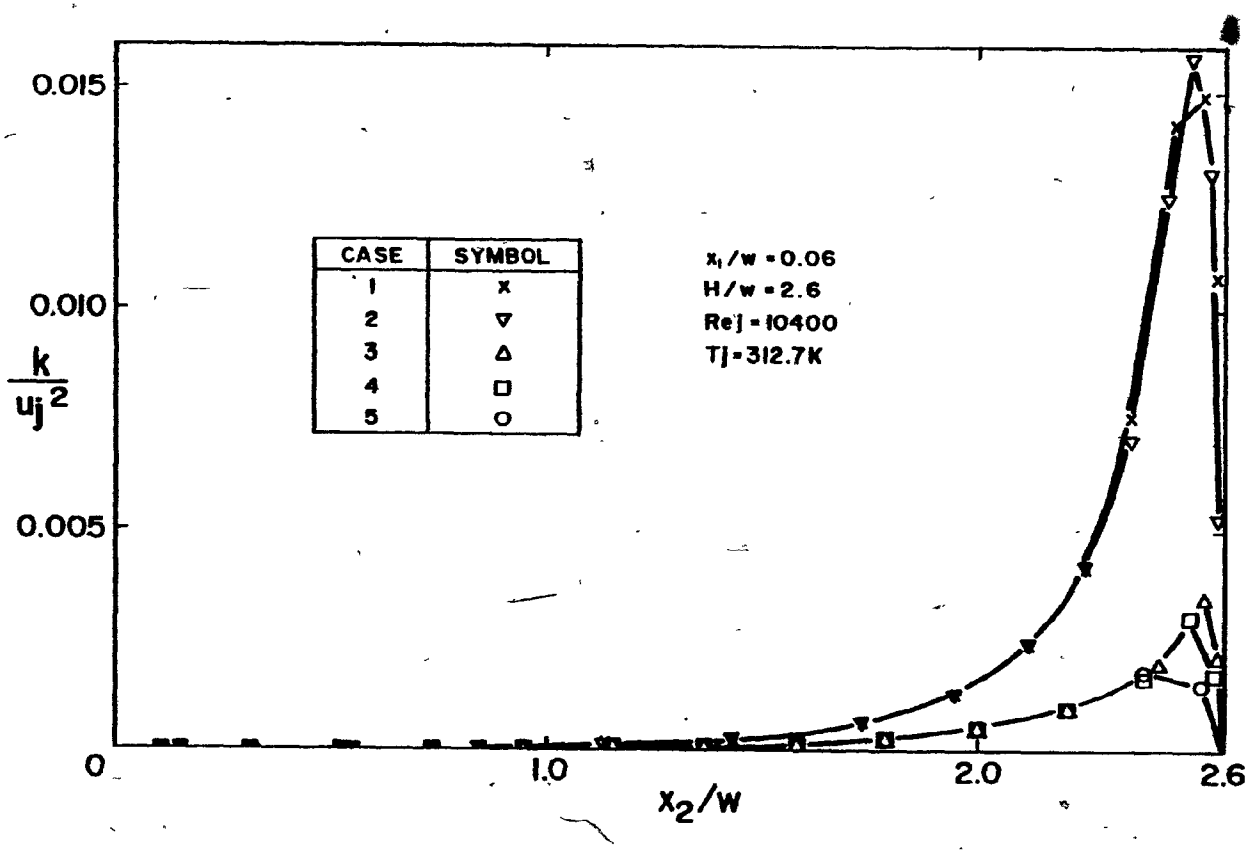


FIGURE 2.54. Turbulent kinetic energy development near the axis of symmetry

comes too large, leading to an erroneously fast increase in the relative kinetic energy near the impingement surface for cases 1 and 2. The recent experimental measurements of Saad (125) indicate that the results computed for cases 1 and 2 are in error. Very close to the impingement surface the computed turbulent kinetic energy is increased by the inaccurate determination of the dissipation of turbulence kinetic energy and the source terms in the F.D.E. for k when the near-wall gridline is in the "laminar" region, $y^+ < 11.63$, as occurs for cases 3 and 4. The relative importance of the computational differences between cases 1 to 5 on turbulence kinetic energy is less pronounced in the wall jet region at $x_1 = 3.62w = 1.39H$, as shown in Figure 2.55. The fact that here the difference between μ_t and μ_{eff} is negligible explains this reduced sensitivity.

Finally in Figure 2.56, the heat transfer distribution is shown for the five cases. Also plotted is the experimental heat transfer distribution obtained in the present work for $Re_j = 10400$ and $H/w = 2.6$. The distributions on either side of the stagnation point along the rotating cylindrical impingement surface, denoted "left side" and "right side", are slightly different as discussed subsequently. Also shown is the experimental heat transfer distribution obtained by Cadek (26) for an unconfined jet on a flat plate at $H/w = 2$. For cases 1 and 2 the computed heat transfer is evidently much too high, thus definitively establishing the importance of the correct treatment of μ_t in the numerical procedure. The agreement is better for cases 3 to 5, although still large differences exist in the

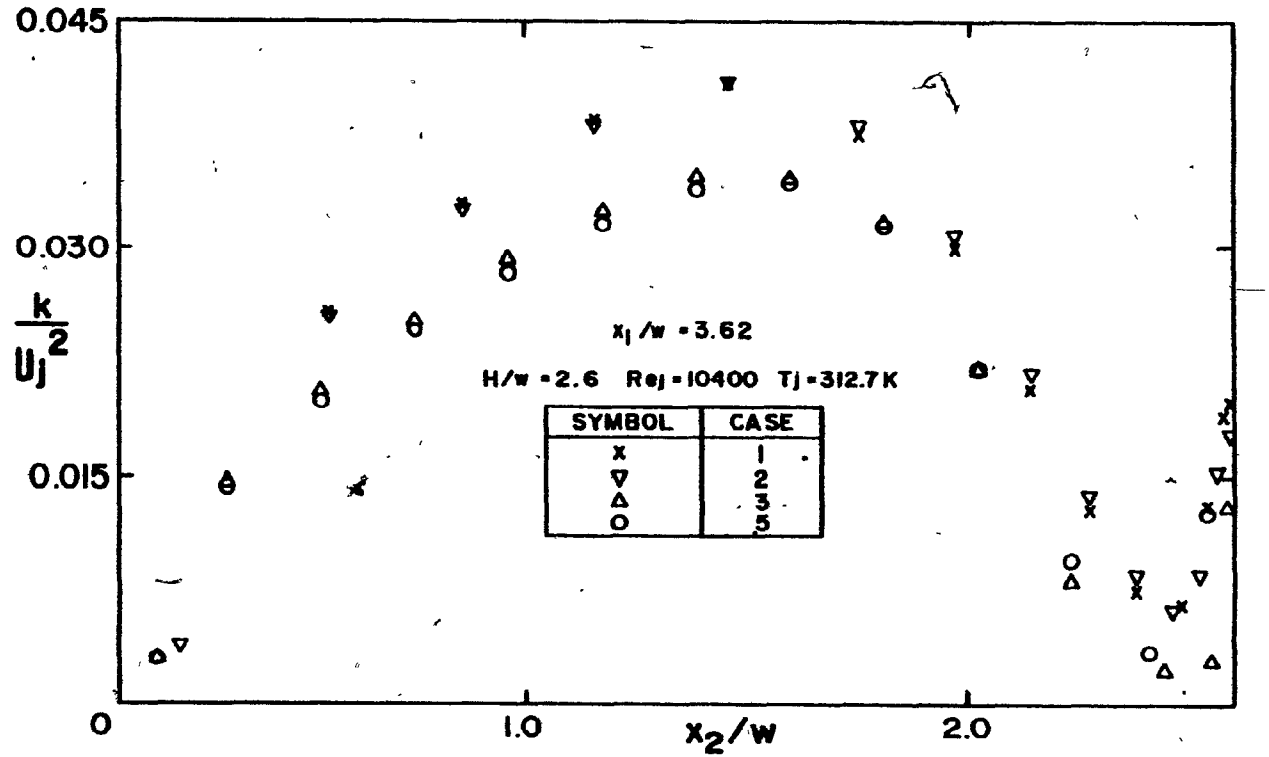


FIGURE 2.55. Turbulent kinetic energy distribution in the wall jet region

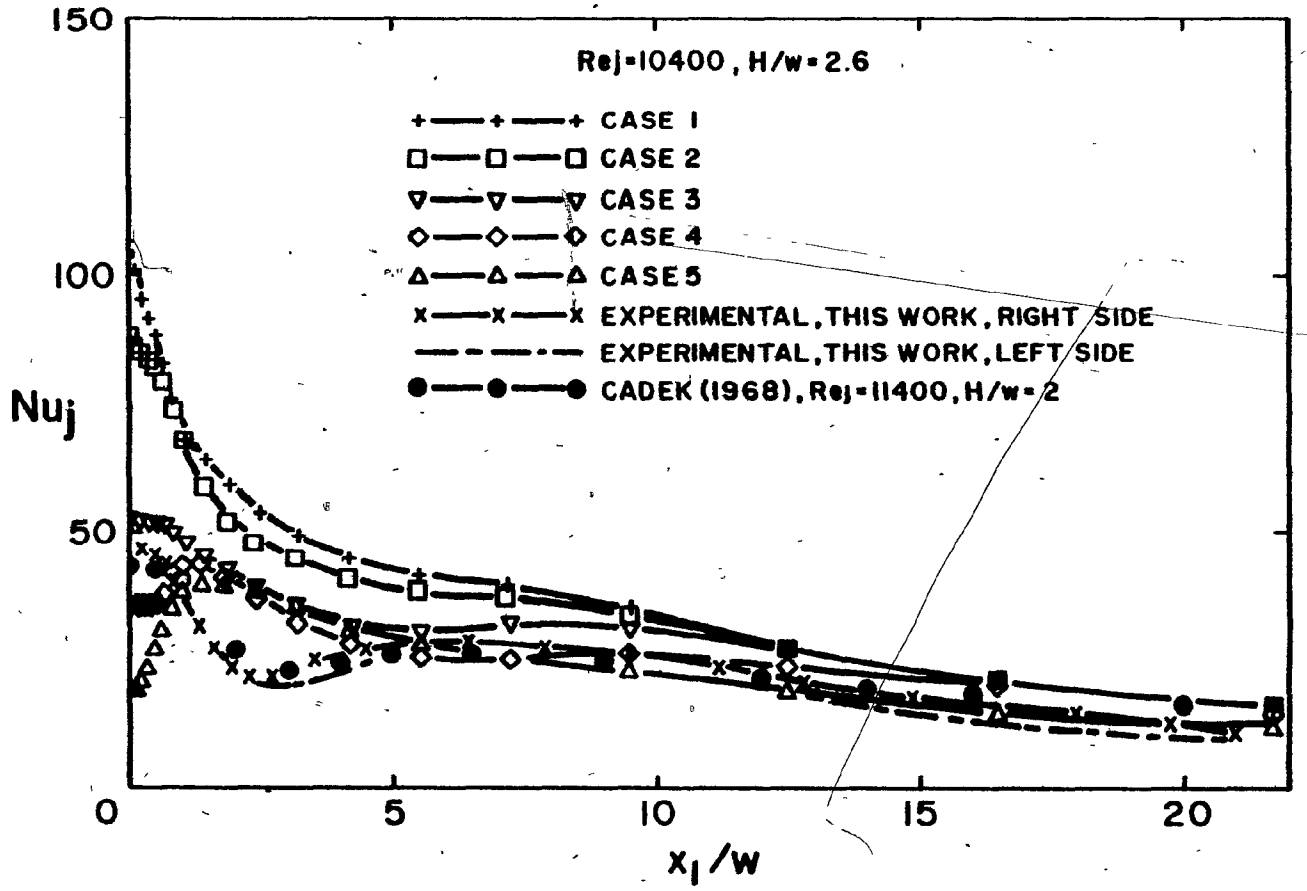


FIGURE 2.56. Heat transfer distribution along the impingement surface for H/w = 2.6 and Re_j = 10400

stagnation and early wall jet regions. The best agreement with the present experimental work is for case 5, in the wall jet region, $x_1/w > 5$, i.e. for the case whereby only "turbulent" wall flux boundary conditions are used. In the region from $x_1 = 5w$ out to $x_1 = 9.5w$, the latter being the limit for which the "turbulent" wall flux boundary condition was used for case 4, there is negligible difference between the results predicted in cases 4 and 5. This observation underlines further the preference for the "turbulent" wall flux boundary condition. It should also be noted that although in Table 2.9 one of the criteria used to differentiate these five cases was ΔX^*_{2Pn}, the separation of the impingement surface from the adjacent gridline, the significant differences in results between these five cases do not derive directly from the gridline spacing but, rather, as the result of other differences which are associated with gridline spacing.

As a result of the investigation of these computational effects, all subsequent numerical simulations were performed with the near-wall gridline in the fully turbulent region ($y^+_{ns} > 11.63$), in order to avoid inaccuracies in determination of the turbulent viscosity, the dissipation of turbulent kinetic energy and the source terms in the finite difference equation for k when applied at a near-wall gridline. Likewise, all subsequent numerical simulations were carried out with the TEACH-T program modified for use of μ_t in the source and diffusion terms of the equations for k and ε, in agreement with the derivation given in Section 2.3.1.2.

It is of interest that Chieng and Launder (32) have recently published a more accurate numerical treatment of k and ε at the near-wall grid nodes, also requiring $y^+_{ns} > 11$. By separate treatment of the viscous sublayer and the adjacent fully turbulent layer in the evaluation of the generation and dissipation terms of turbulent kinetic energy equation, their results for the heat transfer downstream from an abrupt pipe expansion became largely unaffected by moderate variations in the dimension of the near-wall grid cells. Although this procedure became available too late to influence the present study, it is certainly recommended for future numerical work on turbulent impinging jets.

2.3.3.2 Analysis of Turbulence Modelling in the Stagnation Region

It is clear from Figure 2.56 that the heat transfer profile in the stagnation and early wall jet region predicted with the best form of the numerical procedure developed in the present study, i.e. that denoted as case 5, is still far from the actual distribution. Thus where the best predicted Nu_j distribution displays a minimum at the stagnation point and a maximum at $x_1/w = 1.5$, the actual profile has primary and secondary maxima at the stagnation point and at $x_1/w \approx 6.0$, the intervening minimum occurring at $x_1/w \approx 3.0$, the location where the favorable pressure gradient ends (see Figure 2.51). From the discrepancy between computed and actual distributions it is clear that the present modelling of turbulent flow and thermal energy is inade-

quate to describe either the effect of free stream turbulence on heat transfer in the stagnation region or to predict the off-stagnation minimum and maximum in the early wall jet region.

One approach to seeking improved numerical procedures is to incorporate the effect of streamwise pressure gradients. Thus, better simulations of heat transfer should result if the wall flux boundary conditions for u_1 and temperature were extended to include the effect of a streamwise pressure gradient. Such wall flux boundary conditions could be derived from the description of velocity and temperature profiles obtained by Kays et al. (74) for heat transfer to highly accelerated turbulent boundary layers with throughflow. It has been shown by the Stanford group of Kays and Moffat that if a generalized expression for turbulent viscosity and conductivity, based on the above-mentioned measurements, is incorporated into a computer program for numerical computation of turbulent boundary layers, excellent heat transfer predictions for a turbulent boundary layer subjected to intermittent blowing and intermittent streamwise pressure gradient is obtained (Crawford and Kays (34)).

There are however more reasons why the two-equation turbulence model fails to predict the proper heat transfer distribution in the stagnation region. The production term $-\overline{u_i' u_j'} \frac{\partial u_i}{\partial x_j}$ in the turbulent kinetic energy equation is modelled by equation (2.83), i.e. in expanded form for two-dimensional flow

$$\tilde{P} = -\overline{u_i' u_j'} \frac{\partial u_i}{\partial x_j} = \nu_t \left(\frac{\partial u_1}{\partial x_2} + \frac{\partial u_2}{\partial x_1}\right)^2 + 2\nu_t \left(\left(\frac{\partial u_1}{\partial x_1}\right)^2 + \left(\frac{\partial u_2}{\partial x_2}\right)^2\right) \qquad (2.124)$$

(i) (ii)

Comparison of (2.124) with the unmodelled expansion of the production term $\tilde{P}$,

$$\tilde{P} = -\overline{u_i' u_j'} \frac{\partial u_i}{\partial x_j} = -\overline{u_1' u_2'}\left(\frac{\partial u_1}{\partial x_2} + \frac{\partial u_2}{\partial x_1}\right) - \overline{u_1'^2} \frac{\partial u_1}{\partial x_1} - \overline{u_2'^2} \frac{\partial u_2}{\partial x_2} \qquad (2.125)$$

(i) (ii)

shows the origin of modelled terms (i) and (ii) in equation (2.124). In thin shear flow the unmodelled term (i) is dominant. However in the stagnation region of a two-dimensional impinging jet, the second term of equation (2.125) is dominant because $\frac{\partial u_1}{\partial x_1} \approx -\frac{\partial u_2}{\partial x_2}$. Consequently the production term $\tilde{P}$ given in equation (2.125) is quite well approximated by

$$-\overline{u_i' u_j'} \frac{\partial u_i}{\partial x_j} \approx \frac{\partial u_2}{\partial x_2} (\overline{u_1'^2} - \overline{u_2'^2}) \qquad (2.126)$$

in the stagnation region of an impinging jet, and exactly true at the axis of symmetry (Gutmark et al. (54)). In the derivation of equation (2.124), the generalized turbulent viscosity concept in the form of equation (2.76) is used. Isotropy of the turbulent kinetic energy, i.e. $\overline{u_1'^2} = \overline{u_2'^2} = \overline{u_3'^2} = \frac{2}{3} k$, is implicit in this form. Therefore comparison of equation (2.126) with modelled term (ii) suggests that the second term of equation (2.124) should be written as

$$2\nu_t \left(\frac{\partial u_1}{\partial x_1}\left|\frac{\partial u_1}{\partial x_1}\right| + \frac{\partial u_2}{\partial x_2}\left|\frac{\partial u_2}{\partial x_2}\right|\right)$$

which is close or equal to zero, as equation (2.126) would be in case of isotropy of the turbulent kinetic energy.*

However, isotropy of the turbulent kinetic energy does not exist on the axis of symmetry in the stagnation region of an impinging slot jet ($\overline{u_2'^2} > \overline{u_1'^2}$), as has been found experimentally by Gutmark et al. (54), and equation (2.126) gives a sizable contribution to the turbulent energy balance in the stagnation region. As a consequence, the generalized turbulent viscosity concept as given by equation (2.76) cannot be expected to give a proper modelling of the turbulent flow in any stagnation region. So, although the overall flow pattern in the stagnation region is well-predicted by TEACH-T, the heat and momentum transfer at the impingement wall are not, because these transfer rates depend strongly on the kinetic energy at the near-wall gridline. Before resorting to complete Reynolds stress modelling, it seems worthwhile to try the "algebraic stress modelling" (Launder (82)) for $\overline{u_1'u_2'}$, $\overline{u_1'^2}$ and $\overline{u_2'^2}$, i.e. equation (2.101) and similar equations for $\overline{u_1'^2}$ and $\overline{u_2'^2}$.

Another aspect which should be investigated is whether the modelling of term $\frac{\partial}{\partial x_k}\left(-\overline{u_i'k} - \frac{\overline{pu_i'}}{\rho}\right)$ in equation (2.82) for the

---

* This basic error has been pointed out to the writer by Ir. Th.H. van der Meer, working at the department of "Technische Natuurkunde" Technical University of Delft, the Netherlands. Ir. van der Meer experienced comparable problems with prediction of the heat transfer distribution under an impinging round jet, using a similar computer program as TEACH-T called CHAMPION (obtained from Professor Spalding of Imperial College). His numerical investigation with different forms of term (ii) of equation (2.124) will be published in the near future.

turbulent kinetic energy by $\frac{\partial}{\partial x_k}\left(\frac{\nu_t}{\sigma_k}\frac{\partial k}{\partial x_k}\right)$ is adequate because it has been shown by Gutmark et al. (54) that on the axis of symmetry of an impinging slot jet near the impingement plate, the pressure-diffusion term $\frac{\partial}{\partial x_k}\left(-\frac{\overline{pu_i}}{\rho}\right)$ is one of the dominant terms in the turbulent kinetic energy balance. The turbulent diffusion term $\frac{\partial(\overline{u_i k})}{\partial x_k}$ was shown to be negligible.

2.3.3.3 Effect of Re_j and H/w on the Heat Transfer Distribution

Before presenting the heat transfer distributions for the remaining four cases given in Table 2.8, some computed velocity distribution results for H/w = 6 will be compared with experimental measurements for partially similar flow configurations because unfortunately there are no flow measurements for a confined impinging slot jet. Shown in Figure 2.57 is the development of the non-dimensional maximum wall jet velocity for H/w = 6 at jet Reynolds numbers of 5200 and 8100. The computed development is compared with experimental results obtained by Kumada and Mabuchi (79) for an unconfined slot jet impinging on a flat plate, and by Baines and Keffer (9) for an unconfined slot jet impinging on a cylinder of diameter 320.5w. Contrary to the behaviour for H/w = 2.6 in Figure 2.52, the present numerical results are intermediate between the experiments. This difference is not unexpected since the retarding effect of the confinement plate is not felt as close to the stagnation point at H/w = 6.0 as at H/w = 2.6, and the numerical results are in reasonable agreement with the data of Kumada and Mabuchi out to

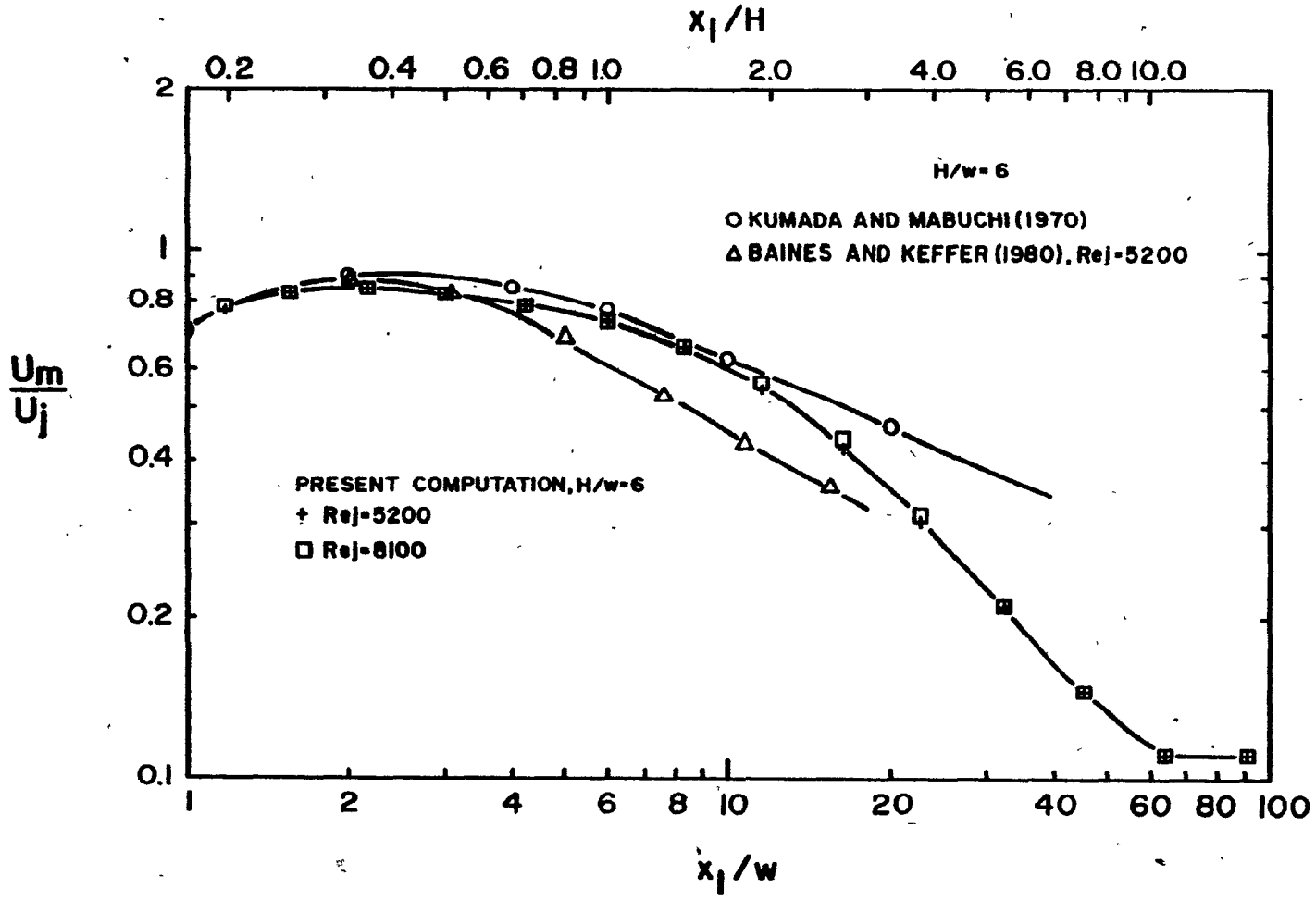


FIGURE 2.57. Development of the maximum wall jet velocity for H/w = 6

approximately $x_1 = 10w = 1.67H$. The rather fast decrease of the maximum wall jet velocity measured by Baines and Keffer is probably due to increased wall jet spreading as a result of impingement surface curvature. As can be seen in Figure 2.58 the spreading rate of the nondimensional half-width $\delta_{\frac{1}{2}}/w$ of the free jet layer of the wall jet obtained by Baines and Keffer is indeed larger than the spreading rate obtained numerically.

Finally in Figure 2.59 the numerically obtained velocity distribution between flat impingement and confinement surfaces for $Re_j = 8100$ and 5200 is compared with that for cylindrical surfaces measured in the SIMTEST apparatus at almost the same distance from the symmetry plane but at a much larger Reynolds number of $Re_j = 32900$. Only positive experimental values of velocity are given here because the measurements were made with a pitot tube. The finding that the experimental wall jet velocities are larger than those computed is rather surprising as the curvature effect is expected to lead to a faster decrease in wall jet velocity. However, the values of Re_j are far from matched between the two cases. It is apparent that detailed flow and turbulence measurements for the confined slot jet impinging on a flat surface at relative close nozzle spacings are required for a proper evaluation of the predictive capability of the TEACH-T program for this type of flow.

The heat transfer distributions along the impingement surface for the remaining four cases given in Table 2.8 are presented in Figures 2.60 to 2.63. Shown in Figure 2.60 is the computed heat transfer distribution for $H/w = 2.6$ and $Re_j =$

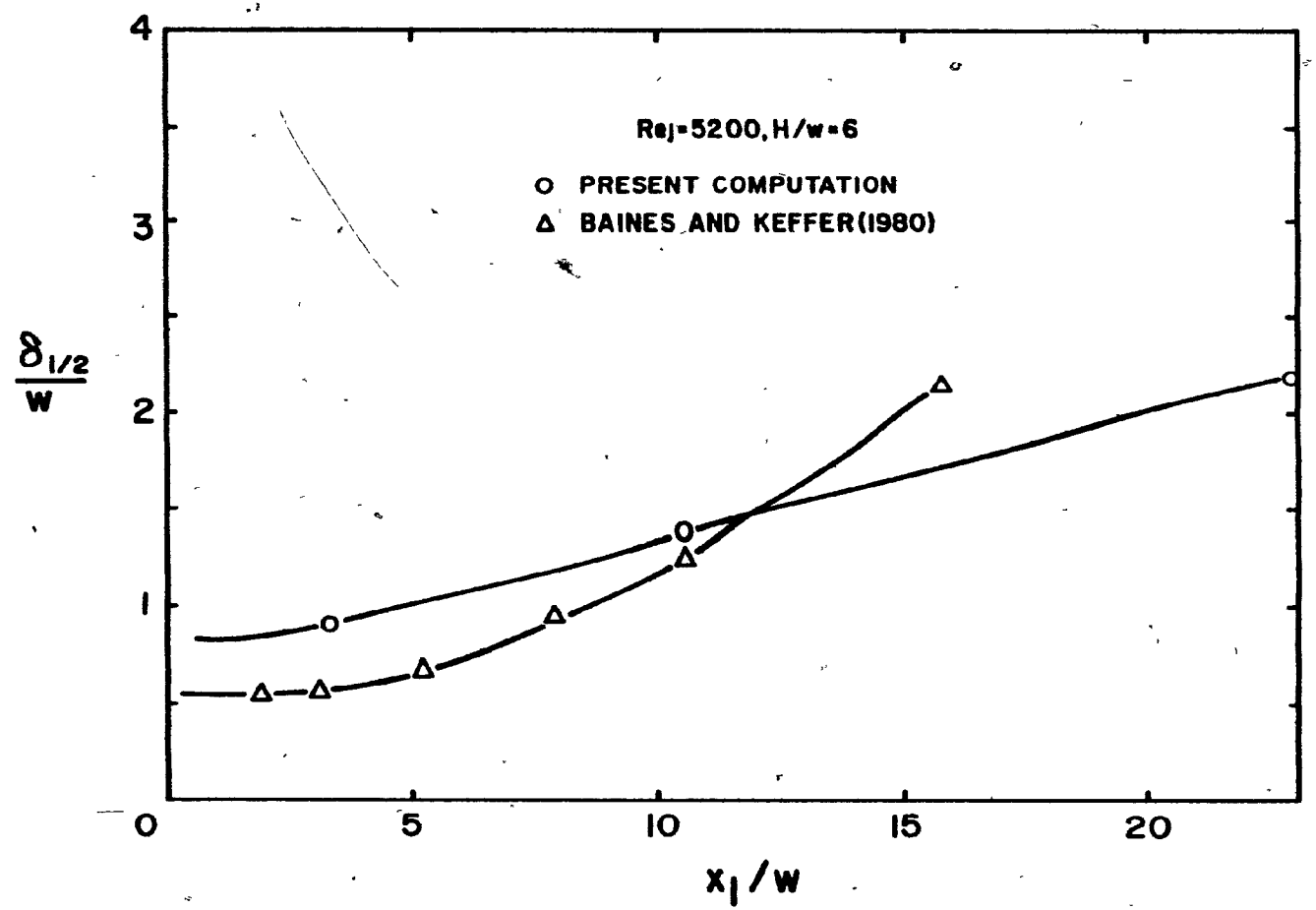


FIGURE 2.58. Spreading of the wall jet half-width

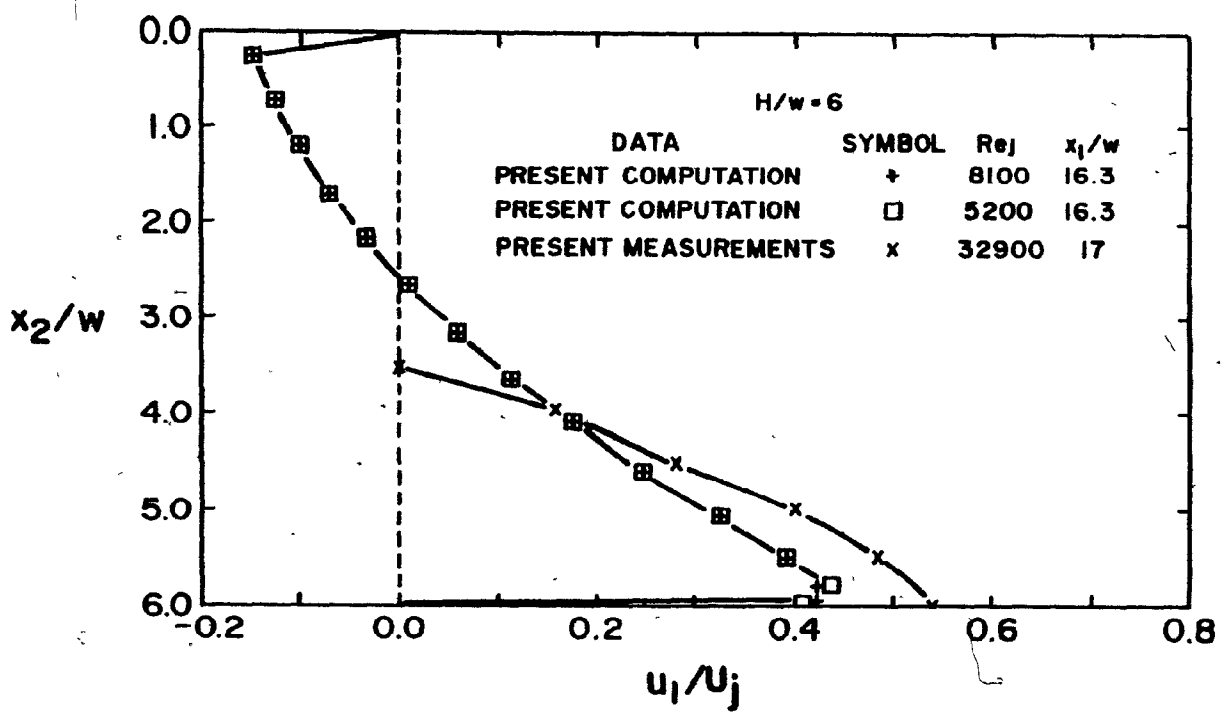


FIGURE 2.59. Velocity distribution in the wall jet region

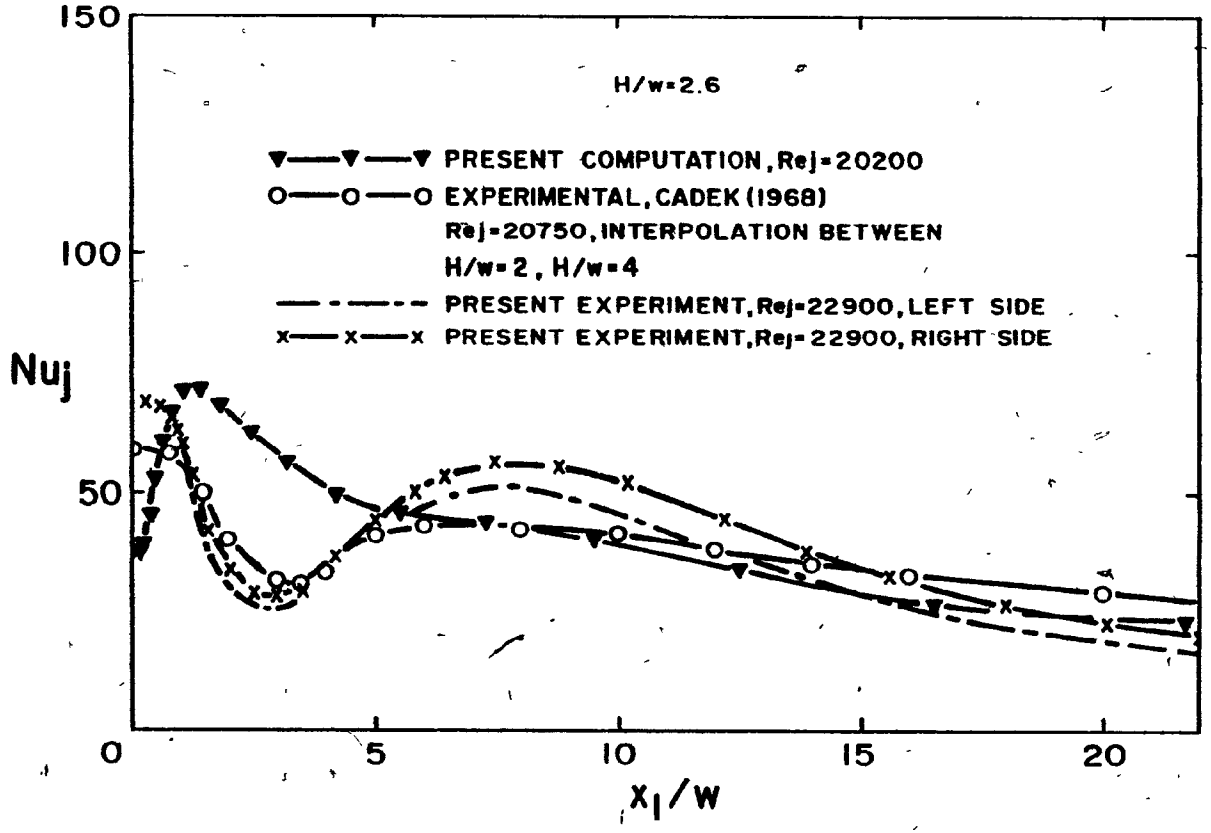


FIGURE 2.60. Heat transfer distribution along the impingement surface for H/w = 2.6 and Re_j = 20200

20200, i.e. at almost twice the Reynolds number in Figure 2.56. All the near-wall grid points are in the "turbulent" region of the boundary layer (y^+_{ns} > 11.63) with the exception of the first two from the axis of symmetry. The general features of Figure 2.60 and the significant discrepancies between predicted and measured heat transfer in the impingement region are as noted already in connection with Figure 2.56. In the wall jet region the agreement between the present computation and the measurements of Cadek (26) for an unconfined jet on a flat surface is reasonable. It would be expected that the lack of a confinement surface in his case would lead to somewhat higher heat transfer in the wall jet region, as is seen on Figure 2.60. Also displayed in Figure 2.60 are the heat transfer distributions obtained for a confined jet with a cylindrical impingement surface with the SIMTEST apparatus (Section 4.3) on both sides of the stagnation point, the notation used for the two sides as already described for Figure 2.56, Section 2.3.3.1.

At the larger nozzle-to-impingement spacing of H/w = 6 portrayed on Figure 2.61, agreement between the experimental heat transfer distribution of Cadek and the present computation appears quite good for x_1/w > 2. At the stagnation point however, the numerical method predicts a minimum instead of a maximum for the reasons already cited, i.e. poor wall boundary conditions for a turbulent boundary layer with a strong favourable pressure gradients, and a "wrong" modelling of that part of the generation term (equation (2.83)) in the turbulent kinetic energy equation which becomes dominant in stagnation flow.

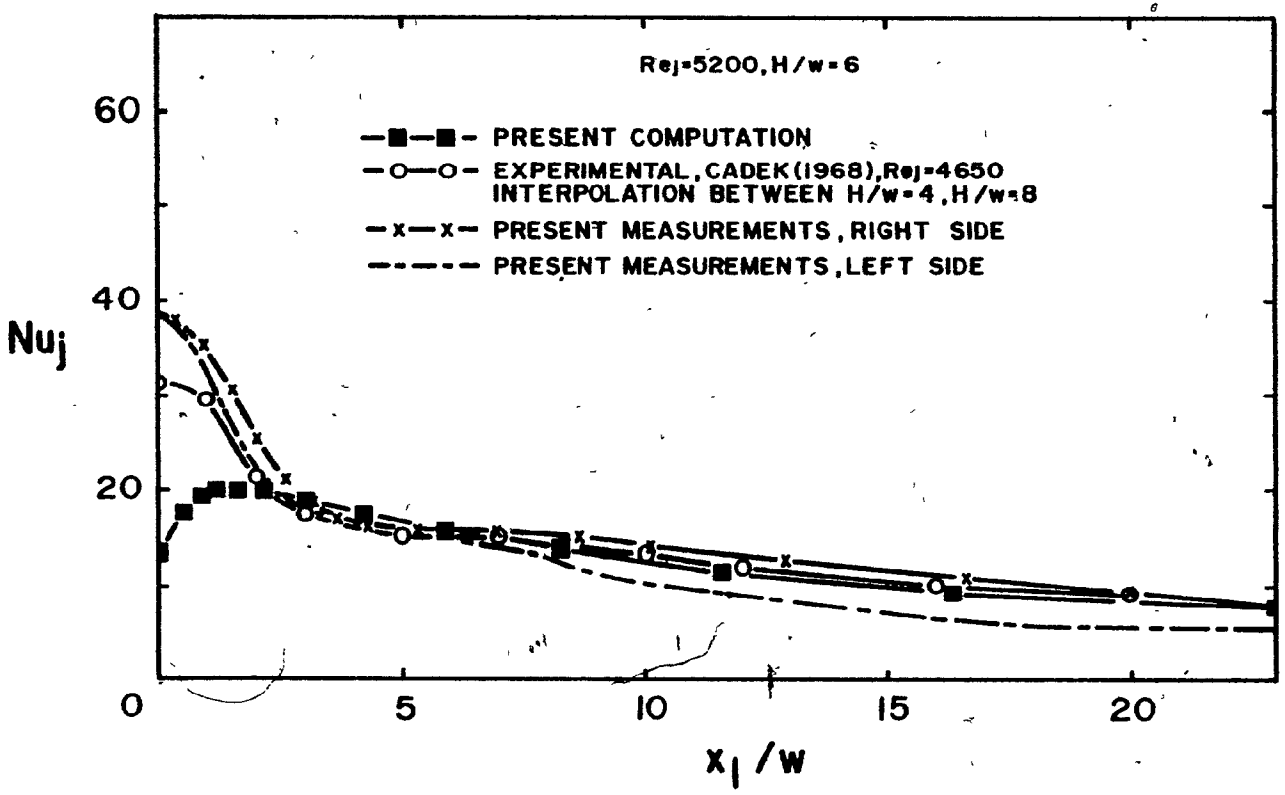


FIGURE 2.61. Heat transfer distribution along the impingement surface for H/w = 6 and Re_j = 5200

For the same spacing, $H/w = 6$, but the higher Re_j, 8100, of Figure 2.62 the secondary heat transfer peak reappears at $x_1 \approx 7w \approx 1.17H$, and the prediction remains poor in the impingement region. For the parameters chosen for Figure 2.63, $Re_j = 20750$ and $H/w = 8$, there are two sets of experimental results, Cadek (26) and Saad (125), and one computational prediction, Wolfshtein (153), available for comparison with the present computed results. The confined flow configuration of Saad (125) is exactly the same as that of the present computations except for a small difference in lateral extent of the impingement system which for Saad extended to $x_1/w = 16$, i.e. $S/H = 2$, slightly smaller than for the present computational case which extended to $x_1/w = 20$, i.e. $S/H = 2.5$. Agreement between the present computed heat transfer distribution and the experimental distributions is again quite good in the wall jet region, poor near stagnation. The discrepancies are clearly greater for the computational results of Wolfshtein who used a one-equation turbulence model (Section 2.3). This figure indicates the extent of improvement in quality of the prediction with the present two-equation model relative to the one-equation model, although both models fail to predict the proper distribution in the stagnation region. The reason for the predicted bell-shaped heat transfer distribution for $H/w = 6$ by Folayan (41) who also used a two-equation model is most probably because of the high level of turbulence in the fully developed jet at the nozzle exit in that case.

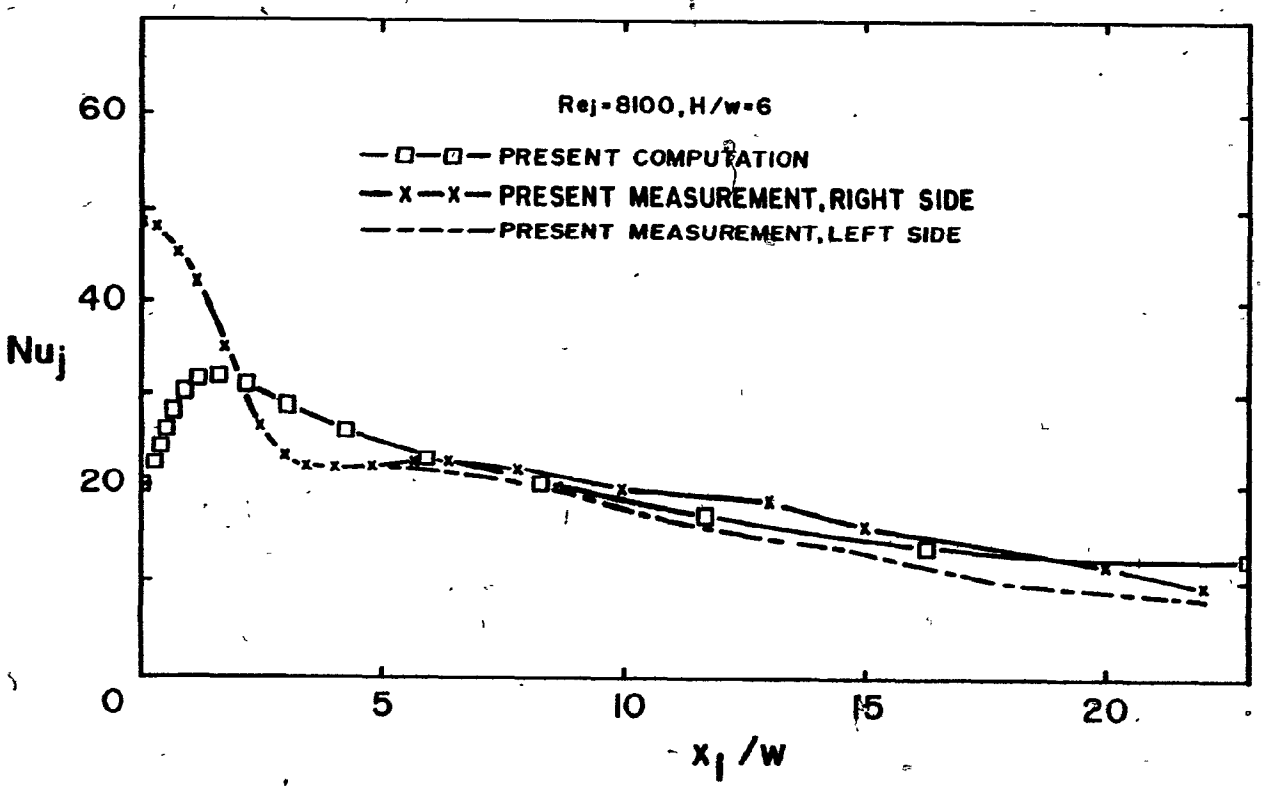


FIGURE 2.62. Heat transfer distribution along the impingement surface for H/w = 6 and Re_j = 8100

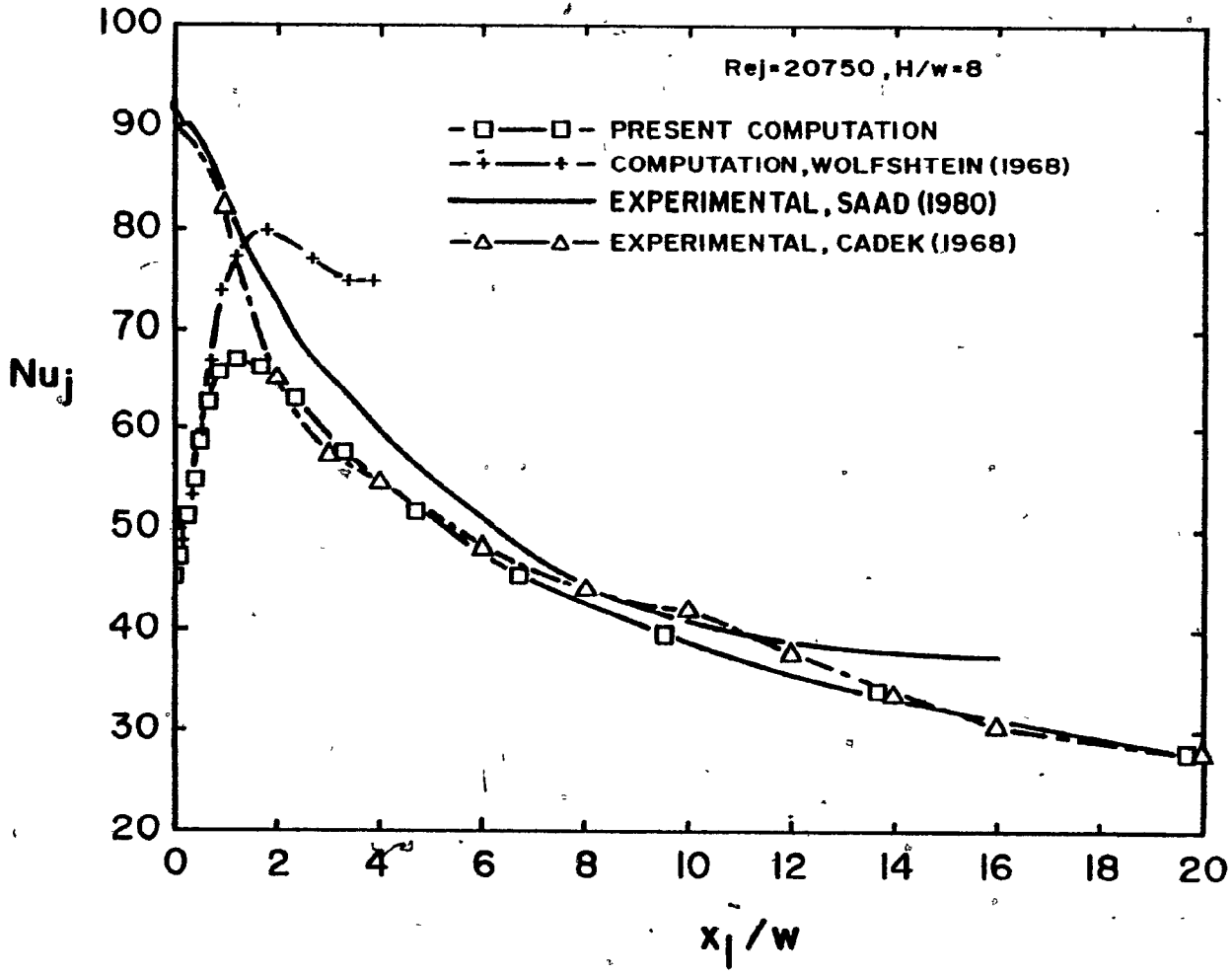


FIGURE 2.63. Heat transfer distribution along the impingement surface for H/w = 8 and Re_j = 20750

2.4 Summary and Conclusions

The enormous amount of experimental work that would be required to obtain a thorough understanding of all the parameters affecting flow and heat transfer under impinging jets and to provide the basic performance characteristics for the full range of parameters of industrial interest provides a strong incentive for development of a reliable theoretical basis of calculation. The first part of the study reported in this chapter documents the validation of such a theoretical framework for laminar impinging slot jets by means of solution of the full equations of motion and thermal energy by an accurate and stable numerical procedure. The starting point was the computational program of Gosman et al. (49), which was developed for the case of a confined laminar slot jet. The specific configuration used was that of a confined jet, a case of more importance industrially than the more frequently studied unconfined jet. The scope of the theoretical framework was extended to incorporate the industrially significant parameter of throughflow at the impingement surface.

Following Gosman et al. the equations of motion and thermal energy are transformed into their stream function-vorticity form and the resulting set of partial differential equations are cast into a general differential equation. A general finite difference equation (F.D.E.) is obtained by integrating the general partial differential equation over a small control volume. Depending on the approximation of the integrals of the convection terms, three alternate formulations of the F.D.E. are ob-

tained. In the central difference scheme, the convective contribution of the dependent variable at a grid node is equally determined by the value of the variable at the surrounding grid nodes. In the so-called "upwind" scheme, however, the convective contribution is determined solely by the value of the variable upstream of this grid node. The "hybrid" scheme is equivalent to the central difference scheme when the convective contribution is smaller than the diffusive contribution but in the reverse situation is equivalent to the "upwind" scheme with the diffusive contribution neglected. Application of the F.D.E. for all variables at all inner grid point, together with the boundary conditions, leads to a converged solution in an iterative procedure.

Several factors influencing the convergence properties and accuracy of the vorticity-stream function program were investigated in great detail: Factors affecting the stability of the procedure which were investigated are: the grid distribution, finite difference scheme, underrelaxation, scanning procedures, specification of the boundary condition at the outflow boundary and the matrix inversion technique.

The influence of grid distribution on stability was investigated because of the difficulty of obtaining a converged solution with very elongated grid cells in the flow region close to the outflow boundary. These elongated grid cells resulted from the attempt to include the extensive recirculation area so as to have only outflow at the outflow boundary but without correspondingly having an unrealistically large number of gridlines in the

x_1-direction. Experience established that the computational procedure had less difficulty with an incompletely defined, inflow-outflow condition at the outflow boundary than with elongated grid cells of high aspect ratio. The qualitative explanation for the numerical instability encountered with high aspect ratio grid cells is that vorticity and stream function at P (Figure 2.1) are almost solely dependent on vorticity and stream function at N, S and P, allowing an error in the center of the flow field to propagate or even amplify in the direction of the walls. The error in vorticity is not corrected at the wall boundaries because of the gradient-type of boundary condition for wall vorticity. This instability problem increased with increasing Re_j and H/w.

The alternate finite difference schemes and choice of underrelaxation factor for vorticity and stream function scarcely influenced the stability of the procedure. Although the "upwind" scheme was slightly more stable and faster than the hybrid scheme, the latter was used for reasons of higher accuracy.

The stability of the numerical procedure was also improved by applying the F.D.E. for all variables successively at one grid point before going to next grid point, instead of scanning all the grid points for one variable before starting with the next variable. A further improvement was obtained when the direction of the main flow was followed in the scanning procedure. In agreement with Roache (117) it was found that the most restrictive specification of the boundary condition at the outflow boundary and not necessarily the most realistic boundary condi-

tion led to an improvement of the convergence properties of the numerical solution.

Finally, the influence of three matrix inversion techniques on the convergence properties of the program were investigated. The three techniques are: the simple Gauss-Seidel point iteration technique, the well-known tridiagonal matrix algorithm (T.M.A.) and the so-called bi-tridiagonal matrix algorithm (B.T.M.A.) given by Von Rosenberg (151). In the first technique the values of the dependent variable are used as soon as they become available, while in the other two block methods the vorticity and stream function are updated successively or simultaneously along gridlines perpendicular to the impingement surface using respectively the T.M.A. or B.T.M.A. The last two algorithms were first tried for the similar stagnation flow. The T.M.A. was unstable because of the lag between the development of the vorticity and stream function field and the strong linkage between these variables especially at the wall via the no-slip boundary condition. The numerical procedure became stable when the main fraction of the lag between the vorticity and stream function was removed by application of the B.T.M.A. An important improvement with the application of the B.T.M.A. was that the number of iterations required to get a solution for plane stagnation flow is an order of magnitude lower than with the Gauss-Seidel point iteration technique. Unfortunately the B.T.M.A. led to an oscillating procedure without convergence for the impinging jet case. As no cure could be found for the instability, the Gauss-Seidel technique was used in all further work.

The factors affecting accuracy of the procedure which were investigated in detail are: the finite difference scheme, treatment of vorticity at the corner of the nozzle and finally, boundary conditions at the outflow boundary.

The hybrid scheme is more accurate than the upwind scheme because the hybrid scheme reduces to the second order accurate central difference scheme when conditions are such that the central difference scheme is stable, while the first order accurate upwind scheme is adopted with the diffusion term in the same flow direction being dropped when the local grid cell Peclet number is larger than 2, as the latter condition would lead to an unstable procedure if central differences were used (Runchal (122)). The diffusion term is neglected when the local grid cell Pe > 2 because it was shown that the diffusion term was already more than accounted for via a numerical error called artificial viscosity, inherent to the upwind scheme (Roache (117)). Another error inherent to the present upwind difference scheme (classified by Roache (117) as the second upwind difference scheme) is identified as "artificial velocity". While the effect of artificial viscosity is to increase the effective numerical viscosity in the flow field, the effect of artificial velocity is to increase the local streamwise velocity.

This last effect is used to explain the higher heat transfer rates in the stagnation region obtained with the upwind scheme compared with the hybrid scheme. The higher accuracy of the hybrid scheme, especially for the heat transfer, was shown for plane stagnation flow as well as for the laminar impinging

slot jet. The differences between results obtained with the upwind and hybrid scheme are however not very large because the diffusion term is generally much smaller than the convective contribution in the regions where the upwind form of the hybrid scheme is used, while the numerical errors related to the upwind scheme are generally much smaller in regions where the central difference form of the hybrid scheme is used. The only flow situation where both numerical schemes lead to significant numerical errors is when the flow direction is at an angle to the grid and has strong crossflow velocity gradients. The numerical error for the vorticity F.D.E. in the curved jet mixing layer, which is such a flow region, is reduced by the choice of a relatively fine grid at this location.

The numerical treatment of the vorticity at the corner of the nozzle had a pronounced effect on the accuracy of the solution depending on the velocity profile at the nozzle. The two cases tested are: a fixed value for the corner vorticity, meaning that the corner is considered as a part of the nozzle, or determination of the vorticity with equation (2.22) considering the corner as a part of the confinement plate. The differences in results between the two treatments are small for a parabolic velocity profile and pronounced for a flat profile at the nozzle exit. From the streamline separation angle at the corner and the velocity distribution in the jet mixing layer it is concluded that application of equation (2.22) for the vorticity at the corner leads to a more realistic spreading behaviour of the jet, and this procedure is used throughout the rest of the

numerical work with the vorticity stream function program. It should be mentioned, however, that the problems with corner vorticity are eliminated when primitive variables are used in the numerical scheme, with a staggered grid for the vector variables (velocities) and scalar variables (pressure, viscosity, etc.), as was shown by Huang (63) for a laminar, round, swirling impinging jet.

It was established that the flow field in the recirculation region was strongly affected by the type of conditions at outflow Boundary III when inflow existed near the confinement plate at this boundary. Elimination of the inflow by completely covering the recirculation area with a grid mesh required either too many gridlines or destabilized the numerical procedure. Fortunately it was established that the flow and heat transfer in the regions of interest, the impingement and wall jet region, were hardly influenced by the boundary condition specification with inflow at that boundary.

Parameters studied which affect the flow and heat transfer characteristics of a confined laminar impinging slot jet are: Reynolds number, Re_j, jet velocity profile at the nozzle, non-dimensional nozzle-to-impingement surface spacing, H/w, Prandtl number, Pr, throughflow at the impingement surface, U_s/U_j, and temperature dependence of physical properties. Analysis of the influence of Re_j and nozzle exit velocity profile is combined because the effect of increasing Reynolds number is to increase momentum and decrease spreading of the jet before impact, similar to the effect of changing nozzle exit velocity profile from

flat to parabolic. Velocity and temperature gradients at the impingement surface are thereby increased and the thermal and viscous boundary layer thickness decreased with either increasing Re_j from 100 to 950 or changing to a sharper velocity profile at the nozzle exit. Comparison of the present boundary layer velocity profiles in the impingement region with theoretical solutions of Sparrow and Lee (138) and Miyazaki and Silberman (97) for respectively a parabolic and flat velocity profile jet (both based on boundary layer solutions with a free stream boundary condition obtained from inviscid flow analysis) shows a close agreement with increasing Re_j or decreasing influence of viscosity. Also, it is interesting to note that for a flat nozzle exit velocity profile the relatively large differences between the present velocity profiles for Reynolds numbers 100 and those for values of 450 and 950 are in agreement with the classification of McNaughton and Sinclair (92) for a round laminar jet. They termed a laminar jet of $Re_j < 300$ a "dissipated laminar jet" and a jet of $300 < Re < 1000$, a "fully laminar jet".

Use of $\frac{C_f}{2}\sqrt{Re_j}$ and $Nu_j/\sqrt{Re_j}$ for nondimensional representation of shear stress and heat transfer at the impingement surface is typical for laminar flow and allows comparison with theoretical studies noted above of Sparrow and Lee and Miyazaki and Silberman. Over the Reynolds number range covered and for both nozzle exit profiles used, the bell-shaped heat transfer distributions $Nu_j/\sqrt{Re_j}$ with a stagnation point maximum, display limited differences from distributions obtained in the theoretical

studies cited. An apparent small off-stagnation maximum for a flat velocity profile is related to a numerical error inherent to the upwind differencing. The lower the Reynolds number, the greater is the overprediction by previous theoretical studies. The reasons why Re_j remains a parameter even when results are expressed as $Nu_j/\sqrt{Re_j}$ or $\frac{C_f}{2}\sqrt{Re_j}$ were noted above. Agreement with the interpolated experimental results of Sparrow and Wong (139) for a parabolic profile is excellent.

Comparison of computed stagnation heat transfer with computed velocity gradient in the stagnation region proves that the stagnation heat transfer results are internally consistent, and therefore also lower than the theoretical results of Sparrow and Lee (138) and Miyazaki and Silberman (97). The ratio of computed stagnation heat transfer for a parabolic nozzle exit profile relative to that for a flat profile was found to be Reynolds number dependent, increasing from 1.5 at $Re_j = 100$ to 1.9 at $Re_j = 950$. The value predicted by Sparrow and Lee (138) for this ratio was almost two. The skin friction results clearly show that the simple Reynolds analogy, $St = \frac{C_f}{2}$, is not valid in the stagnation region, a fact which has on occasion been ignored in previous work. Over the full range of Re_j investigated, maximum skin friction is located at 1w and 0.5w from the stagnation point for respectively flat and parabolic velocity profiles at the nozzle.

The excellent agreement between the heat transfer distribution of Gardon and Akfirat (45) and the present numerical results, both obtained with the same velocity profile at nozzle,

a profile intermediate between flat and parabolic, further confirms the accuracy of the present numerical solution and the high sensitivity to velocity profile at the nozzle exit.

The computed profiles for decay in centerline axial velocity for flat nozzle exit velocity profiles requires comment. The rather steep decrease immediately after the nozzle exit is physically unrealistic as it is well-known that there is a potential core region immediately downstream of the nozzle exit in which velocity remains constant. The erroneous computed decrease in axial velocity derives from the particular treatment of corner vorticity. The resulting underprediction of the stagnation heat transfer is estimated at about 5 to 10%. This effect is scarcely present when the nozzle exit velocity profile is parabolic.

The effect of the nondimensional impingement surface spacing, H/w, was investigated for Re_j = 450 and a flat velocity profile for spacings of 4w, 8w and 12w. It was impossible to obtain a converged solution for H/w = 16 because of the instability generated by the elongated grid cells near the outflow region, as noted earlier. Centerline axial velocity decay profiles are similar in the impingement region and indicate that this region extends 3w from the impingement surface for a flat nozzle exit velocity profile, somewhat larger than the value of about 2w obtained by Miyazaki and Silberman (97) in their theoretical analysis. The result by the present method of numerical prediction should be more accurate due to a more realistic treatment of the effect of viscosity. The finding that, at 2.5w

from an impingement surface for the spacing H/w = 12, the effect of viscosity has just penetrated to the axis of symmetry is in agreement with theoretical "plane half-jet" solution of Schlichting (131). The related fact that for jets with flat nozzle exit profiles the jet with the sharpest velocity profile on impact is for the largest spacing, H/w = 12, explains the otherwise anomalous finding of a slightly higher stagnation heat transfer for this spacing than at H/w = 8. In fact, for laminar jets of flat velocity profile at the nozzle exit, the effect of differences between the heat transfer distribution impingement surface spacing, H/w, is almost negligible over the entire region out to 12w from stagnation. This behaviour is directly associated with the flat velocity profile.

The effect of throughflow at the impingement surface was studied for Re_j = 100, H/w = 4 and a parabolic velocity profile at the nozzle exit. The ratios of throughflow U_s/U_j investigated were -0.01, +0.01 and 0.025, the negative sign indicating blowing from the surface. The influence of throughflow on jet axial velocity is not felt until the beginning of the stagnation region, in agreement with the numerical predictions of Saad (124) and Huang (63) for a round impinging jet. Therefore the reported effects of throughflow on the measured axial velocity outside the impingement region reported by Obot (105) and Abdul-Wahab (1) for a turbulent impinging slot jet may reflect measurement difficulties. As expected, the location of the maximum in lateral velocity is shifted towards the impingement surface with throughflow and vice versa with blowing. However the mag-

nitude of this maximum lateral velocity is scarcely influenced by throughflow, even when 60% of the jet flow has been removed through the plate.

The influence of a normal flux at the impingement surface is to increase heat transfer and skin friction with throughflow and conversely with blowing. The change in skin friction increases rapidly from zero at the stagnation point to a very significant effect at the lateral position where U_m reaches its maximum, thereafter remaining roughly independent of lateral position out to about 1.5H or 6w from stagnation. The change in convective heat transfer at the impingement surface as a result of throughflow is similar to that for skin friction except that the approximately constant change in heat transfer now begins directly at the stagnation point.

It was found that the changes in heat transfer as a result of throughflow are reasonably well-described by the Couette flow model of Mickley et al. (96) and Spalding (136), based on a boundary layer thickness and free stream velocity uninfluenced by throughflow. As the absolute amount of change in heat transfer as a result of throughflow is essentially independent of lateral position and as, at small values of $M_{U_s}/St_{M_{U_s}=0}$, the Couette flow model predicts a change in Stanton number equal to half the fractional mass throughflow ratio, $M_{U_s} = \frac{\rho_s U_s}{\rho_j U_j}$, it follows that the change in heat transfer may be expressed in the form $(St - St_{M_{U_s}=0})/M_{U_s}$. The increase in St at the stagnation point and for a large part of the wall jet region is correlated with an error less than 10% by

$$St - St_{M_{U_s}=0} = 0.58\ M_{U_s} \qquad (2.63)$$

Over a large part of the permeable impingement surface (up to 50% of the jet flow removed) equation (2.63) is in reasonable agreement with the reanalyzed numerical predictions of Saad (125) and Huang (63) for laminar round impinging jets respectively without and with swirl.

Since the increase in St as a result of throughflow, equation (2.63), is independent of the fraction, f, of the jet flow removed through the impingement surface, the average increase in St can reasonably be estimated by

$$\overline{St} - \overline{St}_{M_{U_s}=0} = 0.58\ M_{U_s} \qquad (2.64)$$

By comparison, the equation based simply on a linear combination of the heat transfer contributions of throughflow and impingement that has been given by Crotogino and Allenger (35)

$$\overline{St} - \overline{St}_{M_{U_s}=0} = (1 - 2\frac{S}{H}\frac{H}{w}\overline{St}_{M_{U_s}=0})M_{U_s} \qquad (2.65)$$

would lead to an underestimation of the increase in heat transfer by 15-20%.

The effect of throughflow on drying rates in a mill-trial "Papridryer" have been measured by Burgess et al. (23, 24). When the ability of the two approaches noted above to predict these measured rates was tested it was found that the present

approach (equation (2.64)) gave a better prediction of these results on industrial scale equipment than did that of Crotogino and Allenger, re-expressed here as equation (2.65).

The influence of variable physical properties was studied for $Re_j = 100$, $H/w = 5$ and a parabolic profile at the nozzle exit. The temperatures of the jet were 300, 450 and 600 K, while the impingement surface was kept at 300 K. The effect change in velocity and temperature gradients at the impingement surface with higher jet temperatures could be treated by expressing these gradients in the form of respectively $C_f/2$ and St, with physical properties evaluated at the jet temperature. This procedure is in agreement with the theoretical analysis given in Kays (73). The same effect can also be obtained by using physical properties at the so-called "film" temperature $(T_j + T_s)/2$, but this method requires jet Reynolds number also to be calculated for physical properties at the film temperature.

Another significant finding is that $M_{U_s} = \frac{\rho_s U_s}{\rho_j U_j}$ and not $U_s^* = \frac{U_s}{U_j}$ determines the increase in heat transfer as a result of throughflow. The difference between U_s^* and M_{U_s} becomes increasingly important at higher values of ΔT, i.e. $|T_j - T_s|$.

The influence of Prandtl number was studied for $Re_j = 100$, $H/w = 4$ and a parabolic profile at the nozzle, with values for Pr of 0.73, 2.5 and 7.0. The influence is the same as for the theoretical studies on a round and two-dimensional impinging jet by respectively Sparrow and Lee (138) and Miyazaki and Silberman (97), whereby heat transfer is found to be proportional to $(Pr)^n$ with $n = 0.373$. The same result derives also from the

theoretical analysis of Sibulkin (135) for heat transfer near the forward stagnation point of a body of revolution, where a value of $n = 0.40$ is recommended. The differences are caused by the region of Pr used for the correlation, since it can be derived, (Schlichting (131), that this relationship follows the association $1/2 < n < 1/3$ for $0 < Pr < \infty$. From these results it was concluded that the mass transfer data obtained by the naphthalene sublimation technique are best converted to heat transfer by taking the transfer rate proportional to $Pr^{0.373}$, while the data obtained by the water evaporation technique are better converted to heat transfer by a proportionality to $Pr^{0.40}$.

In conclusion it can be stated that the present vorticity-stream function program generally performed well in predicting the effects on flow and heat transfer characteristics of a confined laminar impinging slot jet caused by Re_j, velocity profile at the nozzle exit, spacing, H/w, throughflow rate, M_{Ug}, temperature dependent physical properties and Pr. Weaknesses of the program in this special case are numerical stability problems encountered for high values of Re_j and H/w and problems related to calculation of vorticity at the corner of the jet which for the case of a flat nozzle exit velocity profile result in prediction of a small decrease of axial velocity immediately downstream of the nozzle exit which does not in fact occur. Both problems could be eliminated by using a numerical program whereby the equations of motion and thermal energy are solved in their primitive form and a staggered grid is used for respectively the vector and scalar variables as was done by Huang (63)

for a confined round laminar impinging jet with swirl. The same program, with extra equations describing the turbulence properties, has been used for the confined impinging turbulent slot jet described next.

The crucial additional requirement for numerical calculation of the flow and temperature field of a confined impinging slot jet which is turbulent rather than laminar is proper mathematical specification of the extra turbulent transport terms in the time-averaged equations of motion and thermal energy. With this specification a closed set of equations is obtained as an approximation of the real turbulent flow. An existing numerical program of the Imperial College group, London, was adapted to the calculation of the turbulent impinging jet system. For reasons of the difficulty of obtaining an accurate prediction for impingement on a flat, stationary impingement surface, the system used for the numerical study did not include the additional complications of impingement surface motion, throughflow, and a curved impingement surface, features in the experimental aspect of the present study. Thus, as only the influence of Re_j and H/w are investigated numerically, these results for the turbulent jet are presented simply as a first step towards the very complex challenge of simulating flow and heat transfer for an impingement system as complicated as the experimental set-up described in Chapter 3.

The turbulent transport terms are incorporated via the concept of a turbulent viscosity and, by extension, a thermal conductivity via a constant turbulent Prandtl number. The turbu-

lent viscosity is evaluated algebraically from the turbulent kinetic energy, k, and the dissipation rate of turbulent kinetic energy, ε, both described by a partial differential transport equation. This turbulence model is called the two-equation k-ε model of turbulence. The k-ε model was originally developed from the Prandtl mixing length theory by replacing the mixing length and the velocity of turbulent blobs of fluid by respectively transport equations for ε and k. Thus the k-ε model was designed to take account of the transport of turbulence while eliminating the problem of specification of the mixing length.

Later, Launder (82) and Rodi (120) have shown that for two-dimensional thin shear flow the turbulent viscosity concept, with k and ε specifying the turbulent viscosity, can be derived from the exact transport equations of the turbulent transport terms by making modest simplifications including the assumption of "local equilibrium", i.e. production of turbulence kinetic energy, $\tilde{P}$, equal to ε. Without the assumption of "local equilibrium" the transport equations for the turbulent stresses can be reduced to algebraic equations relating the stresses ($\overline{u_1'^2}$, $\overline{u_2'^2}$ and $\overline{u_1'u_2'}$) to k, ε, $\tilde{P}$ and velocity gradients. Turbulence models based on these equations are called "algebraic stress models". The reason given by Launder (82) for the good results obtained with the k-ε model is that generally local equilibrium exists in the flow regions where the turbulent transport terms are important (thin shear flow), while in the bulk of the flow the main forces on a fluid element are provided by gradients in static pressure.

In the finite difference program called TEACH-T the equations of motion are solved in their primitive form, i.e. with velocity and pressure as the dependent variables. The equations of motion, thermal energy, turbulence kinetic energy and dissipation rate of turbulence kinetic energy are cast into a general partial differential equation and transformed in finite difference equations by integration of a control volume, using "hybrid" differences for the convection terms, as with the laminar jet calculations. However, contrary to the vorticity-stream function program, a staggered grid is used in TEACH-T for respectively the velocities and all scalar quantities, while continuity is conserved by a so-called pressure-correction equation. Also different from the laminar jet calculations is the specification of variables in the SI system of dimensions, rather than in dimensionless form. Yet another difference is that the wall boundary conditions for temperature, streamwise velocity, k and ε are applied not at the wall but in the fully turbulent near-wall region via a wall-flux relationship. Finally the closed set of finite difference equations are solved in an iterative procedure until convergence is obtained.

The influence of the choice of laminar or turbulent wall flux laws and the effect of alternate treatments of turbulent viscosity in the k and ε diffusion and source terms was studied for $Re_j = 10400$ and $H/w = 2.6$. The choice of wall flux laws depends on whether the near-wall gridline is located in laminar or turbulent flow. With respect to the equations for k and ε, the alternatives tested were use of either effective turbulent vis-

cosity, $\mu_{eff} = \mu_t + \mu$, or just the turbulent viscosity, μ_t. From the computed distributions of pressure along the impingement surface and velocity distribution in the stagnation region it is concluded that the overall features of this internal flow and especially the flow field in the stagnation region is pressure dominated and therefore relatively insensitive to the effect of wall flux laws and use of μ_{eff} or μ_t in the diffusion and source terms of the k and ε equation, or even generally to the treatment of the turbulent stresses.

The influence of both variables are however strongly visible in the distribution of turbulence kinetic energy in the impingement region and heat transfer in the stagnation and early wall jet region. Because μ_t and μ are of the same order of magnitude in the potential core region the use of μ_{eff} instead of μ_t leads to a too rapid diffusion of turbulence kinetic energy produced in the mixing region of the jet. This in turn leads to an increased turbulence kinetic energy near the impingement surface. This effect is even further enhanced by the inaccurate determination of the dissipation of turbulence kinetic energy and the source terms in the finite difference equation for k when the near-wall gridline is in the laminar region, $y^+_{nw} < 11.63$. The resultant overestimation of k at the near-wall gridline leads finally to an overestimation of heat flux in the stagnation region. However, even with the best choice with respect to these two aspects, i.e. use of μ_t in the diffusion and source terms of the k and ε equation and use of turbulent wall flux laws, the predicted heat transfer distribution in the stagnation and

beginning of the wall jet region is poor.

Analysis of the turbulence modelling leads to four recommendations for improving the prediction of flow and heat transfer in impingement and early wall jet region which, as just noted, is not satisfactory with the present procedure.

(1) The wall flux laws for streamwise velocity and temperature should be extended to include the effect of a streamwise pressure gradient, as for example has been done by Crawford and Kays (34) for boundary layer calculations.

(2) The so-called algebraic stress modelling should replace the effective turbulent viscosity concept in order to eliminate the implicit assumption of isotropy of turbulent kinetic energy and a basically incorrect modelling of the production of turbulent kinetic energy in any stagnation region when the turbulent viscosity concept is used.

(3) It should be investigated whether the pressure diffusion term in the transport equation of k is properly modelled in TEACH-T by the diffusion-like term, since Gutmark et al. (54) have shown this term to be one of the dominant terms in the turbulent kinetic energy balance in the stagnation region.

(4) A recently published procedure (Chieng and Launder (32)) for a more accurate calculation of k and ε at the near-wall gridline is recommended for future numerical work on turbulent impinging jets.

Comparison of computed velocity distributions in the wall jet region with experimental measurements for spacings, H/w, of

2.6, 6.0 and 8.0 at a limited number of Reynolds numbers show that the maximum wall jet velocity decreases faster when the flow is restrained by a confinement plate. This effect is stronger at impingement surface spacings of 2.6w than 6.0w. However, for a proper evaluation of the predictive capability of the TEACH-T program for the confined impinging jet flow, detailed flow and turbulence measurements are required for a confined slot jet impinging on a flat surface, especially at relatively small impingement surface spacings which pose a critical test for numerical simulation.

In the wall jet region the computed heat transfer distributions for impingement surface spacings, H/w, of 2.6, 6.0 and 8.0 and jet Reynolds numbers from 5200 to 20750 are in reasonable agreement with experimental results obtained by Cadek (26), Saad (125) and the present investigator. In the impingement region, however, the numerical program used is unable to predict correctly the heat transfer or even the shape of the heat transfer profiles for any of five combinations of Re_j and H/w tested. For every test case the predicted stagnation heat transfer, Nu_o, was low, in the range 1/3 to 2/3 of the correct value. In every test case the program predicts an off-stagnation maximum at 1w to 2w from stagnation, a feature not present in any of these impingement flows.

For combinations of a sufficiently low spacing, H/w, at a sufficiently high Re_j it is well-known that impinging slot jets display an off-stagnation minimum and maximum in heat transfer. In three of the five cases tested in the present study, i.e. for

both values of Re_j at the closest spacing, H/w = 2.6, and for the higher Re_j, 8100, at the intermediate spacing, H/w = 6, the feature of an off-stagnation minimum and maximum in Nu occurs. These off-stagnation peaks are attributed to the onset of boundary layer transition from laminar to turbulent (the minimum) and completion of this transition (the maximum). For the range of Re_j and H/w involved here the distance from the stagnation point at which these peaks occur are about 3w to 4w for the minimum, about 6w to 8w for the maximum. The TEACH-T program is unable to predict this transition, thus in no case can it predict these basic features of impingement heat transfer at small values of the spacing, H/w. The poor prediction of heat transfer profiles in the stagnation region is attributed primarily to the wall-flux laws which are not sufficiently general to include the effect of a streamwise pressure gradient, and to an inadequate modelling of the dominant terms of production of turbulent kinetic energy in the stagnation region.

Comparison with the computational results of Wolfshtein (154) who used a one-equation turbulence model does establish that the present two-equation turbulence model is superior to the one-equation model for prediction of impinging jet heat transfer. A meaningful comparison with the computed results of Folayan (41), who used the same k-ε model, cannot be made because Folayan studied a slot jet with a fully developed turbulent velocity profile at the nozzle exit.

Concluding, the TEACH-T program is able to predict wall jet heat transfer for a confined turbulent impinging slot jet

with reasonable accuracy and without numerical stability problems. However, in the stagnation and early wall jet region the computational program fails to predict correctly the heat transfer or even the shape of the heat transfer profiles. The program always predicts a stagnation point minimum, contrary to actual behaviour, and never predicts the combination of an off-stagnation minimum and maximum at values of Re_j and H/w for which this feature occurs. The distance from the stagnation point at which reliable prediction begins is about 2w in the case of larger H/w spacings for which the heat transfer profile is bell-shaped around the stagnation point, or about 5w to 6w from stagnation for combinations of H/w and Re_j which produce the profile with an off-stagnation minimum and maximum.

The recommendations of changes which should lead to a numerical prediction scheme better able to predict reliably the flow and heat transfer characteristics in the difficult region around the stagnation point are:

(1) The wall-flux laws should be generalized to include the effect of a streamwise pressure gradient.

(2) The two-equation k-ε turbulence model should be replaced by the algebraic stress model of turbulence, to eliminate the assumption of isotropic turbulent kinetic energy implicit in the turbulent viscosity concept.

(3) The procedure of Chieng and Launder (32) should be used for the numerical treatment of k and ε on the near-wall gridline.

CHAPTER 3

EXPERIMENTAL EQUIPMENT AND PROCEDURES

3.1 Overall Design Conception

An experimental facility was built for study of local heat transfer under a single confined turbulent jet of air impinging on a moving surface with or without throughflow at the surface. The moving surface was obtained by forming the impingement surface as the cylindrical wall of a rotating drum, 0.482 m in diameter. Two slot jets, one hot and one cold, impinging on this rotating surface from 180° opposed positions provided overall steady-state operation. The length of each slot jet, 203 mm, equalled the length of the cylindrical impingement surface.

As the prime industrial motivation for this study was drying under impinging jets, for which the impingement system must be closed with a confinement surface matching the impingement (drying) surface, the experimental facility was closed with circular plates at the ends of the rotating drum and with a cylindrical confinement hood concentric with and at a spacing H = 37 mm above the 0.482 m diameter impingement surface. Both jet nozzles were positioned with their exits flush with the confinement surface. Corresponding to the two inlet jets 180° apart, there were in the confinement surface two pairs of exit ports likewise 180° apart, i.e. with each spentflow exiting +90° and -90° from the respective inlet. The two pairs of spentflows were separated from each other by a skimmerplate located at the

midpoint of each exit duct and extending to a few mm from the surface of the rotating drum. Thus the entire apparatus comprised two isolated systems, one hot jet and one cold jet, each system occupying 180° of the rotating cylindrical impingement surface and confinement hood.

The photographs shown as Figures 3.1(a) and 3.1(b) provide a general view prior to insulation of the experimental facility respectively before and after installation in the lab. The experimental facility is termed SIMTEST Apparatus for the objective of its use for testing present and future computer simulations of impingement heat transfer on moving surfaces with throughflow. The inlet jets are located at the top and bottom of the rotating drum assembly, the hot jet beneath the large square heater above the drum. The pair of exhaust ports intermediate between the inlet jets, i.e. at the horizontal positions, are also visible in Figure 3.1(b).

By establishing adiabatic operation for the cylindrical impingement surface, its temperature assumes a steady-state value intermediate between that of the hot and cold jets. Thus the convective heat transfer coefficients obtained with this design correspond to the boundary condition of an isothermal surface.

Provision for throughflow at the impingement surface was incorporated by forming this cylinder from porous metal. Throughflow was achieved when desired by applying suction to the interior of the drum.

The key flow parameter, jet Reynolds number, Re_j, was

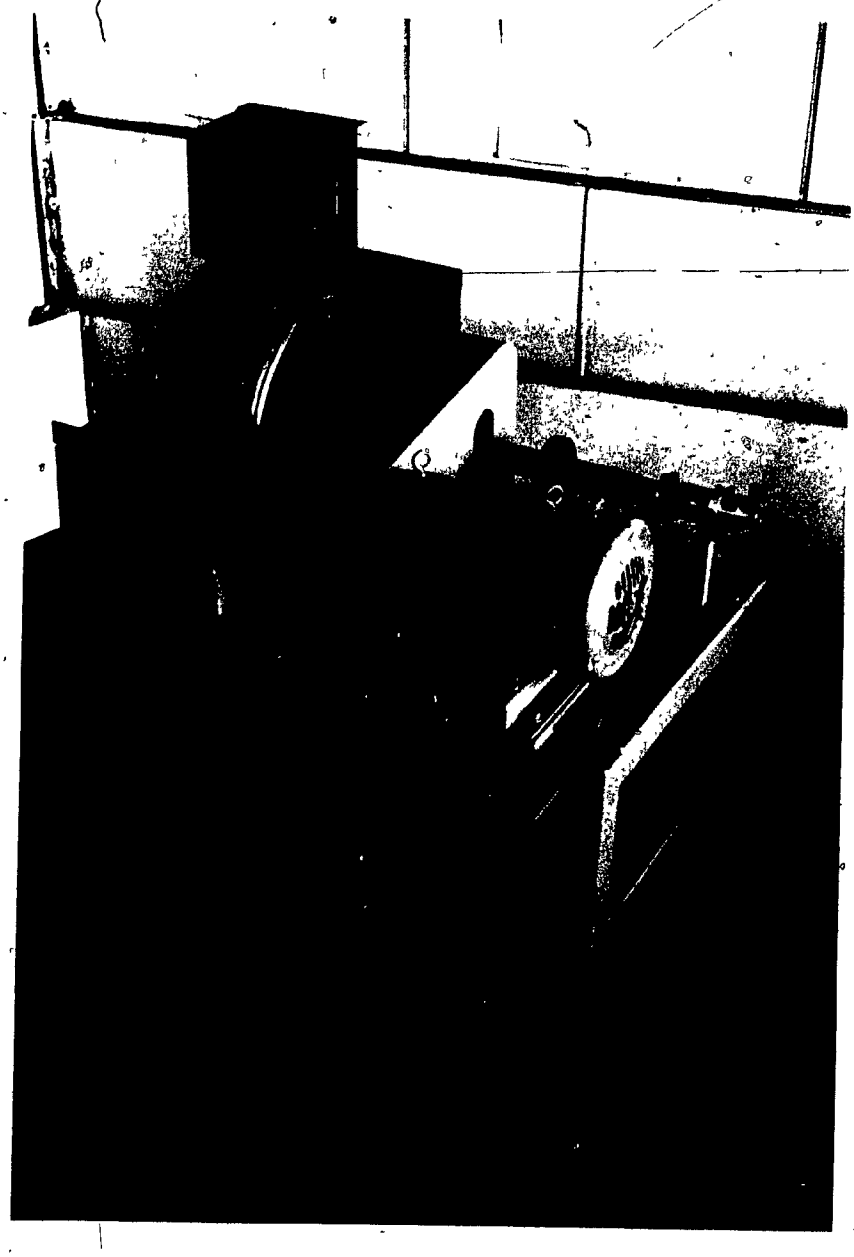


FIGURE 3.1a. General view of experimental facility before installation in laboratory

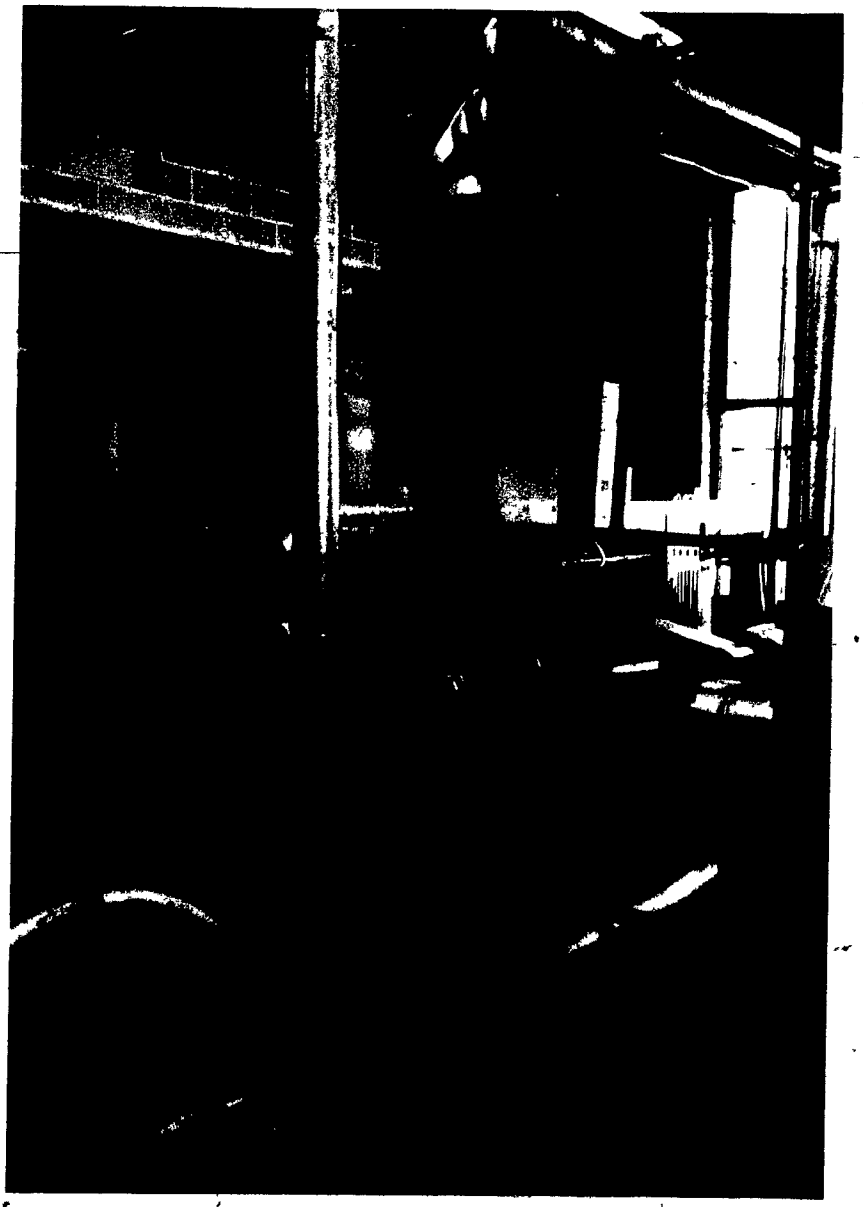


FIGURE 3.1b. General view of experimental facility after installation in laboratory

varied from 5200 to 20300 for the H/w = 6 side (top), and from 9700 to 91800 for the H/w = 2.6 side (bottom).

As to choice of geometrical parameters, selection of nozzle widths, w, of 6.2 and 14.1 mm for the hot and cold jets respectively, combined with spacing the impingement surface at H = 37 mm from the nozzle exits provided data simultaneously for two dimensionless spacings, H/w, of 6.0 and 2.6 for each set of operating conditions. The wider nozzle was used for the cold jet in order to maintain the rotating impingement surface at a significantly lower temperature than would have been the case had the alternate choice been made. The SIMTEST apparatus was designed for future use with the wide range of spacing of impingement surface from the nozzle exit-confinement surface of $26 \leq H \leq 76$ mm, and for nozzles of various widths in order to permit operation subsequently at values of spacing from H/w = 1 up to any spacing relevant to impingement studies.

The range of the other two key experimental parameters, peripheral velocity of the impingement surface, V_s, and throughflow velocity, U_s, were chosen with reference to the proposed "Papridryer" process which represents a projected combination of impingement and through-drying of paper (Burgess et al., 1971a, b). Thus the maximum speed of rotation of the impingement surface, 10 rps, corresponds to V_s = 15 m/s, i.e. to the range of paper machine speeds. Likewise the range of impingement surface throughflow rates, expressed alternately as average throughflow velocity, U_s, or as the ratio of this velocity to the mean jet velocity at the nozzle exit, U_s/U_j, for the

present study and for the pilot plant and mill-trial Papridryer investigations are as follows:

	Papridryer	Present Study
U_s, m/s	0.045-0.26	0-0.164
U_s/U_j, %	0.045-0.45	0-0.895

Another but less significant comparison of variables between the "Papridryer" and the SIMTEST apparatus is that the nozzle area, represented as a fraction of the confinement surface area, is respectively 0.71% and 1.61% for the sides of the apparatus of nozzle width 6.2 and 14.1 mm, values which are in fact in the 1.33-1.67% range of the multiple slot jet Papridryer pilot plant and mill-trial units.

The critical feature and most challenging aspect of the SIMTEST apparatus design is the method for measuring local heat transfer for an impingement surface moving at speeds of up to 15 m/s. Thus at V_s = 15 m/s a point on the impingement surface passes under the 6.2 mm width nozzle in only about 0.4 ms. Moreover, at a point on the impingement surface the local heat flux (or Nusselt number) can vary by a factor in the order of 100 although the local impingement surface temperature may vary by only about 0.2°C (see Appendix 7). The requirement of measuring local heat transfer under such conditions was satisfied by mounting a high sensitivity, fast response heat flux sensor flush with the impingement surface. This thin film heat flux sensor consisted of a specially designed gold film resistance thermometer, extremely thin (about 0.27 μm) and thereby with a

response time of about 10^{-5} seconds. With this sensor it is possible to achieve essentially instantaneous monitoring of surface temperature with a resolution of about $0.001^{\circ}C$ at a sampling speed of 5000 measurements per second (see Appendix 8). The effective width of the sensing section of this heat flux gauge is only 1.15 mm in the 1515 mm circumference of the impingement surface. Instantaneous heat flux, and thereby local Nusselt number, could be determined from this measurement of surface temperature through solution of the unsteady-state heat conduction equation. Use of a computer for on-line data acquisition permits determination of about 500 values of local Nusselt number per rotation, i.e. about 250 values in the Nusselt number profile for each jet for every set of operating conditions for the facility. Profiles of local Nusselt number are produced by a plotter directly as computer output from the data processing.

3.2 The Experimental Facility

The schematic diagram, Figure 3.2, and the close-up photograph, Figure 3.3, illustrate the detailed description of the experimental facility, which begins with consideration of the system for providing ambient and hot air to the jet nozzles. A 3.7 kW one-stage turboblower (0.30 m^3/s at 7 kPa) (1) draws air from the laboratory through an air filter. Dust particles, which could plug the porous drum, are removed by the filter (2) to the extent of 99.97% as measured by the DOP method on 0.3 micron particles. The air from the turboblower is divided into three streams, i.e. the two jets and the excess capacity line

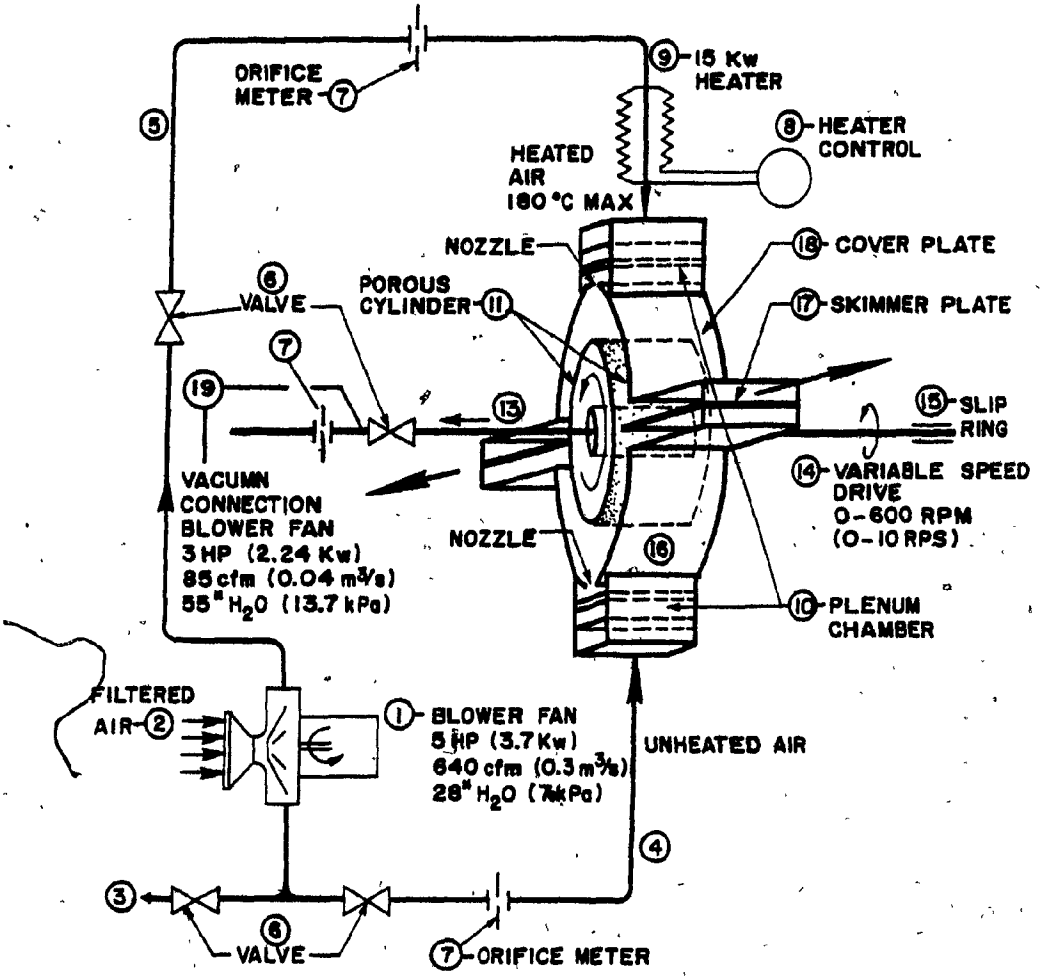


FIGURE 3.2. Schematic diagram of experimental facility



FIGURE 3.3. Close-up photograph of SIMTEST apparatus

(3) which exhausts outside the building through a gate valve. The other two lines (4) and (5) connect to the plenum chambers on opposite sides of the rotating drum assembly. The flowrates in the lines of the two nozzles are controlled by dampers (6) and measured with orifice meters (7). Before entering the upper plenum chamber air from the 0.152 m diameter line is heated by a 15 kW (208 V, 3-phase) duct heater (8). A perforated plate with 7.2% open area (9) at the heater inlet ensures a uniform distribution of air over the heater and hence across the jet nozzle. The heater dimensions are 0.46 x 0.46 x 0.38 m, exclusive of the entry and exit transition sections. The upstream transition section, 0.356 m long, adapts the square heater to the 0.152 m diameter pipe while a 0.254 m long downstream transition section connects to the 0.203 m square plenum chamber. The heater controls include a thermal cutout, duct thermostat, SCR temperature controller (Honeywell R7308-B9044) and a remote potentiometer for manual and automatic control. Air at about 40^{o}C (due to heating by the turboblower) enters the lower plenum chamber via the 0.204 m duct. The identical plenum chambers (10) are 0.305 m long and contain two 100-mesh screens at 0.038 m and 0.191 m from the entrance to reduce the turbulence level of the jets. A 0.051 m thick aluminum honeycomb layer (hexagonal size 4.7 mm) at 0.089 m from the entrance is used to straighten the flow. The nozzles in the hot and cold side are respectively 6.2 mm and ~~14.1~~ mm wide and 0.203 m long, i.e. equal to the length of the cylindrical impingement surface.

Design of a permeable impingement surface as a rotating

drum is the central feature of the SIMTEST apparatus. The two jets impinge on a porous stainless steel cylinder (11) of 3.2 mm wall thickness, 0.482 m outside diameter and 0.22 m long, supported between two 13 mm thick, stainless steel end (support) plates of the same (0.482 m) diameter, shown also by Figure 3.3. The porous cylinder fits into a notch, 5 mm wide and of depth equal to the porous steel thickness (13 mm), which was cut into the inside corner of each support plate. This mounting arrangement accounts for the difference between the length of the porous steel cylinder, 0.22 m, and the length of the impingement surface and slot nozzles, 0.203 m. As suction must be applied for experiments with throughflow at the cylindrical impingement surface, the drum is mounted on a hollow shaft, a 114 mm O.D. x 0.37 m long steel pipe (12), perforated with 28 holes of 25.4 mm diameter from which the throughflow air could be withdrawn to the suction connection (13). To obtain uniform radial flow for operation with throughflow, a 0.165 m diameter cylinder of the same porous S/S is located between the perforated steel shaft and the impingement surface. One end of the 0.114 m O.D. hollow shaft terminates in a bearing sealed with Rulon, which provides the connection to suction system. The other end of the hollow shaft is attached to the main drive shaft, 102 mm O.D. x 16 mm I.D. x 0.85 m long, which is supported by two pillow block bearings spaced 0.457 m apart. A pulley (14) mounted on the shaft between these bearings is driven through a no-slip belt from the drive pulley of a 3.7 kW variable speed motor. Leads from the heat flux sensor, pressure transducer and ther-

mocouples pass through the 16 mm I.D. of the drive shaft to a low-noise, 14-channel slip ring assembly (15) (IEC Corp., Austin, Texas, Model IEC-BX-14) mounted at the end of the shaft.

With a hot and a cold jet impinging on opposite sides of the cylindrical impingement system it is necessary that each spentflow be exhausted without entering the other half of the system. Thus each confined spentflow passes directly from the annular sections (16) to the exhaust ports (17). Skimmerplates (18) at the exhaust ports prevent the spentflow from one half of the system from entering the other half. The end of each skimmerplate is a movable teflon sheet which is positioned to within 3 mm of the drum surface. In the other direction each skimmerplate extends to the end of the 203 mm square exhaust duct, i.e. dividing each of these square ducts into two rectangular exhaust ports, as may be seen on Figure 3.3. The spentflows from the hot and cold sides mix in the 203 mm diameter ducts downstream of the skimmerplates and are exhausted outside the building via duct work designed to equalize pressure drop in each arm.

The suction system (blowers, flow measurement and control), used when impingement surface throughflow is desired, is connected by a 102 mm I.D. flexible S/S line to the bearing which carries the hollow perforated shaft of the rotating drum, shown clearly in Figure 3.1(b). The suction flow is provided by two blowers in series, a 2.24 kW three-stage turboblower (19) (0.040 m^3/s at 13.7 kPa) and a 7.46 kW rotary lobe type blower, not shown, (0.11 m^3/s at -40.7 kPa). The throughflow rate is mea-

sured with an orifice meter. Temperature is measured with a thermometer downstream of the orifice plate. A knock-out drum (not shown) is placed in the line between the blowers. The throughflow rate is controlled by two gate valves before the rotary blower and a gate valve in the inlet of laboratory air to the knock-out drum.

Although the present study involved use of only a single value of spacing of the impingement surface from the nozzle exit-confinement surface (H = 37 mm) and one pair of nozzles (of width 6.2 and 14.1 mm, for H/W of 6 and 2.6 respectively), the SIMTEST apparatus was designed for subsequent use with a choice of 5 values of H over the range 26 to 76 mm and with nozzles of other widths, permitting operation at any relevant value of dimensionless spacing, H/w. Thus any of five confinement hoods, each with the curvature required for the corresponding value of H, may be conveniently installed in the basic facility, as can be seen from Figure 3.3. From this figure it is also evident that the choice of nozzle mounted on the removable confinement surface may readily be changed. Moreover, constructing the confinement hood in removable sections as illustrated in Figure 3.3 facilitated access to the impingement drum. These stationary sections were sealed with silicone against leakage. Air leakage from the interior of the confinement hood around the circumference of the two, 13 mm thick x 0.482 m diameter end plates of the impingement drum was minimized by use of teflon seals. These teflon seal rings, about 0.5 m diameter and 10 mm thick, each supported by a steel retaining ring mounted

on the stationary side plates, are seen on Figures 3.1 and 3.3. As the teflon sealing rings made sliding contact, there was negligible leakage.

The heat flux distribution under each jet is measured with a thin film heat flux sensor. This heat flux probe is mounted flush with the impingement surface in a centrally located, 3.2 mm x 100 mm slot in the porous stainless steel drum, visible in Figure 3.3. Details of the sensor are given in Section 3.3. The pressure distribution under the jets can be measured with a calibrated pressure transducer (Kulite XTH-190-5) mounted in a hole in the drum surface at 180° from the heat flux sensor. Air temperature at the nozzles is measured with a chromel/constantan fine (0.05 mm) wire thermocouple (Medtherm 203-05E10) located in the nozzle on the cold side and just above the nozzle on the hot jet side. The temperature distribution of the curved confinement hood is measured with strategically placed thermocouples. The velocity and temperature distribution in the nozzles and exit ducts can be measured with movable Pitot tubes and thermocouples. To reduce temperature gradients in the axial direction the whole assembly (except the drum end plates) is insulated with a 5 cm layer of fiberglass. However, elimination of axial temperature gradients along the impingement cylinder was only achieved when the end plates of the drum were blackened and were heated with two 250 W infrared heating lamps for each end. The temperature of these drum end plates can be monitored with an IR pyrometer.

Before start-up of the SIMTEST apparatus, the calibration

of the heat flux sensor is checked by measuring its resistance as well as the temperatures at the back of the sensor, the temperature in the nearest nozzle and the room temperature. The difference between the front and back temperature of the sensor should be less than 0.25°C. The variable speed drive, blower for the two jets, and heater are then started, in this sequence. The thermostat setting of the heater is slowly increased to avoid large overshoot of the hot jet temperature, especially at low jet velocities. For experiments with throughflow, the two blowers in the suction line are also started, and the suction flowrate controlled with the gate valve in the line from the knock-out drum to the room. The d.c. power input to the IR heating lamps is manually adjusted until the difference between the three thermocouples at the back of the sensor is reduced to about 0.1°C at steady-state operation.

3.3 The Heat Flux Sensor

3.3.1 Description of the Sensor

3.3.1.1 Selection of Type of Heat Flux Sensor

The most critical problem encountered in the experimental program was selection and manufacture of a sensor which could measure local heat flux under the jets at impingement surface speeds up to 15 m/s and with throughflow. For the narrower nozzle, w = 6.2 mm, a point on the impingement surface traverses one nozzle width in about 0.4 ms when V_s = 15 m/s, i.e. at the maximum speed, and local heat flux or Nusselt number may vary by a factor of 100 although surface temperature may vary by only

about 0.2°C. Such requirements could only be met with a very sensitive and fast response heat flux sensor, imbedded in and flush with the impingement surface. Also, at least one dimension of the sensor should be small so as not to alter significantly the flow at the impingement surface when used with throughflow.

The search for a heat flux sensor which satisfies such specifications led to an extensive review of this field. Fast response heat flux gauges have been used before for applications such as determination of cylinder wall temperature variations in reciprocating engines and determination of heat flux rates to aerodynamic models in shock tubes and shock tunnels (121). The two basic techniques used are thin-film surface thermometry and thick-film calorimetry. A hot-film probe, normally used for skin friction measurements, was first considered for heat transfer measurement in this work as it had been in previous studies, but was rejected on grounds of inapplicability of the analogy between heat transfer and skin friction (see Appendix 9). Selection of the heat flux sensor for the present work was based on the excellent study of D.J. Baines (10) on unsteady heat flux sensors. Besides the two above-mentioned gauges D.J. Baines also included the gradient sensor and thin disk sensor or Gardon foil in his review. For short measuring times or rapidly fluctuating heat flux rates, the thin and thick-film probes are preferred. As the thin-film sensor is the more sensitive gauge, it was selected for the critical requirements of the present investigation.

A thin-film sensor is essentially a slab, the surface temperature of which is measured with a thin-film thermocouple (pile) or thin-film resistance thermometer. The thickness of the slab must be sufficient that it may be considered "semi-infinite", i.e. that fluctuations of surface temperature do not penetrate completely through the slab. As the response time to a sudden change in surface temperature for a film of thickness 0.2-0.3 μm is much smaller than 10^{-5} seconds, (Appendix 10), the surface temperature measurement can be considered instantaneous even with respect to the smallest time scale associated with the highest rotational speed in the present study, 20×10^{-5} s. Because of the small cyclic variation in surface temperature, at the highest rotational speed in the order of $0.2^{\circ}C$, a resistance thermometer rather than a thermocouple (or thermopile) was chosen for measurement of the thin-film temperature. Instantaneous heat fluxes are obtained from surface temperatures by solving the unsteady heat conduction equation for the sensor substrate. A closed solution is available, but because of the presence of an integral with a singularity, a solution can be obtained much faster numerically by a modification of Schmidt's method (2).

In order to satisfy fully the other characteristic desired for the heat flux sensor, i.e. that there be no alteration in flow at the impingement surface for the case of throughflow, it was originally intended to use the porous stainless steel impingement cylinder itself as the substrate for a thin-film resistance thermometer. This objective led to an extensive search for a monomer which could be vacuum deposited on the stainless

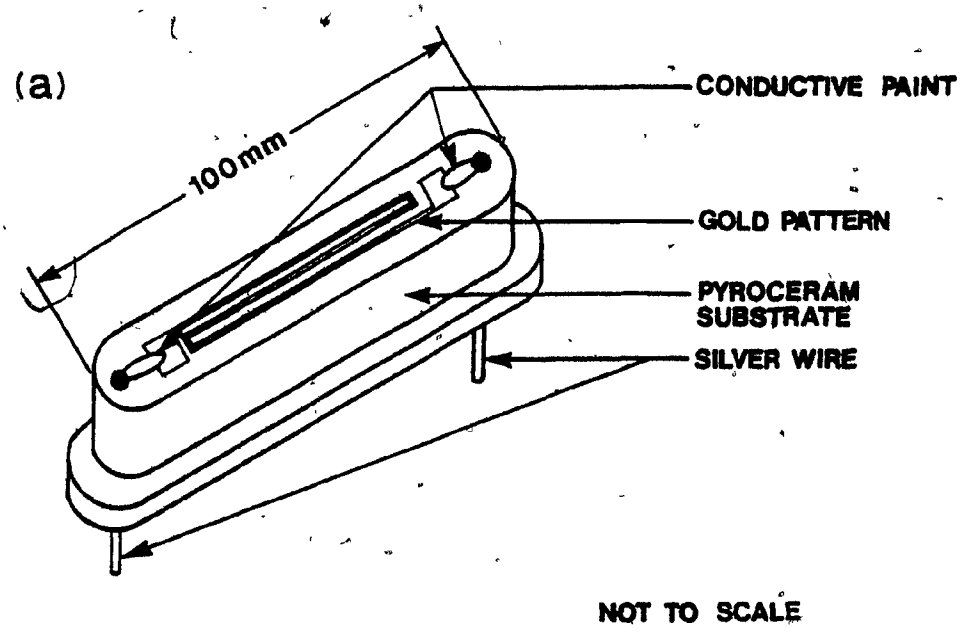
steel particles at the porous impingement surface. What was desired was to deposit on the steel particles at the surface a polymer film that would provide pinhole free electrical insulation from a resistance thermometer metal filament without however blocking the pore structure at the impingement surface. The required insulating material was "Parylene", a thermoplastic polymer, chloro-p-xylene, marketed by Union Carbide Co. Very good pinhole free films have been obtained by Reed and Ripperger (114) by vaporizing the dimer di-p-dichloro-xylene and depositing the monomer on the substrate. As this material was unfortunately no longer available from Union Carbide and as no other monomer was found with which this specification could be achieved, it was necessary to adopt a compromise objective. The alternative selected was to design a thin-film sensor on a solid substrate sufficiently narrow that at the high impingement surface speeds (to 15 m/s) available with the SIMTEST apparatus, the steady boundary layer over the permeable surface would have insufficient time to adjust to the no-throughflow condition during the short time of passing of the narrow impermeable sensor through the flow field. This hypothesis is subsequently examined during analysis in Chapter 4 of the results with throughflow.

It was then necessary to select a solid substrate material which would give the same surface temperature as would exist for the porous stainless steel under the same unsteady state conditions. Under transient conditions the surface temperature response of a material is determined by its $\sqrt{\lambda \rho C_p}$ value (39), ignoring the influence of surface roughness and emissivity. A

simple test assembly was designed and built to measure the thermal conductivity of the porous stainless steel (P.S.S.) from which the drum was manufactured (see Appendix 11,12). The values of thermal conductivity for several samples of P.S.S. grade H, made from 316 SS by Pall Canada, Montreal, varied from 2.9 to 3.5 W/mK at room temperature. With the measured density and specific heat from the literature (107) the average $\sqrt{\lambda \rho C_p}$ value was calculated to be 2.78 $kJ/m^2\,{}^oK(s)^{\frac{1}{2}}$. An electrical insulating material with well-defined thermal properties and a $\sqrt{\lambda \rho C_p}$ value close to that of the P.S.S. used for the impingement surface is "pyroceram 9606" (Corning Glass, Corning, N.Y.). This glass-ceramic material has a $\sqrt{\lambda \rho C_p}$ value of 2.89 $kJ/m^2\,{}^oK(s)^{\frac{1}{2}}$ at 20°C as calculated from the recommended data in literature (146), stated to be accurate within 5%.

3.3.1.2. Manufacture of the Heat Flux Sensor

The thin-film heat flux sensor is shown in Figure 3.4(a). The sensor was mounted centrally in the surface, of the impingement drum, parallel to the drum axis and fastened to the porous stainless steel by epoxy as pictured in Figure 3.4(b). The size of the exposed sensor surface is 3.2 x 100 mm. Thus the sensor is quite narrow (3.2 mm) in the streamwise direction in order to minimize the "blockage effect", and in the longitudinal direction is half the length of the 203 mm long nozzles in order to avoid the end effect region near the walls. A 50 μm polyimide adhesive tape (Dodge Industries Inc., Hoosick Falls, N.Y., Cat. No. 2345) was used to cover the small gap between sensor and



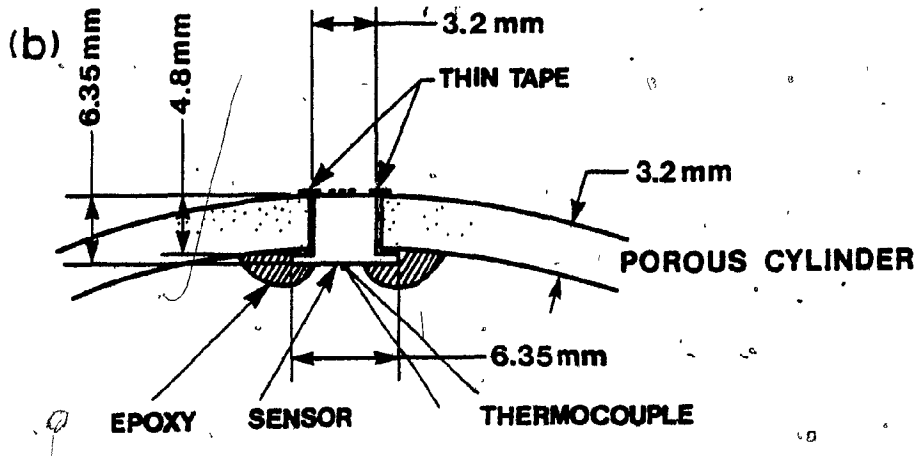


FIGURE 3.4. The heat flux sensor

drum to avoid flow separation at the edges. The pyroceram 9606 substrate was machined at the Research Laboratory of Corning Glass, Corning, N.Y. to have a wider base, thus preventing possible loosening at high rotational speeds. The exposed surface was polished in two steps:

(1) rough polishing with a 5 micron Al_2O_3 suspension in distilled water on a nylon cloth, then washing with distilled water and subsequently cleaning with methanol in an ultrasonic bath.

(2) fine polishing with a 0.3 micron Al_2O_3 suspension on a soft cloth at low (< 250 rpm) rotational speeds, followed by the same washing procedure as above.

Nickel, platinum and gold were considered as alternate materials for the resistance filament to be deposited on the polished surface. By trial it was established that gold films were best, because they were stable in moist air and acetone and benzene, adhered reasonably well to pyroceram and were resistant to slight rubbing. Identical films of nickel or platinum are more sensitive than gold (see Appendix 13) but nickel was unstable in moist air and platinum was very difficult to deposit because of the required high vaporization temperature.

A trial thin-film sensor was made by vacuum deposition of gold on the pyroceram substrate covered by a mask with an opening of 68 x 0.7 mm. Subsequently the gold film was annealed in an oven at 300°C for 1 hour. This thin-film resistor had a resistance of 29 Ω and a temperature coefficient of resistance α of 0.21%/°C (i.e. half the bulk value) at room temperature.

Considerable development of gold deposition techniques was required. Gold film deposition on the pyroceram substrate by sputtering was adopted as being more convenient than vacuum deposition. Trials to further increase adhesion of the gold film to pyroceram by depositing first a thin layer (~ 500 Å) of chromium were unsuccessful, probably because some remaining chromium etchant (HNO_3) attacked the gold film during the annealing process.

In Appendix 13 it is derived that the sensitivity A of the sensor is given by

$$A = \alpha_t L (\delta_f q_{sm}/d)^{\frac{1}{2}} \qquad (3.1)$$

with α_t = temperature coefficient of resistance

δ_f = resistivity

q_{sm} = maximum self-heating heat flux

L = length of film

d = film thickness

Thus by increasing the effective film length, L, by making a filament in the zigzag pattern shown in Figure 3.4(a), the sensor sensitivity is increased proportionally. The length of the film is however limited by the restriction set by the amplifier on the total resistance of the sensor, i.e. 350 Ω.

The gold film pattern of Figure 3.4(a) was obtained by a photofabrication technique, consisting of the following steps:

(1) The front surface of the pyroceram which is completely covered with a thin gold layer, deposited by sputter-

ing rather than vacuum deposition, is uniformly coated in a whirl coating machine with a few drops of a positive photoresist (AZ1350J), and subsequently baked in an oven at 100°C for about 30 minutes. This coating is done under the safe light.

(2) A mask is pressed on to the photoresist after cooling and exposed to UV light from a quartz lamp at about 0.1 m distance for about 2 minutes. This mask was made by miniaturization by Dr. M.C. Jain of the Electrical Engineering Dept., McGill University of a large scale model of the zigzag pattern.

(3) The exposed photoresist is removed with developer in about 100 seconds and again put in the oven for one hour at 100°C.

(4) The underlying gold film is removed by a gold etchant solution consisting out of $KI:I_2:H_2O$ in 4:1:4 by weight, of which 1 part is subsequently diluted with 4 parts of water.

(5) The photoresist over the remaining zigzag gold pattern is removed with acetone, cleaned with benzene and dried in an air jet

After photofabrication of the zigzag gold pattern, the sensor is annealed at 300°C for 12 hours. During this process the resistance decreases by about 30%. Finally a protective SiO_2 layer of about 1000 Å is deposited on top of the gold by sputtering. It is interesting to note that only a 5% resistance decrease occurs after annealing a gold film on glass, prepared

under exactly the same conditions as the pyroceram sensor, indicating the influence of the larger surface roughness of the pyroceram substrate. For different sensors, the resistivity δ and temperature coefficient of resistance α were found to be respectively 6.1×10^{-6} Ω cm and 0.15%/^{o}C at room temperature, independent of the gold film thickness which varied from 1300 Å to 2700 Å. These physical property values are respectively 2.6 times and 1/2.6 times the "bulk" property values of δ_t and α_t.

The particular sensor used to obtain all results of the present study had three gold strips of 0.25 x 70 mm, each separated by 0.20 mm as shown in Figure 3.4. The gold film thickness of 0.27 μ was calculated using the relationship between sputtering frequency and gold film thickness on glass as measured by optical interferometry, and assuming no influence of the substrate. A low contact resistance silver paint was used to make electrical contact between the gold pad at the end of the zigzag pattern and 1.3 mm thick silver lead wires, which were glued with epoxy to the pyroceram substrate. After some experimentation it was found that "Conductive Silver 200" from Degussa gave a stable electrical contact of the lowest electrical resistance. Also, lead wires other than silver (i.e. Cu, Ni, etc.) should be avoided because of oxidation of the contacts leading to large values of contact resistance.

Three thermocouples are glued to the back of the sensor with a high thermal conductivity epoxy adhesive (TRABOND 2151, TRA-CON Inc., Medford, Mass.). The junctions are located at the center and at 30 mm from the center.

3.3.1.3 Calibration of the Heat Flux Sensor

The sensor, protected inside a waterproof plastic bag, was calibrated in a thermostat bath. Temperature was measured to 0.1°C with calibrated thermometers. Sensor resistance was measured with a 5-decade Kelvin bridge, the calibration for which is the lower curve in Figure 3.5. Absence of hysteresis proves that equilibrium was reached during the measurements. The curve is well-described by

$$R = 173.60 + 0.272\ T + 3.4\times10^{-5}\ T^2 \qquad (3.2)$$

with R in ohms, T in °C. As lead wires and a small scratch in one of the gold legs increased the resistance by about 0.5 Ω, the sensor resistance R_s was measured again in place in the drum with the same Wheatstone bridge used during heat transfer measurements. The sensor was placed under the hot air jet and temperature measured with the three thermocouples at the back of the sensor. The bridge reading was taken when the thermocouples gave the same reading, a condition obtained by adjusting the power to the IR heating lamps. The results, given as the upper curve in Figure 3.5, are described by

$$R_s = 174.08 + 0.2742\ T_s + 3.4\times10^{-5}\ T_s^2 \qquad (3.3)$$

with R_s in ohms, T_s in °C. Values recommended by the Thermophysical Properties Research Center at Purdue University for thermal conductivity, thermal diffusivity and specific heat of pyroceram 9606 are given in Figures 3.6, 3.7 and 3.8.

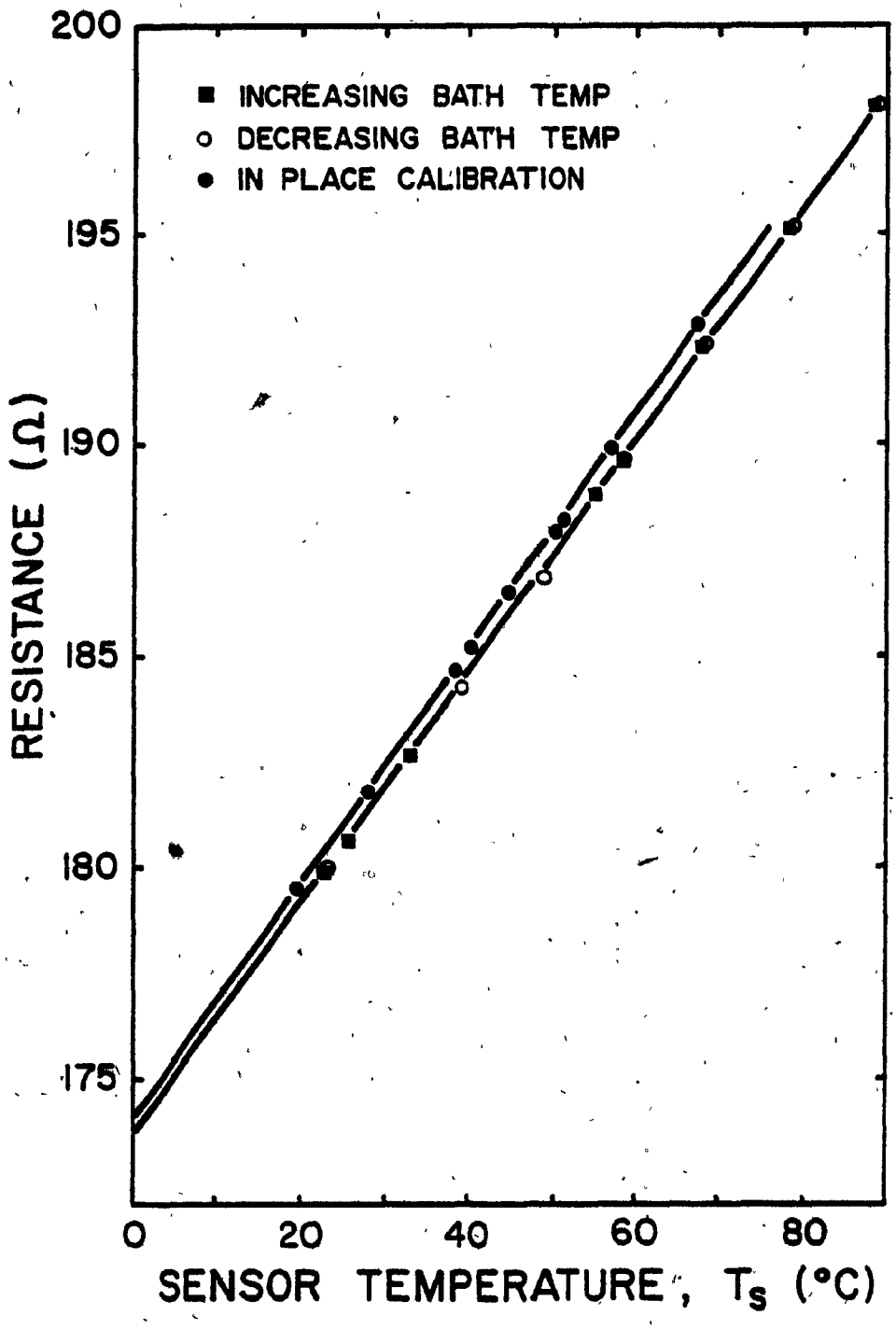


FIGURE 3.5. Calibration curve of heat flux sensor

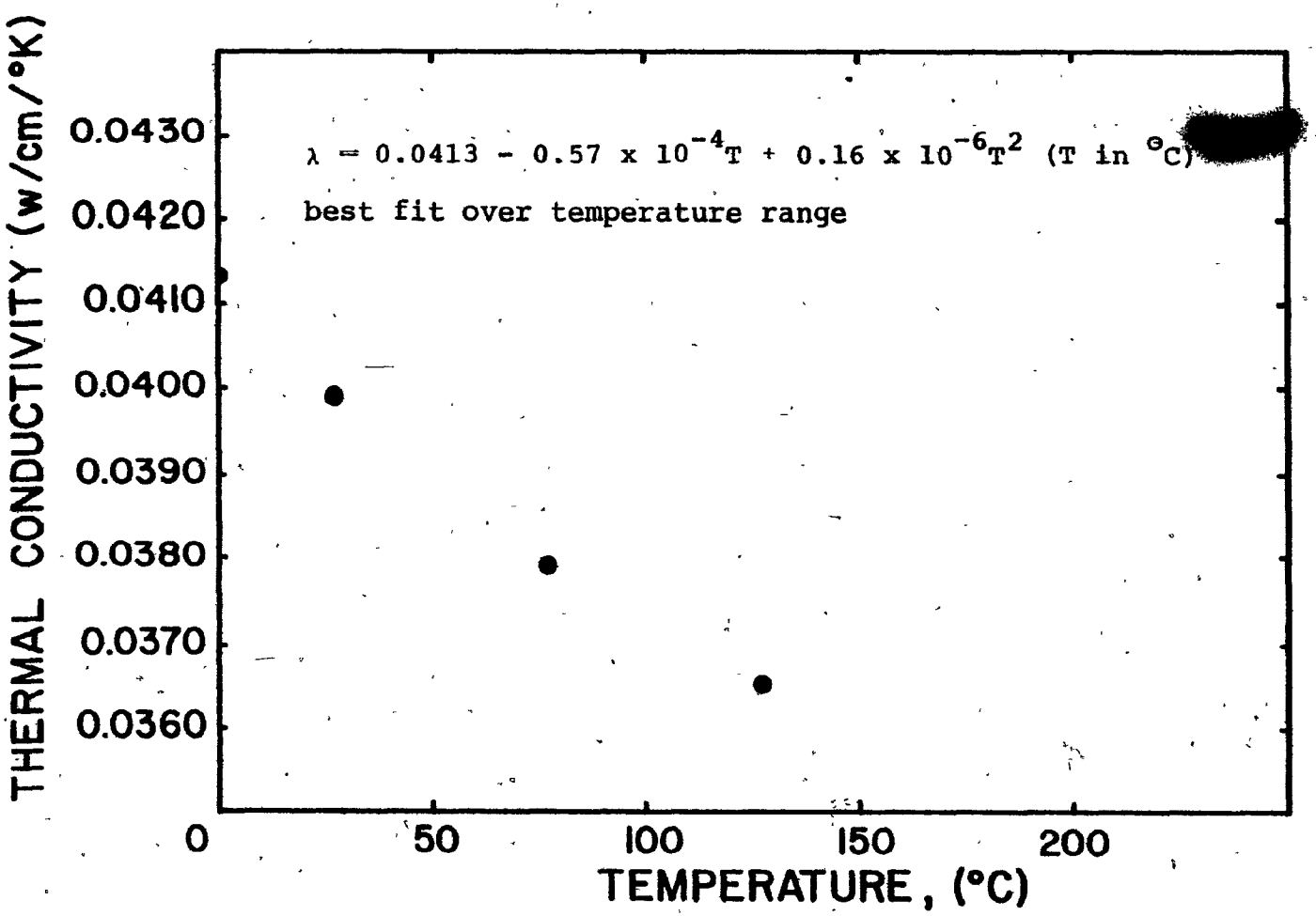


FIGURE 3.6. Thermal conductivity of Pyroceram 9606

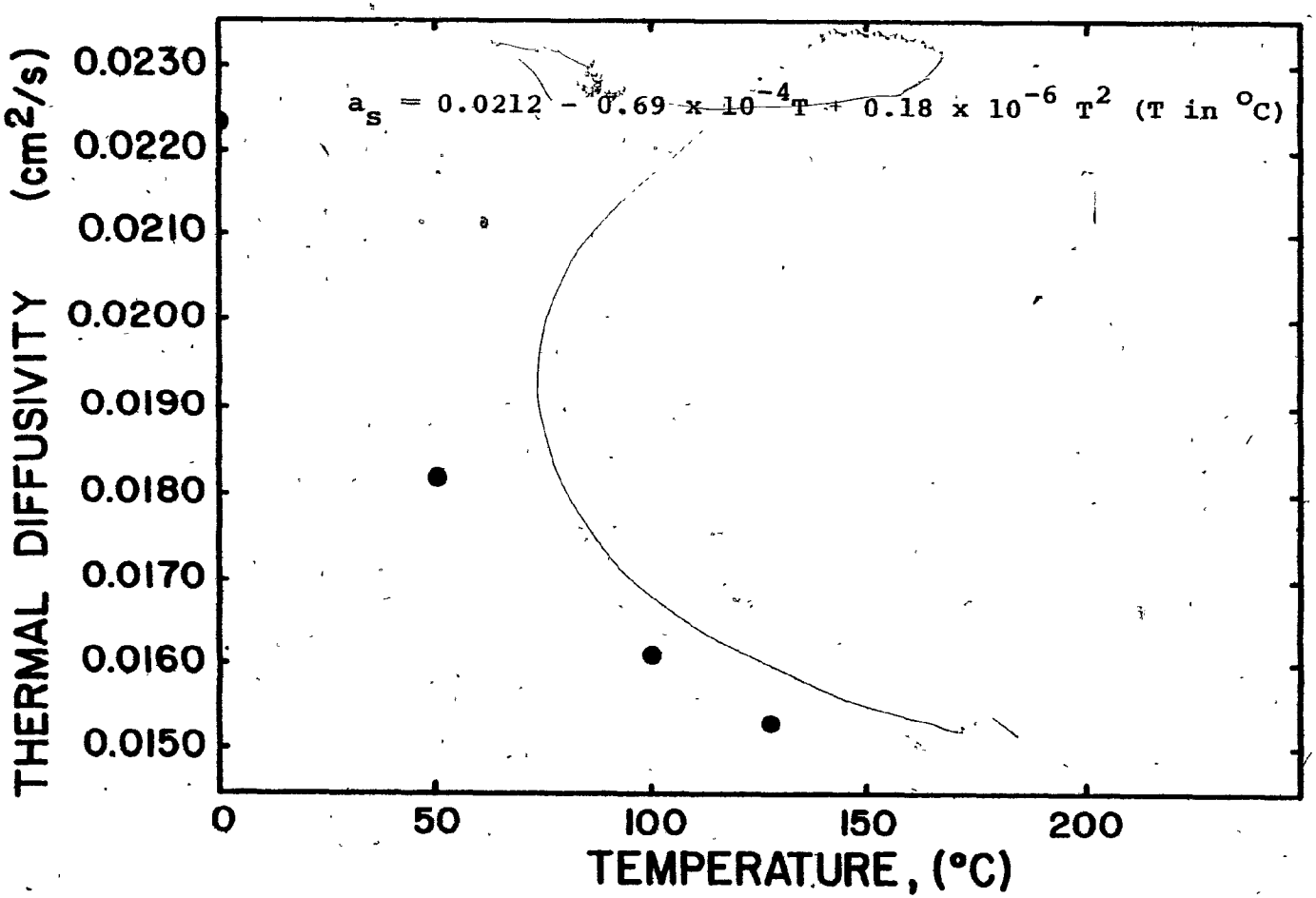


FIGURE 3.7. Thermal diffusivity of Pyroceram 9606

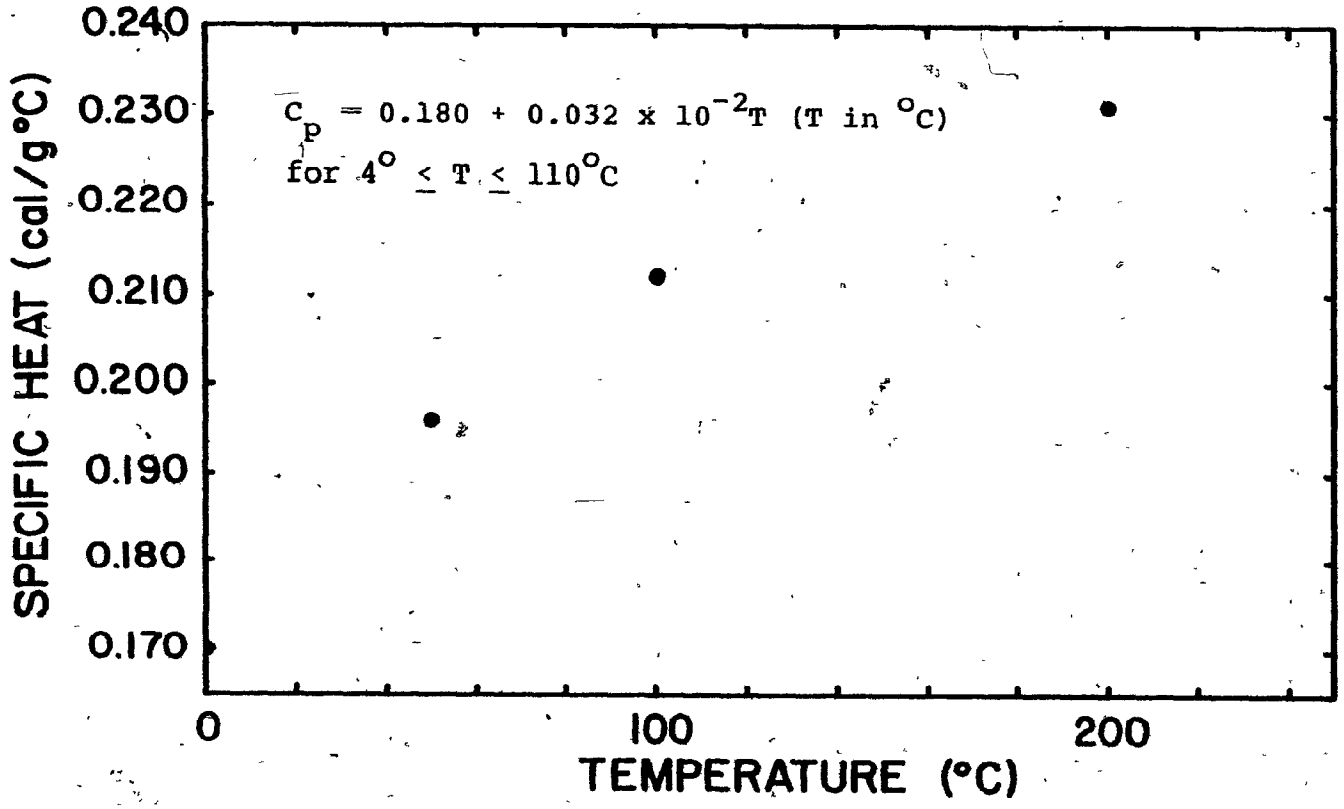
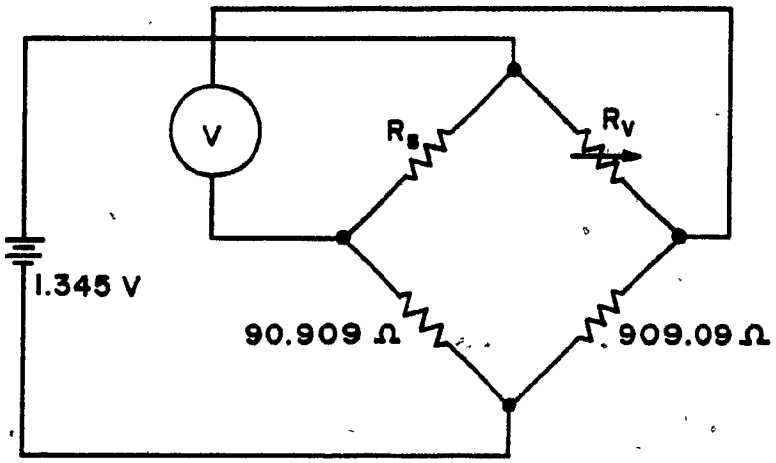


FIGURE 3.8. Specific heat of Pyroceram 9606

3.3.1.4 Instrumentation for the Heat Flux Measurement

The average and fluctuating component of sensor resistance is measured with a 4-decade Wheatstone bridge (J.C. Biddle Co., Cat. No. 601022), the circuit as shown below.



A 1.345 volt mercury battery was used as a stable and noise free power supply. The voltage level of the power supply was determined by the requirement that the self-heating heat flux of the sensor (q_{sm}) could be neglected with respect to the impingement convective heat transfer (see Appendix 14).

In operation the bridge is balanced by setting the variable resistance R_v at 10 times the average of the sensor resistance R_s. Use of an oscilloscope for display of the unbalanced bridge voltage aids this process. The unbalanced bridge voltage v is related to the fluctuating component ΔR_s of the sensor resistance by

$$v = \frac{1.345\ \Delta R_s}{(R_s + 90.909)\left(1 + \frac{R_v}{909.09}\right)} \qquad (3.4)$$

whereby $\Delta R_s = R_s - R_v/10$ (3.5)

Differentiation of equation (3.4) with the use of equations (3.3) and (3.4) gives

$$\frac{\Delta v}{\Delta T_s} = \frac{1.345 \times 909.09(0.2742 + 6.8\times10^{-5} T_s)}{(R_s + 90.909)(909.09 + R_v)} \quad (3.6)$$

in volt/^oC. For a typical experiment, the temperature of the sensor T_s is 60^oC, giving R_s = 190.7 Ω and a setting of the variable resistor R_v at 1907 Ω. Insertion of these values in (3.6) gives

$$\frac{\Delta v}{\Delta T_s} = 429\ \mu V/^oC \quad (3.7)$$

i.e. typically one order of magnitude larger than a thermocouple. Stated otherwise, a variation in bridge voltage output of 1 μV corresponds roughly to a change in sensor temperature of 0.002^oC.

The voltage v is amplified 2500 times with a low noise differential amplifier (DANA Model 2860, noise 1 μV RTI). High frequency noise is subsequently removed with a filter (Rockland Lab. Inc., Model 1022F) of which the two sections are connected in series in the "low-pass" mode. The attenuation slope of the filter is 48 db/oct. A long shielded cable connects the filter to another similar low noise amplifier set to keep the absolute value of the peak output signal slightly smaller than 5 V, the maximum for the 9 bit + sign, 2-channel, high-speed analog to

digital converter (ADC). Consequently, the minimum voltage change which can be differentiated by the ADC is 0.01 volt ($2^9 = 512$ and sign means variation from -5.00 to +5.00 volt). A variation of 0.01 volt at this stage corresponds roughly to a change of $\frac{0.01}{K_d}$ ^oC in the sensor temperature, with K_d being the gain of the second differential amplifier. From the ADC the digitized signal is sent to the digital computer (GEPAC 4020) where it is stored on disk for subsequent data reduction and storage in this computer.

3.3.2 Computation of Instantaneous Local Heat Flux

Instantaneous heat flux is calculated from instantaneous surface temperature of the heat flux sensor by numerically solving the one-dimensional unsteady heat conduction equation for the sensor substrate as a semi-infinite slab. The upper part of the sensor substrate is divided into n layers of thickness h and temperature at the interfaces calculated with the successive substitution formula

$$T_r(t) = \frac{1}{2}\left[T_{r-1}(t - \frac{h^2}{2a_s}) + T_{r+1}(t - \frac{h^2}{2a_s})\right] \qquad (3.8)$$

for $r = 1,2,3...,n-1$. The suffix 0 refers to the impingement surface. Heat flux is calculated with the equation

$$q_0(t - \frac{h^2}{3a_s}) = \frac{\lambda}{h}\left[T_0(t) - T_1(t - \frac{h^2}{2a_s})\right] \qquad (3.9)$$

The derivation of (3.8) and (3.9), given by Sepps (69) and D.J. Baines (10), is reproduced in Appendix 15 as neither reference is readily available. Equation (3.8) is the well-known explicit form of the finite difference approximation to the one-dimensional heat conduction equation with the condition for the Fourier number

$$Fo = \frac{\Delta t a_s}{h^2} \geq \frac{1}{2}$$

with Δt the time between consecutive digitized surface temperature measurements. With this condition equation (3.8) is numerically stable. In the present application the layer thickness h is fixed by the sampling frequency setting of the ADC which determines Δt so that

$$h = \sqrt{2a_s \Delta t} \tag{3.10}$$

Equations (3.8), (3.9) and (3.10) reduce to

$$T_{r,t} = \frac{1}{2}(T_{r-1,t-1} + T_{r+1,t-1}) \tag{3.11}$$

and

$$q_{0,t-\frac{2}{3}} = \frac{\lambda}{h}(T_{0,t} - T_{1,t-1}) \tag{3.12}$$

for $r = 1,2,3,4,\ldots,n-1$

and $t = 1,2,3,4,\ldots,N$

Initial and boundary conditions are required to solve (3.11) and (3.12). The boundary conditions are given by the

measured surface temperature $T_{0,t}$ and the equality $T_{n,t} = T_{n-1,t}$ because the sensor substrate can be considered semi-infinite for rotational speeds larger than 0.36 rps. At this speed the penetration depth Z of the surface temperature fluctuation is roughly equal to the 6.35 mm thickness of the pyroceram substrate. Penetration depth Z is estimated from

$$Z = 1.6\sqrt{\pi a_s \tau_0} \tag{3.13}$$

which gives the depth where the amplitude of a sinusoidal surface temperature variation of frequency τ_0^{-1} is reduced to 1% (10). The initial condition is generated numerically by first taking $T_{n,0}$ to be equal to the drum surface temperature averaged over a complete rotation, then applying equation (3.11) with the boundary conditions for 2 drum rotations for all n. The influence of the estimated uniform temperature $T_{n,0}$ is then completely eliminated. The exact number of measurements during these two rotations is determined by the position of the actuating lever with respect to the microswitch at the time of starting the ADC.

The number of finite difference layer n is calculated as the integer value of the ratio Z/h which is given by

$$Z = 2.0\sqrt{\frac{\tau_0}{\Delta t}} \tag{3.14}$$

using (3.13) and (3.10), τ_0 being the time for one rotation. With an ADC setting of about 500 measurements per rotation,

(3.14) gives a value for n of about 45.

D.J. Baines (10) has given expressions to determine the error in heat flux amplitude and phase shift for a sinusoidal heat flux variation when using equations (3.8) and (3.9) instead of the exact solution to the unsteady heat conduction equation. For a semi-infinite slab the amplitude error is

$$1 - \frac{\sqrt{\sin\left(\frac{\omega_m h^2}{2a_s}\right)}}{\sqrt{\frac{\omega_m h^2}{2a_s}}}$$

and the phase shift is $\frac{\omega_m h^2}{12a_s}$ radians, ω_m being the fastest circular frequency of the heat flux, rad/s. With equation (3.10) the amplitude error and phase shift can be rewritten as respectively

$$1 - \frac{\sqrt{\sin\left(\frac{2\pi\Delta t}{\Delta\tau_m}\right)}}{\sqrt{\frac{2\pi\Delta t}{\Delta\tau_m}}}$$

and $\frac{\pi\Delta t}{3\Delta\tau_m}$, $\Delta\tau_m$ being the time for a complete cycle of the fastest heat flux frequency.

The fastest important heat flux frequency occurs under the hot jet where the heat flux goes from a minimum to a maximum at the stagnation point and again to a minimum in about 45 mm. As

500 measurements per rotation provides about 15 measurements over the 45 mm, the corresponding errors are 1.5% in heat flux amplitude, 4 degrees (or a displacement of 0.5 mm) in phase shift. The amplitude error of 1.5% amounts to an error less than 0.5% with respect to the stagnation heat flux of the hot jet because the amplitude of the heat flux fluctuation over the 45 mm is less than 1/3 of the stagnation heat transfer. The influence of number of measurements per rotation on heat flux distribution is investigated experimentally in Section 3.6.3.

To obtain the mean value of local heat flux, the calculated heat flux at each circumferential position is averaged over a sufficient number (in general 50) rotations, as is documented subsequently in Section 3.6.1. The circumferential location of each measurement point is identified by the number of measurements from a reference point. This point is determined by the first value of about 2.7 V from the digitized square wave voltage of the microswitch, since the microswitch signal is digitized simultaneously with the heat flux sensor signal by the ADC.

Local heat transfer coefficients were evaluated from the definition

$$\alpha = q/(T_j - T_s) \qquad (3.15)$$

Depending on the position of the sensor, the temperature at the nozzle exit T_j was taken to be that of the hot or cold jet. Likewise, for calculation of Nusselt number the corresponding nozzle width was used.

The computer printout includes a listing of conditions of the experiment, local heat flux for both jets for the complete 360 degrees averaged over the desired number of rotations, and average heat flux for both jets. For the latter, five averaging intervals are used, i.e. 150^{o}, 100^{o}, 75^{o}, 50^{o} and 25^{o} centered around the stagnation points for each jet at low rotational speeds, the averaging being carried out according to Simpson's rule.

3.3.3 Display of Nusselt Number Profiles

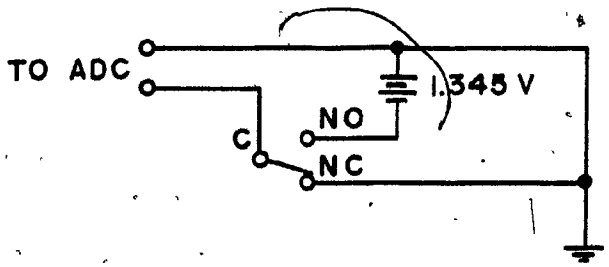
The data processing was completed with production of computer plotted profiles of local Nusselt number. The plotting of circumferential Nusselt number distributions was done with a separate plotting program. Separate plots of Nusselt number distribution are made for both jets. The first and last 15^{o} of each 180^{o} half-cylinder impingement surface is omitted from these plots as conditions in those sections are affected by proximity to the splitter plates and exit ducts. Stated otherwise, 1/6 of each impingement surface was omitted from the local heat transfer plots because of end effects near the splitter plates at which the impingement surfaces terminate. Plotted on the upper horizontal axis of each Nusselt number distribution is the nondimensional position, X_1/w. The position

$X_I/w = 0$ is at the stagnation point for slow rotation (<1 rps), and is at the nozzle centerline for all cases. Thus the entire operation was carried out by computer from data acquisition, through direct processing of this stored data, to plotting of results, i.e. from heat flux sensor voltage signal and impingement surface position identification through to lateral profiles of heat transfer as Nusselt number. The relevant experimental conditions are recorded in the upper corners of the graphs.

3.4 Instrumentation

3.4.1 Circumferential Position Marker

In order to identify the circumferential location of the sensor during rotation, the drum was fitted with a lever which activates a microswitch when passing. This lever closes the microswitch circuit while about 20 mm of the drum surface passes, thus producing a square wave in the circuit shown below.



The signal is amplified by a factor of 2, transmitted to the second channel of the ADC and stored on disk simultaneously with the signal from the sensor.

Some problems were encountered with the microswitch at high rotational speeds. The actual triggering of the microswitch was slowly delayed by about 10 to 20 mm due to the high impact, until finally the switch would break after a few hours of operation at high (~ 12 m/s) rotational speeds. This problem made it very difficult at high rotational speeds of the drum to determine the exact angular position of the lever at the beginning of the square wave. After each switch failure a slow rotation run was performed to establish the exact position of the closing of the new microswitch circuit.

Another problem was the occurrence of interruptions in the microswitch signal at high rotational speeds, probably caused by vibration of the switch lever. This problem was solved computationally in the data reduction program, by ignoring any change in the microswitch signal within a safe margin of 180^{o} from the start of the square wave.

3.4.2 Instrumentation for Pressure Measurement

Local pressure difference across the permeable impingement surface is measured with a differential pressure transducer (Kulite XTH-190-5) with a natural frequency of approximately 70 kHz. The transducer is mounted centrally and flush with the impingement surface, 180° from the heat flux sensor. The reference tube from the back of the transducer is open to the air inside the drum, which is therefore the reference pressure. The transducer is held in a 6.4 mm diameter hole by a hexagonal nut soldered at the inside surface of the impingement drum. The diameter of the pressure transducer housing is 4 mm, leaving a small gap between the sensing diaphragm and the impingement surface. The transducer is complete with a temperature compensating module for the range 66° to 121°C and a factory calibration of 0.059 mV/V/kPa.

The heart of the transducer is a miniature silicon diaphragm on which a Wheatstone bridge has been atomically bonded using diffusion techniques. The Wheatstone bridge input is an 18 volt battery. The output is zeroed by a 7.5 MΩ potentiometer before being amplified 1000 times as shown schematically in Figure 3.9. Electrical connection between the instrumentation and the pressure transducer is made via the slip ring assembly. The signal from the amplifier is sent to a storage oscilloscope for display.

3.4.3 Auxiliary Instrumentation

Temperature is monitored at various locations with chromel-

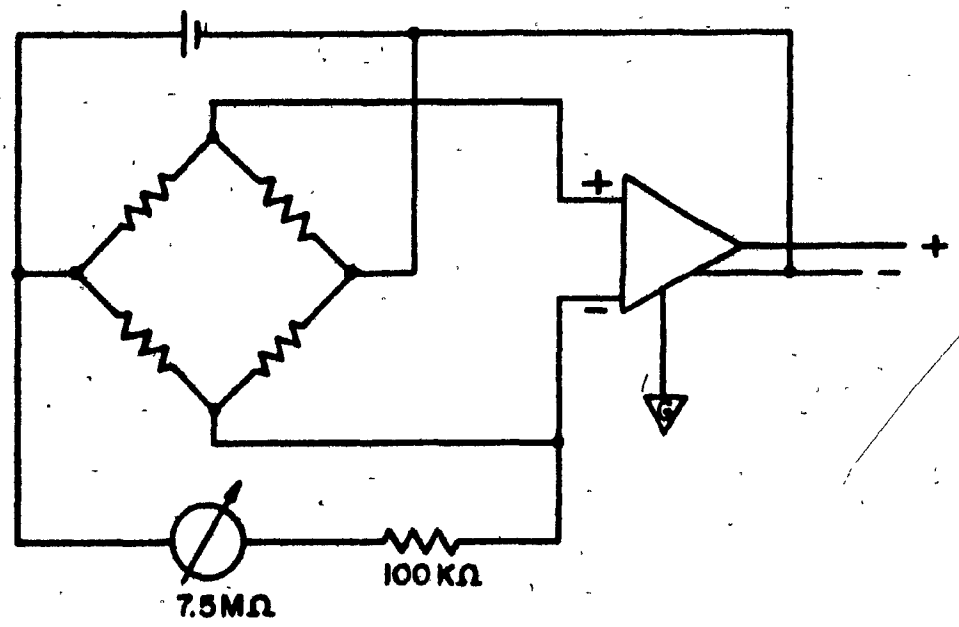


FIGURE 3.9. Electrical circuit of the pressure transducer

constantan thermocouples. The fixed positions are: one in each nozzle and four thermocouples on the upper confinement plates, located along the axial midpoint, at 30 and 200 mm from the hot nozzle centerline. Air temperature profiles in the nozzles and exhaust ducts are measured with movable thermocouples. Reference junctions of all thermocouples are kept at 0°C with an ice point reference (Kaye Instrument K140-4). Thermocouple output is measured with a digital nanovolt meter (Keithley Instruments, Model 180) via a manual 11-position, rotating switch.

3.4.4 Electrical Noise Reduction

Electrical noise in the heat flux signal was reduced to the order of a few μV by the following measures:

- selection of low noise instruments: a) slip ring assembly with 2.5 μV noise per ring with 12 mA into 350 Ω bridge up to 500 rpm; b) amplifier with a noise of 3 μV rms RTI + 2 mV RTO for 10 kHz bandwidth
- use of a mercury battery instead of a regulated d.c. power supply as power source for the sensor
- grounding all instruments to the same ground
- a sliding contact between the drive shaft of the SIMTEST apparatus and the common ground
- shielded wires from the slip ring to the Wheatstone bridge and from there to the amplifier
- use of a low pass filter with 48 db/oct attenuation slope
- use of d.c. current and carbon piles as power supply and control for the IR lamps and proper orientation and

shielding of the instruments.

3.5 Testing and Calibration of Equipment

The temperature and flow field was measured at various locations and sometimes adjusted to obtain the proper two-dimensionality and symmetry before taking heat flux data, as described in the following sections.

3.5.1 Nozzle Flowrate Calibration

The two-dimensional nozzle contours, shown in Figure 3.10, were designed closely to the ASME long radius, circular flow nozzle code (6), using hydraulic diameter of the slot nozzle, D_H, instead of diameter. The hydraulic diameter for the top and bottom nozzle in the SIMTEST apparatus were respectively 12.0 and 26.4 mm. The nozzle type was selected to obtain a close approximation of the flat velocity profile at the nozzle exit which was used as boundary condition in the numerical work of this study. This choice also allowed better comparison with the work of Cadek (26) who used almost identical nozzles.

In traversing the length of both nozzles along the midplane with a total head tube essentially no variation from plenum chamber pressure was measured. Static pressure at the nozzle exit measured with a pitot tube varied along the length of the nozzles as can be seen in Figure 3.11. The magnitude of the variations along the central section (i.e. 1 to 7 inches from the front) are sufficiently small that the jets may be considered to be two-dimensional. Flowrate through the nozzles

Dimensions

Nominal nozzle width, inch	A	B	C	D	E	F	G
1/8	7/16	1/8	0.25	0.167	1/8	$3\frac{15}{16}$	8
1/4	3/8	1/4	0.48	0.320	1/8	3 7/8	8
1/2	1/4	1/2	0.923	0.615	1/8	3 3/4	8

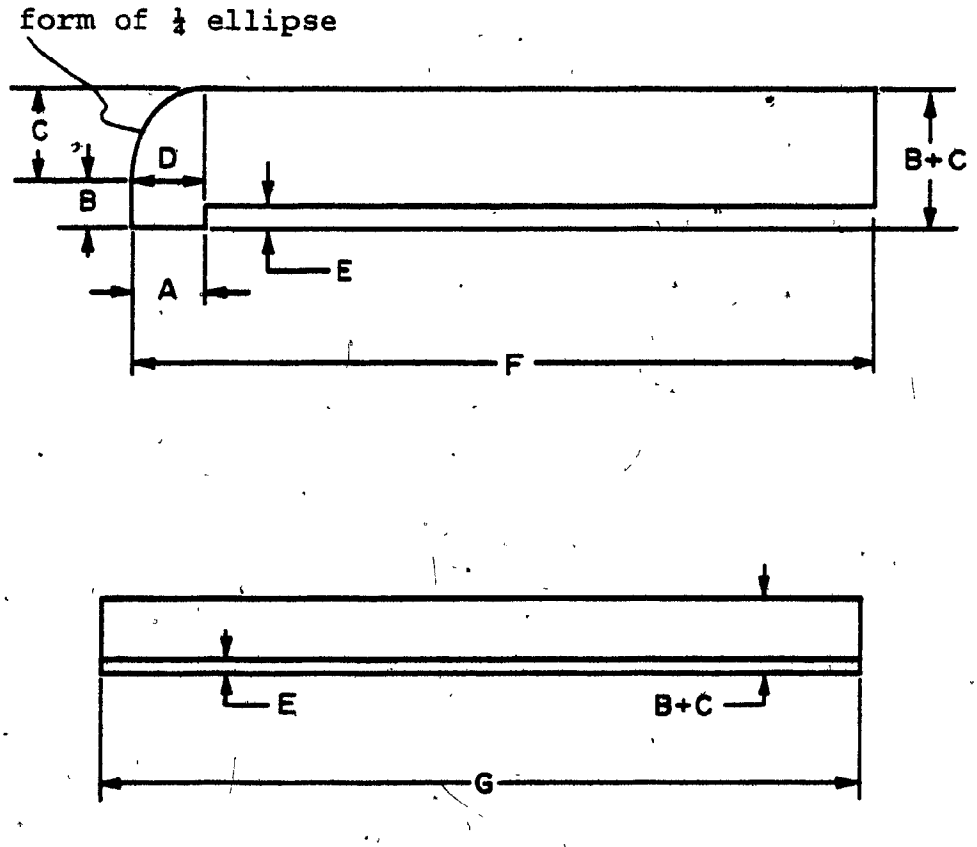


FIGURE 3.10. Design of nozzle blocks

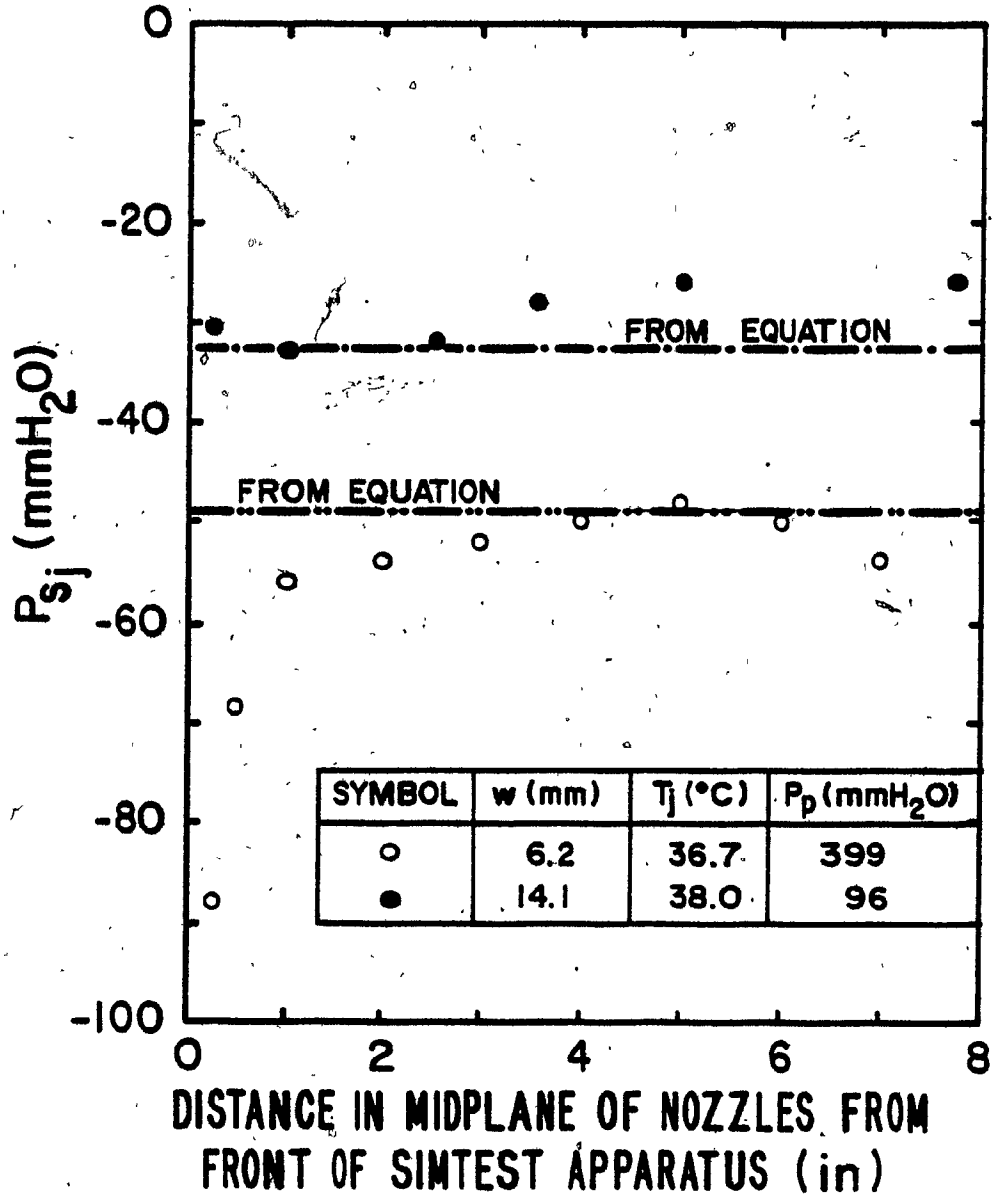


FIGURE 3.11. Static pressure along nozzle midplane

was calibrated against the orifice meters upstream, by measuring the plenum chamber static pressure, (P_p) and temperature and the static pressure at the center of the nozzle exit (P_{sj}). A negative static gauge pressure is measured because the pressure is partly recovered in the confined annular flow sections and to a much lesser extent in the exit ports. A least squares fit of the measurements at the middle of the nozzle exit for the top jet nozzle is:

$$P_{sj} = -0.102(P_p)^{1.05} \tag{3.16}$$

and for the bottom jet nozzle

$$P_{sj} = -0.29(P_p)^{1.07} \tag{3.17}$$

with P_{sj} and P_p in cm H_2O, as indicated in Figures 3.12 and 3.13.

It was found experimentally that the nozzle exit static pressure was not significantly influenced by drum rotation or flowrate through the other nozzle (a maximum ejector effect of 2 mm H_2O was found). Consequently the mass flowrate is completely determined by the plenum chamber pressure and nozzle temperature. The fact that the nozzle exit static pressure was not influenced by flowrate through the other nozzle indicates that pressure recovery occurs in the confined annular sections and exit ports, and not in the exit ducts. This conclusion is further confirmed by the static pressure distribution obtained with the computer program for the turbulent confined impinging jet in Chapter 2. In the computer program the static pressure

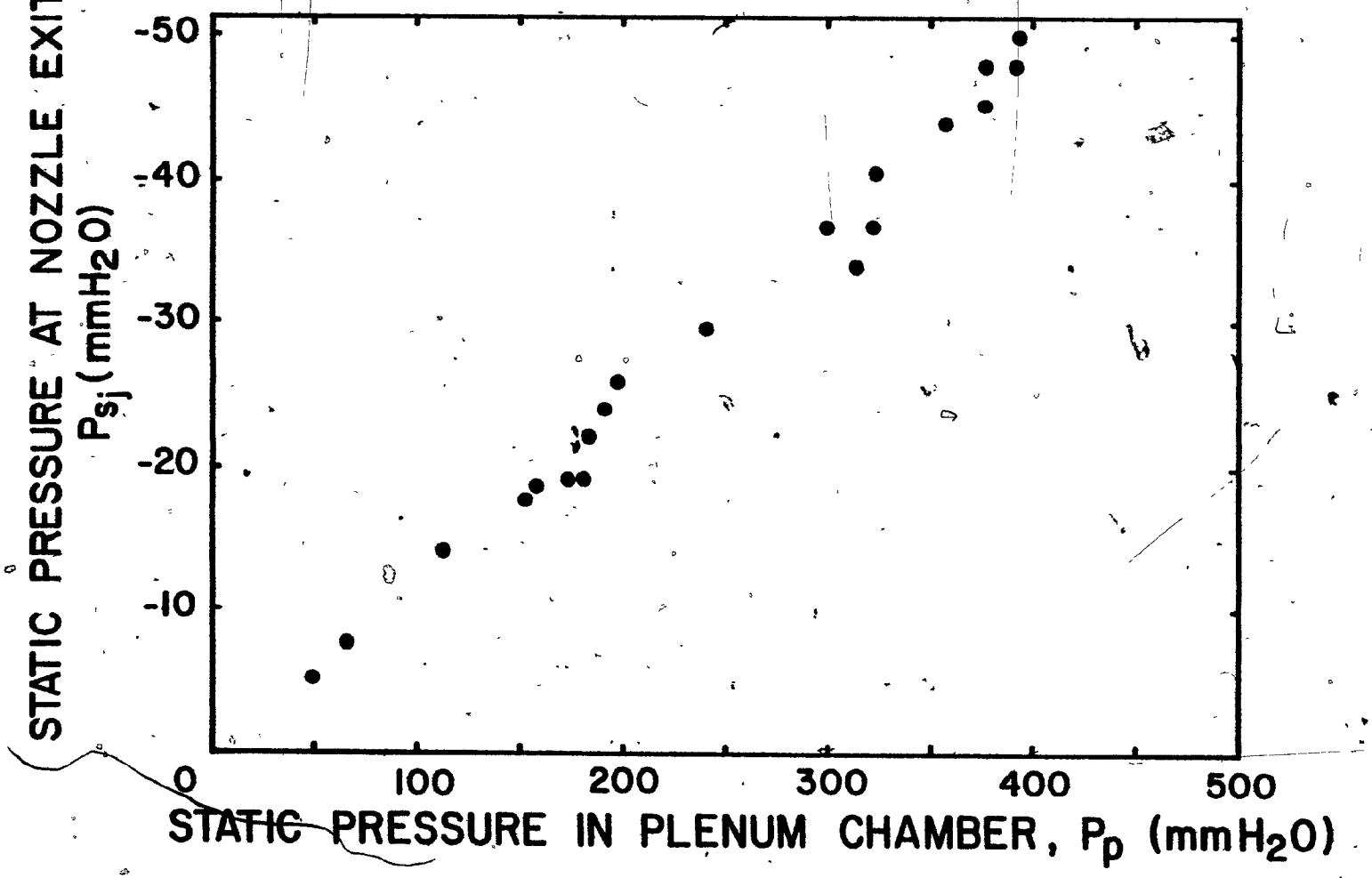


FIGURE 3.12. Relation between static pressure at the nozzle exit and plenum chamber pressure for H/w = 6

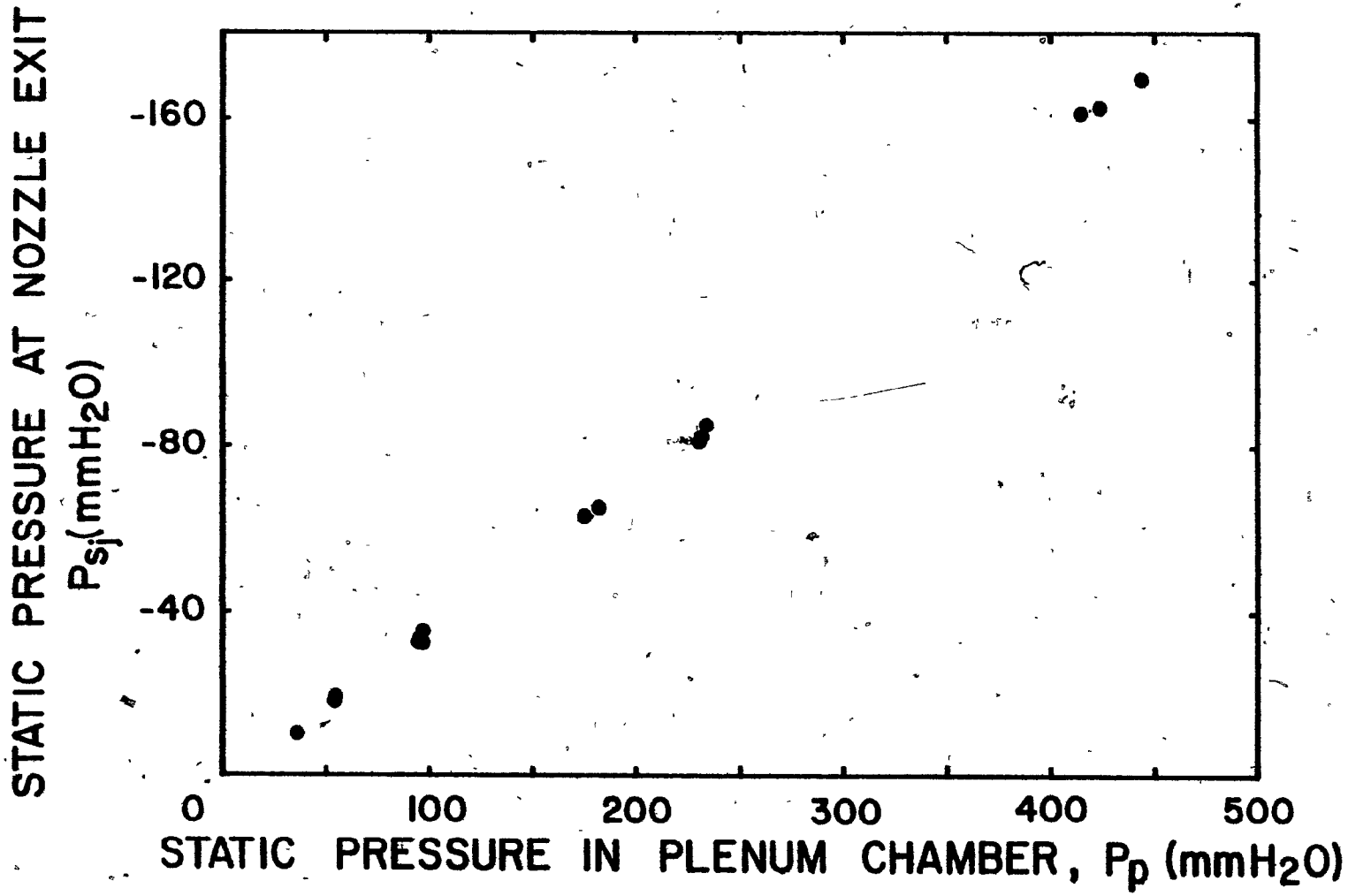


FIGURE 3.13. Relation between static pressure at the nozzle exit and plenum chamber pressure for H/w = 2.6

at the center of the nozzle exit was taken to be the reference pressure and subsequently set at zero. In the confined wall jet region the computed static pressure reached a maximum (P_{sm}) at a fixed distance from the stagnation point (x_{sm}), independent of Re_j. The values of P_{sm} and x_{sm} for the 5 cases computed in Chapter 2 are listed in Table 3.1. Also listed are the pressure difference over the nozzle (ΔP_n) and the ratio $P_{sm}/(\Delta P_n - P_{sm})$.

If the confined flow were exhausting in open air at x_{sm}, the static pressure P_{sj} at the nozzle exit would have been $-P_{sm}$ below atmospheric pressure. Therefore the last column $-P_{sj}/(\Delta P_n + P_{sj})_{exp}$ which is equal to $(-P_{sj}/P_p)_{exp}$ was calculated for comparison for the first four cases given in Table 3.1, using the experimentally obtained static pressure equations (3.16) and (3.17). In all four cases the last column is about 1.1 times the numerically obtained ratio $P_{sm}/(\Delta P_n - P_{sm})$. The close agreement between the two last columns in Table 3.1, and the fact that the static pressure in the SIMTEST apparatus will again increase by a small fraction in the exit ports because of the transition of a $1\frac{1}{2}$ inch wide confinement to a 4" wide confinement, confirm the earlier statement that the pressure recovery leading to equations (3.16) and (3.17) occurs in the confined annular sections and to a much smaller extent in the exit ports of the SIMTEST apparatus.

A consequence of the phenomena leading to pressure recovery is that P_{sj} will be influenced by flow through the porous impingement surface. Unfortunately this effect was not antici-

TABLE 3.1. Comparison of P_s with Theoretical Maximum Recovery Pressure P_{sm}

Re_j	H/w	U_j (m/s)	ρ_j (kg/m^3)	ΔP_n (Pa)	P_{sm} (Pa)	x_{sm}/H	$\left(\frac{P_{sm}}{\Delta P_n - P_{sm}}\right)$	$\left(\frac{-P_s}{\Delta P_n + P_{sj\,exp}}\right)$
20200	2.6	24.05	1.132	327	70.2	~ 7	0.273	0.308
10400	2.6	12.38	1.132	86.9	17.7	~ 7	0.256	0.282
8100	6.0	33.27	0.856	474	43.7	~ 9	0.102	0.110
5200	6.0	21.36	0.856	195	17.0	~ 9	0.096	0.105
20750	8.0	49.08	1.207	1454	113	~ 12	0.084	-

pated during the experimentation. However from the understanding of the causes of the formation of P_{sj} and application of the continuity, energy and momentum equations, plus the insight obtained from the study of the influence of suction on the skin friction in Chapter 2, the underestimation of Re_j due to the influence of suction on P_{sj} was estimated to be only a few percent when less than 50% of the jet flow is removed through the drum surface.

The discharge coefficients determined from the orifice flow measurement and the ideal flowrate calculated from the pressure difference between the plenum chamber pressure and the nozzle exit static pressure are 0.945±0.01 and 0.99±0.01 for respectively the bottom and the top nozzle, as shown in Figures 3.14 and 3.15. The discharge coefficients for the bottom nozzle are in reasonable agreement with the theoretical values (116). The coefficients for the top nozzle are higher than the theoretical values. For calculation of flowrates during experiments the discharge coefficients are taken to be constant and equal to the values given above.

3.5.2 Temperature Distribution in the Nozzles

Temperature of the air entering the top nozzle is measured with a fine wire thermocouple (wire diameter 51 μm) located in the plenum chamber immediately above the center of the nozzle. The same type of fine wire thermocouple (Medtherm 203-05E10) in the bottom nozzle is located in the center of the throat of the nozzle. The temperature drop over the nozzles due to expansion

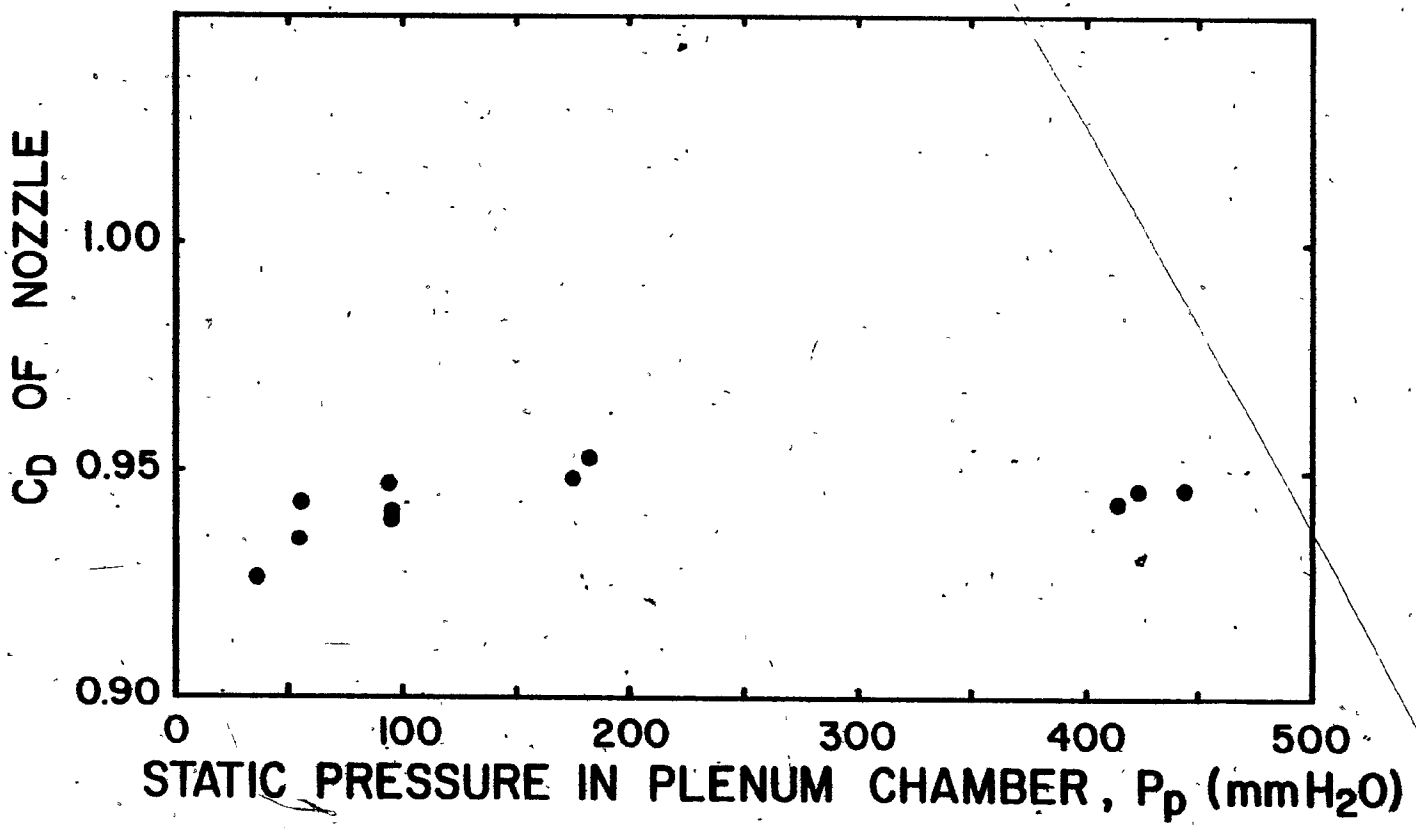


FIGURE 3.14. Discharge coefficient for 14.1 mm nozzle as a function of plenum chamber pressure

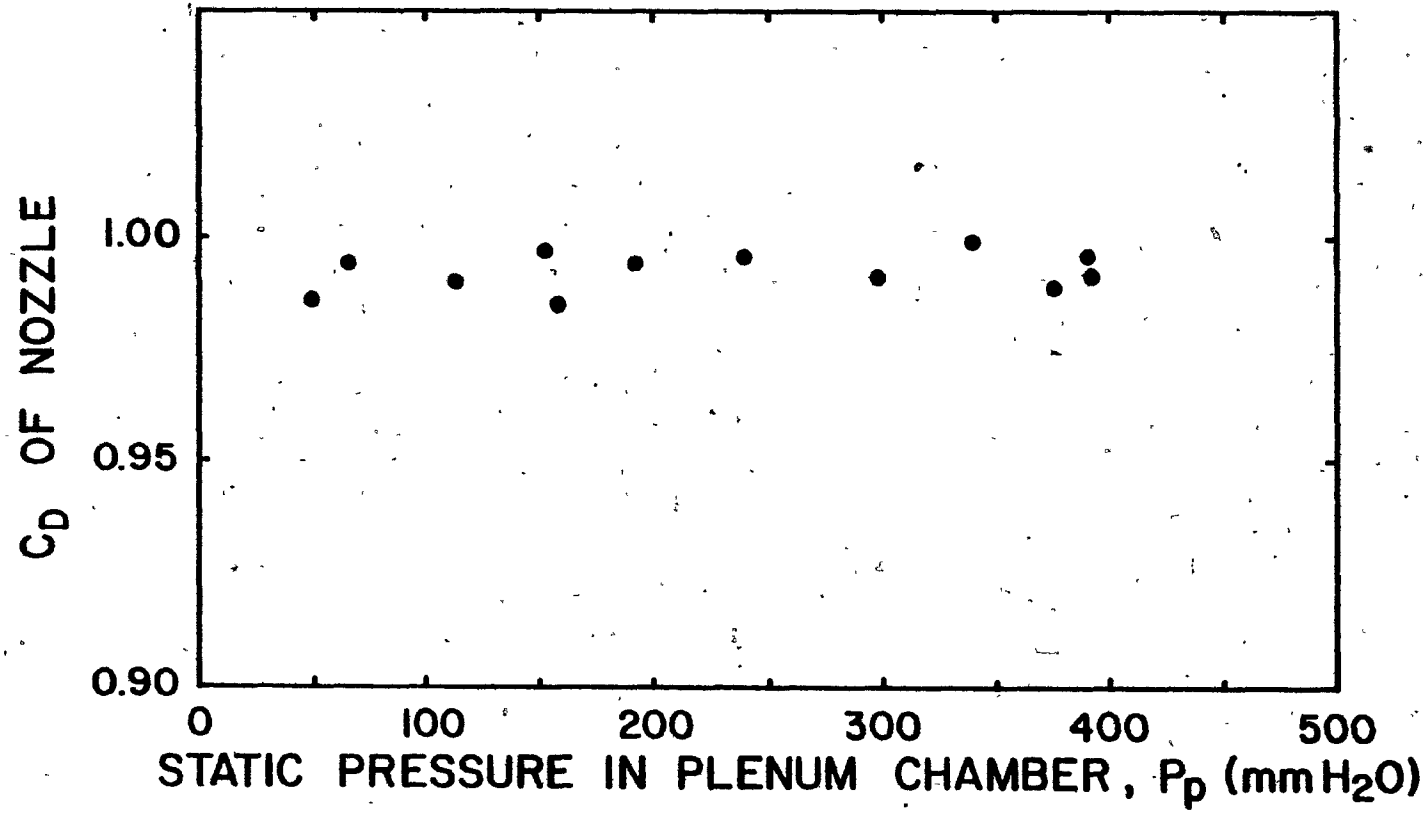


FIGURE 3.15. Discharge coefficient for 6.2 mm nozzle as a function of plenum chamber pressure

was measured with a movable thermocouple under the condition of no heating of the air to the top nozzle. The results in Figure 3.16 show for both nozzles the expected linear relationship between temperature drop and pressure drop.

The temperature distribution at various lateral locations in the hot nozzle exit plane shown in Figure 3.17 is also obtained with a movable thermocouple, in this case for a hot jet temperature of 97°C. The temperature shown is that measured by the movable thermocouple, corrected for the difference between 97°C and the average value of T_j measured by the fine wire thermocouple. The measurements were tedious because of the temperature fluctuations which, for typical temperature controller settings, were ±1°C around the setpoint of 97°C, with a frequency of about 1/20 s^{-1}. The rather uniform hot nozzle temperature distribution shown in Figure 3.17 was obtained only after insulating the plenum chamber and heater with 5 cm thick fiberglass and generating a uniform distribution of air in the heater by placing a perforated plate at the 15.2 cm round entrance of the heater. The 25 holes with a diameter of 8.2 mm were uniformly distributed over the plate, giving an open area of 7.2%. Temperature differences up to 25°C and 12°C over, respectively, the width and length of the nozzle were found previously under similar conditions as in Figure 3.17 but with a 40% open area perforated plate. Maldistribution of air due to location of a pipe bend immediately above the heater could be eliminated only by the large pressure drop across the plate of small open area.

At a nominal jet temperature of 37°C the maximum tempera-

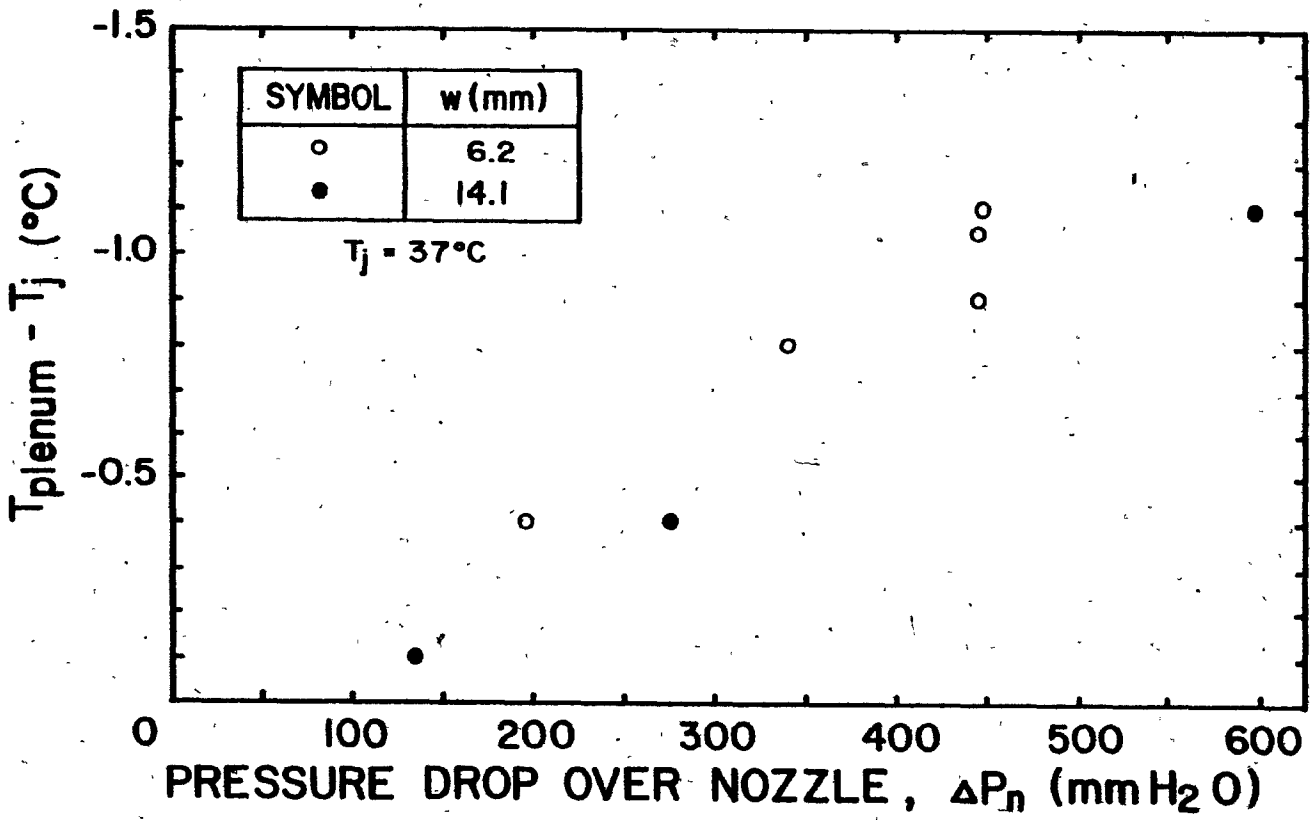


FIGURE 3.16. Temperature decrease across the nozzles caused by expansion

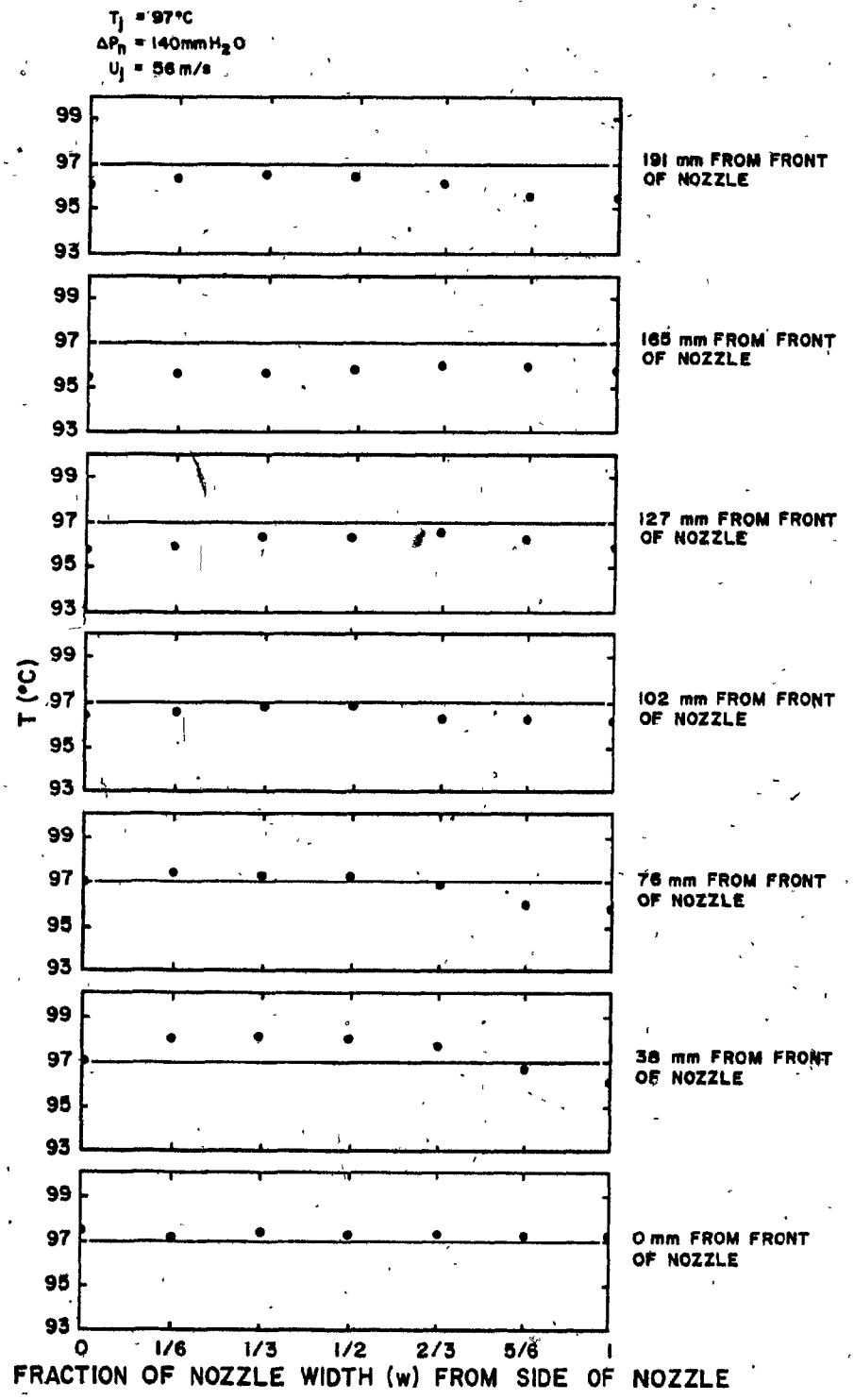


FIGURE 3.17. Temperature distribution in the nozzle of the heating jet

ture variations over the exit plane of the bottom nozzle were 0.3°C and 0.4°C at an average jet velocity of, respectively, 44 m/s and 71 m/s (see Figure 3.18).

Based on these measurements and adjustments the temperatures at the exit planes of both nozzles could be taken as uniform and equal to the temperature measured by the fixed thermocouples, with a small correction for the hot jet for temperature drop due to expansion across the nozzle (see Figure 3.16).

3.5.3 Temperature Effect at an Adiabatic Impingement Surface

A well-known phenomenon in high velocity impingement flows is the increase of jet temperature in the impingement region due to compression (Bouchez and Goldstein (18), Gardon and Cobonpue (43)). Thus, zero convective heat transfer occurs for an impingement surface at a temperature somewhat greater than the nozzle exit temperature. This effect can lead to significant errors in determination of heat transfer coefficients if the difference between nozzle exit temperature and impingement surface recovery temperature cannot be neglected relative to the temperature driving force.

In order to quantify this effect impingement surface temperatures were measured in the stagnation region with the heat flux sensor, with no power supplied to the heater, i.e. with a nozzle exit temperature of approximately 37°C. The results, as temperature difference betweeen the sensor and the nozzle exit, are shown in Figures 3.19 and 3.20 as a function of distance from the stagnation line.

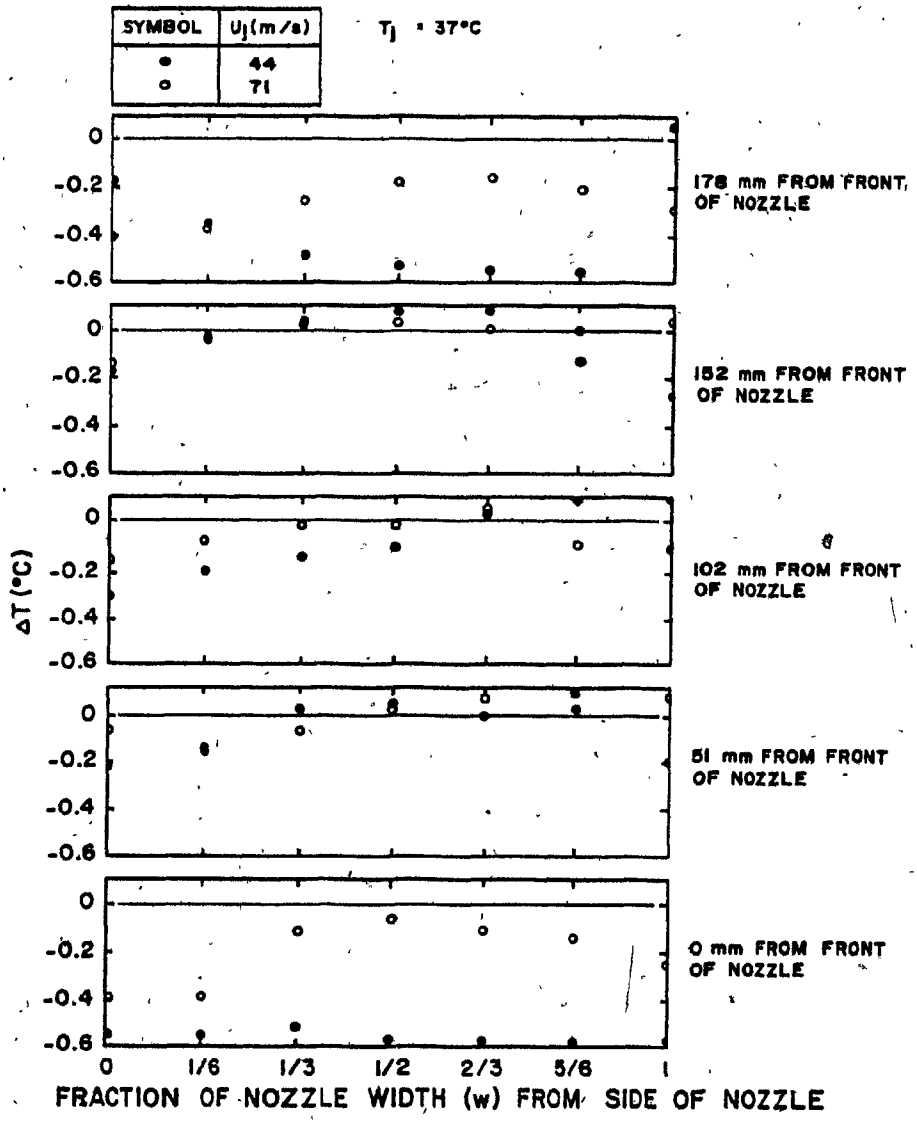


FIGURE 3.18. Temperature distribution in the nozzle of the cooling jet

In interpretation of these results, especially the occurrence of negative values of $T_s - T_j$, it must be appreciated that the experimental impingement surface in this case is not adiabatic. Specifically, as a 37°C jet impinges on an uninsulated surface in an ambient temperature room it is evident that the steady-state condition is not zero convective heat transfer to an adiabatic impingement surface but rather, a small convective heat transfer from the jet to the surface just sufficient to balance the transfer of heat from the impingement surface to the room by conduction from the impingement drum to the associated equipment and eventually by convection to the room. Because of the high rates of impingement heat transfer, the steady-state temperature assumed by the surface may approach the adiabatic recovery temperature but will always be somewhat less than that due to heat loss to the environment. This heat loss is sufficiently large that, for the lower velocity cases, the lower rates of convective heat transfer from the jet allow T_s to be less than T_j. The fact that for the bottom jet a minimum occurs in the T_s profile is another reflection of the convective heat transfer to a non-adiabatic impingement surface. The origin of this minimum in T_s profile is the corresponding minimum in heat transfer coefficient for this nozzle (but not for the top nozzle which determines Figure 3.19) as will be documented subsequently in Chapter 4.

Although interpretation of Figures 3.19 and 3.20 is complicated by these factors, the relevant conclusion is that the temperature driving force $|T_j - T_s|$ during actual heat transfer

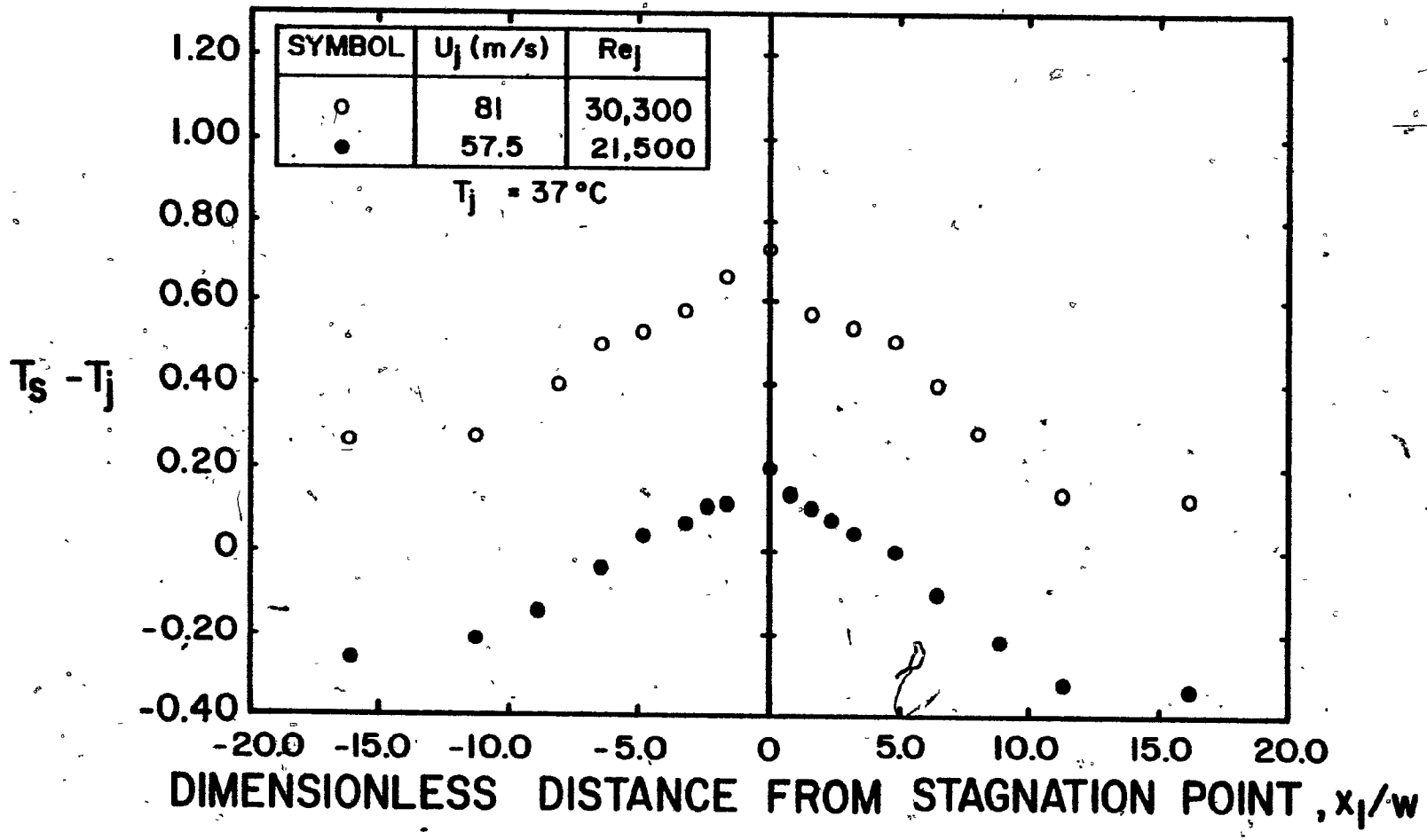


FIGURE 3.19. Adiabatic wall temperature effect for the heating jet

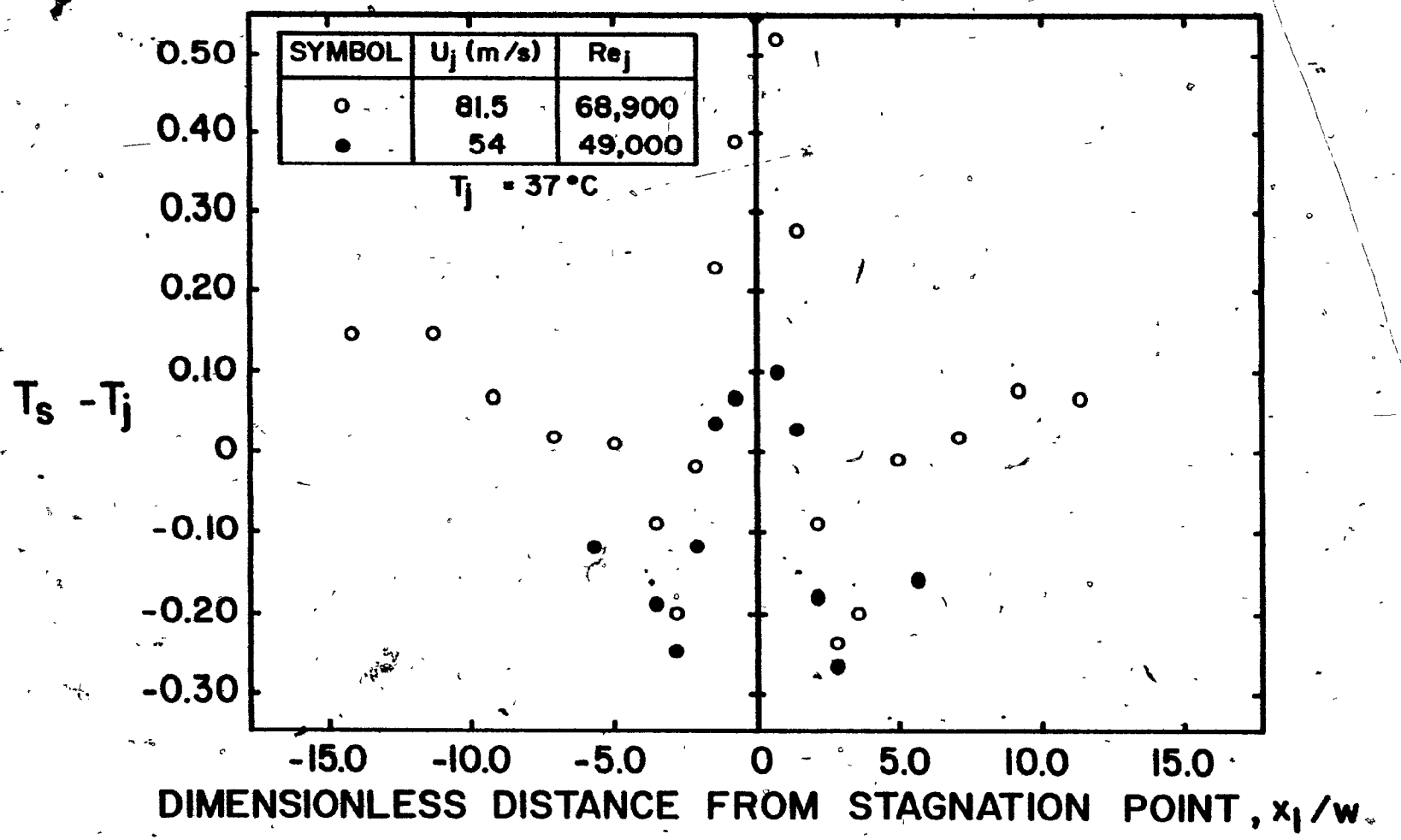


FIGURE 3.20. Adiabatic wall temperature effect for the cooling jet

experiments is over 30 times larger than the values shown in Figures 3.19 and 3.20 for $T_s - T_j$ at the stagnation point. The results of these tests thus establish that the heat transfer driving force may for the present study be taken simply as the temperature difference between the jet at the nozzle exit (T_j) and the impingement surface temperature measured by the sensor at each circumferential position during a heat transfer experiment.

3.5.4 Temperature Measurement at the Back of the Heat Flux Sensor

Temperature of the back of the sensor is measured with three chromel-constantan thermocouples glued to the pyroceram surface with a high thermal conductivity epoxy adhesive. The junctions are located at the center and at 30 mm on either side. During initial testing of the SIMTEST apparatus the temperature of the back of the sensor as indicated by the average temperature from the three thermocouples was $1^{\circ}-2^{\circ}C$ lower than that at the impingement surface of the sensor as measured with the gold film resistance thermometer. The possibility that the difference in temperature indicated between the two sides of the sensor could be due to radial heat losses was eliminated as insulating the back of the sensor with plastic foam had no influence on the apparent $1^{\circ}-2^{\circ}C$ temperature difference between the two sides.

It was finally established that the indicated lower temperature at the back was caused by the temperature difference be-

tween in- and output connections of the slip ring assembly. A schematic diagram of the temperature measurement at the back of the sensor is shown in Figure 3.21. It may be shown that the measured voltage is given by:

$$V = E_{\text{chromel-co}(T_1-T_4)} - E_{\text{chromel-co}(T_2-T_3)} \qquad (3.18)$$

resulting in underestimation of T_4 since during operation T_2 inside the shaft is higher than T_3 in the room. This analysis was verified by measuring T_2 with a calibrated thermistor to eliminate the thermocouple effect over the slip ring assembly. The ture difference between the corrected temperature at the back of sensor and the temperature measured by the gold film was found to be less than 0.15°C. The thermistor was disconnected for further experiments because the essential instrumentation required 12 slip ring connections (2 connections for the heat flux sensor, 6 for the three thermocouples on the back of the sensor, and 4 for the pressure transducer). Only 13 slip rings were available of the 14 slip ring assembly, one slip ring being not connected. The absolute values of temperatures at the back were used only before operation of the SIMTEST apparatus, when $T_2 = T_3$, for checking the output of the heat flux sensor.

3.5.5 Elimination of Axial Heat Conduction Along the Impingement Cylinder

The cylindrical impingement surface assumes a steady temperature, typically in the range 50°-70°C, i.e. intermediate between those of the "cold" (about 40°C) and hot jet. With the

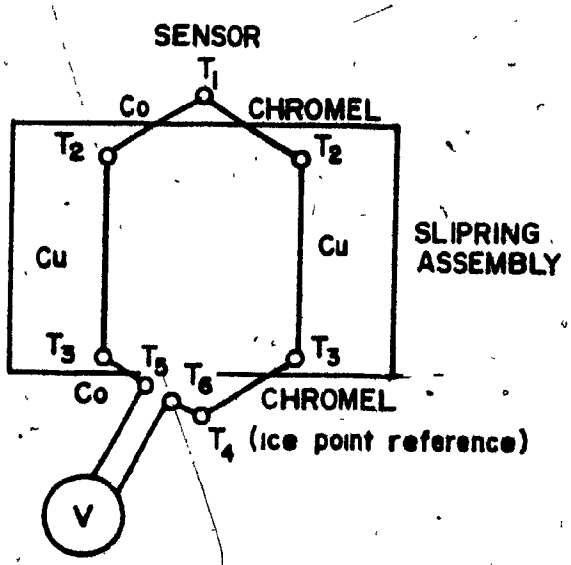


FIGURE 3.21. Electrical circuit for temperature measurement at back of sensor

end plates of the impingement cylinder exposed to ambient air, there would consequently be an axial heat loss. Corresponding to such an external heat loss there would be an outward axial heat conduction to each end of the impingement cylinder, such conduction being reflected by a maximum in any axial temperature profile along the drum. As the experimental technique for obtaining convective heat transfer coefficients requires that the impingement cylinder be adiabatic, it is not acceptable to have such an axial heat conduction. The method used to eliminate axial heat conduction was to heat both impingement cylinder end plates. As this was conveniently done by radiant heating with four 250 W. infrared lamps, the end plates were first blackened. The criterion for adjusting power input to the lamps is to obtain equal temperature readings for the thermocouples at three axial positions along the back of the sensor.

To investigate the influence on calculated heat flux of heating the axial end plates the following experiments were performed: Run 221, no heating; Run 222, optimum heating; Run 223, excessive heating with both lamps at maximum power. The conditions are summarized below.

Run	Lamp Voltage$_R$	Lamp Voltage$_L$	ΔT_R °C	ΔT_L °C	ΔT_{ave} °C
221	0	0	0.02	-0.41	-0.2
222	30	100	0.03	0.03	0.0
223	105	105	0.50	0.06	0.3

Lamp Voltage: Subscripts R and L denote right and left end of the drum (right end carries the suction connection; left end, the drive shaft).

ΔT: Subscripts R and L denote ΔT from center to right and left end of sensor.

The fact that for Run 221 the ΔT from the center to right end of the sensor is positive simply indicates that the maximum in this axial temperature profile lies between the right end of the sensor and the right end of the impingement cylinder. In other words, although in Run 221 the drum is losing heat axially from both ends, the heat loss from the left end (aided by heat conduction along the large shaft on that side) exceeds that from the right end.

The small but significant influence of power input to the lamps on Nu_j distribution is shown in Figures 3.22 and 3.23. The average heat transfer over fixed equal distances on both sides of the stagnation line, in the form of $\overline{Nu}_j$ for both jets is given in Table 3.2. The calculated average heat transfer entering the drum surface on the heating side is equal to the calculated average heat flux on the cooling side because of the adiabatic boundary condition at the back of the sensor in the calculation procedure. This condition is only fulfilled for Run 222 as indicated by the small axial temperature gradients at the back of the sensor. The average heat transfer on the heating side of the drum in Run 222, extending over a half-circumferential distance of 0.72 m is equal to 374 Watt or 2560 W/m^2 for the heat flux to the top half-circumferential section (surface area is 0.146 m^2). The heat loss q_ℓ in Run 221 can be estimated from the average heat transfer on the heating side for Run 222 and the temperature driving forces on the heating and cooling side for Runs 221 and 222.

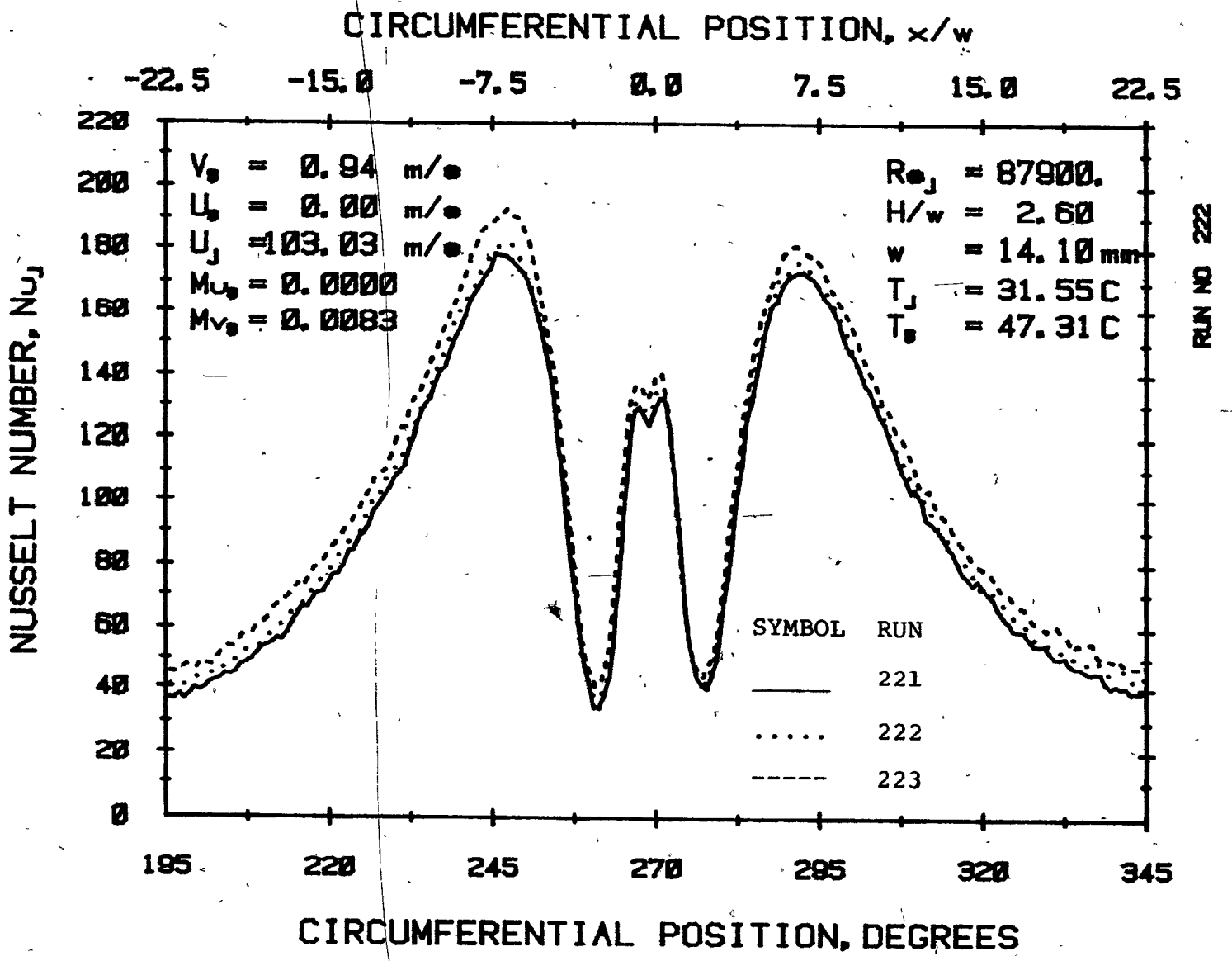


FIGURE 3.22. Effect of power input of heating lamps on heat transfer distribution for the heating jet

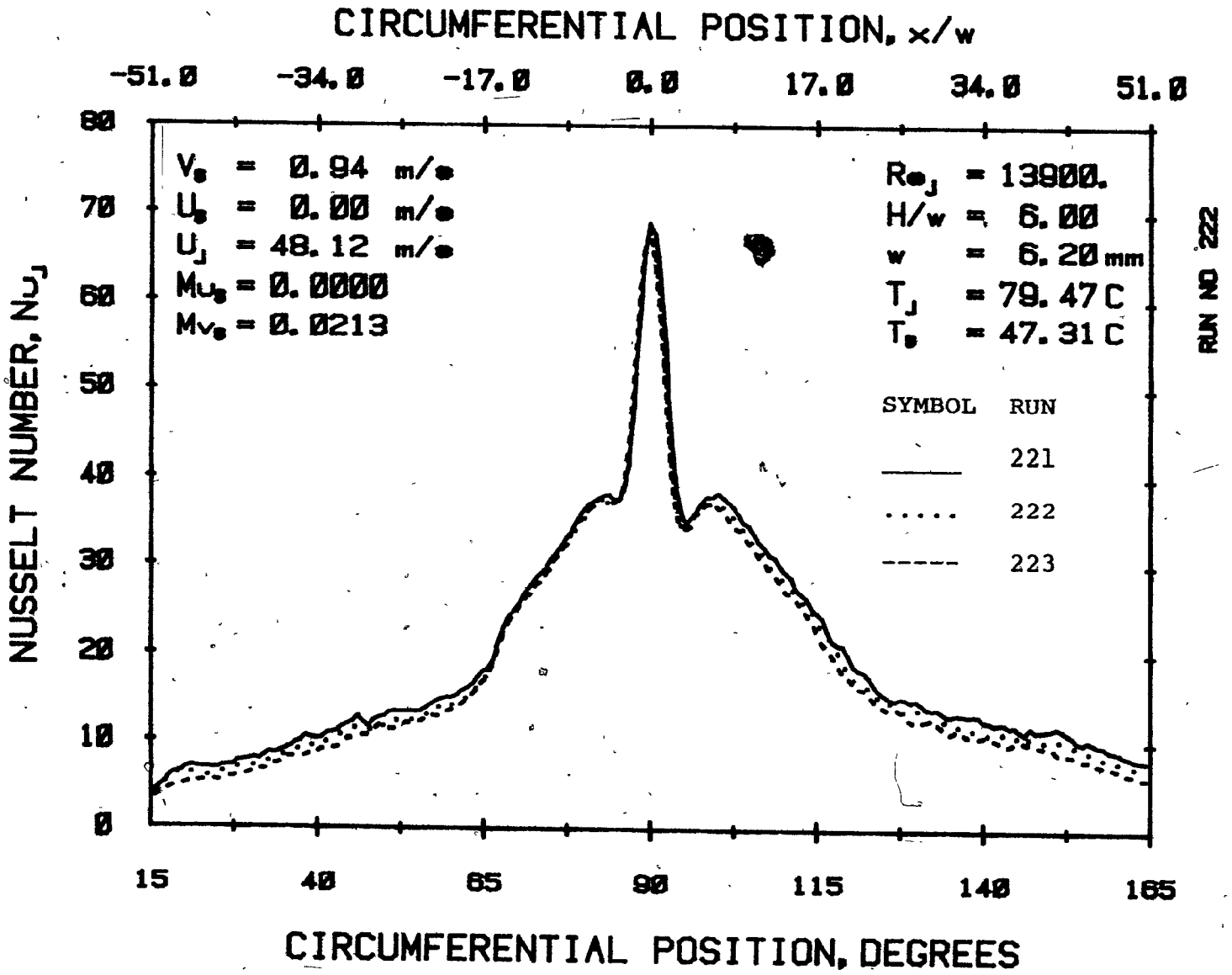


FIGURE 3.23. Effect of power input of heating lamps on heat transfer distribution for the cooling jet

$$q_{\text{heat loss}} = 374\left[\frac{(\Delta T)_{222,t}}{(\Delta T)_{221,t}} - \frac{(\Delta T)_{222,b}}{(\Delta T)_{221,b}}\right] \qquad (3.19)$$

with $(\Delta T)_{222,t}$ and $(\Delta T)_{222,b}$ being $|T_j - T_s|$ for Run 222 at respectively the top and bottom section of the SIMTEST apparatus (see Appendix 16)

or $$q_{\text{heat loss}} = 374\left(\frac{34.2}{33.2} - \frac{14.1}{15.1}\right) = 36 \text{ Watt}$$

The heat transfer loss of 36 W in Run 221 amounts to a heat flux loss of $36/0.308 = 117$ W/m^2 when using the total circumferential heat transfer surface of 0.308 m^2. This is only 4.6% of the total average heat flux on either side of the drum. Expressed nondimensionally as Nu_j, the heat flux loss is equal to 0.71 and -4.4 for respectively the top and bottom side of the drum, and is almost equal to the difference in Nu_{oj} between Runs 222 and 221 for respectively the top and bottom jet (see Table 3.2). Similarly the gain in heat flux for the case of excessive heating of the end plates in Run 223 is calculated as 85 W/m^2 or only 3.3% of the total average heat flux on either side of the drum. In terms of Nu_j the heat gain in Run 223 amounts to 0.55 and -2.9 for respectively the top and bottom side of the drum. From comparison of these values with average temperature difference at the back of the sensor it can be concluded that an average temperature difference at the back of the sensor of $\pm 0.1^{\circ}$C corresponds to a loss in heat flux of roughly ± 50 W/m^2.

For convenience in operation, heating lamp power was set by reference to temperature of the blackened end plates which

TABLE 3.2. Effect of Power Input of Heating Lamps on Local and Average Heat Transfer

Run	Re_j	M_{Vs}	T_j	$T_j - T_s$ (°C)	Nu_{oj}	$\overline{Nu}_j$ 12.5°	$\overline{Nu}_j$ 25°	$\overline{Nu}_j$ 37.5°	$\overline{Nu}_j$ 50°	$\overline{Nu}_j$ 75°	Nu_{jm}
221	87800	0.008	31.3	14.1	131.6	86.1	123.1	133.7	125.7	103.5	186.5
222	87800	0.008	31.7	15.1	127.1	80.4	117.1	127.4	119.5	97.7	178.5
223	87900	0.008	31.6	15.7	123.1	77.5	113.6	125.0	116.9	95.0	175.5
221	13900	0.022	79.6	34.2	63.7	40.3	33.4	27.2	23.1	17.8	35.9
222	13900	0.021	80.0	33.2	64.6	40.3	33.7	27.6	23.5	18.4	35.6
223	13900	0.021	79.5	32.2	65.6	41.0	34.3	28.3	24.4	19.3	36.7

was monitored with an IR pyrometer (Siemens Model Ardonox).

3.5.6 Symmetry of the Flow and Two Dimensionality in the Wall Jet Region

One design objective for the SIMTEST apparatus was that over the total axial dimension of 203 mm (the nozzle and impingement surface length) there should be a region of appreciably axial extent over which the confined annular flow after impingement would be free of axial end effects. The choice of a heat flux sensor filament 70 mm long, located centrally in a 203 mm long impingement cylinder, implies that significant end effects which do not extend more than two-thirds the distance from the ends to the axial midplane do not disturb the flow region scanned by the sensor. Another design objective was that the apparatus should be sufficiently symmetric that, in the absence of impingement surface motion, the nozzle flow would divide equally, half exiting through each exhaust port.

The symmetry of flow around the drum was checked with the drum stationary and without heating the flow to the top nozzle, by comparing the velocity profiles in the exit ducts at 0.09 m downstream from where the square exit duct intersects the curved confinement hood. Traverses were made at the axial midplane, i.e. at 203/2 mm from each end, and at 63.5 mm on both sides of the center (or 38 mm from the side plates). The location of the off-center traverses should be viewed relative to the heat flux sensor filament which extends only 35 mm on either side of the center (or starts 66.5 mm from either end plate). These exit

port profiles were taken with jet Reynolds numbers of 30900 and 38700 at the top and bottom nozzles. The velocity profiles in the top and bottom exit ducts, measured with a pitot tube and inclined manometer and shown respectively in Figures 3.24 and 3.25, prove that the flow is reasonably symmetric in both the upper and lower half of the apparatus. The magnitude of the reversed flow near the outer wall of the exit ducts is uncertain since a pitot tube is not appropriate for such a flow. The combined mass flowrates through the exit ducts (0.12 kg/s and 0.14 kg/s for respectively the top and bottom side) are in good agreement with the corresponding nozzle flowrates (respectively 0.118 and 0.148 kg/s), considering the uncertainties in calculation of mass flowrate in the exit ducts.

The two dimensionality of the confined annular flow was checked in the wall jet region of the upper half of the apparatus with the drum stationary. Profiles of streamwise velocity were measured in a radial plane located at about 105 mm (17w, 2.8H or 25°) along the impingement surface from the stagnation line. This check was made with a jet Reynolds number of 32900 at the top nozzle, and without heating this air. The three axial positions are again at the center and at 38 mm from each side plate. The three plots in Figure 3.26 appear to show a maximum streamwise velocity at the impingement surface whereas in fact this velocity is zero. However numerous investigators of the wall jet region, most recently Obot (1981) have shown that the maximum wall jet velocity lies extremely close to the impingement surface. Also it may be noted that these plots display the

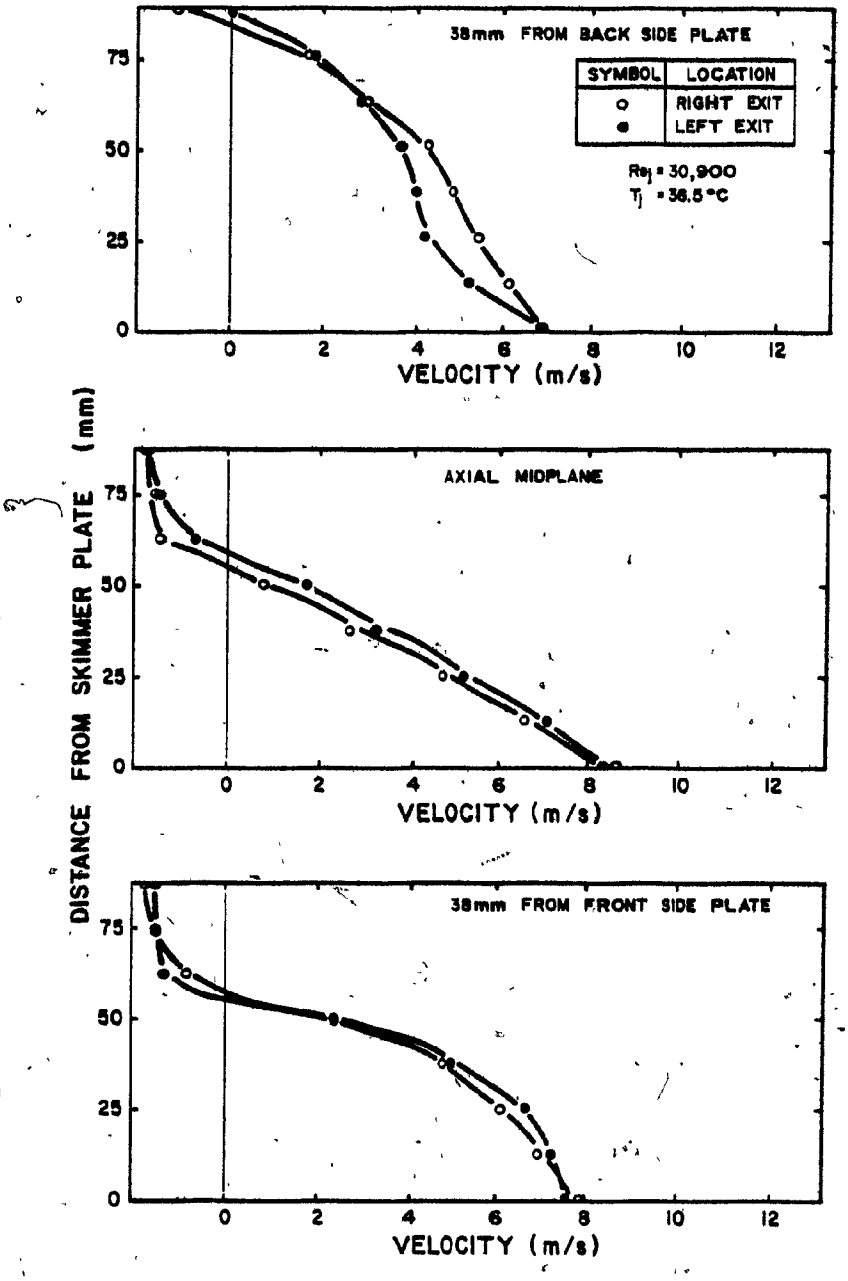


FIGURE 3.24. Velocity distribution in heating jet exit ducts

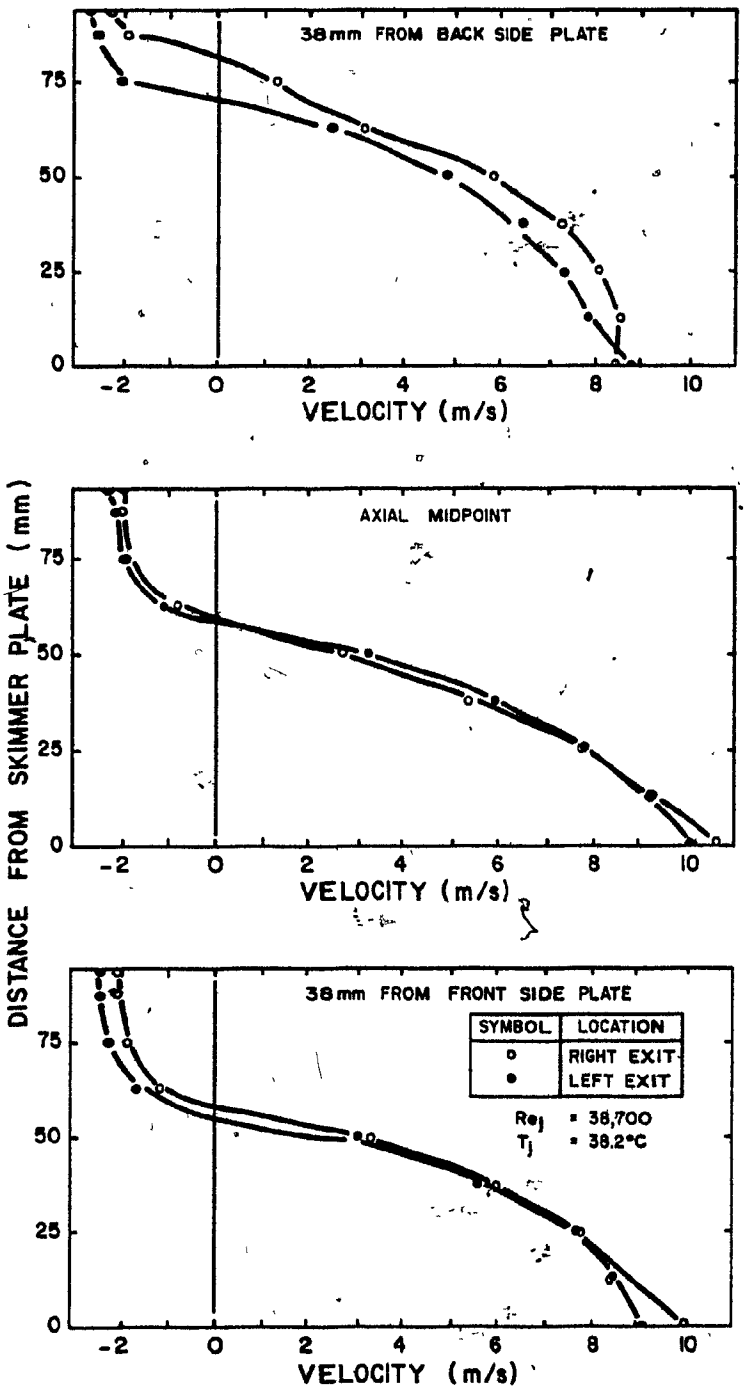


FIGURE 3.25. Velocity distribution in cooling jet exit ducts

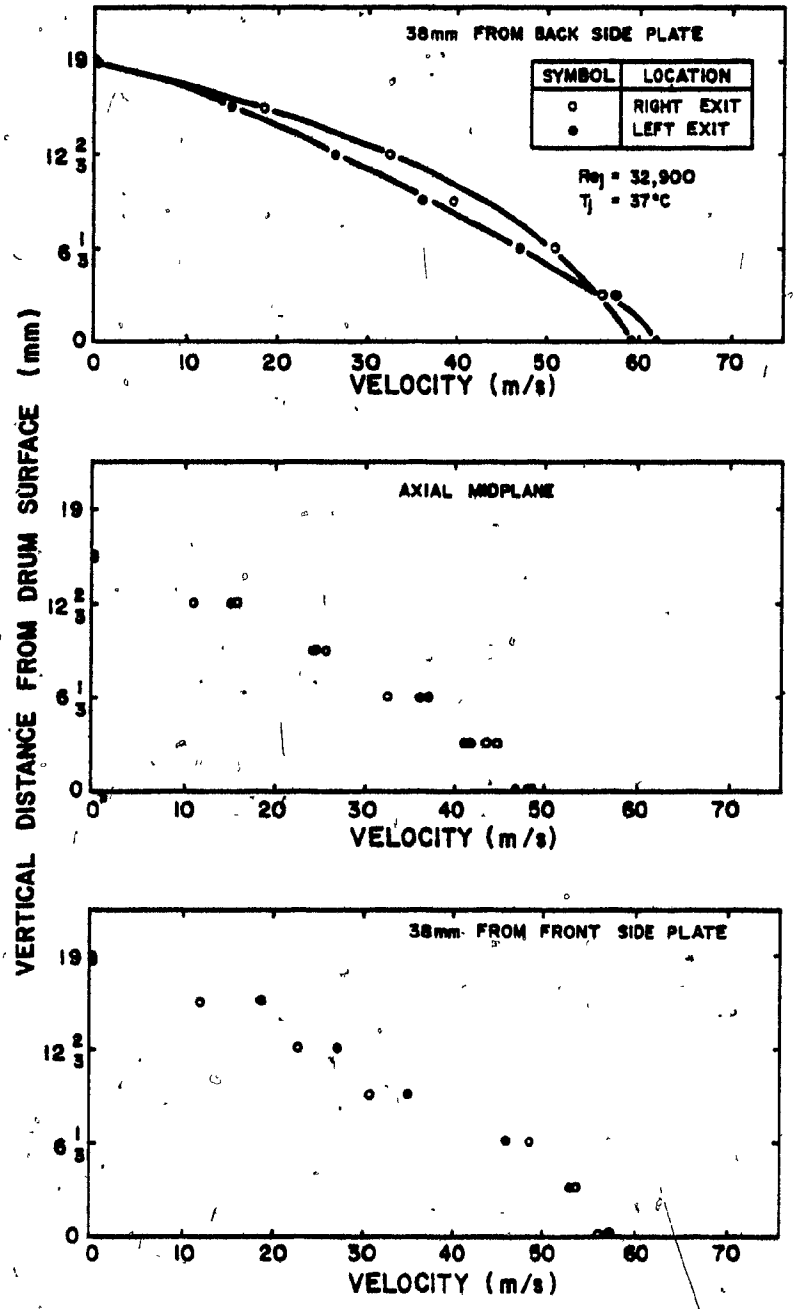


FIGURE 3.26. Velocity distribution in annular confinement section for heating jet

streamwise flow field for only half-way from the impingement to the confinement surface. As is well documented by computer simulations of the flow field obtained in Chapter 2, the region adjacent to the confinement surface contains a recirculating flow for which the mean velocity is towards the jet. The three pairs of profiles of streamwise velocity in the wall jet region displayed in Figure 3.26 show that the distribution in the axial direction is symmetrical. Moreover, at each position from the impingement surface, the distribution in the axial direction has a minimum at the axial midplane. Comparison of flowrates obtained by integrating velocity profiles at the three axial positions with half of the flowrate from the top nozzle leads to estimates for the amount of entrainment of approximately 160, 60 and 140% times half the jet flow at the nozzle at, respectively, the back, axial midplane and front traverse.

The high velocities near the side plates can be explained by the presence of the recirculating flow, which develops in the stagnation region adjacent to the side plates as a result of the large adverse pressure gradient in the corner of the stagnation region formed by the side plates and the drum. The jet flow is displaced from the side plates by this recirculating flow region, leading to higher velocities between the axial midplane and the side plates than at the axial midplane, as is evident on Figure 3.26. The growth of the vortex in the curved corners formed by the side plates and the drum surface causes the wall jet to be displaced even further from the side plates and thus the entrainment rates of the displaced wall jet are increased. These fea-

tures of this complex flow field explain the previously noted higher velocities and entrainment away from the midplane in the annular curved duct.

An extreme example of this phenomenon is given by Russell and Hatton (123) who used a slot jet with an aspect ratio of only 6 (w = 25.4 mm, nozzle length 152.4 mm) impinging on a flat surface at a nondimensional spacing of H/w = 31.5. The whole flow was restrained between two side plates which extended from the impingement surface to the nozzle. By taking two velocity profiles at 90° to each other, both at the midplane (i.e. at 152.4/2 mm from the side plates), one profile perpendicular to the impingement surface at 0.4H from the nozzle centerline to give the wall jet velocity profile, the other profile parallel to and at an unstated distance from the impingement surface, they found that these two velocity profiles corresponded to an outflow 20% greater than inflow. They failed to see the significance of their measurements, which in reality reflect the presence of a component of the flow directed away from the side plates and toward the midplane because of the existence of a recirculating flow adjacent to the side plates, as has been described above. The inappropriately small aspect ratio of the nozzle and the large nozzle-to-plate spacing in the work of Russell and Hatton (123) amplify considerably the effect responsible for the larger off-center velocity profiles displayed in Figure 3.26.

Two other effects complicating the flow near the side plates of the present apparatus are the secondary flow induced by the gradients in the Reynolds stresses in the cross-sectional plane

of a square duct (Brundrett and Baines (64)), and the increased turbulence production in convex curved flows, theoretically explained and experimentally documented by Irwin and Smith (67). Improvement of the two dimensionality of the flow would require use of either a longer impingement cylinder or of side plates inclined outwards and thus leading to an annular flow field with corners smaller than 90^{o} formed by the side plates and drum surface. The angle of inclination should be adjusted experimentally to contain the vortex as much as possible in the corner, so that the annular flow remains two-dimensional over almost the entire axial length of the nozzle.

In this respect it is worthwhile noting the study of Guittan and Newman (51) on self-preserving turbulent wall jets over convex surfaces, a study which documented a similar secondary flow in the corner formed by the side plates and convex surface. The origin of their secondary flow is of course different from that of the present work. Guittan and Newman also give an elegant solution to this problem by using several pairs of side plates, which cut off the boundary layer formed immediately upstream on another pair of more widely spaced end plates.

In the present study it is however believed that the central flow region, i.e. 35 mm on either side of the axial midplane scanned by the gold film is in fact two-dimensional in the impingement and greater part of the wall jet region. This statement is confirmed by comparing the velocity profile of the wall jet region at the axial midplane in Figure 3.26, with the maximum wall jet velocity (U_m) and half-width ($\delta_{.5}$) of the wall jet,

obtained from application to a plane turbulent impinging jet of the theoretical analysis of Meyers, Schauer and Eustis (101) for a plane turbulent wall jet. (No comparison can be made with experimental impinging jet data, since for small values of H/w there is no data available from the literature.) The application noted above is made by considering the present wall jet to be formed by a jet issuing at an average velocity U_j from a nozzle of width $\frac{1}{2}w$ located on the impingement surface a distance H upstream of the stagnation line. This transformation is of course only admissible when the distance downstream from the stagnation line (x_1) is significantly larger than H. The transformed equations are:

$$\frac{U_m}{U_j} = \frac{1}{\sqrt{1 + 0.381\left[\left(\frac{x_1}{w} + \frac{H}{w}\right)/3.5 - 1\right]}} \tag{3.20}$$

and

$$\frac{\delta_{.5}}{w} = \frac{1.025}{\left(\frac{U_m}{U_j}\right)^2 \left(\frac{Re_j}{2}\right)^{0.2}}\left[0.650\left(\frac{Re_j}{2}\right)^{0.2} - 1 + 0.474\left(\frac{U_m}{U_j}\right)^{0.2}\right] \tag{3.21}$$

Insertion of $Re_j = 32900$, $H/w = 6$ and $x_1/w = 17$ gives $U_m/U_j = 0.566$ and $\delta_{.5}/w = 1.81$, which compare closely with experimental values of respectively 0.55 and 1.6 obtained from the velocity profile at the axial midplane in Figure 3.26.

3.5.7. Characterization of the Porous Stainless Steel

The porous stainless steel cylinder is made from two flat sheets of sintered 316 stainless steel (Pall Canada Ltd., Montreal). The two sheets are rolled into two half-cylinders and joined by silver soldering. Some relevant properties are given in Table 3.3.

TABLE 3.3. Properties of the Porous Stainless Steel

Rockwell B Hardness	Mean Pore Size (μm)	Roughness (μm rms)	Thermal Conductivity (W/m/K)	Density (kg/m^3)	Permeability (m)
83	5	7	3.2	4800	0.112×10^{-9}

All properties were measured for flat sheets except for the permeability which was determined with the porous cylinder.

The permeability results are shown in Figure 3.27. The pressure drop across the cylinder wall was measured with the pressure transducer. The suction velocity for the available surface area of the cylinder was calculated from the flowrate through the orifice meter in the suction line. The permeability

$$K = \mu U_s / \Delta p \qquad (3.22)$$

measured for the entire surface is 0.112×10^{-9} m, a value lower

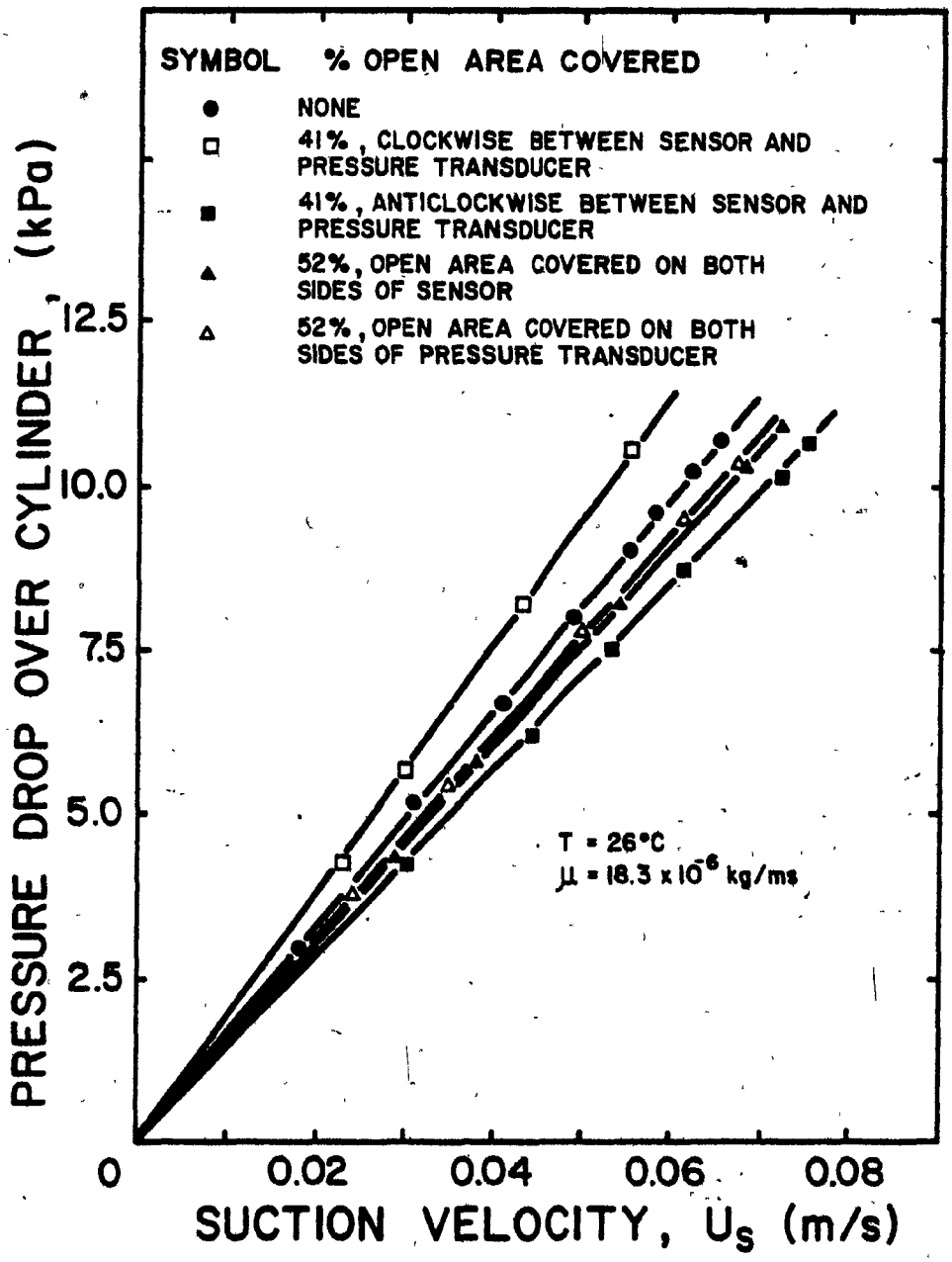


FIGURE 3.27. Uniformity in permeability of porous cylinder

than that given by the manufacturer, 0.32×10^{-9} m, probably due to the rolling of the sheets. Various parts of the drum surface were covered with thin plastic sheet to check the uniformity of permeability. Permeability variations of ±15% are found. The data are consistent, as the permeability for the uncovered surface is between that obtained with either 41% of the surface blocked.

The porous stainless steel impingement surface is considered hydraulically smooth because the rms value of the surface roughness, 7 μm, is smaller than the estimated thickness of the laminar sublayer in the impingement region, even at the highest jet velocities used in this work for the top jet. The thickness of the laminar sublayer in the impingement region was estimated from the shear stress data of Baines and Keffer (7), using the condition for the sublayer thickness of

$$\delta_s = \frac{5\nu}{\sqrt{\frac{\tau_w}{\rho}}} \qquad (3.23)$$

Baines and Keffer measured a maximum friction velocity $\sqrt{\frac{\tau_w}{\rho}}$ of 6.5 m/s at U_j = 53 m/s and H/w = 2.4, giving in a sublayer thickness of 14 μm, i.e. twice the rms roughness of the porous stainless impingement surface.

3.6 Effect of Operating Procedures on Nusselt Number Profiles

3.6.1 Number of Rotations Averaged for a Profile

The local heat flux at a fixed circumferential position

fluctuates with time. These fluctuations are mainly due to the turbulent character of the flow and to some extent to the slower oscillations in the hot jet temperature (oscillations of $\pm 1^{o}C$ with a frequency of 0.1 to 0.05 s^{-1}). The temporal fluctuations can be eliminated by averaging over a number of rotations the local heat flux measured at a specific location since the turbulent flow is steady when averaged over a longer period of time or when averaged over a large number of time instants (ensemble averaging). The influence on the Nusselt distribution of the number of rotations used for averaging is shown in Figures 3.28(a), (b), (c) and (d) for the bottom jet. With increasing number of rotations (1-50) the Nu distribution becomes smoother, while keeping exactly the same basic shape and same position. The latter is clearly shown in Table 3.4 which summarizes the average Nusselt numbers as a function of the number of rotations used for averaging. From the small difference between the distributions obtained for averaging over 25 and 50 rotations, it was concluded that averaging over 50 rotations was sufficient to eliminate most of the temporal fluctuations while keeping computation time within reasonable limits. (Fifty rotations were also found to be sufficient for the averaging of the shear stress in the similar experimental arrangement of Baines and Keffer (7).) Therefore 50 rotations are used for averaging in the present study.

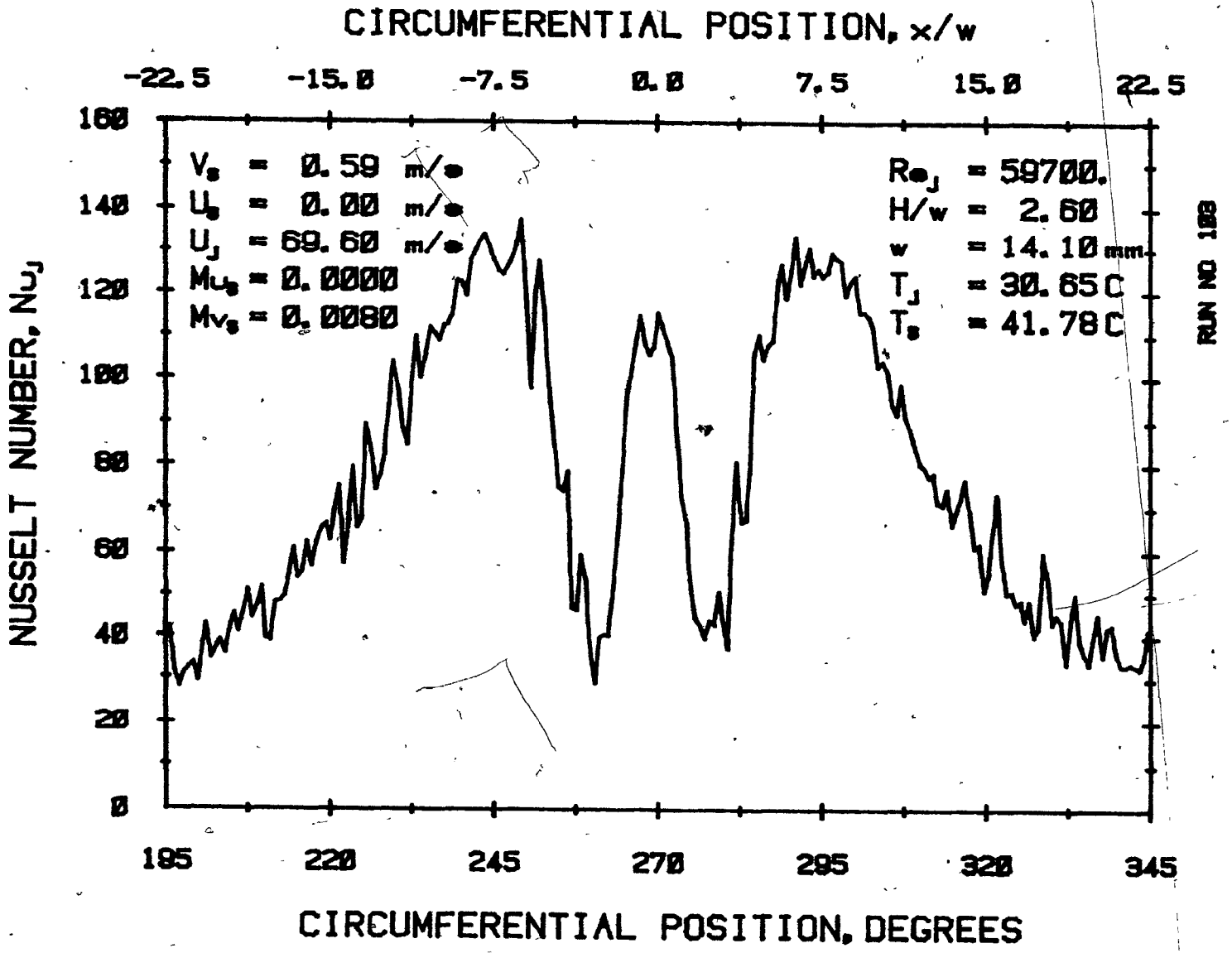


FIGURE 3.28a, Effect of number of rotations for averaging the heat transfer distribution: $N_R = 1$

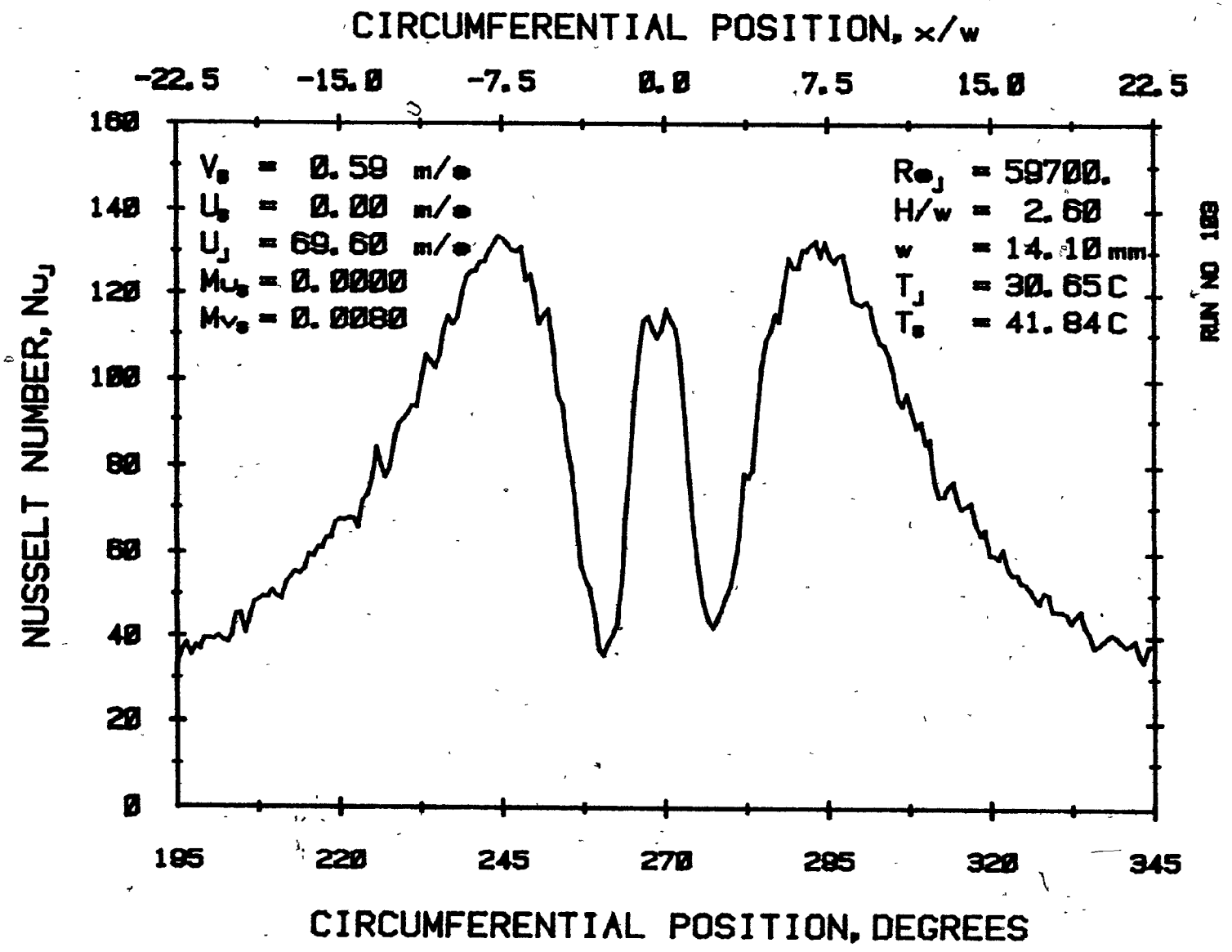


FIGURE 3.28b. Effect of number of rotations for averaging the heat transfer distribution: $N_R = 5$

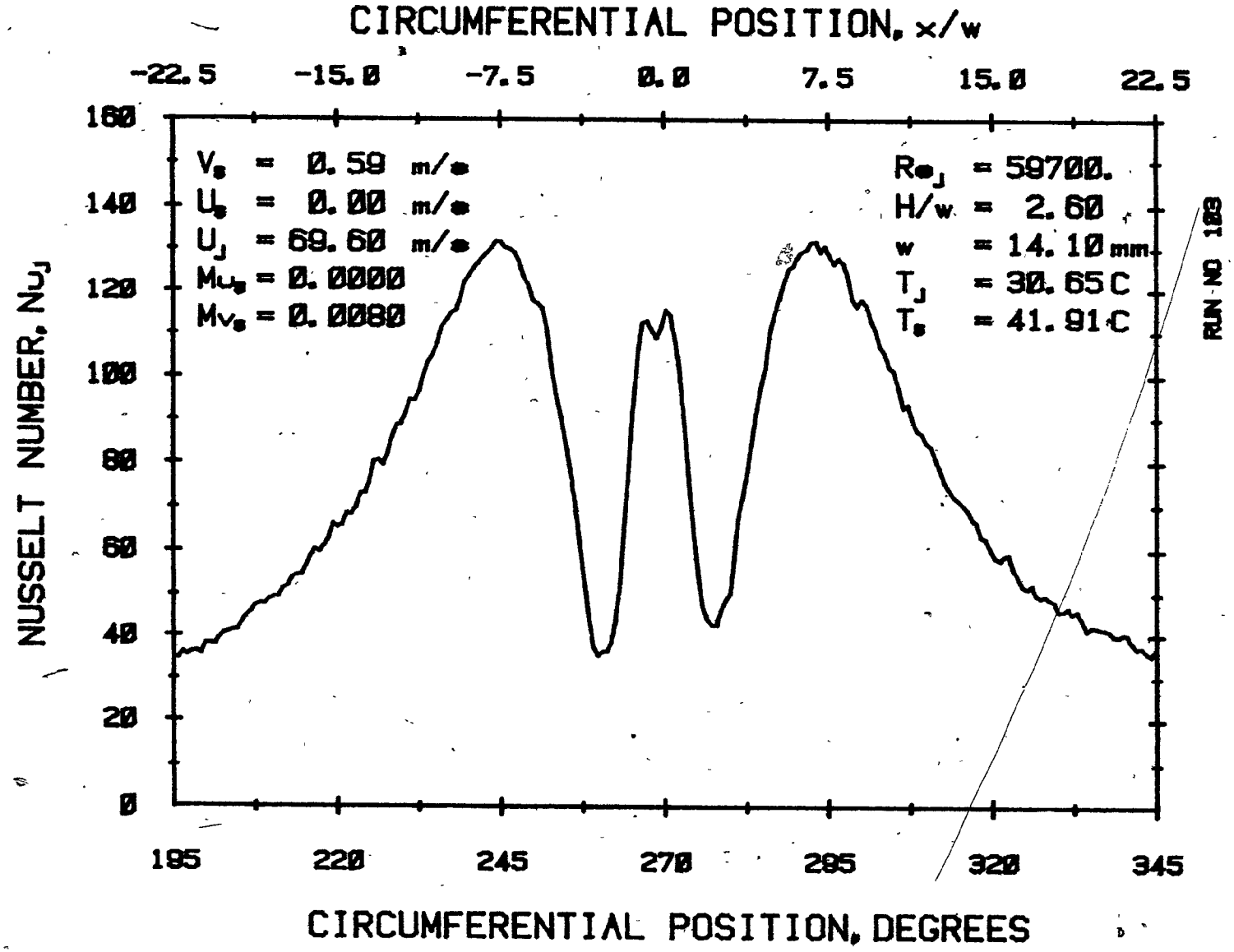


FIGURE 3.28c. Effect of number of rotations for averaging the heat transfer distribution : $N_R = 25$

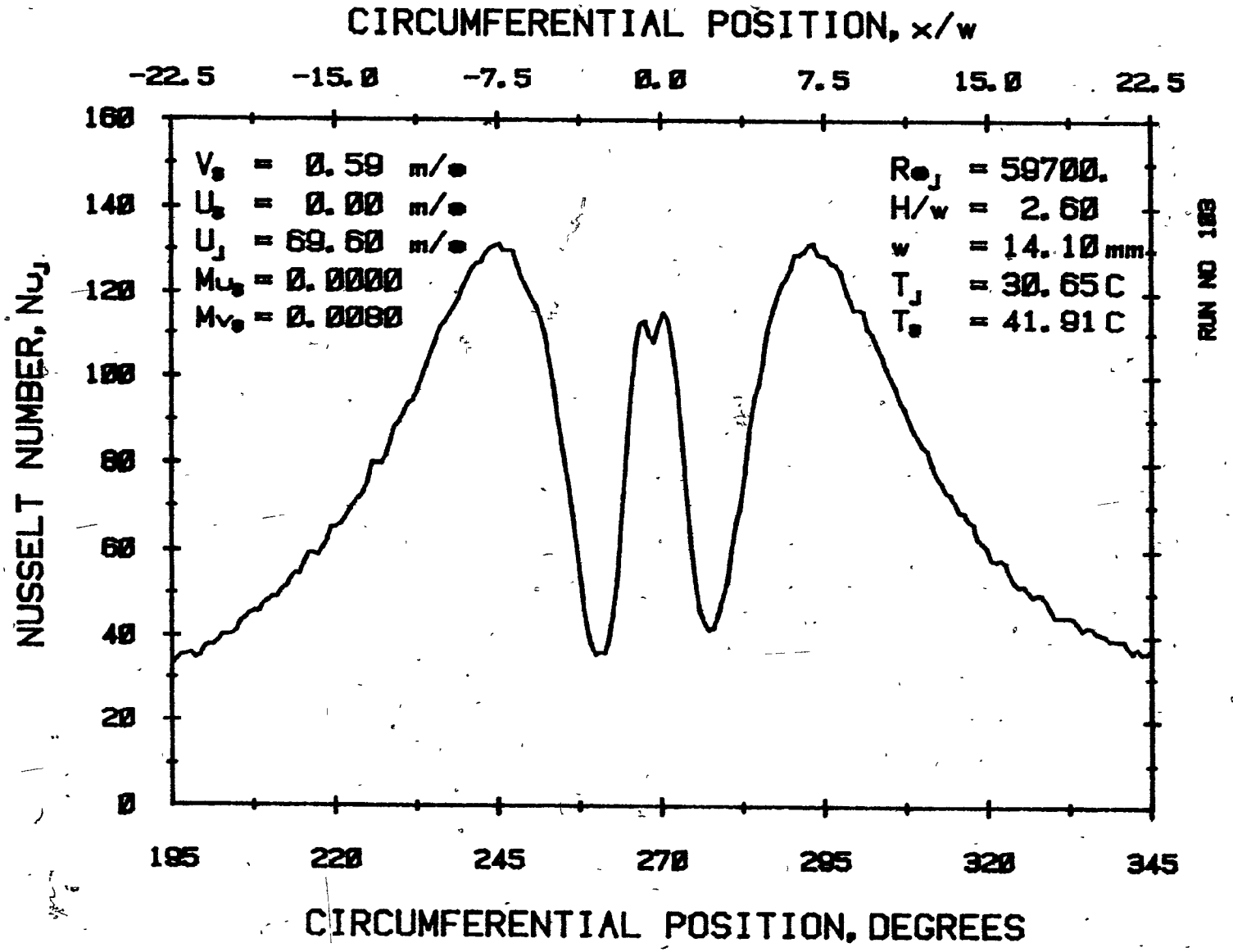


FIGURE 3.28d. Effect of number of rotations for averaging the heat transfer distribution: $N_R = 50$

TABLE 3.4. Effect on Average Nusselt Number for Cold Jet, $\overline{Nu}_j$ of Number of Rotations Averaged

Averaging Interval, degrees	Number of Rotations				
	1	5	10	25	50
150°	78.5	78.5	78.1	78.1	78.0
75°	99.7	99.6	99.4	99.3	99.3
50°	92.3	92.5	92.3	92.1	92.3
25°	76.8	76.5	76.4	76.2	76.3

3.6.2 Filtering of Noise from the Heat Flux Sensor Signal

As the fluctuating voltage from the heat flux sensor is conditioned by a low-pass filter before being digitized by the high speed ADC, care is required to avoid distortion or elimination of information in these two operations. The low-pass filter frequency was varied to establish experimentally the minimum frequency to obtain an undistorted low-noise heat flux signal. The results for a rotational speed of about 25 rpm and an ADC sampling frequency of 200 measurements per second are shown in Figure 3.29 for the bottom jet. The heat flux and angular position at the stagnation point as a function of the filter frequency are given in Table 3.5. The results with a filter frequency of 1000 and 300 Hz do not differ significantly. By decreasing the filter frequency below 300 Hz the heat flux distribution is displaced appreciably in the scanning direction. Filtering at 30 Hz introduces an error of about 5% in the heat flux amplitude. These effects are in agreement with the phase lag

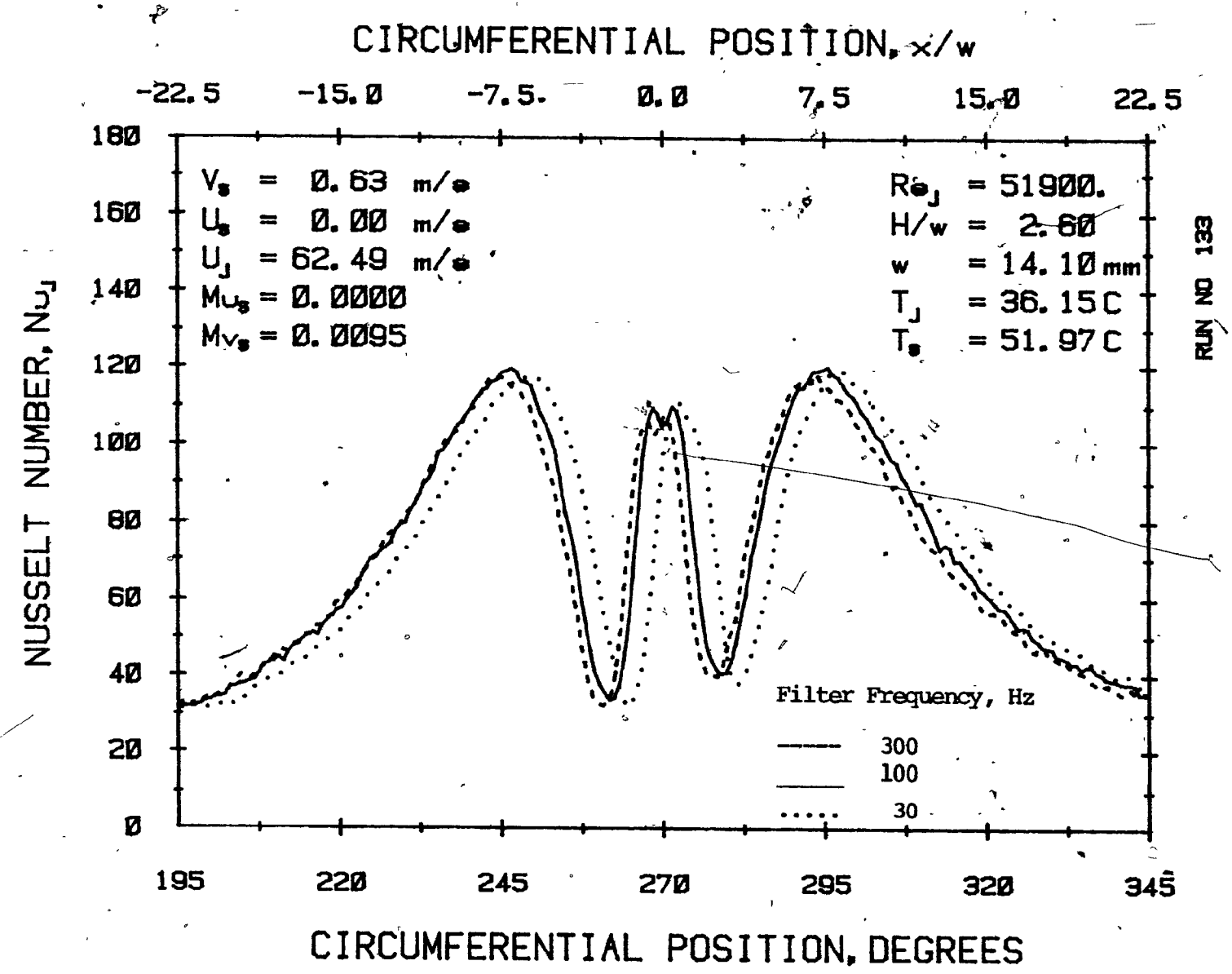


FIGURE 3.29. Effect of frequency of low-pass filter on the heat transfer distribution

and amplitude response of the filter when operating in the 4th order Butterworth response mode.

TABLE 3.5. Effect of Frequency of Filtering of Heat Flux Sensor Signal on Stagnation Point Measurement

Run Number*	Filter Flux Sensor Frequency (Hz)	Nu_{oj}	Position (degrees)
130	1000	102.3	270.4
132	300	100.5	271.0
131	100	101.1	271.7
133	30	107.7	274.0

It can be seen from Figure 3.29 that the small dip and two small maxima in the central heat transfer peak (frequency ~ 60 Hz) of the bottom jet disappear as expected with a filter frequency of 30 Hz. This observation illustrates that use of too low a frequency of noise filtering not only introduces errors in the magnitude and location of Nusselt number profiles but in addition eliminates significant information from the profiles.

Since the number of measurements per rotation was fixed at about 500 for all rotational speeds (cf. Section 3.6.3) it was concluded from the above results that the filter frequency should be larger than the ADC sampling frequency to obtain an essentially undistorted and undisplaced heat flux distribution, while removing most of the high frequency noise.

3.613 Number of Measurements to Define a Profile

The sampling frequency of the ADC was varied to establish experimentally the optimum number of measurements per rotation required to give a detailed and smooth heat flux distribution. The results for the cold jet are shown in Figures 3.30(a), (b) and (c). The average number of measurements per rotation are 239, 412 and 718 for respectively figures (a), (b) and (c). Each is a profile averaged for the standard 50 rotations. The filter was set at a frequency of 500 Hz for all three cases. The only difference between Figures 3.30(c) and (b) is that the profile obtained with 718 measurements per rotation is slightly more noisy than that with 412 measurements. However reduction in resolution to the lowest value, 239 measurements per revolution (Figure 3.30(a)), results in slight reductions in maxima, slight increases in minima due to poorer resolution, and moreover results in elimination of the two small maxima around a small minimum in the central heat transfer peak, features which are consistently present except when the noise filtering frequency is set excessively low (as documented in the previous section) or, as illustrated in the present section, when too few measurements per rotation are used.

From these results and similar results for the hot jet it was concluded that 500 measurements per rotation was roughly the optimum value to which the ADC sampling frequency should be matched.

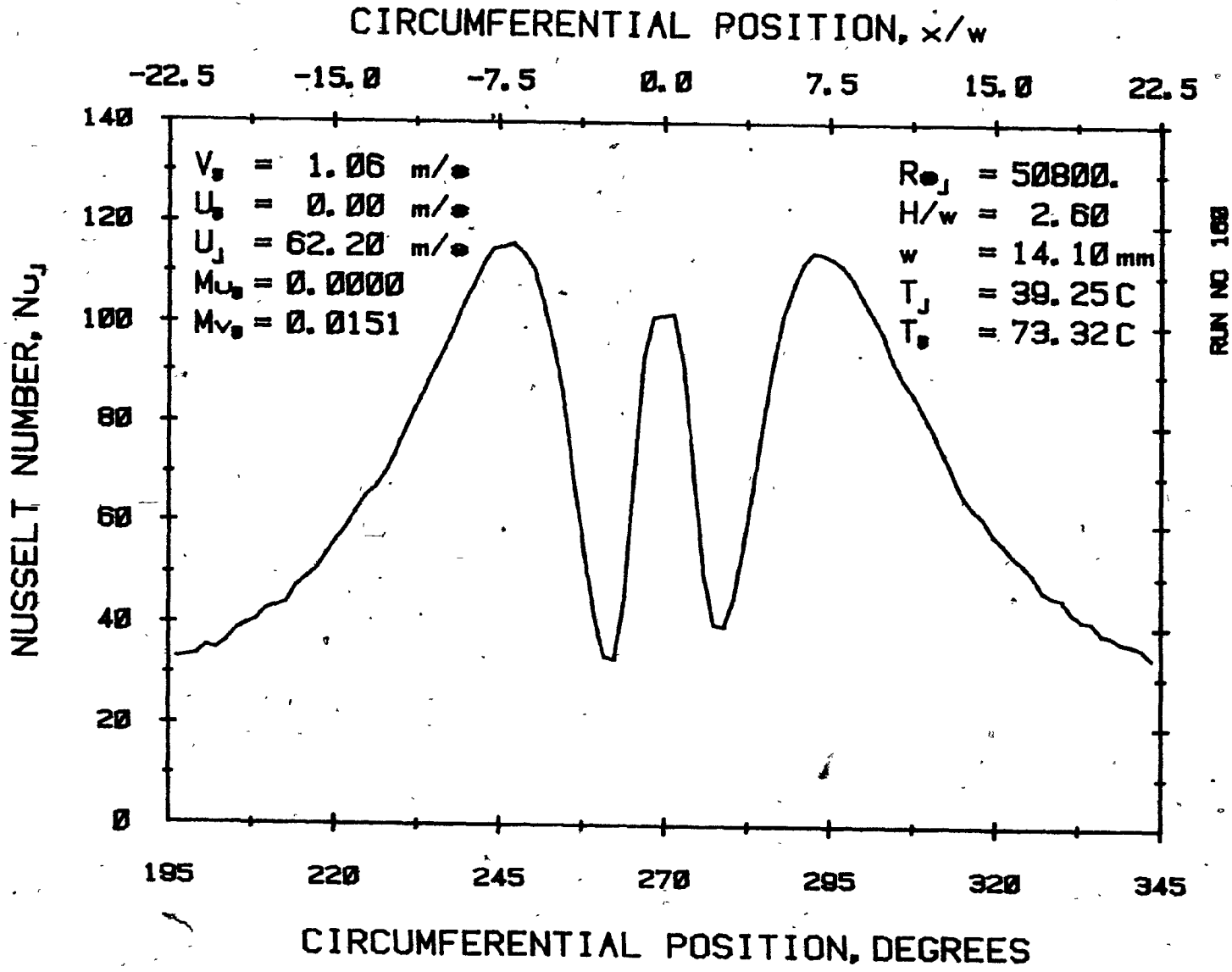


FIGURE 3.30a. Heat transfer distribution for the cooling jet at 239 measurements per rotation

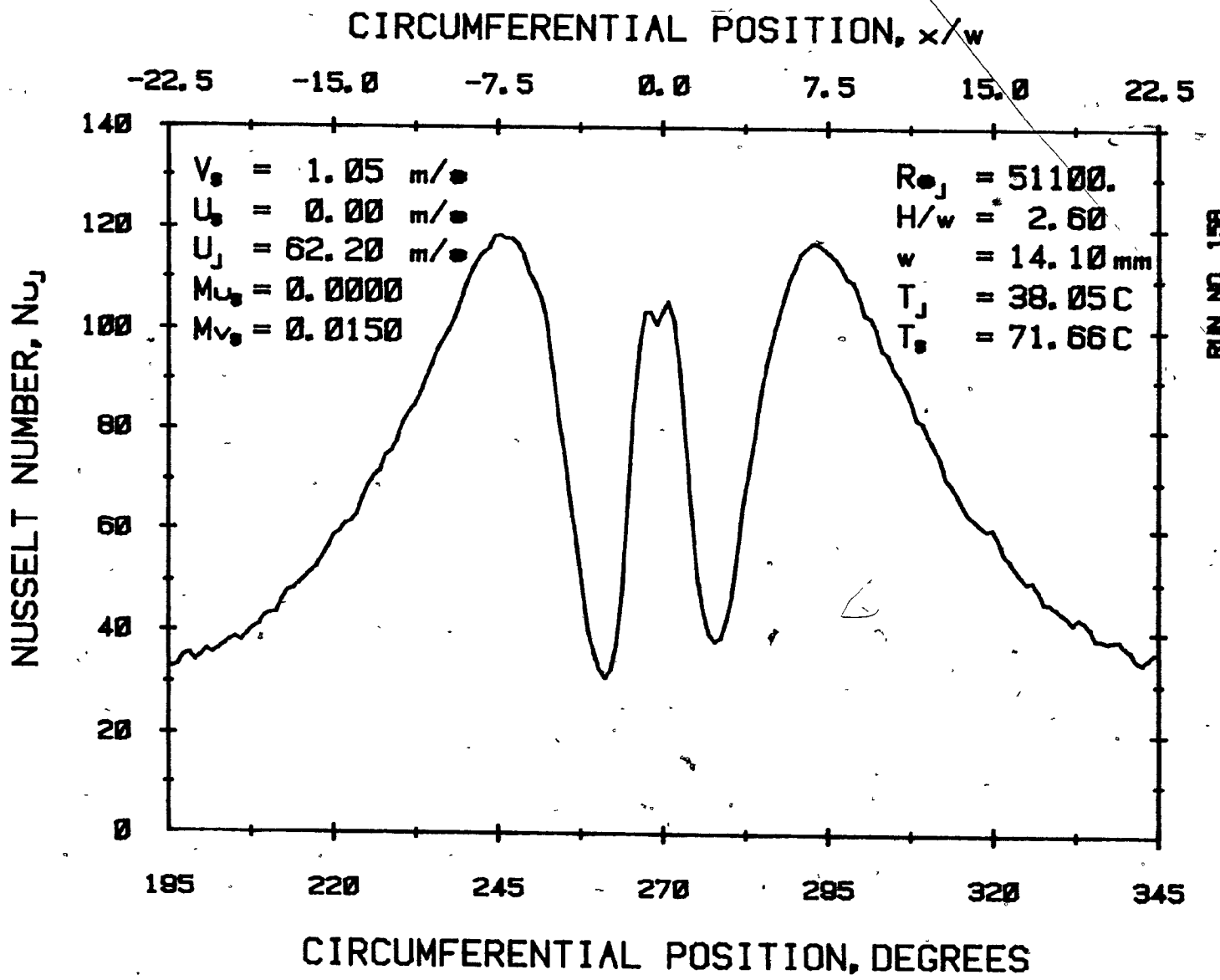


FIGURE 3.30b. Heat transfer distribution for the cooling jet at 412 measurements per rotation

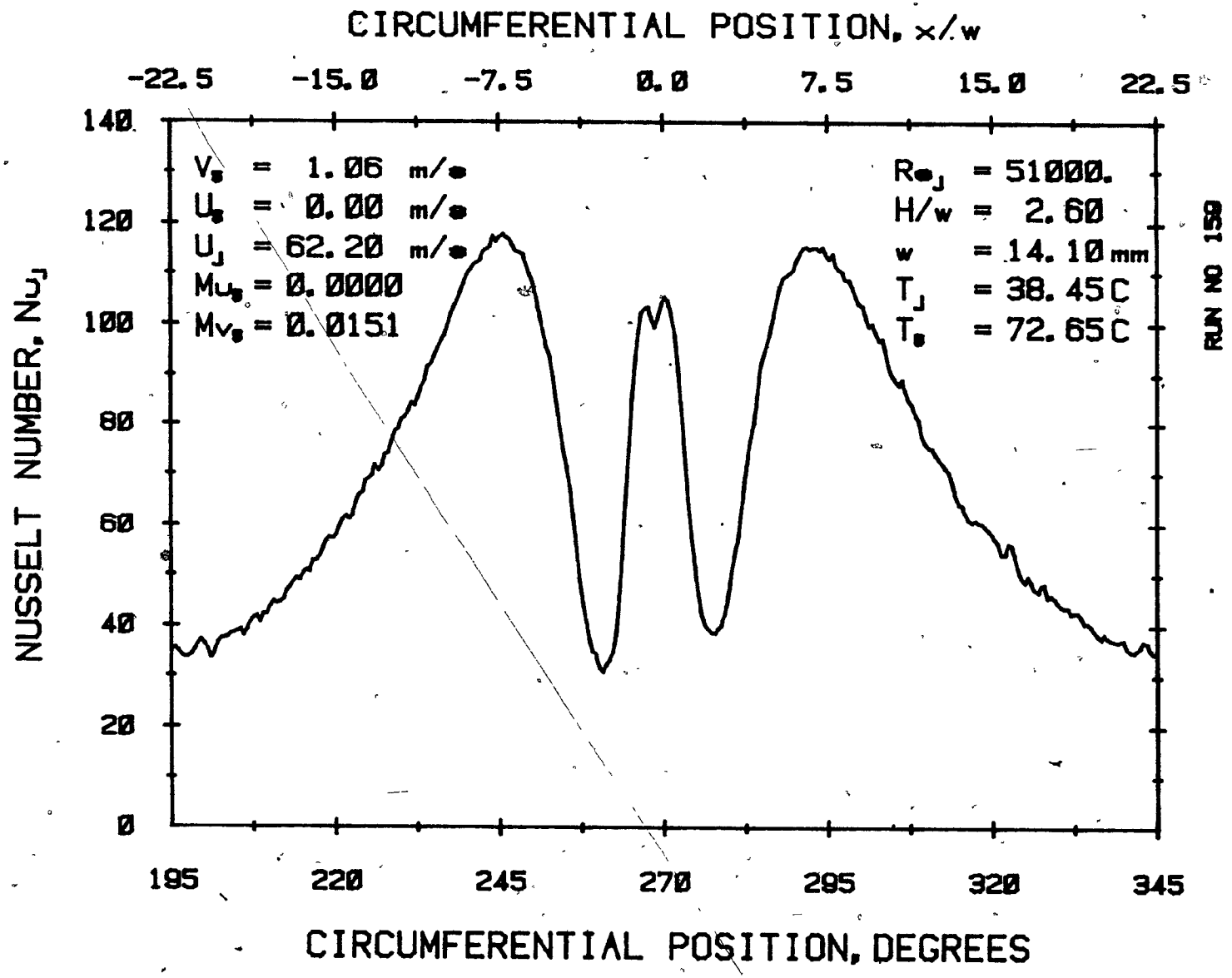


FIGURE 3.30c. Heat transfer distribution for the cooling jet at 718 measurements per rotation

CHAPTER 4

EXPERIMENTAL RESULTS AND DISCUSSION

4.1 Introduction

The experimental results now presented are obtained with the SIMTEST apparatus described in the previous chapter. The first problem treated is determination of a method for allowing adequately for the effect of temperature dependency of physical properties in the case of convective heat transfer under impinging jets. The SIMTEST apparatus for the first time provides heat transfer data for a heating and a cooling jet simultaneously. The temperature difference, ΔT, is varied for the cooling jet from about $11^{o}C$ to $41^{o}C$, and for the heating jet from about $15^{o}C$ to $50^{o}C$. This range, i.e. from about $41^{o}C$ in one direction to $50^{o}C$ in the other, is sufficiently wide to permit the first comprehensive investigation of the physical property dependency effect for impinging jet heat transfer.

Solution of the temperature dependency problem in Section 4.2 made it possible, moreover, to combine all experimental data (i.e. irrespective of either the direction or magnitude of ΔT) in the subsequent analysis of each of the variables studied - jet Reynolds number, Re_j, spacing, H/w, impingement surface motion, V_s, and throughflow at the impingement surface, U_s. The influence of Re_j on local and average heat transfer distribution is then presented in Section 4.3. The heat transfer profiles and correlations obtained in Section 4.3 serve as a basis for

the subsequent analyses of influence of impingement surface motion in Section 4.4 and influence of throughflow at the impingement surface in Section 4.5. Average heat transfer with and without impingement surface motion is compared with data from the literature. The implications of impingement surface motion for the "Papridryer" design is discussed. Problems associated with measurement of the effect of throughflow at the impingement surface are analyzed. The range of the parameters for all the experiments with the SIMTEST apparatus are given in Table 4.1.

4.2 Temperature Independent Correlation of Impingement Heat Transfer with Temperature Dependent Physical Properties

In previous studies of impingement heat transfer the influence of the temperature difference between jet and impingement surface has received little attention. As can be seen from Table 1.2 in Section 1.4.2, in experimental studies the temperature difference factor has been limited in two ways in that, first, ΔT has generally been kept constant and, second, ΔT has usually been at a level of only 10°-30°C and never greater than 70°C. Also, transfer rates obtained with such techniques as water evaporation or naphthalene sublimation are the mass transfer equivalents of heat transfer data at relatively low ΔT. This lack of both high ΔT and variable ΔT experimental data is unfortunate considering the large thermal driving force in important industrial applications as for example turbine blade cooling and paper drying with temperature differences respectively up to 500°C (Livingood et al. (85)) and 350°C (Holik (61), Burgess et al. (23, 24)).

TABLE 4.1. Range of Parameters for Experiments with SIMTEST Apparatus

w (mm)	14.1	6.2
H/w	2.6	6.0
$T_j - T_s$ (^oC)	-10.8 to -38.6	21.3 to 48.7
Re_j	9700 to 91800	5200 to 20300
U_j (m/s)	12 to 115	20 to 70
U_s (m/s)	0 to 0.164	0 to 0.164
V_s (m/s)	0.6 to 12.0	0.6 to 12.0

The temperature driving force used in the present work was varied for the cooling jet from about 10°C to 40°C and for the heating jet from about 20°C to 50°C. Although this ΔT is much smaller than some industrial applications the experimental variation in ΔT is sufficient that this effect cannot be ignored and, moreover, is sufficient to provide the basis for a quantitative analysis of the effect of ΔT. Smaller temperature differences for which physical property effects can be ignored were not used due to the corresponding larger influence on heat transfer coefficients of experimental errors in temperature measurement and of the adiabatic wall temperature effect, discussed in Section 3.5.3.

The objective of all methods of incorporating effects of variable physical properties into heat transfer correlations should be to obtain a form of correlation which is independent of ΔT. Therefore the effectiveness of alternate bases of correlation is conveniently illustrated through graphical representation of the appropriate dimensionless parameters as a function of ΔT. The less sensitive the correlation is to ΔT the more successful is the correlation and hence the more reliable the correlation is for use at high ΔT based on either the more extensive experimental data available at relatively low ΔT or the theoretical "constant property" solutions which do not include temperature dependency of physical properties.

The three alternate methods for incorporating variable physical property effects tested with the present data are:

(1) $\frac{Nu_j}{Nu_{cp}} = \left(\frac{T_s}{T_j}\right)^n$, at constant Reynolds number, with all physical properties evaluated at T_j

(2) $Nu_f = f(Re_f)$, i.e. all properties evaluated at the film temperature, T_f

(3) $Nu_s = f(Re_j)$, i.e. Nusselt number evaluated at the impingement surface temperature, T_s, Reynolds number at the nozzle exit temperature, T_j

The second of these methods is used in all the German literature on impinging jets while most reports in the English literature use correlations where the physical properties are evaluated at the jet temperature, i.e. the first method noted above.

In the set of 12 experiments performed for testing these alternate correlations of temperature effect, relatively low values of Re_j were used, 13800 for the heating jet (H/w = 6) and 51400 for the cooling jet (H/w = 2.6) in order not to obscure examination of the temperature dependent physical properties effect with a significant adiabatic wall temperature effect. The maximum extent of the latter effect on stagnation heat transfer coefficient with these values of Re_j is estimated by the results of Section 3.5.3 to be at a negligible level, about 2%. Likewise, the peripheral velocity of the cylindrical impingement surface was limited to V_s = 0.9 m/s (0.6 rps) and no suction was applied in order to avoid introducing effects of surface motion and throughflow. Each of the above forms of correlation was tested with heat transfer results at three locations, i.e. at the stagnation point, at the off-stagnation maximum and for an

integrated mean heat transfer. Experimental conditions and results are summarized in Tables 4.2 and 4.3 for the heating and cooling jets, respectively.

For the case of stagnation point heat transfer, where it is known that Nusselt number varies with the square root of Reynolds number, the test is best made by reference to the ratio $Nu_o/\sqrt{Re}$. Thus for the heating and cooling data Figures 4.1 and 4.2, respectively, display the stagnation point results as $Nu_{oj}/\sqrt{Re_j}$, $Nu_{of}/\sqrt{Re_f}$ and $Nu_{os}/\sqrt{Re_j}$ as a function of ΔT. For each of the three forms tested the numerical value for $Nu_o/\sqrt{Re}$ is higher on Figure 4.1 than on 4.2 not becuase of the heating-cooling difference but rather because stagnation heat transfer increases with spacing over the range of H/w from 2.6 to 6, as will be discussed subsequently.

A similar procedure is used for testing the three forms of correlation with heat transfer results from the off-stagnation maximum and for mean heat transfer. In these cases the Reynolds number dependency is taken without comment at this time from the results of the succeeding section, 4.3. The values of the appropriate three forms of Nusselt-Reynolds function are listed in Table 4.3 for the off-stagnation maximum and mean heat transfer results, and are presented as a function of ΔT on Figures 4.3 and 4.4 for the heating and cooling results, respectively.

Examination of the correlations displayed on Figures 4.1 through 4.4 shows that, with all three sets of heat transfer data, correlation (3) based on Nu_s and Re_j can be rejected because the corresponding functions are in every case a signifi-

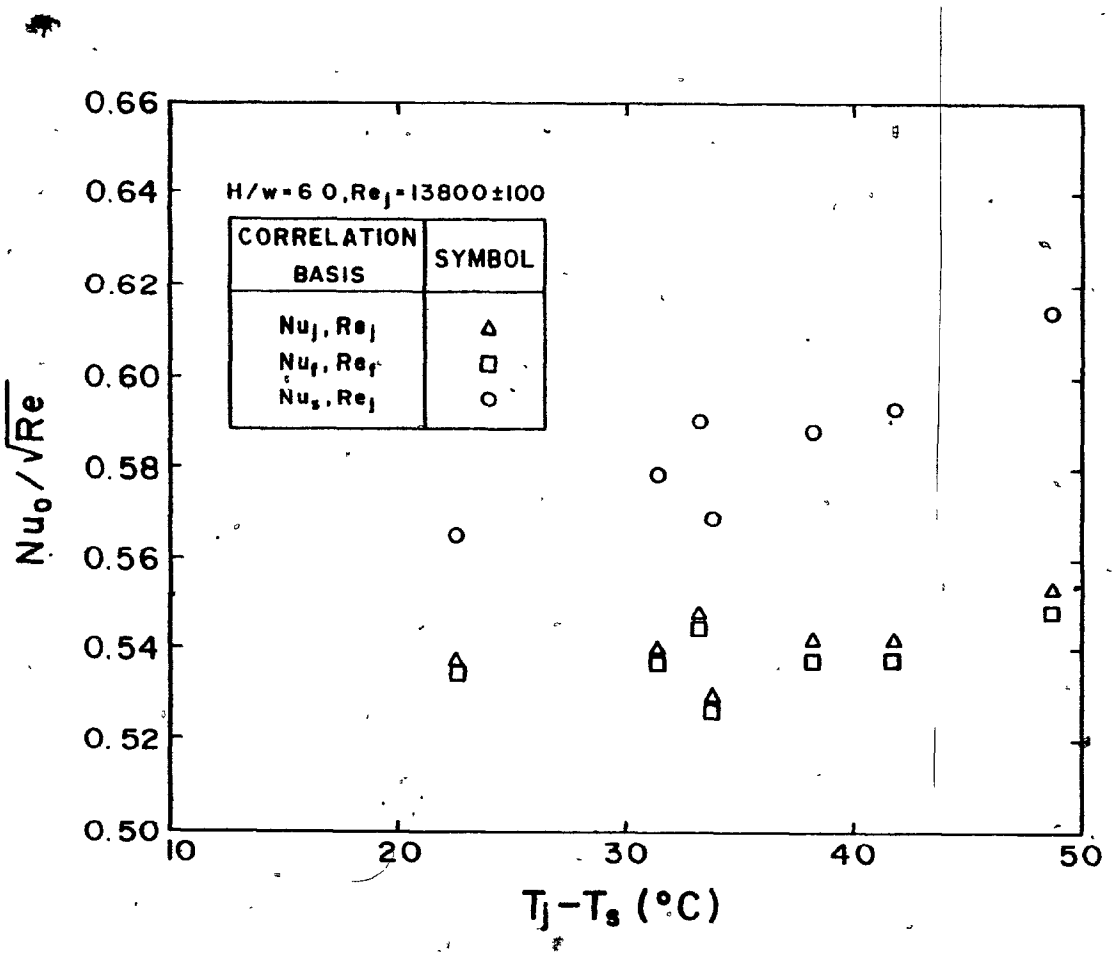


FIGURE 4.1. Test of physical property evaluation basis with stagnation point heat transfer for H/w = 6

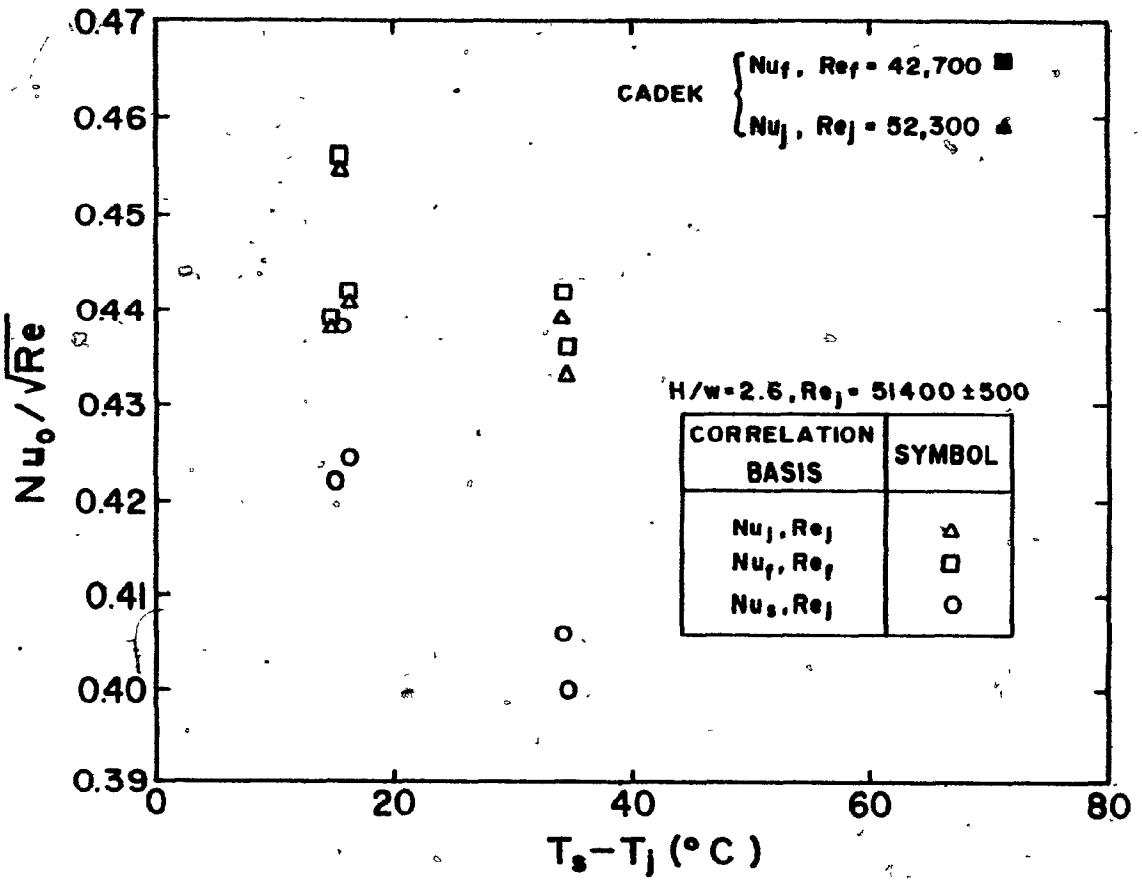


FIGURE 4.2. Test of physical property evaluation basis with stagnation point heat transfer for H/w = 2.6

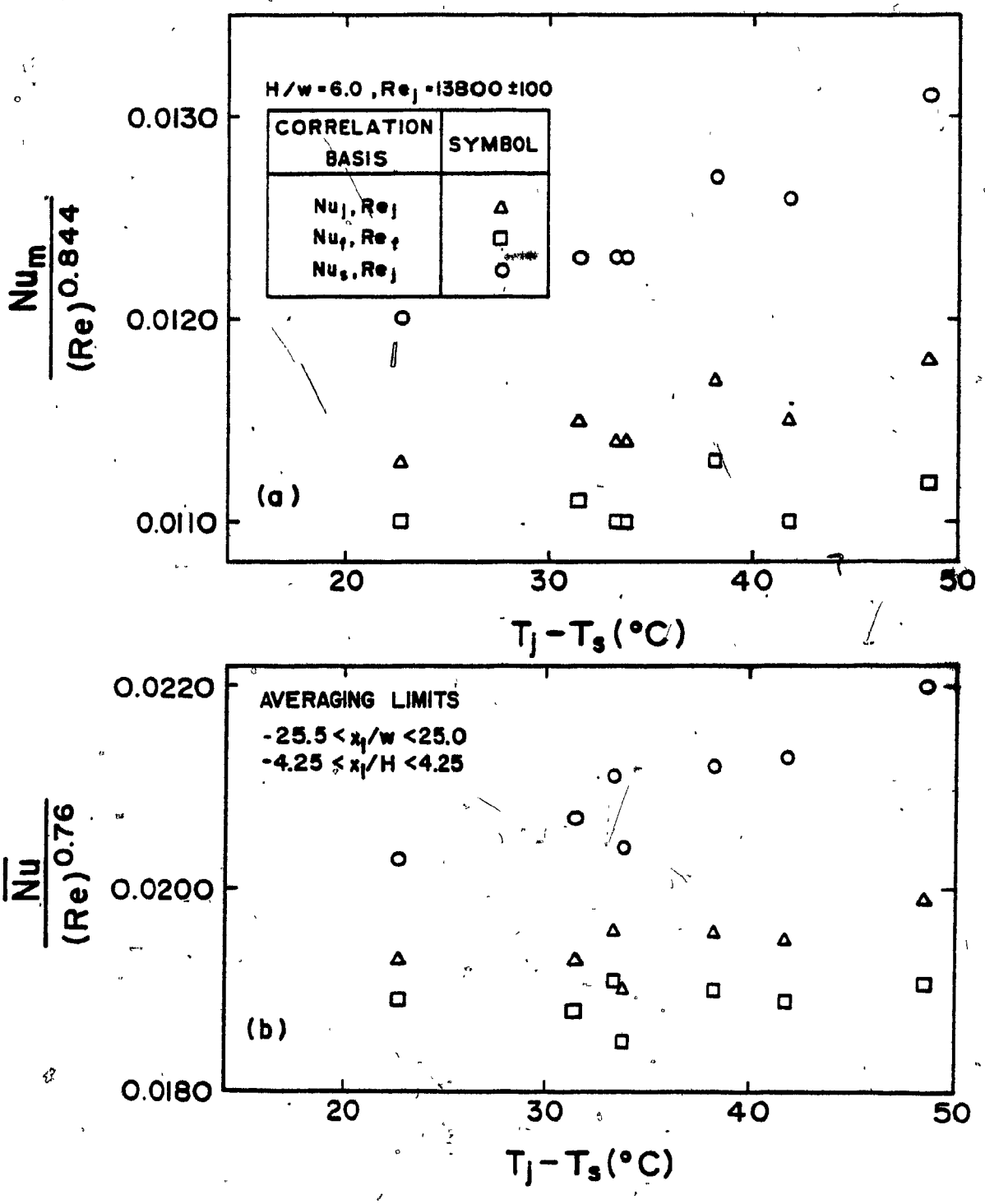


FIGURE 4.3a and b.

Test of physical property evaluation basis with average heat transfer for H/w = 6

TABLE 4.2(a). Influence of $(T_j - T_s)$ on Heat Transfer for the Heating Jet

Run	Re_j	Re_f	T_j °C	T_f °C	$(T_j - T_s)$ °C	ΔP mm H_2O	$Nu_{os}/\sqrt{Re_j}$	$Nu_{oj}/\sqrt{Re_j}$	$Nu_{of}/\sqrt{Re_f}$
185	13700	15200	99.1	78.2	41.8	12.6	0.593	0.542	0.538
186	13800	15100	98.7	79.6	38.2	12.6	0.588	0.542	0.538
187	13700	14900	99.4	82.5	33.8	12.6	0.569	0.530	0.527
218	13900	15600	101.2	76.85	48.7	13.1	0.614	0.554	0.549
222	13900	15100	80.0	63.4	33.2	10.7	0.590	0.548	0.545
224	13900	15100	80.3	64.6	31.4	10.7	0.579	0.540	0.537
225	13900	14700	71.4	60.1	22.6	9.8	0.565	0.537	0.535

TABLE 4.2(b).

Run	(a) $\frac{Nu_{sm}}{(Re_j)^{0.844}}$	(a) $\frac{Nu_{jm}}{(Re_j)^{0.844}}$	(a) $\frac{Nu_{fm}}{(Re_f)^{0.844}}$	(b) $\frac{\overline{Nu}_s}{(Re_j)^{0.76}}$	(b) $\frac{\overline{Nu}_j}{(Re_j)^{0.76}}$	(b) $\frac{\overline{Nu}_f}{(Re_f)^{0.76}}$
185	0.0126	0.0115	0.0110	0.0213	0.0195	0.0189
186	0.0127	0.0117	0.0113	0.0212	0.0196	0.0190
187	0.0123	0.0114	0.0110	0.0204	0.0190	0.0185
218	0.0131	0.0118	0.0112	0.0220	0.0199	0.0191
222	0.0123	0.0114	0.0110	0.0211	0.0196	0.0191
224	0.0123	0.0115	0.0111	0.0207	0.0193	0.0188
225	0.0120	0.0113	0.0110	0.0203	0.0193	0.0189

(a) mean value of the two secondary heat transfer peaks

(b) averaged over $-25.5 \leq \frac{x_1}{w} \leq 25.5$, or $-4.25 \leq \frac{x_1}{H} \leq 4.25$

TABLE 4.3(a). Influence of $(T_s - T_j)$ on Heat Transfer for the Cooling Jet

Run	Re_j	Re_f	T_j ^oC	T_f ^oC	$(T_s - T_j)$ ^oC	ΔP mm H_2O	$Nu_{os}/\sqrt{Re_j}$	$Nu_{oj}/\sqrt{Re_j}$	$Nu_{of}/\sqrt{Re_f}$
159	50900	46300	38.5	55.85	34.7	16.1	0.400	0.433	0.436
158	51100	46500	38.1	55.2	34.2	16.1	0.406	0.439	0.442
111	51800	49600	35.3	43.1	15.6	16.1	0.438	0.455	0.456
113	51600	49400	35.5	43.15	15.3	16.1	0.422	0.438	0.439
132	51900	49600	36.3	44.55	16.5	16.3	0.424	0.441	0.442

TABLE 4.3(b).

Run	(a) $\frac{Nu_{sm}}{(Re_j)^{0.907}}$	(a) $\frac{Nu_{jm}}{(Re_j)^{0.907}}$	(a) $\frac{Nu_{fm}}{(Re_f)^{0.907}}$	(b) $\frac{\overline{Nu}_s}{(Re_j)^{0.739}}$	(b) $\frac{\overline{Nu}_j}{(Re_j)^{0.739}}$	(b) $\frac{\overline{Nu}_f}{(Re_f)^{0.739}}$
159	0.00569	0.00616	0.00645	0.0253	0.0274	0.0282
158	0.00572	0.00619	0.00647	0.0254	0.0275	0.0283
111	0.00593	0.00616	0.00629	0.0268	0.0279	0.0283
113	0.00584	0.00605	0.00618	0.0260	0.0269	0.0273
132	0.00581	0.00603	0.00616	0.0262	0.0272	0.0276

(a) mean value of the two secondary heat transfer peaks

(b) averaged over $-15 \leq \frac{x_1}{w} \leq 15$, or $-5.77 \leq \frac{x_1}{H} \leq 5.77$

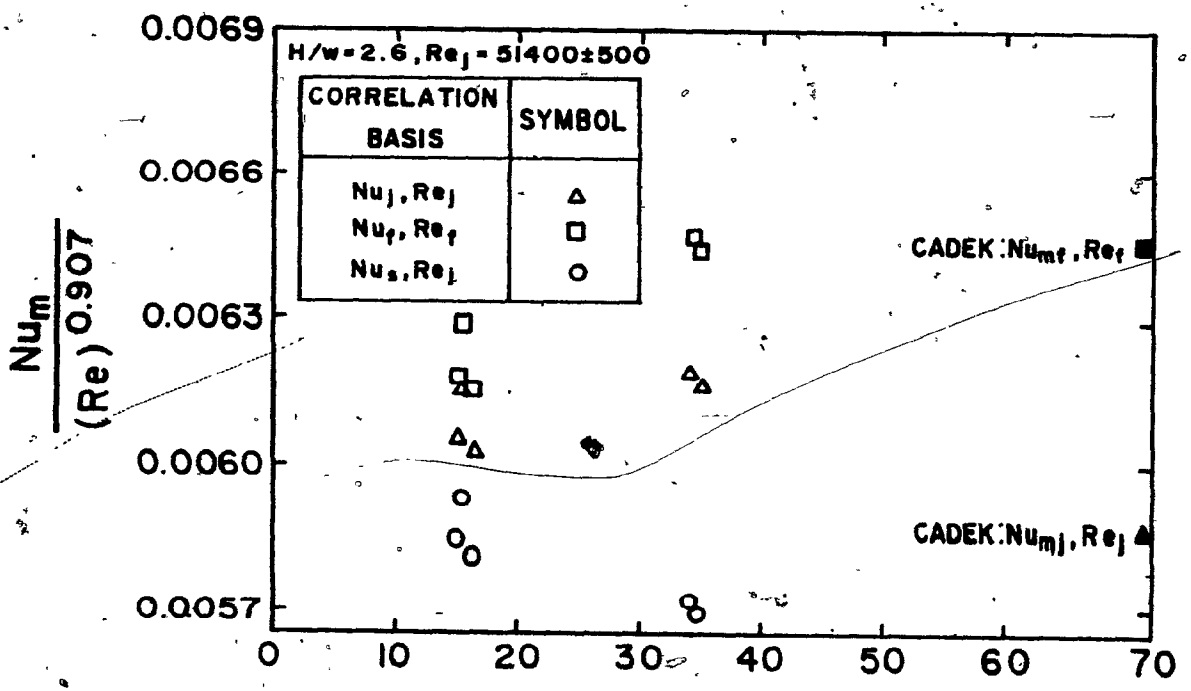


FIGURE 4.4a. Test of physical property evaluation basis with average heat transfer for H/w = 2.6

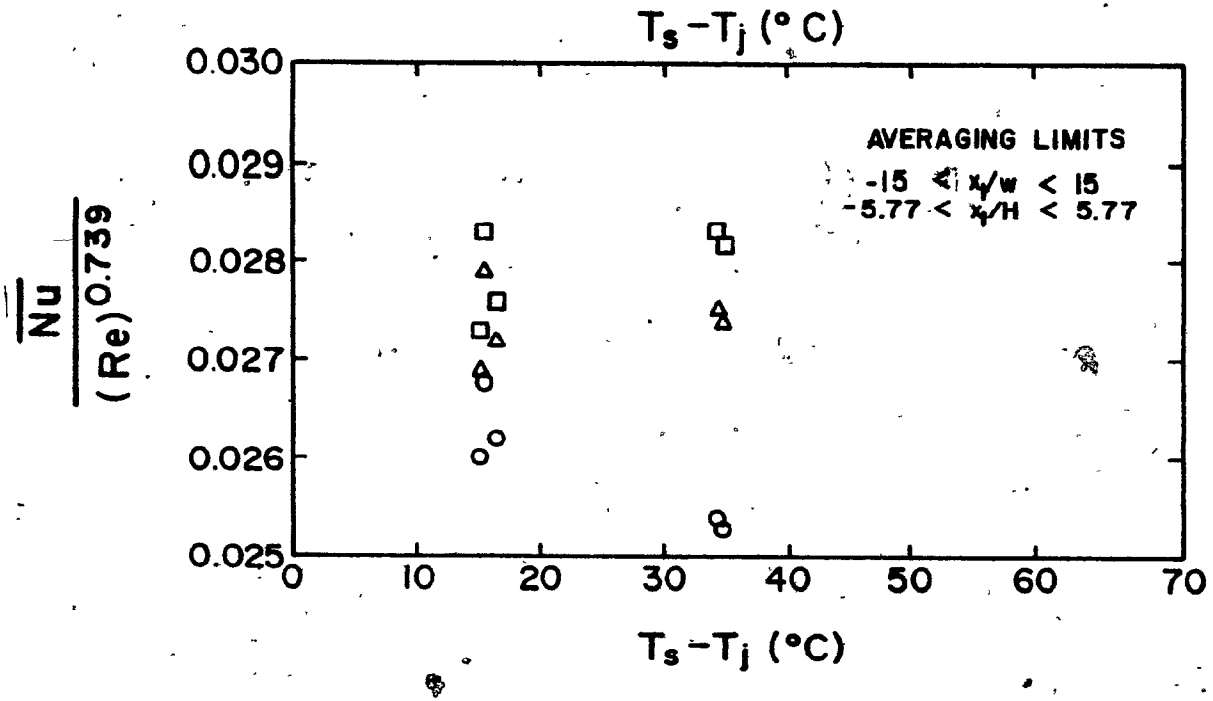


FIGURE 4.4b. Test of physical property evaluation basis with secondary heat transfer maximum for H/w = 2.6

cant function of ΔT. However, from testing the other two correlations using as test criteria the heat transfer results from all three locations and for both heating and cooling, the conclusion is that either the form with all properties at the nozzle exit temperature, (1), or all at the film temperature, (2), is a satisfactory method for obtaining a temperature independent correlation of impingement heat transfer.

Although these two procedures lead to equally successful correlations, the form involving evaluation of all physical properties at the film temperature, which is the most commonly used form of the "reference temperature" method, does have a significant disadvantage from the user viewpoint in that an additional calculation is required, i.e. determination of T_f. In practice, obtaining T_f not only involves an additional step but in design T_f may be unknown, hence leading to iterative solutions to obtain the correct T_f. A second consideration is a preference for use of a characteristic Reynolds number which is independent of temperature at the heat transfer surface, not the case for Re_f. Because the form based on all physical properties evaluated at T_j provides an equally satisfactory correlation of results, is more straightforward for use in design and involves a Reynolds number independent of impingement surface conditions, this form is used subsequently in the presentation and analysis of results from the present investigation, and is recommended as the standard for general use.

It should be recalled from the basis given at the outset for the recommended correlation that, for data at constant Re_j,

it is the parameter $Nu_j (\frac{T_j}{T_s})^n$ which would be independent of temperature and equal to Nu_{cp} of theoretical, constant property solutions or to low temperature difference experimental data at the same Reynolds number. Figures 4.1 through 4.4 establish that within the moderate range of ΔT of the data from the present study, the value of the exponent of the temperature correction term cannot effectively be differentiated from $n = 0$. For a gas with a specific assumed temperature dependence for μ, ρ and k, Kays (73) obtained for the temperature ratio exponent, n, the values of 0.10 for heating and 0.07 for cooling for the case of two-dimensional laminar stagnation flow. However, using Kays' value of $n = 0.1$ for heating, the maximum value of the $(T_j/T_s)^n$ correction term for the present set of test data (ΔT to 50°C; T_j/T_s to 1.18) would in fact be less than 2%. As it is apparent from Figures 4.1 through 4.4 that a correction term of up to 2% is well within the range of experimental error, this term need not be included for the present study nor for any application in the same moderate range of T_j/T_s. However, for use of the present data at higher values of ΔT and T_j/T_s where the effect of physical property temperature dependency become large, this effect may be allowed for by including the temperature ratio term, using the value recommended by Kays (0.10 or 0.07) for the exponent.

Although the representation of experimental data displayed on Figures 4.1 to 4.4 serves primarily to provide a critical test of various procedures used without validation by others

for incorporating the effect of temperature dependent physical properties, such representation as a function of ΔT also establishes that the SIMTEST apparatus and associated procedures produced data of high precision. Moreover, Figures 4.2 and 4.4 display comparative data of Cadek at the stagnation point and at the off-stagnation maximum for essentially the same value of jet Reynolds numbers (Re_j = 52300, Re_f = 42700), expressed here both as Nu_j and Nu_f. As the average Nusselt numbers for these figures are for such a large impingement surface, i.e. to x_1/H = 5.77, it was not considered appropriate to include $\overline{Nu}$ results in this comparison. The basic experimental conditions in Cadek's work differ from those of the current study principally through use here of a rotating cylindrical impingement surface and a long (about 7.5H) region of confined flow after impingement. The data attributed to Cadek on Figures 4.2 and 4.4 are in fact values interpolated for H/w = 2.6 between his results at dimensionless spacings of 2 and 4. The agreement between the interpolated Cadek data and the present study is good for Nu at the stagnation point and at the off-stagnation maxima.

From the testing of experimental results presented in this section, overall conclusions are that the SIMTEST apparatus produced data of high precision and that the new results agree well with those of a reliable reference, Cadek (26), for conditions where such comparisons may be made. With respect to the perennial problem of accounting in heat transfer correlations for the temperature dependency of physical properties, a critical evaluation indicates that for a moderate temperature range

(ΔT to 50°C, T_j/T_s to 1.18) use of a correlation of the form $Nu_s = f(Re_j)$ should be rejected, but that correlations either of the form $Nu_j = f(Re_j)$ or $Nu_f = f(Re_f)$ provide satisfactory methods of incorporating physical property variation in formulations which converge for low ΔT to the $Nu_{cp} = f(Re_{cp})$ form of theoretical solutions. As the form based on all physical properties evaluated at T_j avoids the step of evaluating T_f required for the film temperature based correlation, a temperature which may be unknown in a design problem, the form with all properties evaluated at T_j is the recommended correlation. Although the maximum temperature difference in the present investigation does not require incorporation of the temperature correction term to give the complete form, $Nu_j(\frac{T_j}{T_s})^n = f(Re_j)$, the correlation confirmed by the present test may readily be extended to use for high temperature difference impinging jet heat transfer by the addition of the $(T_j/T_s)^n$ temperature ratio term with values of n from the literature.

4.3 Impingement Heat Transfer without Surface Motion or Throughflow

Studies of local heat and mass transfer for a turbulent impinging slot jet have established the existence of two characteristic shapes of lateral profiles of local heat/mass transfer, depending on the relative impingement surface spacing from the nozzle exit, H/w, and on jet Reynolds number. Thus a bell-shaped distribution is obtained for conditions of large H/w, small Re_j, while a secondary maximum appears for conditions of small H/w, large Re_j. As explained in Section 1.4.2 this be-

haviour for turbulent impinging jets results from the existence of a laminar boundary layer in the impingement region but with some enhancement in this region of transfer rates from those for a laminar boundary layer through the effect of "free stream" turbulence on laminar boundary layer under a favorable pressure gradient. The heat transfer minimum between the stagnation and off-stagnation maxima marks the beginning of transition from this laminar-like boundary layer to a turbulent one, while the off-stagnation maxima occur where boundary layer transition is complete. An important consequence is that different Re_j dependence can be expected for the stagnation and off-stagnation heat transfer maxima, with the Re_j dependence of average heat transfer being a function of extent of averaging area.

The local and average heat transfer results presented in this section were obtained without application of suction and at low speed of rotation of the impingement cylinder, so as to exclude the effect of throughflow and to make the effect of impingement surface motion negligible. Thus the mass velocity ratio $M_{V_s} = U_s\rho_s/(U_j\rho_j)$, which characterizes the effect of impingement surface motion was kept generally less than 0.05 and mostly in the range 0.01 to 0.02, so that conditions do not differ significantly from those for a stationary impingement surface. Consequently these results can be compared with data from literature obtained with slot jets impinging on an impermeable stationary surface. As well as the intrinsic importance of effect of Reynolds number, the correlations obtained in this section serve as the basis for subsequent analyses of influence

on heat transfer of throughflow and impingement surface speed.

Before beginning the presentation of results it should be recalled that all lateral profiles of Nusselt number were computer plotted as the final stage in the totally computerized operation of data acquisition, data processing and plotting of results. These procedures were detailed in Sections 3.3.2 and 3.3.3

The analysis of effect of jet Reynolds number treats first the complete lateral profiles of local heat transfer, including whatever comparisons can be made with studies from the literature which correspond to experimental conditions in the present range of impingement surface spacing, H/w, of 6 and 2.6. The analysis then focuses successively on effect of Reynolds number on heat transfer at the stagnation point, in the stagnation region, at the off-stagnation maximum, in the wall jet region and, finally, for integrated mean heat transfer. In each of these cases comparisons are made with what literature data exist near the H/w dimensionless impingement surface spacings of 6 and 2.6 of the present investigation.

4.3.1 Lateral Profiles of Local Heat Transfer

For H/w = 6, the heating jet, the Reynolds number was varied from 5200 to 20300 and from 9700 to 91800 for H/w = 2.6, the cooling jet. The principal operating conditions and results are summarized in Tables 4.4 and 4.5.

The lateral profiles of local heat transfer for H/w = 6 at four values of Reynolds number are superimposed on Figure 4.5.

TABLE 4.4. Operating conditions and results for influence of Re_j at H/w = 6

Run	Re	P_p (cm H_2O)	M_{V_s}	T_j (^oC)	ΔT (^oC)	$\overline{\Delta T_s}$ (^oC)	$Nu_{oj}/\sqrt{Re_j}$	$\overline{Nu}_{mj}$	$\overline{Nu}_j$ x_1/w=8.5	$\overline{Nu}_j$ x_1/w=17	$\overline{Nu}_j$ x_1/w=25.5	$\overline{Nu}_j$ x_1/w=34	$\overline{Nu}_j$ x_1/w=51
198	5200	1.9	0.053	102.1	38.1	0.0	0.534	-	20.4	15.4	12.6	10.7	8.2
196	8200	4.7	0.034	102.4	38.2	0.15	0.534	22.7	27.3	22.0	18.0	15.3	11.8
193	11000	8.2	0.024	98.8	34.1	0.3	0.550	29.9	34.4	28.3	23.1	19.3	14.9
190	12200	9.9	0.022	98.6	33.6	0.1	0.531	31.6	35.8	29.8	24.2	20.5	15.9
186	13800	12.6	0.019	98.7	38.2	0.05	0.542	36.5	40.4	33.6	27.4	23.2	18.0
169	20300	21.6	0.013	75.9	21.3	0.0	0.532	48.8	51.4	43.6	35.2	29.7	23.2

TABLE 4.5. Operating conditions and results for influence of Re_j at $H/w = 2.6$

Run	Re	ΔP (cm H_2O)	M_{V_s}	T_j (^oC)	ΔT (^oC)	$\overline{\Delta T_s}$ (^oC)	$Nu_{oj}/\sqrt{Re_j}$	$\overline{Nu}_{mj}$	$\overline{Nu}_j$ $x_1/w=3\frac{3}{4}$	$\overline{Nu}_j$ $x_1/w=7.5$	$\overline{Nu}_j$ $x_1/w=11\frac{1}{4}$	$\overline{Nu}_j$ $x_1/w=15$	$\overline{Nu}_j$ $x_1/w=22.5$
148	9700	0.6	0.047	34.8	32.3	+0.1	0.474	28.5	30.7	28.9	27.8	25.9	21.6
150	10400	0.7	0.041	36.1	38.6	+0.25	0.449	27.4	29.9	28.1	26.9	24.9	20.8
199	16400	1.8	0.044	38.3	25.7	0.0	0.449	39.2	37.3	36.7	36.8	34.7	29.3
142	22900	3.4	0.030	39.7	22.1	+0.3	0.452	53.7	42.6	43.7	46.0	43.9	36.9
155a	22900	3.4	0.032	39.1	17.7	+0.05	0.452	53.1	41.8	43.4	45.7	43.5	36.7
147	23200	3.5	0.030	40.0	26.0	+0.1	0.443	52.7	42.2	43.2	45.4	43.3	36.4
124	24400	3.8	0.030	38.5	24.0	+0.1	0.463	58.5	48.0	48.4	50.4	48.3	40.6
174	24400	3.8	0.029	37.0	17.8	0.0	0.441	57.1	43.6	45.6	48.0	45.9	38.9
196	25100	4.0	0.029	37.8	26.4	+0.15	0.454	59.8	45.2	47.4	50.4	48.2	40.6
110	28600	5.0	0.012	34.9	16.6	0.0	0.462	66.8	51.4	53.9	56.7	54.1	45.7
193	30100	5.7	0.023	37.5	27.2	+0.3	0.455	69.6	48.1	52.5	56.7	54.3	45.8
179	35100	7.7	0.020	37.9	21.3	+0.05	0.449	79.4	52.4	59.5	64.1	61.3	51.8
108	37400	8.6	0.009	36.2	11.9	0.0	0.454	86.2	58.5	64.5	69.2	66.1	55.6
166	38600	9.6	0.018	40.7	24.4	0.0	0.462	91.0	56.8	65.7	71.8	68.9	58.1
225	41100	9.9	0.018	32.2	16.6	+0.2	0.440	90.2	54.8	63.8	70.2	67.2	56.2
109	48000	13.7	0.007	34.5	10.8	+0.05	0.445	107.2	65.2	76.8	83.0	79.1	65.6
159	50900	16.1	0.015	38.5	34.7	-0.1	0.433	114.5	63.0	79.7	86.5	82.3	69.0
158	51100	16.1	0.015	38.1	34.2	-0.2	0.439	115.4	64.1	79.0	86.8	82.9	69.3

TABLE 4.5. (continued)

Run	Re	ΔP (cm H_2O)	M_{V_s}	T_j (°C)	ΔT (°C)	$\overline{\Delta T_s}$ (°C)	$Nu_{oj}/\sqrt{Re_j}$	$\overline{Nu}_{mj}$	$\overline{Nu}_j$ $x_1/w=3\frac{1}{2}$	$\overline{Nu}_j$ $x_1/w=7.5$	$\overline{Nu}_j$ $x_1/w=11\frac{1}{2}$	$\overline{Nu}_j$ $x_1/w=15$	$\overline{Nu}_j$ $x_1/w=22.5$
111	51800	16.1	0,006	35.3	15.6	-0.1	0.455	116.7	68.6	82.7	89.3	84.9	70.6
113	51600	16.1	0.021	35.5	15.3	-0.05	0.438	114.7	66.0	80.1	86.4	81.8	67.8
132	51900	16.3	0.010	36.3	16.5	0.0	0.441	114.4	65.6	79.6	87.2	83.2	69.7
130	52200	16.3	0.009	35.5	16.2	-0.05	0.448	117.2	65.8	81.1	88.5	84.3	70.6
154	53800	18.3	0.041	40.6	14.1	+0.05	0.441	116.9	64.1	80.2	87.4	83.0	68.6
169	57200	20.4	0.011	39.3	15.4	0.0	0.442	127.0	65.9	86.6	94.7	89.7	74.1
103	59800	20.1	0.008	30.7	11.3	0.0	0.443	130.5	76.3	93.0	99.3	93.8	78.0
186	63400	25.1	0.010	40.1	20.4	+0.05	0.441	139.4	69.4	93.4	102.6	97.3	80.9
224	66800	25.4	0.011	31.9	17.0	+0.15	0.430	139.9	69.4	92.9	102.4	96.9	80.4
117	71300	30.0	0.008	35.8	16.2	0.0	0.429	149.3	79.3	103.3	110.8	104.1	85.6
116	83700	40.5	0.007	35.0	17.2	-0.3	0.434	176.3	89.5	121.2	128.8	120.3	98.8
185	84700	43.4	0.008	39.1	18.3	+0.05	0.439	183.0	80.4	119.5	130.2	122.2	100.1
222	87800	42.7	0.008	31.7	15.1	+0.05	0.429	181.5	80.4	117.1	127.4	119.5	97.7
218	89300	43.3	0.008	29.9	22.7	+0.15	0.419	181.3	79.7	118.4	129.2	121.1	99.4
161	91300	50.0	0.008	39.2	28.5	+0.05	0.438	199.0	85.8	129.7	140.8	131.9	108.1
162	91600	50.3	0.008	39.2	20.3	+0.05	0.411	184.2	82.0	119.0	129.8	121.6	99.2
163	91500	50.5	0.008	39.5	19.8	-0.15	0.439	196.1	85.0	127.3	138.9	130.0	106.2
164	91800	50.8	0.009	39.7	14.1	0.0	0.418	182.6	85.1	118.1	128.4	120.2	98.2
165	91600	50.6	0.009	39.5	9.4	+0.05	0.416	176.5	84.5	114.5	124.0	115.4	93.5

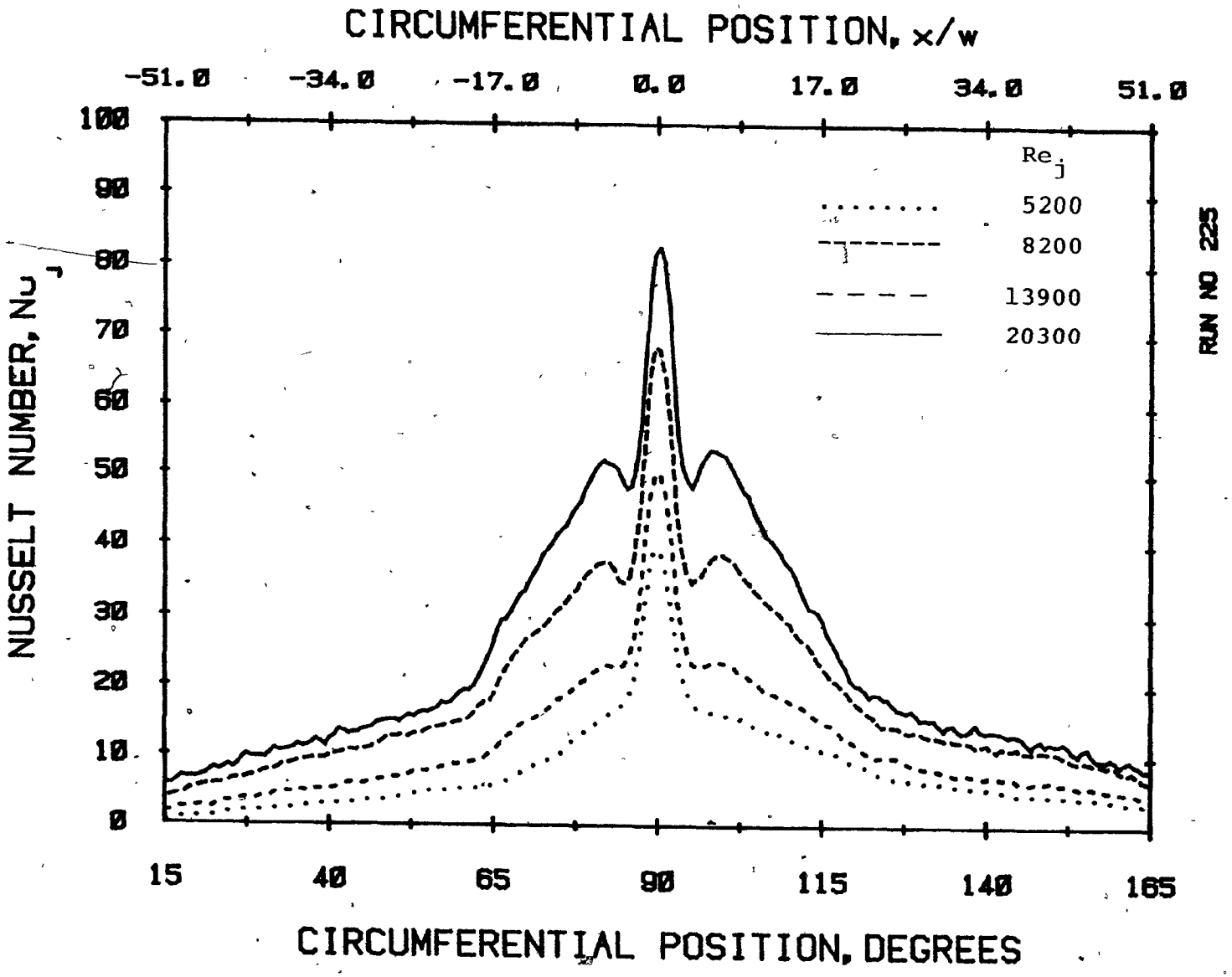


FIGURE 4.5. Lateral profiles of Nu_j at H/w = 6: Effect of Re_j

The lateral distance from the stagnation point over which these profiles are symmetric increases as Re_j increases, i.e. as M_{V_s} decreases. This trend will be seen again subsequently, and even more clearly, in Figure 4.16 where heat transfer distributions from both sides of the stagnation point are folded on to a single scale. Significant differences occur only in the far wall jet region, a region of minimal interest and importance, and are of the order of 20% (absolute $\Delta Nu_j \approx 2$). Essentially complete symmetry is obtained for $Re_j = 20300$, i.e. at $M_{V_s} = 0.013$. These observations confirm the achievement of two important objectives, i.e. that the rotating cylindrical impingement cylinder can be operated to give reliable data at sufficiently low speed to exclude any significant effect of impingement surface motion, and that symmetric flow and heat transfer conditions can be obtained in the SIMTEST apparatus, as discussed in section 3.5.6

Figure 4.5 indicates that, for the spacing $H/w = 6$, the heat transfer profiles over the indicated range of Re_j are characterized by a sharp central stagnation heat transfer maxi- and a smaller secondary maximum. Only at the lowest Reynolds number, $Re_j = 5200$, does the secondary maximum not appear, and even at this low Re_j the sudden change in slope of the profile at $x_1/w \approx 3.5$ indicates that this basic feature is present but not yet to the extent of a secondary peak. Over the 5000-20000 Reynolds number range for $H/w = 6$ the results indicate that the transition point minimum in the profiles occurs between 3.5w and 4w, i.e. at about 0.6H from the stagnation point, this dis-

tance decreasing slightly with increasing Re_j (see also Figure 4.16). The secondary maxima occur at 6w, i.e. 1H from the stagnation point, this location being independent of Re_j. Close examination of the data of Cadek (26) at spacings, H/w, of 2 and 4, give support to the location of the maxima at $x_1/w \approx 6$ and its independence of Re_j. Saad (125), on the other hand, reports a shift of the location of the maximum from 7w to 5w from the stagnation point with increasing Re_j for H/w = 4. Both references agree however on the shift in location of the minimum from 3w to 1.8w from the stagnation point with increasing Re_j for H/w = 4, in accordance with the trend found in the present work for H/w = 6.

From two previous studies with an impingement surface spacing of 6w there are heat transfer profiles available at Reynolds numbers which permit direct comparison with results of the present study, specifically, from Gardon and Akfirat (45), at Re_j = 11000 and Cadek (26), at Re_j = 11400. As the present profiles are essentially symmetric, both sides of the profiles of the present study for Re_j = 11000 are for convenience used in Figure 4.6 to display measurements of these investigators. Both reference studies were for cooling jets on flat impingement surfaces without a confinement surface, i.e. open to the surroundings. Cadek's nozzle geometry was identical to that of the present study, while Gardon and Akfirat used a long nozzle of width 3.17 mm. From Figure 4.6 it is seen that these prior results, both of which are considered of high reliability, are in excellent agreement with local heat trans-

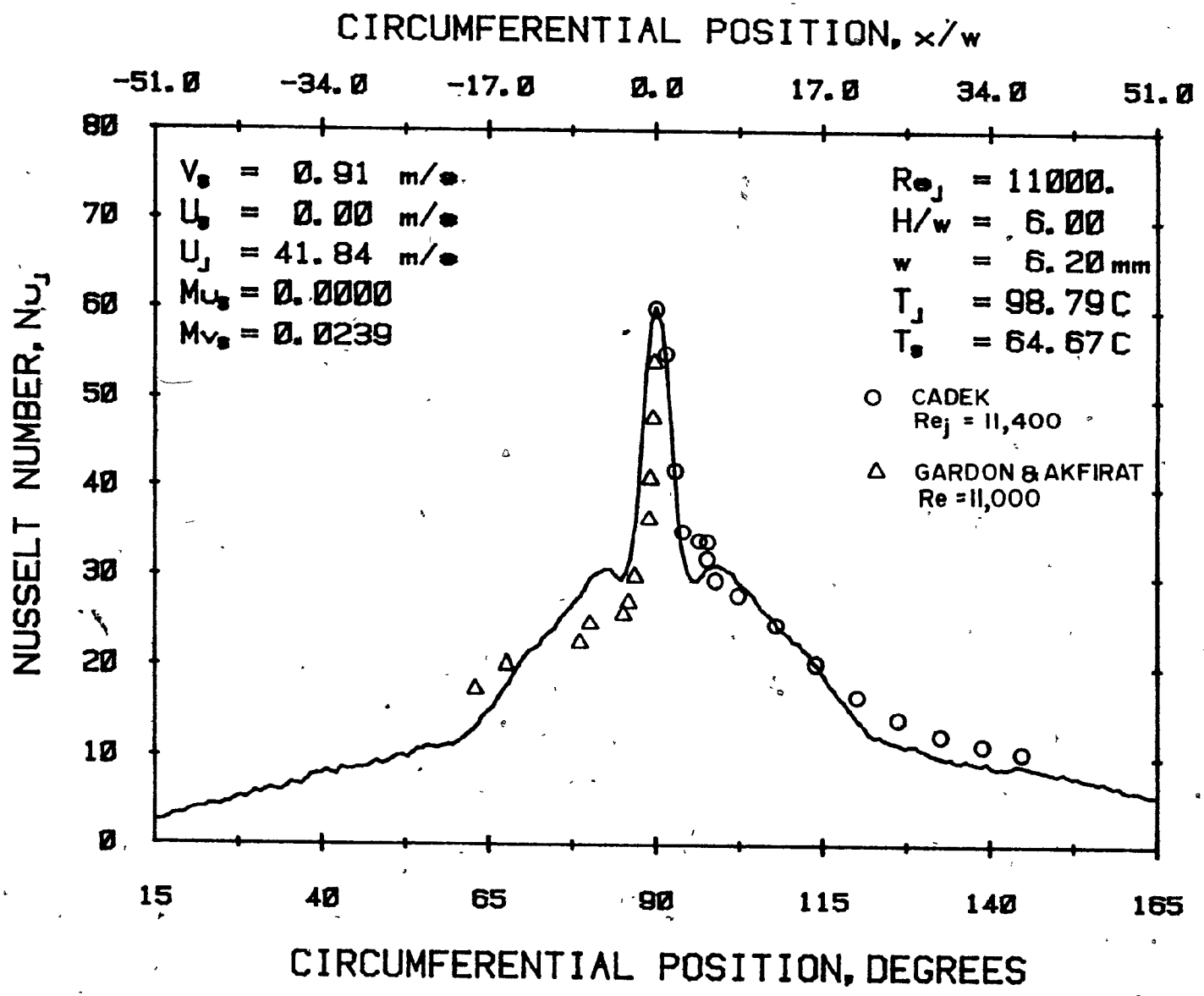


FIGURE 4.6. Lateral profiles of Nu_j at H/w = 6: Comparison of results

fer profiles obtained in the present study over the critical impingement region. This evidence for the accuracy of results from the rotating impingement cylinder and thin-film heat flux sensor of the SIMTEST apparatus provides substantial confirmation of the reliability of data from this new experimental facility. In fact, examination of Figure 4.6 indicates that the transition point minimum and the secondary maximum are defined more precisely by the experimental techniques developed for the present study.

For the far wall jet region, beyond about $x_1/w = 15$ or $x_1/H = 2.5$, Figure 4.6 indicates that the Nusselt number from the two reference studies becomes significantly higher than from the present investigation. An important feature of the two reference studies is that their jets were unconfined, and hence would entrain air from the surroundings, something which does not occur in the confined impingement system of the present study. Thus for their case of unconfined cooling jets, entrainment of ambient air and the mixing of this entrained air acts to lower the temperature of the wall jet, thus increasing the local effective ΔT in the far wall jet region. Such an increase in heat flux appears experimentally as an enhanced Nusselt number, which is the effect noted on Figure 4.6 for these two studies.

The lateral profiles of local heat transfer are examined for $H/w = 2.6$, the cooling jet, for which the range of jet Reynolds number is 9100 to 91800 and other conditions as listed in Table 4.5. Lateral profiles at several values of Reynolds

number are superimposed on Figure 4.7. As was the case in Figure 4.5 for H/w = 6, the profiles of Figure 4.7 are again reassuringly symmetric around the nozzle centerline, thus confirming both that the flow and hence heat transfer was symmetric in the SIMTEST apparatus and that data could be obtained at rotational speeds sufficiently low that the results correspond to those for stationary impingement surfaces. By comparison of the profiles displayed on these two figures, it is seen that, for the same value of Re_j, the features of the transition point minimum and the off-stagnation maxima at the completion of boundary layer transition are much more pronounced at the closer spacing of H/w = 2.6. The more pronounced minima and off-stagnation maxima at the closer spacing are related to the origin of these features, namely the "free stream" turbulence and the lateral gradient in pressure in the impingement region. The "free stream" turbulence decreases and the pressure gradient increases as the spacing H/w is decreased at constant Re_j. The combination of the lower heat transfer around the stagnation point due to the first effect and the higher pressure gradient due to the second effect explains the more pronounced profile at H/w = 2.6. At this close spacing the secondary peaks become higher than the stagnation peak for $Re_j > 40000$.

The transition point minima move slightly inward from about 2.9w from the stagnation point at low values of Re_j, to about 2.3w at $Re_j = 91500$, i.e. at locations of approximately 1H from stagnation. The minimum on the side approaching stagnation (the left side of all profiles) is marginally lower than

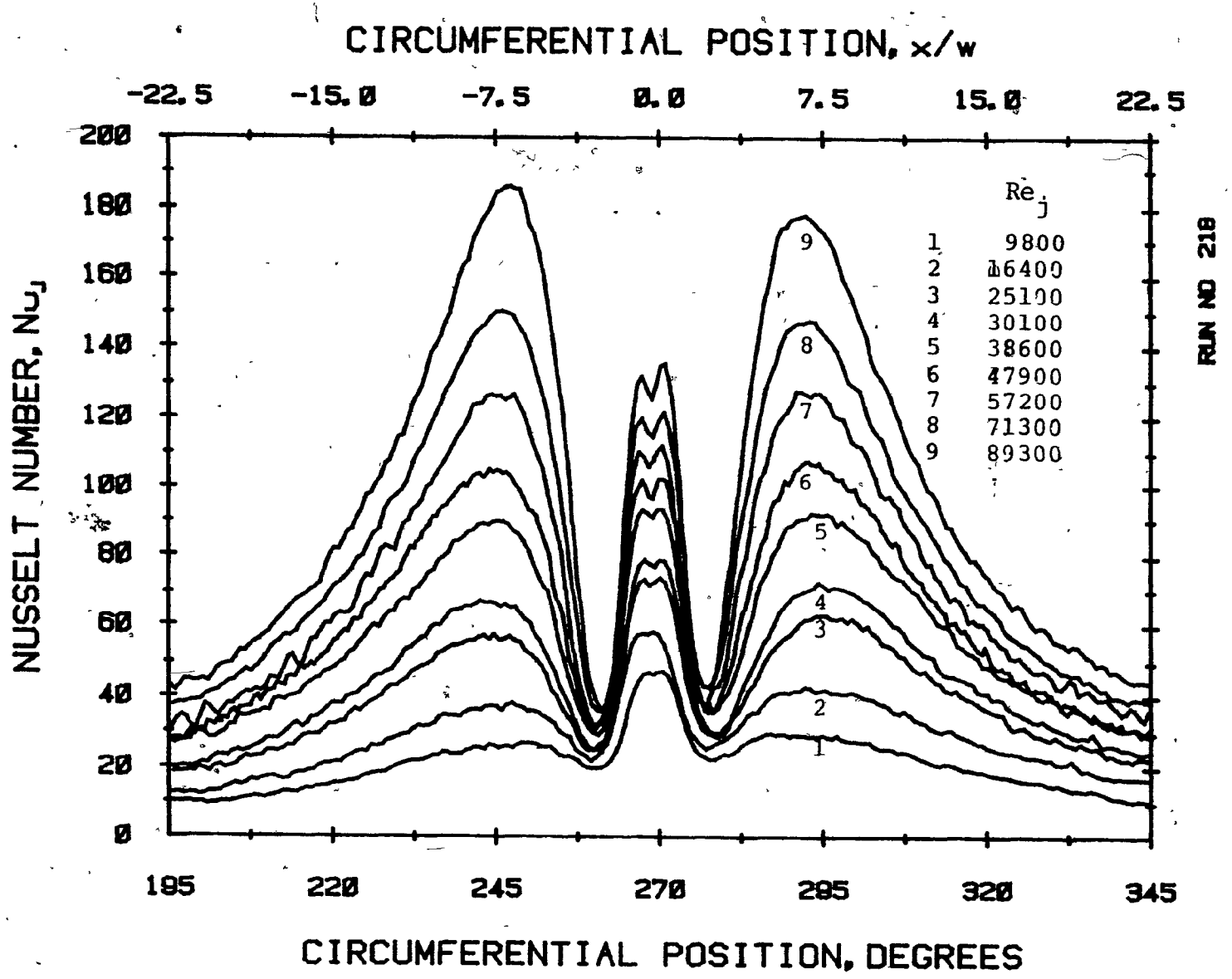


FIGURE 4.7. Lateral profiles of Nu_j at H/w = 2.6: Effect of Re_j

on the side leaving stagnation (on the right of all profiles). The off-stagnation maxima occur at about 7.5w or 2.9H from the stagnation point at about Re_j = 30000. This position appears to decrease slightly with both Reynolds number increases and decreases from Re_j = 30000, a position of about 6.5w or 2.5H from stagnation for both the highest and lowest values of Re_j used. The locations of the maxima and minima are very close to the locations reported by Cadek (26) for H/w = 2 and to the earlier reported locations for H/w = 6.0.

A more general perspective may be gained by collecting for both impingement surface spacings, 2.6w and 6w, the observations made concerning the location of the off-stagnation minima and maxima. At both spacings the distance from stagnation at which the minima occur decreases somewhat with Re_j but the effect of Re_j is slight on the location of the secondary maxima. Although such distances have generally been expressed nondimensionally with respect to nozzle width, w, the use of spacing, H, as characteristic dimension is also pertinent. Interest in H as the reference dimension is reinforced by the recent observation by Saad (125) that, for a wide range of w (3.3 to 8.3 mm) and H/w (4 to 16 for both values of w), a single normalized impingement surface pressure profile is obtained provided lateral distance is expressed relative to H rather than w. From this general pressure profile Saad found that the surface pressure drops to half the stagnation pressure at about 0.15H from stagnation, and to 5% of stagnation pressure at about 0.5H from stagnation. The present study indicates that, as H/w is decreased from 6 to

2.6, the location of the transition point minimum moves closer to stagnation if measured relative to w (i.e. moves from 3.5w-4w at H/w = 6, to 2.9w-3.3w at H/w = 2.6), but moves further from stagnation when expressed in terms of H (i.e. from about 0.6H for H/w = 6, to about 1H for H/w = 2.6). Thus in both cases the boundary layer transition occurs shortly beyond the location (0.5H according to Saad) at which impingement surface pressure has dropped to 5% of stagnation pressure. The fact that the location of the minimum, marking the onset of transition to a turbulent boundary layer, increases from about 0.6H to about 1H as H/w is decreased from 6 to 2.6 is consistent with Saad's observation that the normalized pressure profile remains essentially unchanged when lateral distance is expressed relative to H, because the reduction in arrival turbulence intensity which accompanies a decrease in H/w from 6 to 2.6 explains the increase in distance required (from 0.6H to 1H) before boundary layer transition begins.

As the surface pressure gradient is very small beyond the location of the heat transfer profile minimum, distance beyond that point should be expressed nondimensionally relative to w rather than H. The distance required from the onset to completion of boundary layer transition, i.e. from the minimum to the off-stagnation maximum, increases from about (6w-3.75w =) 2.25w for H/w = 6, to about (7.5w-2.6w =) 4.9w for H/w = 2.6. This difference in distance required for completion of transition is consistent with the much higher arrival turbulence intensity for the wider spacing, a fact documented by previous

work and most recently by Saad (125).

Similar to Figure 4.6, both sides of the profile for H/w = 2.6, Re_j = 10900 given on Figure 4.8 are used to display measurements from five previous studies. The measurements of Cadek (26) and Schlünder et al. (133) were obtained by interpolation of their profiles for H/w = 2.0 and 4.0. For the other three references the distribution at H/w = 2.0 is taken because the differences in the profiles for spacings of 2w and 2.6w are very small. The mass transfer rates obtained by Korger and Krizek (78), Schlünder et al. (133) and Kumada et al. (80) are converted to heat transfer with the aid of equation

$$Nu_j = (Pr/Sc)^n Sh_j \qquad (4.1)$$

with n being 0.42, in accordance with the recommendations of Hausen (55) for turbulent flow and the German literature on impinging jets. This value of n is larger than the value 0.373 obtained in Section 2.2.3.5 for the laminar impinging slot jet, and slightly larger than 0.4 normally used in the English literature on turbulent impinging jets.

Good agreement exists between the heat transfer data for an unconfined jet on a flat plate of Cadek (26), Gardón and Akfirat (44) and the present results, except for large values of x_1/w, as was the case also for the H/w = 6 spacing in Figure 4.6. The tendency for heat transfer for an unconfined cooling jet to be enhanced in the far wall jet region, already noted in connection with the comparisons on Figure 4.6, is again evident

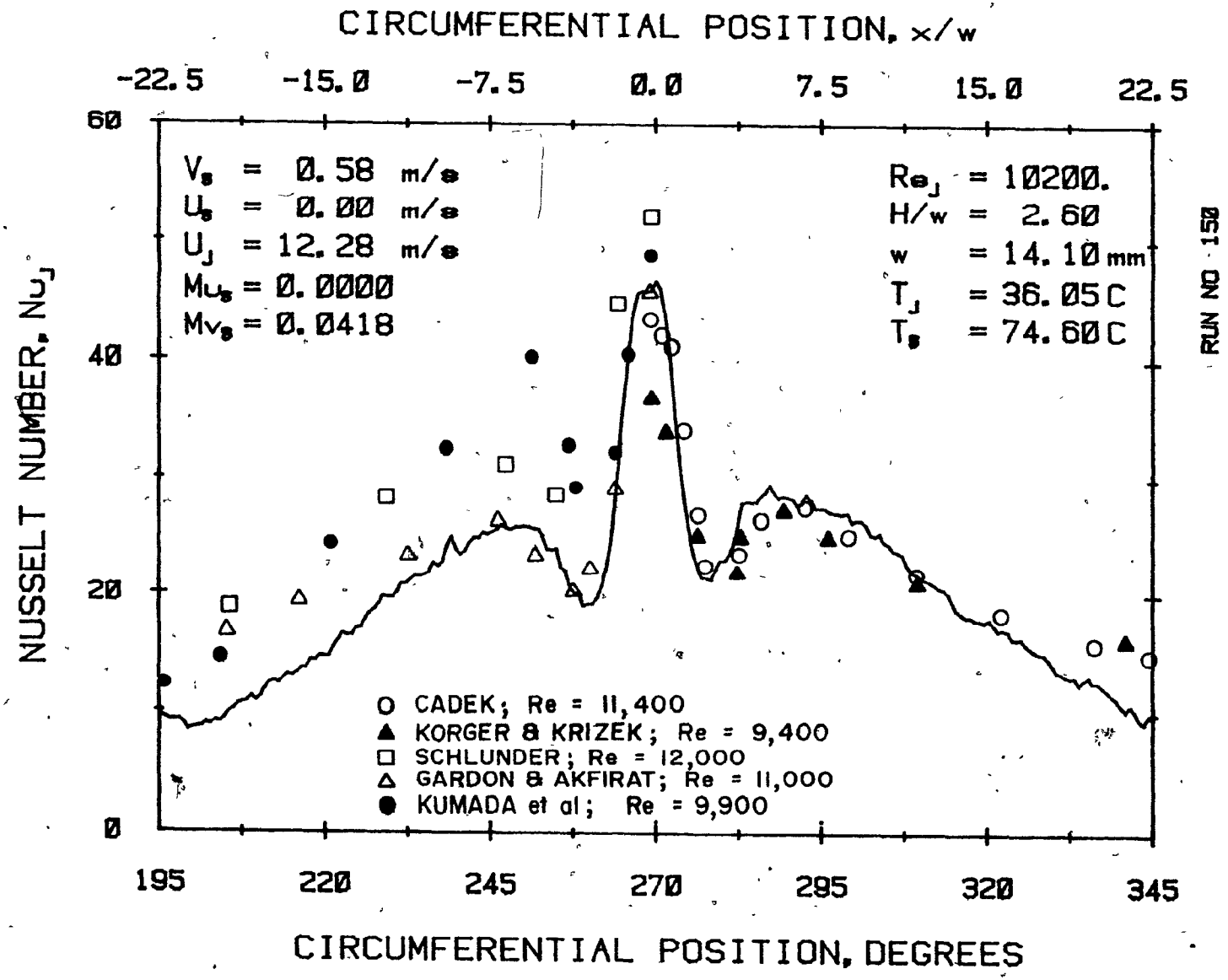


FIGURE 4.8. Lateral profiles of Nu_j at H/w = 2.6: Comparison of results for Re_j 9400 to 12000

on Figure 4.8. The agreement in the impingement and earlier wall jet region with the flat plate mass transfer data of Schlünder et al. (133) and Korger and Krizek (78) is reasonable considering the differences in Re_j. As the mass transfer distribution determined by Kumada et al. (80) for an unconfined slot jet impinging on a small cylinder (only 15w in diameter) shows quite different behaviour in the wall jet region from that found by all previous investigations as well as the present one, it is clear that their results cannot be used to confirm the accuracy of results from the present study.

Another example of the excellent agreement with the heat transfer data of Cadek (26) in the impingement and early wall jet region as well as the high resolution of the present experimental technique is given in Figure 4.9 for the higher Reynolds number of 52100. This figure also illustrates again the higher heat transfer in the far wall jet region that is found for an unconfined cooling jet.

4.3.2 Stagnation Point Heat Transfer

It is now generally agreed that at values of H/w sufficiently low and of Re_j sufficiently high there exists a laminar type boundary layer in the impingement region under even highly turbulent jets. It follows that, within this range of H/w and Re_j values, stagnation heat transfer for turbulent jets may be analyzed based on laminar boundary layer theory. This view, presented in Section 1.4, has been substantiated in the analysis of experimental heat transfer profiles from the present

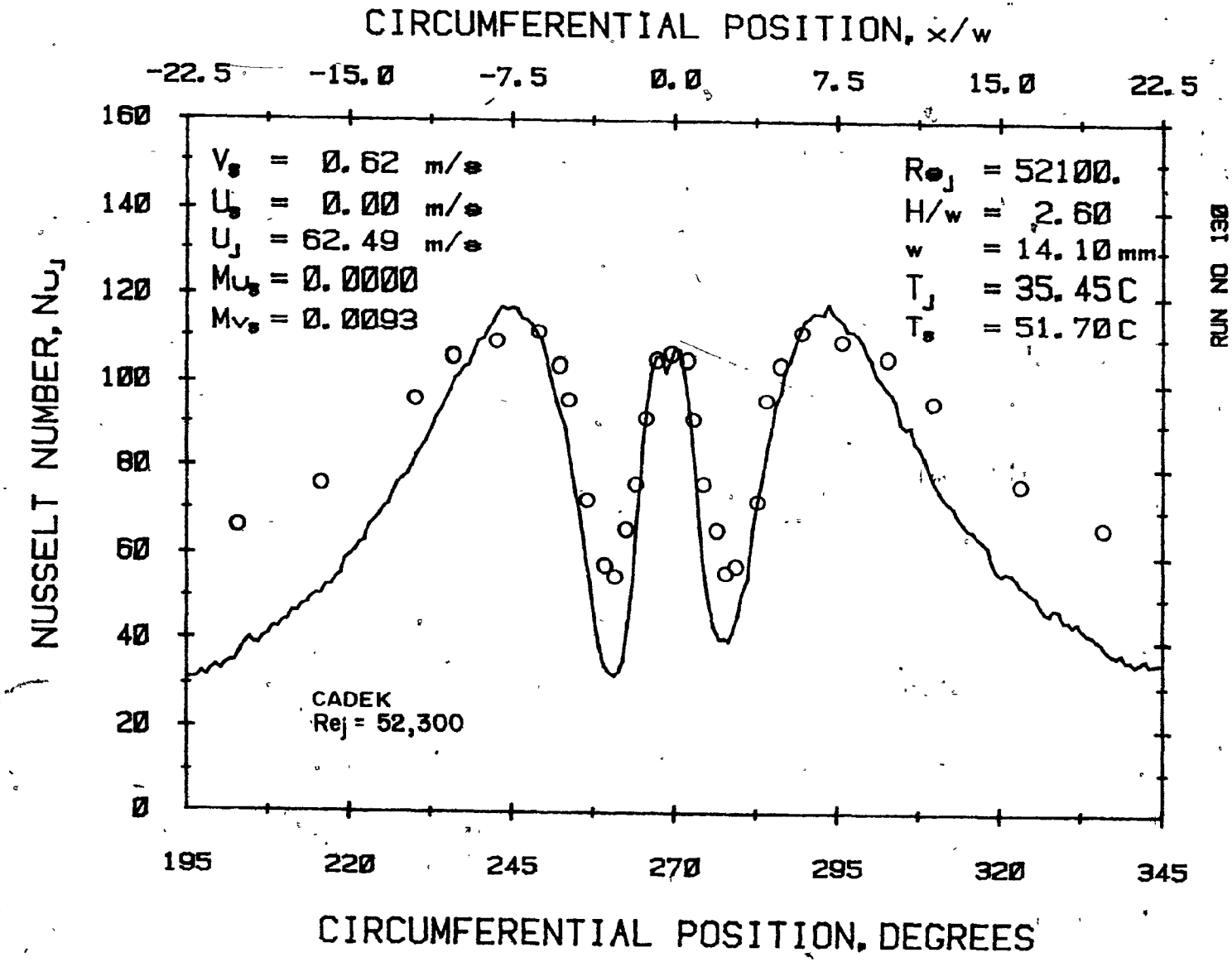


FIGURE 4.9. Lateral profiles of Nu_j at H/w = 2.6: Comparison of results for Re_j = 52200

study in Section 4.3.1. Theoretical expressions for stagnation point heat transfer derived from solution of the laminar boundary layer equations have the form

$$Nu_{oj} = C\sqrt{Re_j} \tag{4.2}$$

with C being a function of H/w and of the method used to calculate the free-stream boundary conditions. The two free-stream boundary conditions used for the impinging slot jet analysis are obtained from potential flow theory (Miyazaki and Silberman (97)) and experimental pressure distribution in the stagnation region (Cadek (26) and Andreyev et al. (4)). In accordance with these analyses the present stagnation point heat transfer data for the two impingement surface spacings, H/w of 2.6 and 6, are presented with $Nu_{oj}/\sqrt{Re_j}$ as a function of Re_j in respectively Figures 4.10 and 4.11.

The present data in Figure 4.10 for H/w = 2.6 show a small decrease in $Nu_{oj}/\sqrt{Re_j}$ with increasing Re_j over the very wide experimental range of the latter variable. The magnitude of the decrease at high Reynolds number could be explained for the most part by the small decrease in effective temperature driving force at the stagnation point accompanying the development of a small adiabatic wall temperature effect, as described in Section 3.5.3. Therefore it is concluded that the stagnation heat transfer at H/w = 2.6 for the present flow configuration over the range $10^4 \leq Re_j \leq 10^5$ is well described by equation (4.2) with C = 0.455. This value of the proportionality constant is

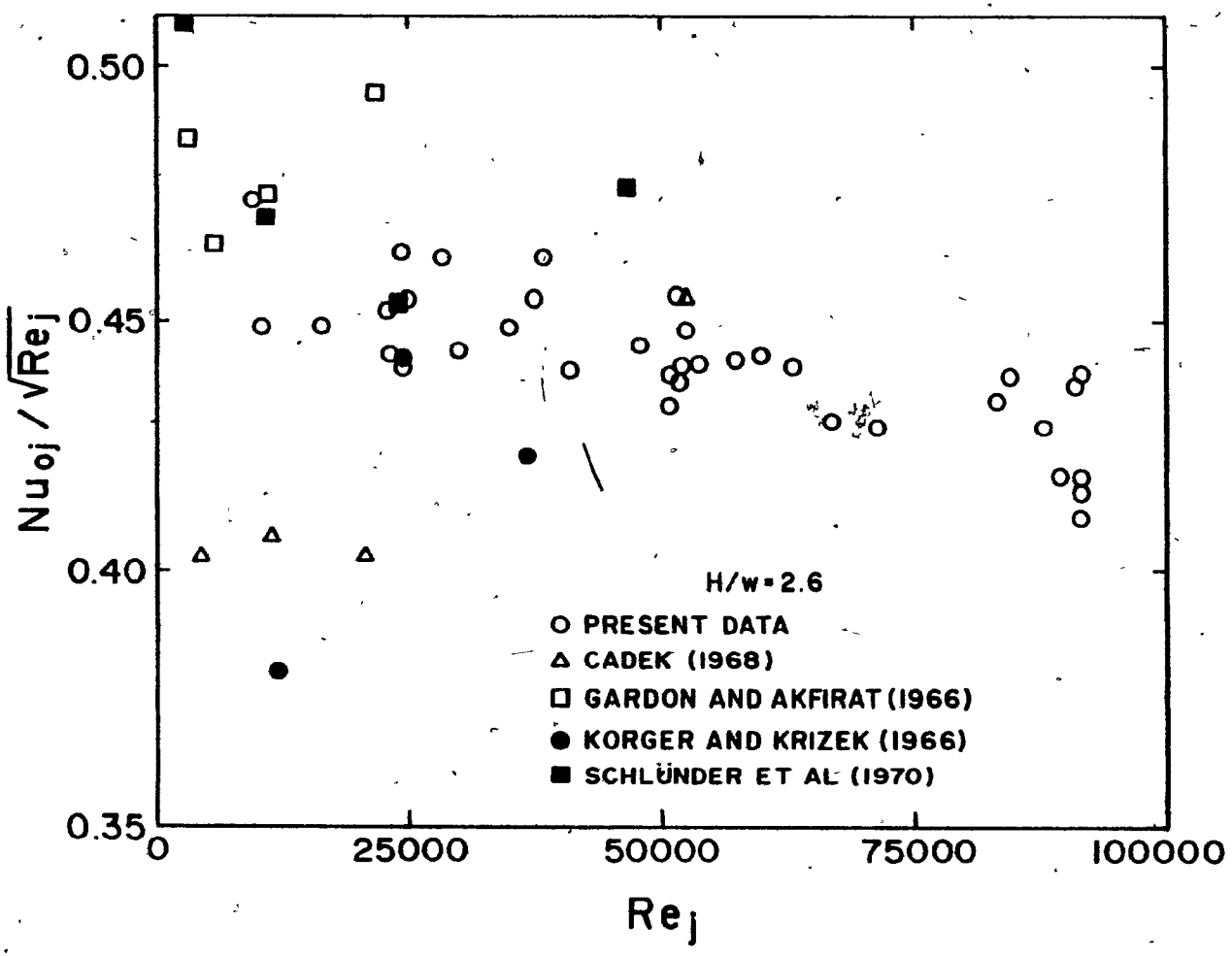


FIGURE 4.10. Stagnation point heat transfer at H/w = 2.6: Effect of Re_j

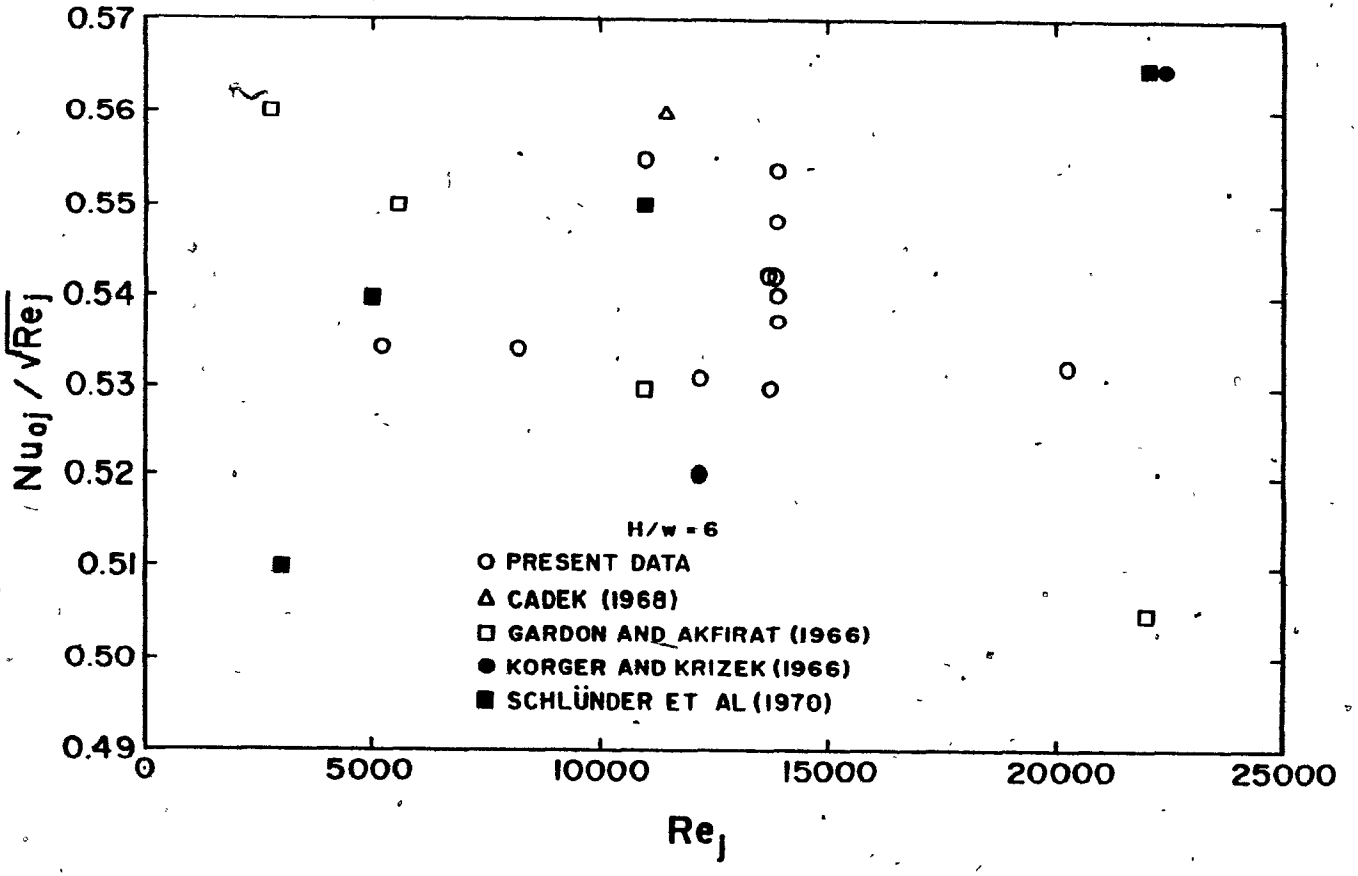


FIGURE 4.11. Stagnation point heat transfer at H/w = 6: Effect of Re_j

very close to the theoretical value of 0.44 obtained by both Miyazaki and Silberman (97) and Andreyev et al. (4). A constant of 0.458 is obtained when interpolating the semi-theoretical results of Cadek (26) between his spacings, H/w, of 2 and 4.

The influence of cylinder curvature on stagnation point heat transfer of an impinging slot jet for $H/w \leq 4$ has been studied experimentally by Kumada et al. (80). Their work indicates that for cylinder diameters of 25w, 15w and 7.5w, the proportionality constants C of equation (4.2) are 0.46, 0.49 and 0.54. The experimental results of Kumada et al. for cylinders of diameter less than 15w are confirmed by the subsequent potential flow analysis of Miyazaki and Sparrow (98). From the close agreement between the values obtained by Kumada et al. of $C = 0.46$ for a slot jet impinging on a cylinder of diameter 25w and the flat plate constants of 0.44 and 0.458, obtained by respectively Miyazaki and Silberman (97) and Cadek (26), it is concluded that the effect of curvature in the impingement region can be neglected for the present study at $H/w = 2.6$ as for this case the impingement cylinder diameter is 34w.

The close agreement between the equation proposed for the stagnation point heat transfer for $H/w = 2.6$

$$Nu_{oj} = 0.455\sqrt{Re_j} \qquad (4.3)$$

and the semi-theoretical results referred to above for $H/w = 2.6$, confirms the appropriateness of the laminar boundary layer

based theory in this range of Re_j and H/w for a turbulent impinging slot jet. It should be stressed that this agreement by no means implies that the jet is laminar on arrival at the impingement surface. Thus although the length of the potential core is indeed greater than 2.6w, the recent measurements of Saad (125) have shown that for the same type of nozzle used in the present study, for which nozzle exit turbulence intensity is less than 1%, the arrival turbulence level increases by a factor of from 3 to 5 times, i.e. to 3%-5% turbulence intensity by only 2.6w from the nozzle exit.

The flat plate stagnation heat transfer data obtained by Cadek (26) (interpolation between his spacings, H/w, of 2 and 4) and Gardon and Akfirat (45) are also shown in Figure 4.10. The mass transfer data of Schlünder et al. (133) and Korger and Krizek (78) displayed are likewise interpolated between H/w spacings of 2 and 4 before being converted to heat transfer using equation (4.1). The deviations from equation (4.3) of the transfer data derived from these references are generally less than 12%.

A similar representation of stagnation point heat transfer at H/w = 6 from the present study is shown in Figure 4.11, these data being well-described by

$$Nu_{oj} = 0.54\sqrt{Re_j} \qquad (4.4)$$

over the range of Re_j considered. For this spacing it can be

seen that for some value of Reynolds number in the range $5200 < Re_j < 8200$ does the transition to turbulence lead to a sufficient increase in heat transfer to produce a secondary heat transfer maximum. It should therefore be noted that at $Re_j = 5200$, Figure 4.11 indicates a proportionality constant, C, no different than at the higher values of Re_j which produce a laminar boundary layer in the impingement region. The agreement of data at $H/w = 6$ with the same four references as in Figure 4.10 is again quite good, considering the differences in nozzle design and experimental set-up which lead to different velocity distributions and, especially, to different levels of arrival turbulence intensity.

Whereas at $H/w = 2.6$, there was close agreement between the experimentally determined proportionality constant for equation (4.2) and that predicted based on laminar boundary layer theory, this is not the case at the larger spacing. Thus at $H/w = 6$ the experimentally determined value of the constant in equation (4.4), 0.54, is much larger than the theoretical values obtained by Miyazaki and Silberman (97) and Cadek (26) of respectively 0.44 and 0.40. The higher proportionality constant C at $H/w = 6$ is attributed to the augmenting effect of jet turbulence on heat transfer through the laminar-like boundary layer. Beyond considerations from previous studies presented in Section 1.4.2 it is pertinent to note also that the recently reported results of Saad (125) show that by 6w from the nozzle exit, turbulence intensity from the same type of nozzle used in the present study increases to a value in the range 9%-14%. The large increase in nozzle centerline turbulence intensity

documented by Saad, i.e. from about 3%-5% at 2.6w from the nozzle exit, to 9%-14% at 6w from the nozzle, may than be taken as the reason for the considerable increase in C over the laminar boundary layer value for H/w = 6, in contrast to the close agreement at H/w = 2.6.

Most impinging jet studies report a small increase in the turbulence augmenting effect with increasing Reynolds number when H/w = 4. Correlation of such results as Nu_{oj} as a function of Re_j^n leads to exponents, n, slightly larger than 0.5, as can be seen in Figure 1.8. The results of five investigations presented in Figure 4.11 indicate however no predominant trend in this regard. The upward trend of C with increasing Re_j is shown in Figure 4.11 for the data of Schlünder et al. (133) and Korger and Krizek (78) but the reverse trend is indicated by the data of Gardon and Akfirat (44) at H/w = 6. The trend in the latter case may be caused by their special nozzle design. The result of Cadek (26), obtained with exactly the same ASTM long radius nozzle as in the present study, is in reasonable agreement with the proposed correlation, equation (4.4).

4.3.3 Heat Transfer Distribution in the Stagnation Region

The influence of Reynolds number on heat transfer in the stagnation region over the wide Re_j range of the present study can conveniently be seen by normalizing local Nusselt number to the stagnation point value.

In Figures 4.12 and 4.13 these normalized stagnation heat transfer distributions are compared with theoretical solutions

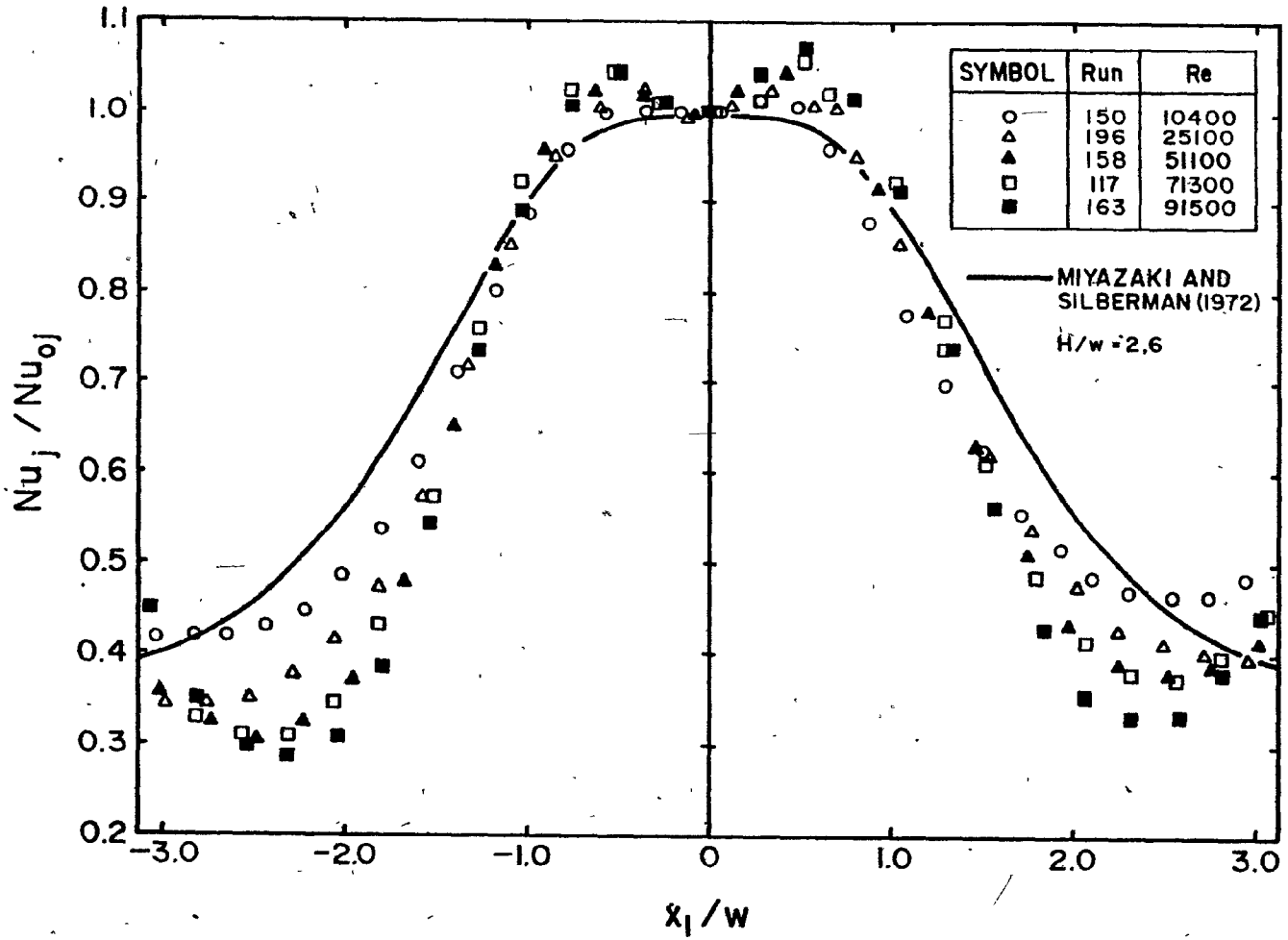


FIGURE 4.12. Heat transfer distribution in the stagnation region at H/w = 2.6: Effect of Re_j

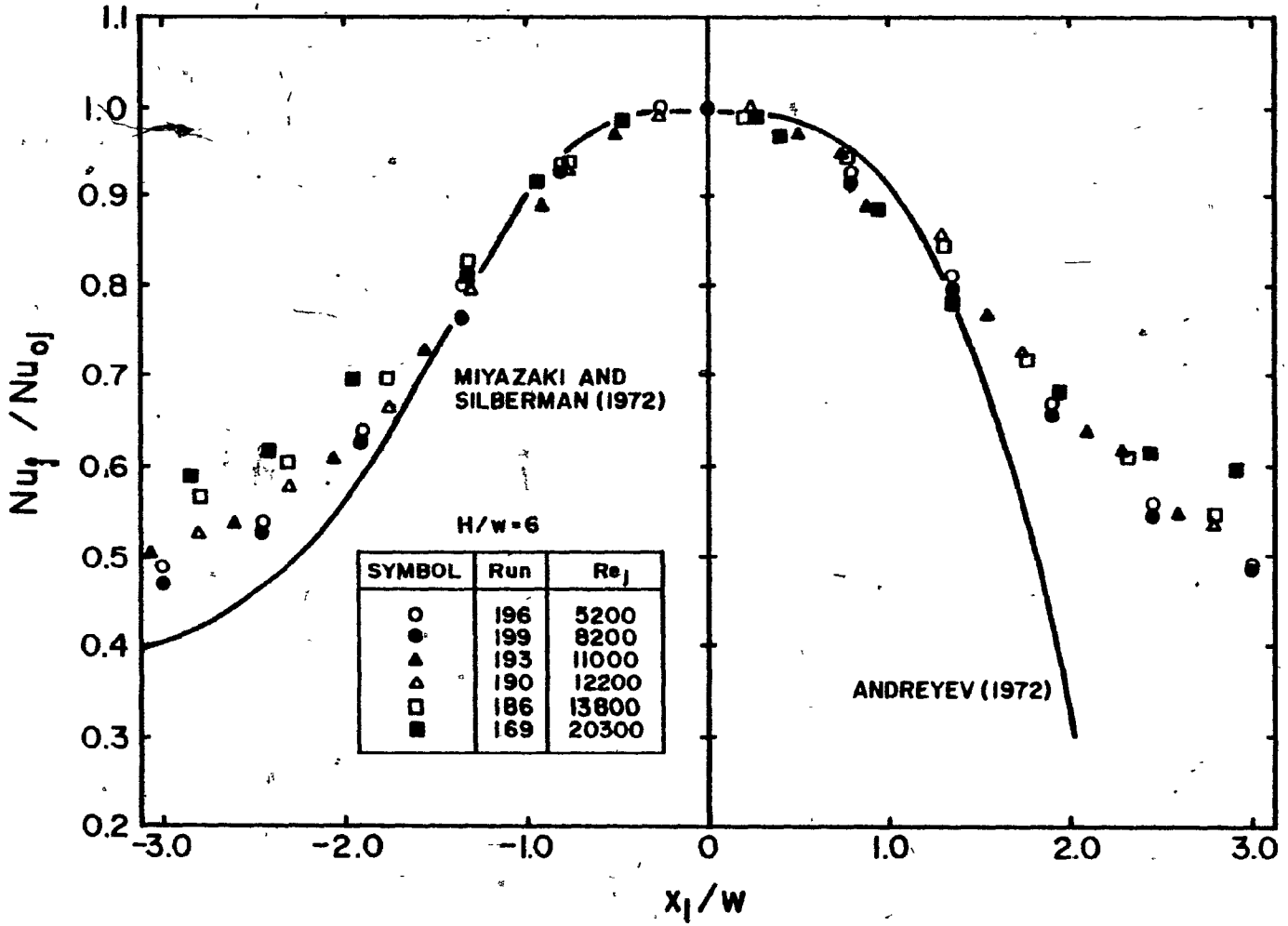


FIGURE 4.13. Heat transfer distribution in the stagnation region at H/w = 6.0: Effect of Re_j

for spacings, H/w, of 2.6 and 6.0, respectively. The agreement between the present data and the theoretical solution of Miyazaki and Silberman (97), based on potential flow theory and a laminar boundary layer solution, is reasonable for both impingement surface spacings used. The theoretical prediction of Andreyev et al. (4) is clearly not as good. The fact that a theoretical solution based on a laminar boundary layer can give a reasonable estimate of heat transfer out to the position of the minimum in the heat transfer profile provides further confirmation that for low H/w-high Re_j, the associated high pressure gradient in this region is able to maintain a laminar boundary layer even under these highly turbulent jets, as discussed earlier in Sections 4.3.1 and 4.3.2. The relatively small scatter of the normalized data over the wide range of Reynolds numbers in Figures 4.12 and 4.13 implies that out to the transition point minimum in the profile, Nu_j dependence with Re_j^n is represented reasonably well with the same exponent used at the stagnation point, $n = 0.5$, the exponent characteristic of a laminar boundary layer. At $H/w = 6$, there is indication in Figure 4.13 of this exponent becoming greater than 0.5. The slight shift inward of the transition point minimum with large increases in Re_j, noted in Section 4.3.1, can be seen more clearly on Figure 4.12.

It is believed that a high turbulence level at $x_1/w = \pm 0.5$ is responsible for the small peaks in heat transfer at these locations. For the same type of slot nozzles used in the present study, the recent work of Saad (125) has documented the

extremely high peaks in turbulence directly under the nozzle walls, i.e. at $x_1/w = \pm 0.5$. Thus at 1w downstream from the nozzle exit Saad found that the turbulence intensity was about 25% at $x/w = 0.5$ although only 2.5% at the nozzle centerline. The phenomena cannot be explained by temperature variations across the width of the nozzle because the size of the peaks was not a function of $T_s - T_j$ and the variations in recovery temperature over 1w around the stagnation point are too small to explain the size of the peaks. Thus the turbulence profile for impingement surface spacings as close as $H/w = 2.6$ can be accepted as the cause of these small heat transfer peaks under the nozzle walls.

4.3.4 The Secondary Heat Transfer Maximum

Shown in Figures 4.14 and 4.15 is the effect of Reynolds number on the secondary heat transfer maxima for both spacings, H/w, of the present study. The values used for these maxima are the average of the right and left peaks from each complete profile. The present data are well-correlated by

$$Nu_{jm} = 0.0060\ Re_j^{0.907} \tag{4.5}$$

for $H/w = 2.6$, and by

$$Nu_{jm} = 0.0114\ Re_j^{0.844} \tag{4.6}$$

for $H/w = 6$.

The only previous correlation of secondary heat transfer

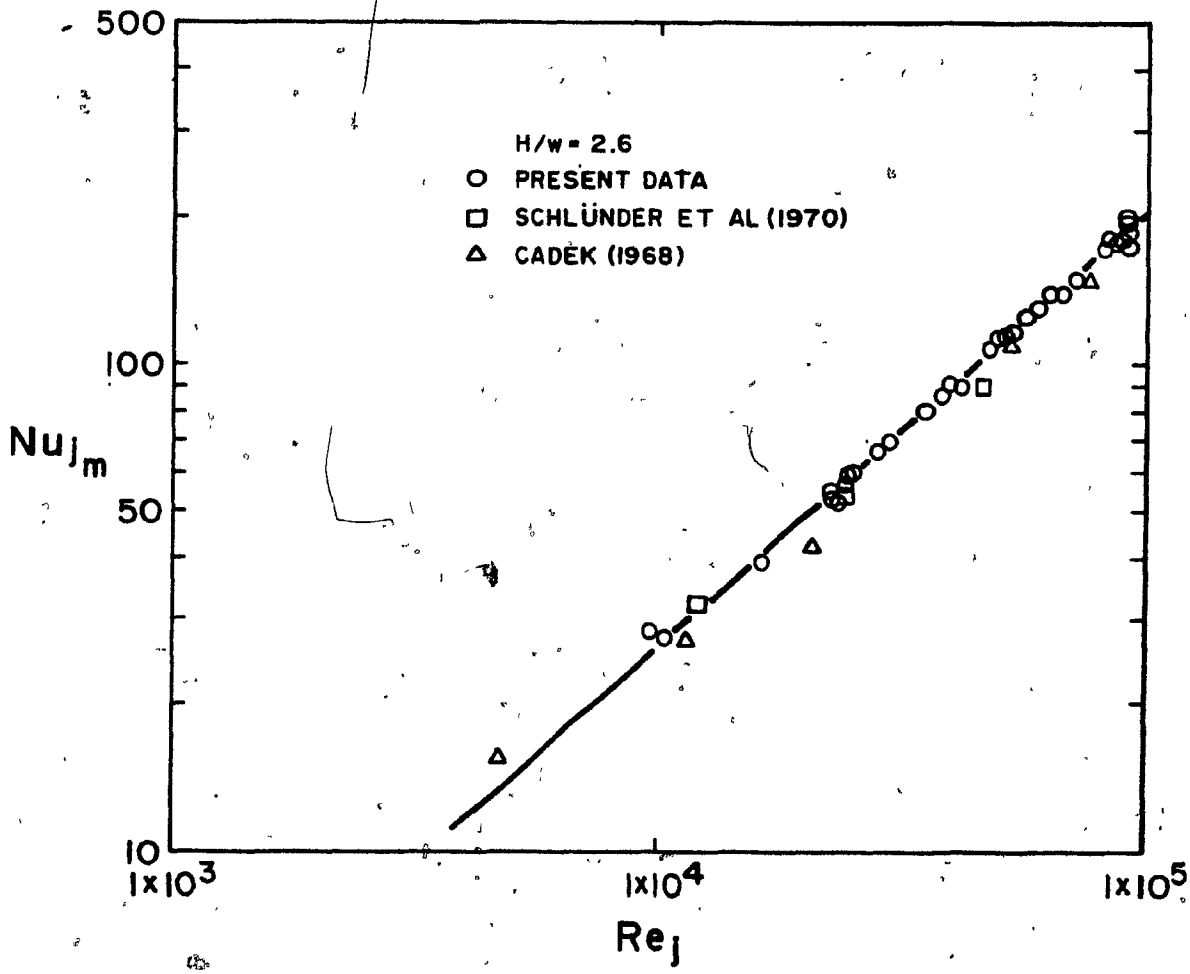


FIGURE 4.14. Secondary heat transfer maximum at H/w = 2.6: Effect of Re_j

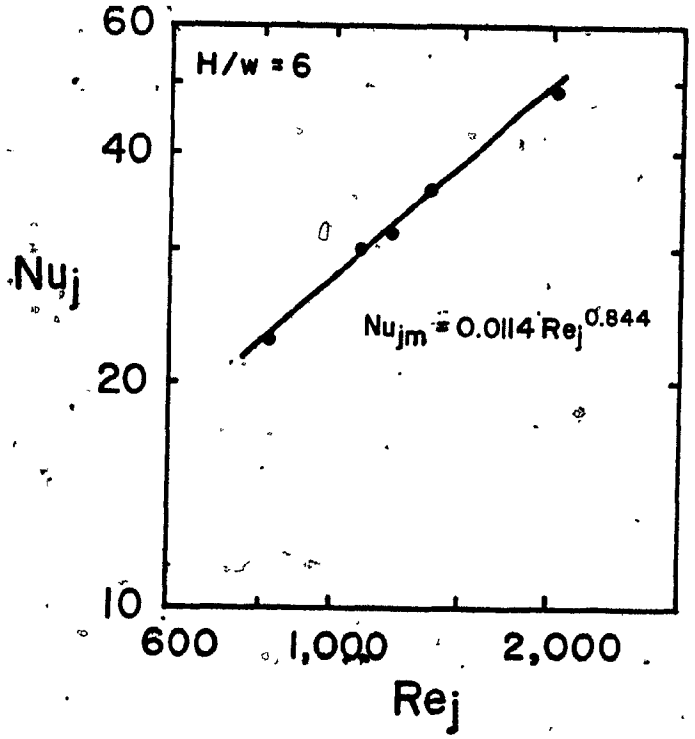


FIGURE 4.15. Secondary heat transfer maximum at H/w = 6: Effect of Re_j

maxima was by Kumada et al. (80) for their results at H/w = 2.0. Their Re_j exponent of 2/3 is considerably lower than the present value of 0.907. However, it has already been noted in Section 4.3.1 in connection with the display of their data on Figure 5.8 that their results are completely out of line relative to those of all other studies, a difference which is attributed to the fact that their unconfined jets impinged on a small cylinder only 15w in diameter. However, reasonable agreement can be seen on Figure 4.14 between the present results and those of Cadek (26) and Schlünder et al. (133) for unconfined slot jets impinging on flat plates. This comparison is again based on interpolation between their data for H/w of 2 and 4. Finally, as stagnation heat transfer is proportional to $Re_j^{0.5}$ because of laminar boundary layer conditions around this point, while the Reynolds number dependence at the secondary heat transfer maxima reflects a fully turbulent boundary layer, the latter increase faster with increasing Re_j and finally dominate the heat transfer profiles, as was shown spectacularly in Figure 4.7.

4.3.5 Heat Transfer Distribution in the Wall Jet Region

The first observation in the analysis of heat transfer in the wall jet region beyond the secondary maximum derives from the complete profiles of Figure 4.5 of Section 4.3.1, which give the best overall perspective as they extend 51w from stagnation. These profiles indicate that, over a wide range of Re_j, there is a distinct change in slope at about 20w from stagnation, the decay in heat transfer with lateral distance being

greater before, less subsequent to this break in the profiles. In order to examine the wall jet region further, some of the profiles of Figure 4.5 have been replotted on Figure 4.16. On the latter figure, both halves of the profiles for each run have been folded on to a single scale by using only the absolute value of the lateral position, $|x_1/w|$. Moreover, the profiles are expressed in terms of total distance from the nozzle exit through use of the coordinate $H/w + |x_1/w|$. Thus the three complete profiles for the indicated values of Re_j appear on Figure 4.16 as three pairs of profiles. The choice of this total distance coordinate and the switch to logarithmic scales relates to the theoretical derivation of Cadek (26) that wall jet heat transfer is proportional to $(H/w + |x_1/w|)^{-0.5714}$ for large $|x_1/w|$. This behaviour was confirmed by his experiments. The form $H/w + |x_1/w|$ was obtained by Cadek using the assumption, based on extensive experimental evidence, that the outer layer of the wall jet behaves as half a free jet, the origin of which is from a fictitious nozzle discharging parallel to the impingement surface, from the side opposite to the wall jet and at a distance H from the stagnation point.

Three factors which may affect conditions in the wall jet region are whether the jet is confined or unconfined, and whether the impingement surface is curved or flat, in motion or stationary. As the effect of surface motion appears as a loss of symmetry in a complete profile, the presence of this effect may readily be detected in Figure 4.16 by failure of a pair of half-profiles to superimpose. As noted earlier, the quantitative

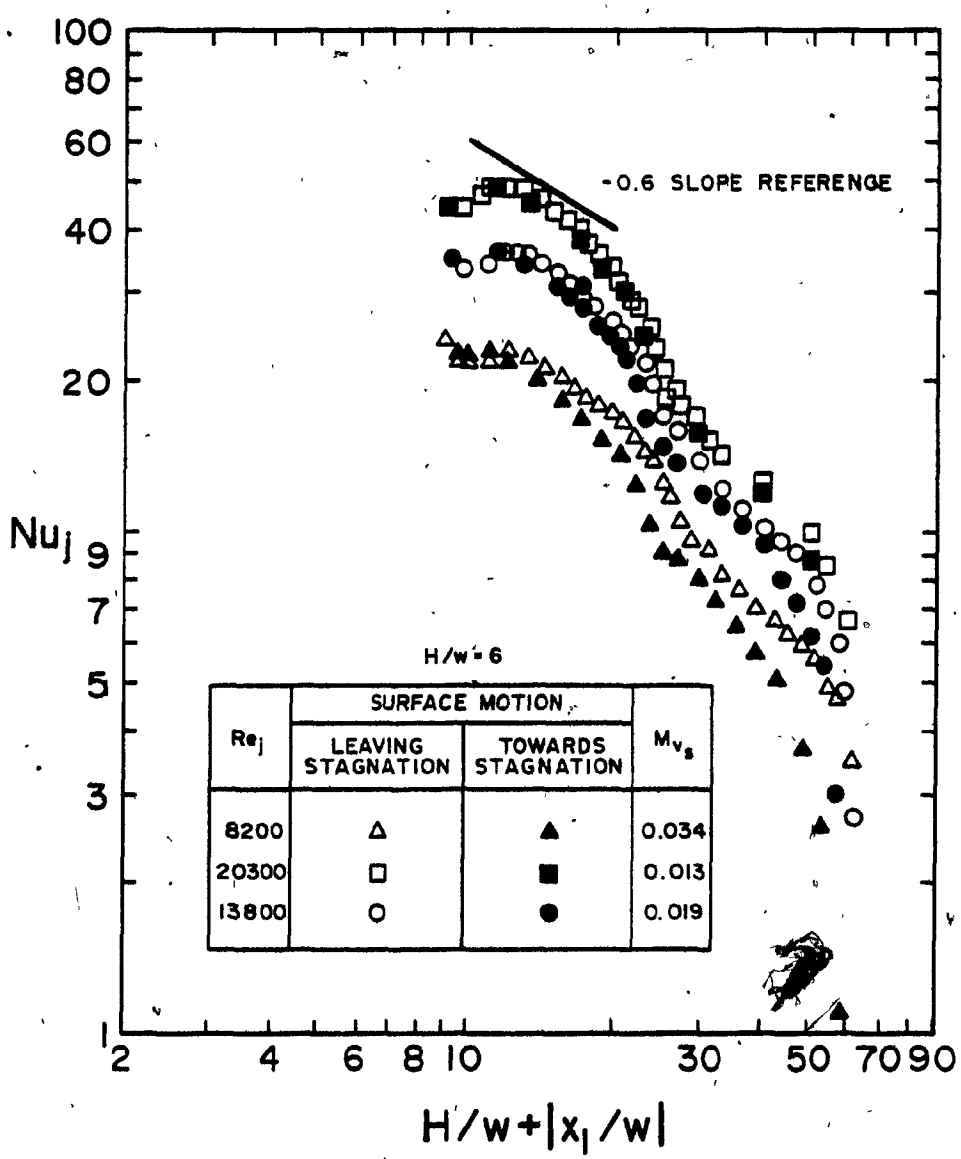


FIGURE 4.16. Heat transfer in the wall jet region at H/w = 6: Effect of Re_j and M_{v_s}

measure of surface motion is provided by the dimensionless parameter, M_{V_s}. Thus in Figure 4.16 it is evident that a surface motion effect is clearly present for $M_{V_s} = 0.034$, marginally present for $M_{V_s} = 0.019$, and absent for $M_{V_s} = 0.013$. As the effect of surface motion is treated extensively in the subsequent section 4.4, the present analysis is restricted to cases for which this is not a significant variable.

For the case for which there is no surface motion effect ($M_{V_s} = 0.013$) Figure 4.16 indicates that the slope of the profile from the secondary maximum to the break in the profile noted earlier, i.e. from 12 to 26 on the abscissa, is clearly steeper than the -0.57 slope obtained by Cadek. Beyond the break in the profile at $H/w + |x_1/w| = 26$, the slope is less steep, but never fully as flat as a slope of -0.6. The profile for the case without surface motion effect, $M_{V_s} = 0.013$, is shown as a line on Figure 4.17 along with comparative data by Cadek (26) for an unconfined jet on a flat surface at spacings, H/w, of 4 and 8. The present results for $H/w = 6$ are envelopped by the measurements of Cadek at spacings of 4 and 8 up to $H/w + |x_1/w| = 20$, i.e. to $x_1/w = 14$ at $H/w = 6$, indicating that the influence of confinement and impingement surface curvature are of minor importance in this region. However, the slope of the line for the present results is clearly more steep than the reference results, starting at about $H/w + |x_1/w| = 15$, i.e. after 9w from stagnation.

Heat transfer in the wall jet region beyond the secondary maximum appears to reflect interaction between the effects of

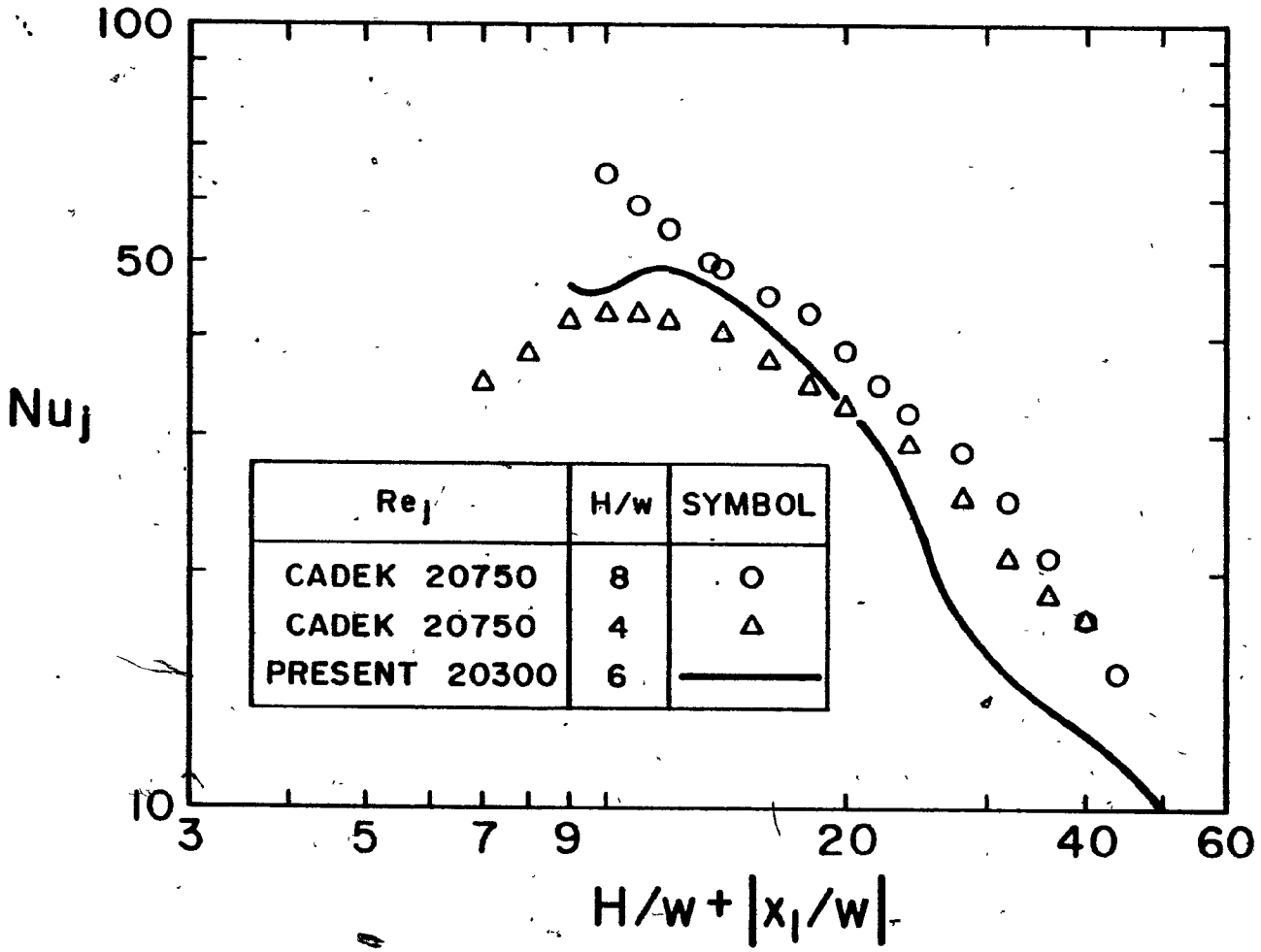


FIGURE 4.17. Heat transfer in the wall jet region at H/w = 6: Comparison of results

curvature of the impingement surface and the unconfined/confined alternative for impingement systems. As most previous studies have been of unconfined jets impinging on flat surfaces while the present one is exceptional in use of the combination of a confined, cylindrical impingement system, complete separation of the effects of these interacting variables is therefore not possible. Two effects may be attributed to confinement. While an unconfined air jet entrains large amounts of air from the surroundings, thereby enhancing the wall jet flow, the totally confined impingement system of the present study restricts this effect to the amount of exhaust air which can be entrained in a recirculating flow along the confinement surface to the region of the jet and eventually into the wall jet flow. Clearly this effect of confinement acts to reduce the wall jet velocity relative to that for an equivalent unconfined jet, a reduction which in turn reduces impingement surface transfer rates. However another, and an opposite effect, of the presence of a confinement surface is to restrain the expansion of the wall jet, an effect which would decrease the rate of decay of velocity of a confined wall jet, thereby slowing the decay in impingement surface transfer rates. The effect of the wall jet flowing over a convex surface, the case in the present study with a cylindrical impingement surface, would be to allow the wall jet width to increase more quickly and hence the wall jet velocity to decay more rapidly.

Of these three effects, that of the convex impingement surface permitting the wall jet velocity, and hence transport rates,

to decay more quickly would act over the entire curved surface. The effect of confinement on reducing entrainment and hence reducing wall jet velocity and surface transport rates may become effective only at some distance from stagnation, i.e. after mixing and interaction with the entrained flow has begun to influence the wall jet. The third effect, enhancement of wall jet velocity and surface transfer rates by restriction of spreading of the wall jet, would start to be felt the farthest from stagnation, i.e. at the position when the width of an unconfined wall jet would have grown to approach the spacing of the confinement surface from the impingement surface (H, in the present study).

While the three heat transfer effects noted above are all the results of changes in the flow field, yet another factor is a thermal effect. For unconfined impingement systems, the standard configuration for previous studies, entrainment of surrounding air would also affect the local effective ΔT for convective heat transfer with the wall jet. Thus for an unconfined cooling jet on a heated surface, entrainment of ambient air tends to decrease the temperature of the wall jet, hence increases local effective values of ΔT, thereby leading experimentally to an apparently enhanced heat transfer coefficient. Entrainment of ambient air into an unconfined heating jet on a cooler surface would have the inverse effect, i.e. of decreasing local effective ΔT at the impingement surface. As most previous studies have been of unconfined cooling jets on heated surfaces, this thermal effect acts to exaggerate the heat transfer coefficients

in all such studies.

The above analysis concerning transfer rates for a confined cylindrical impingement surface relative to an unconfined jet on a flat surface suggests, then, that of the three flow field effects, one effect acts to reduce transfer rates over the entire convex surface, a second effect (reduction of entrainment by confinement) begins to reduce transfer rates after some distance from stagnation, while a third effect (reduction in decay of wall jet velocity by restriction of wall jet spreading by confinement) begins only far out in the wall jet. The heat transfer profile for the $M_{V_s} = 0.013$ case of Figures 4.16 and 4.17, for which the further complication of surface motion is absent, appears consistent with the above analysis. Specifically, starting shortly after the secondary maximum, this profile shows a steeper decay than the -0.6 slope derived theoretically and confirmed experimentally by Cadek for an unconfined cooling jet on a flat surface. However, the steepness of the decay continues to increase out to about 20w from stagnation, consistent with an increasing effect of reduction of heat transfer through a wall jet flow decreased by confinement, plus the thermal effect which, for Cadek's unconfined cooling jet, results in exaggeration of the heat transfer rates in the wall jet. Finally, the reduction in rate of decay of heat transfer after about 26w from the nozzle exit is consistent with the effect of the confinement surface restraining wall jet expansion and velocity decay.

Complete identification of the location and quantitative effects of these four factors requires more extensive measure-

ment than has yet been undertaken in this field. Figure 2.56 indicated that comparison of the velocity measurements by Kumada and Mabuchi (79) for an unconfined impinging jet with the present computational results for a confined impinging jet on a flat surface showed no influence of the confining plate up to $x_1/w \approx 12$ at $H/w = 6$. However for $x_1/w > 12$ at this spacing, i.e. for $(H/w + |x_1/w|) > 18$, the decrease in maximum wall jet velocity in Figure 2.56 is much stronger for the computed confined jet than the experimental unconfined results of Kumada and Mabuchi. Figure 2.56 also indicates that the decrease in computed maximum wall jet velocity is stopped at around $H/w + |x_1/w| \approx 70$ due to restraint by the confinement plate of growth in wall jet width and corresponding wall jet velocity decay. This position is much later than the break in the profiles of Figures 4.16 and 4.17, i.e. about 26w from the nozzle exit. The relevance of this comparison is however limited by the fact that the experimental impingement surface is cylindrical, for which wall jet growth is expected to be increased, leading to an earlier onset of the restraint of wall jet growth by the confinement surface, as shown by Wilson and Goldstein (152).

The wall jet heat transfer for $H/w = 2.6$ is similarly displayed in Figure 4.18. Shown in addition to the pairs of profiles for three Reynolds numbers at $H/w = 2.6$ from the present study are the reference line of the symmetric distribution for $Re_j = 20300$ at $H/w = 6$ (from Figure 4.17) and the flat plate, unconfined jet heat transfer data of Cadek (26) at $Re_j = 52300$ and $H/w = 2.0$. Dealing first with the additional effect of sur-

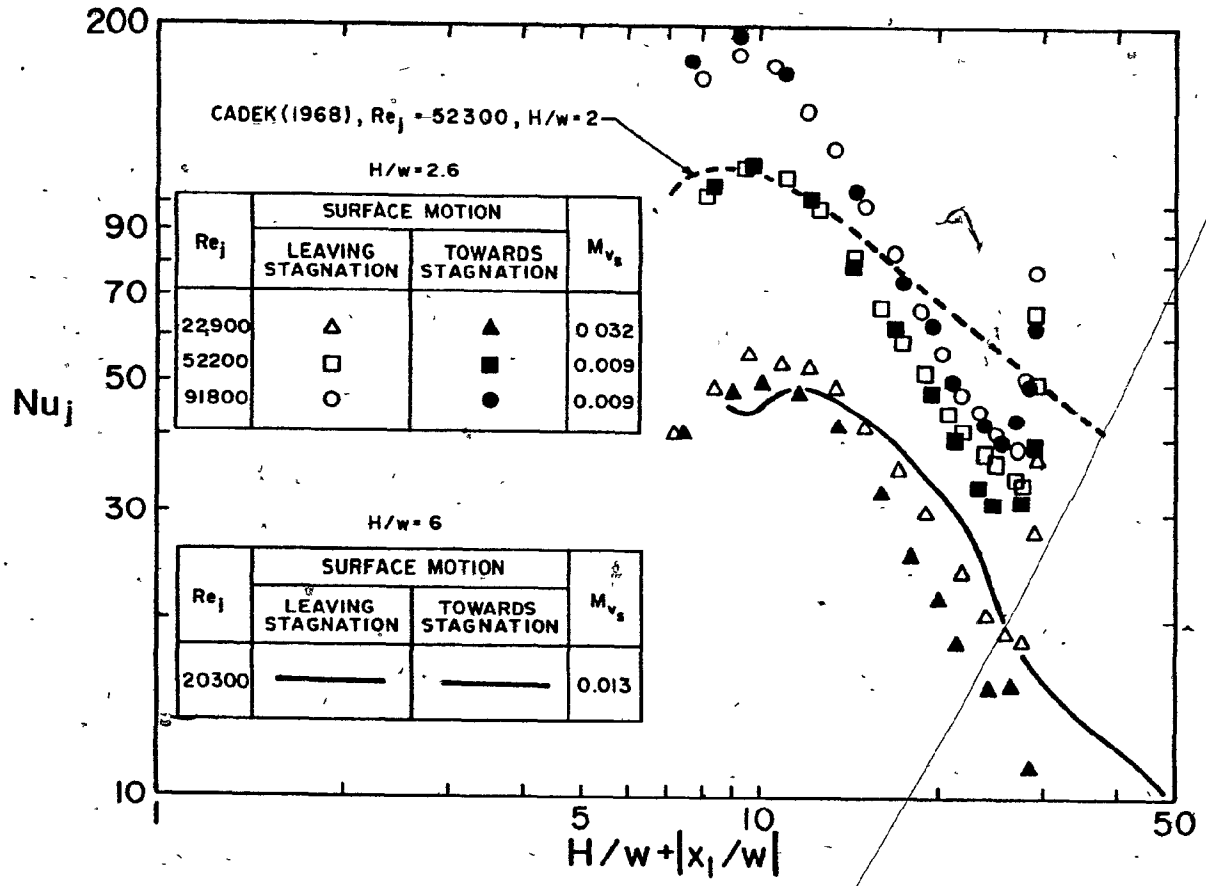


FIGURE 4.18.— Heat transfer in the wall jet region at H/w = 2.6: Effect of Re_j and M_{Vs}

face motion, it is seen that such an effect is present for M_{V_s} = 0.032 in that this pair of profiles do not superimpose, while at M_{V_s} = 0.009 the profiles are symmetric within limits of experimental accuracy, thus indicating that, for these two profiles, surface motion is not a factor. As was done in discussion of the H/w = 6 data of Figure 4.16, the present analysis excludes the effect of surface motion, this being treated extensively in the next section, 4.4.

The heat transfer behaviour in the wall jet region for the closer spacing of H/w = 2.6 differs appreciably from that noted on Figures 4.16 and 4.17 for H/w = 6. The reference line for H/w = 6 on Figure 4.18 indicates that the initial rate of decay of Nusselt number beyond the secondary maximum is not much more steep than Cadek's slope of -0.57, becoming progressively steeper with increasing distance until reaching the break-point in the profile at about $H/w + |x_1'/w| = 26$. By contrast, for H/w = 2.6 there is no initial period of decay at a rate not much steeper than the -0.57 reference slope. In this regard it is pertinent to recall the three flow field effects enumerated in the discussion of the H/w = 6 profiles of Figures 4.16 and 4.17, namely, the effect of a convex surface in enhancing growth of wall jet width and decreasing wall jet velocity, the effect of confinement on reducing the wall jet flow, and the effect of confinement of restraining the wall jet in the region far from stagnation. Relative to the jet, the curvature of the impingement surface for H/w = 2.6 is significantly greater than for H/w = 6. This relationship derives from the fact that H is maintained

the same as for the H/w = 6 case, while w is increased - from 6.2 mm to 14.1 mm. Thus the diameter of the impingement surface is 77.7w when H/w = 6, but only 34.2w for H/w = 2.6. Thus the curvature effect on increasing wall jet growth and decreasing wall jet velocity and thereby decreasing heat transfer relative to a flat impingement surface can be one factor in the difference between the wall jet results at these two spacings. The second basic flow field effect, that of confinement reducing the wall jet flow, this effect will also be greater, the closer the relative spacing between the confinement and impingement surfaces. Quantitative evidence is available in this regard. Thus the computational results in Figure 2.51 show that for $x_1/w > 4$ or $(H/w + |x_1/w|) > 7$ the computed maximum wall jet velocity becomes lower than the unconfined flat plate results of Kumada and Mabuchi (79). Thus both the increased curvature of the convex impingement surface and the closer relative proximity of the confinement plate to the impingement surface combine to yield wall jet heat transfer profiles which decay faster at H/w = 2.6 than at H/w = 6 for the present study, and much faster than the reference case of an unconfined cooling jet on a flat surface of Cadek. It is clear that reliance on results such as those of Cadek would lead to serious overestimation of heat transfer for confined jet systems on cylindrical impingement surfaces.

It will be recalled that the results of Figures 4.16 and 4.17 for H/w = 6 provided evidence for the third effect, i.e. that at about 26w from the nozzle exit, the wall jet began to

be constrained by the confinement surface and hence the rate of decay of heat transfer with increasing distance was reduced. At the H/w = 2.6 spacing however, the length of the wall jet region relative to the slot width, w, is considerably reduced, with the result that the position 26w from the nozzle exit is now reached just as the disturbance caused by the defection of the wall jet into the exhaust ports starts. If the lateral extent of the confined wall jet region had been greater, presumably the same sort of break in the heat transfer profiles would have appeared as was found for H/w = 6 when the wall jet could be monitored for about 60w from the nozzle exit. The sharp increase in Nu_j shortly before the skimmer plates which is apparent at the end of the profiles on Figure 4.18 is caused by flow recirculation in the corner formed by the skimmer plate and the cylindrical impingement surface, and is therefore simply an end effect of this particular equipment.

4.3.6 Average Heat Transfer

Average heat transfer was obtained by integrating the local heat transfer distribution from $-x_1/w$ to x_1/w in the data reduction program. For H/w = 6 the data for average heat transfer data in Table 4.4 were correlated by a relatively simple equation

$$\overline{Nu}_j = \frac{0.91}{\frac{x_1}{w} + 22} Re_j^{0.76} \qquad (4.7)$$

for $8.5 \leq x_1/w \leq 51$ and $5200 \leq Re_j \leq 20300$. It will be recalled

from Section 4.3.1 that for $H/w = 6$, the secondary maximum occurs at about 6w or 1H from stagnation. Thus the smallest impingement surface for which the equation (4.7) correlation of average heat transfer is valid, i.e. $x_1/w = 8.5$ or $x_1/H = 1.4$, is one which is slightly larger than that which contains the two maxima and the intervening minimum. The comparison, which may be seen on Figure 4.19, of $\overline{Nu}_j$ from Table 4.4 with values of $\overline{Nu}_j$ calculated from equation (4.7) shows that the data are well correlated by equation (4.7).

The correlation of average heat transfer by Schlünder et al. (133) for an unconfined slot jet impinging on a flat impingement surface is, in the notation of the present work

$$\frac{\overline{Nu}_j}{(Pr)^{0.42}} = \frac{1.53}{\frac{x_1}{w} + \frac{H}{w} + 2.78} (2\ Re_j)^m \qquad (4.8)$$

where

$$m = 0.695 - \frac{2}{\frac{x_1}{w} + 0.80\left(\frac{H}{w}\right)^{1.33} + 6.12}$$

The differences between the two correlations (4.7) and (4.8) are generally less than 10%, as can be seen in Figure 4.20. From this comparison it appears that the influence on average heat transfer of confinement and of the curvature of the cylindrical impingement surface is small at an impingement surface spacing of 6w over the range of Re_j and averaging distance x_1/w of the present study.

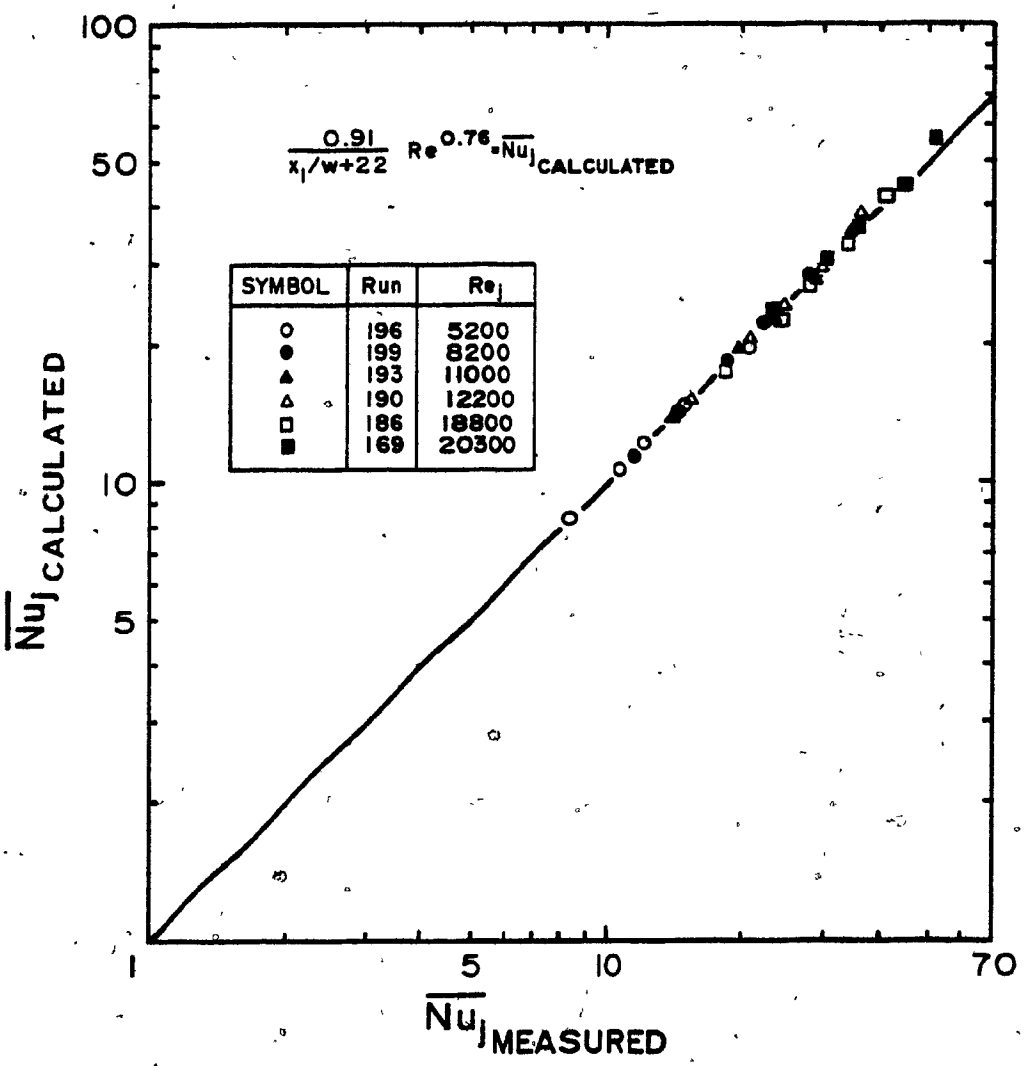


FIGURE 4.19. Correlation of average heat transfer for H/w = 6

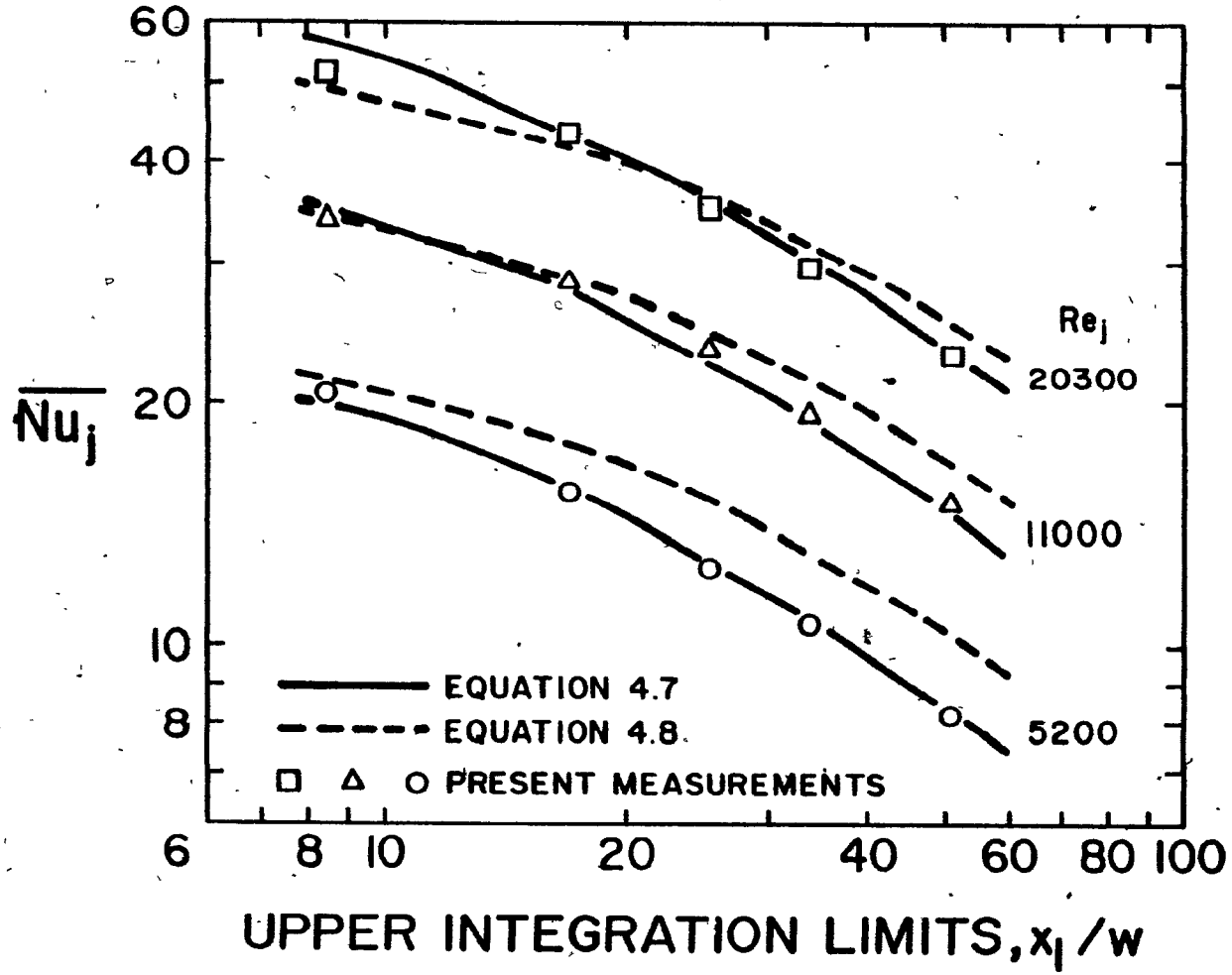


FIGURE 4.20. Average heat transfer at H/w = 6: Comparison of results

For the close impingement surface spacing of 2.6w the complicated shape of the heat transfer distribution makes it impossible to obtain as simple an expression as equation (4.7) for average heat transfer. However, the values of average heat transfer in Table 4.5 are correlated by

$$\overline{Nu}_j = aRe_j^b \qquad (4.9)$$

with a and b both functions of the upper integration limit, x_1/w, as given in Table 4.6.

TABLE 4.6. Parameters in Average Heat Transfer Correlation for H/w = 2.6

x_1/w	a	b
3.75	0.285	0.50
7.5	0.0410	0.699
11.25	0.0272	0.744
15	0.0270	0.739
22.5	0.0260	0.726

With respect to the upper integration limits of Table 4.6 it is useful to recall from Section 4.3.1 that, for H/w = 2.6, the transition minimum in the heat transfer profile occurs at about 2.6w or 1H from stagnation, and the off-stagnation maximum at about $x_1/w = 7$. Thus the smallest impingement surface for which

the correlation of $\overline{Nu}_j$ given by equation (4.9) and Table 4.6 is valid is one which is large enough that it includes the transition minimum but not large enough to include the off-stagnation maximum. The accuracy of the correlations is good as can be seen in Figure 4.21a. The average heat transfer correlation, equation (4.9), cannot be compared with equation (4.8) of Schlünder et al. (133) because their equation is valid only for $4 \leq H/w \leq 20$.

It is of considerable interest to compare average heat transfer for the two experimental values of impingement surface spacing, 6 and 2.6. Thus the corresponding correlations, equations (4.7) and (4.9), are presented on Figure 4.21b for two values of Re_j within the limits of applicability of both correlations. It is apparent from this figure that, regardless of the extent of the impingement surface, average heat transfer is higher at the higher spacing, $H/w = 6$. The spread in $\overline{Nu}_j$ between the two spacings, H/w, is particularly large for values of x_1/w near the low end of the range of applicability because this includes the effect of the low values of Nu at the transition point minimum, these minima being much more depressed for the smaller spacing, $H/w = 2.6$, as discussed in Section 4.3.1. It is also worth noting that the Reynolds number exponent is always higher for the larger impingement surface spacing, $H/w = 6$. Consequently, the higher the value of Re_j, the larger the advantage of the higher spacing.

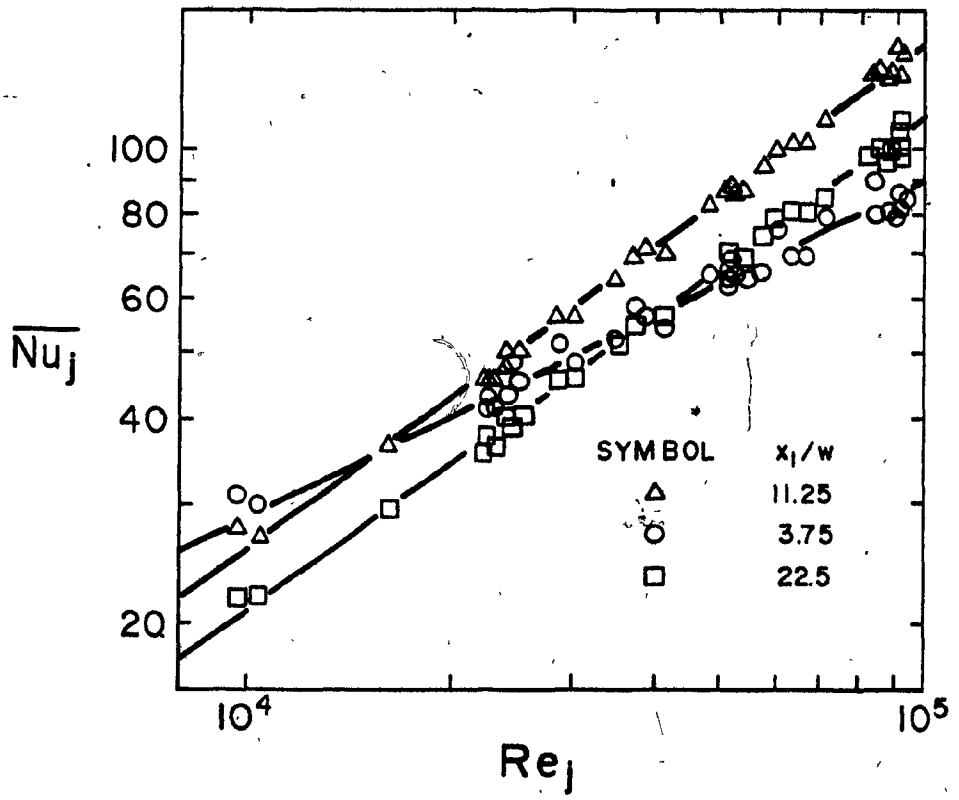


FIGURE 4.21a. Correlations of average heat transfer at H/w = 2.6

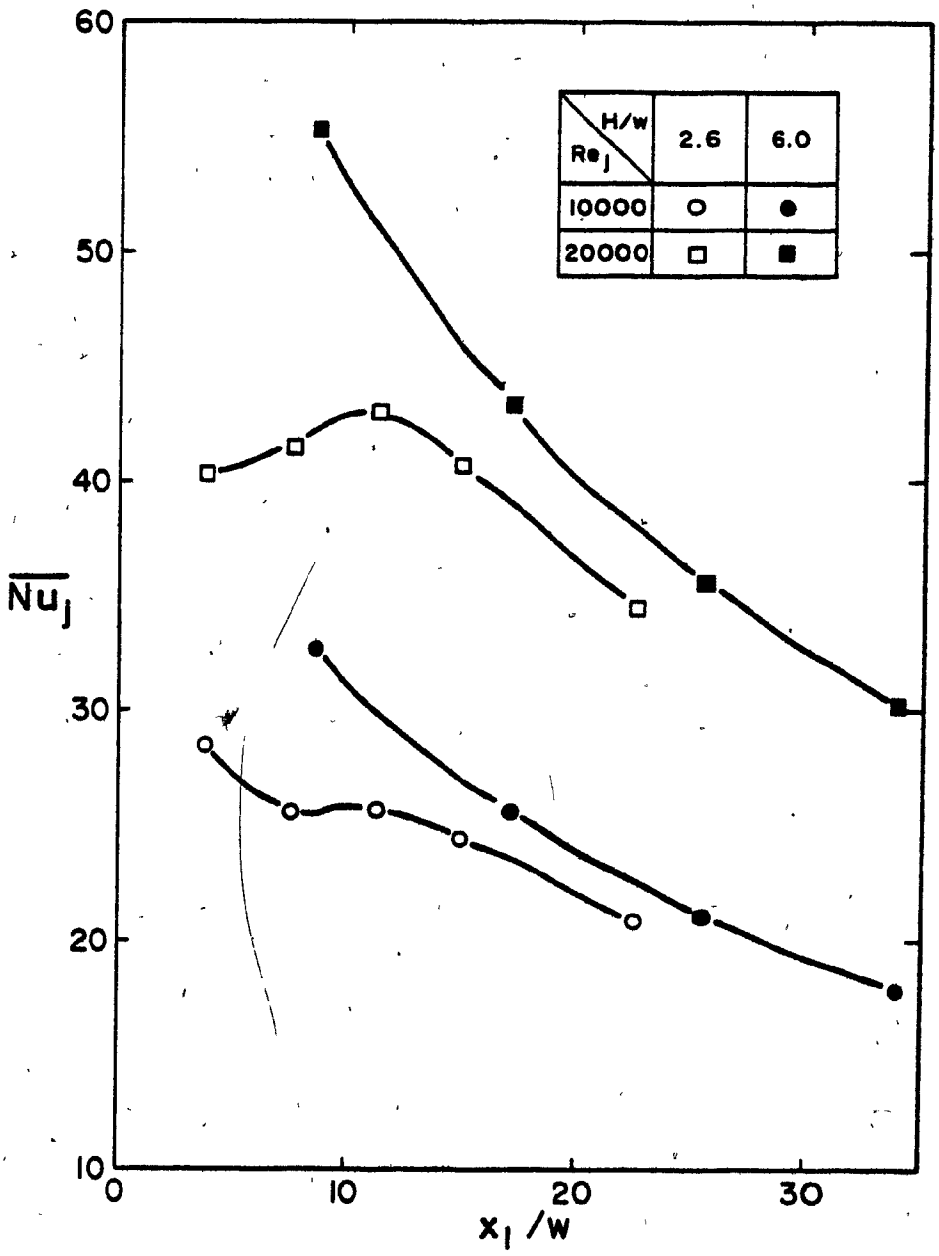


FIGURE 4.21b. Comparison of present correlation for average heat transfer for experimental H/w spacings

4.4 Influence of Impingement Surface Motion

Although impingement heat and mass transfer at continuously moving surfaces are encountered in a variety of engineering situations, little experimental work has been reported on this subject. Average heat transfer between a hot rotating cylinder and an unconfined impinging slot jet has been reported by Kays and Bjorklund (75), Yildiz (155) and Fechner (40). Subba Raju and Schlünder (142) measured average heat transfer between an unconfined impinging slot jet and a continuously moving heated flat surface, while recently Hardisty (57) reports that the effect of surface motion on the impingement flow field was negligible for practical situations in the ink drying process. Related studies of the effect of surface motion on average heat or mass transfer at the impingement surface with unconfined round jets are reported by Maxwell and Nash (90) for a rotating cylinder and by Popiel et al. (108) and Metzger and Grochowsky (95) for a rotating disk. A significant factor is that all these studies report average transfer rates for unconfined jets whereas in typical industrial applications the jets are confined with a hood in order to prevent entrainment from the surroundings and to recirculate or control the exhaust of spent fluid after impingement. For this reason the present study of effect of impingement motion is carried out for the more realistic case of a confined slot jet. The two limiting regimes in the heat and mass transfer studies of impingement surface motion are the high jet velocity case, for which the flow is dominated by the impingement flow, and the high surface velocity case,

where the flow induced by surface motion dominates the flow field.

The local and average heat transfer results presented in this section were obtained without throughflow, and at varying speeds of rotation of the impingement cylinder. Surface motion is expressed as the surface velocity mass ratio $M_{V_s} = V_s\rho_s/U_j\rho_j$, the appropriate nondimensional parameter. The results are compared with those of Section 4.3 for an effectively stationary surface and with the average heat transfer data of Fechner (40) and Subba Raju and Schlünder (142). As in the previous section, the sequence of analysis of the influence of impingement surface motion is to consider first the lateral profiles of local heat transfer, followed by examination of the influence on heat transfer at the stagnation point, in the stagnation region, at the off-stagnation maximum, in the wall jet region and, finally, the influence of surface motion on mean heat transfer.

4.4.1 Lateral Profiles of Local Heat Transfer

The rotational speed of the impingement cylinder was varied from about 24 rpm (0.6 m/s) to slightly more than 475 rpm (12.0 m/s). The principal operating conditions and the stagnation and average heat transfer results are summarized in Tables 4.7 and 4.8. Surface motion is expressed nondimensionally through combination with the jet mass velocity in the form of the surface velocity mass ratio $M_{V_s} = V_s\rho_s/U_j\rho_j$. For impingement on a rotating cylinder Fechner (40) used Re/Re_{rot}, which is equal to $1/M_{V_s}$ for constant property flow ($Re = U_jD_c/\nu$,

TABLE 4.7 Operating Conditions and Results for Influence of M_{V_s} at H/w = 6

Run	Re	V_s (m/s)	M_{V_s}	U_s (m/s)	T_j (°C)	T_j-T_s (°C)	$\overline{\Delta T_s}$ (°C)	$Nu_{oj}/\sqrt{Re_j}$	$\overline{Nu}_j$ $x_1/w=8.5$	$\overline{Nu}_j$ $x_1/w=17$	$\overline{Nu}_j$ $x_1/w=25.5$	$\overline{Nu}_j$ $x_1/w=34$	$\overline{Nu}_j$ $x_1/w=51$
196	8200	0.95	0.034	0.0	102.4	38.2	0.15	0.534	27.3	22.0	18.0	15.3	11.8
207	8200	1.77	0.063	0.0	100.0	39.2	0.0	0.550	27.8	22.4	18.1	15.3	11.7
202	8200	6.23	0.222	0.0	99.7	38.4	-0.15	0.567	26.5	19.9	16.8	14.4	11.1
203	8300	12.00	0.423	0.0	100.5	40.6	-0.6	0.561	22.2	16.7	14.3	-	-
193	11000	0.91	0.024	0.0	98.8	34.1	0.3	0.550	34.4	28.3	23.1	19.3	14.9
210	11000	2.57	0.067	0.0	101.0	37.0	-0.05	0.524	33.4	27.6	22.6	19.1	14.6
212	11000	7.73	0.203	0.0	101.8	39.3	-0.3	0.581	33.5	26.0	21.5	18.1	13.7
213	11200	11.82	0.307	0.0	101.3	40.5	-0.65	0.595	31.3	23.5	20.1	17.2	-
218	13900	0.86	0.018	0.0	101.2	48.7	0.15	0.554	40.9	34.0	27.9	23.8	18.5
215	13800	3.09	0.066	0.0	100.0	46.6	0.10	0.571	41.5	34.1	28.0	23.6	18.3
219	13900	11.76	0.251	0.0	102.2	50.4	-0.05	0.607	39.0	30.0	25.6	22.1	17.1

TABLE 4.8. Operating conditions and results for influence of M_{V_s} at H/w = 2.6

Run	Re	V_s (m/s)	M_{V_s}	U_s (m/s)	T_j (°C)	$T_j - T_s$ (°C)	$\overline{\Delta T_s}$ (°C)	$Nu_{oj}/\sqrt{Re_j}$	$\overline{Nu}_j$ $x_1/w=3\frac{1}{2}$	$\overline{Nu}_j$ $x_1/w=7.5$	$\overline{Nu}_j$ $x_1/w=11\frac{1}{2}$	$\overline{Nu}_j$ $x_1/w=15$	$\overline{Nu}_j$ $x_1/w=22.5$
148	9700	0.60	0.047	0.0	34.8	32.3	-0.1	0.474	30.7	28.9	27.8	25.9	21.6
150	10400	0.57	0.041	0.0	36.1	38.6	0.25	0.449	29.9	28.1	26.9	24.9	20.8
149	10400	3.69	0.263	0.0	36.0	36.8	-0.3	0.443	30.0	27.1	25.6	24.0	20.5
151	10400	8.88	0.634	0.0	36.3	35.9	-0.7	0.508	33.5	27.1	25.6	24.0	20.5
152	11100	12.84	0.857	0.0	36.6	35.6	-1.2	0.480	29.5	25.2	22.4	20.5	17.9
142	22900	0.91	0.030	0.0	39.7	22.1	0.3	0.452	42.6	43.7	46.0	43.9	36.9
143	22800	2.81	0.094	0.0	39.9	21.3	-0.1	0.450	43.2	44.0	46.3	44.2	37.7
144	22800	6.53	0.219	0.0	40.0	22.1	-0.1	0.448	44.2	43.0	43.3	41.5	35.5
145	23100	9.27	0.301	0.0	40.1	25.6	+0.1	0.444	46.1	42.0	41.0	39.4	33.6
146	23100	12.74	0.414	0.0	40.3	24.9	0.05	0.481	53.2	43.3	41.7	39.6	32.9
147	23200	0.91	0.030	0.0	40.0	26.0	0.1	0.443	42.2	43.2	45.4	43.3	36.4
132	51900	0.63	0.010	0.0	36.3	16.5	0.0	0.441	65.6	79.6	87.2	83.2	69.7
113	51600	1.37	0.021	0.0	35.5	15.3	-0.05	0.438	66.0	80.1	86.4	81.8	67.8
135	52000	2.39	0.036	0.0	37.0	15.4	-0.05	0.442	66.6	79.6	87.0	83.2	69.6
114	51700	2.67	0.041	0.0	36.0	15.8	-0.15	0.456	67.7	80.0	86.3	81.9	68.2
136	51700	5.58	0.085	0.0	37.5	15.6	-0.1	0.467	68.9	82.9	87.7	83.6	70.3

TABLE 4.8. (continued)

Run	Re	V_s (m/s)	M_{V_s}	U_s (m/s)	T_j (°C)	$T_j - T_s$ (°C)	$\overline{\Delta T_s}$ (°C)	$Nu_{oj}/\sqrt{Re_j}$	$\overline{Nu}_j$ $x_1/w=3\frac{1}{2}$	$\overline{Nu}_j$ $x_1/w=7.5$	$\overline{Nu}_j$ $x_1/w=11\frac{1}{2}$	$\overline{Nu}_j$ $x_1/w=15$	$\overline{Nu}_j$ $x_1/w=22.5$
137	51800	5.61	0.085	0.0	37.9	15.6	0.0	0.440	64.4	76.4	82.9	79.0	65.8
138	51700	8.73	0.131	0.0	38.3	18.6	-0.4	0.453	70.3	83.3	87.3	83.3	70.3
140	50600	11.76	0.177	0.0	41.4	17.7	-0.5	0.466	67.8	80.9	85.3	80.9	68.0
218	89300	0.86	0.008	0.0	29.9	22.7	0.15	0.419	79.7	118.4	129.2	121.1	99.4
215	87400	3.09	0.027	0.0	32.7	20.7	0.10	0,457	83.6	119.4	130.7	123.0	101.0
219	89000	11.76	0.102	0.0	30.0	21.8	-0.05	0.475	89.1	121.6	129.8	122.0	100.8
196	25100	0.95	0.029	0.0	37.8	26.4	0.15	0.454	45.2	47.4	50.4	48.2	40.6
207	26200	1.77	0.052	0.0	33.5	27.3	0.0	0.439	44.8	46.9	50.1	48.1	40.7
202	25900	6.23	0.184	0.0	35.3	26.0	-0.15	0.444	44.9	46.5	48.5	46.3	39.7
203	26500	12.00	0.349	0.0	34.5	25.4	-0.6	0.467	49.4	49.0	48.3	45.8	39.3
193	30100	0.91	0.023	0.0	37.5	27.2	0.3	0.444	47.2	51.6	55.6	55.3	44.8
210	30100	2.57	0.065	0.0	35.7	28.3	-0.05	0.458	49.0	53.5	57.4	55.2	46.9
212	30900	7.73	0.194	0.0	33.3	29.2	-0.3	0.448	48.7	53.4	55.8	53.6	43.9
213	31400	11.82	0.290	0.0	32.5	28.8	-0.65	0.464	52.0	54.6	55.1	52.7	45.4

$Re_{rot} = V_s D_c/\nu$, with D_c the diameter of the cylinder). The choice of the M_{V_s} parameter for surface motion is also consistent with the usage for impinging jets with crossflow by Bouchez (17) and Sparrow et al. (137).

Also listed in Tables 4.7 and 4.8 are the average temperature differences $\overline{\Delta T_s}$ between the central thermocouple and the two other thermocouples at the back of the sensor. The rather large negative values of $\overline{\Delta T_s}$ ($\approx 0.6^{\circ}C$) at the highest rotational speed of about 12 rpm indicate that, at this high velocity of the impingement surface, the axial heat loss could not completely be countered by temperature control of the impingement cylinder end plates. In Section 3.5.5 it was estimated that $\overline{\Delta T_s} = 0.1^{\circ}C$ corresponds to a heat loss of 50 W/m^2. From this estimate, the largest error in the stagnation Nusselt number, caused by axial heat losses at high rotational speeds, was calculated to be 3 and 2% for spacings, H/w, of 6 and 2.6, respectively.

Lateral profiles of local heat transfer for H/w = 6 at three values of surface velocity mass ratio M_{V_s} are superimposed on Figures 4.22, 4.23 and 4.24 for jet Reynolds numbers respectively of 8200, 11000 and 13900. For H/w = 2.6, profiles at various values of surface velocity mass ratio, M_{V_s}, are likewise superimposed on Figures 4.25, 4.26 and 4.27 for Reynolds numbers respectively of 11000, 23000 and 51000.

The value of the surface velocity parameter, M_{V_s}, at which surface motion begins to have a significant effect depends on the criterion used, some variables being more sensitive than

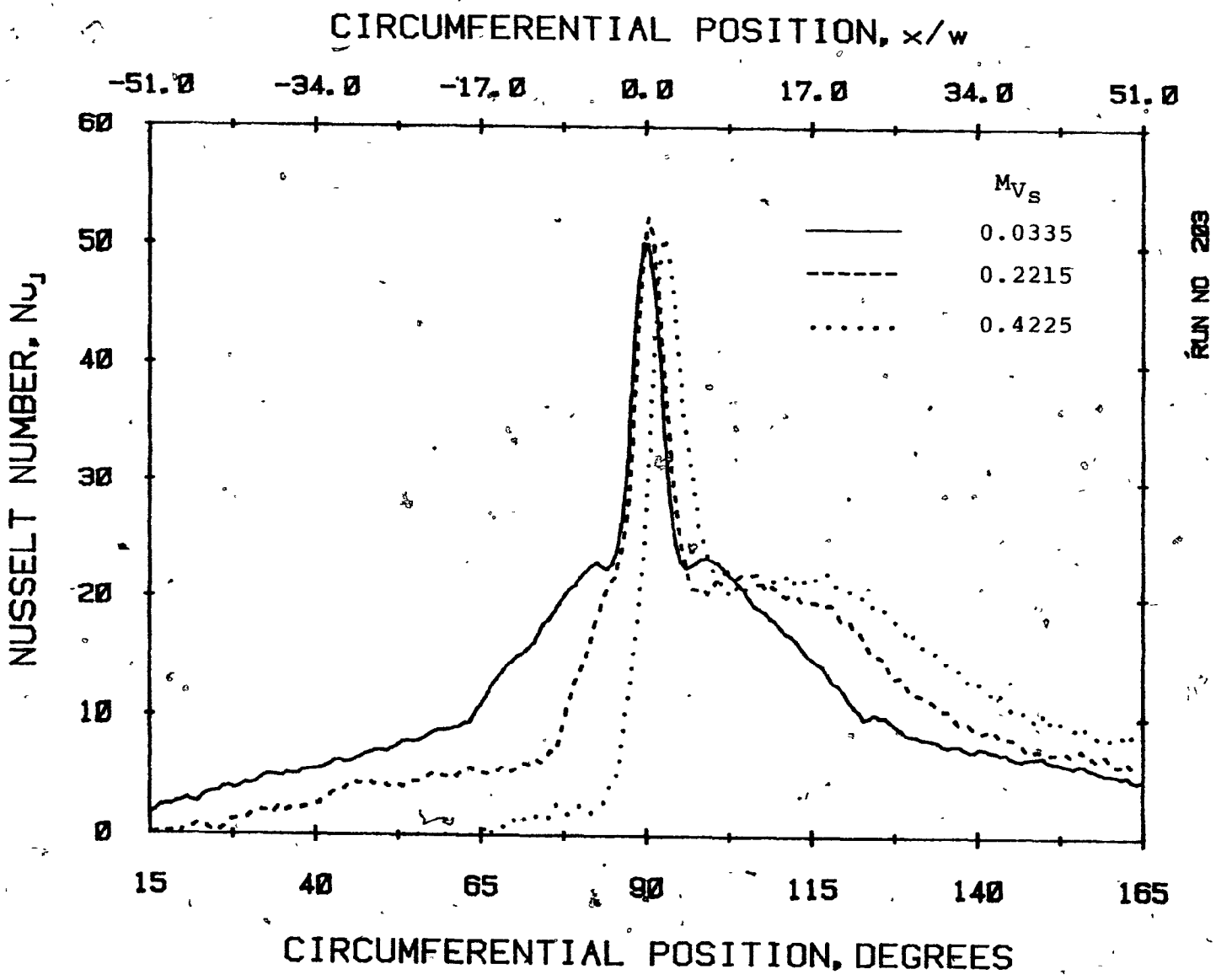


FIGURE 4.22. Effect of M_{V_s} on lateral profile of heat transfer at Re_j = 8200 and H/w = 6

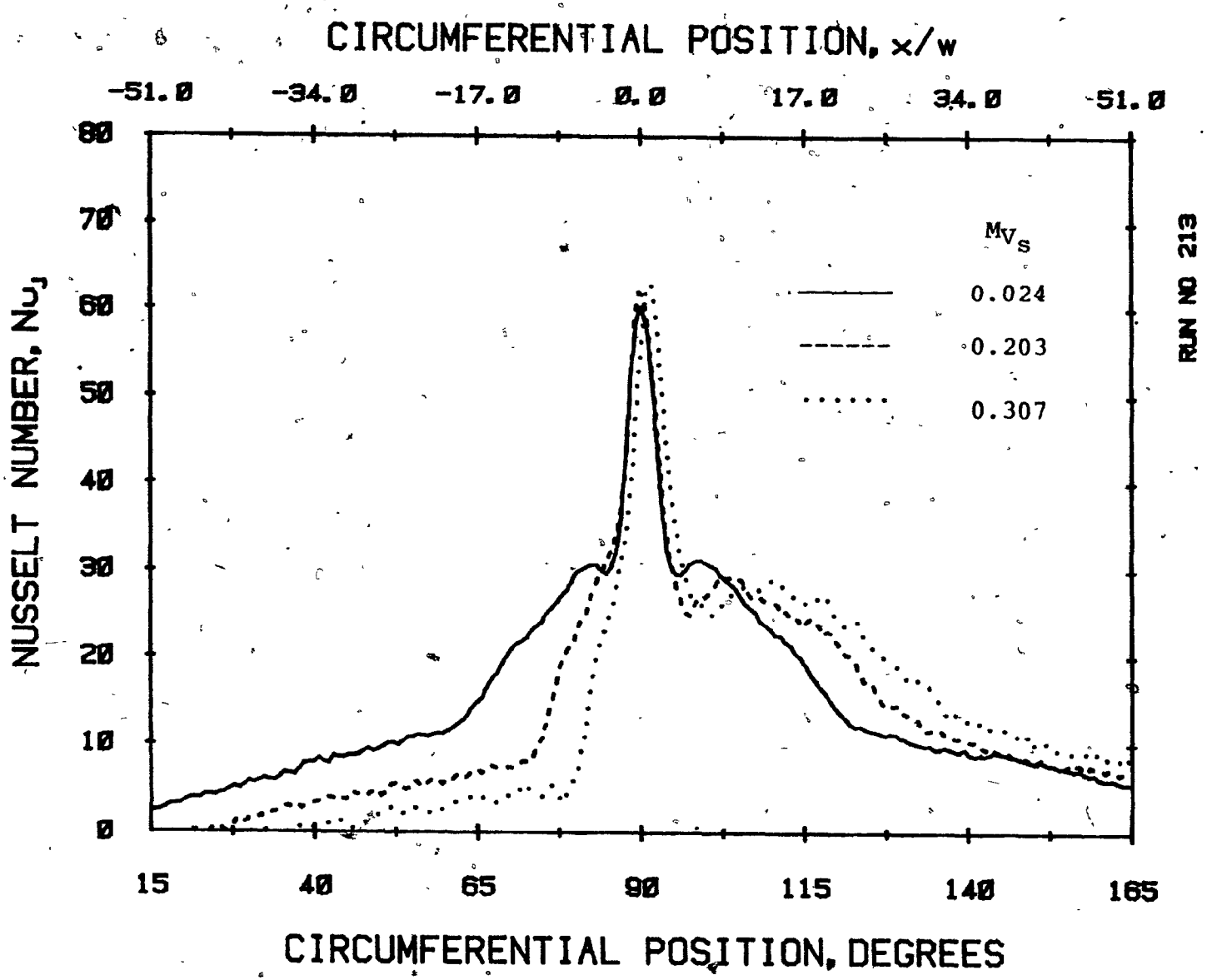


FIGURE 4.23. Effect of Mv_s on lateral profile of heat transfer at Re_j = 11000 and H/w = 6

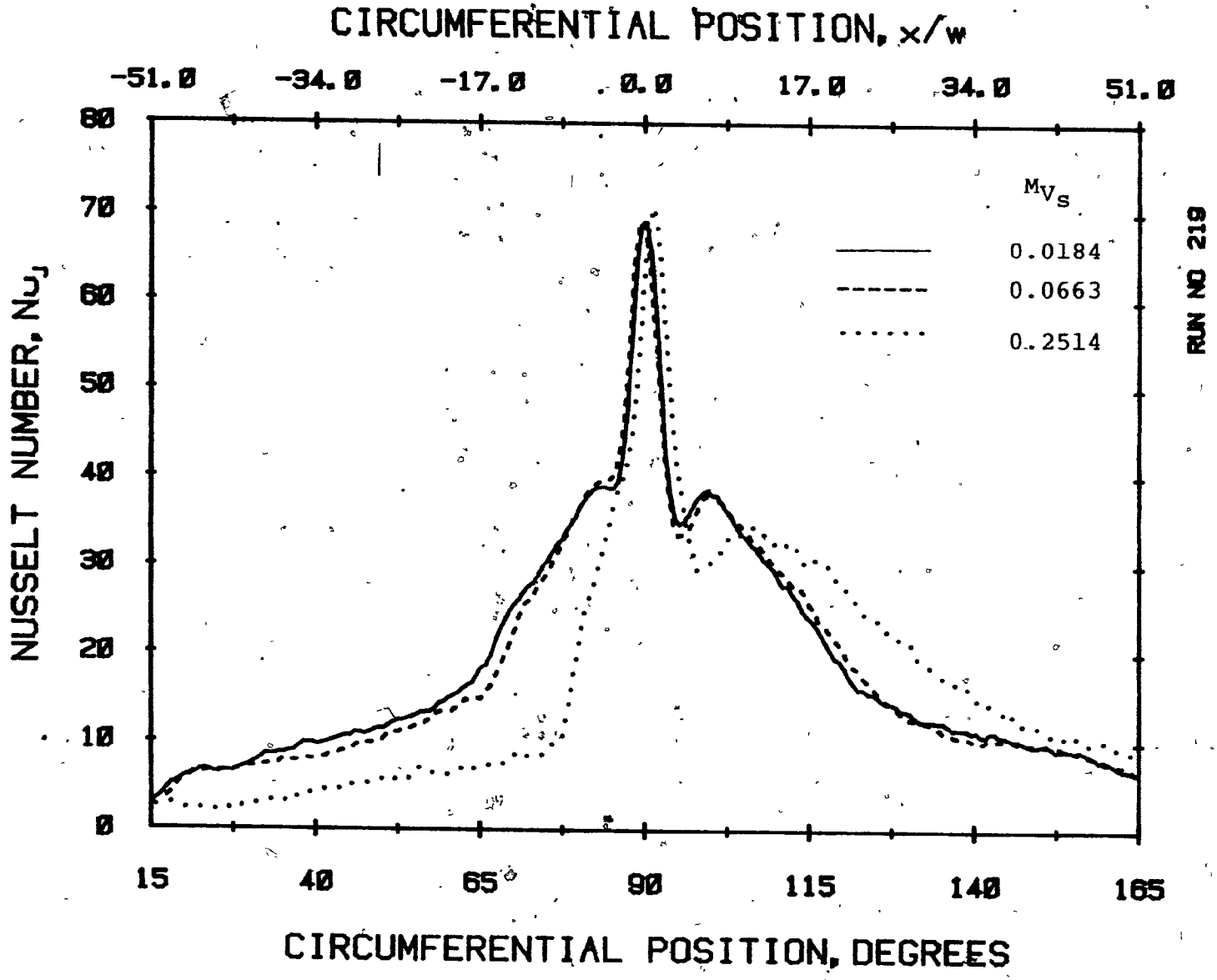


FIGURE 4.24. Effect of M_{V_S} on lateral profile of heat transfer at Re_j = 13900 and H/w = 6

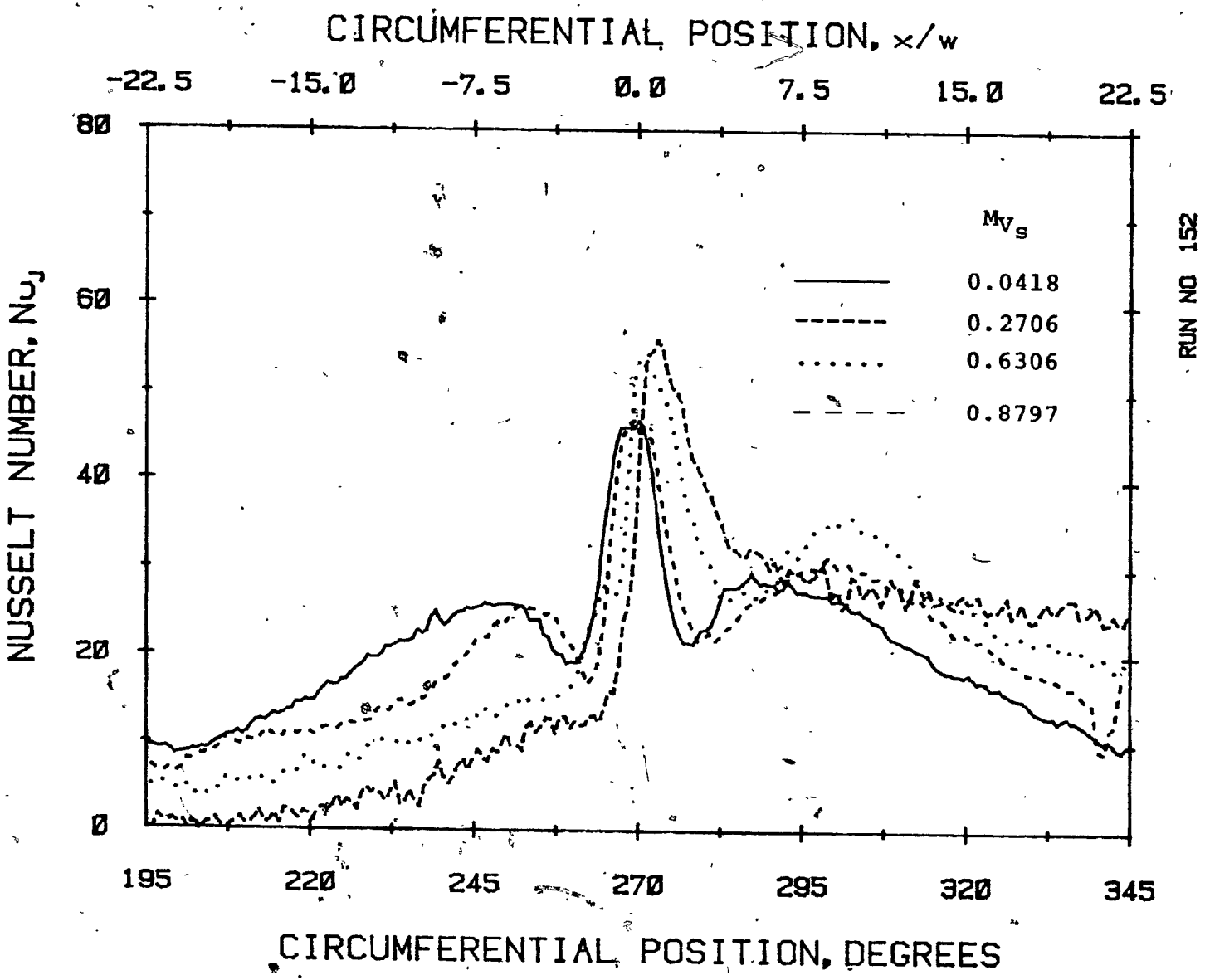


FIGURE 4.25. Effect of M_{V_s} on lateral profile of heat transfer at Re_j = 11000 and H/w = 2.6

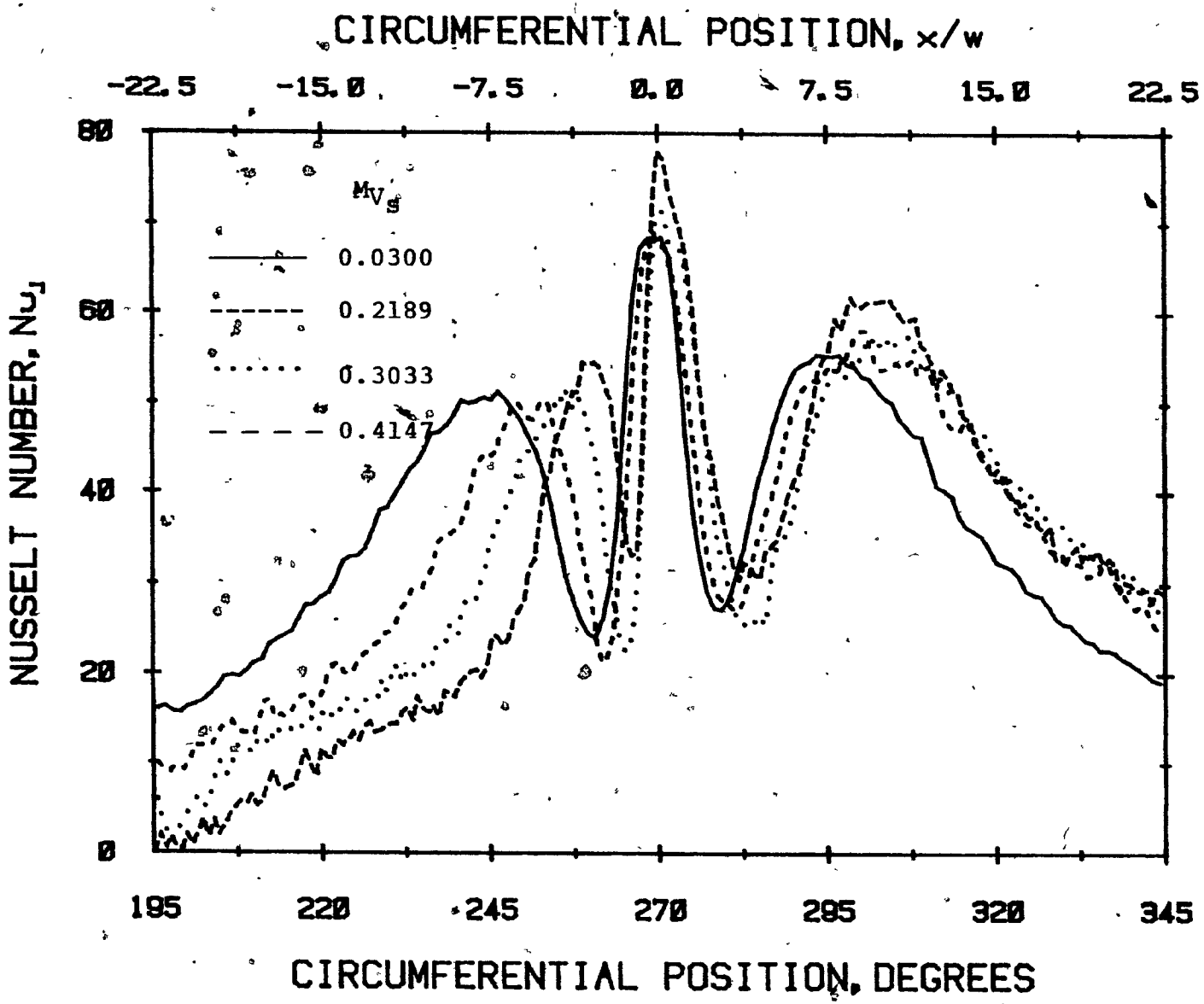


FIGURE 4.26. Effect of M_{V_S} on lateral profile of heat transfer at Re_j = 23000 and H/w = 2.6

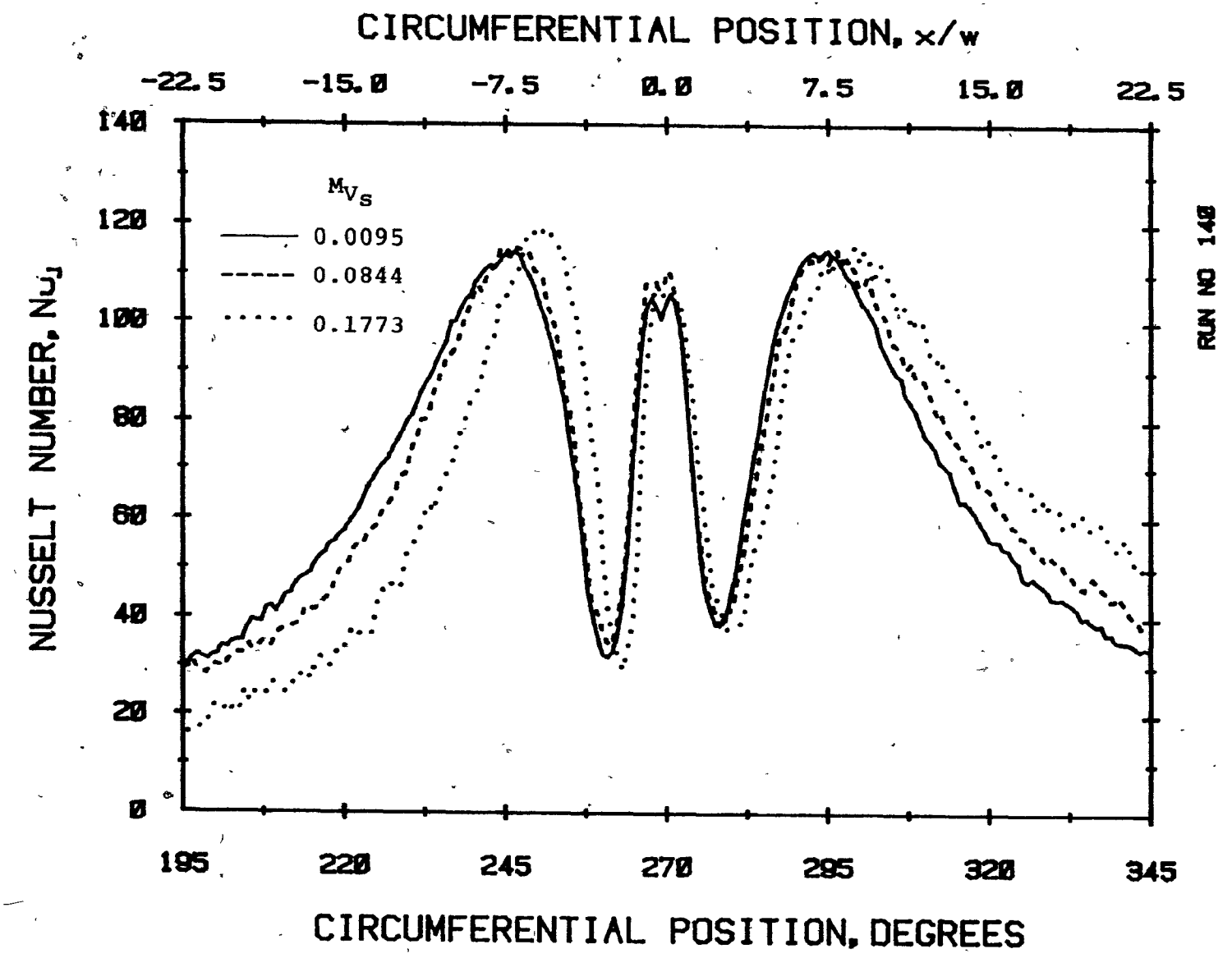


FIGURE 4.27. Effect of M_{V_S} on lateral profile of heat transfer at Re_j = 51000 and H/w = 2.6

others to surface motion. Previously the symmetry of heat transfer profiles including the far wall jet region was demonstrated in Figure 4.16 to be a parameter particularly sensitive to M_{V_s}. It can be seen from the results for the lower two values of M_{V_s} on Figure 4.24 that there are only small differences in the profiles between M_{V_s} values of 0.018 and 0.066. As the minimum value of M_{V_s} on each of the six figures, 4.22 to 4.27, is in the range 0.010 to 0.041, the profile for the minimum M_{V_s} value on each of these figures may then be taken as representing the base case of no significant surface motion effect.

The following general effects of surface motion on the profiles can be distinguished.

(a) An increase in the stagnation heat transfer peak, but no significant displacement of the peak. Thus even at the two highest values of M_{V_s} used, 0.634 and 0.857 in Figure 4.25, the central peak is only displaced in the direction of the surface motion by about 0.5w and 1w respectively.

(b) Off-stagnation features of the profiles, i.e. the minima and off-stagnation maxima on both sides of the nozzle centerline are displaced in the direction of the surface motion. Because of this displacement the minimum and the secondary maximum on the side where the impingement surface is approaching the nozzle centerline (always the left hand side of the profiles

as shown) disappear into the stagnation heat transfer peak at a sufficiently high value of M_{V_s}, while the location of the minimum and maximum on the other side is displaced progressively further from the nozzle centerline as M_{V_s} is increased.

(c) Another off-stagnation feature of the profiles, the sudden change in slope in the wall jet region, which for H/w = 6 occurs around 20w from the nozzle centerline without wall motion, is likewise displaced in the direction of the surface motion.

(d) On the side of the nozzle centerline with surface motion approaching the nozzle, heat transfer becomes negative at high values of M_{V_s}.

Overall it can be said that heat transfer increases where impingement surface motion is in the direction away from the nozzle centerline, while the reverse is the case where surface motion is in the direction towards the nozzle centerline. Such behaviour is clearly evident on all three figures for H/w = 6, and for the lowest value of Re_j at H/w = 2.6, Figure 4.25. The same type of lateral displacements are evident for the two higher values of Re_j at H/w = 2.6, Figures 4.26 and 4.27, but the overall trends are not so apparent due to the very large off-stagnation peaks.

The trends noted above conflict with those reported by Holik (61) and Subba Raju and Schlünder (142) in their studies of influence of impingement surface motion, as will be further discussed subsequently.

The quantitative aspects of effect of surface motion for each region, i.e. stagnation point, stagnation region, secondary maxima and wall jet region, will be documented subsequently in separate sections directed to each of these regions. However, it is useful first, in connection with Figures 4.22 to 4.27, to provide an overall perspective for the entire impingement surfaces concerning factors which affect the results. This perspective must reflect the overall character of the effect of surface motion, characterized by M_{V_s}, the surface velocity mass ratio. Operation at values of M_{V_s} used in the present experiments has the effect of skewing all off-stagnation features of the profiles while having relatively little effect on the position and only a moderate effect on the magnitude of the central heat transfer maximum. Thus over the central impingement region, of total width approximately 6w for H/w spacings of both 2.6 and 6, the impingement flow predominates over the flow induced by motion of the impingement surface. Another general consideration is that, because the presence of surface motion destroys the symmetry of the impingement system, it is necessary that the interaction of factors affecting results be considered separately for the two unsymmetric sections of

the impingement system, i.e. where the surface is approaching the nozzle centerline and where surface motion is away from the nozzle.

For turbulent impinging slot jets in the present range of Re_j and H/w, heat transfer profiles in the absence of surface motion generally reflect a laminar boundary layer around the stagnation point, onset of transition to a turbulent boundary layer (marked by a heat transfer minimum) after the strong pressure gradient which maintains the laminar boundary layer is no longer present, and an off-stagnation maximum marking completion of transition. The drag exerted by the surface motion skews the jet in the direction of this motion. The resulting skewing in the direction of surface motion of the sharp pressure profile of the impingement region is reflected in a shift in location of the onset of boundary layer transition, evident in Figures 4.22 to 4.27 in the corresponding shift in heat transfer minima.

While shift in pressure profile is one factor affecting boundary layer transition and hence the heat transfer profile minimum, surface motion also effects results through the consequences of change in velocity gradient at the surface. As surface motion increases it is evident that velocity gradient at the surface increases where surface motion is approaching the nozzle centerline and decreases for motion away from the nozzle. The corresponding increase and

decrease in momentum transfer for surface motion respectively approaching and leaving the stagnation region in turn advances and retards, respectively, the onset of transition to a turbulent boundary layer. Thus in that part of the stagnation region where surface motion is directed towards the nozzle, the point of boundary layer transition is shifted towards the nozzle centerline by a combination of two effects, i.e. the shift of pressure profile in that direction and the advancement of transition by increased velocity gradient and momentum transfer at the surface. In the stagnation region where surface motion is directed away from the nozzle, the heat transfer minimum is shifted away from the nozzle centerline by combination of the same two effects now both acting in the opposite direction.

In the region from a minimum to an off-stagnation maximum in a heat transfer profile, pressure gradient is no longer a consideration but alteration by surface motion of the velocity gradient and momentum transfer at the surface continues its same role. Thus, as with the shift of a heat transfer minimum, the location of a secondary maximum is shifted closer to the nozzle because of faster boundary layer transition to turbulence where surface motion is directed towards the nozzle, and vice versa. For all conditions for which minima or secondary maxima exist on Figures 4.22 to 4.27, such peaks are invariably shifted in the direction

of surface motion in accordance with the physical analysis presented above.

For regions with surface motion directed towards the nozzle the range of M_{V_s} used is always sufficient to destroy marginal peaks at H/w = 6, while for H/w = 2.6 only at the lowest Reynolds number, 10900, and the highest value of M_{V_s}, 0.857, is the effect of surface motion sufficiently strong that these peaks are shifted into the central stagnation peak.

Although the fact that velocity gradients and momentum transfer at the surface are increased where surface motion is towards the nozzle and decreased on the other side has been discussed above only for the region out to the secondary maxima, the same effects would apply also for the wall jet region. However, the trend observed in Figures 4.22 to 4.27 for heat transfer to decrease for surface motion directed towards the nozzle centerline, and vice versa, which is opposite to the effects that would be caused by velocity gradient and momentum transfer changes at the surface. However, an important additional effect on the wall jet region is the effect of surface motion on the maximum velocity of the wall jet, in turn controlled by the rate of spreading of the wall jet. Thus the tendency for an increased velocity gradient and momentum transfer rate at the impingement surface, in the region of surface motion approaching the nozzle, in turn increases the rate of spreading of

the wall jet, thereby increasing the rate at which maximum wall jet velocity decays with distance from the nozzle centerline. As these are counteracting effects, it is not possible to predict from qualitative reasoning which effect is predominant. It is clear, however, from inspection of the wall jet regions of the profiles on Figures 4.22 to 4.27 that the general trend is for a reduction in heat transfer for surface motion approaching the nozzle, and vice versa. If there were no other effects present, this observation would indicate that the predominant effect is an increased rate of spreading and reduction in mean velocity of the wall jet for surface motion approaching the nozzle, and the corresponding effects on the other side of the nozzle where surface motion is away from the nozzle.

In addition to these various effects of surface motion on the flow characteristics in the critical region adjacent to the impingement surface, there are also thermal effects which may influence heat transfer. In this regard it should be recalled that all local heat transfer coefficients for impingement systems have conventionally been determined using $|T_j - T_s|$ as the temperature difference. Thus, for a given set of conditions, a lateral profile of local heat transfer coefficient is in fact a profile of local heat flux divided by a constant, $|T_j - T_s|$. This convenient calculation procedure thus ignores the reality that the effective local ΔT for convective heat transfer at an impingement

surface decreases continuously to values of effective ΔT in the far wall jet region which may be greatly lower than the maximum value of ΔT at the stagnation point. This analysis provides a basis for a more complete understanding of the effect of surface motion. Thus, in the region where surface motion is directed towards stagnation, the velocity gradient at the surface is increased as already noted, and as a consequence the wall jet velocity is decreased by the opposing surface motion. A decreased wall jet velocity allows the boundary layer fluid to approach the impingement surface temperature more quickly, i.e. results in an effective local ΔT which decreases with lateral distance more rapidly than without surface motion. Where surface motion is directed towards the stagnation point, there is then a thermal effect which reduces the local effective ΔT. This effect, which acts to reduce heat flux, appears ultimately as a reduced Nusselt number. The fact that the reduction in heat transfer in the wall jet regions on the left hand side of the profiles of Figures 4.22 to 4.27 is too large to be explained solely by the flow field effects already described indicates that the additional thermal mechanism may play an important role in reducing heat transfer in wall jet regions where surface motion is opposite to the wall jet velocity.

This thermal effect operates to produce the opposite result where surface motion is directed away from the stagnation point. Thus for the case of aiding flow (wall jet and surface velocity in the same direction) the wall jet velocity is increased by surface motion, and consequently at the same distance from the nozzle centerline the approach of the boundary layer fluid temperature to the impingement surface temperature is reduced. The effective local ΔT is thus increased, thereby increasing the actual heat flux and hence the calculated Nusselt number for such regions. The increased Nusselt number on the right side of Figure 4.22 to 4.27 profiles with increased surface motion indicates the effectiveness of this mechanism for increasing heat transfer where surface motion is directed away from the stagnation point.

Another view of the thermal effect results from noting that, because of the no-slip condition at the wall, a moving impingement surface tends to drag fluid from one region to another. On the side where the impingement surface is approaching the nozzle any fluid dragged by the surface is from regions farther from the nozzle centerline, where the boundary layer is closer to thermal equilibrium with the impingement surface, into regions closer to the nozzle where the boundary layer would otherwise be further from thermal equilibrium. On this side, therefore, the consequences of

the non-slip condition with surface motion would be to decrease the local effective ΔT, hence decrease the heat flux, and thereby decrease the calculated heat transfer coefficient and Nusselt number. By contrast, on the other side, i.e. where the surface motion is away from the nozzle centerline, any fluid dragged by the surface is from the impingement region, where the boundary layer is furthest from thermal equilibrium, into the wall jet region. Thus on this side the no-slip condition for a moving surface tends to increase local ΔT and consequently the local heat flux, which would be reflected in increased Nusselt number as calculated.

With development of this overall perspective concerning the flow field and thermal mechanisms by which surface motion affects heat transfer over the entire impingement surface from the nozzle centerline to the far wall jet region, it is now appropriate to proceed to a detailed inspection of the quantitative effects of surface motion in each region of the impingement system.

4.4.2 Stagnation Point Heat Transfer

In order to examine the effect of surface motion on stagnation point heat transfer the effect of Reynolds number can effectively be eliminated by expressing the results as $Nu_{oj}/\sqrt{Re_j}$. The effect of surface motion, expressed again

as M_{V_s} for the experimental spacings, H/w, of 2.6 and 6, may then be seen on Figures 4.28 and 4.29. The reference value of $Nu_{oj}/\sqrt{Re_j}$ for essentially stationary conditions, obtained in section 4.3.2, is recorded on each graph. It should be noted that for the case of H/w = 2.6 the value taken for Nu_o may not be the maximum value of the central heat transfer peak, for reasons discussed subsequently. It is clear that the stagnation point heat transfer increases with increasing M_{V_s}. However, the sensitivity of Nu_o to M_{V_s} is not great, the increase in Nu_o for values of M_{V_s} up to the quite high maximum employed being only in the order of 10% relative to that for a stationary surface.

The explanation for the increased stagnation point heat transfer is the higher velocity gradient and momentum transfer at the nozzle centerline and in the immediately adjacent stagnation region on the side where surface motion is approaching the nozzle centerline. In fact, due to the effect of surface motion on velocity gradient at the surface, it follows that the stagnation point is also shifted so that, with surface motion, the stagnation point is displaced somewhat from the nozzle centerline in the direction of the surface motion. As the explanation given for the effect of surface motion on stagnation point heat transfer relates to conditions at the immediate approach to the stagnation point from the direction

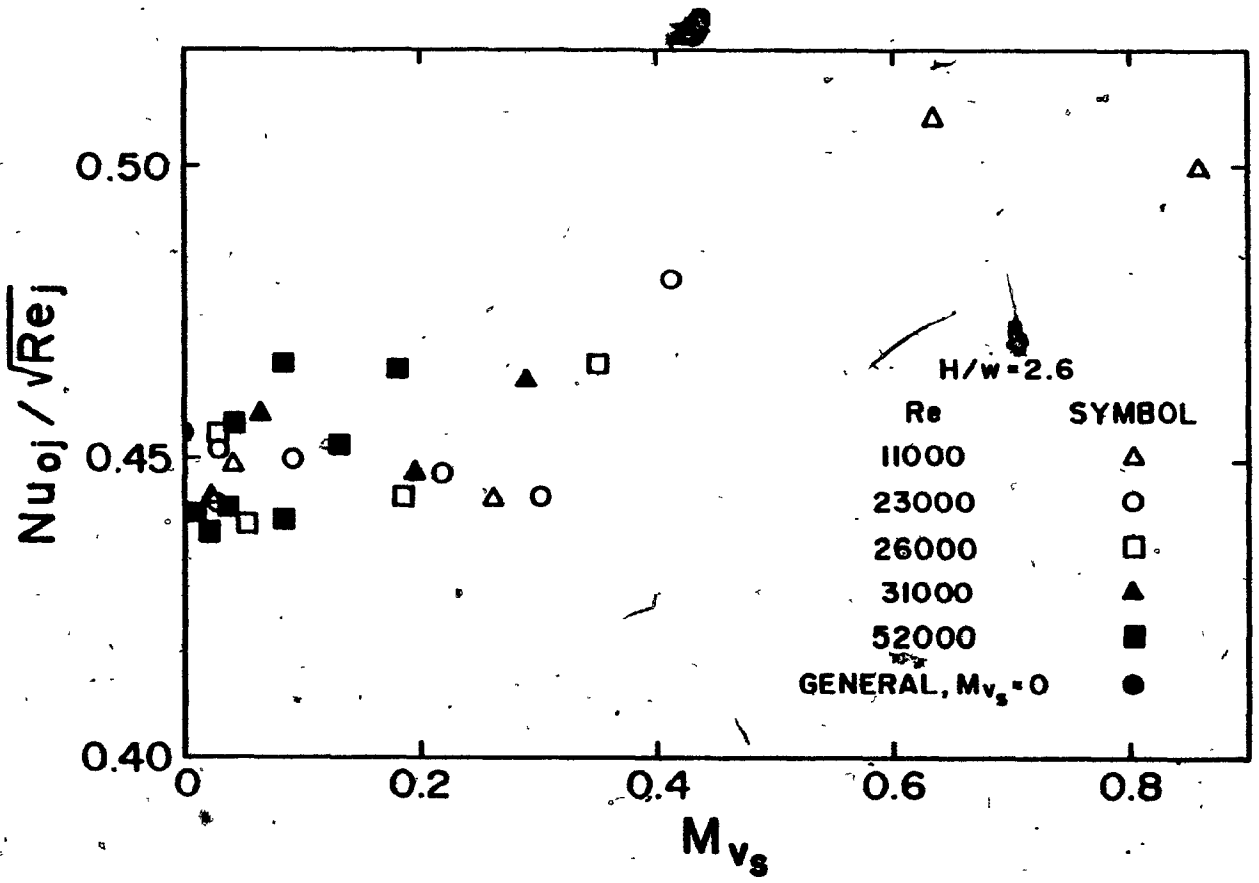


FIGURE 4.28. Effect of M_{v_s} on stagnation point heat transfer at H/w = 2.6

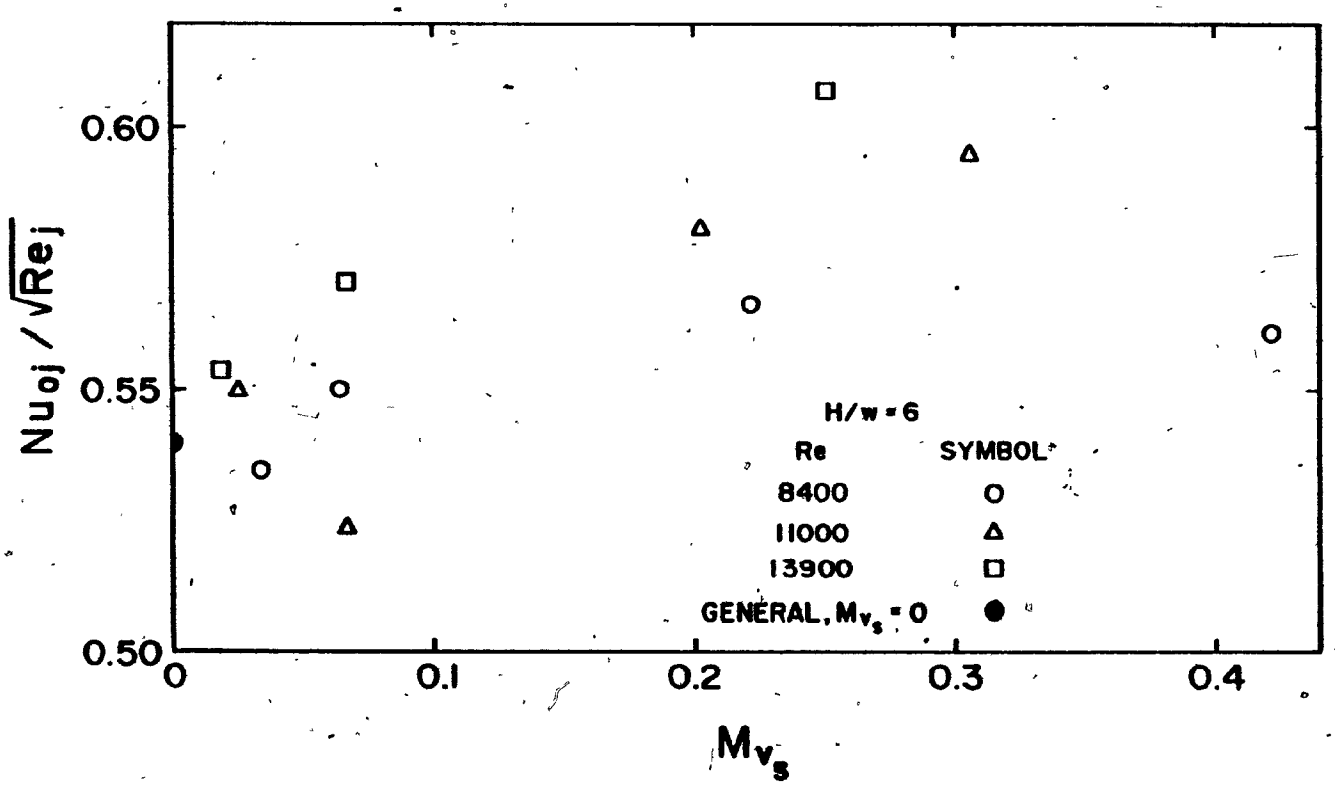


FIGURE 4.29. Effect of M_{V_s} on stagnation point heat transfer at H/w = 6

of the surface motion, it is significant to note that on those profiles of Figures 4.25 to 4.27 for which some assymetry appears in the central heat transfer peak, the assymetry is always in the direction of a higher heat transfer on the side of the peak from which the impingement surface is arriving. Such assymetry within the central peak is consistent with the view that mechanism for enhancement of Nu_o derives from the arrival side of the central peak. An increase in turbulence level with increasing M_{V_s} has been measured by Fechner (40) on the mid-plane of the jet very close to the his rotating cylinder. His measurement of increased turbulence along the nozzle centerline close to the impingement surface is consistent with the effects that would be expected for the increased velocity gradient at the impingement surface which was described above. However, for a proper perspective it should be kept in mind that the effect of M_{V_s} on Nu_o is in fact rather small.

4.4.3 Heat Transfer Distribution in the Stagnation Region

A detailed picture of the influence of surface motion on heat transfer distribution in the stagnation region for H/w = 2.6 is shown in Figure 4.30 for Re_j = 11000 and 26000. Small variations in Re_j are eliminated by expressing results as $Nu_j/\sqrt{Re_j}$. For reasons already noted in section 4.4.1 the transition point minimum in heat transfer is shifted by surface motion in the direction of surface motion. Thus

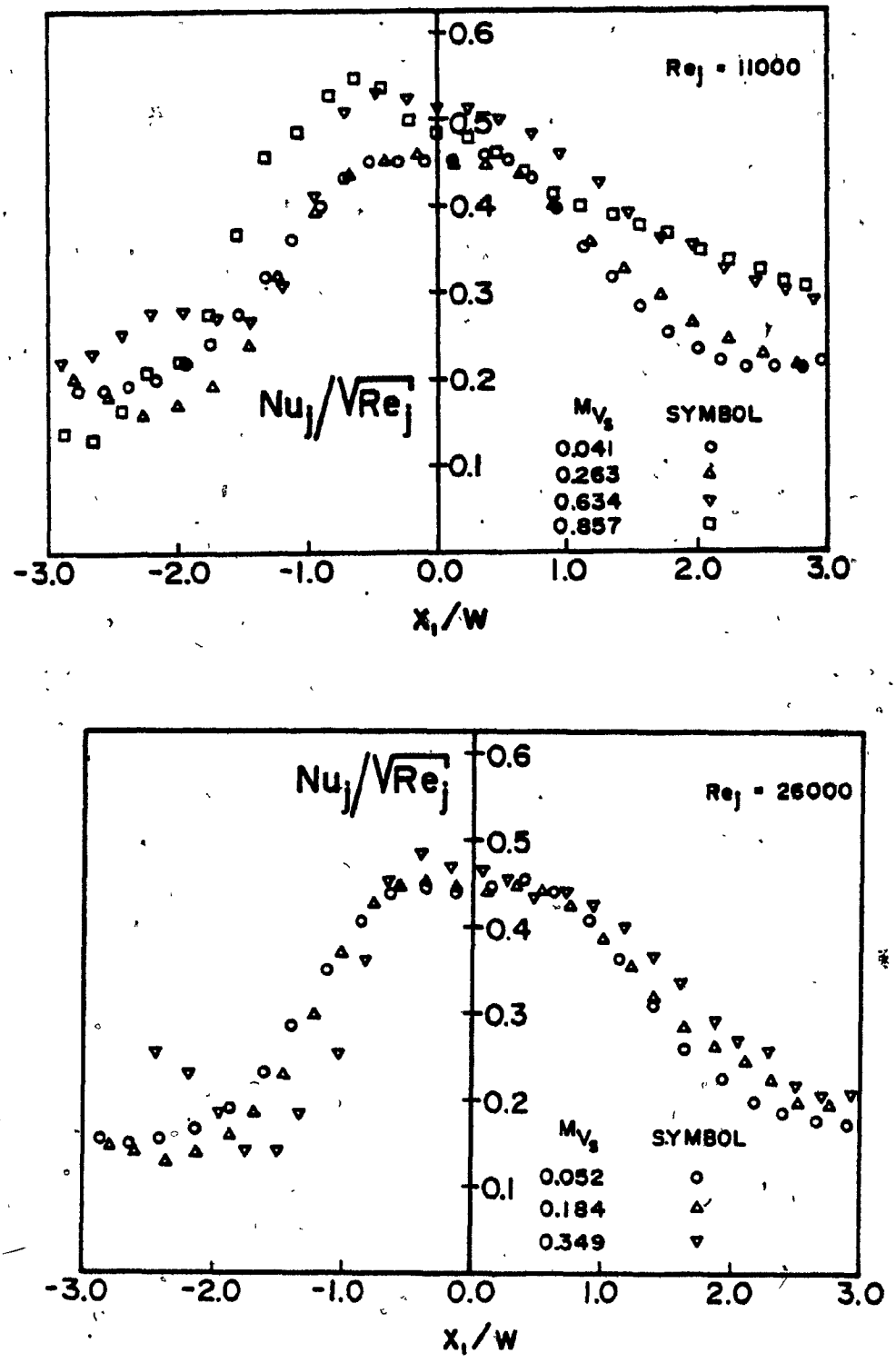


FIGURE 4.30. Effect of M_{V_s} on heat transfer distribution in stagnation region for H/w = 2.6

on Figure 4.30, at Re_j = 11000, the displacement of the transition point minimum on the side from which the surface is approaching the nozzle centerline (the left side of the figure) can clearly be seen. Thus this minimum moves from values of x_1/w of -2.7 to -2.3 to -1.4 as M_{V_s} is increased from 0.041 to 0.263 to 0.634. At the latter value of M_{V_s} the secondary maximum, visible at x_1/w = -2.1, has almost engulfed the minimum at -1.4. At the highest value of M_{V_s}, 0.857, the minimum and secondary maximum have disappeared, indicating that for these operating conditions, transition from a laminar to turbulent boundary layer occurs so quickly that these events are no longer marked by separate peaks in the heat transfer profile.

4.4.4 The Secondary Heat Transfer Maximum

The basic reasons why the location and size of the secondary heat transfer maxima are influenced by impingement surface motion were given in section 4.4.1.

The extent of the displacement of these peaks by surface motion is shown in Figure 4.31 for both sides of the profiles and in Figure 4.32 for the peak on the side of the nozzle where the surface is directed away from the nozzle for H/w = 6. Figures 4.22 to 4.24 show that for H/w = 6 the other secondary peak disappears into the central peak at all but the lowest values of M_{V_s} investigated. At H/w = 2.6

as well, it can be seen from Figure 4.31 that the location of the off-stagnation maximum on the side with surface motion approaching the nozzle is appreciably more sensitive to M_{V_s}. Thus from Figure 4.31 it can be seen that the location of the peak on the approach side of the nozzle shifts towards the nozzle centerline, linearly with M_{V_s}, until this secondary peak ceases to exist at $M_{V_s} \simeq 0.8$. Figure 4.25 shows that this secondary peak disappears by $M_{V_s} = 0.857$.

The lateral displacement of the other secondary peak, i.e. on the leaving side of the nozzle is, as already noted, less sensitive to surface motion than the peak on the approach side. The location of the leaving side secondary maximum does, however, shift with surface motion until $M_{V_s} \simeq 0.3$, after which its position seems independent of M_{V_s}. Figure 4.25 indicates that, for some value of $M_{V_s} < 0.857$, there no longer is a secondary maximum on the leaving side of the nozzle, at least for $H/w = 2.6$. The disappearance of this peak would be expected when V_s approaches the velocity of the wall jet. Figure 4.32 indicates that for $H/w = 6$, the increasing displacement of the secondary maximum on the leaving side of the nozzle continues at least to surface velocities as high as $M_{V_s} = 0.4$.

Switching to the aspect of height of the secondary maxima, Figure 4.33 indicates that, at $H/w = 2.6$, the height increases slightly with increasing M_{V_s}, with about the same

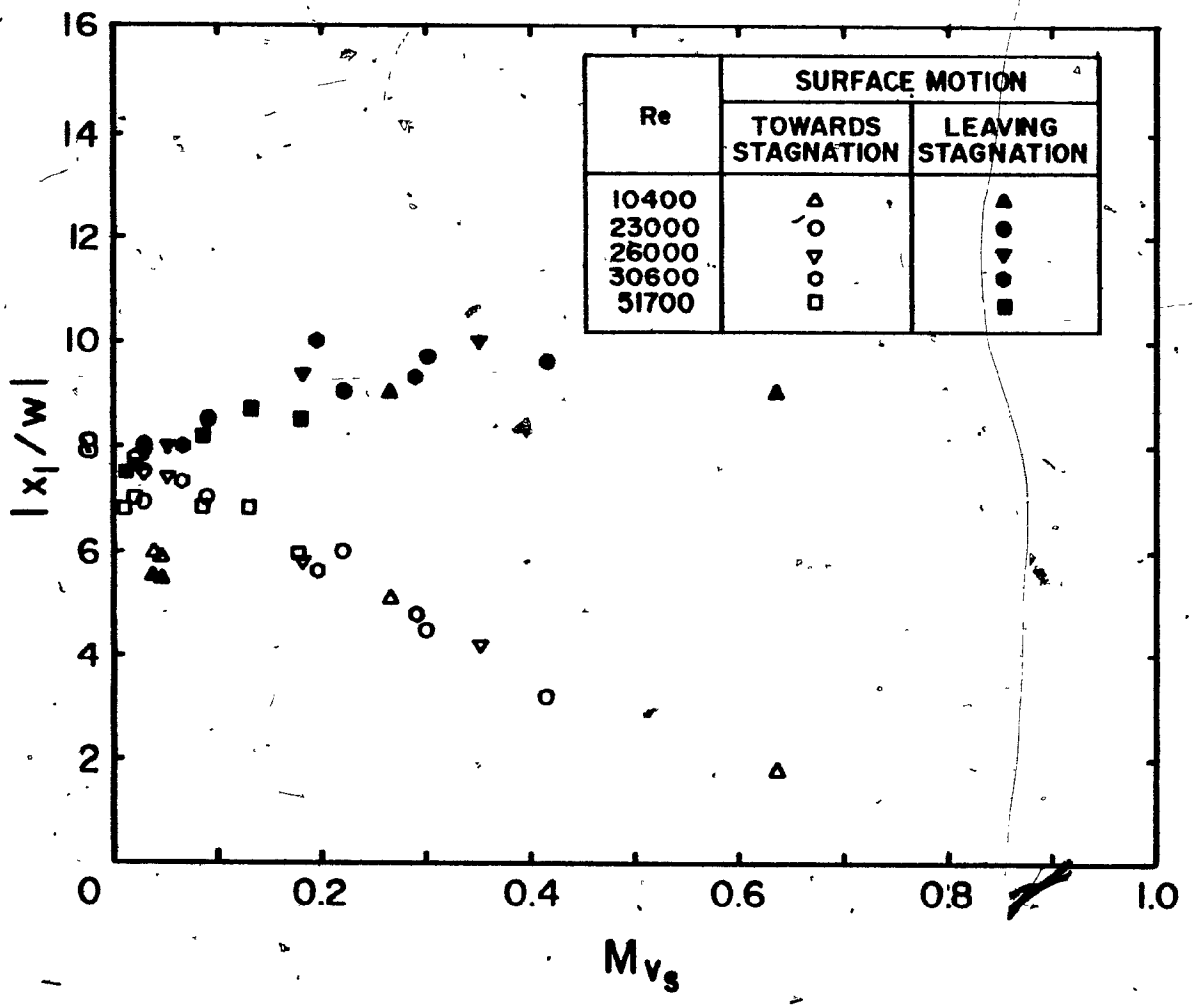


FIGURE 4.31. Effect of M_{V_S} on location of secondary heat transfer maxima at H/w = 2.6

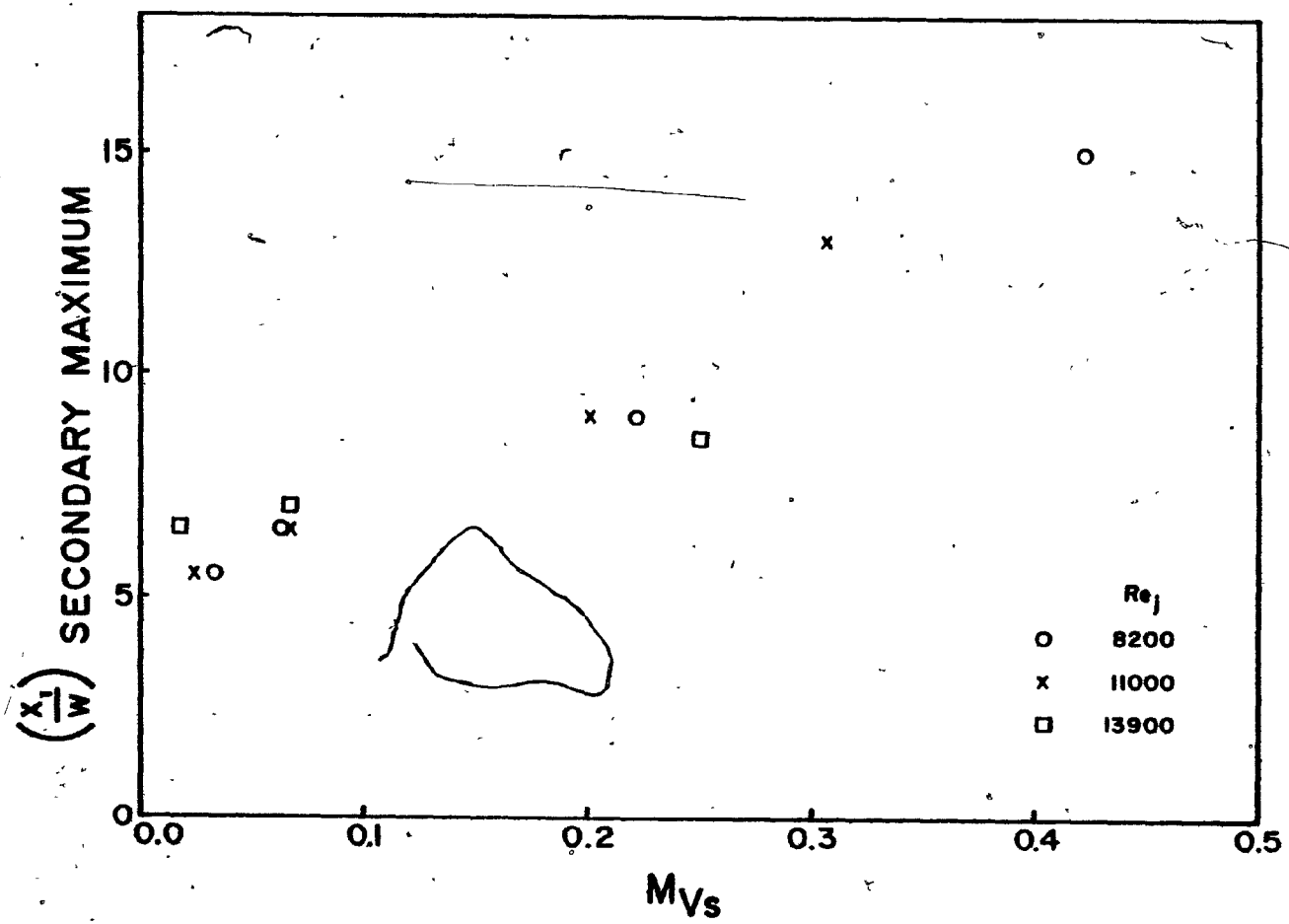


FIGURE 4.32. Effect of M_{Vs} on location of secondary heat transfer maxima for impingement surface leaving stagnation, H/w = 6

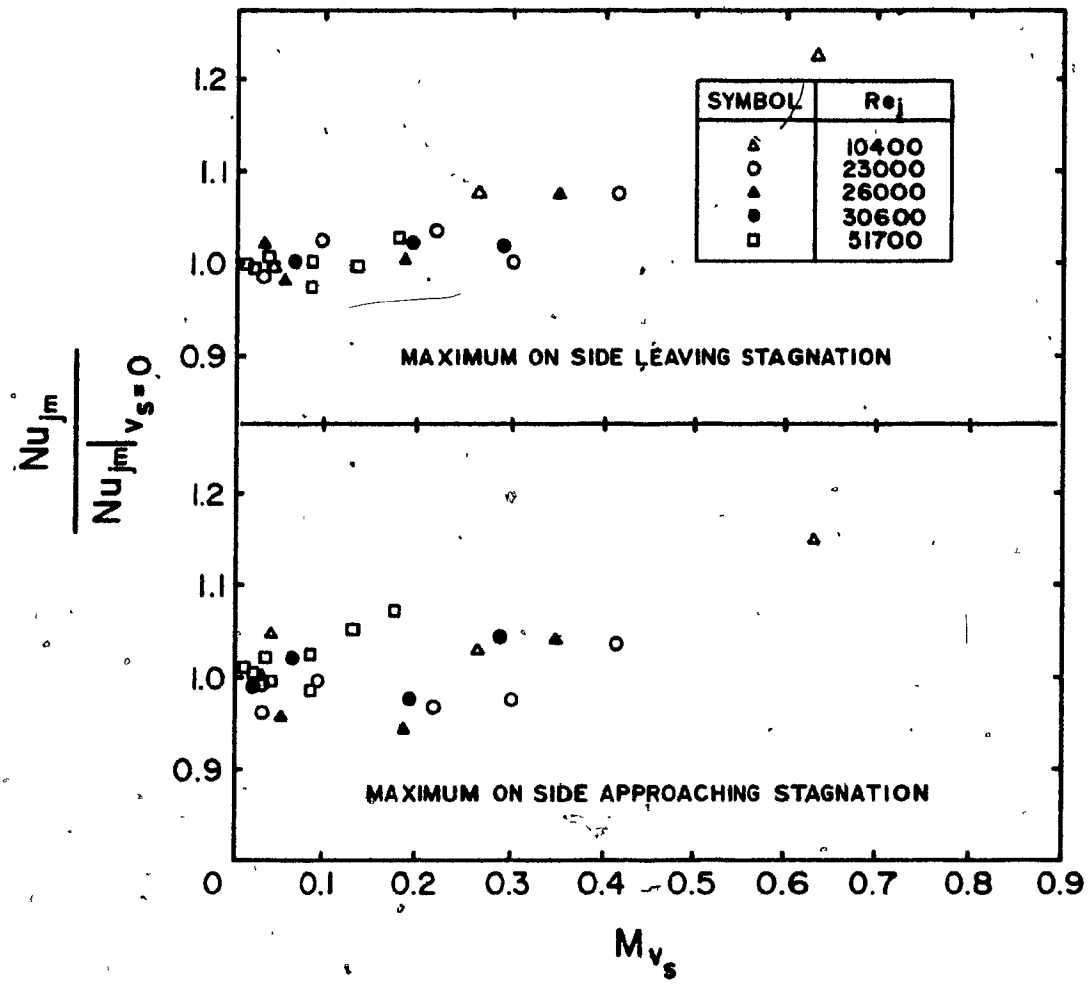


FIGURE 4.33. Effect of M_{V_s} on secondary heat transfer maxima at H/w ≐ 2.6

low sensitivity to surface motion as already noted on Figure 4.28 and 4.29 for stagnation heat transfer.

4.4.5 Heat Transfer Distribution in the Wall Jet Region

As was developed in section 4.4.1, it has been pointed out that heat transfer in the wall jet region reflects a combination of several interacting effects, i.e. of two flow field effects - the opposing effects of surface motion on velocity gradient at the surface and on wall jet velocity, and the thermal effect that surface motion has on local effective ΔT for convective heat transfer. Examination of the profiles of Figures 4.22 to 4.27 provides support for the view that the effect of surface motion on the rate of spreading of the wall jet is an important consideration. The clear change in slope of the profiles at about 20w from stagnation for $H/w = 6$ in the absence of significant surface motion effect was attributed in section 4.3.5 to the constraint exerted by the confinement surface against further spreading of the wall jet. On all profiles at $H/w = 6$ of Figures 4.22 to 4.24 it can be seen that, on the surface motion approach side of the nozzle, this clear change in slope remains but is displaced progressively closer to the nozzle by increasing surface motion. This consistent behaviour supports the view that the rate of spreading of the wall jet is appreciably increased by surface motion in the direction opposite to the

wall jet velocity, because a consequence of the faster spreading would be an earlier constraint by the confinement surface against further spreading. Conversely, on the leaving side of the nozzle the reduction in rate of wall jet spreading which was indicated as a consequence of surface motion on that side would have the effect of extending the distance required before constraint by the confinement surface would occur. This is indeed the effect noted on the right hand side of Figures 4.22 to 4.24.

Further confirmation for this view is provided by the results for H/w = 2.6 which, for a stationary surface, did not extend sufficiently far into the wall jet region for the effect of constraint on spreading by the confinement surface to be felt. For all values of M_{V_s} of 0.262 (Figure 4.25) and above, this change of slope is evident on the left hand profiles for H/w = 2.6, indicating the onset of constraint by the confinement surface on further wall jet spreading. Future investigations should provide velocity, turbulence and temperature measurements to explore the inferences made here concerning the effect of motion of the impingement surface.

In addition to the general features already noted, there is also an equipment-specific effect of surface motion on the profiles. As there must be some gap between the surface of the impingement cylinder and the two skimmer plates

which separate the heating and cooling jet sides of the apparatus, a layer of air from the other side always enters with the surface. At high values of M_{V_s} this layer of air from the other side of the apparatus, with high momentum from the impingement surface, tends to lift the wall jet from the cylinder in that region, i.e. in the regions after 0° and 180°. The fact that the surface enters the cooling jet half of the apparatus accompanied by a layer of hot air, and vice versa, means that there may be a section of impingement surface beginning at 0° and 180° for which the heat transfer is negative. Such sections may be seen on some profiles of Figures 4.22 to 4.27. This effect constitutes then an end effect in the particular experimental equipment.

In pointing out in section 4.4.4 that for $H/w = 2.6$ at the highest surface velocity, $M_{V_s} = 0.857$, the secondary maximum ceased to exist on the leaving side of the nozzle (Figure 4.25), it was noted that the approach of surface velocity, V_s, to the wall jet velocity would be expected to affect the occurrence of a secondary maximum. It is interesting to note that for the profile just referred to, for which $V_s = 12.94$ m/s, the mean velocity of the channel flow equivalent to half the nozzle flow rate ($U_j w/2H$) would be only 2.53 m/s. Lack of detailed information on velocity distributions for this annular confined flow at high impingement surface speeds makes more specific comment impossible.

A final remark is that the fluctuating behaviour of the heat transfer in the wall jet region at high values of M_{V_s} is caused by electrical noise, which becomes relatively more important at high rotational speeds.

4.4.6 Average Heat Transfer

Average heat transfer was obtained by integrating the profiles from $-x_1/w$ to x_1/w, with $x_1/w = 0$ located at the nozzle centerline. In order to isolate the effect of impingement surface motion, the values of average heat transfer in Tables 4.7 and 4.8 are normalized by the average heat transfer without significant surface motion effect, but at the same Re_j and extent of area averaged, i.e. by equations 4.7 and 4.9 for spacings, H/w, respectively, of 6 and 2.6. The normalized heat transfer for several values of the upper integration limit x_1/w are displayed in Figures 4.34a and b and 4.35 for spacings of 2.6 and 6. The significance of the extent of impingement surface over which the heat transfer is averaged may readily be seen by comparing these integration limits with typical profiles from Figures 4.22 to 4.27.

Figures 4.34 and 4.35 indicate that the normalized average heat transfer for both spacings, 2.6 and 6, decrease slightly with increasing M_{V_s} except when the heat transfer is averaged only over the stagnation region. Thus it can be seen from Figure 4.34a that, at H/w = 2.6, when the upper

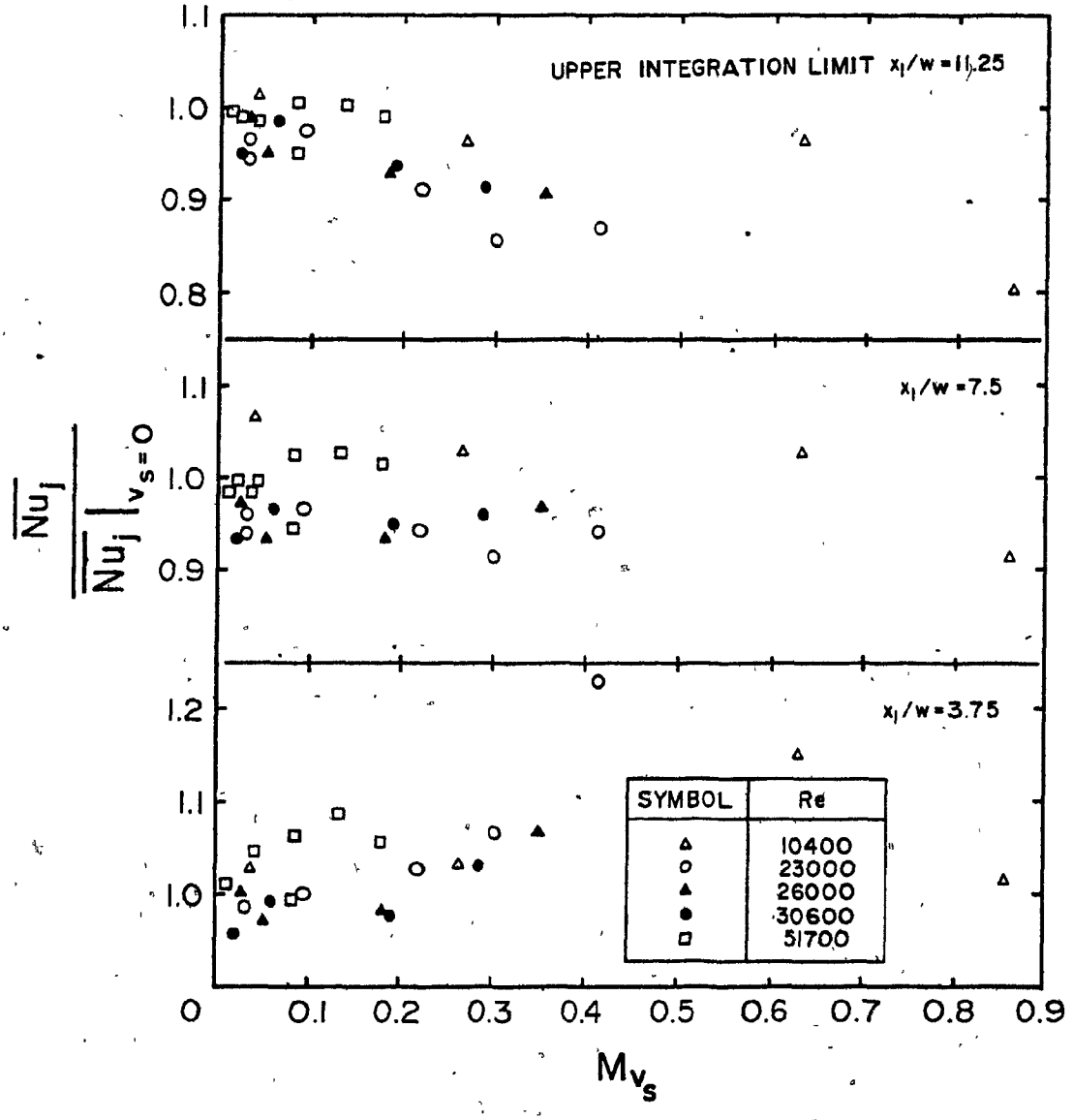


FIGURE 4.34a. Effect of M_{V_s} and upper integration limit on average heat transfer for H/w = 2.6

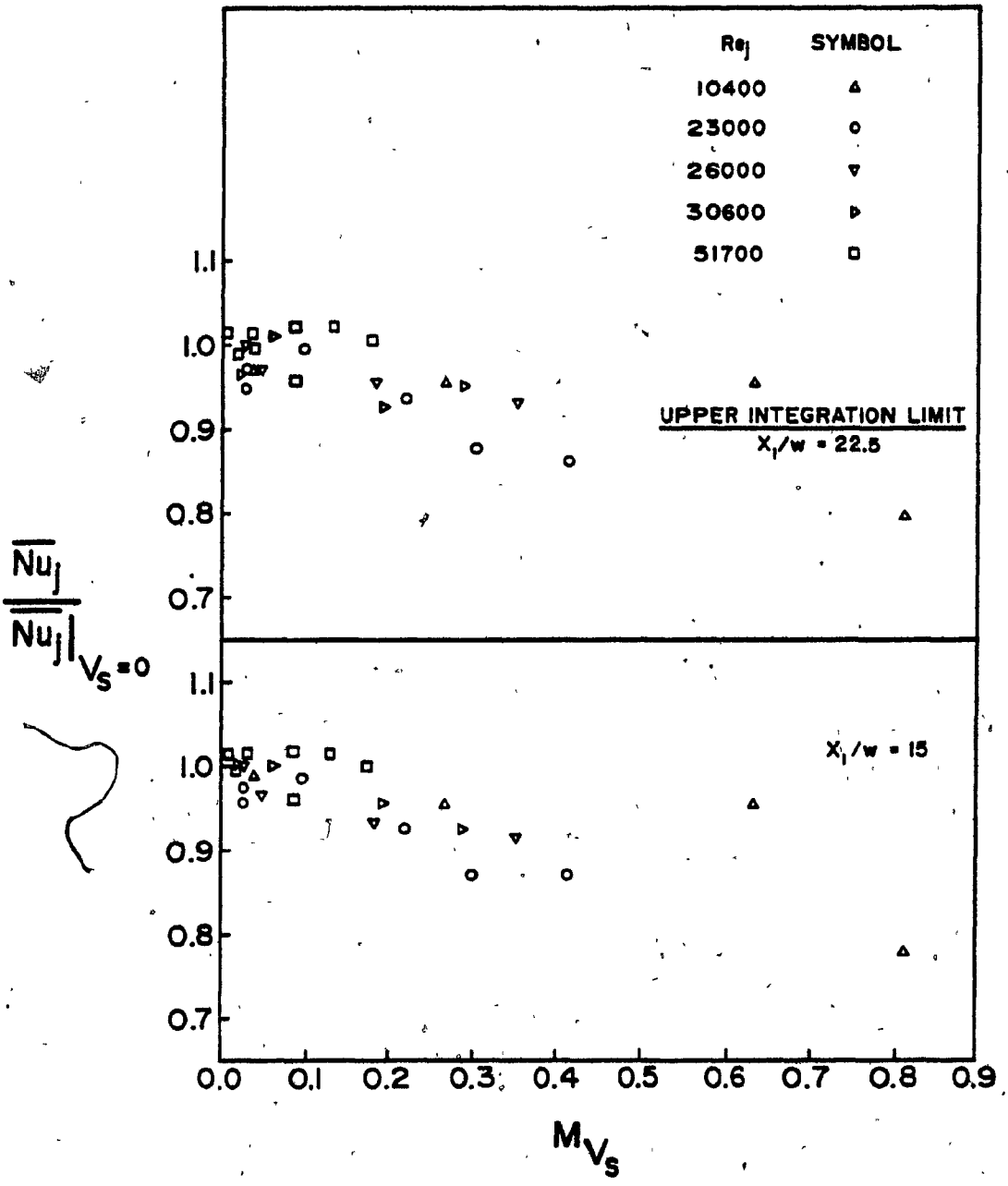


FIGURE 4.34b. Effect of M_{V_s} and upper integration limit on average heat transfer for H/w = 2.6

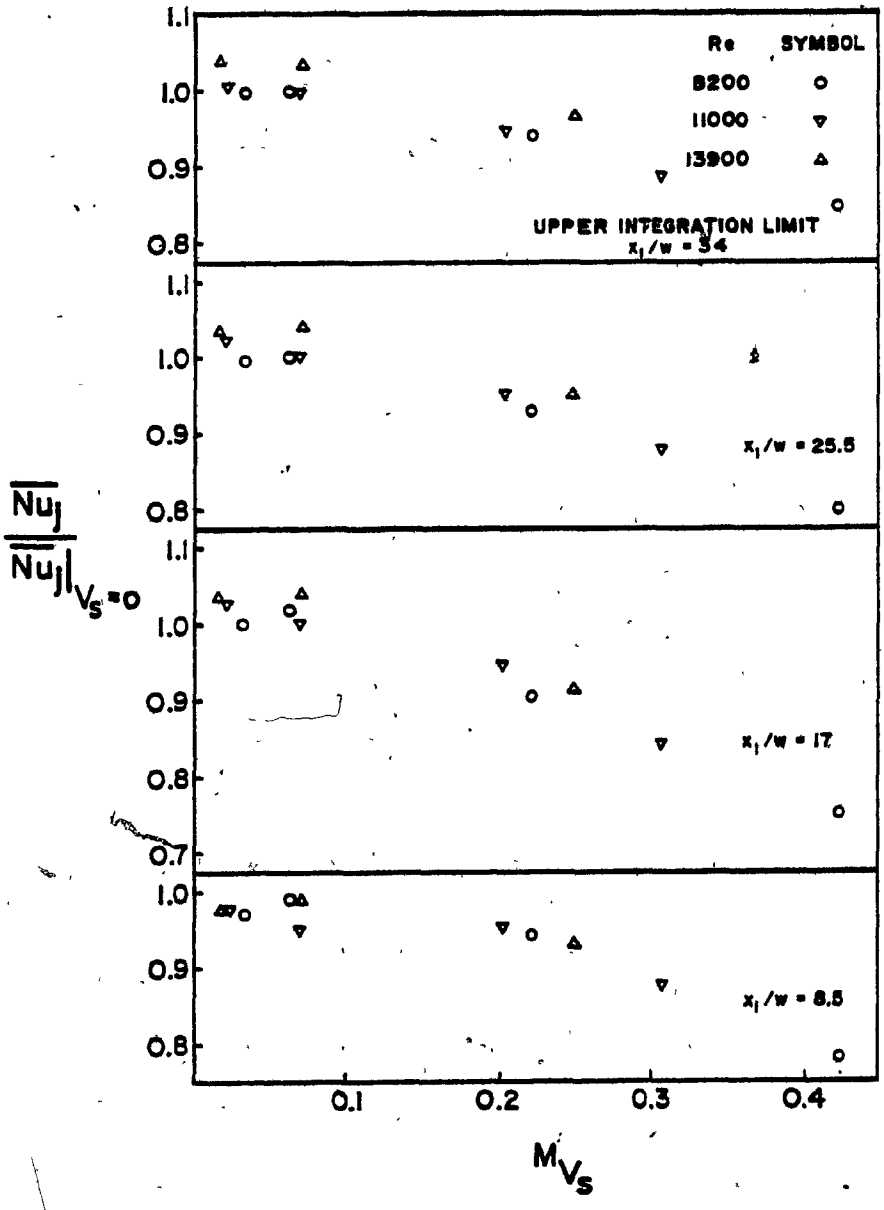


FIGURE 4.35. Effect of M_{V_s} and upper integration limit on average heat transfer for H/w = 6

integration limit is $x_1/w = 3.75$, $\overline{Nu_j}$ increases with M_{V_s}, and when the integration limit is $x_1/w = 7.5$, $\overline{Nu_j}$ is independent of M_{V_s}. Fechner (40) however, obtained an increase in average heat transfer with increasing M_{V_s} for multiple jets impinging symmetrically on a rotating cylinder. His results are shown in Figures 4.36 and 4.37 for respectively four symmetrically placed jets and for three and two symmetrically placed jets.

The geometrical parameters of Fechner's experiment are close to the present heating jet, i.e. $H/w = 5.3$ and $D_c/w = 60$ as compared to $H/w = 6$ and $D_c/w = 78$ for the heating jet. However, Fechner's experiment was with unconfined jets and did not employ skimmer plates between the regions of different jets. Thus whereas the present study corresponds to a single confined jet at two values of H/w, Fechner's investigation is of multiple unconfined jets.

Before proceeding further with comparisons between studies which are different in these basic ways, the extent to which interaction between Fechner's multiple jets may have influenced his results should be known. In this respect the only guide available is the recent study by Saad (125) of multiple confined slot jets impinging on a flat stationary surface. Saad found that for an aspect ratio, $S/H \geq 1.5$, significant interaction did not exist, i.e. a multiple jet system is effectively an assembly of

single jets. Here the aspect ratio, S/H, is the non-dimensional expression of the spacing, S, between centerlines of adjacent inlet nozzles and exit ports, i.e. 2S is the centerline spacing between adjacent nozzles. When Fechner's system is re-interpreted in this way, the aspect ratio for his case of most closely spaced nozzles is S/H = 4.4. It may therefore be concluded that his multiple jets are effectively an array of widely spaced single jets. Admittedly the criterion of multiple jet interaction derived by Saad is for impingement on a flat stationary surface, but his is the only criterion available. Therefore, as the aspect ratio, S/H, equivalent to Fechner's system is so much greater than the limit determined by Saad, it seems reasonable to make comparisons of results between Fechner's widely spaced multiple jets and the present single jet case.

The average heat transfer which would be equivalent to Fechner's system at the limit of $M_{V_s} \rightarrow 0$ was therefore calculated with equation 4.7 for H/w = 6, now with the upper integration limit x_1/w being determined for values of x_1 equal to 1/8, 1/6 or 1/4 of the circumference of the cylinder used by Fechner, with w also as the nozzle width employed by Fechner, for respectively 4, 3 and 2 symmetrically placed impinging jets. The values so calculated appear on Figures 4.36 and 4.37 at $M_{V_s} = 0$. The agreement between the average heat transfer calculated with equation 4.7 and that obtained by extrapolating the data of Fechner to $M_{V_s} = 0$, is remarkably

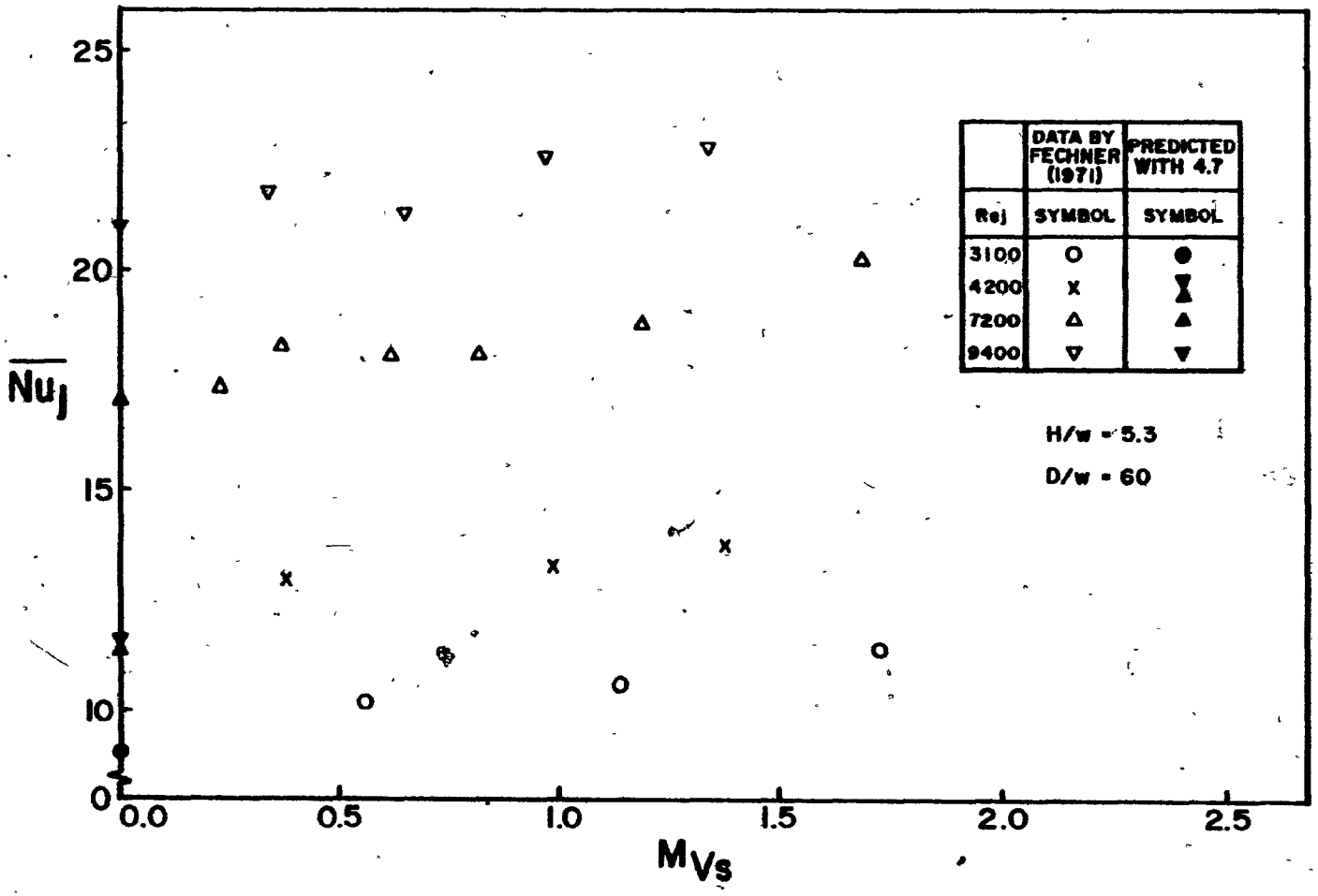


FIGURE 4.36. Average heat transfer between four symmetrically placed jets and a rotating cylinder, as measured by Fechner

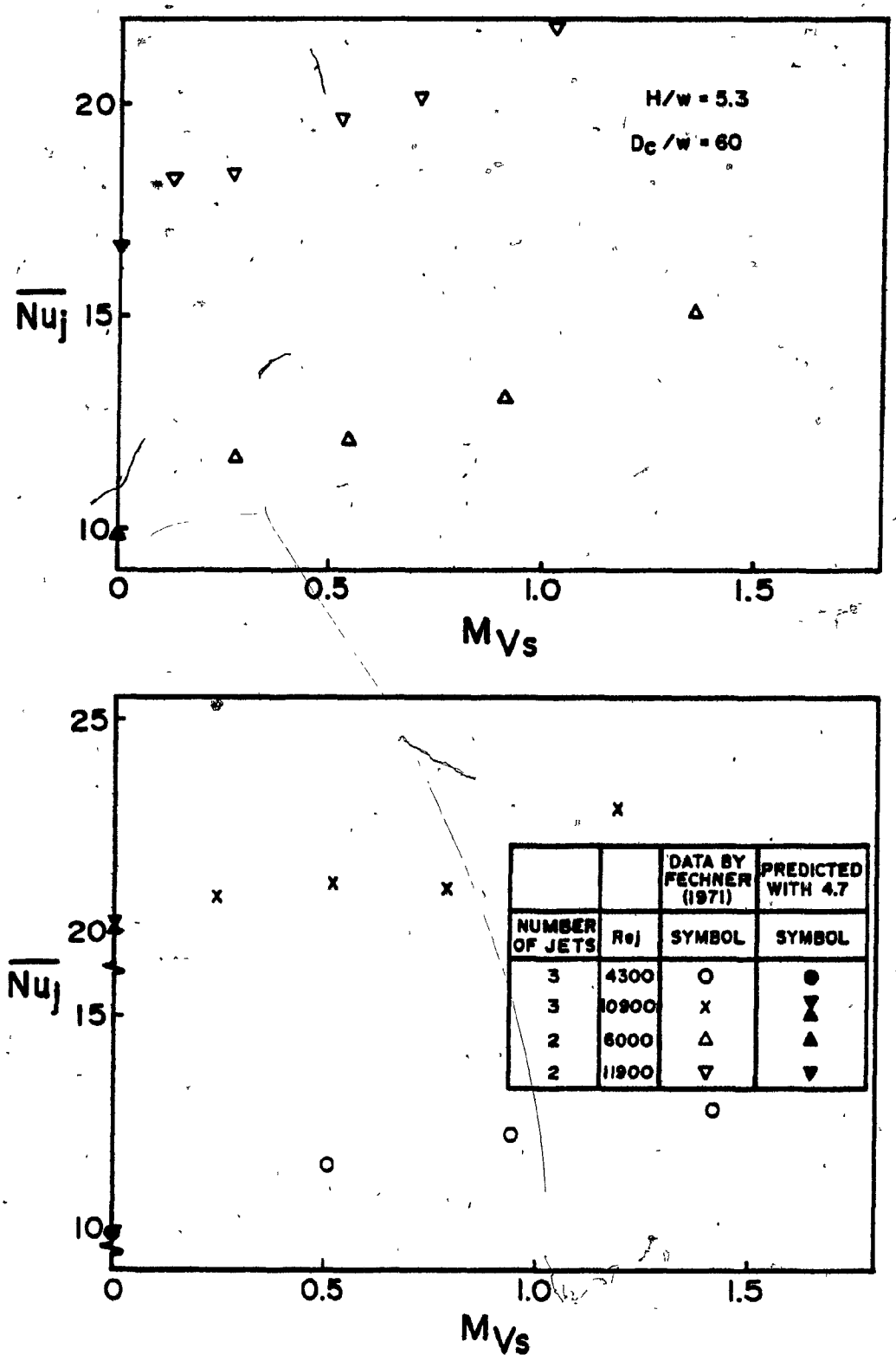


FIGURE 4.37. Average heat transfer between symmetrically placed jets and a rotating cylinder, as measured by Fechner

good, especially for the case of four impinging jets in Figure 4.36, where the influence of confinement would be least important.

In view of this good agreement between results from Fechner's study and the present investigation, the disagreement concerning effect of M_{V_s} on $\overline{Nu_j}$ takes on added significance. However, there is a straightforward explanation for these opposing trends. The present heat transfer profiles have established that, with increasing M_{V_s}, Nu_j increases on the leaving side of the nozzle but decreases somewhat more than that on the approach side. This behaviour causes $\overline{Nu_j}$ to decrease with increasing M_{V_s} when the averaging is carried out symmetrically around the nozzle centerline.

However, in the multiple jet case of Fechner, the lack of symmetrically placed splitter plates leads to a distinctly different behaviour. In Fechner's case the high heat transfer region for the nozzle leaving side would extend over more than half the circumferential distance to the next jet, while the low heat transfer region on the nozzle approach side extends correspondingly over less than half the peripheral distance between jets. This assymetry derives from the greater momentum of the wall jet flowing on the leaving side of the nozzle where the wall jet velocity is in the same direction as the surface motion. By contrast, the other wall jet flows on the approach side of the nozzle, and hence against the direction of the surface motion, and therefore

would have significantly lower momentum. Overall this assymetry of the wall jets leads then to more of the surface being covered by the wall jet with the higher heat transfer, which leads thereby to an increase in average heat transfer with increasing M_{V_s}.

The analysis developed above concerning Fechner's results for unconfined multiple jets has implications for confined impingement systems as well. Specifically, for a confined system it would appear that mean heat transfer would increase if exhaust ports were located not equidistant between the inlet nozzles but rather, displaced from the equidistant position in the direction of the surface motion. In this way less than half of the impingement surface would be covered by the wall jet which flows in the direction opposite to the surface motion, and correspondingly more than half the surface would be covered by the wall jet with higher heat transfer, i.e. flowing in the same direction as the impingement surface motion. For a particular spacing between nozzles, an estimate of the optimum location of exhaust ports could be obtained by determining from profiles such as Figures 4.22 to 4.27 what assymetric averaging limits would lead to maximum value of $\overline{Nu}$.

Finally, it is necessary to comment on the data obtained by Subba Raju and Schlünder (142) for a slot jet impinging on a continuously moving flat belt. For very small values of surface motion, i.e. $M_{V_s} << 0.1$, they reported an increase of 1.5 to 2 times the average heat transfer predicted by equation 4.8 for a stationary surface. The averaging area

was of the same order as in the present work. Considering the results of Fechner and of the present study, it seems impossible to believe their findings.

4.5 Influence of Throughflow at the Impingement Surface

The influence on heat transfer of throughflow at the impingement surface has received even less attention than has the influence of impingement surface motion, discussed in the preceding section. Most of the limited amount of work has been reported by the Impinging Jet Group of the Department of Chemical Engineering, McGill University. One of the main motivations for the work of the Impinging Jet Group is the large increase in drying rate which can be obtained by combining impingement and throughflow drying in the drying of newsprint, as has been shown by Burgess et al. (23, 24) with the "Papridryer" process. The work of the McGill Impinging Jet Group has been mainly theoretical (see section 2.2.3.3). The only two published experimental studies are the early investigation by Obot (105) of heat transfer for a single impinging round jet, including throughflow at a porous impingement surface, and the recent Ph.D. thesis by Saad (125), which included a preliminary study of the effect of throughflow on heat transfer for confined impinging slot jets.

The original objectives of the present work included study of the effect of throughflow at the impingement surface by measurement of the heat flux at the surface using a porous

sensor having the same permeability and transient surface temperature response as the porous stainless steel used for the impingement cylinder of the SIMTEST apparatus. However, for reasons documented in section 3.3.1.1 concerning selection of the heat flux sensor, development of a non-porous substrate based sensor of the exacting specifications of sensitivity and response time required was found to be sufficiently difficult that it was necessary to drop the further complication of use of a porous substrate.

The use of a small impermeable sensor installed in a moving, permeable impingement surface with throughflow will yield results which are representative of the throughflow case provided that the steady boundary layer over the permeable surface has insufficient time to adjust to the no-throughflow condition during the short transit time of a small impermeable sensor. The high impingement surface speeds of up to 12 m/s in the present study are favorable to this experimental approach. Some theoretical support for the possibility of using a small impermeable sensor in a moving permeable surface to measure heat transfer with throughflow was obtained from a computer simulation of heat transfer under a laminar impinging slot jet with throughflow at a stationary impingement surface. The relevant simulation results, shown in Figure 4.38, are obtained with the vorticity-stream function program described in section 2.2.

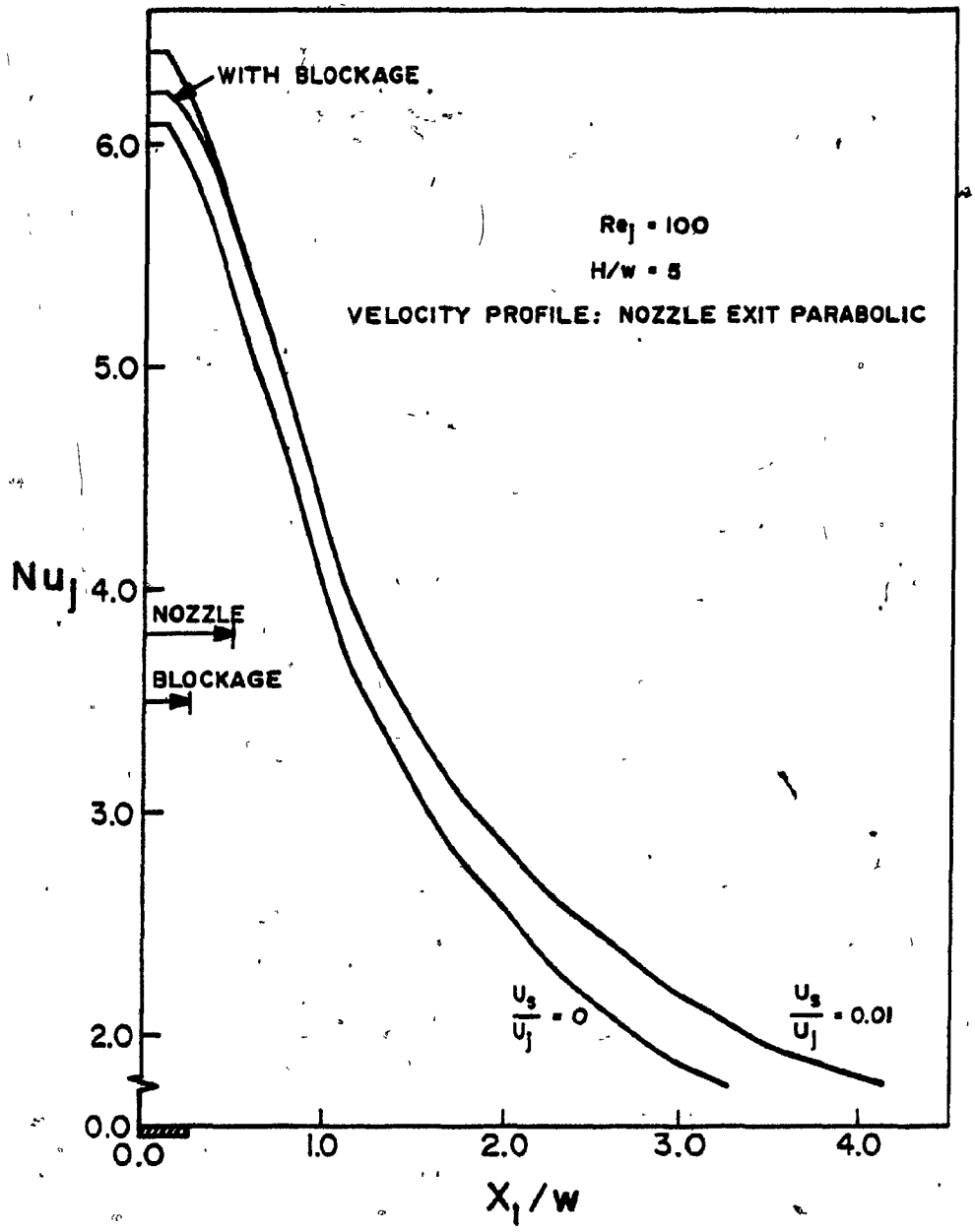


FIGURE 4.38. Effect of impermeable sensor on impingement heat transfer with throughflow

The three cases shown are: no throughflow ($U_s/U_j = 0$), uniform throughflow ($U_s/U_j = 0.01$) and the same uniform throughflow but with a small impermeable blockage around the stagnation point. The size of the blockage was set at half the nozzle width, similar to the width of the sensor relative to the nozzle width for the heating jet side of the SIMTEST apparatus. It can be seen that the stagnation point heat transfer which would be measured by the impermeable sensor in a stationary impingement surface is roughly midway between the values for the limiting cases of uniform throughflow and no throughflow.

These results for a stationary surface, plus the fact that the effect of blockage on the steady flow and temperature field would be less at high impingement surface speeds, provided support for the possibility that results from a small impermeable sensor in a moving permeable impingement surface would yield a reasonable approximation for heat transfer in the case of throughflow at the impingement surface. In fact, it was subsequently established that an impermeable sensor, even of this small size, in a moving impingement surface cannot give results which are representative of heat transfer under turbulent impinging jets with throughflow, for the following two reasons:

1. The thickness of the boundary layer with turbulent impinging jets is of the order of 1 mm or less,

compared with the effective width of the blockage (including the epoxy glue; see Figure 3.4) of the order of 10 mm. In the case of the numerical simulation of Figure 4.38, the ratio of boundary layer thickness to width of the blockage is much larger, namely 0.44.

2. The speed with which a turbulent boundary layer adapts to changes in the thermal boundary condition at the wall is higher by at least a factor 100 than for a laminar boundary layer. The thermal response of a turbulent boundary layer can be characterized by a turbulent Fourier number

$$Fo_t = \frac{\bar{a}_{eff}\, t}{\delta^2}$$

with $\bar{a}_{eff}$ the average effective thermal diffusivity for the turbulent boundary layer, t the exposure time and δ the boundary layer thickness. When $\bar{a}_{eff}$ is taken as $100(a_{laminar}) \simeq 25 \times 10^{-4}$ m^2/s for air at about 50°C, $\delta \leq 10^{-3}$ m and the exposure time t is 4×10^{-4} seconds (the time for a fluid particle at the edge of the boundary layer to travel from the beginning of the blockage to a position perpendicularly above the gold film), then $Fo_t \geq 1$. At Fourier numbers of this size, the boundary layer is completely adapted to the new thermal boundary condition.

Although heat transfer coefficients obtained by the present technique do not then represent the case of heat transfer with throughflow, they do nonetheless reflect an aspect of heat transfer in the flow field of impingement with throughflow. In section 2.2.3.3 the concept was discussed of partitioning heat transfer with throughflow into an impingement contribution and a throughflow contribution. The results by the present technique constitute, specifically, this impingement contribution because, with an impermeable sensor, the heat flux measured is that for pure impingement without throughflow but in the overall flow field of impingement with throughflow.

4.5.1 Lateral Profiles of Local Heat Transfer

The interpretation just established for heat transfer as determined by the present technique can be confirmed by reference to an overall energy balance, applied to the results for the limiting case of a throughflow rate essentially equal to the nozzle exit flow rate. Shown in Figure 4.39 are the heat transfer profiles for two levels of throughflow at $Re_j = 5200$, $H/w = 6$ and a relatively low impingement surface velocity, $M_{V_s} = 0.05$, along with the reference profile for zero throughflow. The throughflow velocity is again expressed nondimensionally as M_{U_s}, the ratio of throughflow mass velocity to jet mass velocity. The differences between the three profiles are quite small, especially when it is realized

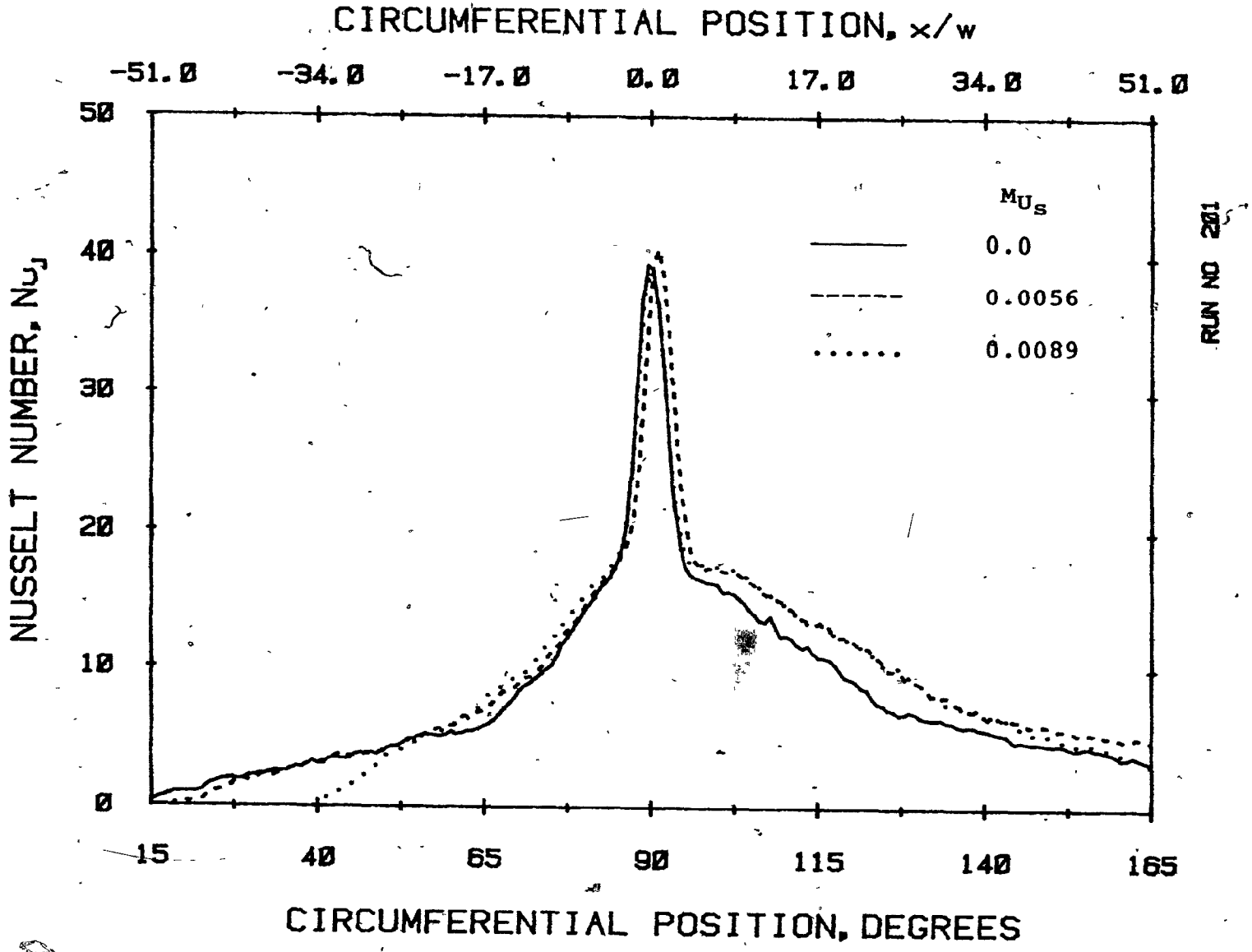


FIGURE 4.39. Effect of M_{U_S} on lateral profiles of heat transfer at Re_j = 5200 and H/w = 6

that for $M_{U_s} = 0.00895$ the total mass of throughflow air withdrawn through the impingement cylinder surface on the heating jet side is 0.026 kg/s compared with 0.024 kg/s supplied by the heating jet. The fact that the measured heat transfer goes to zero at an angular position of 40° reflects the entrance of cooler air from the exhaust port at 0° for the case where throughflow exceeds nozzle flow. This inflow apparently comes entirely from the exhaust duct at 0° because of the assymetry of the nozzle exit flow caused by surface motion in the direction of the exhaust duct at 180°.

Application of an overall heat balance to the space bounded by the confinement surface, nozzle, impingement surface and radial planes on both sides of the stagnation point leads to the requirement for average heat transfer as

$$\overline{Nu}_j \geq M_{U_s} \, Re_j \, Pr \qquad (4.10)$$

or

$$\overline{St}_j \geq M_{U_s} \qquad (4.11)$$

The equality in equations (4.10) and (4.11) applies when throughflow across the surface used for averaging of the heat transfer exactly equals nozzle exit flow, the inequality when throughflow is less than the jet flow. It should be noted that equation (4.11) is the same as equation (2.62) derived from the theoretical analysis of Mickley et al. (96) and Spalding (136).

Application of equation 4.10 to the case of $M_{U_s} = 0.00895$ in Figure 4.39 gives $\overline{Nu}_j \geq 33$. This is clearly much larger than the average heat transfer obtained by the impermeable sensor from an angular position of 40° to 165°, and establishes again the limitations in use of this sensor for heat transfer measurements with throughflow.

Another interesting result is obtained when the flow in the impingement region is approximated by laminar plane stagnation flow with uniform throughflow. From the exact solutions in graphical form of Hartnett and Eckert (59) it can be derived that the increase in heat transfer due to throughflow is reasonably well represented by

$$St_j - St_{j_{M_{U_s}=0}} = 0.65\, M_{U_s} \qquad (4.12)$$

This equation is again similar to equation (2.61) obtained from the theoretical analysis of Mickley et al. (96), and even closer to equation (2.63) which is the correlation of the numerical results of the influence of throughflow obtained in section 2.2.3.3. Application of equation (4.12) to the case of $M_{U_s} = 0.00895$ in Figure 4.39 gives an increase in the Nusselt number due to throughflow of 21.5, compared with a negligible increase in Figure 4.39.

Other heat transfer distributions for H/w = 6 obtained by the sensor at relatively small values of M_{V_s} (<0.03) are shown in Figures 4.40 and 4.41 for values of Re_j respectively of 11000 and 13800. Also here it is found that the influence of throughflow on the heat transfer distribution as measured by the impermeable sensor is negligible. The applied throughflow velocities are 0, 0.10 and 0.16 m/s. A complete listing of relevant experimental conditions and results at H/w = 6 for all runs with throughflow is given in Table 4.9.

The experimental runs with throughflow for H/w = 2.6 are given in Table 4.10. The influence of throughflow on heat transfer distributions from the impermeable sensor for H/w = 2.6 at small values of M_{V_s} are shown in Figures 4.42 to 4.45.

There is an apparent increase in Nu_j with increasing M_{U_s}, especially at the lower Reynolds numbers. This apparent increase, however, is mainly caused by extra axial heat loss from the ends of the impingement cylinder. Normally this heat loss is compensated by heating lamps but for the cases of high throughflow and high rotational speed the maximum heating rate of these lamps was insufficient to counter this heat loss. As a result the average temperature difference between the thermocouples at the back of the sensor ($\overline{\Delta T_s}$) reached values of -0.95°C (see Table 4.10).

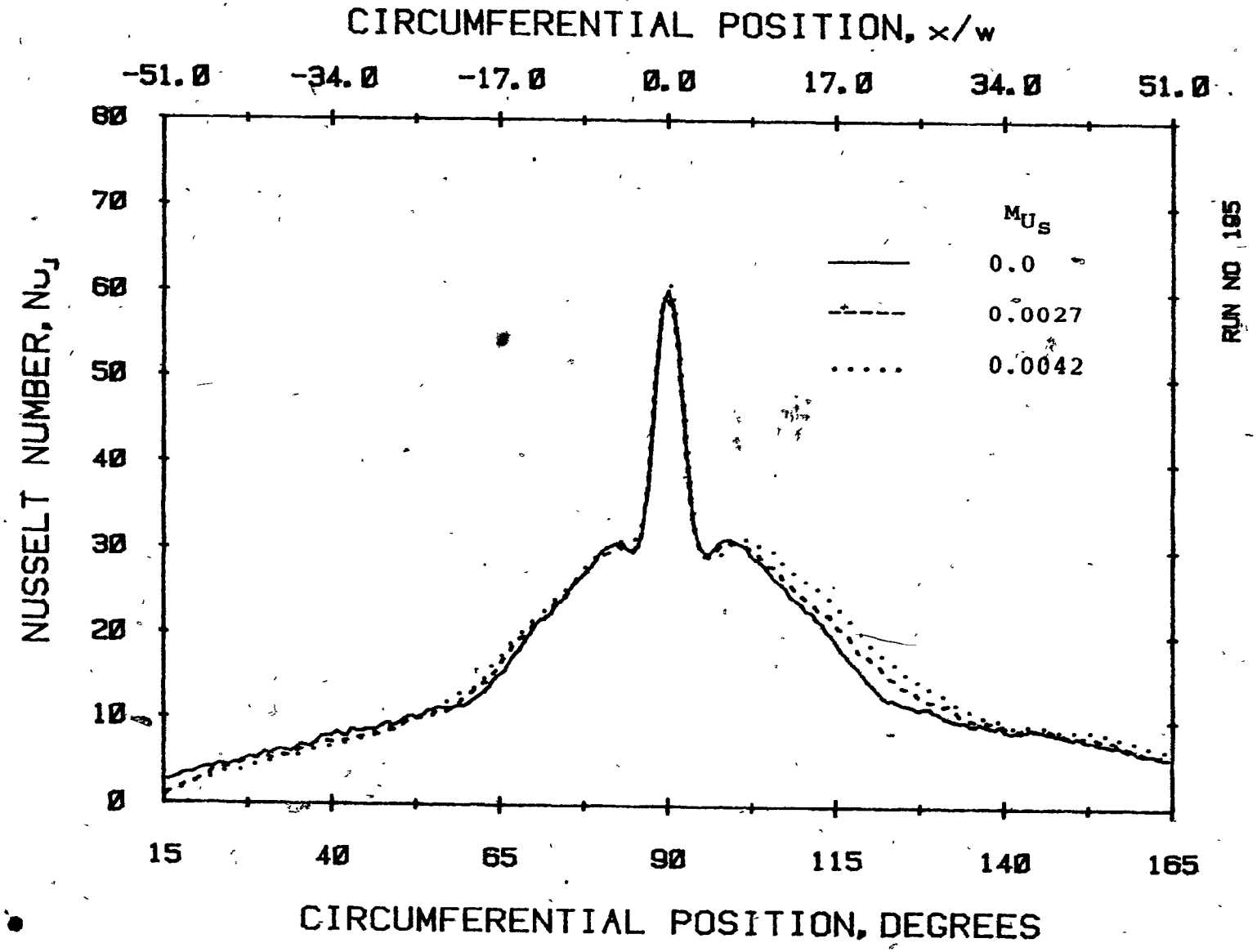


FIGURE .4.40. Effect of M_{U_s} on lateral profiles of heat transfer at $Re_j = 11100$ and $H/w = 6$

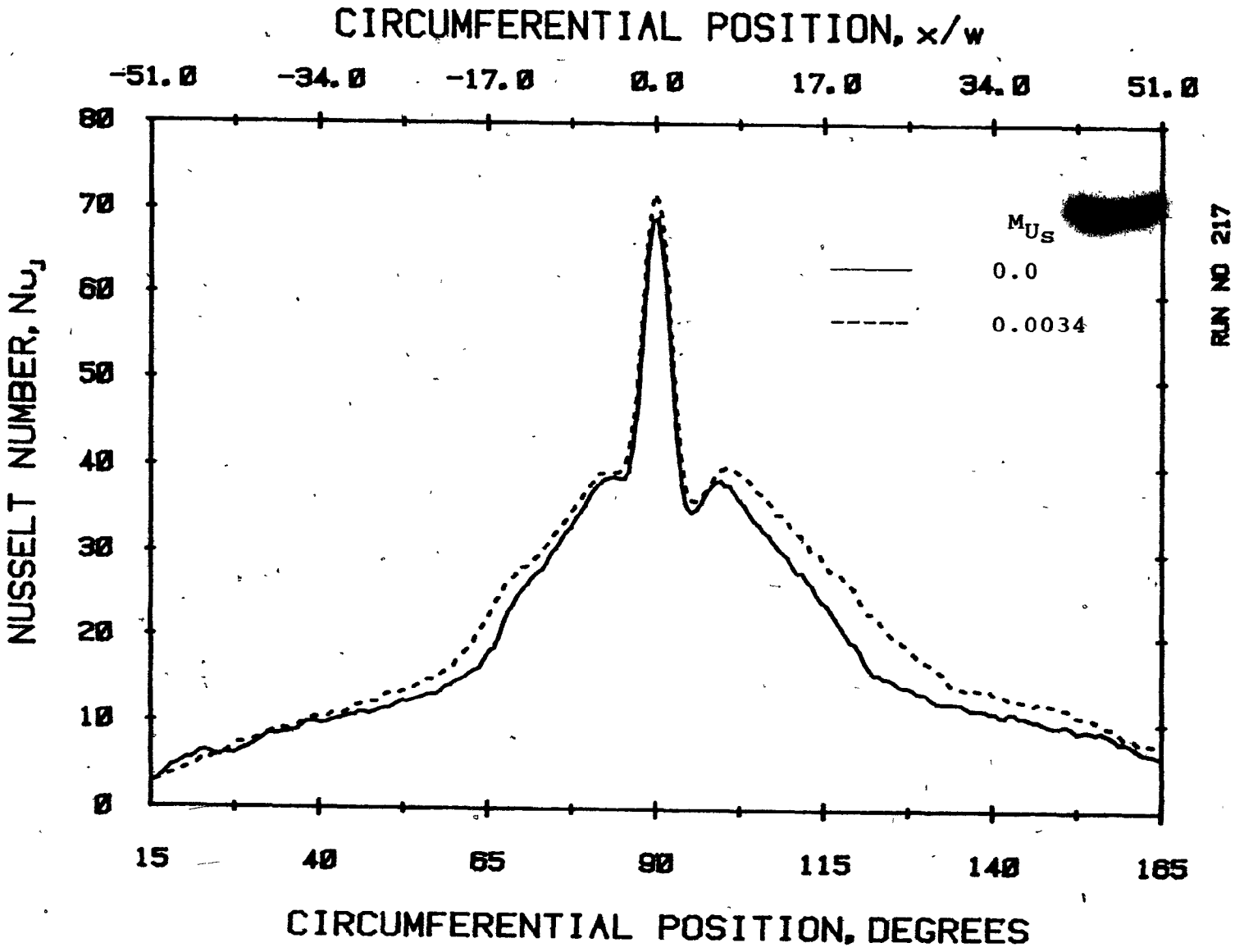


FIGURE 4.41. Effect of M_{U_S} on lateral profiles of heat transfer at Re_j = 13800 and H/w = 6

TABLE 4.9. Operating conditions and results for influence of M_{U_s} at H/w = 6

Run	Re_j	M_{V_s}	U_s (m/s)	M_{U_s}	T_j (°C)	$T_j - T_s$ (°C)	$\overline{\Delta T_s}$ (°C)	$Nu_{oj}/\sqrt{Re_j}$	$\overline{Nu}_j$ $x_1/w=8.5$	$\overline{Nu}_j$ $x_1/w=17$	$\overline{Nu}_j$ $x_1/w=25.5$	$\overline{Nu}_j$ $x_1/w=34$	$\overline{Nu}_j$ $x_1/w=51$
199	5200	0.053	0.0	0.0	102.1	38.1	0.0	0.534	20.4	15.4	12.6	10.7	8.2
200	5200	0.051	0.101	0.00561	102.4	39.2	-0.1	0.546	21.3	16.7	13.9	11.9	9.1
201	5200	0.052	0.160	0.00895	103.6	43.2	-0.55	0.528	21.0	16.5	13.9	11.7	-
196	8200	0.034	0.0	0.0	102.4	38.2	0.15	0.534	27.3	22.0	18.0	15.3	11.8
197	8000	0.033	0.098	0.00353	102.8	37.5	0.10	0.548	27.7	22.7	19.0	16.2	12.5
198	8000	0.034	0.160	0.00575	101.9	35.7	-0.05	0.545	27.7	23.0	19.4	16.5	12.7
207	8200	0.063	0.0	0.0	102.4	38.2	0.15	0.534	27.3	22.0	18.0	15.3	11.8
208	8200	0.062	0.164	0.00621	101.1	39.2	-0.25	0.553	28.6	23.7	19.8	16.8	12.9
202	8200	0.222	0.0	0.0	99.7	38.4	-0.15	0.567	26.5	19.9	16.8	14.4	11.1
204	8200	0.220	0.162	0.00577	100.5	39.0	-0.65	0.564	28.3	23.0	19.4	16.7	13.3
203	8300	0.423	0.0	0.0	100.5	40.6	-0.6	0.561	22.2	16.7	14.3	-	-
209	8200	0.419	0.161	0.00572	100.3	39.1	-0.95	0.537	26.9	21.8	18.8	16.3	13.2
193	11000	0.024	0.0	0.0	98.8	34.1	0.3	0.550	34.4	28.3	23.1	19.3	14.9
194	11000	0.027	0.103	0.00271	99.8	36.0	0.15	0.542	34.4	28.6	23.7	20.1	15.5
195	11100	0.023	0.162	0.00425	98.3	35.1	0.0	0.552	34.6	29.3	24.7	21.0	16.0
213	11200	0.307	0.0	0.0	101.3	40.5	-0.65	0.595	31.3	23.5	20.1	17.2	

TABLE 4.9. (continued)

Run	Re_j	M_{V_s}	U_s (m/s)	M_{U_s}	T_j (°C)	$T_j - T_s$ (°C)	$\overline{\Delta T_s}$ (°C)	$Nu_{oj}/\sqrt{Re_j}$	$\overline{Nu}_j$ $x_1/w=8.5$	$\overline{Nu}_j$ $x_1/w=17$	$\overline{Nu}_j$ $x_1/w=25.5$	$\overline{Nu}_j$ $x_1/w=34$	$\overline{Nu}_j$ $x_1/w=51$
214	11000	0.311	0.163	0.00429	102.3	39.3	-0.80	0.577	33.3	27.2	22.9	19.7	15.5
219	13900	0.251	0.0	0.0	102.2	50.4	-0.05	0.607	39.0	30.0	25.6	22.1	17.1
220	13800	0.254	0.159	0.00339	99.7	42.9	-0.30	0.611	41.9	34.3	29.1	25.2	19.8
218	13900	0.018	0.0	0.0	101.2	48.7	0.15	0.553	40.9	34.0	27.9	23.8	18.5
217	13800	0.018	0.160	0.00339	100.6	45.1	0.60	0.578	42.4	36.2	30.7	26.3	20.5
216	13800	0.066	0.161	0.00343	100.2	44.4	0.50	0.586	43.2	36.7	31.0	26.6	20.6
169	20300	0.013	0.0	0.0	75.9	21.3	0.0	0.532	51.4	43.6	35.2	29.7	23.2
170	20100	0.013	0.101	0.00154	76.7	20.9	-0.25	0.549	51.1	43.7	35.6	30.2	23.4
171	20000	0.013	0.157	0.00241	76.7	20.5	-0.4	0.517	50.4	43.4	35.8	30.4	23.4

TABLE 4.10. Operating conditions and results for influence of M_{U_s} at H/w = 2.6 .

Run	Re_j	M_{V_s}	U_s (m/s)	M_{U_s}	T_j (°C)	$T_j - T_s$ (°C)	$\overline{\Delta T_s}$ (°C)	$Nu_{oj}/\sqrt{Re_j}$	$\overline{Nu}_j$ $x_1/w=3\frac{1}{2}$	$\overline{Nu}_j$ $x_1/w=7.5$	$\overline{Nu}_j$ $x_1/w=11\frac{1}{2}$	$\overline{Nu}_j$ $x_1/w=15$	$\overline{Nu}_j$ $x_1/w=22.5$
199	16400	0.0443	0.0	0.0	38.3	25.7	0.0	0.449	37.3	36.7	36.8	34.7	29.3
200	16600	0.0425	0.101	0.00464	36.4	26.8	-0.1	0.448	40.8	39.3	39.4	37.5	31.8
201	16300	0.0435	0.160	0.00751	37.1	23.3	-0.55	0.469	44.3	42.7	42.6	40.8	35.2
174	24400	0.0297	0.0	0.0	37.0	17.8	0.0	0.441	43.6	45.6	48.0	45.9	38.9
123	23900	0.0295	0.052	0.00167	39.7	16.1	-0.15	0.475	51.3	49.7	51.8	49.8	42.8
177	24800	0.0248	0.107	0.00338	35.0	18.0	-0.15	0.458	50.1	49.9	52.5	50.4	42.8
176	24600	0.0289	0.158	0.00506	35.5	17.1	-0.25	0.478	54.0	52.9	55.2	53.3	45.5
196	25100	0.0286	0.0	0.0	37.8	26.4	0.15	0.454	45.2	47.4	50.4	48.2	40.6
197	24900	0.0278	0.098	0.00297	38.8	26.5	0.10	0.458	48.7	48.6	51.7	50.1	42.8
198	24600	0.0285	0.160	0.00485	41.1	25.1	-0.05	0.463	51.4	50.1	52.6	50.8	43.3
207	26200	0.052	0.0	0.0	33.5	27.3	0.0	0.439	44.8	46.9	50.1	48.1	40.7
208	26100	0.0515	0.164	0.00481	34.2	27.7	-0.25	0.448	50.3	49.5	52.8	51.1	43.6
202	25900	0.184	0.0	0.0	35.3	26.0	-0.15	0.444	44.9	46.5	48.5	46.3	39.7
204	26000	0.183	0.162	0.00478	33.4	28.1	-0.65	0.461	51.8	51.7	54.0	52.2	45.0
203	26500	0.349	0.0	0.0	34.5	25.4	-0.6	0.467	49.4	49.0	48.3	45.8	39.3
209	26300	0.347	0.161	0.00473	32.7	28.5	-0.95	0.448	51.1	51.4	53.6	51.1	44.4
193	30100	0.0229	0.0	0.0	37.5	27.2	0.3	0.444	47.2	51.6	55.6	55.3	44.8

TABLE 4.10. (continued)

Run	Re_j	M_{V_s}	U_s (m/s)	M_{U_s}	T_j (°C)	$T_j - T_s$ (°C)	$\overline{\Delta T_s}$ (°C)	$Nu_{oj}/\sqrt{Re_j}$	$\overline{Nu_j}$ $x_1/w=3\frac{1}{2}$	$\overline{Nu_j}$ $x_1/w=7.5$	$\overline{Nu_j}$ $x_1/w=11\frac{1}{2}$	$\overline{Nu_j}$ $x_1/w=15$	$\overline{Nu_j}$ $x_1/w=22.5$
194	30100	0.0226	0.103	0.00259	36.5	27.3	0.15	0.466	53.9	55.1	59.6	57.7	49.3
195	30100	0.0225	0.162	0.00409	36.6	26.6	0.0	0.466	56.1	56.3	60.6	58.9	50.3
213	31400	0.2904	0.0	0.0	32.5	28.8	-0.65	0.464	52.0	54.6	55.1	52.7	45.4
214	30600	0.2966	0.163	0.00409	32.8	30.2	-0.8	0.460	54.9	56.3	59.9	57.6	49.9
179	35100	0.0203	0.0	0.0	37.9	21.3	0.05	0.449	52.4	59.5	64.1	61.3	51.8
180	34800	0.0203	0.103	0.00225	38.4	20.4	-0.2	0.469	58.4	61.8	66.8	64.7	55.3
181	34700	0.0201	0.160	0.00352	38.7	20.0	-0.3	0.479	62.1	64.6	69.4	67.3	57.7
183	34800	0.1813	0.0	0.0	39.6	20.8	-0.4	0.461	53.0	57.8	60.5	58.1	49.7
182	34500	0.1824	0.158	0.00348	39.0	19.7	-0.8	0.484	61.6	63.2	67.6	65.5	56.8
169	57200	0.0121	0.0	0.0	39.3	15.3	0.0	0.442	65.9	86.6	94.7	89.7	74.1
170	56200	0.0123	0.101	0.00135	41.0	14.8	-0.25	0.473	71.5	86.3	95.6	91.9	77.3
171	55800	0.0123	0.157	0.00213	42.1	14.1	-0.4	0.473	73.9	85.8	95.8	92.6	77.9
218	89300	0.0074	0.0	0.0	29.9	22.6	0.15	0.419	79.7	118.4	129.2	121.1	99.4
217	88000	0.0074	0.160	0.00138	31.4	24.1	0.6	0.429	79.1	105.1	120.8	115.8	95.7
215	87400	0.0265	0.0	0.0	32.7	20.7	0.10	0.457	83.6	119.4	130.7	123.0	101.0
216	87800	0.0265	0.161	0.00139	32.2	23.6	0.5	0.431	79.4	105.4	120.3	115.9	95.5
219	89000	0.1020	0.0	0.0	30.0	21.8	-0.05	0.475	89.1	121.6	129.8	122.0	100.8
220	85500	0.1047	0.159	0.00140	34.5	22.3	-0.3	0.460	83.0	106.6	119.2	114.2	94.4

From the results of section 3.5.5 it can be calculated that a change of $-0.1^{o}C$ in $\overline{\Delta T_s}$ corresponds to a change in Nu_j of 1.0 on the cooling jet side, when $T_j \simeq 35^{o}C$ and $T_s - T_j \simeq 25^{o}C$ (as is typical for most experiments listed in Table 4.10). When the heat transfer distribution in Figures 4.42 to 4.45 are corrected for this heat loss it is found that there is essentially no influence of throughflow on the heat transfer distribution measured by the sensor. The influence of this heat loss on the heating side of the impingement cylinder is less important because here a change in $\overline{\Delta T_s}$ of $-0.1^{o}C$ corresponds to -0.25 in Nu_j when $T_j \simeq 100^{o}C$ and $T_j - T_s \simeq 40^{o}C$ (typical for the runs in Table 4.9).

Aside from the most important observation that heat transfer measured by the sensor is hardly influenced by throughflow, the only small but significant change in the profiles is the slight displacement of the secondary maxima from the nozzle centerline with increasing M_{U_s}. The most probable explanation for this behaviour is delayed boundary layer transition and slower spreading of the wall jet caused by throughflow at the impingement surface.

No comparison can be made with experimental data from literature because the only work reported is the recent preliminary investigation at $H/w = 8$ by Saad (125). Moreover, the average heat transfer found by Saad with throughflow is inconsistent with equation (4.10), raising the possibility that his throughflow results are too low.

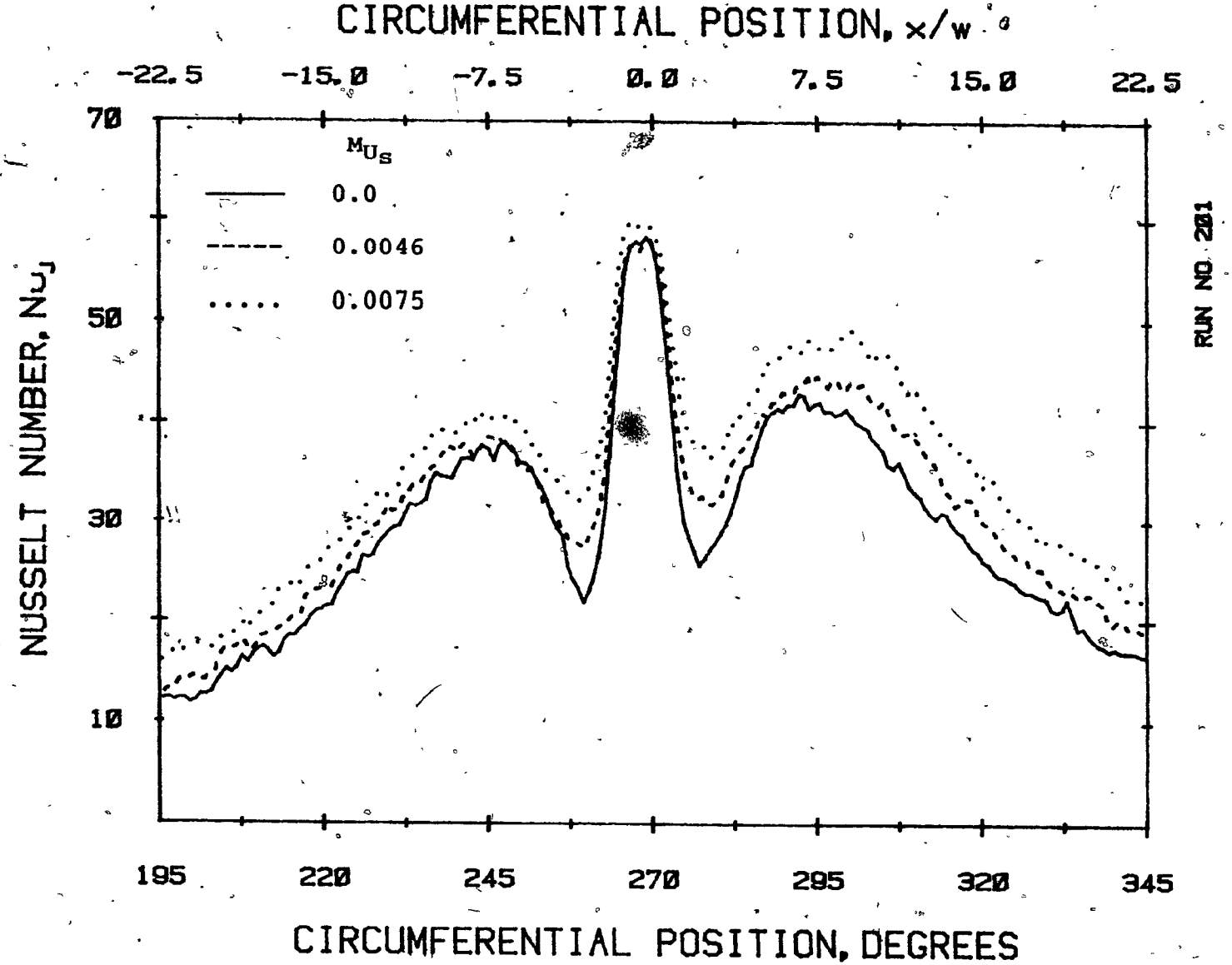


FIGURE 4.42. Effect of M_{U_S} on lateral profiles of heat transfer at Re_j = 16300 and H/w = 2.6

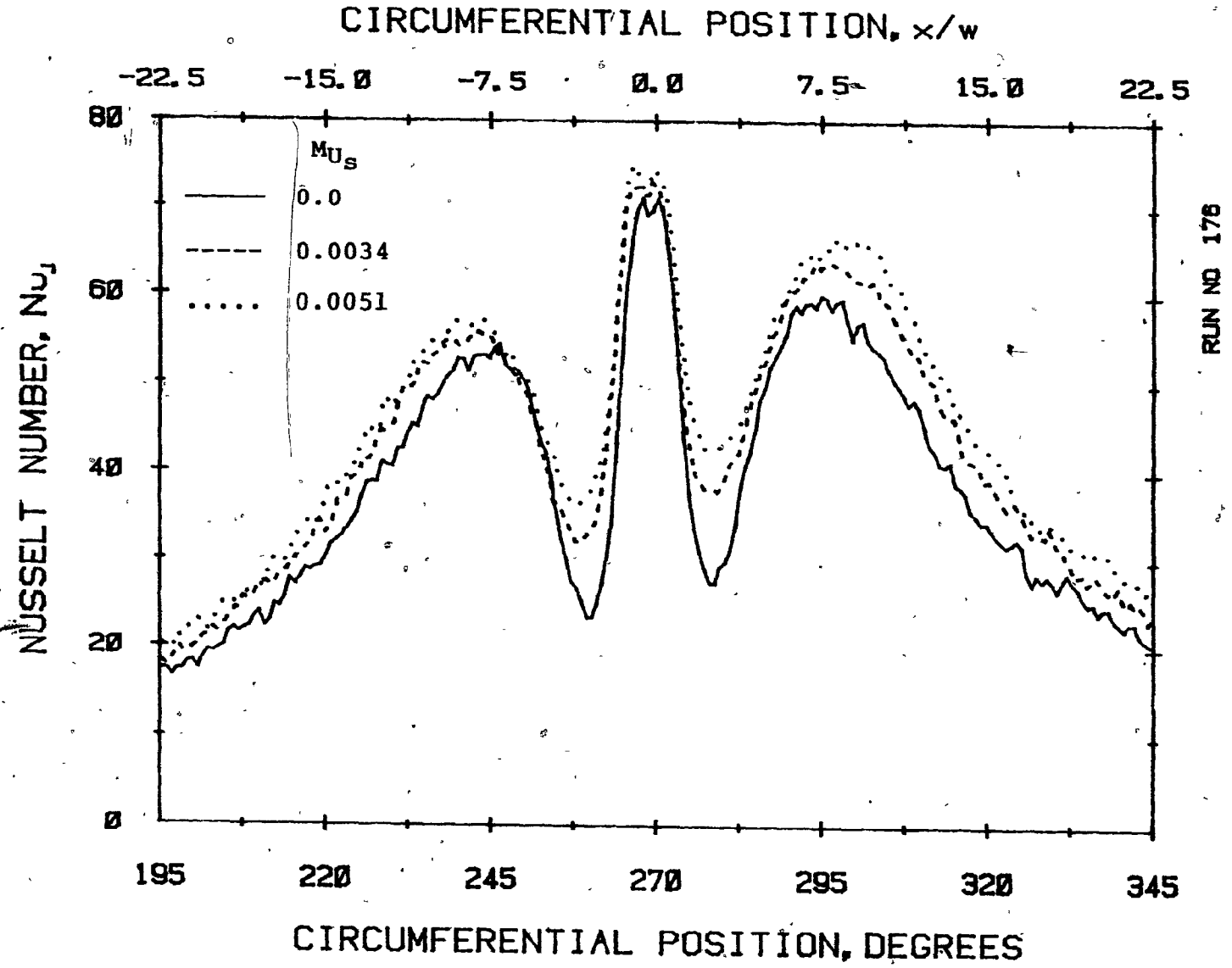


FIGURE 4.43. Effect of M_{U_s} on lateral profiles of heat transfer at Re_j = 24600 and H/w = 2.6

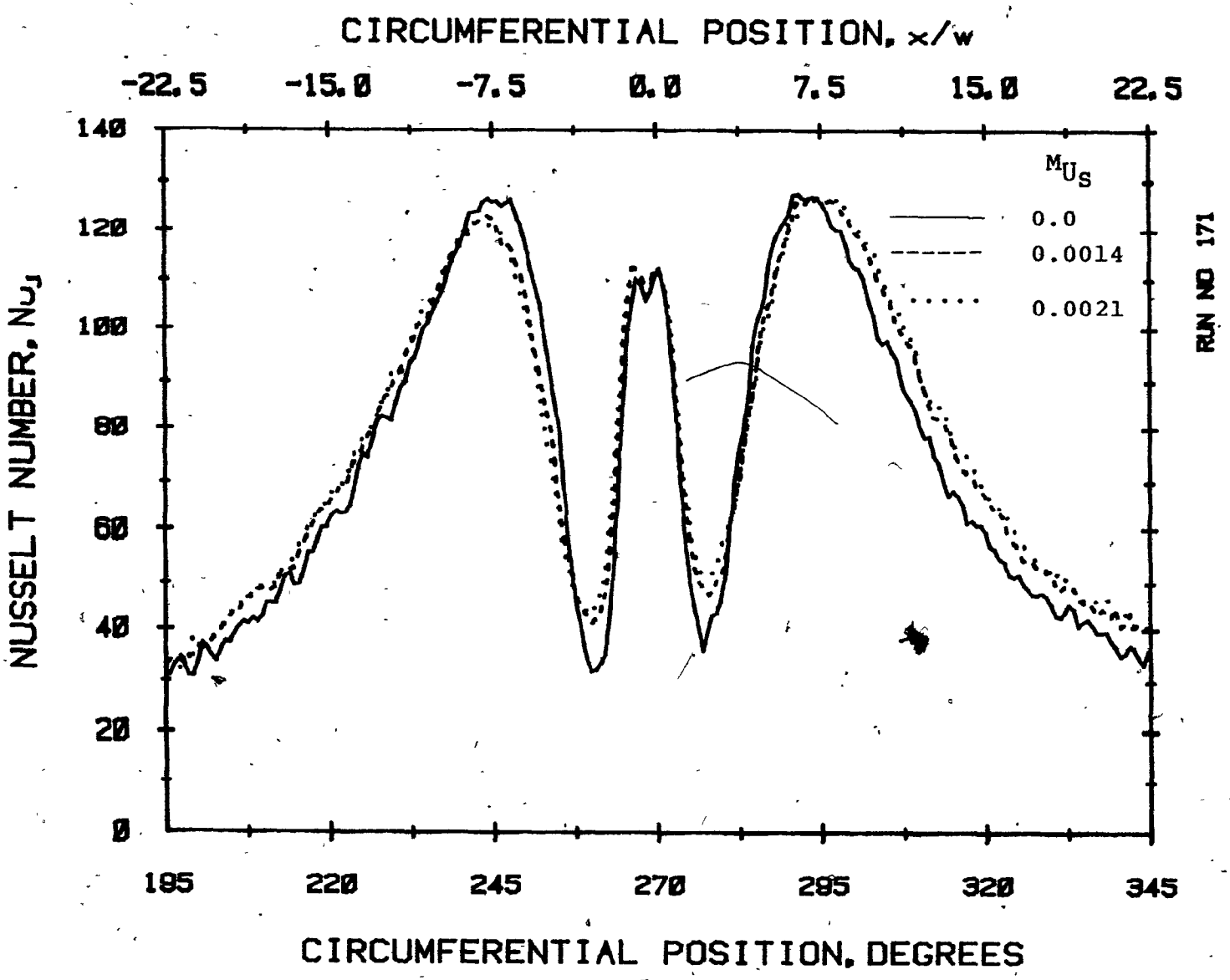


FIGURE 4.44. Effect of M_{Us} on lateral profiles of heat transfer at $Re_j = 55000$ and $H/w = 2.6$

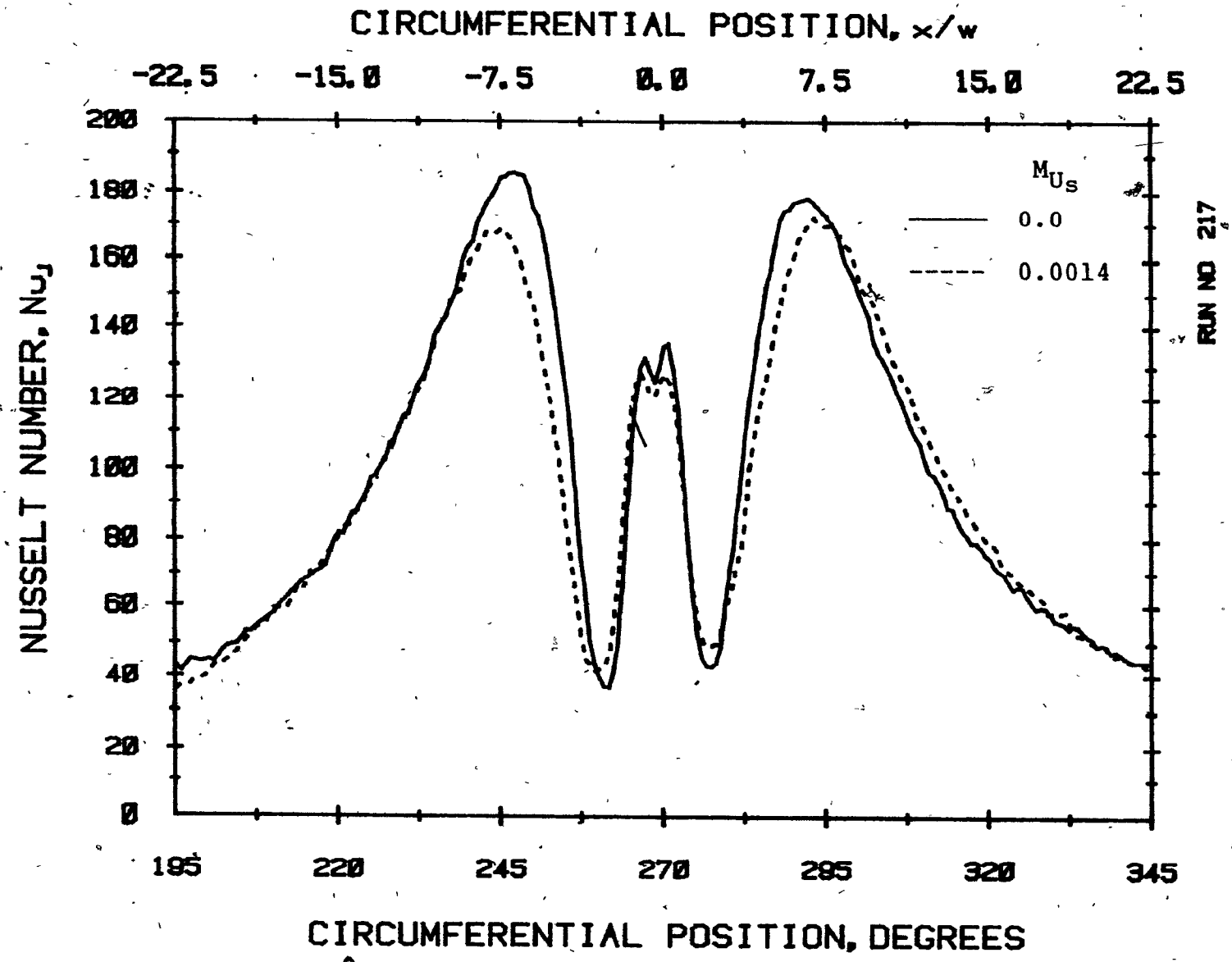


FIGURE 4.45. Effect of M_{Us} on lateral profiles of heat transfer at Re_j = 88000 and x/w = 2.6

The influence of impingement surface motion on the measured heat transfer distributions at high throughflow rates are shown in Figures 4.46 and 4.47 for respectively H/w = 6 at Re_j = 8200 and H/w = 2.6 at Re_j = 26200. The influence of M_{V_s} is quite small, especially when compared with the influence of M_{V_s} for the no-throughflow case in section 4.4. For example, the profiles on Figure 4.46 correspond to those for the no-throughflow case in Figure 4.22.

The overall effect is that a more symmetric measured heat transfer distribution is obtained, relative to profiles without throughflow. This effect may be attributed to removal by throughflow of the flow induced by the surface motion. A similar comparison of the effect of throughflow at relatively high surface motion is shown in Figures 4.48 and 4.49 for respectively H/w = 6 and 2.6, from which the effect of throughflow in producing more symmetric profiles is again evident.

4.5.2 Significance of the Impermeable Sensor Results

In the theoretical work of Crotogino and Allenger (35) the rate for through drying of permeable wet paper under an impinging slot jet was divided into an impingement and a throughflow contribution. From the analysis given in section 4.5 it was concluded that the heat flux measured by the impermeable sensor could be considered as the impingement contribution to the total heat flux because the turbulent

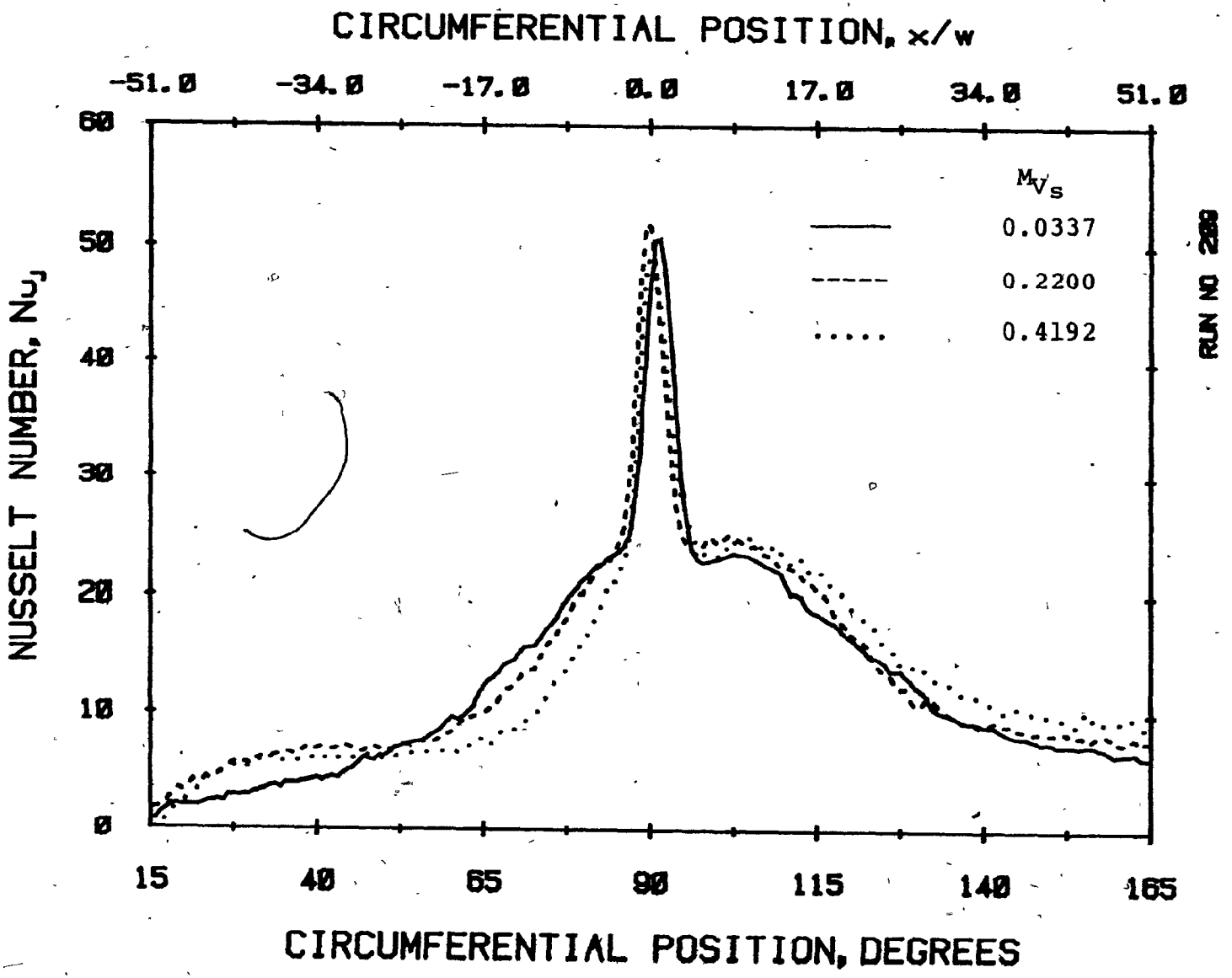


FIGURE 4.46. Effect of impingement surface motion on heat transfer distribution at [illegible] = 8200 and H/w = 6 and the highest throughflow, $M_{U_S} \simeq 0.0059$

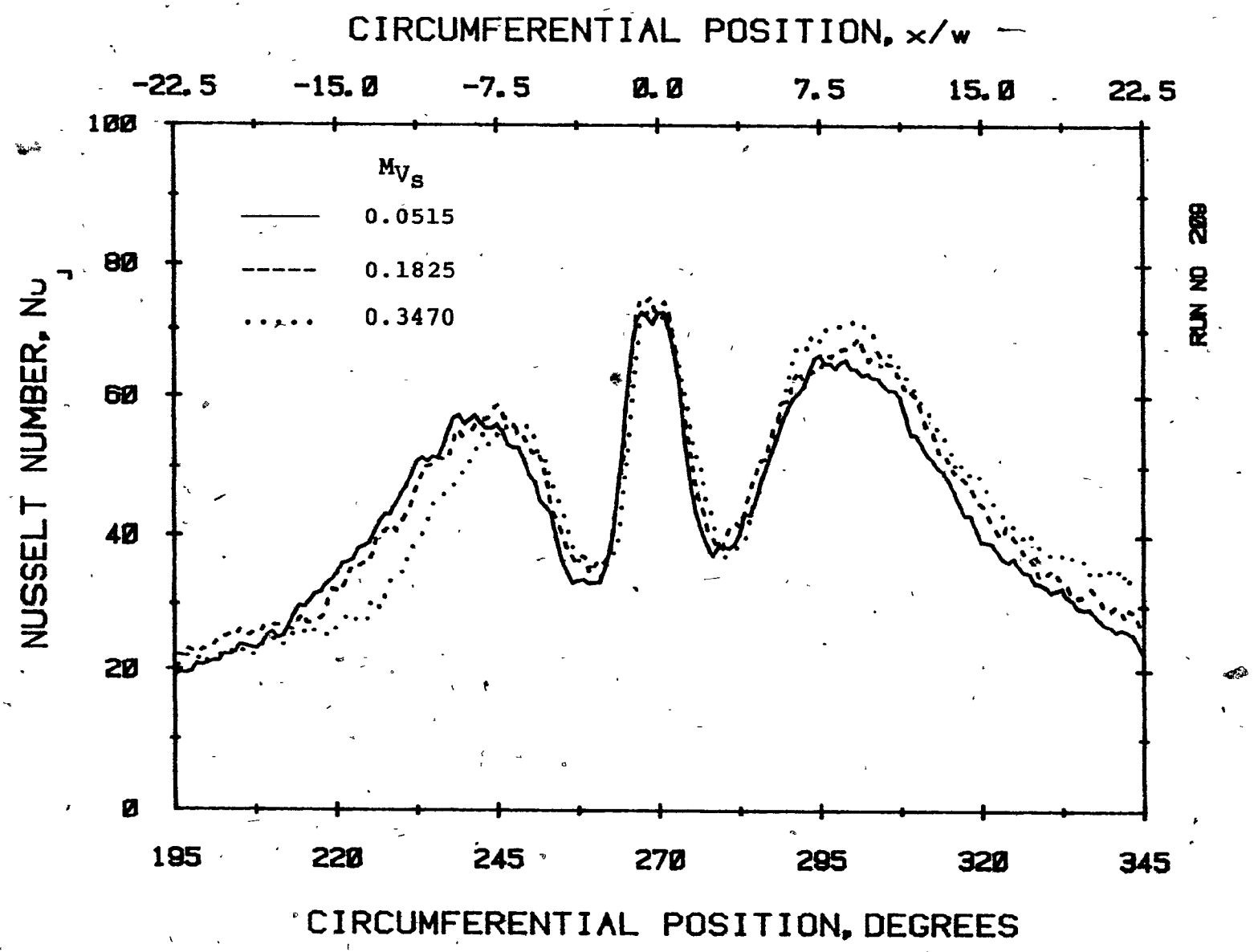


FIGURE 4.47. Effect of impingement surface motion on heat transfer distribution at $Re_j \simeq 26000$, H/w = 6 and the highest throughflow, $M_{U_S} \simeq 0.0049$

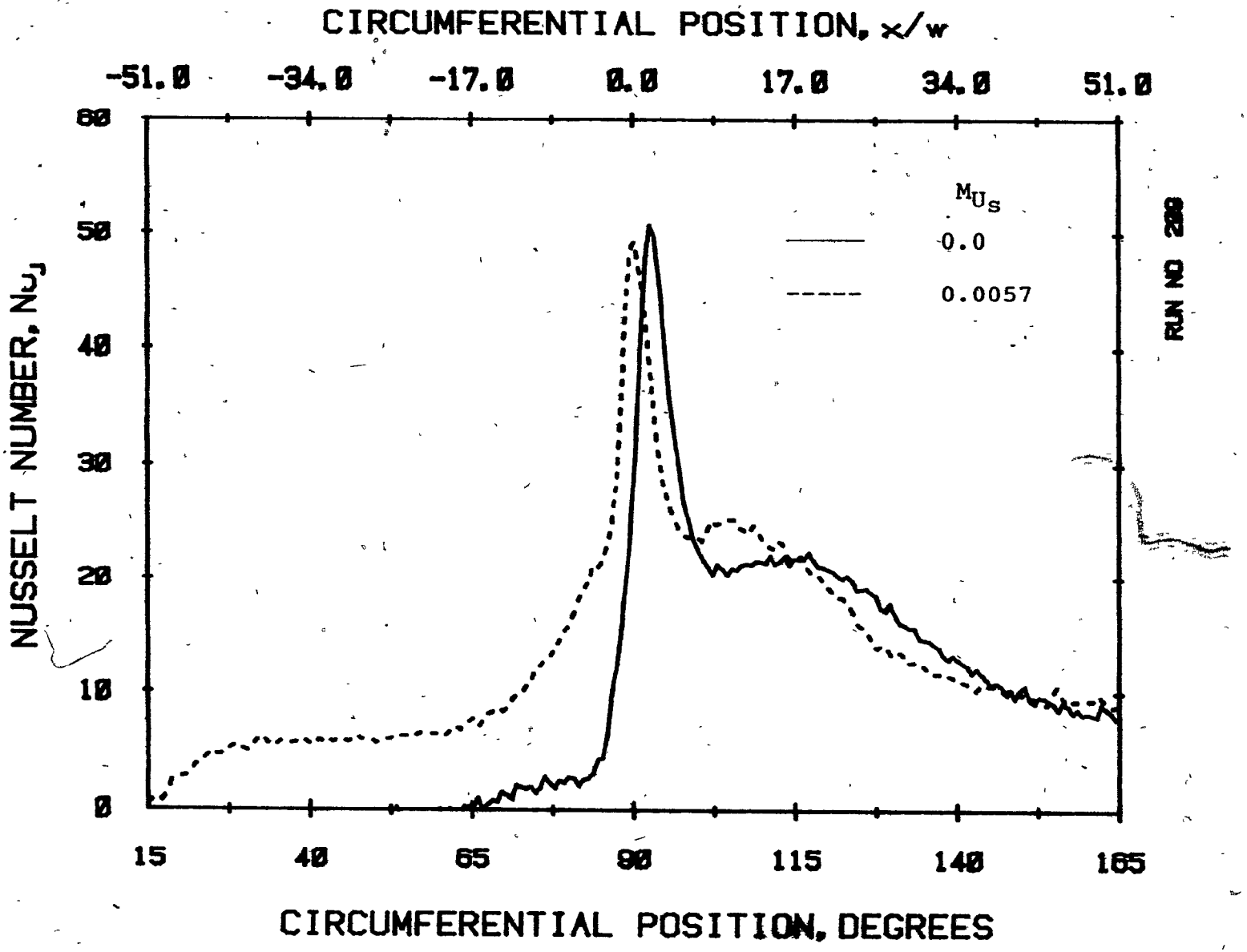


FIGURE 4.48. Effect of M_{U_S} on lateral profiles of heat transfer at Re_j=8200 H/w = 6 and high impingement surface speed, $M_{V_S} = 0.42$

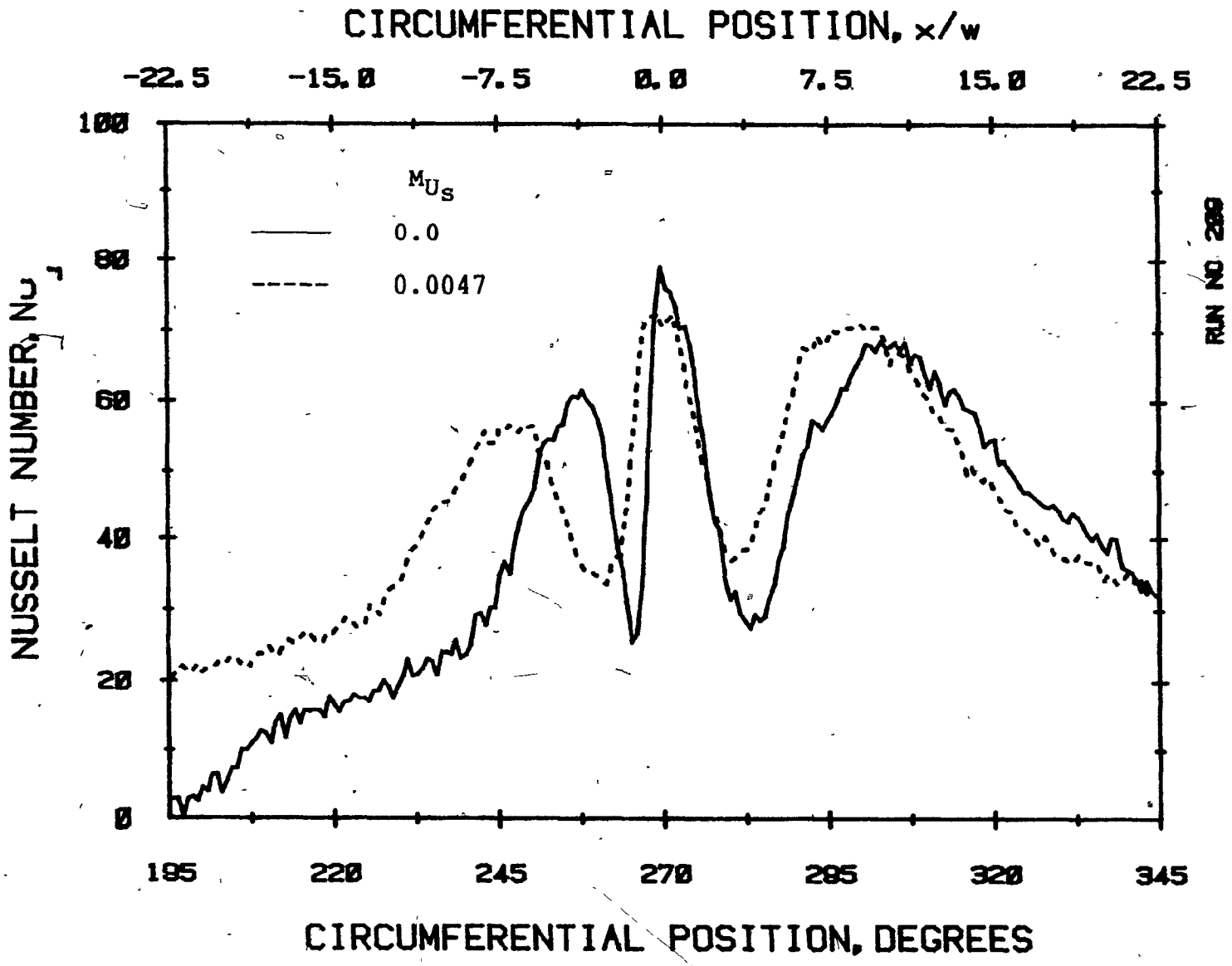


FIGURE 4.49. Effect of M_{U_S} on lateral profiles of heat transfer at $Re_j = 26400$, $H/w = 2.6$ and high impingement surface speed, $M_{V_S} = 0.348$

boundary layer can adapt to the no-throughflow condition immediately above the sensor and gold film ($Fo_t \geq 1$). The results presented in section 4.5.1 showed that the heat transfer distribution measured by the sensor was hardly influenced by throughflow, while those effects which were caused by throughflow (i.e. a more symmetric distribution at high values of M_{V_s} and the slight displacement of the secondary maxima) could be explained from the global features of the flow pattern of the impinging jet with throughflow. The experimental finding that local heat transfer in the wall jet region is not greatly influenced by throughflow, even when a substantial fraction of the jet flow has thereby been removed (see Figure 4.39) is consistent with previous indications. Specifically, this trend is in agreement both with the numerical results presented in section 2.2.3.3 showing that the maximum wall jet velocity was hardly influenced even when 60% of the flow had been removed by throughflow, and with the results of Baines and Keffer (9) for an unconfined turbulent slot jet impinging on a large porous cylinder.

Based on these observations, it is now proposed that a good estimate of the real heat transfer with throughflow can be made by applying the Couette flow analysis of Mickley et al. (96) and Spalding (136), as described in section 2.2.3.3, to the present heat transfer results with throughflow obtained with the impermeable sensor, i.e.

$$Nu_j = -M_{U_s} Re_j Pr/(e^{-M_{U_s} Re_j Pr/Nu_{j_{is}}} - 1) \qquad (4.13)$$

in which $Nu_{j_{is}}$ is the local Nusselt number obtained by the impermeable sensor. Further support for equation 4.13 is the good agreement in Figure 2.42 of section 2.2.3.3 between the numerical results for the laminar slot jet and the Couette flow analysis, and the improved prediction of the influence of throughflow on the drying rate of the Papridryer with equation (2.64), based on Couette flow analysis, rather than with equation (2.65) used by Crotogino and Allenger.

Finally, it should be noted that for multiple jet impingement at appreciable impingement surface velocities, the rather more symmetric heat transfer distributions obtained with throughflow suggest that maximum average heat transfer would be achieved with a more symmetric positioning of the exhaust ports with throughflow than for the no-throughflow case described in section 4.4.6.

4.6 Summary and Conclusions

The experimental heat transfer distributions presented in this chapter are obtained for a confined slot jet impinging on the surface of a rotating porous cylinder with the possibility of having throughflow at the impingement surface. The experimental equipment called SIMTEST apparatus is

described in detail in Chapter 3. The influence of the temperature driving force for the heating jet at H/w = 6 and the cooling jet at H/w = 2.6 was investigated first. The size of the temperature driving force was varied from about 15° to 50°C. Three methods of incorporating the variable physical property effects into correlations of heat transfer were tested using the results at the stagnation point, at the off-stagnation maximum and for the integrated mean heat transfer. One method is with all physical properties evaluated at the nozzle exit temperature, the second is with all properties evaluated at the film temperature, $T_f = (T_j + T_s)/2$, while the third method relates Nusselt number evaluated at the surface temperature, T_s, with Reynolds number at the nozzle exit temperature, T_j. The first two methods were equally successful in producing temperature independent correlations at all three locations, while the last method was rejected as not eliminating the influence of temperature driving force on the correlations. Because the second method, based on the film temperature, requires the additional calculation of T_f and leads to a Reynolds number dependent on temperature of the heat transfer surface, the first method with all physical properties evaluated at T_j is adopted for the present investigation. Elimination of the influence of temperature driving force on the correlations with all physical properties evaluated at T_j is in close

agreement with the theoretical analysis of Kays (73) for laminar plane stagnation flow over the moderate temperature range (ΔT to $50^{o}C$). Elimination of the temperature dependency of physical properties on the heat transfer results allows analysis of the other variables, Re_j, V_s and U_s at the two nozzle to impingement surface spacings of 2.6w and 6w, irrespective of the direction and magnitude of the temperature driving force. An additional conclusion from the analysis of results for variation of the temperature driving force is that the SIMTEST apparatus and associated procedures produced data of high precision.

Through operation at sufficiently low peripheral velocities of the impingement cylinder, V_s, and without throughflow at the surface, an extensive investigation was made of the effect of Re_j without surface motion or throughflow effect. Thus Reynolds number was varied from 5200 to 20300 for $H/w = 6$, and from 9700 to 91800 for $H/w = 2.6$. Heat transfer profiles for $H/w = 6$ are characterized by a sharp central stagnation heat transfer peak, with a smaller secondary maximum or sudden change in slope on both sides of the stagnation point, depending on the value of Re_j. The heat transfer profile for $Re_j = 11000$ over the critical impingement region and beginning of wall jet region is in excellent agreement with the reliable experimental results of Gardon and Akfirat (45) and Cadek (26). In the wall jet region beyond about $x_1/w = 15$ however, the Nusselt number from the present study becomes significantly

lower than in either of these reference studies. At $H/w = 2.6$, the features of the transition point minimum and the off-stagnation maximum are much more pronounced for the same Re_j than at $H/w = 6$.

The more pronounced profile at $H/w = 2.6$ is explained by the lower heat transfer around the stagnation point due to lower turbulence in the arrival jet and the abrupt transition from laminar to turbulent flow at the location where the favorable pressure gradient ends. The secondary peaks at $H/w = 2.6$ become even higher than the stagnation peak for Re_j greater than about 40000. The same excellent agreement with the impingement heat transfer data of Cadek (26) and Gardon and Akfirat (45) is obtained at $H/w = 2.6$ and Re_j of about 11000, and the present wall jet heat transfer is also lower than in the above-mentioned investigations. Good agreement is also obtained with the impingement mass transfer studies of three other references, after application of the analogy between heat and mass transfer. Superposition of the two halves of the complete profiles established that the rotating cylindrical impingement cylinder could give reliable and totally symmetric profiles at sufficiently low speeds to exclude any significant effect of surface motion. This observation and the fact that close agreement was obtained with all reliable published data for stationary impingement surfaces led to the general conclusion that for the wide range of jet Reynolds number investigated, the present profiles are of a higher resolution than ever before published.

The stagnation point heat transfer results are correlated as

$$Nu_{oj} = C \sqrt{Re_j} \qquad (4.2)$$

from theoretical expressions for laminar flow because the boundary layer in the vicinity of the stagnation point is laminar even under the highly turbulent jets of the present study. For impingement surface spacings of 2.6 and 6, the present stagnation heat transfer results are well correlated over the range of experiments by respectively C = 0.455 and 0.54, compared with respectively 0.458 and 0.40 derived by Cadek (26) from his own pressure distribution at a flat impingement plate and laminar boundary layer theory.

From comparison with the experimental results of Kumada et al. (80) for an unconfined slot jet impinging on a cylinder, as well as from the theoretical analysis of Miyazaki and Sparrow (98) it is concluded that, for spacings, H/w, of 2.6 and 6, the effect of curvature on stagnation point heat transfer can be neglected for the corresponding values of D_c/w, 34 and 78, of the present study. The close agreement between the semi-theoretical results of Cadek and the present stagnation heat transfer for H/w = 2.6, as well as with the potential flow-boundary layer analysis of Miyazaki and Silberman (97), (i.e. C = 0.44), confirms that the potential core still exists in the arrival jet.

The reason for the higher constant C for H/w = 6 is the augmenting effect of jet ("free stream") turbulence on heat transfer in the presence of a favorable pressure gradient, as documented most recently by the turbulence and heat transfer measurements by Saad (125) for the same design of slot jet. The differences between the present stagnation point heat transfer at H/w = 2.6 and the interpolated and/or converted experimental data of four references is generally less than 12%. Likewise the agreement with the same four references is quite good for H/w = 6, considering the differences in nozzle design and experimental set-up.

Examination of the distribution of heat transfer in the stagnation region out to about 3w from stagnation indicates reasonable agreement at the experimental spacings of 2.6 and 6 between normalized heat transfer distributions and the theoretical solution of Miyazaki and Silberman (97). This agreement shows that heat transfer in this region is proportional to $\sqrt{Re_j}$. At H/w = 2.6 the heat transfer minimum, which marks the onset of transition to a turbulent boundary layer, moves inward from $x_1/w = 2.9$ at $Re_j = 10000$ to $x_1/w = 2.3$ at $Re_j = 91500$. At H/w = 6 this transition minimum is located at about 3.5w to 4w from stagnation.

As to the secondary heat transfer maximum which marks completion of transition from a laminar to turbulent boundary layer, it was found that the value, Nu_{jm}, of this peak could be correlated by

$$Nu_{jm} = 0.0060\ Re_j^{0.907} \qquad (4.5)$$

for $H/w = 2.6$, and by

$$Nu_{jm} = 0.0114\ Re_j^{0.844} \qquad (4.6)$$

for $H/w = 6$.

The location of the secondary maximum is at about 7w and 6w from the stagnation point for spacings respectively of 2.6 and 6.

Significant differences are found in the wall jet region between previous studies of unconfined jets on flat impingement surfaces and the present study of confined jets on a cylindrical impingement surface. Three flow field effects which may in turn affect heat transfer are identified. Flow over a convex surface permits the wall jet velocity, and hence transfer rates, to decay more quickly. Confinement reduces entrainment, which may thereby decrease wall jet velocity and transfer rates. Finally, far from the stagnation point confinement can restrain wall jet spreading, thereby slowing the rate of decay of transfer rates. A separate, thermal factor is that confinement reduces the modification of wall jet temperature that results with unconfined jets from mixing of entrained flow with wall jet flow. Complete documentation of these various factors would require more comprehensive future investigation. Thus the present finding for $H/w = 2.6$ of a stronger decrease of Nu_j for $14 \leq x_1/w \leq 20$ is indirectly

caused by the presence of the confinement hood which is responsible for the steeper decrease in the maximum wall jet velocity and faster growth of the width of the wall jet, as was shown numerically in section 2.2.3.3. On the other hand, the slower rate of decrease in Nu_j at $H/w = 6$ for $x_1/w \geq 20$ is attributed to the limitation of further growth of the wall jet by the confinement surface. The fast decrease in wall jet heat transfer for $H/w = 2.6$ starts immediately after the secondary peak, in agreement with the numerical finding of a faster decrease of maximum wall jet velocity for $x_1/w \geq 4$ as a result of the recirculating flow induced by the confinement surface. For $H/w = 2.6$ the second region, i.e. of a slower heat transfer decrease, begins in the present apparatus only very close to the impingement system boundary at the skimmer plate.

Average heat transfer could be correlated at $H/w = 6$ by the relatively simple equation

$$\overline{Nu_j} = \frac{0.91}{\frac{x_1}{w} + 22} Re_j^{0.76} \qquad (4.7)$$

for $8.5 \leq x_1/w \leq 51$ and $5200 \leq Re_j \leq 20300$. Comparison with the average heat transfer correlation of Schlünder et al. (133) for an unconfined slot jet impinging on a flat surface shows that the influence of the confinement surface and impingement cylinder curvature on average heat transfer is small over the range of validity of equation 4.7.

The complicated shape of the heat transfer distribution at $H/w = 2.6$ lead in this case to a less simple correlation form than equation 4.7. Average heat transfer is higher for $H/w = 6$, with this advantage for the wider spacing becoming greater as the extent of impingement area averaged is reduced.

Study of the effect of impingement surface motion on impinging slot jet heat transfer was undertaken because of the industrial importance of this effect, especially for impingement drying of wet webs. Of the few attempts which have been made to investigate the effect of surface motion there is none which has attempted to obtain the distribution of local heat transfer; i.e. previous experiments have been only of average transfer rates. Determination of average transfer rates provides very little insight into impingement processes. Moreover, even for average heat transfer it now appears that only one previous study, that of Fechner (40), provides reliable data. Also, previous work has been restricted to unconfined jets whereas in important industrial applications the jets are confined with a hood. Results with unconfined jets may provide quite unreliable estimates of the performance of a confined impingement system. Thus measurement of effect of surface motion for confined jet impingement heat transfer responds to an important industrial need not met by previous work.

The influence of impingement surface motion on heat transfer profiles is analysed in terms of the appropriate non-dimensional parameter, surface velocity mass ratio,

$M_{V_s} = V_s\rho_s/U_j\rho_j$. Rotational speed of the impingement cylinder was varied from about 24 rpm (0.6 m/s) to about 475 rpm (12 m/s). The highest values of M_{V_s} are 0.857 and 0.423 for impingement surface spacings, H/w, of respectively 2.6 and 6.

Impingement surface motion of this magnitude causes relatively little effect on stagnation heat transfer. Nu_o does increase linearly with M_{V_s}, but the maximum increase is only by about 10% for the maximum values of M_{V_s} used. The location of the stagnation point is shifted in the direction of surface motion but this aspect is also relatively insensitive to surface motion, the maximum shift about 1 w for the highest value of M_{V_s}.

Off-stagnation features of the profiles, i.e. minima and secondary maxima on both sides of the nozzle centerline, are likewise displaced in the direction of surface motion. Surface motion has even less effect on the magnitude of the secondary maxima than on Nu_o, with the increase of heat transfer at the secondary maxima being generally less than 5%. The sensitivity to surface motion of the location of the various features of the profiles increases with distance from the nozzle centerline, i.e. this sensitivity is least for the position of the stagnation point, greatest for position of the secondary maximum. Thus on the side with surface motion approaching the nozzle, i.e. where both the minima and secondary maxima shift towards the nozzle centerline with increasing M_{V_s}, the greater sensitivity to M_{V_s} of the secondary maxima

can lead at some moderate value of M_{V_s} to the minima being engulfed by the secondary maxima, then at some higher value of M_{V_s}, can lead to the secondary maxima disappearing into the central stagnation peak. As the off-stagnation peaks are more pronounced at closer impingement surface spacings and higher values of Re_j, amount of surface motion, expressed as M_{V_s}, required for disappearance of the off-stagnation peaks on the side with surface motion approaching the nozzle depends on H/w and Re_j. Thus the off-stagnation peaks on the approach side of the nozzle disappear at a very low value of surface motion, about $M_{V_s} = 0.07$, for $H/w = 6$ and $Re_j = 13900$, while for $H/w = 2.6$ and $Re_j = 10900$ these peaks do not disappear until a quite high value, around $M_{V_s} = 0.65$, is reached. By contrast, on the side with surface motion leaving the nozzle, the same characteristic of greater shift in the direction of surface motion by secondary maxima then by minima means that on this side, increasing surface motion simply leads to a lateral stretching apart of these peaks. The sensitivity in shift of location of off-stagnation peaks increases also with increasing impingement surface spacing, the maximum case being a shift of about 10 w in location of the secondary maximum on the leaving side of the nozzle for $M_{V_s} = 0.42$ at $H/w = 6$. Consistent with the characteristic that surface motion shifts features of the profiles in the direction of the surface motion, heat transfer in the wall jet region is reduced on the side with surface motion approaching the nozzle and

increased on the leaving side of the nozzle. Moreover, even the break in the profile, which without surface motion occurs at around 20 w from stagnation, is clearly seen to move in the direction of wall motion. As this is the feature located furthest from the nozzle centerline, it displays the greatest sensitivity of all, shifting on the approach side of the nozzle by about 15 w in the direction of surface motion for the case of $H/w = 6$, $Re_j = 8200$.

The influence of surface motion on the location and magnitude of the heat transfer profiles summarized above depends on the interaction of a number of flow and thermal effects. The minima are associated with the onset of transition from a laminar to a turbulent boundary layer that is associated with the end of the strong pressure gradient in the stagnation region. Thus the shift in these minima reflects the corresponding shift in the direction of surface motion experienced by the impingement surface pressure profiles. On the side with surface motion approaching the nozzle, i.e. where surface motion is opposite to the wall jet velocity, surface motion tends to increase the velocity gradient at the impingement surface, which would favor faster completion of transition to a turbulent boundary layer. On the side with surface motion leaving the nozzle, i.e. on the aiding flow side where the wall jet velocity and surface motion direction are the same, increased surface motion tends to decrease velocity gradient

at the impingement surface, hence to retard completion of boundary layer transition. These effects are consistent with the shift in location of secondary maxima on both the approach and the leaving side of the nozzle. The tendency on the approach side of the nozzle for surface motion to increase the velocity gradient at the surface is consistent with the small increase with surface motion noted for both stagnation heat transfer and heat transfer at the secondary maximum on the approach side of the nozzle.

With increasing distance from the nozzle centerline, more effects yet come into play. Thus on the approach side, the opposed flow relationship between the wall jet and the surface motion enhances the rate of spreading of the wall jet, thereby tending to reduce heat transfer. As this effect is just the opposite of the first noted flow effect, it is not clear whether the net result of flow effects would be to increase or decrease heat transfer in the wall jet region. The same pair of flow effects exists in just the opposite sense in the wall jet region on the side where surface motion is away from the nozzle, i.e. on the aiding flow side. In addition to the influence on heat transfer via direct effects of surface motion on the flow field, there is also an indirect or thermal effect. As impinging jet heat transfer coefficients have conventionally been determined using $|T_j - T_s|$ as the temperature difference, it must be kept in mind that profiles of heat

transfer coefficients or of Nusselt number thus calculated are in fact profiles of local heat flux divided by a constant. This procedure ignores the reduction in local effective ΔT for convective heat transfer from a maximum value of this driving force under the nozzle exit to progressively lower values with increasing distance from the nozzle centerline. Because of the no-slip condition, a moving impingement surface on the approach side of the nozzle drags fluid from the wall jet region towards the impingement region, i.e. from a region of low local ΔT for convective heat transfer into a region of high local ΔT. This thermal effect thus tends to decrease heat transfer on the approach side of the nozzle by reduction in the local effective ΔT for convection heat transfer. On the leaving side of the nozzle the drag associated with the no-slip condition has the opposite effect, i.e. of enhancing heat transfer by increasing local effective ΔT. Thus for the wall jet region three mechanisms whereby surface motion influences heat transfer have been identified, i.e. a pair of opposed effects on heat transfer via flow field modification, and an additional thermal effect. The fact that three effects have been identified, not all affecting heat transfer in the same way, makes it impossible to know the relative importance of each of these effects.

While there are these three quite general effects of surface motion in the wall jet region, there is an additional, purely equipment specific effect which is present only in the far wall jet region on the approach side. This effect

results from carry over of a thin layer of fluid from the heating side to the cooling side, and vice versa, through the small gap between the splitter plate and the surface of the impingement cylinder. This carry-over reduces heat transfer for some distance after the 0° and the 180° positions, reducing the Nusselt number below the correct value in that section of the profiles.

Average heat transfer, obtained experimentally by integration of the profiles out to the same distance on both sides of the nozzle centerline, decreases with increasing M_{V_s}. By contrast, for unconfined multiple slot jets impinging on a rotating cylinder, Fechner (40) found just the opposite effect of surface motion. Both experimental findings appear to be correct. The source of the difference is attributable to the fact that, in Fechner's unconfined multiple jet case, more than half the impingement surface is covered by the higher momentum wall jet which flows in the same direction as the surface motion, and this wall jet region has higher heat transfer than the one on the opposed flow side. As a consequence, it can be predicted on the basis of the present analysis that, for a "Papridryer" type of dryer, average heat transfer can be maximized through use of an asymmetric location of the exhaust ports. A shift of the exhaust ports in the direction of surface motion would reduce the extent of influence of the low heat transfer region, increase the extent of the high heat transfer region, thereby leading to an increased overall heat transfer.

Although the drying of continuous wet webs under impinging jets with throughflow is of industrial importance, little attention has been given to basic studies of the relevant phenomena. As the present experimental study included determination of the effect of surface motion on the distribution of heat transfer without throughflow, measurements with throughflow at the impingement surface were also made using the same experimental technique. The central feature of the experimental technique involves use of a small, highly sensitive, impermeable heat flux sensor in a permeable rotating impingement cylinder. Analysis indicates that even at the highest impingement surface velocity, about 12 m/s, the boundary layer over the impermeable sensor is able to adapt to the no-throughflow condition at the sensor surface in less time than that required for the sensor to pass. Hence the experimental technique of the present investigation measures heat transfer under an impinging jet whose overall flow and thermal features are determined by throughflow at the impingement surface, as only the boundary layer on the small sensor is adapted to the no-throughflow condition. Thus the heat transfer that is measured for the first time in the present study with throughflow is the component referred to by Crotogino and Allenger (35) as the impingement contribution of the "total" heat transfer where the latter is considered to consist of an impingement and a throughflow contribution.

Three throughflow velocities were applied at the impingement surface, 0.05, 0.10 and 0.16 m/s. Use of these levels of throughflow velocity U_s provided values of the non-dimensional throughflow parameter, M_{U_s}, up to about 0.009 or, expressed otherwise, corresponded in the extreme case to slightly more than 100% of the nozzle exit flow being withdrawn as throughflow. In addition to measuring heat transfer profiles over these levels of M_{U_s} and at various values of Re_j for low impingement surface velocities where the latter is not a factor, profiles with throughflow were also determined for quite high surface velocities corresponding to values of M_{V_s} up to about 0.42.

At low values of impingement surface velocity, for which the profiles without throughflow are symmetrical, there is strikingly little influence of throughflow on heat transfer distribution at either of the impingement surface spacings, 2.6 and 6, even when up to 60% of the jet flow is removed through the impingement surface. By contrast, at values of M_{V_s} sufficiently high that, without throughflow the profiles are highly assymetric, there is a more pronounced effect of throughflow, and this effect is to counteract the effect of surface velocity, i.e. is to shift the profiles back in the direction of being more symmetrical. The mechanism of this effect is that throughflow removes into the impingement surface the flow induced by the motion of that flow boundary. Because of the tendency for compensating changes to occur in

difference sections of the profiles, average heat transfer at high impingement surface velocities is, however, hardly influenced by throughflow.

Based on these observations and the analysis given of the influence of throughflow on heat transfer, it is then proposed that the "total" heat transfer with throughflow can be estimated from the present heat transfer results by applying the Couette flow analysis of Mickley et al. (96) and Spalding (136), i.e.

$$Nu_j = -M_{U_s} Re_j Pr/(e^{-M_{U_s} Re_j Pr/Nu_{jis}} - 1) \qquad (4.13)$$

with Nu_{jis} being the local Nusselt number obtained with an impermeable sensor in the flow and temperature field with throughflow. Further support for equation (4.13) was presented in section 2.2.3.3, where the influence of throughflow on the laminar jet calculation was described.

In conclusion, it has been shown possible to obtain accurate heat transfer profiles with a high resolution using the SIMTEST apparatus and procedures developed for this study and operated over a wide range of jet Reynolds numbers and impingement surface velocities. The design of the SIMTEST apparatus also allows the study of non-dimensional impingement surface spacings, H/w, other than the pair of values, 2.6 and 6, used in the present investigation. Even at the high values of impingement surface velocity possible (to 12 m/s), use of the small impermeable heat flux sensor of the SIMTEST apparatus in the flow and temperature field produced with

throughflow at the impingement surface does not yield the heat flux. However, this impermeable sensor does yield a meaningful result, namely, the impingement contribution to the total heat flux. Moreover, a theoretically based equation is proposed whereby the total heat transfer in the presence of throughflow may be calculated from the impingement contribution measured in the present investigation. Direct measurement of heat flux with throughflow could only be made with a permeable thin film heat flux sensor having the same permeability and surface temperature response as the surrounding impingement surface.

CHAPTER 5

CONCLUSIONS

5.1 Contributions to Knowledge

1. The influence of the matrix inversion technique on stability and convergence characteristics of the finite difference formulation of the vorticity-stream function equations was analysed. It was established that simultaneous solution of the vorticity and stream function equation along a gridline perpendicular to a wall leads to a stable and fast numerical procedure for plane laminar stagnation flow by removing the lag in development of the vorticity and stream function field which occurs when solving the two equations successively along the gridlines. Application of the simultaneous solution procedure to a laminar confined impinging slot jet leads to an unstable system because of the combination of fast development of the flow with this algorithm and the recirculating and non-linear character of respectively the flow and equations describing the flow.

2. In addition to the numerical error generally called artificial viscosity, another error, termed "artificial velocity", has been identified in the second upwind difference formulation of the convection terms in the equations of motion.

This "artificial velocity" is responsible for the higher heat transfer rates in a stagnation region when the upwind finite difference scheme is used instead of the more accurate hybrid scheme.

3. The flow and temperature field as well as the skin friction and heat transfer at the impingement surface for a laminar confined impinging slot jet has been calculated numerically with a vorticity-stream function program. The influence on the flow and heat transfer characteristics were well predicted for the following variables: jet Reynolds number, jet velocity profile at the nozzle exit, non-dimensional nozzle to impingement surface spacing, Prandtl number, throughflow at the impingement surface and variable physical properties.

4. It has been shown that the numerically calculated changes in heat transfer as a result of throughflow at the impingement surface are reasonably well predicted by application of the Couette flow model of Mickley et al. (96) and Spalding (136), based on a boundary layer thickness and free stream velocity uninfluenced by throughflow. The increase in heat transfer is correlated with an error less than 10% by

$$St - St_{M_{U_s}=0} = 0.58\, M_{U_s} \qquad (2.63)$$

The use of equation (2.63) leads to a better prediction of the increase in drying rate with throughflow for the full scale "Papridryer" (Burgess et al., 19a, b) than with the model of

Crotogino and Allenger (35) based on a linear combination of heat transfer contributions of throughflow and impingement.

5. The flow and temperature field as well as the skin friction and heat transfer at the impingement surface for a turbulent confined impinging slot jet has been numerically calculated with a velocity-pressure finite difference program including the 2-equation $k - \varepsilon$ turbulence model. The influence on the flow and heat transfer characteristics was documented for jet Reynolds number and for non-dimensional nozzle to impingement surface spacing, H/w, over the range 2.6 to 8. The computed heat transfer distribution in the wall jet region are in reasonable agreement with the experimental results obtained by Cadek (26), Saad (125) and the present author.

6. The failure of the numerical program to predict the correct heat transfer distribution in the stagnation and beginning of the wall jet region is caused by the wall-flux laws, which are not sufficiently general to include the effect of a streamwise pressure gradient and by an incorrect modelling of the dominant terms of production of turbulent kinetic energy in the stagnation region.

7. A high sensitivity, fast response thin film heat flux sensor was developed as the critical component for measurement of local heat transfer at the surface of a rotating impingement cylinder. With this sensor, a unique experimental facility

was developed, comprising a heating and a cooling confined slot jet impinging on opposite sides of a cylinder, thereby achieving overall steady-state operation. This new experimental technique permitted local heat transfer profiles to be determined over a range of peripheral speeds from those sufficiently low to eliminate impingement surface motion as a variable, up to impingement surface velocities of about 12 m/s. By constructing the impingement cylinder from porous metal the flow and temperature field corresponding to the industrially significant condition of throughflow at the impingement surface could be obtained.

8. Analysis of experimental data for temperature differences of from 15° to 50°C and for both heating and cooling jets established that a temperature independent form of correlation is obtained by evaluating all physical properties at the jet temperature at the nozzle exit or at the film temperature $(T_j + T_s)/2$, the former being the more convenient and the recommended procedure.

9. The effect of jet Reynolds number on local heat transfer distribution of a confined turbulent impinging slot jet in the absence of any impingement surface motion effect was documented for two non-dimensional impingement surface spacings, H/w, 2.6 and 6. The accurate Nusselt number profiles obtained are of the highest resolution ever published, and permit

identification of the several factors influencing heat transfer from the stagnation point to the far wall jet. It was found that results of previous studies of unconfined jets would significantly overestimate the heat transfer in the wall jet region of confined jet systems. However, comparison with the average heat transfer correlation of Schlünder et al. (133) for an unconfined jet impinging on a flat surface indicates that the combined effects of presence of confinement and of impingement surface curvature on average heat transfer is small.

10. The present investigation of effect of impingement surface motion is the first to study the more industrially important case of a jet system which is confined, and is the first to measure effect of impingement surface motion on local heat transfer profiles. The quantitative effect of influence of impingement surface motion on heat transfer profiles is documented for values of surface velocity, V_s, expressed in the appropriate non-dimensional parameter, $M_{V_s} = V_s\rho_s/U_j\rho_j$ up to 0.857 at non-dimensional spacings, H/w, of 2.6 and 6. As profiles of impingement heat transfer reveal much more information than does average heat transfer, the profiles enable identification of several mechanisms by which impingement surface motion affects heat transfer. Integrated mean heat transfer decreases slightly with increasing M_{V_s} when the integration limits are the same on both sides of the nozzle centerline. For multiple confined slot jet systems it is

predicted that a shift in the exhaust ports in the direction of wall motion would increase average heat transfer.

11. For the flow and temperature field produced by throughflow at the impingement surface, use of an impermeable sensor yields not total heat flux but rather, the impingement contribution to the total flux. An equation is suggested whereby total heat flux may be estimated from this impingement component of the total flux.

5.2 Recommendations and Suggestions for Future Work

1. The stability problems encountered with the fast numerical procedure whereby the finite difference formulations of the vorticity and streamfunction equation are solved simultaneously along gridlines perpendicular to a wall should be further investigated. The stability could be improved by "following the flow" and by use of values of vorticity and stream function at the previous iteration instead of using the values as soon as they come available.

2. It should be investigated whether the following three changes in the TEACH-T program would improve the prediction of heat transfer in the impingement region and beginning of wall jet region of a turbulent impinging slot jet.

   a. The wall-flux laws for the streamwise velocity and the temperature should be generalized to include the effect of a streamwise pressure gradient, throughflow at the impingement

surface, surface roughness, etc., as has been done by Crawford and Kays (34) for boundary layer calculations.

b. The so-called algebraic stress modelling should replace the effective turbulent viscosity concept, to eliminate the implicit assumption of isotropy of turbulent kinetic energy and an essentially incorrect modelling of the production of turbulent kinetic energy in any stagnation region when the turbulent viscosity concept is used.

c. The more accurate calculation procedure of k and ε at the near-wall gridline published by Chieng and Launder (32) should be used.

3. Only when the changes mentioned under (2) have the required effect on the prediction of the heat transfer in the stagnation region of a turbulent impinging slot jet should the numerical calculation be extended over a wider range of Reynolds number, and finally be applied to the SIMTEST configuration with throughflow at the impingement surface.

4. A thorough experimental study of the turbulent structure in the impingement and early wall jet region, analogous to the study of Gutmark et al. (54) should accompany the recommendations under (2) and (3). Contrary to Gutmark

(54), this study should be done for a confined slot jet at impingement surface spacings between 2 and 16 nozzle widths, not at H/w = 100. Also, such an investigation should not be restricted to measurements on the nozzle centerline only.

5. The heat flux measurements with the SIMTEST apparatus should be extended to other values of H/w and to higher temperature differences than used in the present work. Also, the use of more practical nozzles than the ASTM standard nozzle design used in this work is recommended.

6. Instead of the present determination of the flowrate through the nozzles from the static pressure in the preceding plenum chambers, it is recommended to drill a hole in the straight section of the throat of the nozzle and to determine the flowrate from the pressure difference between the static pressure in the plenum chamber and the straight section of the nozzle throat. For other types of nozzles one could use other total flow measurement devices.

7. The velocity and temperature profiles in the wall jet region of the SIMTEST apparatus should be measured both with and without throughflow and significant impingement surface motion.

8. The proposed equation (4.13), for the correction of the influence of the impermeable character of the sensor on the heat transfer with throughflow, could be checked experimentally by performing the following experiment with the SIMTEST apparatus:

The hot jet conditions should be,
$w = 3.175 \times 10^{-3}$m, $H = 12.7 \times 10^{-3}$m, $U_j = 12.5$ m/s, $T_j = 525^{o}$K, $T_s = 350^{o}$K, $U_s = 0.083$ m/s and $V_s = 0.42$ m/s, leading to $Re_j = 950$, $H/w = 4$, $M_{U_s} = 0.01$, $M_{V_s} = 0.05$ and $T_s^* = 2/3$.

For these conditions a numerical solution could be obtained with the vorticity-stream function program described in section 2.2. Comparison of the experimental and numerical results should indicate whether the proposed equation (4.13) is valid.

9. The possibility of manufacturing a porous sensor based on the same principle as the present sensor should be investigated.

A porous glass substrate should be polished without blocking the pores or otherwise changing its permeability. Then it should be investigated whether it is possible to deposit an electrical continuous thin gold film on the porous glass. This sensor should be mounted in a porous cylinder made of the same material as the sensor, i.e. having the same surface temperature response and permeability as the sensor.

10. If recommendation (9) can be realized, the influence of the porous character of the sensor on the data reduction technique described in section 3.3.2 should be investigated.

REFERENCES

1. Abdul-Wahab, H., A.S. Mujumdar and W.J.M. Douglas (1975): Flow measurements in a bounded turbulent impinging slot jet with suction, Technical Report, McGill University.

2. Abramovitch, G.N. (1963): The theory of turbulent jets; trans. by Scripta Technica, MIT Press.

3. Akfirat, J.C. (1966): Transfer of heat from an isothermal flat plate to a two-dimensional wall jet, Proceedings of Third International Heat Transfer Conference, Chicago, August, pp 274-279.

4. Andreyev, A.A., V.N. Dakhno, V.K. Savin and B.N. Yudayev (1972): Investigation of heat transfer in a gradient flow region for plane turbulent jet impinging on a plate situated normal to the flow, NASA-TT-F-14195.

5. Arganbright, D.G. and H. Resch (1971): A review of basic aspects of heat transfer under impinging air jets, Wood Science and Technology, Vol. 5, pp 73-94.

6. ASME (1971): Research Report on Fluid Meters, ASME, New York, N.Y.

7. Baines, W.D. and J.F. Keffer (1975): Measurements of shear stress on a moving surface under an impinging jet, PPRIC Technical Report, February.

8. Baines, W.D. and J.F. Keffer (1976): Shear stress and heat transfer at a stagnation point, Int. J. Heat and Mass Transfer, Vol. 19, pp 21-26.

9. Baines, W.D. and J.F. Keffer (1980): Observations of effects of suction on a two-dimensional jet impinging on a porous surface, Drying '80, Vol. I, pp 376-382, Hemisphere Publishing Corporation.

10. Baines, D.J. (1970): A comparative theoretical evaluation of five commonly used types of unsteady heat flux sensor, Report HSA 27, Australian Defence Scientific Service, Weapons Research Establishment, January.

11. Baines, D.J. (1972): Selecting unsteady heat flux sensors; Instruments and Control Systems, May, pp 80-83.

12. Beltaos, S. (1976): Oblique impingement of plane turbulent jets, Proceedings of ASCE, Vol. 102, No. HY9, pp 1177-1192.

13. Beltaos, S. and N. Rajaratnam (1973): Plane turbulent impinging jets, J. of Hydraulic Research, Vol. 11, No. 1, pp 29-59.

14. Biceroglu, O., A.S. Mujumdar, A.R.P. van Heiningen and W.J.M. Douglas (1976): Thermal conductivity of sintered metal powders at room temperature, Letters in Heat and Mass Transfer, Vol. 3, pp 183-192.

15. Bird, R.B., W.E. Stewart and E.N. Lightfoot (1960): Transport Phenomena, Wiley, New York.

16. Black, J. and H. Hardisty (1976): Heat and mass transfer in ink-drying and infra-red dryness measurement, 6th Thermodynamics and Fluid Mechanics Convention, Univ. of Durham.

17. Bouchez, J.P. (1973): Heat transfer to an impinging circular jet in a crossflow, Ph.D. thesis, Univ. of Minnesota.

18. Bouchez, J.P. and R.J. Goldstein (1975): Impingement cooling from a circular jet in a crossflow, Int. J. Heat and Mass Transfer, Vol. 18, pp 719-730.

19. Bower, W.W., D.R. Kotansky and G.H. Hoffman (1977): Computations and measurements of two-dimensional turbulent jet impingement flow fields, Symposium on Turbulent Shear Flows, University Park, Pennsylvania, April 18-20, Vol. I, pp 3.1-3.8.

20. Brown, G.L. (1967): Theory and application of heated films for skin friction measurement, Proc. 1967 Heat Transfer and Fluid Mech. Inst., Stanford Univ. Press, pp 361-368.

21. Brundrett, E. and W.D. Baines (1964): Production and diffusion of vorticity in duct flows, J. Fluid Mech., Vol. 19, pp 375-394.

22. Bui, H.T. (1978): Internal laminar swirling flow at high temperatures: Flow and heat transfer characteristics, Technical Report, McGill University.

23. Burgess, B.W., S.M. Chapman and W. Seto (1972a): The Papridryer Process, Part I, The basic concepts and laboratory results, Pulp and Paper Mag. Can., Vol. 73, No. 11, pp 314-322.

24. Burgess, B.W., W. Seto, E. Koller and I.T. Pye (1972b): The Papridryer Process, Part II, Mill Trials, Pulp and Paper Mag. Can., Vol. 73, No. 11, pp 323-331.

25. Cadek, F.F. and R.D. Zerkle (1974): Local heat transfer characteristics of two-dimensional impinging air jets theory and experiment, Int. Heat Transfer Conf., FC 1.4, pp 15-19.

26. Cadek, F.F. (1968): A fundamental investigation of jet impingement heat transfer, Ph.D. thesis, Univ. of Cincinnati.

27. Caretto, L.S., A.D. Gosman, S.V. Patankar and D.B. Spalding (1973): Two calculation procedures for steady, three-dimensional flows with recirculation, Proc. 3rd Int. Conf. on Numerical Methods in Fluid Mechanics. Editors J. Ehlers, K. Hepp and H.A. Weidenmüller, Vol. II, Springer Verlag, Berlin.

28. Carnahan, B., H.A. Luther and J.O. Wilkes (1969): Applied Numerical Methods, John Wiley and Sons, Inc.

29. Carslaw, H.S. and J.C. Jaeger (1976): Conduction of Heat in Solids, The Clarendon Press, Oxford.

30. Cartwright, W.G. and P.J. Russell (1967): Characteristics of a turbulent slot jet impinging on a plane surface, Proc. Instn. Mech. Engrs., Vol. 182, Pt. 3H, pp 309-319.

31. Chien, J.C. and J.A. Schetz (1975): Numerical solution of the three-dimensional Navier-Stokes equations with applications to channel flows and a buoyant jet in a cross-flow, J. of Applied Mech., Trans. of ASME, Vol. 97, Series E, No. 3, pp 575-583.

32. Chieng, C.C. and B.E. Launder (1980): On the calculation of turbulent heat transport downstream from an abrupt pipe expansion, Numerical Heat Transfer, Vol. 3, pp 189-207.

33. Chudnovskii, A.F. (1961): Various steady-state methods for measuring the thermal conductivity of semi-conductors, Soviet Physics-Solid State, 2, 11, pp 2610-2616.

34. Crawford, M.E. and W.M. Kays (1975): STAN-5 - A program for numerical computation of two-dimensional internal/external boundary layer flows, Mech. Eng. Dept. Report HMT-23, Stanford Univ.

35. Crotogino, R.H. and V. Allenger (1979): A mathematical model of the Papridryer process, Trans. Tech. Sect. CPPA, Vol. 5(4), December, pp TR84-91.

36. de Vahl Davis, G. and G.D. Mallinson (1972): False diffusion in numerical fluid mechanics, Report No. 1972/FMT/1, School of Mech. Ind. Eng., Univ. of New South Wales.

37. Dosdogru, G.A. (1969): Über die Ausführung von Schlitzdüsen im Unterschallbereich, Mitteilungen Heft 2, Forschungsgesell-schaft Druckmachinen e.V.

38. Dosdogru, G.A. (1972): Einfluß des Turbulenzgrades auf den Wärme-und Stoffübergang in Schlitzdüsentrocknern, Chemie-Ingenieur-Technik, Vol. 24, pp 1340-1345.

39. Eckert, E.R.G. and R.M. Drake, Jr. (1959): Heat and Mass Transfer, McGraw-Hill, New York.

40. Fechner, G. (1971): Wärmeübertrogung bei senkrecht auf treffendem Strahl an der Platte und am Rohr, Dissertation T.U. München.

41. Folayan, C.O. (1976): Impingement cooling, Ph.D. thesis, Imperial College, London.

42. Folayan, C.O. and J.H. Whitelaw (1977): Impingement cooling and its application to combustion, Joint Gas Turbine Congress, ISME, GTSJ, ASME, Paper No. 07, pp 1-7, Tokyo.

43. Gardon, R. and J. Cobonpue (1962): Heat transfer between a flat plate and jets of air impinging on it, Proc. 2nd Int. Heat Transfer Conf., ASME, pp 454-460.

44. Gardon, R. and J.C. Akfirat (1965): The role of turbulence in determining the heat transfer characteristics of impinging jets, Int. J. Heat and Mass Transfer, Vol. 8, pp 1261-1272.

45. Gardon, R. and J.C. Akfirat (1966): Heat transfer characteristics of impinging two-dimensional air jets, J. Heat Transfer, Vol. 88, No. 1, pp 101-108.

46. Gauntner, J.W., J.N.B. Livingood and P. Hrycak (1970): Survey of literature on flow characteristics of a single turbulent jet impinging on a flat plate, NASA TND-5652.

47. Glauert, M.B. (1956): The wall jet, J. Fluid Mech., Vol. 1, Part 6, pp 625-643.

48. Gosman, A.D., J.H. Whitelaw and B.E. Launder (1976): Flow, heat and mass transfer in turbulent recirculating flows - prediction and measurements, Short course notes, Chem. Eng. Dept., McGill University.

49. Gosman, A.D., W.N. Pun, A.K. Runchal, D.B. Spalding and M. Wolfshtein (1969): Heat and Mass Transfer in Recirculating Flows, Academic Press, N.Y.

50. Gosman, A.D. and G.S. Samuelson (1972): Modeling radial dilution air injection in axial flow combustors, Fall Meeting of the Western States Section of the Combustion Institute, October 30-31, Monterey.

51. Guitton, D.E. and B.G. Newman (1977): Self-preserving turbulent wall jets over convex surfaces, J. Fluid Mech., Vol. 81, Part 1, pp 155-185.

52. Gutmark, E. and I. Wygnanski (1976): The planar turbulent jet, J. Fluid Mech., Vol. 73, Part 3, pp 465-495.

53. Gutmark, E., I. Wygnanski and M. Wolfshtein (1977): Selective amplification of fluctuations in a turbulent impinging jet, Symposium on Turbulent Shear Flows, University Park, Pennsylvania, April 18-20, Vol. I, pp 3.27-3.33.

54. Gutmark, E., M. Wolfshtein and I. Wygnanski (1978): The plane turbulent impinging jet, J. Fluid Mech., Vol. 88, Part 4, pp 737-756.

55. Hausen, H. (1959): Neue Gleichungen für die Wärmeübertragung bei freier oder erzwungener Strömung, Allgemeine Wärmetechnik, Zeitschrift für Wärme-, Kälte und Verfahrenstechnik, Band 9, nr 4/5, pp 75-79.

56. Hardisty, H. (1973): Industrial drying using impinging air jets, Parts 1 and 2 (Reports 226 and 227), School of Engineering, Univ. of Bath.

57. Hardisty, H. (1980): Drying printed ink coatings by impinging air jets, Drying '80, Vol. I, pp 367-375, Hemisphere Publishing Corporation.

58. Harlow, F.H. and P. Nakayama (1968): Transport of turbulence energy decay rate, Los Alamos Sci. Lab. Report LA-3854.

59. Hartnett, J.P. and E.R.G. Eckert (1957): Mass-transfer cooling in a laminar boundary layer with constant fluid properties, Trans. of ASME, February, pp 247-254.

60. Hinze, J.O. (1959): Turbulence, an Introduction to Jets Measurements and Theory, McGraw-Hill Inc.

61. Holik, H. (1971): Zur Prallströmtrocknung von Papier, Das Papier, 25, Vol. 6, pp 289-300.

62. Huang, B., A.S. Mujumdar and W.J.M. Douglas (1981): Flow characteristics of a swirling laminar impinging jet, Can. J. Chem. Eng., Vol. 59, pp 423-429.

63. Huang, B. (1977): Prediction of flow and heat transfer under a laminar swirling impinging jet, M.Eng. thesis, Chem. Eng. Dept., McGill University.

64. Huang, B., W.J.M. Douglas and A.S. Mujumdar (1978): Heat transfer under a laminar swirling impinging jet - a numerical study, 6th Int. Heat Transfer Conf., Paper Fc(b)-23, Vol. 5, pp 311-316.

65. Ioffe, A.V. and A.F. Ioffe (1958): Measurements of thermal conductivity of semiconductors in the vicinity of room temperature, Soviet Physics-Technical Physics, 3, 11, pp 2163-2168.

66. Irwin, H.P.A.H. (1974): Measurements in blown boundary layers and their prediction by Reynolds stress modelling, Ph.D. thesis, Mech. Eng. Dept., McGill University.

67. Irwin, H.P.A.H. and P. Arnot Smith (1975): Prediction of the effect of streamline curvature on turbulence, Physics of Fluids, Vol. 18, No. 6, pp 624-630.

68. Januszewski, J., M.I. Khokhar and A.S. Mujumdar (1977): Thermal conductivity of some porous metals, Letters in Heat and Mass Transfer.

69. Jepps, G. (1965): Heat conduction in single-layer and double-layer walls, with boundary conditions appropriate to aerodynamic heating, AARC Report ACA-66.

70. Jones, W.P. and B.E. Launder (1972): The prediction of laminarization with a two-equation model of turbulence, Int. J. Heat and Mass Transfer, Vol. 15, pp 301.

71. Kaganov, M.A. (1958): A theoretical analysis of the method of measuring thermal conductivity of semiconductors proposed by A.V. Ioffe and A.F. Ioffe, Soviet Physics-Technical Physics, 3, 11, pp 2169-2172.

72. Kataoka, K. and T. Mizushina (1974): Local enhancement of the rate of heat-transfer in an impinging round jet by free-stream turbulence, Int. Heat Transfer Conf., FC 8.3, pp 305-309.

73. Kays, W.M. (1980): Convective Heat and Mass Transfer, McGraw-Hill Book Co.

74. Kays, W.M., R.J. Moffat and W.H. Thielbahr (1970): Heat transfer to the highly accelerated turbulent boundary layer with and without mass addition, J. Heat Transfer, August, pp 499-505.

75. Kays, W.M. and I.S. Bjorklund (1956): Heat transfer from a rotating cylinder with and without crossflow, Trans. of ASME, Paper No. 56-A71, pp 1-8.

76. Keeble, T.S. (1969): Impingement cooling, Dept. of Supply, Australian Defence Scientific Service, Aero. Res. Lab., Mech. Eng. Note No. 308.

77. Kolmogorov, A.N. (1942): Equations of turbulent motion in an incompressible fluid, Izv. Akad. Nauk. USSR, Seria fizicheska VI, No. 12, pp 56-58.

78. Korger, M. and F. Krizek (1966): Mass transfer coefficient in impingement flow from slotted nozzles, Int. J. Heat and Mass Transfer, Vol. 9, pp 337-344.

79. Kumada, M. and I. Mabuchi (1970): Studies on the heat transfer of impinging jets (1st Report, Mass transfer for two-dimensional jet of air impinging normally on flat plate), Bull. of JSME, Vol. 13, No. 55, pp 77-85.

80. Kumada, M., I. Mabuchi and Y. Kawashima (1972): Mass transfer on a cylinder in the potential core region of a two-dimensional jet, Trans. Japan Soc. Mech. Engrs., 38, pp 315.

81. Kumada, M., I. Mabuchi, Y. Kawashima and M. Hirati (1976): Mass transfer on a cylinder in developed region of a two-dimensional jet, Heat Transfer, Japanese Research, Vol. 5, No. 3.

82. Launder, B.E. (1975): Progress in the modelling of turbulent transport, Supplementary Notes for course "Turbulent Recirculating Flows - Prediction and Measurement", July 28-August 1, Penn. State Univ.

83. Launder, B.E. and D.B. Spalding (1972): Mathematical Models of Turbulence, Academic Press, London.

84. Launder, B.E., A.P. Morse, W. Rodi and D.B. Spalding (1973): The prediction of free shear flows - A comparison of six turbulence models, Proc. Langley Free Shear Flows Conf., July 20-21, Vol. 1, NASA SP-320.

85. Livingood, J.N.B., H. Ellerbrock and A. Kaufman (1971): NASA Turbine Cooling Research Status Report, NASA TMX-2384.

86. Livingood, J.N.B. and P. Hrycak (1973): Impingement heat transfer from turbulent air jets to flat plates: A literature survey, NASA TMX-2778.

87. Marple, V.A., B.Y.H. Liu and K.T. Whitby (1974): On the flow fields of inertial impactors, J. of Fluids Engineering, Trans. of ASME, Series I, Vol. 96, pp 394-400.

88. Martin, H. (1977): Heat and mass transfer between impinging gas jets and solid surfaces, Advances in Heat Transfer, Vol. 13, Academic Press.

89. Masliyah, J.H. and T.T. Nguyen (1979): Mass transfer due to an impinging slot jet, Int. J. Heat and Mass Transfer, Vol. 22, pp 237-244.

90. Maxwell, R.W. and K.L. Nash (1973): Convective mass transfer from stationary and moving surfaces using a mercury evaporation technique, Int. J. Heat and Mass Transfer, Vol. 16, pp 385-393.

91. McMurray, D.C., P.S. Myers and O.A. Uyehara (1966): Influence of impinging jet variables on local heat transfer coefficients along a flat surface with constant heat flux, Proc. 3rd Int. Heat Transfer Conf., Vol. 2, Paper No. 71, pp 292-299.

92. McNaughton, K.J. and C.G. Sinclair (1966): Submerged jets in short cylindrical flow vessels, J. Fluid Mech., Vol. 25, pp 367-375.

93. Metzger, D.E. (1962): Spot cooling and heating of surfaces with high velocity impinging air jets, Technical Report No. 52, Mech. Eng. Dept., Stanford Univ.

94. Metzger, D.E., K.N. Cummings and W.A. Ruby (1974): Effect of Prandtl number on heat transfer characteristics of impinging liquid jets, Int. Heat Transfer Conf., Tokyo.

95. Metzger, D.E. and L.D. Grochowsky (1977): Heat transfer between an impinging jet and a rotating disk, Trans. of ASME, J. Heat Transfer, Vol. 99, pp 663-667.

96. Mickley, H., R.C. Ross, A.L. Squyers and W.E. Stewart (1954): Heat, mass and momentum transfer for flow over a flat plate with blowing and suction, NACA TN-3208.

97. Miyazaki, H. and E. Silberman (1972): Flow and heat transfer on a flat plate normal to a two-dimensional laminar jet issuing from a nozzle of finite height, Int. J. Heat and Mass Transfer, Vol. 15, pp 2097-2107.

98. Miyazaki, H. and E.M. Sparrow (1976): Potential flow solution for crossflow impingement of a slot jet on a circular cylinder, J. of Fluids Eng., Trans. of ASME, June, pp 249-255.

99. Mujumdar, A.S. (1971): The effect of free-stream turbulence on heat transfer from cylinders in cross-flow, Ph.D. thesis, Chem. Eng. Dept., McGill University.

100. Mujumdar, A.S. and W.J.M. Douglas (1972): Impingement heat transfer - A literature review, Paper presented at TAPPI Conf., New Orleans.

101. Myers, G.E., J.J. Schauer and R.H. Eustis (1963a): Plane turbulent wall jet flow development and friction factor, J. of Basic Engineering, Trans. of ASME, Vol. 85, Series D, March, pp 47-54.

102. Myers, G.E., J.J. Schauer and R.H. Eustis (1963b): Heat transfer to plane turbulent wall jets, J. Heat Transfer, Vol. 85, Series C, August, pp 209-214.

103. Obot, N.T. (1975): An apparatus for study of effect of suction on heat transfer for impinging round jets, M.Eng. thesis, Chem. Eng. Dept., McGill University.

104. Obot, N.T., A.S. Mujumdar and W.J.M. Douglas (1979): Design correlations for heat and mass transfer under various turbulent impinging jet configurations, Developments in Drying, Hemisphere Publications, pp 388-402.

105. Obot, N.T. (1981): Flow and heat transfer for round turbulent jets impinging on permeable and impermeable surfaces, Ph.D. thesis, Chem. Eng. Dept., McGill University.

106. Patankar, S.V. (1974): Numerical prediction of three-dimensional flow, Studies in Convection: Theory and Applications, Academic Press, London.

107. Perry, J.H. (1963): Chemical Engineers' Handbook, McGraw-Hill Book Co.

108. Popiel, Cz. O., E. Tuliszka and O. Buglaslawski (1974): Heat transfer from a rotating disk in an impinging air jet, Int. Heat Transfer Conf., Tokyo.

109. Popiel, C.O. and O. Trass (1981): Ordered flow structure and skin friction measurements on the plate in an impinging round jet, 7th International Congress of Chemical Engineering, Chemical Equipment Design and Automation, Prague, August 31-September 4.

110. Poreh, M. and J.E. Cermak (1959): Flow characteristics of a circular submerged jet impinging normally on a smooth boundary, 6th Mid-Western Conf. on Fluid Mechanics, Univ. of Texas, pp 198.

111. Prandtl, L. (1945): Über ein neues Formelsystem für die ausgebildete Turbulenz, Nachr. Akad. Wiss., Göttingen, Math.-Phys., pp 6.

112. Priddin, C.H. (1975): The behaviour of the turbulent boundary layer on curved, porous walls, Ph.D. thesis, Univ. of London.

113. Raithby, G.D. (1976): A critical evaluation of upstream differencing applied to problems involving fluid flow, Computer Methods in Applied Mechanics and Engineering, 9, pp 75-103.

114. Reed, R.P. and E.A. Ripperger (1972): Deposited thin film thermocouples of microscopic dimensions, Temperature, Its Measurement and Control in Science and Industry, Instrument Society of America, Pittsburg, Vol. 4, Part 3, pp 2209-2220.

115. Reynolds, O. (1895): On the dynamical theory of incompressible fluids and the determination of the criterion, Phil. Trans. of the Roy. Soc. of London, Series A, 186, 123.

116. Rivas, M.A. and A.H. Shapiro (1956): On the theory of discharge coefficients for rounded-entrance flow meters and venturis, Trans. of ASME, April, pp 489-497.

117. Roache, P.J. (1972a): Computational Fluid Mechanics, Hermosa Publishers, Albuquerque, N.M.

118. Roache, P.J. and T.J. Mueller (1972): Numerical solutions of laminar separated flows, AIAA J., Vol. 8, No. 3, pp 530-538.

119. Roache, P.J. (1972b): On artificial viscosity, J. of Comp. Physics, Vol. 10, pp 169-184.

120. Rodi, W. (1975): A note on the empirical constant in the Kolmogorov-Prandtl eddy-viscosity expression, J. of Fluids Engineering, September, pp 386.

121. Rose, P.H. (1958): Development of the calorimeter heat transfer gauge for use in shock tubes, AVCO Research Report 17, February.

122. Runchal, A.K. (1972): Convergence and accuracy of three finite difference schemes for a two-dimensional conduction and convection problem, Int. J. for Num. Meth. in Eng., Vol. 4, pp 541-550.

123. Russell, P.J. and A.P. Hatton (1972): Turbulent flow characteristics of an impinging jet, Proc. Instn. Mech. Engrs., Vol. 186, 52/72, pp 635-644.

124. Saad, N.R. (1975): Simulation of flow and heat transfer under a laminar impinging round jet, M.Eng. thesis, Chem. Eng. Dept., McGill University.

125. Saad, N.R. (1981): Flow and heat transfer for multiple turbulent impinging slot jets, Ph.D. thesis, Chem. Eng. Dept., McGill University.

126. Saad, N.R., W.J.M. Douglas and A.S. Mujumdar (1977): Prediction of heat transfer under an axisymmetric laminar impinging jet, Ind. Eng. Chem. Fundam., Vol. 16, pp 148-154.

127. Samuels, M.R. and C.M. Wetzel (1972): Velocity profiles in the exit region of a submerged laminar jet, Chem. Eng. J., Vol. 4, pp 41-45.

128. Schauer, J.J. and R.H. Eustis (1963): The flow development and heat transfer characteristics of plane turbulent impinging jets, Technical Report No. 3, Mech. Eng. Dept., Stanford Univ.

129. Scheuter, K.R. and G.A. Dosdogru (1970): Die Messung der örtlichen Wärmeübergangszahl mittels eines geheizten Bandes, Schweizer Archiv für angewandte Wissenschaft und Technik, 36, 10, pp 3-19.

130. Scheuter, K.R. and G.A. Dosdogru (1971): Investigation of impinging air jet dryers with respect to possible automation, Technical Association of Graphic Arts Proceedings, pp 224-250.

131. Schlichting, H. (1968): Boundary Layer Theory, Sixth Edition, McGraw-Hill Book Co., New York.

132. Schlünder, E.U. and V. Gnielinski (1967): Wärme-und Stoffübertragung zwischen Gut und aufprallendem Düsenstrahl, Chemie-Ingenieur-Technik, 39, 9/10, pp 578-584.

133. Schlünder, E.U., P. Krötzsch and W. Hennecke (1970): Gesetzmäßigkeiten der Wärme-und Stoffübertragung bei der Prallströmung aus Rund-und Schlitzdüsen, Chemie-Ingenieur-Technik, 42, 6, pp 333-338.

134. Schuh, H. and R. Pettersson (1966): Heat transfer by arrays of two-dimensional jets directed normal to surfaces including the effects of superimposed wall parallel flow, Proc. 3rd Int. Heat Transfer Conf., Vol. 2, pp 280 (Paper No. 70).

135. Sibulkin, M.J. (1965): Heat transfer near the forward stagnation point of a body of revolution, J. Aero. Sci., 19, pp 570-571.

136. Spalding, D.B. (1960): A novel finite difference formulation for differential expressions involving both first and second order derivatives, Int. J. for Num. Meth. in Eng., Vol. 4, pp 551-559.

137. Sparrow, E.M., R.J. Goldstein and M.A. Rouf (1975): Effect of nozzle-surface separation distance on impingement heat transfer for a jet in a crossflow, Trans. of ASME, J. Heat Transfer, Vol. 97, pp 528-533.

138. Sparrow, E.M. and L. Lee (1975): Analysis of flow field and impingement heat and mass transfer due to a non-uniform slot jet, Trans. of ASME, Series C, J. Heat Transfer.

139. Sparrow, E.M. and T.C. Wong (1975): Impingement transfer coefficients due to initially laminar slot jets, Int. J. Heat and Mass Transfer, Vol. 18, pp 597-605.

140. Squire, H.B. (1938): Section of Modern Developments in Fluid Dynamics, ed. by S. Goldstein, Oxford, II, pp 623-627.

141. Strand, T. (1962): Inviscid-incompressible-flow theory of static two-dimensional solid jets in proximity to the ground, J. Aero. Sci., Vol. 29, pp 170-173.

142. Subba Raju, K. and E.U. Schlünder (1977): Heat transfer between an impinging jet and a continuously moving flat surface, Wärme-und Stoffübertragung, Thermo- and Fluid Dynamics, Vol. 10, pp 131-136.

143. Swann, W.F.B. (1959): Theory of the A.F. Ioffe method for rapid measurement of the thermal conductivity of solids, J. Franklin Inst., 267, 5, pp 363-380.

144. Tanner, R.I. (1967): Theory of a thermal flux meter in a shear flow, J. of Applied Mechanics, December, pp 801-805.

145. Tennekes, H. and J.L. Lumley (1972): A First Course in Turbulence, MIT Press.

146. Touloukian, Y.S. (1970): Thermophysical Properties of Matter, IFI/Plenum, New York.

147. van Heiningen, A.R.P., A.S. Mujumdar and W.J.M. Douglas (1976a): On the use of hot and cold-film sensors for skin friction and heat transfer measurements in impingement flows, Letters in Heat and Mass Transfer, Vol. 3, pp 523-528.

148. van Heiningen, A.R.P., A.S. Mujumdar and W.J.M. Douglas (1976b): Numerical prediction of the flow field and impingement heat transfer caused by a laminar slot jet, Trans. of ASME, J. Heat Transfer, Vol. 98, No. 4, pp 654-658.

149. van Heiningen, A.R.P., A.S. Mujumdar and W.J.M. Douglas (1976c): Comment on "Numerical solution of the three-dimensional Navier-Stokes equations with applications to channel flows and a buoyant jet in a crossflow", J. of Applied Mechanics, Vol. 43, Series E, No. 2, Trans. of ASME, Vol. 98, pp 379-380.

150. van Heiningen, A.R.P., A.S. Mujumdar and W.J.M. Douglas (1977): Flow and heat transfer characteristics of turbulent slot jet impinging on a moving wall, Turbulent Shear Flow Symposium, Penn. State University.

151. Von Rosenberg, D.U. (1969): Methods for the Numerical Solution of Partial Differential Equations, American Elsevier Publishing Company, New York.

152. Wilson, D.J. and R.J. Goldstein (1976): Turbulent wall jets with cylindrical streamwise surface curvature, J. of Fluids Engineering, June, Paper No. 76-FE-0.

153. Wolfshtein, M. (1967): Convective process in turbulent impinging jets, Ph.D. thesis, Imperial College, London.

154. Wolfshtein, M. (1968): Numerical smearing in one-sided difference approximations to the equations of non-viscous flow, Imperial College Report EF/TN/A/3, Mech. Eng. Dept.

155. Yildiz, A. (1964): Zum Wärmeübergang am Kommutabor, Dissertation, T.H. Berlin.

156. Yokobori, S., N. Kasagi and M. Hirata (1977): Characteristic behaviour of turbulence in the stagnation region of a two-dimensional submerged jet impinging normally on a flat plate, Symposium on Turbulent Shear Flows, University Park, Pennsylvania, April 18-20, pp 3.17-3.25.

APPENDIX 1

DERIVATION OF THE BOUNDARY CONDITION OF THE VORTICITY AT THE WALL

(a) Integral Method

The derivation of Gosman et al. (49) is followed with the effect of variable density taken into account. Near a wall, gradients in the direction parallel to the wall are much smaller than those in the normal direction so by neglecting them, the stream function equation (2.11) reduces to

$$\frac{d}{dx_2}\left(\frac{1}{\rho}\frac{d\psi}{dx_2}\right) = -\omega \tag{1}$$

Integrating from $x_2 = 0$ to Δx_2

$$\left(\frac{1}{\rho}\frac{d\psi}{dx_2}\right)\Bigg|_{x_2=\Delta x_2} - \left(\frac{1}{\rho}\frac{d\psi}{dx_2}\right)\Bigg|_{x_2=0} = -\int_0^{\Delta x_2} \omega dx_2 \tag{2}$$

For a stationary wall

$$\frac{d\psi}{dx_2}\Bigg|_{x_2=0} - (\rho u_1)\Big|_{x_2=0} = 0 \tag{3}$$

Inserting (3) in (2) and integrating again from $x_2 = 0$ to Δx_2

$$\psi_w - \psi_{nw} = \int_0^{\Delta x_2} \left[\rho \int_0^{\Delta x_2} \omega dx_2 \right] dx_2 \qquad (4)$$

Now ω and ρ are assumed to vary linearly with distance from the wall, so that

$$\omega = \omega_w + \frac{\omega_{nw} - \omega_w}{\Delta x_2} x_2 \qquad (5)$$

and

$$\rho = \rho_w + \frac{\rho_{nw} - \rho_w}{\Delta x_2} x_2 \qquad (6)$$

Insertion of (5) and (6) in (4) and performing the integration gives

$$\psi_w - \psi_{nw} = \omega_w (\Delta x_2)^2 \left(\frac{3}{24} \rho_w + \frac{5}{24} \rho_{nw}\right) + \omega_{nw} (\Delta x_2)^2 \left(\frac{1}{24} \rho_w + \frac{3}{24} \rho_{nw}\right) \qquad (7)$$

or

$$\omega_w = \frac{-3(\psi_{nw} - \psi_w)}{\left(\frac{3}{8} \rho_w + \frac{5}{8} \rho_{nw}\right)(\Delta x_2)^2} - \frac{1}{2} \frac{\left(\frac{1}{4} \rho_w + \frac{3}{4} \rho_{nw}\right)}{\left(\frac{3}{8} \rho_w + \frac{5}{8} \rho_{nw}\right)} \omega_{nw} \qquad (8)$$

After non-dimensionalization equation (2.22) is obtained.

(b) Taylor Series Expansion Method

The derivation of Roache (117) is followed with the effect of variable density taken into account.

The Taylor series expansion of the stream function at the wall gives

$$\psi_{nw} = \psi_w + \left.\frac{\partial \psi}{\partial x_2}\right|_w \Delta x_2 + \frac{1}{2}\left.\frac{\partial^2 \psi}{\partial x_2^2}\right|_w (\Delta x_2)^2 + \frac{1}{6}\left.\frac{\partial^3 \psi}{\partial x_2^3}\right|_w (\Delta x_2)^3 + O\left[(\Delta x_2)^4\right] \tag{9}$$

From the no-slip condition and the definition of the stream function (2.5) it follows that

$$\left.\frac{\partial \psi}{\partial x_2}\right|_w = 0 \tag{10}$$

With an impermeable wall the vorticity at the wall becomes

$$\omega_w = -\left.\frac{\partial u_1}{\partial x_2}\right|_w \tag{11}$$

With the introduction of the stream function equation (11) becomes

$$\left.\frac{\partial^2 \psi}{\partial x_2^2}\right|_w = -\rho_w \omega_w \tag{12}$$

The vorticity gradient at the wall is equal to

$$\left.\frac{\partial \omega}{\partial x_2}\right|_w = -\left.\frac{\partial^2 u_1}{\partial x_2^2}\right|_w \tag{13}$$

With the introduction of the stream function equation (13) becomes

$$\left.\frac{\partial \omega}{\partial x_2}\right|_w = -\frac{1}{\rho_w}\left.\frac{\partial^3 \psi}{\partial x_2^3}\right|_w - \frac{2}{\rho_w}\left.\left(\frac{\partial \rho}{\partial x_2}\right)\right|_w \cdot \omega_w \tag{14}$$

or $$\left.\frac{\partial^3 \psi}{\partial x_2^3}\right|_w = -2\left.\frac{\partial \rho}{\partial x_2}\right|_w \omega_w - \rho_w \left.\frac{\partial \omega}{\partial x_2}\right|_w \tag{15}$$

Assuming a linear variation of ρ and ω near the wall gives

$$\left.\frac{\partial \rho}{\partial x_2}\right|_w = \frac{\rho_{nw} - \rho_w}{\Delta x_2} \tag{16}$$

and $$\left.\frac{\partial \omega}{\partial x_2}\right|_w = \frac{\omega_{nw} - \omega_w}{\Delta x_2} \tag{17}$$

Introduction of equations (10), (12), (15), (16) and (17) in equation (9) gives

$$\psi_{nw} - \psi_w = -\frac{1}{3}\rho_{nw}\omega_w(\Delta x_2)^2 - \frac{1}{6}\rho_w\omega_{nw}(\Delta x_2)^2 \tag{18}$$

or $$\omega_w = -\frac{3(\psi_{nw} - \psi_w)}{\rho_{nw}(\Delta x_2)^2} - \frac{1}{2}\frac{\rho_w}{\rho_{nw}}\omega_{nw} \tag{19}$$

APPENDIX 2

CONVECTION AND DIFFUSION TERMS IN FINITE DIFFERENCE EQUATION (2.28)

Convection Terms

$$AE_\phi = \frac{1}{2} a^*_\phi (\psi^*_S + \psi^*_{SE} - \psi^*_N - \psi^*_{NE}) / ((X^*_{2N} - X^*_{2S})(X^*_{1E} - X^*_{1W}))$$

$$AW_\phi = \frac{1}{2} a^*_\phi (\psi^*_N + \psi^*_{NW} - \psi^*_S - \psi^*_{SW}) / ((X^*_{2N} - X^*_{2S})(X^*_{1E} - X^*_{1W}))$$

$$AN_\phi = \frac{1}{2} a^*_\phi (\psi^*_E + \psi^*_{NE} - \psi^*_W - \psi^*_{NW}) / ((X^*_{2N} - X^*_{2S})(X^*_{1E} - X^*_{1W}))$$

$$AS_\phi = \frac{1}{2} a^*_\phi (\psi^*_W + \psi^*_{SW} - \psi^*_E - \psi^*_{SE}) / ((X^*_{2N} - X^*_{2S})(X^*_{1E} - X^*_{1W}))$$

Diffusion Terms

$$BE_\phi = (b^*_{\phi E} + b^*_{\phi P}) / ((X^*_{1E} - X^*_{1P})(X^*_{1E} - X^*_{1W}))$$

$$BW_\phi = (b^*_{\phi W} + b^*_{\phi P}) / ((X^*_{1P} - X^*_{1W})(X^*_{1E} - X^*_{1W}))$$

$$BN_\phi = (b^*_{\phi N} + b^*_{\phi P}) / ((X^*_{2N} - X^*_{2P})(X^*_{2N} - X^*_{2S}))$$

$$BS_\phi = (b^*_{\phi S} + b^*_{\phi P}) / ((X^*_{2P} - X^*_{2S})(X^*_{2N} - X^*_{2S}))$$

With elongated grid cells near the wall and negligible variation in physical properties, equation (2.28) for the vor-